

Geotechnical, Geological and Earthquake Engineering

Gian Paolo Cimellaro
Sebastiano Marasco

Introduction to Dynamics of Structures and Earthquake Engineering

EXTRAS ONLINE



Springer

Geotechnical, Geological and Earthquake Engineering

Volume 45

Series Editor

Atilla Ansal, School of Engineering, Özyeğin University, Istanbul, Turkey

Editorial Advisory Board

Julian Bommer, Imperial College London, U.K.

Jonathan D. Bray, University of California, Berkeley, U.S.A.

Kyriazis Pitilakis, Aristotle University of Thessaloniki, Greece

Susumu Yasuda, Tokyo Denki University, Japan

More information about this series at <http://www.springer.com/series/6011>

Gian Paolo Cimellaro • Sebastiano Marasco

Introduction to Dynamics of Structures and Earthquake Engineering



Springer

المنارة للاستشارات

EXTRAS ONLINE

Gian Paolo Cimellaro
Department of Structural, Geotechnical
and Building Engineering (DISEG)
Politecnico di Torino
Torino, Italy

Sebastiano Marasco
Department of Structural, Geotechnical
and Building Engineering (DISEG)
Politecnico di Torino
Torino, Italy

Additional material to this book can be downloaded from <http://extras.springer.com>.

ISSN 1573-6059 ISSN 1872-4671 (electronic)
Geotechnical, Geological and Earthquake Engineering
ISBN 978-3-319-72540-6 ISBN 978-3-319-72541-3 (eBook)
<https://doi.org/10.1007/978-3-319-72541-3>

Library of Congress Control Number: 2017963746

© Springer International Publishing AG 2018

This work is subject to copyright. All rights are reserved by the Publisher, whether the whole or part of the material is concerned, specifically the rights of translation, reprinting, reuse of illustrations, recitation, broadcasting, reproduction on microfilms or in any other physical way, and transmission or information storage and retrieval, electronic adaptation, computer software, or by similar or dissimilar methodology now known or hereafter developed.

The use of general descriptive names, registered names, trademarks, service marks, etc. in this publication does not imply, even in the absence of a specific statement, that such names are exempt from the relevant protective laws and regulations and therefore free for general use.

The publisher, the authors and the editors are safe to assume that the advice and information in this book are believed to be true and accurate at the date of publication. Neither the publisher nor the authors or the editors give a warranty, express or implied, with respect to the material contained herein or for any errors or omissions that may have been made. The publisher remains neutral with regard to jurisdictional claims in published maps and institutional affiliations.

Printed on acid-free paper

This Springer imprint is published by the registered company Springer International Publishing AG part of Springer Nature.

The registered company address is: Gewerbestrasse 11, 6330 Cham, Switzerland

*I would like to dedicate this book to my
grandfather, master of life and culture.*

Foreword

It is a great pleasure to present *Introduction to Dynamics of Structures and Earthquake Engineering* by Gian Paolo Cimellaro and Sebastiano Marasco. The book locates itself between elementary books and books for advanced graduate studies. The book is divided into three parts: “Part I – Dynamics of Structures” introduces the main concepts of dynamics of structures. “Part II – Introduction to Earthquake Engineering” introduces the basic concepts of seismology, seismic hazard analysis, and different analysis methods. “Part III – Seismic Design of Buildings” describes how to model structures in seismic zones and the basic concepts of capacity design as well as new innovative techniques for the design of new and retrofit of existing buildings. The typical coverage of “Dynamics of Structures” starts properly with an introduction of the fundamental concepts of structural dynamics, with emphasis on the application of energy methods, analysis on the frequency domain, and signal processing, which are essentials necessary for the study of earthquake engineering. Part II introduces the main concepts of seismology, and probabilistic seismic hazard analysis, and provides a chapter dedicated to earthquake prediction methods. Part III introduces the basic concepts of capacity design within the context of Italian seismic design standards and highlights new and innovative techniques to improve structural performance, such as base isolation, tuned mass dampers, and supplemental viscous dampers. An entire chapter is also dedicated to the modeling of infill walls and the seismic behavior of masonry structures. The book presents also illustrative examples that help in understanding the subject and the link between theory and finite element programs, such as SAP2000. The information presented in this book can be used not only by students but also by those engineers engaged in the seismic design and retrofit of buildings who want to improve their understanding on the subject.

Berkeley, USA
September 2017

Prof. Stephen Mahin

Preface

The aim of this new book is to provide an elementary, but comprehensive, textbook which can be adopted for the courses of earthquake engineering at both the School of Engineering and the School of Architecture of the Politecnico di Torino, providing in an easy and accessible way the latest updates in the field. No previous knowledge of structural dynamics is assumed, making this book suitable for the reader that is learning the subject for the first time. However, the following background is required:

- *Static analysis of structures including statistically indeterminate structures and matrix formulation*
- *Rigid body dynamics*
- *Mathematics: linear algebra and ordinary and partial differential equation*

With respect to other classical books on dynamics of structures, this book emphasizes the application of energy methods and the analysis in the frequency domain with the corresponding visualization in the Gauss-Argant plan. Emphasis is also given to the applications of numerical methods for the solution of the equation of motion and to the ground motion selection to be used in time history analysis of structures which are more frequently used in current practice due to the increasing computational power of computers in the last decade.

The book is organized in three main parts:

- I. “*Dynamics of Structures*”
- II. “*Introduction to Earthquake Engineering*”
- III. “*Seismic Design of Buildings*”

Part I introduces the main concepts of dynamics of structures. Part II introduces the basic concepts of seismology, the seismic hazard analysis, and the different analysis methods. Part III describes how to model structures in a seismic zone and the basic concepts of capacity design (Chap. 15) as well as the new innovative techniques for the retrofit of new and existing buildings, such as passive energy dissipating systems (Chap. 17), tuned mass dampers (Chap. 18), and base isolation (Chap. 19). Chapter 20 focuses on the seismic behavior of masonry structures,

while Chap. 21 provides a brief introduction to a structural analysis program called SAP2000. An appendix has also been included with some basic concepts of probability.

Several figures have been carefully designed and executed to be pedagogically effective. Many of them involve the use of computer simulations. Most of the references have been omitted in the book to avoid distracting the reader; however, a selected list of publications has been added at the end of each book chapter for further reading.

Torino, Italy
July, 2017

Gian Paolo Cimellaro

Acknowledgments

This book has been written during a year of sabbatical leave that I spent at the University of California, Berkeley. It is the result of the research experience with my students and of the years that I have taught in the course of seismic engineering at the Politecnico di Torino. I am grateful to several present and former students who helped in the revision of the book such as my current Ph.D. student, Sebastiano Marasco, who is the coauthor of this book and is one of the developers of the computer software OpenSignal which is included in the book. He has also generated most of the numerical results which appear in the figures. Bridget Bassi, a student from MIT who was a visiting scholar at the Politecnico di Torino, helped with the revision of the English language of the script. Students Alessandro Cardoni, Ali Zamani Noori, Omar Kammouh, Glen Dervishaj, Erfan Sheikhi, Gerardo Leo, Marzia Bianco, Tommaso Romanazzi, Chiara Lesbo, and Sumaia Shek Yussuf Abdirashid assisted in editing and preparing the LaTeX document of the book.

I also wish to express my deepest appreciation to Prof. Andrei M. Reinhorn, Prof. T.T. Soong, and Prof. Steve Mahin for the influence they have had and still have on my professional growth.

We did our best to avoid any errors or misprints in this first edition of the book. Nevertheless, we would like to invite instructors, students, and professional engineers to contact me (gianpaolo.cimellaro@polito.it) if you identified any errors or if you have suggestions for improvements or need clarifications.

Gian Paolo Cimellaro

Contents

Part I Dynamics of Structures

1	Introduction	3
1.1	Idealization of the Structures	3
1.2	Degrees of Freedom	4
1.3	Stiffness	7
1.4	Mass	9
1.5	Damping	10
1.6	Equations of Motion	13
1.6.1	Free Vibrations	15
1.6.2	External Excitations	16
	References	16
2	SDOF Systems	17
2.1	Linear SDOF Systems	17
2.1.1	Free Vibrations	17
2.2	Response to Harmonic Excitations	28
2.2.1	Undamped Systems	28
2.2.2	Viscously Damped Systems	32
2.3	Response to an Impulsive Excitation	44
2.4	Response to a Periodic Excitation	49
2.5	Earthquake Response	50
2.6	Transmissibility Function	51
2.7	Nonlinear System Response	54
	References	55
3	Methods of Solution of the Equation of Motion	57
3.1	Analytical Methods	57
3.2	Duhamel's Integral	63
3.3	Fourier Series	65

3.4	Numerical Methods	68
3.4.1	Explicit Methods	70
3.4.2	Implicit Methods	75
3.4.3	Comparison Between the Different Numerical Methods	78
3.4.4	Numerical Methods for Nonlinear Problems	81
	References	94
4	MDOF Systems	95
4.1	Discretization	95
4.2	Shear Type and Bending Type Frames	96
4.3	Mass, Stiffness and Damping Matrix	96
4.3.1	Bending Type Frames	99
4.3.2	Shear Type Frames	104
4.4	Reduction of DOFs	107
4.5	Modal Analysis	109
4.5.1	Vibrational Modes Response	115
4.5.2	Modal Expansion of Displacements	116
4.5.3	Energetic Considerations	118
4.6	Free Vibrations	118
4.6.1	Undamped Systems	118
4.6.2	Damped Systems	126
4.7	Response to Harmonic Excitation	131
4.7.1	Undamped Systems	131
4.7.2	Viscously Damped Systems	139
4.8	Earthquake Response	142
4.8.1	Numerical Example	146
4.9	3D MDOF Multistory Buildings	150
	References	160
5	Energy Dissipation	161
5.1	Energy Balance Equation	161
5.2	Damping Energy	163
5.2.1	Logarithmic Decrement Analysis (LDA)	164
5.2.2	Half-Power Method (HPM)	166
5.3	Plastic Energy	166
	References	172
6	Distributed Mass and Elasticity Systems	173
6.1	Introduction	173
6.2	Vibrational Modes Analysis	174
6.3	Vibrational Modes Analysis of Forced Systems	177
	References	178

7	Generalized SDOF Systems	179
7.1	Lagrangian Approach	179
7.2	Approximated Solution	181
7.2.1	Example 1: System with Distributed Mass and Elasticity	182
7.2.2	Example 2: System with Distributed Elasticity and Lumped Mass	186
7.2.3	Example 3: General Systems	188
	References	190

Part II Introduction to Earthquake Engineering

8	Seismology and Earthquakes	193
8.1	Basic Concepts of Seismology	193
8.1.1	Earthquake Genesis	193
8.1.2	Seismological Parameters	201
8.1.3	Waves Propagation	209
8.1.4	Attenuation Relationship	214
8.2	Ground Motion Parameters	216
8.2.1	Peak Parameters	216
8.2.2	Frequency and Energetic Content	216
8.2.3	Duration	226
8.2.4	Other Parameters	227
	References	228
9	Major Seismic Events That Occurred in Italy and in the World	229
9.1	Introduction	229
9.2	Earthquakes Occurred in Italy in the Past 150 Years	230
9.3	Earthquakes Occurred in the World from 1960 to the Present Day	240
	References	249
10	Seismic Hazard Analysis	251
10.1	Introduction	251
10.2	Deterministic Seismic Hazard Analysis (DSHA)	252
10.3	Probabilistic Seismic Hazard Analysis (PSHA)	256
	References	261
11	Earthquake Prediction	263
11.1	Introduction	263
11.2	General Aspects	264
11.3	Prediction Methods	265
11.3.1	Animal Behavior	265
11.3.2	Changes in VP/VS	266
11.3.3	Radon Emission	267
11.3.4	Electromagnetic Variations	268
11.3.5	Precursory Seismicity Patterns	269

11.4	Earthquake Prediction and Time-Dependent Seismic Hazard Scenarios	269
11.4.1	Algorithms for Intermediate-Term Middle Range Earthquake Prediction	270
11.4.2	Neo-Deterministic Time-Dependent Seismic Hazard Scenarios for the Italian Territory	271
11.5	Notable Predictions	273
11.5.1	Haicheng (China, 1975)	273
11.5.2	Parkfield (USA, 1985–1993)	274
11.5.3	Loma Prieta (USA, 1989)	277
11.5.4	L'Aquila (Italy, 2009)	278
	References	279
12	Seismic Input	281
12.1	Introduction	281
12.2	Brief History of Italian Seismic Standards	282
12.3	Elastic Response Spectra	283
12.4	Uniform Hazard Spectrum (UHS)	285
12.5	Design Response Spectrum (DS)	288
12.5.1	Design Response Spectrum According to NTC08 and EC8	288
12.5.2	Conditional Mean Spectrum (CMS)	296
12.6	Use of Acceleration Time Histories	298
12.6.1	Ground Motion Selection and Modification	299
12.6.2	Available Databases for Signal Processing and Ground Motion Selection	304
	References	306
13	Opensignal	309
13.1	Introduction	309
13.2	State of Art	310
13.3	Structure of the Software	311
13.4	Strong Motion Databases	311
13.5	Signal Processing and Filtering	312
13.5.1	Response Spectra Analysis	313
13.6	Seismic Records Selection	315
13.6.1	Real Time History Selection	315
13.6.2	Artificial Time-History Selection	317
13.6.3	Synthetic Time-History Selection	317
13.7	Approximated Site Response Analysis	320
13.8	Case Study	323
	References	329
14	Methods of Analysis	331
14.1	Introduction	331
14.2	Linear Static Analysis	334

14.3	Linear Dynamic Analysis	336
14.4	Nonlinear Static Analysis: Pushover	337
14.4.1	Capacity Spectrum Analysis Method	343
14.4.2	N2 Method	345
14.5	Direct Displacement-Based Seismic Design Procedure	347
14.6	Nonlinear Dynamic Analysis	350
	References	351
Part III Seismic Design of Buildings		
15	Capacity Design	355
15.1	Introduction	355
15.2	Capacity Design of a Multi-story Building	356
15.3	Design Approach by Codes	359
15.3.1	Design of Beams for Bending	360
15.3.2	Design of Beams for Shear	360
15.3.3	Design of Columns in Bending	360
15.3.4	Design of Columns in Shear	362
15.3.5	Beam-Column Joint	363
	References	366
16	Seismic Modeling of Infill Walls	369
16.1	Introduction	369
16.2	Influential Parameters	370
16.2.1	Strength of the Masonry Infill	370
16.2.2	Characteristics of the Reinforced Concrete Frame	370
16.2.3	Relative Stiffness	370
16.2.4	Gaps Between Infills and Surrounding Frame	371
16.2.5	Openings	371
16.3	Mechanisms of Failure	371
16.3.1	Failure Modes of Infills	371
16.3.2	Failure Modes of Surrounding Reinforced Concrete Frames	374
16.4	Existing Analytical Models	377
16.4.1	Stiffness Methods	377
16.4.2	Strength Methods	384
	References	389
17	Passive Energy Dissipating Systems	391
17.1	Introduction	391
17.2	Energy Balance Equation	392
17.3	Types of Passive Energy Dissipating System	394
17.3.1	Displacement-Activated Dampers	395
17.3.2	Viscous and Viscoelastic Dampers	407
17.4	Mechanical Model of Dampers	411
17.5	Characteristics of the Braces	412

17.6	Seismic Behavior of a Passive Brace	413
17.7	Seismic Design of Damping Systems	414
17.8	Geometric Amplification of Dampers	417
	References	418
18	Tuned-Mass Dampers	421
18.1	Introduction	421
18.2	Undamped TMD Under Harmonic Loading	421
18.3	Undamped TMD Under Harmonic Base Motion	424
18.4	Damped TMD Under Harmonic Loading	427
18.5	Active TMD	431
18.6	Analysis of a MDOF Structure Equipped with TMD	433
18.7	Design Considerations	435
18.8	Application of TMD	435
18.9	Application of ATMD	436
	References	438
19	Base Isolation	439
19.1	Introduction	439
19.2	History	441
	19.2.1 First Base Isolation System	443
19.3	Equation of Motion of a Base Isolated Building	443
19.4	Characteristics of Base Isolation System	452
19.5	Seismic Isolation Systems	453
	19.5.1 Low-Damping Natural or Synthetic Rubber Bearings	454
	19.5.2 High-Damping Rubber Bearings (HDRBs)	454
	19.5.3 Lead Rubber Bearings	460
	19.5.4 Friction Pendulum System (FPS)	461
	19.5.5 Spring-Type System	463
19.6	Limitations of a Base Isolation System	464
19.7	Installation Methodology for New and Existing Buildings	464
	19.7.1 Retrofit Construction Sequence for Existing Buildings	464
	19.7.2 Retrofit Construction Costs for New Buildings	467
	19.7.3 Mid-Story Base Isolation	468
19.8	Simplified Methodology to Design a Seismically Isolated Building with Rubber Bearings	471
	References	473
20	Masonry Structures	475
20.1	Introduction	475
20.2	Types of Masonry	476
20.3	Collapse Mechanisms of Masonry Buildings	480
	20.3.1 In-Plane Failure Mechanisms of a Single-Story Masonry Building	484

20.3.2	In-Plane Failure Mechanisms of a Multi-story Masonry Building	489
20.3.3	Out-of-Plane Failure Mechanisms of a Single-Story Masonry Building	491
20.3.4	Out-of-Plane Failure Mechanisms of a Multi-story Masonry building	504
20.4	Applications of Kinematic Equilibrium Method	508
20.4.1	Example 1: Simple Overturning	508
20.4.2	Example 2: Design of a Reinforcing Tie System	509
20.5	Retrofit Interventions	511
20.5.1	Traditional Retrofit Interventions	511
20.5.2	Modern Retrofit Interventions	511
20.5.3	Classification of Interventions	513
	References	531
21	Modeling of Structures in Seismic Zone	533
21.1	Introduction	533
21.2	Structural Analysis	533
21.2.1	Structural Idealization	534
21.2.2	Materials	534
21.2.3	Load Analysis	535
21.2.4	Solution of the Problem Through a Given Method of Analysis	535
21.2.5	Safety Assessment	536
21.3	Brief Introduction to SAP2000	536
21.3.1	Files Type	536
21.3.2	Coordinate System	537
21.3.3	Elements	537
21.3.4	Materials and Sections	538
21.3.5	Loads	538
21.3.6	Restraints and Constraints	540
21.4	SAP2000 Case Study	541
21.4.1	Model Definition	543
21.4.2	Materials Definition	547
21.4.3	Sections Definition	548
21.4.4	Vertical Load Definition	549
21.4.5	Seismic Action	550
21.5	Seismic Retrofitting	565
21.5.1	Seismic Isolated Structures	566
21.5.2	Shear Walls	570
21.5.3	Effects of the External Walls	577
21.6	Comparisons of the Structural Models	579
	References	582

A	Fundamentals of Probability and Statistics	585
A.1	Important Definitions	585
A.2	The Venn Diagram	585
A.3	Mathematics of Probability	585
A.4	Conditional Probability	586
A.5	The Theorem of Total Probability	587
A.6	Probability Distribution of a Random Variable	588
A.7	Useful Probability Distributions	589
A.8	Multiple Random Variables	590
A.9	The Conditional and Marginal Distributions.....	591
	Glossary	593
	Index	595

Acronyms

ABV	Assembly-based vulnerability
ASD	Allowable stress design method
CCF	Cross correlation function
CDF	Cumulative distribution function
CM	Center of mass
CMS	Conditional mean spectrum
CLS	Collapse prevention limit state
CSM	Capacity Spectrum Method
CQC	Complete Quadratic Combination
DBE	Design basis earthquake
DFT	Discrete Fourier transform
DOF	Degree of freedom
DRR	Disaster risk reduction
DS	Design spectrum
DSHA	Deterministic seismic hazard analysis
DV	Decision variable
EC	Eurocode
EDP	Engineering Demand Parameter
ESMD	European Strong Motion Database
FEA	Finite element analysis
FEMA	Federal Emergency Management Agency
FFT	Fast Fourier transform
GIS	Geographic information system
GMPE	Ground motion prediction equation
GMSM	Ground motion selection and modification
HPM	Half-power method
ICEF	International Commission on Earthquake Forecasting for Civil Protection
INGV	Italian National Institute of Geophysics and Volcanology

IM	Intensity measure
IR	ICEF Report
ITACA	Italian Accelerometric Archive
LDA	Logarithmic decrement analysis
LSD	Limit state design
MAE	Mid-America Earthquake Center
MCE	Maximum capable earthquake
MCEER	Multidisciplinary Earthquake Engineering to Extreme Events Center
MCS	Mercalli-Cancani-Sieberg
MDOF	Multi-degree-of-freedom
MMI	Modified Mercalli Intensity
NDP	Nonlinear dynamic procedures
NIBS	National Institute of Building Sciences
NIST	National Institute of Standards and Technology
NOAA	National Oceanic and Atmospheric Administration
NPS	Nuclear power station
NYCDOT	New York City Department of Transportation
NYPD	New York City Police Department
OCIPEP	Office of Critical Infrastructure Preparedness and Emergency Preparedness
OLS	Operational limit state
PACT	Performance Assessment Calculation Tool
PBEE	Performance-based earthquake engineering
PBSE	Performance-based seismic engineering
PDF	Probability density function
PEER	Pacific Earthquake Engineering Research Center
PGA	Peak ground acceleration
PGD	Peak ground displacement
PGV	Peak ground velocity
PL	Performance levels
PRA	Probabilistic risk analysis
PSA	Maximum pseudo spectral acceleration
PSHA	Probabilistic seismic hazard analysis
PSSRA	Probabilistic seismic structural response analysis
RBD	Resilience-based design
RHA	Response history analysis
RPL	Resilience performance levels
RSA	Response spectrum analysis
Sa	Spectral acceleration
SDOF	Single-degree-of-freedom
SLS	Serviceability limit state
SRA	Seismic risk analysis
SRSS	Square root of the sum of the square

T	Period (s)
TF	Transmissibility function
UDS	User-defined spectrum
UHS	Uniform hazard spectrum
ULS	Ultimate limit state
UNISDR	The United Nations International Strategy for Disaster Risk Reduction
USGS	United States Geological Survey

Part I
Dynamics of Structures

Chapter 1

Introduction



Abstract This chapter formulates the structural dynamics problem for structures that can be idealized as systems with a massless supporting element, a lumped mass and an equivalent viscous damping element. The equations of motion are formulated for a single-degree-of-freedom system.

1.1 Idealization of the Structures

Dynamic analysis of structures is used to evaluate the behavior of systems subjected to vibrations. Such systems in civil engineering are usually complex structures that can be simplified and idealized as discrete models.

The main goal of dynamics of structures is to determine the stress and strain levels caused by vibrations employing the extended methods of static analysis.

As shown in Sect. 1.3, an immediate advantage of using discrete models is that the system equations become ordinary differential equations.

Figure 1.1 illustrates a typical example of structural idealization to perform dynamic analysis.

From the actual configuration of the structure, the total mass m can be assumed concentrated at the top (lumped mass) while the lateral displacement u is controlled by the vertical element by means of its stiffness k . In any case, the idealization of the structure can be suggested by its simple geometry. According to this consideration, the multi-story buildings can be idealized in a 2D frame where the mass is concentrated at the roof level and the elastic inextensible massless elements provide stiffness to the system. Furthermore, the dissipative capacity of the structure is modeled using a viscous damper (dashpot) element for each elementary frame (Fig. 1.2).

Each structural member of the model contributes to inertial (mass), elastic (stiffness) and energy dissipation (viscous damping) properties of the structure. Each of these terms is separated from one another, and the sum of them all gives information about the dynamic response of the structure (Friswell and Mottershead 2013).

Fig. 1.1 Idealization of a tank with thin column

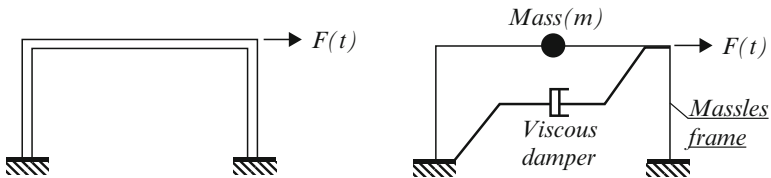
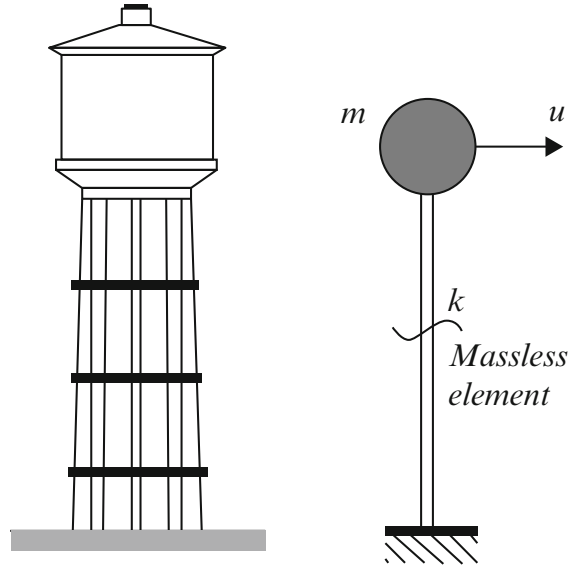


Fig. 1.2 Idealization of one-story frame

1.2 Degrees of Freedom

In classical mechanics, the number of independent parameters that define the configuration of a system is referred to as the degrees of freedom (DOFs). In dynamic analysis, this value represents the number of independent displacements required to define the displaced positions of all the masses relative to their original position. Naturally, the DOFs depend on the body stiffness distribution and on the reference system in which the body is described. Figure 1.3 shows an example of DOFs definition for a rigid 3D body with diffused mass.

In the dynamic analyses, the idealization of the structures can lead to a simplification of the problem. Considering the generic elastic frame illustrated in Fig. 1.4 subjected to a lateral force, with mass applied in the middle of the beam and with rigid columns, only the lateral displacement is permitted. This type of idealized structure is called Single Degree Of Freedom (SDOF) since it has only one DOF (Humar 2012).

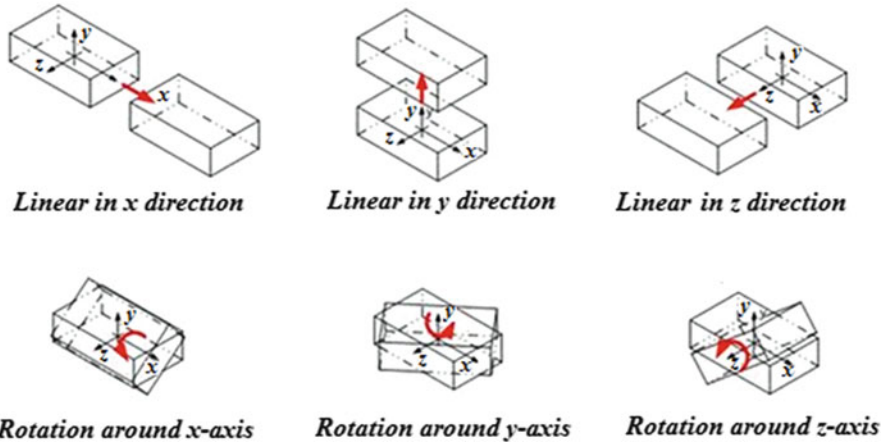


Fig. 1.3 Degrees of freedom of a 3D rigid element

Fig. 1.4 Idealized one-story buildings for dynamic analysis

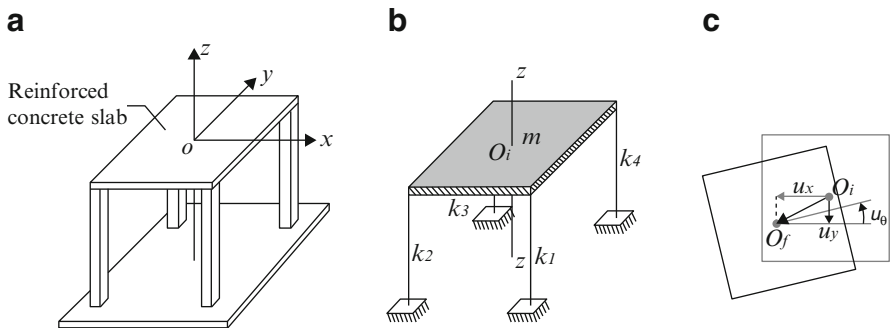
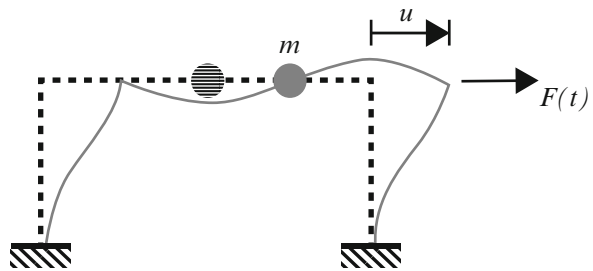


Fig. 1.5 3D structure (a) and its idealization (b). Identification of DOFs of the structures (c)

This represents the typical flexural system considered in the structural analyses of frames (bending type frame). The following example (Fig. 1.5) shows a practical case of DOFs identification in a 3D structure.



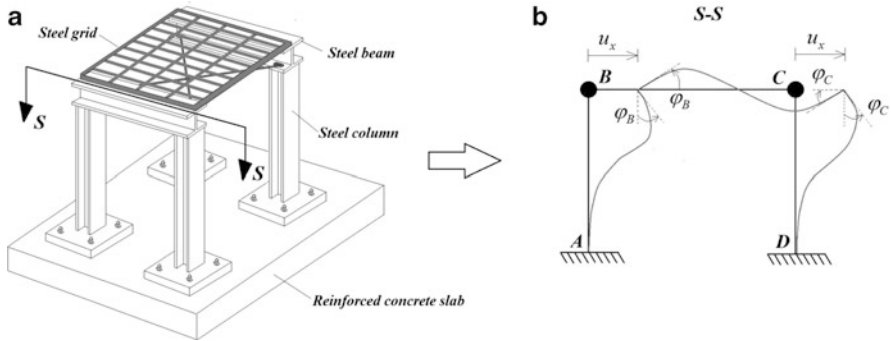


Fig. 1.6 3D view of a one story steel frame (a) and its 2D idealization for section S-S (b)

Each column can be assumed to be fixed at the basement level, while the mass is assumed concentrated at the roof level. This assumption is always valid for reinforced concrete or steel buildings, since the horizontal deck can be assumed more rigid and heavy than the column system (*shear type frame*).

Considering columns as inextensible elastic elements, the structure has three DOFs, which are the following:

- linear shifting in x direction (u_x);
- linear shifting in y direction (u_y);
- rotation around z-axis (ϑ_z);

Figure 1.6 shows a 3D one story steel frame composed of a double “T” beam and columns. A steel grid defines the roof of the system, in which two diagonal elements are inserted to improve the horizontal stiffness. All the elements can be assumed inextensible while the stiffness of the horizontal deck is assumed infinite. In addition, the total mass of the frame is assumed concentrated at the connections between beams and columns.

The static DOFs of the system are identified by the rotation around the nodes B and C and by the linear translation in the x direction. The assumption that the masses are lumped has led to neglect the rotational degrees of freedom, since the inertia associated with the rotation of concentrated mass with respect to its mass center can be assumed equal to zero. This last observation is very important to understand the difference between the DOFs required for static analyses and the ones for the dynamic case. For this reason, only one DOF can be assumed in the dynamic analysis since the rotation DOF is much smaller than the linear DOFs. On the other hand, in the dynamic analysis only the shift in x direction has to be considered (u_x). This example focuses on the reduction of DOFs due to the idealization of lumped mass structure.

1.3 Stiffness

Consider the simple frame shown in Fig. 1.7 subjected to a static external lateral force $F(t)$ causing a displacement u . Assuming that the columns at the top are cut, the sum of the resulting elastic reactions F_s must be equal to the external force (static equilibrium) (Clough and Penzien 1993).

The resisting force F_s depends on the displacement u and on the mechanical behavior of the frame elements. To illustrate this, Fig. 1.8 shows the classical force-displacement relationship for structural materials.

One can notice how the relationship is linear for small value of displacements, while it becomes nonlinear for displacements greater than a given value. The first case is representative of the linear elastic field in which the $F_s - u$ relationship is expressed in Eq. 1.1

$$F_s = k \cdot u \tag{1.1}$$

where k represents the elastic modulus of the material. When the displacement on the structure exceeds the yielding threshold (u_y), the force-displacement

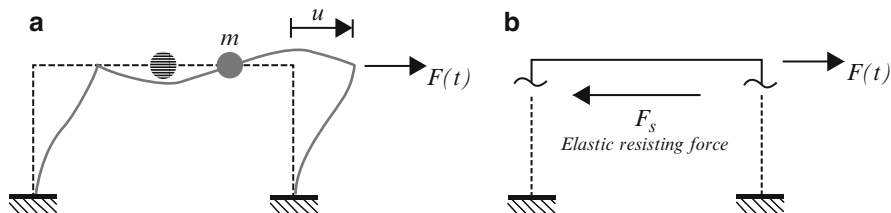


Fig. 1.7 Deformed shape of elastic SDOF system (a) and static equilibrium (b)

Fig. 1.8 Generic force-displacement relationship

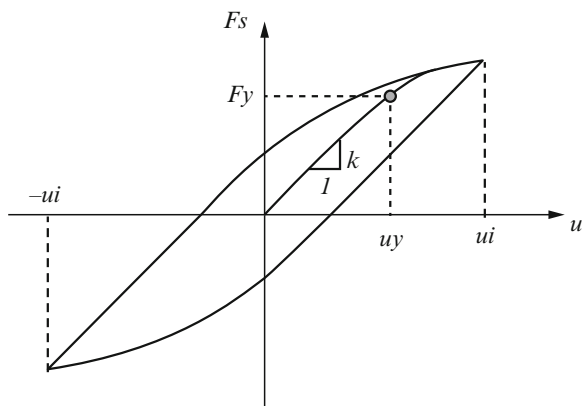
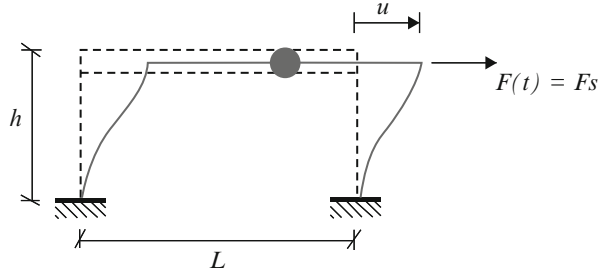


Fig. 1.9 SDOF elastic frame with rigid beam



relationship cannot be described by a linear expression, but it will be evaluated by referring to the real deformations history (Eq. 1.2).

$$F_s = F_s(u, u) \quad (1.2)$$

where u is the deformation gradient. Equation refers to all inelastic behavior of elements, since it is able to describe the hysteretic curve for any given material. The following considerations will be referred to in the linear elastic case only.

The definition of the elastic modulus leads to the definition of the elastic force in terms of displacements. Consider the frame shown in Fig. 1.9, with inextensible columns and rigid beam.

In general, it is clear that the elastic parameter k_{ij} represents the force that should be applied at the location i to produce a unit displacement at location j .

The lateral displacement u represents the unique DOF of the system. In this simple case, the stiffness coefficient k can be expressed as the sum of the elastic coefficients of the two columns (Eq. 1.3)

$$k = \sum_{\text{columns}} \frac{12EI_c}{h^3} = \sum_{i=1}^2 \frac{12(EI_c)_i}{(h^3)_i} = \frac{24EI_c}{h^3} \quad (1.3)$$

where EI_c and EI_b are the flexural stiffnesses of the columns and the beams, respectively, where $EI_b \rightarrow \infty$. The geometric parameters L and h refer to the bay width and height of the frame.

Thus the equilibrium equation can be written as shown in Eq. 1.4.

$$F_s = \frac{24EI_c}{h^3} \cdot u \quad (1.4)$$

It can be observed that the elastic coefficient is expressed as force over length [FL^{-1}]. This unit measurement is valid for linear displacement, while the elastic coefficients associated with the rotational DOFs are expressed as force [F].

1.4 Mass

The inertia of a physical system represents the resistance to motion changes. So, when a stress perturbation F_m is applied to a mass m , an acceleration u will arise according to Newton's second law (Eq. 1.5).

$$F_m = m \cdot u \quad (1.5)$$

The acceleration term is expressed as the second derivative of displacement with respect to time (u). The identification of the mass coefficients for a lumped mass system is easy, since they are equal to the mass values. For a generic system, the mass parameter m_{ij} represents what force should be applied at the location i to produce a unit of acceleration at location j . Figure 1.10 shows the same frame as in Fig. 1.9, but considering the inertial characteristics.

If ρ_l is the linear density of the frame materials, the mass M calculation can be assumed as expressed in Eq. 1.6.

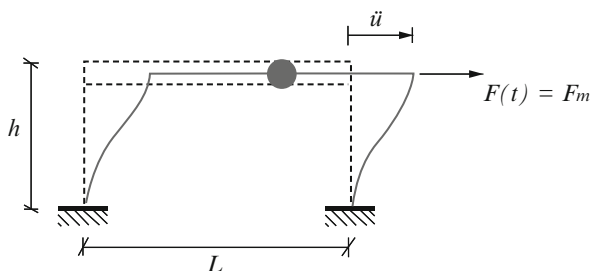
$$M = \rho_l \frac{h}{2} + \rho_l L + \rho_l \frac{h}{2} = \rho_l (h + L) \quad (1.6)$$

Since only one lumped mass is used to describe the inertia properties of the frame, the coefficient m will be equal to M . As observed in Sect. 1.2, assuming the mass is concentrated at the roof level, will lead to neglect the rotational inertia terms associated with the corresponding rotational DOFs. A numerical example is proposed to validate this assumption. Consider a circular mass with very small radius (Fig. 1.11). For this mass, the polar inertia moment (mass coefficient associated with a rotational DOF) is calculated and compared with the total mass that is representative of the linear shifting DOF.

The inertia moment referred to its center O is expressed in Eq. 1.7.

$$I_O = \int_0^R r^2 dm = \rho_A \int_0^R r^2 2\pi \cdot r \cdot dr \quad (1.7)$$

Fig. 1.10 SDOF elastic frame with rigid beam and mass concentrated at roof level



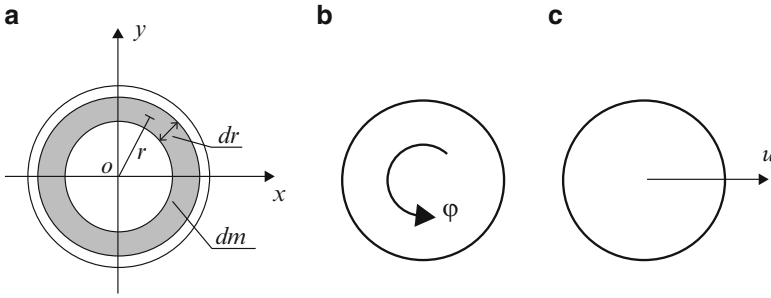


Fig. 1.11 Elementary mass of a circular body (a), rotational DOF (b) and linear shifting DOF (c)

where ρ_A represents the density per unit surface. The total mass of the system can be evaluated as the product of the density and the total area (Eq. 1.8).

$$m = \rho_A \cdot \pi \cdot R^2 \quad (1.8)$$

Since for lumped mass system, the radius R is a small value, one will notice that the coefficient m is much larger than the I_O parameter. Thus, the polar inertia of a concentrated mass can be assumed equal to zero.

1.5 Damping

The vibrational energy is dissipated by various mechanisms, such as the thermal effects caused by the repetition of stress cycles and from the internal friction of a deformed element. In the structural applications, the dissipative mechanisms depend on the materials and on their interactions (friction between structural and nonstructural elements). The mathematical description of dissipated energy in a structure can be very difficult to estimate. In practice, all the dissipative processes that arise on a structure can be idealized with an equivalent viscous damping model. The generic dissipative force-displacement relationship for a structural element is plotted in Fig. 1.12. The dissipative force-displacement curve will enclose an irregular area, referred to as the “hysteresis loop”, that is proportional to the energy lost per cycle (Ikhouane et al 2007). Considering an equivalent regular elliptical area, the energy dissipation W_D can be evaluated as shown in Eq. 1.9.

$$W_D = \int F(t) du = \pi \cdot a \cdot b = f(F_d, u_{max}) \quad (1.9)$$

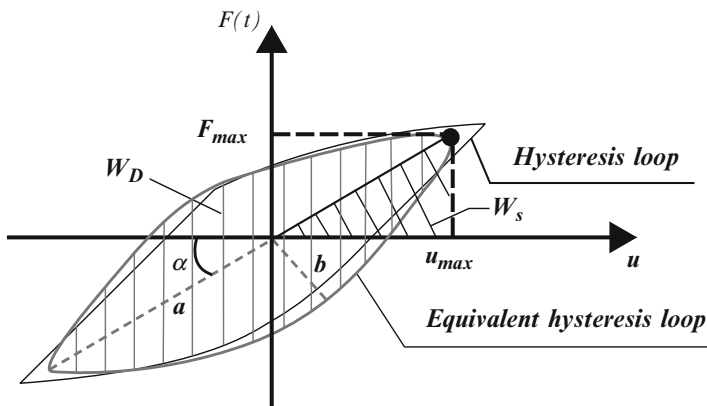


Fig. 1.12 Equivalent hysteresis loop and associated dissipated energy

where a and b represent the semi axis length of the elliptical hysteresis loop, while W_D and W_S are the dissipated energy in a single load-unload cycle and the associated strain energy, respectively. The equivalent damping capacity can be expressed as the ratio between the two aforementioned energy values. It was observed from experimental data that the strain energy depends on the frequency of excitation ω . Considering the resonance conditions (Sect. 2.2.1) the energy dissipated in a vibration cycle of the actual structure and an equivalent viscous system can be supposed equal to the following expression (Eq. 1.10).

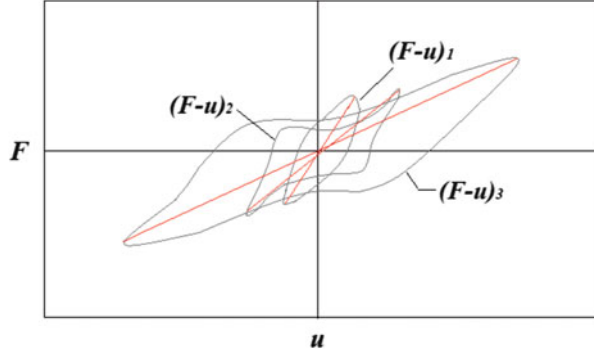
$$4 \cdot \pi \cdot \xi_{eq} \cdot W_S = W_D \quad (1.10)$$

where ξ_{eq} defines the equivalent viscous damping ratio and it can be evaluated from the energy balance as shown in Eq. 1.11.

$$\xi_{eq} = \frac{1}{4\pi} \frac{W_D}{W_S} \quad (1.11)$$

Experiments indicate that the energy dissipated per cycle (and the corresponding force) is independent of frequency and is proportional to the square of the amplitude of vibration (unlike viscous damping in which the energy loss per cycle is proportional to the square of the amplitude and directly proportional to the frequency of motion). This is because damping forces are not viscous in nature, but instead arise from internal friction. In the viscous damping formulation, the dissipated energy is dependent upon the frequency of excitation, since the damping ratio will as a result be defined in reference to the frequency of the dynamic force. It has been observed that the number of the load-unload cycles per units of time controls the

Fig. 1.13 Comparison between three different F - u functions referencing loads with different values of frequency and amplitude



inclination of the elastic part of the hysteretic cycle. On the other hand, the width of the hysteretic loop depends on the amplitude of the dynamic force applied on the system (Fig. 1.13).

Figure 1.13 clearly shows the effects of the load frequency variation. In fact, with the increasing frequency of the dynamic load, the gradient of the equivalent elastic line decreases. Nevertheless, the equivalent damping ratio, evaluated from a dynamic test at exciting frequency equal the resonant frequency (Chap. 7) results a satisfactory approximation.

In the structural applications, the equivalent linear viscous damping approach leads to evaluation of the damping force F_d as a linear relation of the velocity (Eq. 1.12).

$$F_d = c \cdot u \quad (1.12)$$

where c is the viscous damping coefficient and it has units of force per time/length [FTL^{-1}]. One will notice that the generic coefficient c_{ij} represents the damping force that should be applied at the location i to produce a unit velocity at location j . This coefficient is strongly related to the equivalent viscous damping by means of the expression reported in Eq. 1.13.

$$c = \xi \cdot 2 \cdot \omega \cdot m \quad (1.13)$$

The viscous damping coefficient is directly proportional to the equivalent viscous damping ratio and to the vibrational frequency of the system. This characteristic will be discussed in detail in the next paragraph.

Figure 1.14 illustrates the dashpot model and the damping force in a SDOF frame.

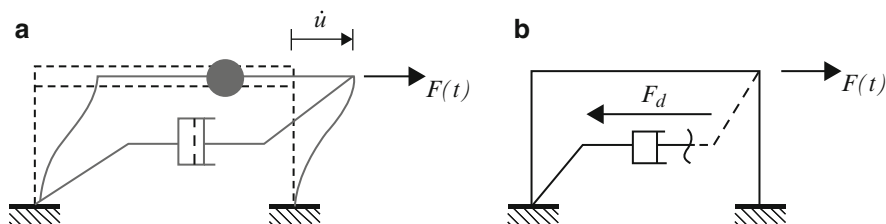


Fig. 1.14 Dashpot model (a) and damping resisting force for a SDOF frame (b)

1.6 Equations of Motion

The equations of motion are the mathematical expressions of the dynamic equilibrium of a physical system (Hertz 1894). They can be derived from Newton's second law or from D'Alembert principle. Considering the system response at a given time t_i , the applied load $F(t_i)$ generates the elastic force $F_s(t_i)$ and the damping force $F_d(t_i)$ in the opposite direction. From Newton's second law, the algebraic sum of these three forces should balance the inertial force, proportional to the mass system (Eq. 1.14).

$$F(t_i) - F_s(t_i) - F_d(t_i) = m \cdot u \quad (1.14)$$

The same result can be obtained using D'Alembert principle based on the dynamic equilibrium at a given time t_i (d'Alembert 1743). In any time instant, a dynamic system can be evaluated as an equilibrated system if a fictitious inertia force (proportional to the mass system) is applied in the opposite direction of the dynamic load $F(t_i)$. Considering the elastic $F_s(t_i)$ and damping $F_d(t_i)$ contribution at a given time t_i , the equation of motion will assume the same expression as the previous one.

By applying the contributions due to stiffness and damping discussed previously, the equations of motion can be modified as shown in Eq. 1.15.

$$m \cdot \ddot{u} + c \cdot \dot{u} + k \cdot u = F(t) \quad (1.15)$$

Equation 1.15 shows that the external applied force in a structural system is equilibrated from three different force contributions schematically outlined in the Fig. 1.15.

The main goal of earthquake engineering is to predict the dynamic response of a structure subjected to a seismic excitation, which can be seen as a ground displacement u_g . The ground shaking will induce a perturbation u on a generic structure rigidly constrained at the base (Fig. 1.16).

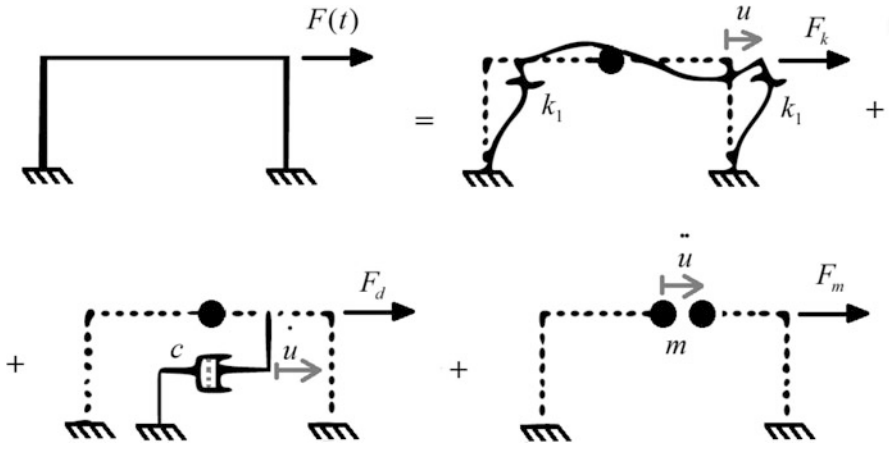


Fig. 1.15 Different contributions to the dynamic equilibrium (Chopra 2001)

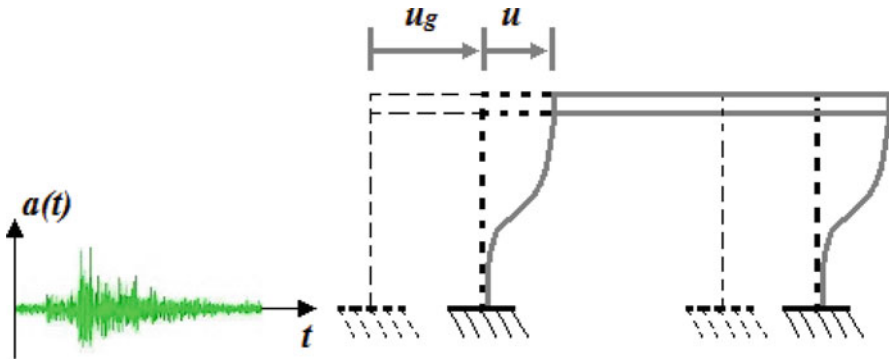


Fig. 1.16 Displacements components induced by the ground shaking

Thus, the absolute displacement U at given time can be expressed as the sum of the two aforementioned parameters (Eq. 1.16).

$$U(t) = u(t) + u_g(t) \tag{1.16}$$

The inertia force is expressed in terms of absolute accelerations, while the elastic and damping actions can be evaluated from the relative displacement and velocity, respectively. Thus, the equation of motion can be rewritten (Eq. 1.17) in terms of absolute accelerations.

$$m \cdot (u(t) + u_g(t)) + c \cdot \dot{u} + k \cdot u = 0 \rightarrow m \cdot \ddot{u} + c \cdot \dot{u} + k \cdot u = -m \cdot \ddot{u}_g \tag{1.17}$$



where the product between the mass and the ground acceleration represents the seismic excitation on the structure and it is also referred to as effective earthquake force. This result highlights the importance of the earthquake's effects on structures with large mass values.

The equation of motion can be characterized for two different cases, discussed below.

1.6.1 Free Vibrations

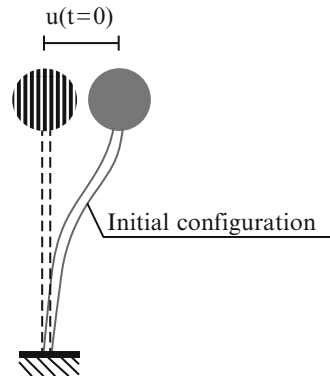
When a physical system is disturbed from its static equilibrium configuration, it will tend to return to its equilibrium position without external excitation. This mechanism is called free vibration and from the dynamic motion, some information about the intrinsic vibrational characteristics of the system can be extrapolated (e.g. natural vibration period). In this case, the external perturbation is defined by variation of the motion parameters. The classic case of free vibration can be observed from a system in which its mass is subjected to a given displacement at time zero $u(t = 0)$ (Fig. 1.17).

The equation of motion can be expressed as illustrated in the Eq. 1.18.

$$m \cdot \ddot{u} + c \cdot \dot{u} + k \cdot u = 0 \quad (1.18)$$

The solution to the problem is obtained by setting up the initial conditions which include the displacement and velocity at time zero.

Fig. 1.17 Perturbed SDOF system at time $t = 0$



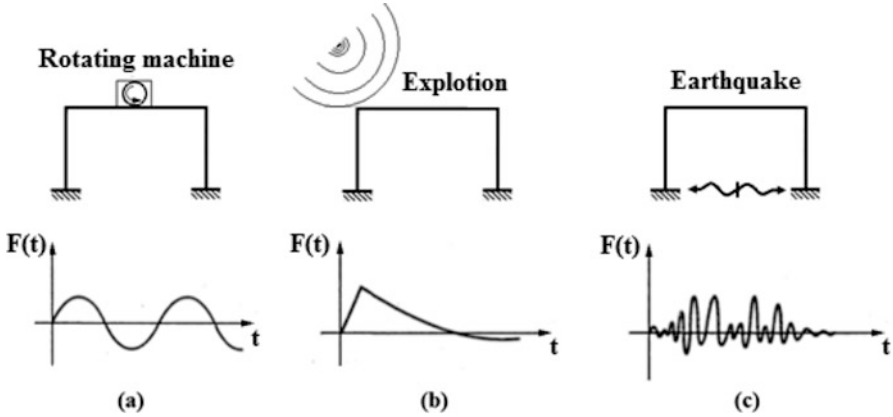


Fig. 1.18 Harmonic excitation (a), impulsive excitation (b) and irregular excitation (c)

1.6.2 External Excitations

If the static equilibrium condition of a system is changed by an external periodic force, the system dynamic response is governed by the natural vibration characteristics and from the external applied force. Thus, the total response of the system can be separated into the permanent response (due to the external force) and temporary response (due to the free vibration). The mathematical solution of the equations of motion depends on the type of the external force applied. It can be considered as impulsive, harmonic or irregular. Figure 1.18 illustrates a comparison between the real situation's dynamic system and the relative periodic force which arises.

References

- Chopra AK (2001) Dynamics of structures: theory and applications to earthquake engineering, 2nd edn. Prentice-Hall, Upper Saddle River
- Clough R, Penzien J (1993) Dynamic of structures. McGraw-Hill, New York
- D'Alembert JLR (1743) *Traité de dynamique*, 1st edn. David, Paris. (Reprint of the second augmented edition (1758) by Gauthier-Villars Publishers, in two volumes, Paris, 1925; also Facsimile reprint by Editions Gabay, Paris, 1998)
- Friswell M, Mottershead JE (2013) Finite element model updating in structural dynamics, vol 38. Springer Science & Business Media
- Hertz H (1894) *Die Prinzipien der Mechanik*, vol 3. JA Barth, Leipzig
- Humar J (2012) Dynamics of structures. Prentice Hall, Englewood Cliffs
- Ikhouane F, Hurtado JE, Rodellar J (2007) Variation of the hysteresis loop with the Bouc–Wen model parameters. *Nonlinear Dyn* 48(4):361–380

Chapter 2

SDOF Systems



Abstract This chapter analyzes linear single-degree-of-freedom systems and their response to harmonic, impulsive and periodic excitations. The response to such excitations is important because it provides insight into how the system will respond to other types of forces. Finally also the response to earthquake records is considered. The chapter ends with some considerations about the nonlinear response.

2.1 Linear SDOF Systems

The dynamic analyses performed in this chapter assume that the inertial contributions (mass) are lumped as a finite number of discrete elements. Such models are defined lumped mass systems, in which all of the mass elements move in the same direction (SDOF systems) (Chopra 2001). The undamped and damped systems will be discussed with reference to the free vibrations case and external force applications case. Damping in structures is assumed according to the linear equivalent viscous damping and its contribution is assumed a discrete element. Some examples of simplified idealization of SDOF systems are shown in Fig. 2.1.

The case (a) represents the simplest idealization of a system, in which every property is assumed as a lumped characteristic (discrete system). This will be the assumed schematization in this chapter for solving the associated equations of motion.

2.1.1 Free Vibrations

A discrete SDOF system subjected to free vibrations is assumed in order to explain the analytical results for undamped and damped systems (Rao 2007).

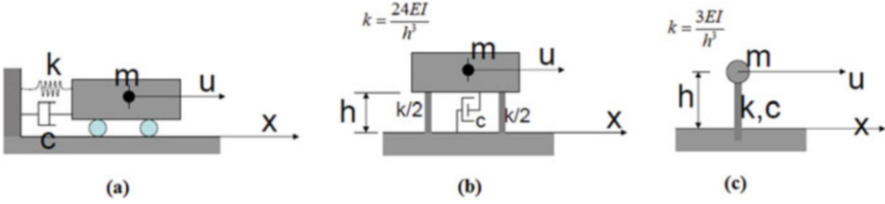
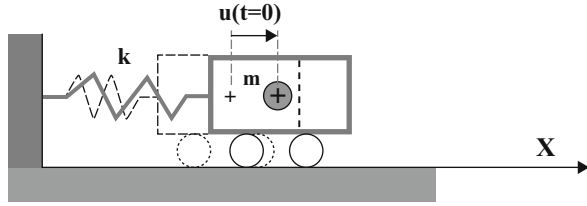


Fig. 2.1 Lumped mass–stiffness–damping system (a), lumped mass–damping system (b), lumped mass system (c)

Fig. 2.2 Discrete undamped SDOF system



2.1.1.1 Elastic Undamped Systems

Figure 2.2 shows the reference system in which a given displacement at time zero has been applied to the lumped mass m .

The equation of motion is reported in Eq. 2.1.

$$m \cdot \ddot{u} + k \cdot u = 0 \tag{2.1}$$

Only the inertia and stiffness contributions are considered. Introducing the term ω , which represents the angular frequency of the system defined as square of the ratio between the stiffness coefficient and the mass ($\omega = \sqrt{k/m}$), the equation of motion can be rewritten as following (Eq. 2.2).

$$\ddot{u} + \omega^2 \cdot u = 0 \tag{2.2}$$

Setting $z = u$, the differential equation can be expressed in the characteristic polynomial form (Eq. 2.3).

$$z^2 + \omega^2 = 0 \rightarrow z_{1,2} = +\sqrt{-\omega^2} = \pm i \cdot \omega \tag{2.3}$$

Since the complex solutions values z_1 and z_2 are different, the generic solution can be expressed in the following exponential form (Eq. 2.4).

$$u(t) = C_1 \cdot e^{i\omega t} + C_2 \cdot e^{-i\omega t} \tag{2.4}$$



Remembering the Eulerian relation reported in Eq. 2.5.

$$e^{\pm i\omega t} = \cos(\omega \cdot t) \pm i \cdot \sin(\omega \cdot t) \tag{2.5}$$

The solution of the equation of motion can be rewritten as illustrated in Eq. 2.6

$$u(t) = A_1 \cdot \sin(\omega \cdot t) + A_2 \cdot \cos(\omega \cdot t) \tag{2.6}$$

in which the constants A_1 and A_2 can be evaluated from the initial conditions of the system. Alternatively, the solution $u(t)$ can be expressed in terms of the amplitude A and phase φ (Eq. 2.7).

$$u(t) = A \cdot \sin(\omega \cdot t + \phi) \tag{2.7}$$

Equation 2.8 illustrates the relationship between the amplitude and the phase.

$$\begin{cases} A = \sqrt{A_1^2 + A_2^2} \\ \phi = \text{tg}^{-1}\left(\frac{A_1}{A_2}\right) \end{cases} \tag{2.8}$$

Assuming the initial conditions given in the Eqs. 2.9,

$$u(0) = u_0; \quad \dot{u}(0) = \dot{u}_0 \tag{2.9}$$

from these conditions, the solution of the equation of motion can be calculated as shown below (Eq. 2.10).

$$u(t) = \frac{\dot{u}_0}{\omega} \cdot \sin(\omega \cdot t) + u_0 \cdot \cos(\omega \cdot t) \tag{2.10}$$

Figure 2.3 illustrates the $u(t) - t$ relationship for the analyzed case and the associated conditions of the system in four different configurations.

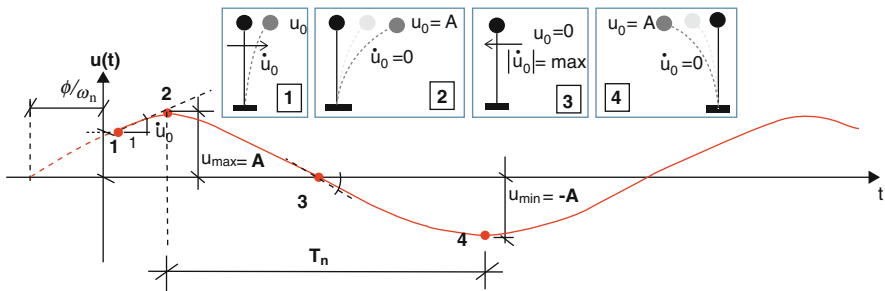


Fig. 2.3 Displacement response of a SDOF undamped system



In particular Fig. 2.3 shows several interesting aspects of the dynamic response of an SDOF undamped system. First, it can be observed that the amplitude of the motion is unchanged ($|A|=const$) over time, since the system was considered without damping. In addition, some dynamic information can be extrapolated from the $u(t)$ - t relationship, such as the natural vibrational period of the system (Eq. 2.11).

$$T_n = \frac{2\pi}{\omega_n} = 2\pi \sqrt{\frac{m}{k}} \quad (2.11)$$

This represents the time required for the undamped system to complete one cycle of free vibration. The inverse of the period defines the natural frequency and is reported in Eq. 2.12.

$$f_n = \frac{\omega_n}{2\pi} = \frac{1}{2\pi} \sqrt{\frac{k}{m}} \quad (2.12)$$

The natural characteristics (represented by the n index) of a generic system are independent from the attenuation phenomena (damping) and are referred to as the free vibration mechanism. It is interesting to express the solution given in Eq. 2.10 in terms of velocity and accelerations, in order to compare all of the trends in the time domain. For this purpose, Eq. 2.13 illustrates the generic mathematical expression of velocity and acceleration in terms of amplitude and phase, obtained from the $u(t)$ function by derivation.

$$\begin{cases} \dot{u}(t) = \omega \cdot A \cdot \cos(\omega \cdot t + \phi) \\ \ddot{u}(t) = -\omega^2 \cdot A \cdot \sin(\omega \cdot t + \phi) = -\omega^2 \cdot u(t) \end{cases} \quad (2.13)$$

In Fig. 2.4 a comparison between displacement, velocity and acceleration is reported over time.

It is possible to observe that the acceleration response is in-phase with the displacement response, while the velocity trend is shifted by $\pi/2$ with respect to the other ones. This information can be obtained from the Fig. 2.3 in which the four different configurations clearly show that when velocity response achieves its maximum value, the displacement value is equal to zero and vice versa. Thus, the time period between $u(t) = 0$ and $u(t) = max = |A|$ represents the offset between velocity and displacement and its value is equal to $\pi/2$.

2.1.1.2 Elastic Viscously Damped Systems

Figure 2.5 shows the referenced damped system, in which a given displacement at time zero has been applied to the lumped mass m .

Fig. 2.4 Comparison between displacement (a), velocity (b) and acceleration (c) response for a SDOF undamped system

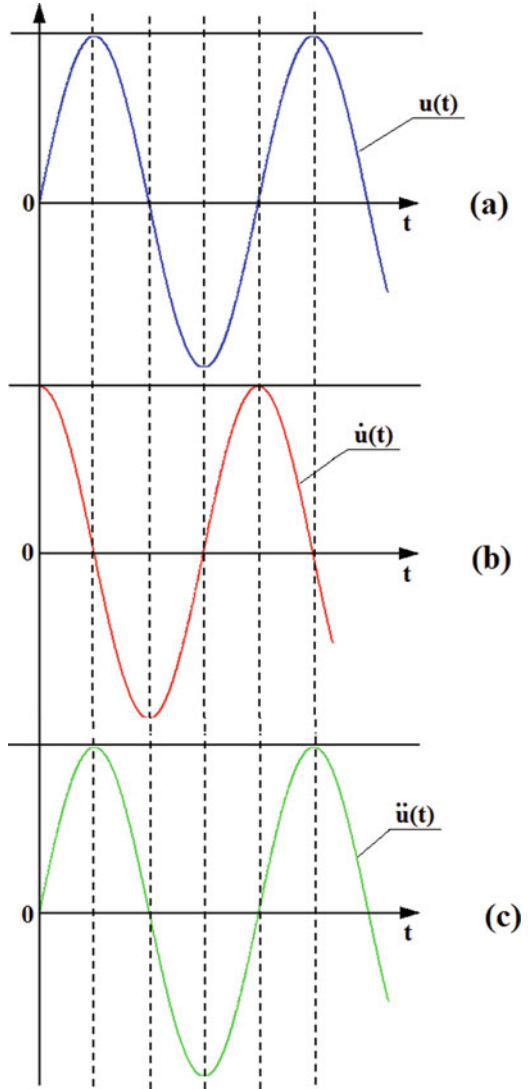
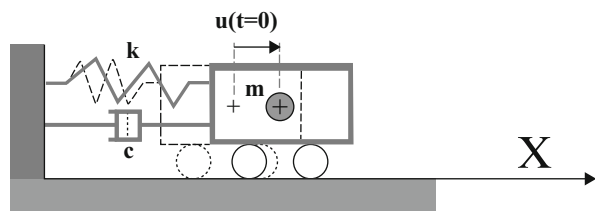


Fig. 2.5 Discrete damped SDOF system



In this case, the equation of motion can be expressed as (Eq. 2.14).

$$m \cdot \ddot{u} + c \cdot \dot{u} + k \cdot u = 0 \quad (2.14)$$

Now, introducing the *angular frequency* ω of the system the equation of motion can be rewritten (Eq. 2.15).

$$\ddot{u} + \frac{c}{m} \cdot \dot{u} + \omega^2 \cdot u = 0 \quad (2.15)$$

It is also useful to express the viscous coefficient c as function of the damping ratio ξ (Eq. 2.16), which represents the ratio between the viscous coefficient and its critical value c_c .

$$\xi = \frac{c}{c_c} = \frac{c}{2 \cdot \sqrt{k \cdot m}} \quad (2.16)$$

The equation of motion becomes the one shown below (Eq. 2.17).

$$\ddot{u} + 2 \cdot \xi \cdot \omega \cdot \dot{u} + \omega^2 \cdot u = 0 \quad (2.17)$$

The damping ratio is a dimensionless term and it depends on the natural frequency of the system. Setting $z = u$, the differential equation can be expressed in the characteristic polynomial form (Eq. 2.18).

$$z^2 + 2 \cdot \xi \cdot \omega \cdot z + \omega^2 = 0 \rightarrow z_{1,2} = \omega \cdot \left[-\xi \pm \sqrt{\xi^2 - 1} \right] \quad (2.18)$$

The solution of the above equations depends on the damping ratio value. As a result, three different cases can be analyzed.

- *Case I*: Underdamped system ($\xi < 1 \rightarrow c < c_c$). This is the more realistic case, since most of the structural systems (e.g. buildings, etc.) have a viscous damping coefficient that is less than the critical one. Two different and complex solutions can be evaluated from the characteristic polynomial (Eq. 2.19).

$$z_{1,2} = -\xi \cdot \omega \pm i\omega_D \quad (2.19)$$

In the equation above, ω_D represents the natural damped angular frequency and is evaluated as shown in the Eq. 2.20.

$$\omega_D = \omega \cdot \sqrt{1 - \xi^2} \quad (2.20)$$

From this value, it is possible to evaluate the natural damped period T_D (Eq. 2.21).

$$T_D = \frac{1}{\omega_D} = \frac{1}{\omega \cdot \sqrt{1 - \xi^2}} \quad (2.21)$$

The general solution illustrated in Eq. 2.22 can be obtained.

$$u(t) = e^{-\xi \cdot \omega \cdot t} \cdot [C_1 \cdot e^{i \cdot \xi \cdot \omega_D \cdot t} + C_2 \cdot e^{-i \cdot \xi \cdot \omega_D \cdot t}] \quad (2.22)$$

Using Euler's relation, the above equation can be replaced with the following (Eq. 2.23).

$$u(t) = A_1 \cdot e^{-\xi \cdot \omega \cdot t} \cdot \cos(\omega_D \cdot t) + A_2 \cdot e^{-\xi \cdot \omega \cdot t} \cdot \sin(\omega_D \cdot t) \quad (2.23)$$

It can then be expressed in terms of amplitude and phase contributions (Eq. 2.24).

$$u(t) = A \cdot e^{-\xi \cdot \omega \cdot t} \cdot \sin(\omega_D \cdot t + \phi) \quad (2.24)$$

The similarity between this expression and the function reported in the Eq. 2.7 can now be observed. Only the exponential term is added in the response of the damped system, while the damped angular frequency is not significantly different from the undamped one. Considering a reinforced concrete SDOF system for which the damping ratio is assumed to equal 5%, the difference between the two mentioned angular frequencies can be neglected (Eq. 2.25).

$$\omega_D = \omega \cdot \sqrt{1 - \xi^2} = \omega \cdot \sqrt{1 - (0.05)^2} \approx \omega \quad (2.25)$$

The exponential term provides information about the attenuation of motion. In fact, its value increases with the time, causing a reduction in the amplitude of motion. The generic initial conditions given in Eq. 2.26 are assumed.

$$u(0) = u_0; \quad \dot{u}(0) = \dot{u}_0 \quad (2.26)$$

The solution to the problem, in terms of system displacement, is given in Eq. 2.27.

$$u(t) = e^{-\xi \cdot \omega \cdot t} \cdot \left\{ u_0 \cdot \cos(\omega_D \cdot t) + \frac{u_0 + \xi \cdot \omega \cdot u_0}{\omega_D} \cdot \sin(\omega_D \cdot t) \right\} \quad (2.27)$$

Figure 2.6 shows the trend of the displacement system response in the time domain.

The dashed lines represent the exponential functions that control the reduction of the displacement amplitude ($u_{III} < u_{II} < u_I$). In addition, the ratio between two adjacent positive displacement amplitudes is always approximately constant (Eq. 2.28).

$$\frac{u_n}{u_{n+1}} \simeq e^{2\pi\xi \frac{\omega}{\omega_D}} \quad (2.28)$$

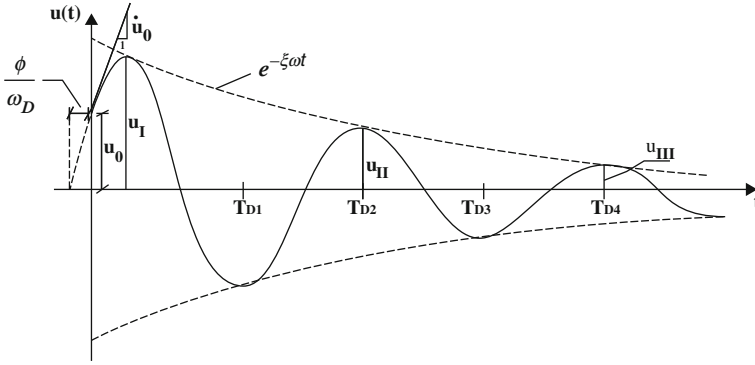


Fig. 2.6 Displacement response of a SDOF underdamped system

This observation is commonly used to estimate the damping ratio of a specific structure with given displacement response. In fact, the logarithm of the ratio reported above (logarithmic decrement) is assumed as a viscous damping index (Eq. 2.29).

$$\delta = \ln \left(\frac{u_n}{u_{n+1}} \right) \simeq 2\pi\xi \frac{\omega}{\omega_D} \quad (2.29)$$

As observed previously, the damped frequency and the natural frequency can be assumed to be equal. From this hypothesis, the logarithmic decrement can be evaluated as shown in Eq. 2.30.

$$\delta \simeq 2\pi\xi \quad (2.30)$$

Thus, by using this relation it is possible to estimate the damping ratio of the system. In order to emphasize the effects of the damping on the dynamic response of a system, vector motion representation is proposed. The dynamic response $u(t)$ can be efficiently illustrated in the *Argand-Gauss plane*, in which the x-axis represents the real contributions and the y-axis the imaginary ones (Fig. 2.7).

Naturally, if the damping is equal to zero the dashed circular line coincides with the external circular line ($e^{-\xi\omega t} = 0$)

- *Case 2: Critical damping system* ($\xi = 1 \rightarrow c = c_c$). In this case, the two solutions are real, coincident and they can be evaluated from the characteristic polynomial (Eq. 2.31).

$$z_{1,2} = -\xi \cdot \omega \quad (2.31)$$

So, the general solution shown in Eq. 2.32 can be obtained.

$$u(t) = C_1 \cdot e^{-\xi\omega t} + C_2 \cdot t \cdot e^{-\xi\omega t} \quad (2.32)$$

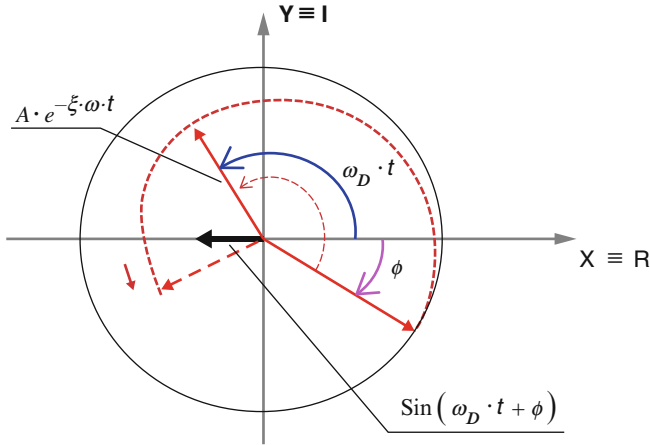


Fig. 2.7 Vector representation of a dynamic response of SDOF underdamped system

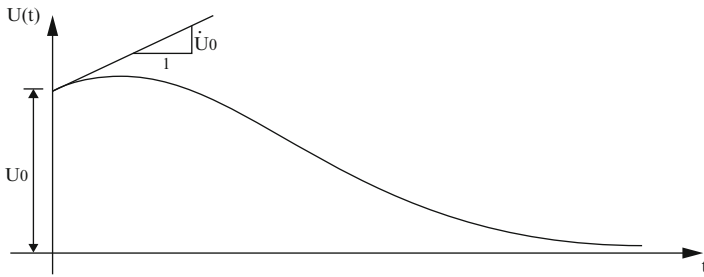


Fig. 2.8 Displacement response of a SDOF system with critical damping

Assuming the generic initial conditions given in Eq. 2.33,

$$u(0) = u_0; \quad \dot{u}(0) = \dot{u}_0 \tag{2.33}$$

the solution of the problem in terms of system displacement is given in Eq. 2.34

$$u(t) = e^{-\omega \cdot t} \cdot \{u_0 \cdot (1 + \omega \cdot t) + \dot{u}_0 \cdot t\} \tag{2.34}$$

A solution of this type is not periodic and it presents an exponential attenuation. Figure 2.8 shows the trend of the displacement system response in the time domain.

- *Case 3: Overdamped system* ($\xi > 1 \rightarrow c > c_c$). The characteristic polynomial has two distinct and real solutions (Eq. 2.35).

$$z_{1,2} = \omega \cdot \left[-\xi \pm \sqrt{\xi^2 - 1} \right] \tag{2.35}$$

The general solutions shown in Eq. 2.36 can be obtained,

$$u(t) = C_1 \cdot e^{-\omega \cdot (\xi - \sqrt{\xi^2 - 1}) \cdot t} + C_2 \cdot e^{-\omega \cdot (\xi + \sqrt{\xi^2 - 1}) \cdot t} \quad (2.36)$$

while the Eq. 2.37 represents the solution of the equation of motion associated with the generic initial conditions ($u(0) = u_0$; $\dot{u}(0) = \dot{u}_0$).

$$u(t) = \frac{1}{2 \cdot \sqrt{\xi^2 - 1}} \cdot e^{-\omega \cdot (\xi - \sqrt{\xi^2 - 1}) \cdot t} \cdot \left[u_0 \cdot \omega \cdot (\sqrt{\xi^2 - 1} + \xi) + \dot{u}_0 \right] + \frac{1}{2 \cdot \sqrt{\xi^2 - 1}} \cdot e^{-\omega \cdot (\xi + \sqrt{\xi^2 - 1}) \cdot t} \cdot \left[u_0 \cdot \omega \cdot (\sqrt{\xi^2 - 1} - \xi) - \dot{u}_0 \right] \quad (2.37)$$

Even in this case, the dynamic response of the system is not described by a periodic function and therefore it will not be a pure oscillation of the system. Figure 2.9 compares the dynamic response of the system with different values of damping ratio, including the case of critical damping ($\xi = 1$).

For increasing values of damping ratio ($\xi > 1$), the equilibrium condition is achieved after a long period of time. Naturally, the overdamped case is not realistic in structural applications. Figure 2.10 illustrates the three different cases of damped SDOF system, focusing on the dynamic response over several time steps.

2.1.1.3 Energetic Considerations

The dynamic configuration of a free vibrational SDOF system can be expressed in terms of energy. The input energy E_{in} shown in Eq. 2.38 is evaluated as the sum

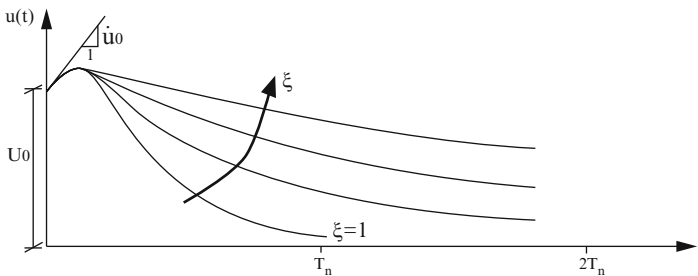


Fig. 2.9 Comparison between displacement response of a SDOF system with critical damping and with $\xi > 1$

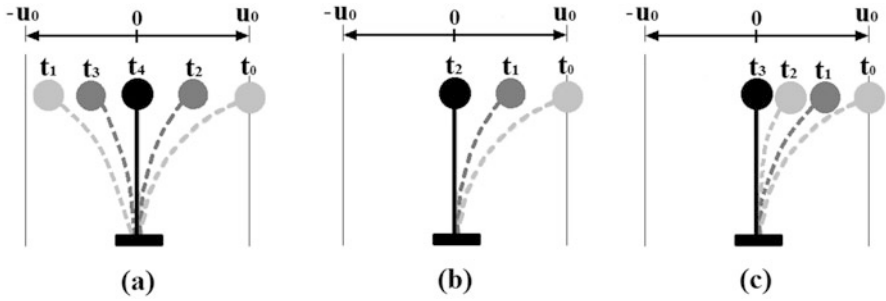


Fig. 2.10 Sequence of dynamic response for a SDOF underdamped system (a), with critical damping system (b) and for an overdamped system (c)

of the kinetic energy and potential energy due to velocity ($\dot{u}(t)$) and displacement ($u(t)$), respectively.

$$E_{in} = \frac{1}{2} \cdot k \cdot [u(t)]^2 + \frac{1}{2} \cdot m \cdot [\dot{u}(t)]^2 \tag{2.38}$$

Considering the most important case of an underdamped system with the generic initial conditions, the previous energy balance equation can be expressed as follows (Eq. 2.39):

$$E_{in} = \frac{1}{2} \cdot A^2 \cdot e^{-\xi \cdot \omega \cdot t} \cdot \left\{ k \cdot [\sin(\omega_D \cdot t + \phi)]^2 + \frac{1}{2} \cdot m \cdot [-\xi \cdot \omega \cdot \sin(\omega_D \cdot t + \phi) + \omega_D \cdot \cos(\omega_D \cdot t + \phi)]^2 \right\} \tag{2.39}$$

It is possible to observe how the square amplitude of the motion is directly proportional to the energy of the system and represents the greatest contribution. In addition, the exponential terms represent the viscous dissipated energy. Replacing E_0 for the energy contribution associated with conservative terms, the previous equation can be rewritten as expressed in Eq. 2.40.

$$E_{in} = e^{-\xi \cdot \omega \cdot t} \cdot E_0 \tag{2.40}$$

In order to evaluate the energy variation due to the damping, the first derivative of the conservative energy E_0 with respect to the time has to be performed together with the normalization with respect to the total input energy (Eq. 2.41).

$$\frac{dE_{in}}{dt} = -\xi \cdot \omega \cdot E_{in} \tag{2.41}$$



The parameter $(\xi \cdot \omega)^{-1}$ represents the decay time that is the lost energy rate referred to in the system. It is possible to see that this coefficient depends on the vibrational property of the system and on the damping ratio (material characteristics).

2.2 Response to Harmonic Excitations

The evaluation of the dynamic response of a SDOF system is one of most important goals in structural earthquake engineering. Clearly, the dynamic response of a system depends on the nature of the applied force. In order to obtain a simple solution, the harmonic excitation will be considered as external force. The harmonic excitation is characterized by a constant value of angular frequency ω_f , also called *exciting frequency*, and also by a given value of amplitude. Usually the time variation of the external force has a sinusoidal trend. In the following paragraphs, the dynamic solution of the equation of motion will be derived for undamped and damped elastic SDOF systems (Meirovitch 2010).

2.2.1 Undamped Systems

Figure 2.11 illustrates the typical scheme of an undamped system subjected to an external periodic force.

Considering the external force variable with sinusoidal law ($F(t) = F_0 \cdot \sin(\omega_f \cdot t)$), the equation of motion can be expressed as shown below (Eq. 2.42).

$$m \cdot \ddot{u} + k \cdot u = F_0 \cdot \sin(\omega_f \cdot t) \quad (2.42)$$

This represents a second order nonhomogeneous differential equation with constant coefficients, and therefore the solutions can be evaluated as the sum of a homogeneous associated solution (u_0) and a particular solution (u_p). The first one represents the free vibration response, while the second term refers to the dynamic response due to the external force. The u_0 solution has been evaluated in the previous

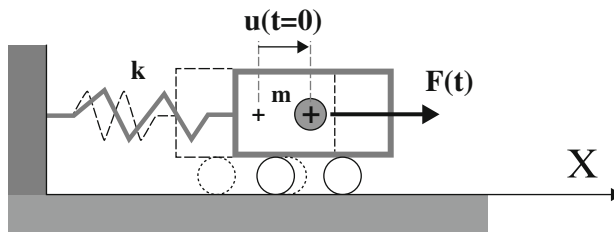


Fig. 2.11 Discrete undamped SDOF system subjected to an external force

paragraph and the particular solution can be expressed as shown in a simple form, since the external force is a sinusoidal function (Eq. 2.43).

$$\begin{cases} u_0(t) = A_1 \cdot \sin(\omega \cdot t) + A_2 \cdot \cos(\omega \cdot t) \\ u_p(t) = C \cdot \sin(\omega_f \cdot t) \end{cases} \quad (2.43)$$

The constant C can be evaluated by substituting the particular solution into the equation of motion (Eq. 2.44).

$$-C \cdot \omega_f^2 \cdot m \cdot \sin(\omega_f \cdot t) + C \cdot k \cdot \sin(\omega_f \cdot t) = F_0 \cdot \sin(\omega_f \cdot t) \quad (2.44)$$

Simplifying the sinusoidal and dividing the two members by the mass, Eq. 2.45 is obtained.

$$C \cdot (\omega^2 - \omega_f^2) = \frac{F_0}{m} \quad (2.45)$$

Introducing the ratio between the exciting force frequency and the natural frequency ($\beta = \omega_f/\omega$) also called *frequency ratio*, the value of the constant C can be evaluated as shown in the Eq. 2.46.

$$C = \frac{F_0}{k \cdot (1 - \beta^2)} \quad (2.46)$$

Thus the particular solution is defined below (Eq. 2.47).

$$u_p(t) = \frac{F_0}{k \cdot (1 - \beta^2)} \cdot \sin(\omega_f \cdot t) \quad (2.47)$$

The dynamic response of the system will assume the following form (Eq. 2.48).

$$u(t) = u_0(t) + u_p(t) = A_1 \cdot \sin(\omega \cdot t) + A_2 \cdot \cos(\omega \cdot t) + \frac{F_0}{k \cdot (1 - \beta^2)} \cdot \sin(\omega_f \cdot t) \quad (2.48)$$

The free vibration coefficients (A_1 and A_2) can be evaluated by imposing the initial conditions. The generic initial conditions with velocity and displacement not equal to zero are considered (Eq. 2.49).

$$u(0) = u_0; \quad \dot{u}(0) = \dot{u}_0 \quad (2.49)$$

Thus, the dynamic response of the SDOF undamped system is given in Eq. 2.50.

$$\begin{aligned} u(t) = u_0(t) + u_p(t) = & u_0 \cdot \cos(\omega \cdot t) \\ & + \left[\frac{\dot{u}_0}{\omega} - \frac{F_0}{k \cdot (1 - \beta^2)} \cdot \beta \right] \cdot \sin(\omega \cdot t) + \frac{F_0}{k \cdot (1 - \beta^2)} \cdot \sin(\omega_f \cdot t) \end{aligned} \quad (2.50)$$

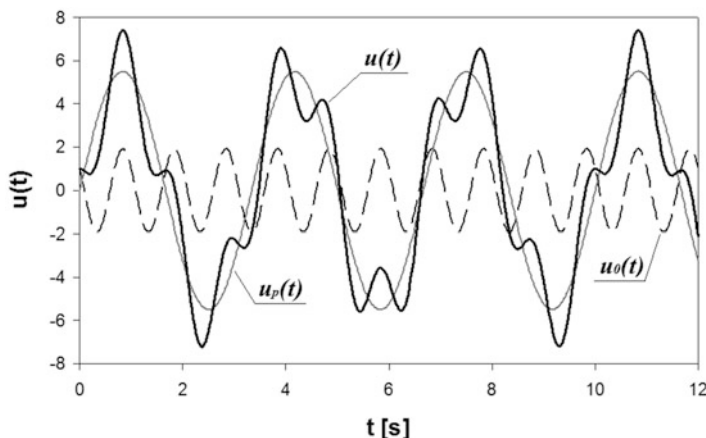


Fig. 2.12 Different contributions to the dynamic response of an undamped SDOF system subjected to a harmonic excitation with $\beta = 0.3$ and $u_0 = \dot{u}_0 = 0$

The response associated with the free vibrations is called the *transient contribution* because in the realistic case (damped system) it tends to zero as time increases. Instead, the term due to the external force is permanent and it defines a *steady state of vibration*. In other words, the dynamic response of the system is the sum of two oscillations having different frequencies. In addition, one can notice that the dynamic response due to the external force contribution is not dependent upon the initial conditions. In order to understand the aspects previously discussed, the Fig. 2.12 shows the dynamic response of a forced SDOF undamped system with $\beta = 0.3$ and $u_0 = \dot{u}_0 = 0$, distinguishing between the permanent and transient contributions.

It is interesting to observe the dynamic coefficient $\frac{F_0}{k \cdot (1 - \beta^2)}$ for which the ratio between the external amplitude and the elastic coefficient represents the elastic displacement that arises under static conditions. Thus the parameter $(1 - \beta^2)^{-1}$ tends to amplify the static response of the system and it is called the dynamic amplification coefficient. This value assumes high values if β is approximately equal to one. For this reason, according to the values assumed by β , two particular conditions can occur:

- *Resonance phenomenon*: when the exciting force frequency is equal to the natural frequency of the system. This condition causes an infinite amplification of the dynamic response, since the denominator of the $u(t)$ function is equal to zero. Naturally, this condition cannot occur in real systems because they have an intrinsic energy dissipation during the motion. In the resonance case ($\omega = \omega_f$), the dynamic response shown in Eq. 2.50 loses significance, since it

tends to infinity for any time value. In this case, the particular solution has to be substituted from the following form (Eq. 2.51).

$$u_p(t) = C \cdot t \cdot \cos(\omega \cdot t) \rightarrow \text{for } \omega = \omega_f \quad (2.51)$$

Substituting this expression into the equation of motion, the following value of the constant C is found (Eq. 2.52).

$$C = -\frac{F_0}{2 \cdot k} \cdot \omega \quad (2.52)$$

Considering the generic free vibrational solution, the dynamic response of the system is given by Eq. 2.53.

$$u(t) = A_1 \cdot \sin(\omega \cdot t) + A_2 \cdot \cos(\omega \cdot t) - \frac{F_0}{2 \cdot k} \cdot \omega \cdot t \cdot \cos(\omega \cdot t) \quad (2.53)$$

For the sake of simplicity, the initial conditions $u(t) = 0$ and $\dot{u}_0(t) = 0$ are considered and the total dynamic response in terms of displacements can be expressed as shown in Eq. 2.54.

$$u(t) = \frac{F_0}{2 \cdot k} \cdot [\sin(\omega \cdot t) - \omega \cdot t \cdot \cos(\omega \cdot t)] \quad (2.54)$$

The amplitude dynamic response increases linearly and it tends to infinity for an infinitely long time (Fig. 2.13).

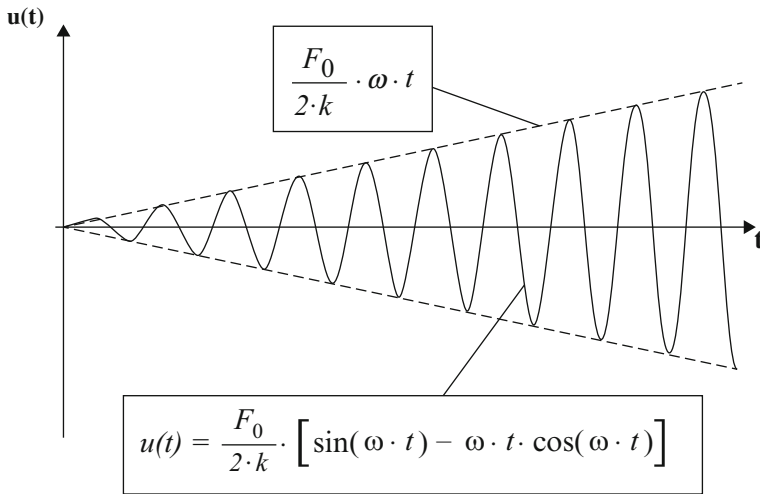


Fig. 2.13 Resonance phenomenon in terms of displacement response

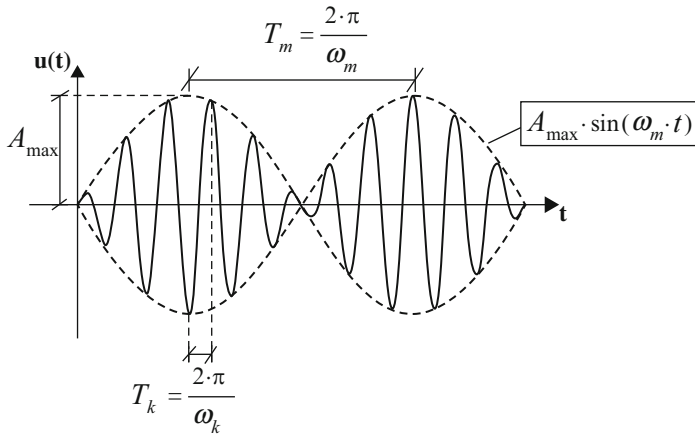


Fig. 2.14 Beat phenomenon in terms of displacement response

- *Beats phenomenon*: when the exciting force frequency value is very close to the natural frequency. In this case the dynamic response of the system is characterized by sudden amplitude variations. This leads to obtaining an increase and decrease of the signal amplitude, depending on the phase concordance or discordance, respectively. Figure 2.14 shows an example of the beats phenomenon in terms of displacement response. The dynamic response is described by a harmonic function with given frequency $\omega_n = \frac{|\omega_f + \omega|}{2}$ whose amplitude is modulated by a sinusoidal function having frequency $\omega_m = \frac{|\omega_f - \omega|}{2}$

2.2.2 Viscously Damped Systems

When the damping force is also considered in the SDOF system (Fig. 2.15), the equation of motion becomes as shown in Eq. 2.55.

$$m \cdot \ddot{u} + c \cdot \dot{u} + k \cdot u = F_0 \cdot \sin(\omega_f \cdot t) \quad (2.55)$$

Substituting the angular natural frequency (ratio between the stiffness and mass) and the damping ratio coefficient, the equation of motion can be rewritten (Eq. 2.56).

$$\ddot{u} + 2 \cdot \omega \cdot \xi \cdot \dot{u} + \omega^2 \cdot u = \frac{F_0}{m} \cdot \sin(\omega_f \cdot t) \quad (2.56)$$

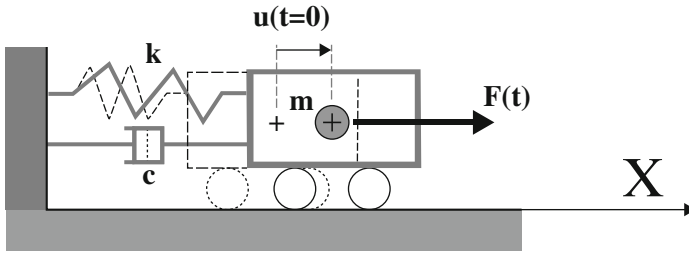


Fig. 2.15 Discrete damped SDOF system subjected to an external force

The particular solution assumes the mathematical form given in Eq. 2.57.

$$u_p(t) = C_1 \cdot \sin(\omega_f \cdot t) + C_2 \cdot \cos(\omega_f \cdot t) \quad (2.57)$$

As obtained previously, the associated homogeneous solution for underdamped SDOF system is given by Eq. 2.58.

$$u_0(t) = A_1 \cdot e^{-\xi \cdot \omega \cdot t} \cdot \cos(\omega_D \cdot t) + A_2 \cdot e^{-\xi \cdot \omega \cdot t} \cdot \sin(\omega_D \cdot t) \quad (2.58)$$

Substituting the particular solution and its first derivative into the equation of motion in terms of displacement and velocity, the constants C_1 and C_2 can be evaluated (Eq. 2.59)

$$\begin{cases} C_1 = \frac{F_0}{k} \cdot \frac{1 - \beta^2}{(1 - \beta^2)^2 + (2 \cdot \xi \cdot \beta)^2} \\ C_2 = \frac{F_0}{k} \cdot \frac{-2 \cdot \xi \cdot \beta}{(1 - \beta^2)^2 + (2 \cdot \xi \cdot \beta)^2} \end{cases} \quad (2.59)$$

The complete solution assumes the following form (Eq. 2.60).

$$u(t) = e^{-\xi \cdot \omega \cdot t} \cdot [A_1 \cdot \cos(\omega_D \cdot t) + A_2 \cdot \sin(\omega_D \cdot t)] + \frac{F_0}{k} \cdot \frac{1}{(1 - \beta^2)^2 + (2 \cdot \xi \cdot \beta)^2} \cdot [(1 - \beta^2) \cdot \sin(\omega_f \cdot t) - 2 \cdot \xi \cdot \beta \cdot \cos(\omega_f \cdot t)] \quad (2.60)$$

In this case, the first part of the equation represents the transient contribution and is evaluated from the initial conditions. The second part of the equation defines the steady state of the system and it depends on the exciting force frequency. It can be observed that the last contribution is out of phase compared to the sinusoidal

external force. The parameters expressed in the Eq. 2.61 can be considered in order to clarify the last claim.

$$u_p(t) = A_{\max} \cdot \sin(\omega_f \cdot t - \phi) \rightarrow \begin{cases} A_{\max} = \frac{F_0}{k} \cdot \frac{1}{\sqrt{(1 - \beta^2)^2 + (2 \cdot \xi \cdot \beta)^2}} \\ \phi = \text{tg}^{-1} \left(\frac{2 \cdot \xi \cdot \beta}{1 - \beta^2} \right) \end{cases} \quad (2.61)$$

This mathematical representation focuses the out of phase of the permanent contribution of motion, compared to the external applied force. In addition, the dynamic amplification parameter can be evaluated from the amplitude A_{\max} . Remembering that it represents the ratio between the steady state amplitude contribution (A_{\max}) and the static one (F_0/k), it can be expressed as shown in Eq. 2.62.

$$|A| = \frac{1}{\sqrt{(1 - \beta^2)^2 + (2 \cdot \xi \cdot \beta)^2}} \quad (2.62)$$

Differing from the undamped system cases, the dynamic amplification is never equal to infinity since the damping has been considered. Naturally, the resonance case can be achieved for the $\omega = \omega_f$, for which the aforementioned coefficient assumes the following value (Eq. 2.63).

$$|A|_{\text{resonance}} = \frac{1}{2 \cdot \xi} \quad (2.63)$$

One of the most common mathematical representations of the dynamic response of an SDOF forced system is the function $|A| - \beta$, which provides some information about the amplification response for a given frequency ratio. In Fig. 2.16 different trends of dynamic amplification coefficients with their damping ratio are compared. Each of them is characterized by a given value of damping ratio.

It can be observed that the dynamic response for an undamped SDOF system tends to infinity for $\beta = 1$. Generally, the maximum response for a damped system takes place when the frequency ratio is equal to one (resonance phenomenon). Specifically, the resonance condition is slightly influenced by the damping ratio of the system (dashed line in Fig. 2.16). It can be observed that over a given damping ratio value, the peak of the curve $|A| - \beta$ no longer exists. In order to evaluate this level of damping ratio (ξ_m), the first derivative of the amplification function with respect to frequency ratio is evaluated and is assumed to equal zero (Eq. 2.64).

$$\frac{d|A|}{d\beta} = 0 \rightarrow \beta = \sqrt{1 - 2 \cdot \xi^2} \quad (2.64)$$

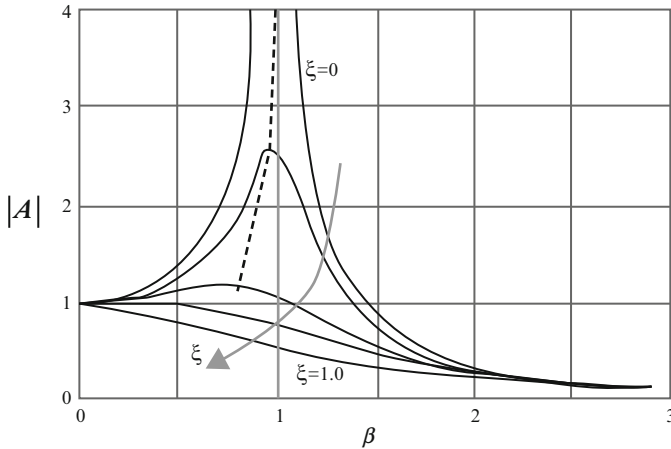


Fig. 2.16 Dynamic amplification functions for different values of damping ratio

The resonance frequency ratio can be evaluated by substituting the damping ratio value. As observed previously, the peak values refer to the resonance phenomena and therefore the frequency ratio can be assumed approximately equal to one for every value of damping ratio. From this assumption the ξ_m parameter can be evaluated in Eq. (2.65).

$$\xi_m \approx \frac{1}{\sqrt{2}} \approx 0.70 \tag{2.65}$$

Thus, for damping ratio values less than the level ξ_m the dynamic amplification function has a peak. In addition, for these cases one can observe values of dynamic amplification coefficients less than the one for the entire frequency ratio domain. In these particular cases the applied force on the system leads to a dynamic response with smaller amplitude than the static case. The same consideration can be made in order to study the variation of the phase angle with the frequency ratio. For this purpose, Fig. 2.17 compares some trends of $\phi - \beta$ function with different values of damping ratio.

Returning to the general dynamic response of a damped SDOF system (Eq. 2.60), the particular solution can be written in terms of dynamic amplitude coefficient (Eq. 2.66).

$$u(t) = e^{-\xi \cdot \omega \cdot t} \cdot [A_1 \cdot \cos(\omega_D \cdot t) + A_2 \cdot \sin(\omega_D \cdot t)] + \frac{F_0}{k} \cdot (|A|)^2 \cdot [(1 - \beta^2) \cdot \sin(\omega_f \cdot t) - 2 \cdot \xi \cdot \beta \cdot \cos(\omega_f \cdot t)] \tag{2.66}$$



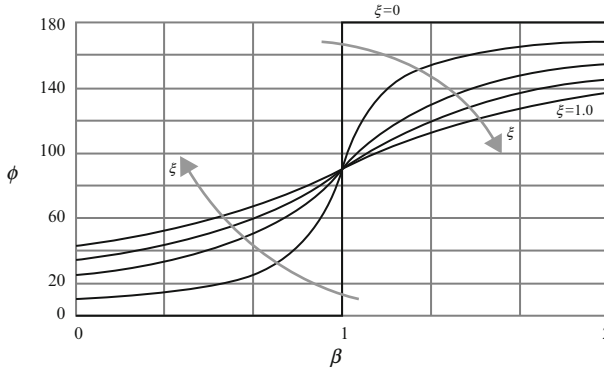


Fig. 2.17 Phase angle for different values of damping ratio and frequency ratio

Imposing $\omega = \omega_D$ and considering the simple initial conditions referring to a configuration at rest $u(0) = 0; \dot{u}(0) = 0$ the free vibration constants A_1 and A_2 can be evaluated (Eq. 2.67).

$$A_1 = 2 \cdot \frac{F_0}{k} \cdot (|A|)^2 \cdot \xi \cdot \beta \quad A_2 = \frac{F_0}{k} \cdot (|A|)^2 \cdot \beta \cdot [2\xi^2 - (1 - \beta^2)] \quad (2.67)$$

The dynamic response is given in Eq. 2.68.

$$\begin{aligned} u(t) = & \frac{F_0}{k} \cdot (|A|)^2 \cdot (1 - \beta^2) \cdot [\sin(\omega_f \cdot t) - e^{-\xi \cdot \omega \cdot t} \cdot \beta \cdot \sin(\omega \cdot t)] \\ & - \frac{F_0}{k} \cdot (|A|)^2 \cdot 2 \cdot \xi \cdot \beta \cdot [\cos(\omega_f \cdot t) - e^{-\xi \cdot \omega \cdot t} \cdot \cos(\omega \cdot t)] \\ & + e^{-\xi \cdot \omega \cdot t} \cdot 2 \cdot \xi^2 \cdot \beta \cdot \sin(\omega \cdot t) \end{aligned} \quad (2.68)$$

Figure 2.18 illustrates the trend of the total dynamic response compared with the exciting force and free vibrations ones for a system damped at 5% with $\beta = 0.3$.

Since the free vibrations are damped, the dynamic response of the system is equal to the particular solution (steady state) after a given amount of time. Furthermore, if the resonance condition is taken into account ($\omega = \omega_f \rightarrow \beta = 1$), the dynamic response of the system can be written as follows (Eq. 2.69).

$$u(t) = \frac{F_0}{k} \cdot \frac{1}{2 \cdot \xi} \cdot \{e^{-\xi \cdot \omega \cdot t} \cdot [\xi \cdot \sin(\omega \cdot t) + \cos(\omega \cdot t)] - \cos(\omega_f \cdot t)\} \quad (2.69)$$

It can be observed that for large values of time the maximum amplitude of the dynamic response is equal to the resonance dynamic amplification coefficient ($\frac{1}{2 \cdot \xi}$) (Fig. 2.19). Thus, the dynamic response of the system tends to an amplified steady state, apart from infinity.

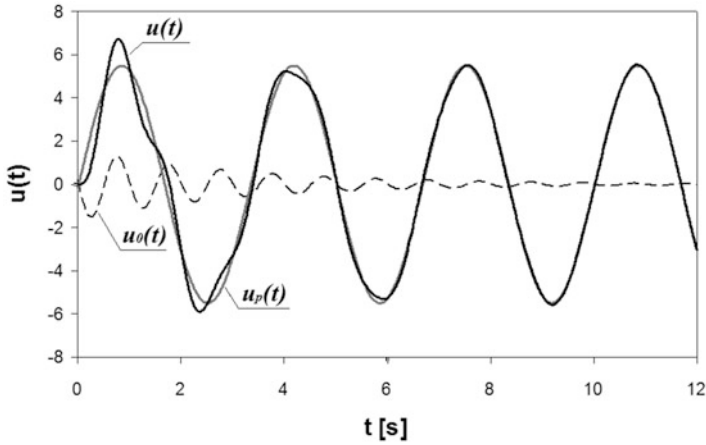


Fig. 2.18 Different contributions in the dynamic response of a SDOF system at 5% damping, subjected to a harmonic excitation with $\beta = 0.3$ and $u_0 = \dot{u}_0 = 0$

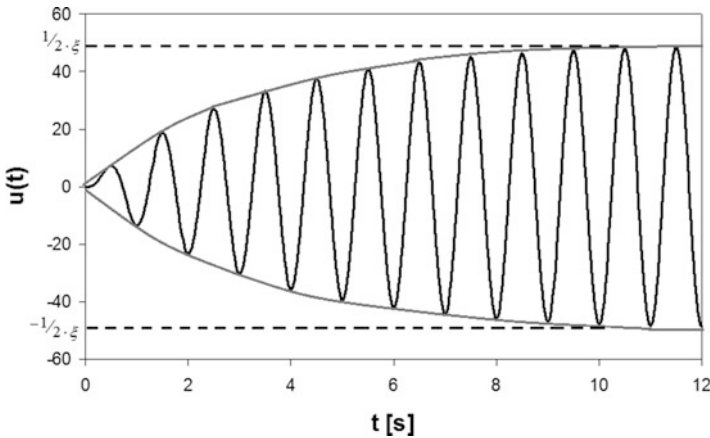


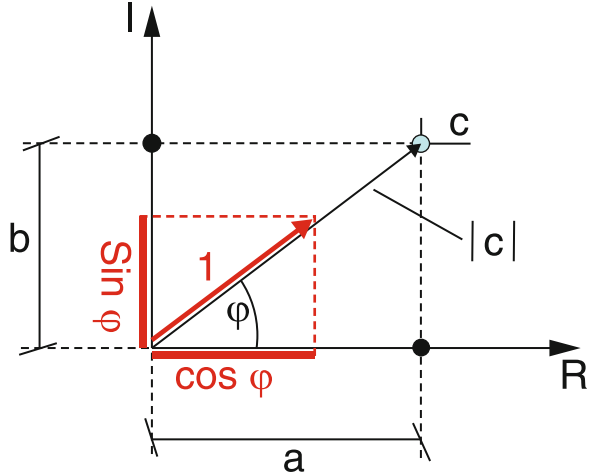
Fig. 2.19 Resonance dynamic response for a SDOF system damped at 5% with initial condition $u_0 = \dot{u}_0 = 0$

The grey curve represents the boundary of the response and it is possible to observe how it tends to the maximum amplitude value ($|A|_{resonance} = \frac{1}{2 \cdot \xi}$) over time.

2.2.2.1 Representation of Dynamic Response in the Argand-Gauss Plane

The identification of the system response in the *Argand-Gauss Plan* is very useful, since some information can be evaluated (Burton 1988). In order to introduce the problem, a brief description of complex algebra is shown in Fig. 2.20.

Fig. 2.20 Complex representation of a vector



Assuming the angle φ as linear function of the time ($\varphi = \omega \cdot t$) the Eq. 2.70 collects all the mathematical information about the vector c represented in Fig. 2.20.

$$\begin{cases} c = a + ib \\ |c| = \sqrt{a^2 + b^2} \Rightarrow c = |c| \cdot (\cos(\omega \cdot t) + i \cdot \sin(\omega \cdot t)) \\ \operatorname{tg}(\varphi) = \frac{b}{a} \end{cases} \quad (2.70)$$

In addition, the first and second derivative of c with respect to the phase angle is expressed in Eq. 2.71.

$$\begin{cases} \frac{dc}{d\varphi} = |c| \cdot \omega \cdot (-\sin(\omega \cdot t) + i \cdot \cos(\omega \cdot t)) \Rightarrow \frac{dc}{d\varphi} = i \cdot c \cdot \omega \\ \frac{d^2c}{d\varphi^2} = |c| \cdot \omega^2 \cdot (-\cos(\omega \cdot t) - i \cdot \sin(\omega \cdot t)) \Rightarrow \frac{d^2c}{d\varphi^2} = -c \cdot \omega^2 \end{cases} \quad (2.71)$$

The complex trigonometric parameters can be expressed in terms of an exponential function, using Euler's relations (Eq. 2.72).

$$\begin{cases} \cos(\omega \cdot t) = \frac{e^{i\omega t} + e^{-i\omega t}}{2} \\ \sin(\omega \cdot t) = \frac{e^{i\omega t} - e^{-i\omega t}}{2 \cdot i} \end{cases} \quad (2.72)$$

These relationships can be applied to the equation of motion for a SDOF damped system subjected to a harmonic external load (Eq. 2.73).

$$\ddot{u} + 2 \cdot \omega \cdot \xi \cdot \dot{u} + \omega^2 \cdot u = \frac{F_0}{m} \cdot \cos(\omega_f \cdot t) = 2 \cdot A_0 \cdot \frac{e^{i\omega_f t} + e^{-i\omega_f t}}{2} \quad (2.73)$$

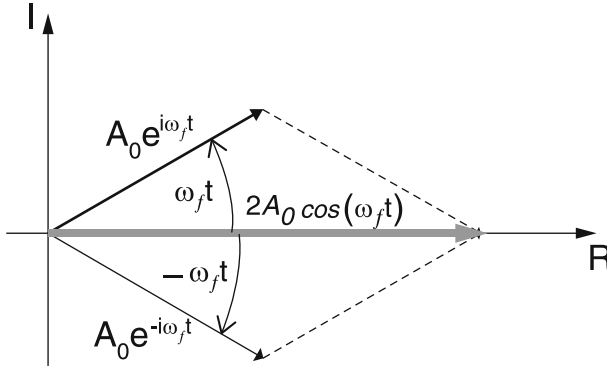


Fig. 2.21 Vector composition of external force

For the sake of simplicity, the constant F_0/m was substituted by the other constant expressed as $2A_0$. Observing the equation reported above, the solution of the problem can be obtained as the sum of two solutions separated further (Eq. 2.74).

$$\begin{cases} \ddot{u}_1 + 2 \cdot \omega \cdot \xi \cdot \dot{u}_1 + \omega^2 \cdot u_1 = A_0 \cdot e^{i\omega_f t} \\ \ddot{u}_2 + 2 \cdot \omega \cdot \xi \cdot \dot{u}_2 + \omega^2 \cdot u_2 = A_0 \cdot e^{-i\omega_f t} \end{cases} \quad (2.74)$$

Figure 2.21 illustrates the vector components associated with the two contributions of the external exciting force.

Considering the first equation, the particular solution can be expressed as shown in Eq. 2.75.

$$u_1 = C \cdot e^{i\omega_f t} \rightarrow \begin{cases} \dot{u}_1 = i \cdot \omega_f \cdot C \cdot e^{i\omega_f t} \\ \ddot{u}_1 = -\omega_f^2 \cdot C \cdot e^{i\omega_f t} \end{cases} \quad (2.75)$$

Substituting these expressions and simplifying the equation of motion gives (Eq. 2.76):

$$-\omega_f^2 \cdot C + i \cdot \xi \cdot \omega_f \cdot \omega \cdot C + \omega^2 \cdot C = A_0 \quad (2.76)$$

Dividing all the terms by ω^2 and replacing with $\beta = \omega_f/\omega$, the constant C can be evaluated from the previous equation (Eq. 2.77).

$$C = \frac{A_0}{\omega^2} \cdot \left\{ \frac{(1 - \beta^2)}{\left[(1 - \beta^2)^2 + (2 \cdot \xi \cdot \beta)^2 \right]} - i \cdot \frac{2 \cdot \xi \cdot \beta}{\left[(1 - \beta^2)^2 + (2 \cdot \xi \cdot \beta)^2 \right]} \right\} \quad (2.77)$$

The constant C represents the amplitude of the response due to the exciting force and is defined as the sum of a real (a) and an imaginary (b) part (Eq. 2.78).

$$C = \frac{A_0}{\omega^2} \cdot (a + i \cdot b) \rightarrow \begin{cases} a = \frac{(1 - \beta^2)}{[(1 - \beta^2)^2 + (2 \cdot \xi \cdot \beta)^2]} \\ b = \frac{2 \cdot \xi \cdot \beta}{[(1 - \beta^2)^2 + (2 \cdot \xi \cdot \beta)^2]} \end{cases} \quad (2.78)$$

Equation 2.79 shows the absolute value of C .

$$|C| = \frac{A_0}{\omega^2} \cdot |a + i \cdot b| = \frac{A_0}{\omega^2} \cdot \sqrt{a^2 + b^2} = \frac{A_0}{\omega^2} \cdot \frac{1}{\sqrt{(1 - \beta^2)^2 + (2 \cdot \xi \cdot \beta)^2}} \quad (2.79)$$

Coherently with the symbols used in the previous paragraph, the two last equations can be expressed below (Eq. 2.80)

$$\begin{cases} C = \frac{A_0}{\omega^2} \cdot A \\ |C| = \frac{A_0}{\omega^2} \cdot |A| \end{cases} \quad (2.80)$$

where $|A|$ is the dynamic amplification coefficient. It can be observed that the term A can be broken down into its real and imaginary parts as shown in the Eq. 2.81.

$$A = (a + i \cdot b) \rightarrow \begin{cases} a = \text{Re}(A) \\ b = \text{Im}(A) \end{cases} \quad (2.81)$$

The phase angle of the response is evaluated in Eq. 2.82.

$$\text{phase}(C) = \frac{A_0}{\omega^2} \cdot \text{phase}(A) = \frac{A_0}{\omega^2} \cdot \phi_A \rightarrow \text{tg}(\phi_A) = -\frac{\text{Im}(A)}{\text{Re}(A)} = \frac{2 \cdot \xi \cdot \beta}{(1 - \beta^2)} \quad (2.82)$$

After these considerations, the steady dynamic response can be expressed in terms of $|A|$ and β_A (Eq. 2.83).

$$u_1 = \frac{A_0}{\omega^2} \cdot A \cdot e^{i \cdot \omega_f \cdot t} = \frac{A_0}{\omega^2} \cdot |A| \cdot \left\{ \frac{\text{Re}(A)}{|A|} + i \cdot \frac{\text{Im}(A)}{|A|} \right\} \cdot e^{i \cdot \omega_f \cdot t} \quad (2.83)$$

Referring to the Fig. 2.20, the ratio of real and imaginary part of A with respect to its absolute value can be expressed as shown in Eq. 2.84.

$$\begin{cases} \frac{\text{Re}(A)}{|A|} = \cos(\phi_A) \\ \frac{\text{Im}(A)}{|A|} = \sin(\phi_A) \end{cases} \quad (2.84)$$

Thus, the u_1 function can be simplified (Eq. 2.85).

$$\begin{aligned} u_1 &= \frac{A_0}{\omega^2} \cdot |A| \cdot \{\cos(\phi_A) + i \cdot \sin(\phi_A)\} \cdot e^{i\omega_f t} \\ &= \frac{A_0}{\omega^2} \cdot |A| \cdot e^{i\phi_A} \cdot e^{i\omega_f t} = \frac{A_0}{\omega^2} \cdot |A| \cdot e^{i(\omega_f t + \phi_A)} \end{aligned} \quad (2.85)$$

Figure 2.22 illustrates the vector representation of the response u_1 . Using the same procedure, the u_2 solution can be evaluated (Eq. 2.86).

$$u_2 = \frac{A_0}{\omega^2} \cdot |A| \cdot e^{-i(\omega_f t + \phi_A)} \quad (2.86)$$

Equation 2.87 shows the sum of the two aforementioned functions, which provides the total dynamic permanent response of the system.

$$u_p(t) = u_1 + u_2 = \frac{A_0}{\omega^2} \cdot |A| \cdot [e^{i(\omega_f t + \phi_A)} + e^{-i(\omega_f t + \phi_A)}] = \frac{F_0}{k} \cdot |A| \cdot \cos(\omega_f t + \phi_A) \quad (2.87)$$

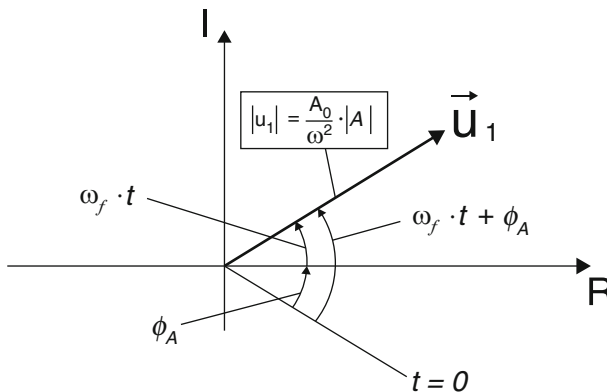


Fig. 2.22 Vector representation of the response u_1

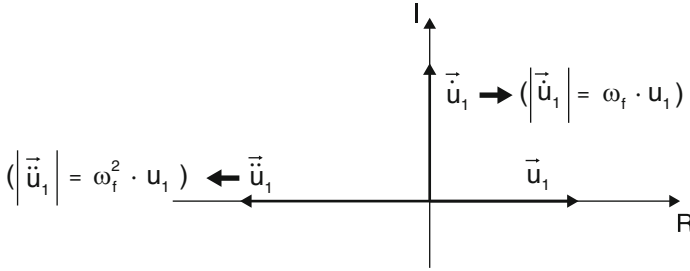


Fig. 2.23 Vector representation of displacement, velocity and acceleration permanent response at given time

The above mathematical formula contains some information about the permanent response of a damped SDOF system. It is a harmonic function with angular frequency equal to the external force's and with amplitude expressed by $|A|$ coefficient. Furthermore, it is generated with a time delay evaluated as ϕ_A/ω_f with respect to the external exciting force. If the external force is applied statically ($\omega_f = 0$; $\beta = 0$), the previous equation becomes equal to the ratio between amplitude F_0 and the stiffness k (static displacement $u_{p,static}$). Thus, the dynamic amplification coefficient is the ratio between the dynamic response of the system and the static one (Eq. 2.88).

$$|A| = \frac{u_p}{u_{p,static}} \quad (2.88)$$

The representation of the dynamic response of a SDOF damped system in the complex plan can be very useful for explaining all the forces that arise in the dynamic system for a given time instant. For the sake of simplicity, the partial permanent dynamic response u_1 at a given time is considered coincident with the real axis. Figure 2.23 illustrates the displacement, velocity and acceleration response in the condition previously mentioned.

In order to respect to the dynamic equilibrium, the elastic, damping and inertial force will arise in the opposite direction of the displacement, velocity and acceleration, respectively. Figure 2.24 shows the vector representation of the three reactions.

Naturally, the three forces will equilibrate the external exciting force which will be represented as a vector having a slope of (ωt) with respect to the real axis. All these components can be used to clearly explain the dynamic behavior of the forced system in terms of amplitude. For this purpose, the dynamic amplitude function is proposed again (Fig. 2.25) in order to identify the three characteristic ranges of frequency ratio discussed below.

- **Zone 1:** $\beta \ll 1$ (small β values). The dynamic response of the system is not influenced by the damping and all the amplification values are equal to one. This result means that the dynamic response of the system is essentially equal to the

Fig. 2.24 Vector representation of elastic, damping and inertial force at given time

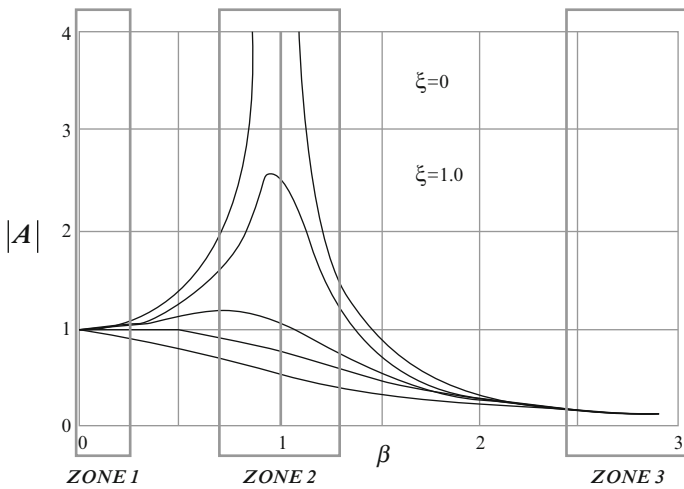
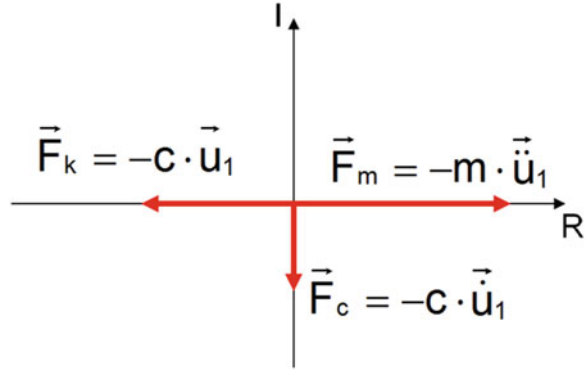


Fig. 2.25 Individuation of three characteristic zones in the dynamic amplification function

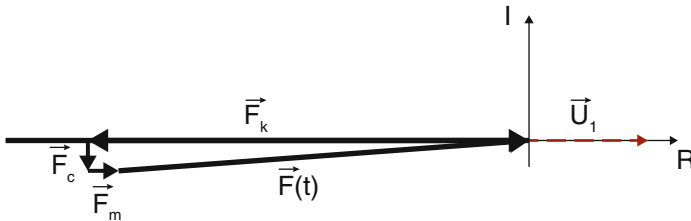


Fig. 2.26 Forces equilibrium in the complex plan for $\beta \ll 1$ system

static one. This is accurate because the exciting force frequency tends to zero. In other words the external force is applied in a quasi-static way. Since ω_f assumes very small values, the external force has a very low inclination with respect to the real axis (Fig. 2.26).

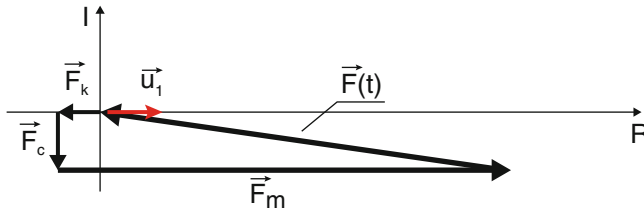


Fig. 2.27 Forces equilibrium in the complex plan for $\beta \approx 1$ system

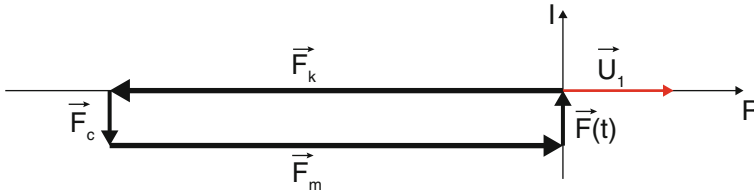


Fig. 2.28 Forces equilibrium in the complex plane for $\beta \gg 1$ system

The damping and inertial forces are much smaller than the elastic and external ones. This demonstrates how the response of the system is largely static. In addition, the displacement u_1 results in phase coincidence with external applied force (phase lag $\rightarrow \varphi_{u_1-F} 0$).

- **Zone 2: $\beta \approx 1$ (resonance).** As discussed, in these cases the dynamic response of the system is at maximum (for $\xi \leq \xi_m$) and the amplification strongly depends on the damping. In the Fig. 2.27 the vector dynamic equilibrium is shown.

In this case, the inertial force provides the main contribution that equilibrates with the external dynamic force. It is possible to observe how the displacement has a discordant phase with respect to the external force (phase lag $\rightarrow \Delta\varphi_{u_1-F} \pi$).

- **Zone 3: $\beta \gg 1$ (high β values).** The dynamic response of the system tends to zero. Figure 2.28 shows the dynamic equilibrium in the complex number plane.

The damping force is equal to the external one, while elastic force is equal to the inertial force. If the action due to the dissipative processes is neglected, the equilibrium is not achieved. In addition, the phase difference between displacement u_1 and external dynamic force is equal to 90° (phase lag $\rightarrow \Delta\varphi_{u_1-F} \approx \pi/2$). The phase lags evaluated for the three cases can be observed in the $\varphi - \beta$ function (Fig. 2.29).

2.3 Response to an Impulsive Excitation

If a generic SDOF damped system is subjected to a brief external excitation, the damping effects are not strictly important for evaluating the maximum response of the system. In fact, the peak of $u(t)$ function will be reached before the dissipative

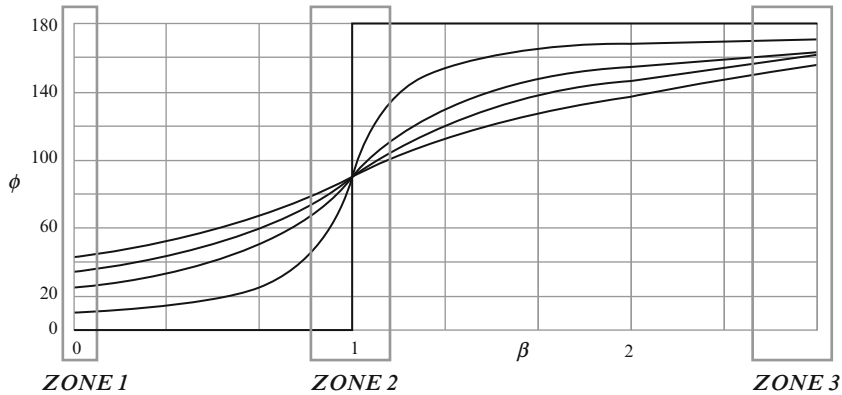


Fig. 2.29 Individuation of the three characteristic zones in the dynamic response phase

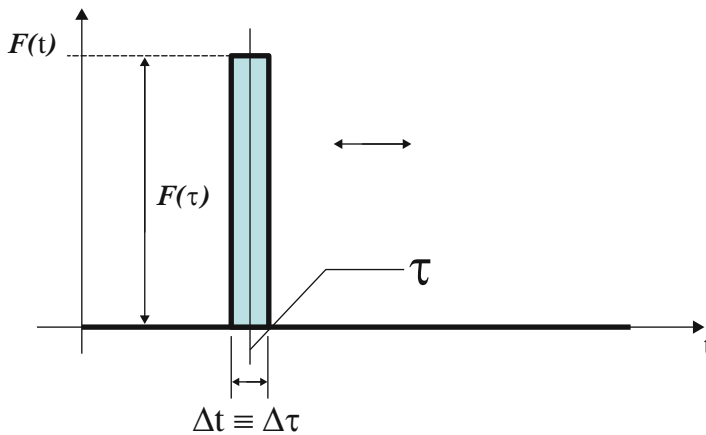


Fig. 2.30 Dirac function for a given generic time τ

force is able to cause damping. Figure 2.30 illustrates the classic impulsive force represented as a Dirac function.

The area of the rectangular elementary impulse is equal to one (Eq. 2.89)

$$I = \int_{-\infty}^{+\infty} F(t) \cdot dt = 1 \rightarrow F(t) = \frac{1}{\Delta t} \tag{2.89}$$

where I represents the impulse and Δt is the small finite value of the time range close to the given instant τ . Assuming the generic damped SDOF system on which

an impulse I is applied at time τ . The dynamic response of the system for $t > \tau$ can be evaluated according to the integrated equation of motion reported in Eq. 2.90.

$$I = \int_{-\infty}^t F(t) \cdot dt = \int_{-\infty}^t m \cdot \ddot{u} \cdot dt + \int_{-\infty}^t c \cdot \dot{u} \cdot dt + \int_{-\infty}^t k \cdot u \cdot dt \quad (2.90)$$

Each of the integral terms can be expressed as sum of three different contributions (Eq. 2.91).

$$\left\{ \begin{array}{l} \int_{-\infty}^{\tau^-} F(t) \cdot dt = \int_{-\infty}^{\tau^-} m \cdot \ddot{u} \cdot dt + \int_{-\infty}^{\tau^-} c \cdot \dot{u} \cdot dt + \int_{-\infty}^{\tau^-} k \cdot u \cdot dt \\ \int_{\tau^-}^{\tau^+} F(t) \cdot dt = \int_{\tau^-}^{\tau^+} m \cdot \ddot{u} \cdot dt + \int_{\tau^-}^{\tau^+} c \cdot \dot{u} \cdot dt + \int_{\tau^-}^{\tau^+} k \cdot u \cdot dt \\ \int_{\tau^+}^t F(t) \cdot dt = \int_{\tau^+}^t m \cdot \ddot{u} \cdot dt + \int_{\tau^+}^t c \cdot \dot{u} \cdot dt + \int_{\tau^+}^t k \cdot u \cdot dt \end{array} \right. \quad (2.91)$$

The first and third contributions of the external impulsive force are equal to zero by definition. In addition, all the reaction forces can be assumed null for $t < \tau^-$ since the impulse has not been applied yet. According to the momentum conservation principle (or impulse theorem), the damping and elastic terms evaluated in the range $\Delta t = (\tau^+ - \tau^-)$ are equal to zero. Furthermore, the inertia, stiffness and damping terms for $t > \tau^+$ have to be equilibrated with the external force which is null (vibrations conditions). Equation 2.92 reflects the aforementioned claims.

$$\begin{aligned} \int_{\tau^-}^{\tau^+} F(t) \cdot dt &= \int_{\tau^-}^{\tau^+} m \cdot \ddot{u} \cdot dt = 1 \\ \int_{\tau^-}^{\tau^+} F(t) \cdot dt &= \int_{\tau^+}^t m \cdot \ddot{u} \cdot dt + \int_{\tau^+}^t c \cdot \dot{u} \cdot dt + \int_{\tau^+}^t k \cdot u \cdot dt = 0 \end{aligned} \quad (2.92)$$

Since the impulse is defined for a small range time Δt the second term of the first equation can be expressed as shown in the Eq. 2.93.

$$\int_{\tau^-}^{\tau^+} F(t) \cdot dt = m \cdot [\dot{u}(\tau^+) - \dot{u}(\tau^-)] = 1 \quad (2.93)$$

Assuming the system is at rest before the application of the impulse ($\dot{u}(\tau^-) = 0$), the velocity immediately after the impulse can be evaluated (Eq. 2.94).

$$\dot{u}(\tau^+) = \frac{\int_{\tau^-}^{\tau^+} F(t) \cdot dt}{m} = \frac{1}{m} \quad (2.94)$$

Naturally, the displacement at time τ^+ is equal to zero since the system is at rest when the impulse is applied. Therefore, the problem is represented by the evaluation of the dynamic response of the system after the application of the impulsive external force ($u(t - \tau)$). As observed previously, it can be integrated into a free vibrations problem in which the initial conditions ($u(\tau(+)) = 0; \dot{u}(\tau(+)) = \frac{1}{m}$) are deduced according to the Eq.2.93 Remembering the solution found in Eq.2.24, the free vibrations response of the damped SDOF system is given by (Eq. 2.95).

$$u(t)_{\forall t > \tau} = \frac{\dot{u}(\tau^+)}{\omega_D} \cdot e^{-\xi \cdot \omega \cdot (t-\tau)} \cdot \sin [\omega_D \cdot (t - \tau)] = \frac{1}{m \cdot \omega_D} \cdot e^{-\xi \cdot \omega \cdot (t-\tau)} \cdot \sin [\omega_D \cdot (t - \tau)] \tag{2.95}$$

In Eq.2.96 the displacement response can be expressed in terms of differential value.

$$du(t)_{\forall t > \tau} = \frac{F(\tau) \cdot d\tau}{m \cdot \omega_D} \cdot e^{-\xi \cdot \omega \cdot (t-\tau)} \cdot \sin [\omega_D \cdot (t - \tau)] \tag{2.96}$$

Equation 2.96 represents the response due to an elementary impulse applied on the system at a given time τ . Thus, this definition can be used in order to evaluate the dynamic response of a SDOF system subjected to a generic time dependent excitation $F(t)$. In fact, an external force can be considered as sum of different elementary impulses (Harris and Piersol 2002) as shown in Fig. 2.31.

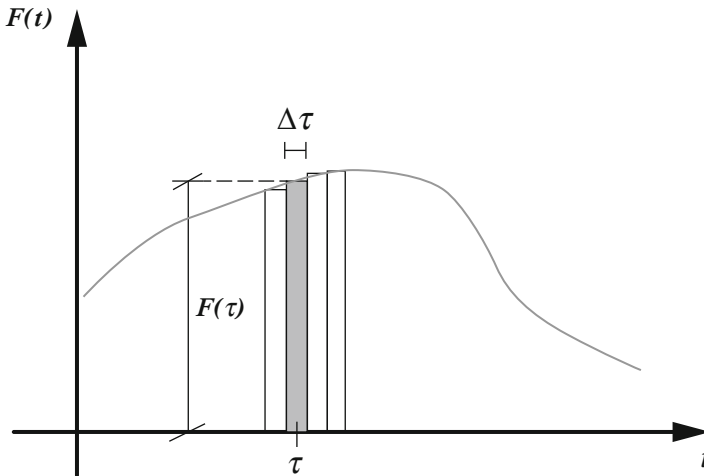


Fig. 2.31 Idealization of a generic external dynamic excitation in different elementary impulses

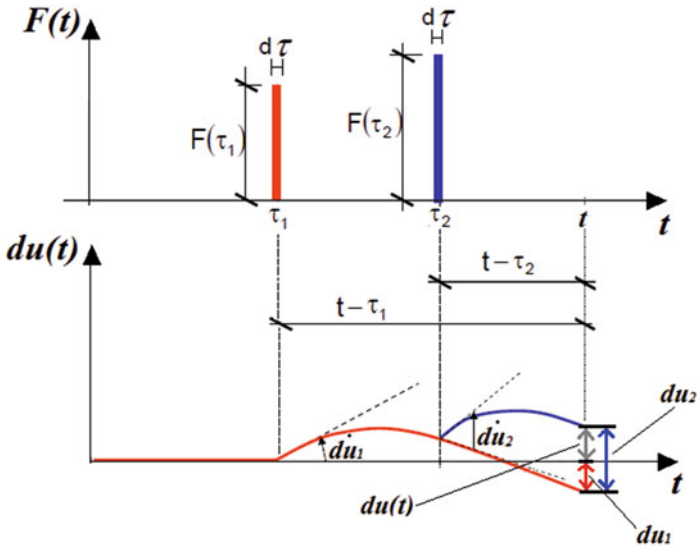


Fig. 2.32 Dynamic response of a system subjected to two impulses

Equation 2.97 defines the total dynamic response of a system subjected to a generic excitation.

$$du(t)_{\forall t > \tau} = \sum_{i=1}^n \frac{F(\tau_i) \cdot d\tau_i}{m \cdot \omega_D} \cdot e^{-\xi \cdot \omega \cdot (t - \tau_i)} \cdot \sin [\omega_D \cdot (t - \tau_i)] \quad (2.97)$$

In order to understand the mathematical approach proposed, an example is reported in the Fig. 2.32 where the external excitation is expressed by two shifted impulses.

Therefore, the total dynamic response of a forced SDOF system at a specific time t can be mathematically expressed by an integral between zero and the given time. The resulting expression is named the Duhamel integral and it is represented in the Eq. 2.98 (Clough and Penzien 1993).

$$u(t) = \frac{1}{m \cdot \omega_D} \int_0^t F(\tau_i) \cdot e^{-\xi \cdot \omega \cdot (t - \tau_i)} \cdot \sin [\omega_D \cdot (t - \tau_i)] \cdot dt \quad (2.98)$$

This dynamic response refers to the generic case in which the system is initially at rest. In order to provide the dynamic response having different initial conditions, the free vibration contribution has to be assumed (Eq. 2.99).

$$u(t) = \frac{\dot{u}_0}{\omega} \cdot \sin(\omega \cdot t) + u_0 \cdot \cos(\omega \cdot t) + \frac{1}{m \cdot \omega_D} \int_0^t F(\tau_i) \cdot e^{-\xi \cdot \omega \cdot (t - \tau_i)} \cdot \sin [\omega_D \cdot (t - \tau_i)] \cdot dt \quad (2.99)$$

One can notice that the Duhamels integral represents the convolution between the impulse and the free vibration response (Eq. 2.100).

$$u(t) = \int_0^t f(\tau) \cdot h(t - \tau) \cdot d\tau \rightarrow \begin{cases} f(\tau) = F(\tau) \\ h(t - \tau) = e^{-\xi \cdot \omega \cdot (t - \tau_i)} \cdot \sin[\omega_D \cdot (t - \tau_i)] \end{cases} \quad (2.100)$$

Since the mathematical procedure used for the Duhamel's integral is based on the superposition of effects, it is valid only for linear elastic systems. In addition, if the external force is described by a simple function, the Duhamel integral can be solved in closed form.

2.4 Response to a Periodic Excitation

When the external exciting force is periodic, it can be expressed as sum of trigonometric harmonic functions. This approach is named Fourier series analysis (Brigham 1988) and will be discussed in detail in the Sect. 3.3 (Brigham 1988). Equation 2.101 shows the series decomposition of the periodic excitation according to Fourier.

$$F(t) = a_0 \cdot \sum_{n=1}^{\infty} a_n \cdot \cos(\omega_f \cdot n \cdot t) + \sum_{n=1}^{\infty} b_n \cdot \sin(\omega_f \cdot n \cdot t) \quad (2.101)$$

Remembering that the period T_f of the external force can be expressed as ratio between 2π and the frequency of the excitation ω_f , the coefficients of the Fourier series are given by Eq. 2.102.

$$\begin{cases} a_0 = \frac{1}{T_f} \int_0^{T_f} F(t) \cdot dt \\ a_n = \frac{2}{T_f} \int_0^{T_f} F(t) \cdot \cos\left(\frac{2\pi \cdot n}{T_f} \cdot t\right) \cdot dt \\ b_n = \frac{2}{T_f} \int_0^{T_f} F(t) \cdot \sin\left(\frac{2\pi \cdot n}{T_f} \cdot t\right) \cdot dt \end{cases} \quad (2.102)$$

Therefore, each of the harmonic functions produces a permanent dynamic response of the system depending on its exciting frequency and amplitude (Eq. 2.103).

$$u_p(t) = u_{p,a_0}(t) + \sum_{n=1}^{\infty} u_{p,a_n}(t) + \sum_{n=1}^{\infty} u_{p,b_n}(t) \quad (2.103)$$

The terms illustrated in the above equation are referred to as a_0 , a_n and b_n components of the total periodic excitation, respectively. The first contribution is a constant, while a_n and b_n vary with cosine and sinusoidal law. Naturally, the total permanent response is the superposition of the three aforementioned particular solutions (Eq. 2.104).

$$\begin{cases} u_{p,a_0}(t) = \frac{a_0}{k} \\ u_{p,a_n}(t) = \frac{a_n}{k} \cdot \frac{1}{(1-\beta_n^2)^2 + (2\xi\beta_n)^2} \cdot [2 \cdot \xi \cdot \beta_n \cdot \sin(\omega_n \cdot t) + (1 - \beta_n^2) \cdot \cos(\omega_n \cdot t)] \\ u_{p,b_n}(t) = \frac{b_n}{k} \cdot \frac{1}{(1-\beta_n^2)^2 + (2\xi\beta_n)^2} \cdot [(1 - \beta_n^2) \cdot \sin(\omega_n \cdot t) - 2 \cdot \xi \cdot \beta_n \cdot \cos(\omega_n \cdot t)] \end{cases} \quad (2.104)$$

where the n th frequency is expressed as n times the frequency of the exciting force ($\omega_n = n \cdot \omega_f$). Since β_n represents the ratio between ω_n and ω , it can be also defined as shown in Eq. 2.105.

$$\beta_n = \frac{\omega_n}{\omega} = n \cdot \frac{\omega_f}{\omega} = n \cdot \beta \quad (2.105)$$

Equation 2.106 illustrates the total dynamic response of the SDOF system.

$$\begin{aligned} u(t) = & e^{-\xi\omega t} \cdot [A_1 \cdot \cos(\omega_D \cdot t) + A_2 \cdot \sin(\omega_D \cdot t)] + \frac{a_0}{k} \\ & + \frac{1}{k} \cdot \sum_{n=1}^{\infty} \cdot \frac{1}{(1-\beta_n^2)^2 + (2 \cdot \xi \cdot \beta_n)^2} \cdot a_n \cdot [2 \cdot \xi \cdot \beta_n \cdot \sin(\omega_n \cdot t) + (1 - \beta_n^2) \cdot \cos(\omega_n \cdot t)] \\ & + \frac{1}{k} \cdot \sum_{n=1}^{\infty} \cdot \frac{1}{(1-\beta_n^2)^2 + (2 \cdot \xi \cdot \beta_n)^2} \cdot b_n \cdot [(1 - \beta_n^2) \cdot \sin(\omega_n \cdot t) - 2 \cdot \xi \cdot \beta_n \cdot \cos(\omega_n \cdot t)] \end{aligned} \quad (2.106)$$

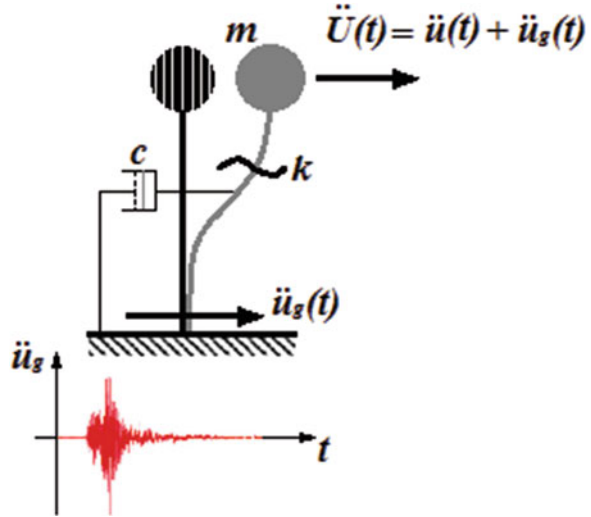
The coefficients A_1 and A_2 can be deduced by imposing the initial conditions.

2.5 Earthquake Response

The general definition of the problem is introduced in this paragraph, while all the solution methods will be discussed in detail in the Chap. 3. In Sect. 1.6 the generic equation of motion has been particularized for the earthquake excitation case (Eq. 2.107).

$$m \cdot \ddot{u} + c \cdot \dot{u} + k \cdot u = -m \cdot \ddot{u}_g \quad (2.107)$$

Fig. 2.33 Earthquake excitation on a SDOF damped system



In this case, the external excitation is composed by the inertial force due to the acceleration at the base (\ddot{u}_g) of the SDOF system (Eq. 2.108).

$$F(t) = -m \cdot \ddot{u}_g(t) \tag{2.108}$$

Figure 2.33 assumes the aforementioned characteristics for a generic SDOF system.

2.6 Transmissibility Function

It has been observed that the permanent dynamic response of a system subjected to an harmonic excitation can be expressed as a sinusoidal function having a phase lag. Equation 2.109 assumes the displacement and velocity response.

$$\begin{cases} u_p(t) = \frac{F_0}{k} \cdot |A| \cdot \sin(\omega_f \cdot t + \phi) \\ \dot{u}_p(t) = \omega_f \cdot \frac{F_0}{k} \cdot |A| \cdot \sin(\omega_f \cdot t + \phi) \end{cases} \tag{2.109}$$

Figure 2.34 shows a discrete SDOF damped system for which the evaluation of the action transmitted at its base (F_{TR}) will be explained.



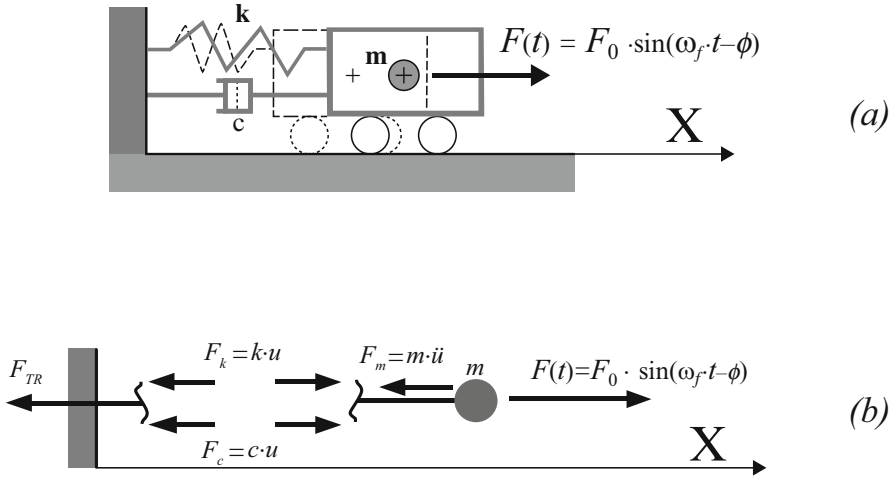


Fig. 2.34 Discrete SDOF damped system (a) and associated equilibrated forces arise (b)

For the dynamic equilibrium, the transmitted force is equal to the elastic and damping contribution. By substituting the value of displacement and velocity of the previous equation, the F_{TR} action can be evaluated (Eq. 2.110).

$$F_{TR}(t) = \frac{F_0}{k} \cdot |A| \cdot [c \cdot \omega_f \cdot \cos(\omega_f \cdot t + \phi) + k \cdot \sin(\omega_f \cdot t + \phi)] \quad (2.110)$$

Replacing c and k with the associated values in terms of natural angular frequency, the Eq. 2.111 can be written.

$$F_{TR}(t) = F_0 \cdot |A| \cdot [2 \cdot \xi \cdot \beta \cdot \cos(\omega_f \cdot t + \phi) + \sin(\omega_f \cdot t + \phi)] \quad (2.111)$$

Equating the first derivative of the above force with respect to the time to zero, it is possible to obtain the time in which the transmitted force achieves its maximum value (Eq. 2.112).

$$\frac{dF_{TR}(t)}{dt} = 0 \rightarrow t_{F_{TR}=\max} = \frac{1}{\omega_f} \cdot [\arctg(2 \cdot \xi \cdot \beta) + \phi] \quad (2.112)$$

Thus, the maximum transmissible force can be rewritten as a single harmonic function with phase lag due to the ϕ and $t_{F_{TR}=\max}$ contributions (Eq. 2.113).

$$F_{TR,MAX}(t) = F_0 \cdot |A| \cdot \sqrt{1 + (2 \cdot \xi \cdot \beta)^2} \cdot \sin(\omega_f \cdot t + \phi + t_{F_{TR}=\max}) \quad (2.113)$$

Since the equation reported above refers to a maximum value, the trigonometric term will be equal to the unit. With reference to this consideration, the ratio between

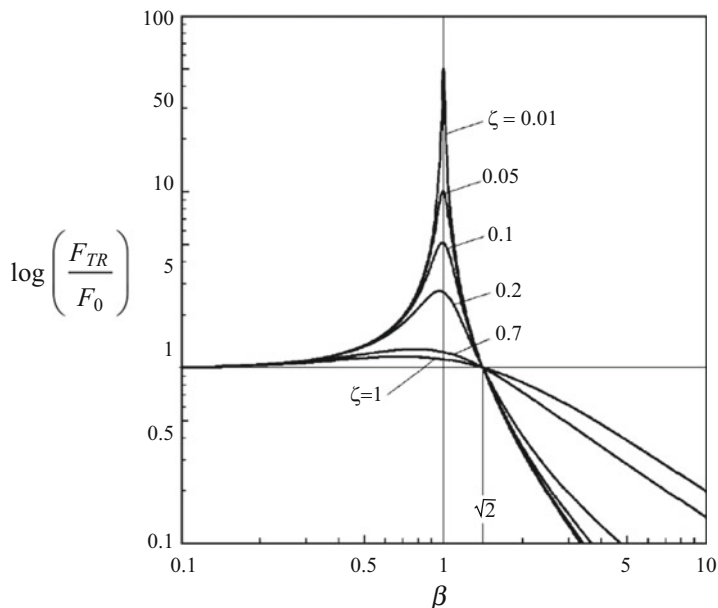


Fig. 2.35 Transmissibility functions for different values of damping ratios (Chopra 2001)

the maximum transmitted force at the base and the amplitude of the external force defines the maximum portion of the external harmonic excitation at the base of the system and is named the *transmissibility function* TF (Eq. 2.114).

$$TF = |A| \cdot \sqrt{1 + (2 \cdot \xi \cdot \beta)^2} = \sqrt{\frac{1 + (2 \cdot \xi \cdot \beta)^2}{(1 - \beta^2)^2 + (2 \cdot \xi \cdot \beta)^2}} \quad (2.114)$$

Figure 2.35 illustrates the trend of the $TF - \beta$ function including different values of damping ratio.

- $\beta < \sqrt{2}$: the *transmissibility function* is greater than one for every value of damping ratio. Furthermore, damping tends to decrease the value of the force transmitted to the base (amplification zone).
- $\beta > \sqrt{2}$: the *transmissibility function* is less than one while an increase in the damping ratio leads to values of transmissibility tending to one (attenuation zone).

The last case represents the isolation region for which the action at the base of the system is attenuated, compared with the external force. In this region small values of damping are desirable, since they tend to amplify the transmitted force. The concepts discussed represent the starting point for all the procedures and methodologies used to isolate a structure subjected to an earthquake. In addition, as

specified in Sect. 2.4, the irregular and periodic excitation due to an earthquake can be decomposed as the sum of infinite harmonic contributions with given frequency of excitation ω_n . In the case of earthquake excitation, the function TF indicates the transmitted action at the mass system due to the earthquake.

2.7 Nonlinear System Response

The amplitude of the external excitation may be such that the displacements of the system are greater than the elastic limit. In this case, the permanent deformations of the system must be considered, since the dynamic response is governed by the cyclic stress path. The stress-deformation function of the system component material is not regular, but it can be assumed regular by using simplified models. The elasto-plastic model is widely used in structural analyses since it is an idealized and consistent representation of the material behavior. Figure 2.36 illustrates the comparison between a real $F-u$ function and the elasto-plastic model for it.

The dashed line in Fig. 2.36a illustrates the real complete hysteretic cycle while the thick line shows its idealization with an elasto-plastic model. In Fig. 2.36b the main parameters describing the model are shown, while the list is indicated below:

- F_y and u_y represents the yielding force and displacement, respectively;
- u_e is the reversible displacement at the end of the positive load-unload cycle (elastic displacement);
- u_p is the irreversible displacement at the end of the positive load-unload cycle (plastic displacement);
- u_{max} defines the maximum displacement tolerated by the system.

It can be observed that the maximum allowable displacement is an index of the plastic dissipation. The total capacity of a system to dissipate energy as plastic deformation energy can be evaluated by the ratio reported below (Eq. 2.115).

$$\mu = \frac{u_{max}}{u_y} \quad (2.115)$$

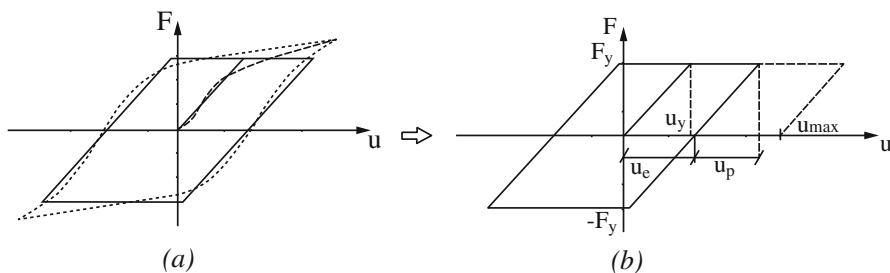


Fig. 2.36 Idealization of the load cycle (a) and characteristics of the elasto-plastic model (b)

This ratio is also called ductility factor. Naturally, other mechanical models are proposed in literature in attempts to define the referenced problem with different precision and complexity. In this case the equation of motion can be expressed as below reported (Eq. 2.116).

$$m \cdot \ddot{u} + c \cdot \dot{u} + k(u) \cdot u = F(t) \quad (2.116)$$

Different from the elastic case, the stiffness coefficient has to be evaluated according to the stress path idealized with the mechanical model. Nonlinear dynamic problems are solved using the numerical methods.

References

- Brigham E (1988) Oran: the fast Fourier transform and its applications. Prentice-Hall, Engelwood Cliffs
- Burton D (1988) The history of mathematics an introduction. McGraw Hill, New York
- Chopra AK (2001) Dynamics of structures: theory and applications to earthquake engineering, 2nd edn. Prentice Hall, Upper Saddle River
- Clough R, Penzien J (1993) Dynamic of structures. McGraw-Hill, New York
- Harris CM, Piersol AG (2002) Harris' shock and vibration handbook, vol 5. McGraw-Hill, New York
- Meirovitch L (2010) Fundamentals of vibrations. Waveland Press, Long Grove
- Rao SS (2007) Vibration of continuous systems. Wiley, Hoboken

Chapter 3

Methods of Solution of the Equation of Motion



Abstract The chapter analyzes different methods of solution of the equation of motion. The equation of motion for a forced SDOF system can be solved in closed form if the external excitation can be expressed as a harmonic function (analytical solution). Moreover, the dynamic response of a system subjected to a generic excitation can be evaluated using other approaches based on the decomposition of the irregular external force (*Fourier series* or *Duhamel integral* application). In these cases, the solution is achieved by the superposition property, so that they can be applied for a linear system. Clearly, this represents a limit to of the dynamic response of a real system in which the applied excitation causes irreversible deformation. In order to bypass the intrinsic limit of the previously proposed solution approaches, numerical methods are used. All the following examples and considerations are related to a damped SDOF system subjected to an external excitation.

3.1 Analytical Methods

In previous sections, it was observed that the response of a SDOF system is easily estimated in analytical form if the external force is expressed in a regular and periodic function. Figure 3.1 shows an exciting sinusoidal force acting on a SDOF system having an angular frequency $\omega_f = 2 \text{ rad/s}$ and an amplitude of $F_0 = 5 \text{ N}$.

The SDOF system having the characteristics reported in the Table 3.1 is considered as example.

In addition, the system is considered with initial displacement and velocity equal to zero ($u_0 = 0$ and $\dot{u}_0 = 0$). The equation of motion is expressed as follows (Eq. 3.1).

Fig. 3.1 External sinusoidal excitation with $\omega_f = 2$ rad/s and $F_0 = 5$ N

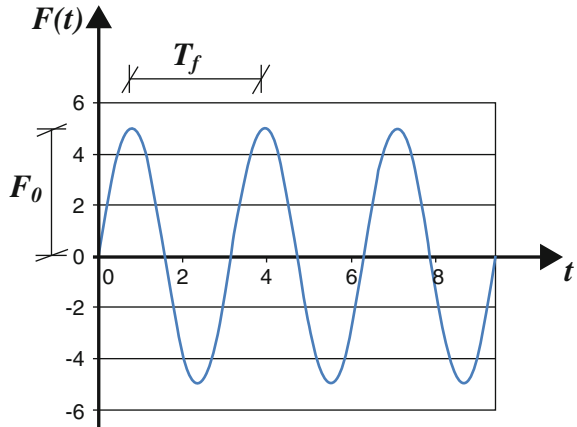


Table 3.1 Characteristics of the SDOF system

k [N/m]	ξ [%]	m [kg]
150	5	20

$$\begin{aligned}
 u(t) = & \frac{F_0}{k} \cdot (|A|)^2 \cdot (1 - \beta^2) \cdot [\sin(\omega_f \cdot t) - e^{-\xi \cdot \omega \cdot t} \cdot \beta \cdot \sin(\omega \cdot t)] + \\
 & - \frac{F_0}{k} \cdot (|A|)^2 \cdot (1 - \beta^2) \cdot 2 \cdot \xi \cdot \beta \cdot [\cos(\omega_f \cdot t) - e^{-\xi \cdot \omega \cdot t} \cdot \cos(\omega \cdot t)] + \\
 & + e^{-\xi \cdot \omega \cdot t} \cdot 2 \cdot \xi^2 \cdot \beta \cdot \sin(\omega \cdot t)
 \end{aligned} \quad (3.1)$$

The ratio between the elastic coefficient and mass gives information about the natural frequency (Eq. 3.2).

$$\omega = \sqrt{\frac{k}{m}} = 2.74 \text{ rad/s} \quad (3.2)$$

Thus, the frequency ratio and the dynamic amplification function can be evaluated (Eq. 3.3).

$$\left\{ \begin{array}{l} \beta = \frac{\omega_f}{\omega} = 0.73 \\ |A| = \frac{1}{\sqrt{(1-\beta^2)^2 + (2\xi\beta)^2}} = 1.46 \end{array} \right. \quad (3.3)$$

Substituting every calculated parameter, and supposing $\omega = \omega_D$, in the Eq. 3.1 the dynamic response of the system is found and is shown in Fig. 3.2.

Furthermore, Fig. 3.2 shows the maximum dynamic response (u_{max}) and the static one (u_s). It is possible that the maximum response occurs initially because the damping effects are not able to provide a sensible contribution yet. On the contrary, after a long period, the dissipated energy has achieved its maximum value and the free vibration term is equal to zero.

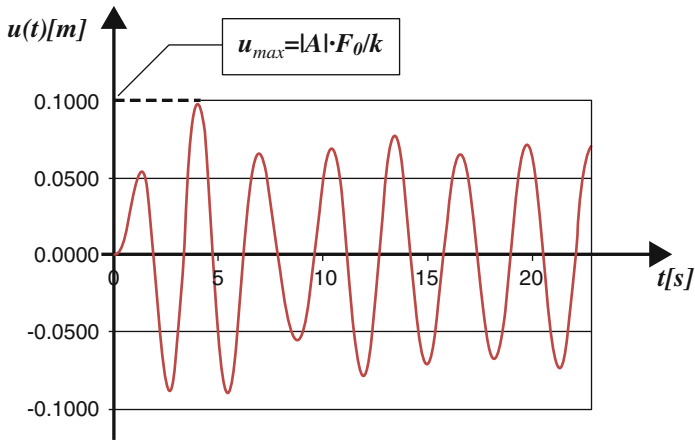
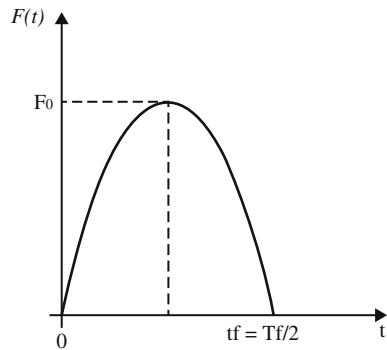


Fig. 3.2 Dynamic response of the SDOF system

Fig. 3.3 Impulsive sinusoidal excitation



The same system is considered with a sinusoidal force defined in the interval $[0, T_f/2]$ (Fig. 3.3).

This case can be represented as a system subjected to a sinusoidal impulse with amplitude F_0 (Chopra 2001). The dynamic response of the system is defined with reference to two different contributions:

- response of damped SDOF forced system for $t \leq t_f$;
- response of damped SDOF system in free vibrations for $t > t_f$ and with initial conditions coming from the previous response.

Since the load is applied impulsively, the maximum response of the system will be achieved suddenly after the application of the load. This consideration leads to the neglect of the damping effects in the response of the system because they are not able to dissipate a significant quantity of energy. Thus, the consideration of a forced response will be in reference to an undamped SDOF system. Equation 3.4 assumes the partial solution in terms of displacement, considering the system initially in rest.

$$\left\{ \begin{array}{l} t \leq t_f : u(t) = \frac{F_0}{k \cdot (1 - \beta^2)} \cdot [\sin(\omega_f \cdot t) - \beta \cdot \sin(\omega \cdot t)] \\ t > t_f : u(t) = e^{-\xi \cdot \omega \cdot (t - t_f)} \cdot \left\{ u(t_f) \cdot \cos(\omega_D \cdot (t - t_f)) + \frac{\dot{u}(t_f) + \xi \cdot \omega \cdot u(t_f)}{\omega_D} \cdot \sin(\omega_D \cdot (t - t_f)) \right\} \end{array} \right\} \quad (3.4)$$

Imposing $t = t_f$ in the first equation, the initial condition for the free vibrations can be evaluated (Eq. 3.5).

$$\left\{ \begin{array}{l} u(t_f) = \frac{F_0}{k \cdot (1 - \beta^2)} \cdot [\sin(\omega_f \cdot t_f) - \beta \cdot \sin(\omega \cdot t_f)] \\ \dot{u}(t_f) = \omega_f \cdot \frac{F_0}{k \cdot (1 - \beta^2)} \cdot [\cos(\omega_f \cdot t_f) - \cos(\omega \cdot t_f)] \end{array} \right\} \quad (3.5)$$

Substituting $t_f = T_f$ the Eq. 3.6 is obtained.

$$\left\{ \begin{array}{l} u(t_f) = \frac{F_0}{k \cdot (1 - \beta^2)} \cdot \left[\sin\left(\omega_f \cdot \frac{\pi}{2}\right) - \beta \cdot \sin\left(\omega \cdot \frac{\pi}{2}\right) \right] \\ \dot{u}(t_f) = \omega_f \cdot \frac{F_0}{k \cdot (1 - \beta^2)} \cdot \left[\cos\left(\omega_f \cdot \frac{\pi}{2}\right) - \cos\left(\omega \cdot \frac{\pi}{2}\right) \right] \end{array} \right\} \quad (3.6)$$

It can be observed that the displacement and velocity response of the system at time t_f depends on the frequency ratio and on the time duration of the impulse. Considering the studied case in which $t_f = T_f = \pi/2$, the Eq. 3.7 resumes the dynamic response at time t_f .

$$\left\{ \begin{array}{l} u(t_f) = 4.78 \cdot 10^{-2} \text{ m} \\ \dot{u}(t_f) = -8.58 \cdot 10^{-2} \text{ m/s} \end{array} \right\} \quad (3.7)$$

Substituting the values in the free vibration equation for damped SDOF system (Eq. 3.4), it is possible to obtain the dynamic response for $t > t_f$. Figure 3.4 illustrates the function $u(t) - t$ considering $\omega = \omega_D$ in the free vibration contributions.

Naturally, the response to an impulsive force depends on the time range over which it is defined, on the frequency ratio and on the shape. For this purpose, in the next part we will propose the case of a rectangular impulsive load (Fig. 3.5).

Even in this case, the dynamic response of the system can be decomposed into the forced and free vibration contribution. For the first one, the equation of motion can be expressed in the following way (Eq. 3.8).

$$m \cdot \ddot{u} + k \cdot u = F_0 \quad (3.8)$$

The damping contribution has been neglected as explained above, while the second term of the equation assumes a constant value. In this case, the particular homogeneous associated solutions can be expressed as shown in the Eq. 3.9.

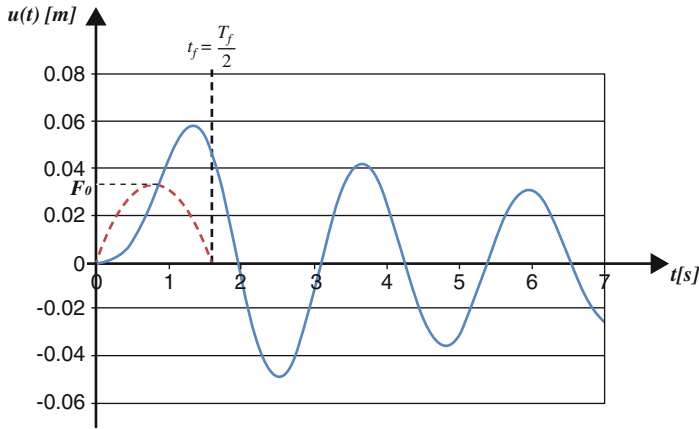
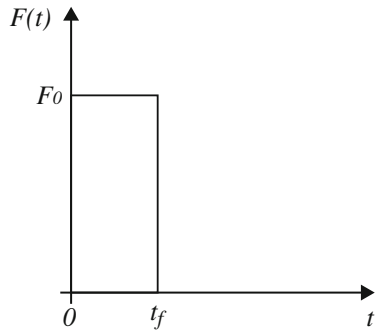


Fig. 3.4 Dynamic response for a SDOF system subjected to a sinusoidal impulse

Fig. 3.5 Rectangular impulse



$$\begin{cases} u_p(t) = \frac{F_0}{k} \\ u_0(t) = A_1 \cos(\omega \cdot t) + A_2 \sin(\omega \cdot t) \end{cases} \quad (3.9)$$

Imposing the initial conditions associated to a system at rest, the solution of the equation of motion for the forced SDOF system is given as (Eq. 3.10).

$$t \leq t_f : u(t) = \frac{F_0}{k} \cdot [1 - \cos(\omega \cdot t)] \quad (3.10)$$

From this equation, the displacement and velocity at time t_f can be evaluated to define the free vibrations response for $t > t_f$ (Eq. 3.11).

$$\begin{cases} u(t_f) = \frac{F_0}{k} \cdot [1 - \cos(\omega \cdot t_f)] \\ \dot{u}(t_f) = \omega \cdot \frac{F_0}{k} \cdot [1 + \sin(\omega \cdot t_f)] \end{cases} \quad (3.11)$$

Fig. 3.6 Dynamic response for a SDOF system subjected to a rectangular impulse

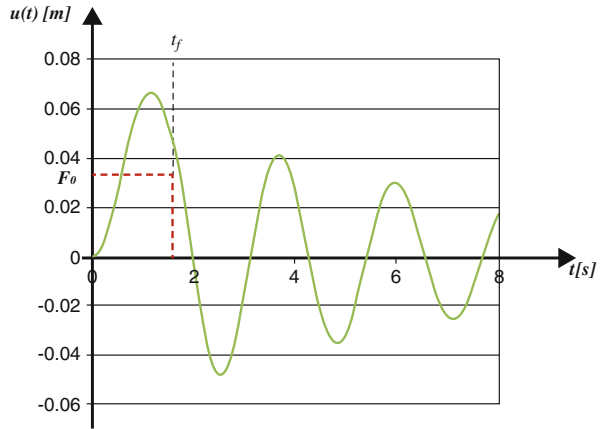
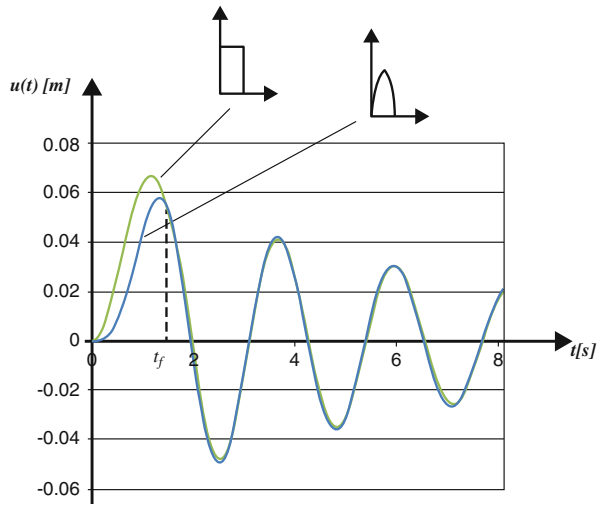


Fig. 3.7 Comparison between the responses of a SDOF system subjected to rectangular and sinusoidal impulse



Assuming also in this case that $t_f = \pi/2$, the Fig. 3.6 shows the dynamic response of the system to the rectangular impulse.

In order to highlight the difference in the response between rectangular and sinusoidal impulse, the Fig. 3.7 is proposed.

The dynamic responses for rectangular and sinusoidal impulses have the same shape in the free vibration range, but different amplifications. In fact, it is possible to observe that the rectangular impulse produces a greater amplification than the sinusoidal one. As observed previously, the dynamic response of the system is a function of the impulse duration and the frequency ratio. In reference to the first aspect, a comparison of the $|A| - (t_f/T_f)$ function between different shapes of the impulse is proposed in Fig. 3.8.

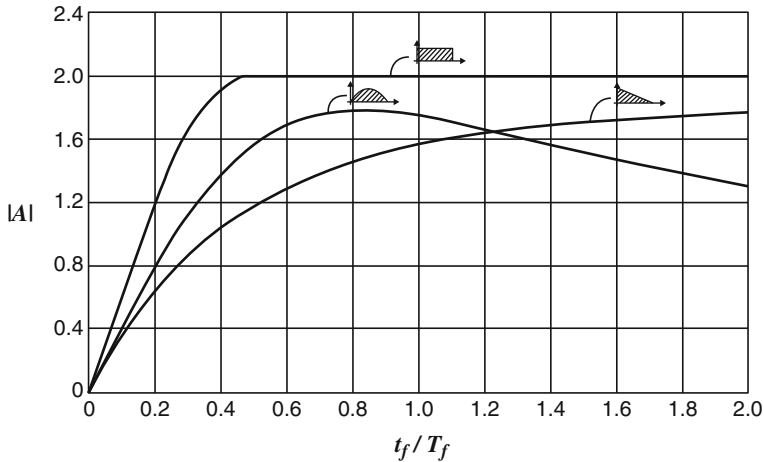


Fig. 3.8 Dynamic amplification function depending on the duration of the impulse for rectangular, sinusoidal and triangular shapes (Carpinteri 1998)

3.2 Duhamel's Integral

In Sect. 2.3 the Duhamel integral has been introduced to evaluate the dynamic response of a linear SDOF system subjected to a generic excitation (Harris and Piersol 2002). Equation 3.12 shows again the Duhamel's integral which is valid for a SDOF damped system initially at rest.

$$u(t) = \frac{1}{m \cdot \omega_D} \int_0^t F(\tau_i) \cdot e^{-\xi \cdot \omega \cdot (t-\tau_i)} \cdot \sin [\omega_D \cdot (t - \tau_i)] \cdot dt \tag{3.12}$$

Usually the external force assumes a complex form that leads to a non-closed form solution of the problem. In many cases, the Duhamel integral is expressed in discrete form to obtain the solution numerically. At this purpose, the generic excitation is expressed as the sum of several finite small rectangular force contributions. Thus, if Δt is the sampling time interval, the previous relation can be expressed as shown in Eq. 3.13.

$$u(t) = \frac{1}{m \cdot \omega_D} \sum_{j=1}^N F(j \cdot \Delta t) \cdot e^{-\xi \cdot \omega \cdot (t-j \cdot \Delta t)} \cdot \sin [\omega_D \cdot (t - j \cdot \Delta t)] \cdot \Delta t \tag{3.13}$$

Consider the sinusoidal impulse problem observed in the previous section, divided into four rectangular contributions (Fig. 3.9).

Assuming $t_f = \pi/2$, the sampling time chosen is equal to $\Delta t = \pi/8$. In addition, the force values associated with each rectangle is assumed to be a mean value

Fig. 3.9 Discretization of half sinusoidal excitation

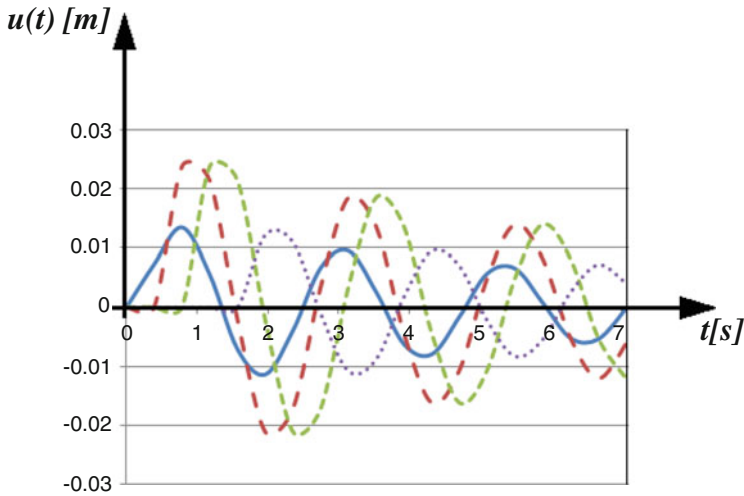
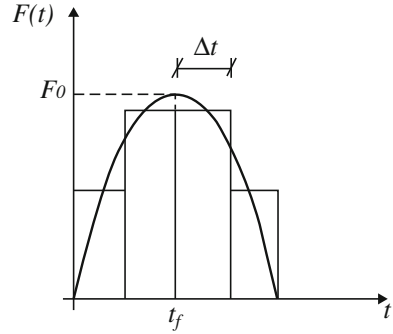


Fig. 3.10 Different dynamic response contributions due to the four discretized rectangular impulses

deduced from the exciting function. Assuming $\omega = \omega_D$, the dynamic response of the system is evaluated by the sum of the four discrete contributions. For this purpose, Fig. 3.10 illustrates each of the dynamic responses.

The sum of all the contributions gives the total dynamic response of the SDOF system (Fig. 3.11).

Typically, the accuracy of the method used depends on the sampling interval chosen to discretize the exciting force. It is very interesting to compare the results obtained with the analytical method and with the discretized Duhamel's formulation (Fig. 3.12).

The difference between the two functions is due to the different idealizations of the exciting force. Clearly, if $\Delta t \rightarrow \infty$, then the Duhamel's solution will be equal to the analytical one.

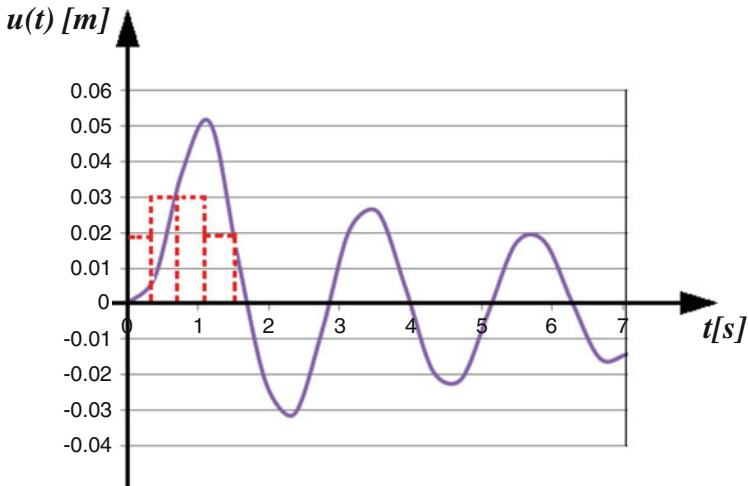


Fig. 3.11 Total dynamic response due to a discretized sinusoidal exciting force

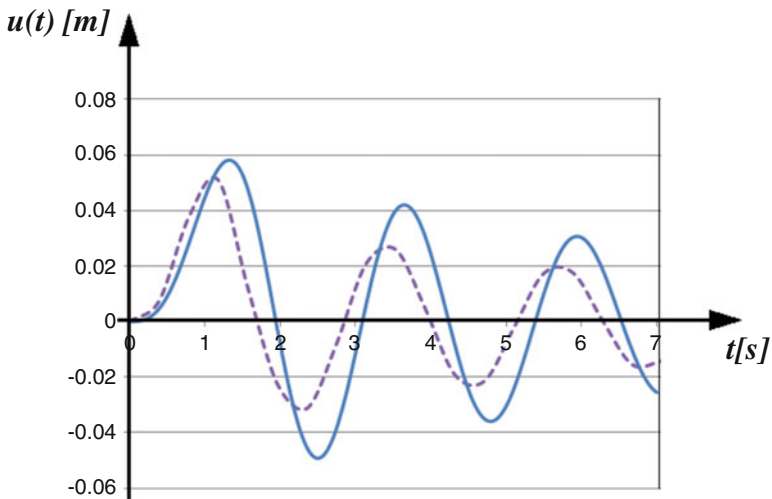
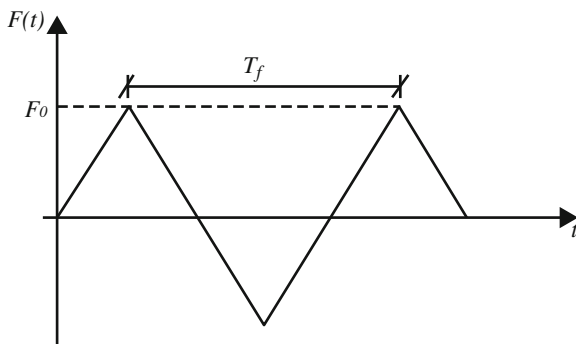


Fig. 3.12 Comparison between the dynamic response obtained using an analytical solution and discrete Duhamel's integral (dashed line)

3.3 Fourier Series

The irregular periodic excitation can be decomposed into several harmonic functions with given frequency and phase (Brigham 1988). Equation 2.106 proposed in Sect. 2.4 shows the total response of the system, in which the external excitation has been expressed in Fourier series. The number of harmonic functions required to

Fig. 3.13 Triangular periodic excitation



achieve the convergence of the series is infinite, but in practice, a finite number is sufficient for achieving an adequate convergence. For example, a periodic triangular excitation with period $T_f = \pi$ and amplitude $F_0 = 5$ N is used to evaluate the dynamic response of the system according to the Fourier series approach (Fig. 3.13).

The definition of the periodic excitation in its period is reported in Eq. 3.14.

$$\begin{cases} F(t) = 8 \cdot \frac{F_0}{T_f} \cdot t \rightarrow \text{for } : 0 \leq t < T_f/2 \\ F(t) = -8 \cdot \frac{F_0}{T_f} \cdot t \rightarrow \text{for } : T_f/2 \leq t < T_f \end{cases} \quad (3.14)$$

The triangular excitation can be defined as shown in Eq. 3.15 using Eq. 2.102 of Sect. 2.4 to evaluate the characteristic coefficients.

$$F(t) = \frac{8 \cdot F_0}{\pi^2} \cdot \sum_{n=0}^{\infty} (-1)^n \cdot \frac{\sin(\omega_f \cdot t \cdot (2 \cdot n + 1))}{(2 \cdot n + 1)^2} \quad (3.15)$$

In order to simplify the calculation procedure, only four harmonic contributions will be considered. Figure 3.14 illustrates the comparison between the triangular function and the associated series obtained with $n = 1$.

Summing all the harmonic contributions, we obtain the Fourier series (Fig. 3.15).

It can be observed that the number of harmonic contributions chosen to define the triangular function results adequate. Therefore, the dynamic response of the system can be evaluated by superposition of the effects due to every harmonic function. Assuming the case of an undamped system, the dynamic response can be expressed as shown in the Eq. 3.16.

$$u(t) = A_1 \cdot \cos(\omega \cdot t) + A_2 \cdot \sin(\omega \cdot t) + \frac{\frac{8 \cdot F_0}{\pi^2} \cdot \sum_{n=0}^1 (-1)^n \cdot \frac{\sin(\omega_f \cdot t \cdot (2 \cdot n + 1))}{(2 \cdot n + 1)^2}}{k \cdot (1 - \beta^2)} \quad (3.16)$$

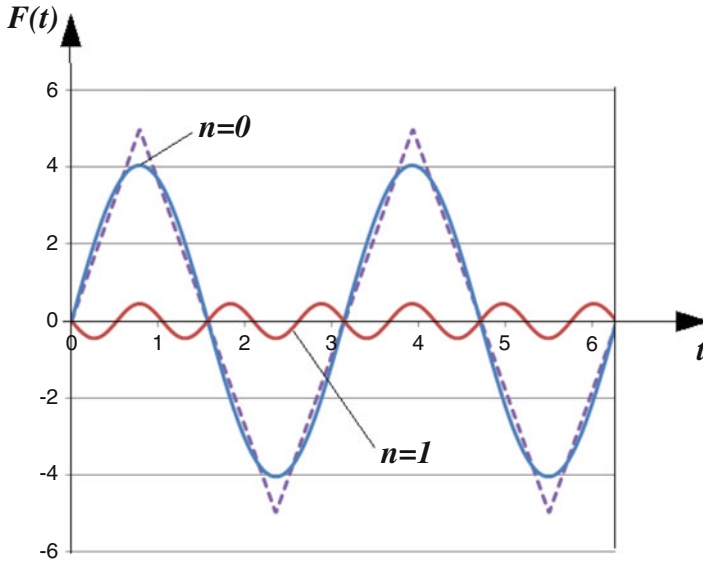


Fig. 3.14 Comparison between triangular function and four harmonic functions

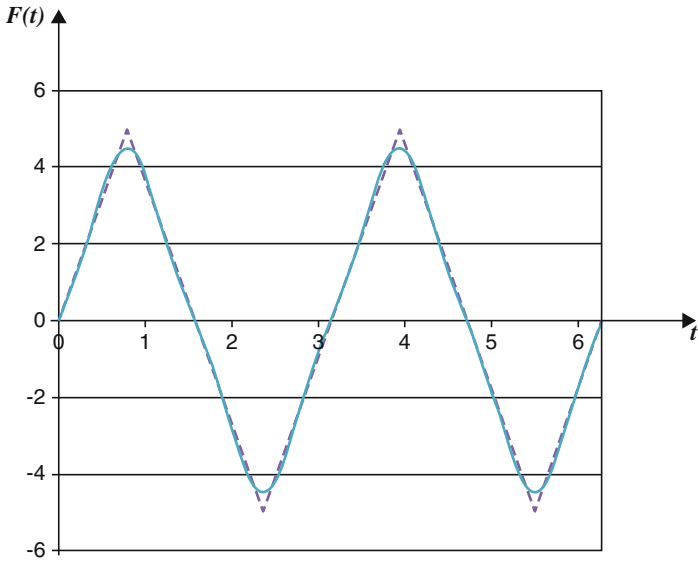


Fig. 3.15 Triangular function (dashed line) and Fourier series obtained with $n = 1$

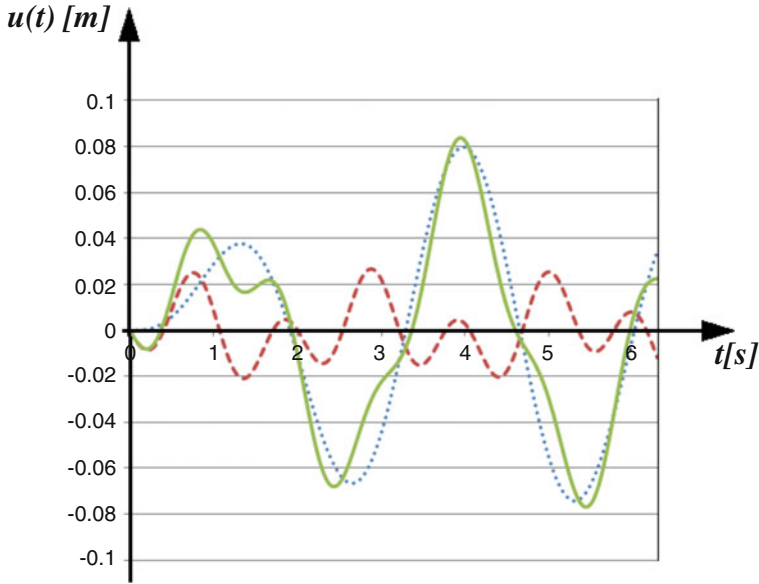


Fig. 3.16 Total dynamic response (continuous line) and response due to the two harmonic functions (dashed lines)

Imposing the initial conditions $u(0) = 0$ and $\dot{u}(0) = 0$, the coefficient A_1 and A_2 can be determined (Eq. 3.17).

$$A_1 = 0$$

$$A_2 = -\frac{8 \cdot F_0}{k \cdot \pi^2 \cdot (1 - \beta^2)} \cdot \beta \cdot \sum_{n=0}^{\infty} \frac{(-1)^n}{(2n+1)^2} \quad (3.17)$$

Equation 3.18 illustrates the dynamic response of the undamped system.

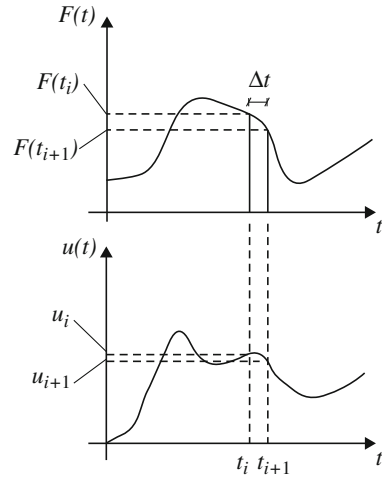
$$u(t) = \frac{8 \cdot F_0}{k \cdot \pi^2 \cdot (1 - \beta^2)} \cdot \sum_{n=0}^{\infty} \frac{(-1)^n}{(2n+1)^2} \cdot [\sin(\omega_f \cdot t \cdot (2n+1)) - (2n+1) \cdot \beta \cdot \sin(\omega \cdot t)] \quad (3.18)$$

In the Fig. 3.16 the response of the SDOF undamped system is compared to the two solutions due to the harmonic function of the Fourier series.

3.4 Numerical Methods

An analytical solution of the equation of motion for SDOF system is not usually possible, since the exciting force has an irregular trend in the time domain (e.g. earthquake excitation). Additionally, the amplitude of the load can induce nonlinear

Fig. 3.17 Time stepping schematization for a given time interval



mechanical effects on the system, so the method based on the superposition of the effects (e.g. Duhamel's integral and Fourier series) cannot be applied. Thus, the numerical time-stepping methods based on the integration of differential equations of motion are commonly used for the dynamic analysis. In the time stepping approach, the solutions are achieved by discretization of the time domain with constant or variable time interval Δt_i . Therefore, the problem is expressed in terms of evaluation of the dynamic response of the system at time step $i+1$, knowing its conditions at the previous time step i . Figure 3.17 illustrates graphically the concepts just explained.

Different time stepping procedures can be developed and each of them is characterized by the following requirements:

- *Stability*: refers to the error propagation and a numerical method can be defined stable if the round-off errors are not increasing in the calculation procedure;
- *Accuracy*: if the numerical method gives a solution closer to the real one;
- *Convergence*: if the absolute error tends to zero as the time step decreases.

The solution at generic time t_{i+1} can be evaluated with reference to the solution at previous time t_i . In this case, the numerical method is named the *explicit method*, while if the solution at instant t_{i+1} is defined directly from the equation at the same time step, the numerical method is called *implicit* (Chopra 2001). In the next part, the main numerical methods used in the dynamic analysis will be discussed.

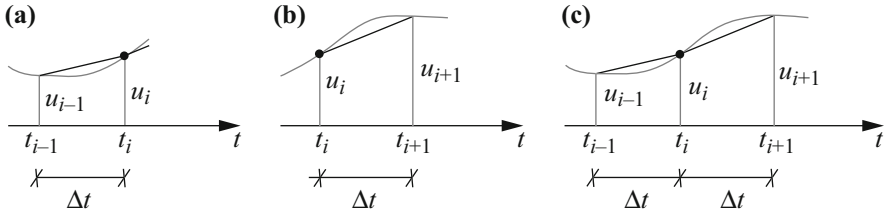


Fig. 3.18 Forward difference (a), backward differences (b) and central difference (c)

3.4.1 Explicit Methods

3.4.1.1 Finite Differences Method

This method is based on the assumption that the displacement and its derivatives are finite differences ($dt \rightarrow \Delta t$ and $du \rightarrow \Delta u$) (Klaus-Jurgen and Wilson Edward 1976). The first and second finite derivatives of displacement with respect to the time can be defined according to forward, backward or central difference approaches (Fig. 3.18).

Equations 3.19 and 3.20 show the first and second finite derivatives of displacement with respect to the time for the cases of *forward* and *central differences*, respectively.

$$\begin{cases} \dot{u}_i \approx \frac{u(t_{i+1}) - u(t_i)}{\Delta t} \\ \ddot{u}_i \approx \frac{u(t_{i+1} + \Delta t) - 2 \cdot u(t_{i+1}) + u(t_i)}{\Delta t^2} \end{cases} \quad (3.19)$$

$$\begin{cases} \dot{u}_i \approx \frac{u(t_{i+1}) - u(t_{i-1}))}{2 \cdot \Delta t} \\ \ddot{u}_i \approx \frac{u(t_{i+1}) - 2 \cdot u(t_i) + u(t_{i-1}))}{\Delta t^2} \end{cases} \quad (3.20)$$

The central difference method is more accurate than the forward or backward ones. Thus, the central differences method is preferred in practical applications. Substituting the expression of the first and second derivatives, obtained as finite differences, into the generic equation of motion for a SDOF damped system subjected to an exciting force $F(t)$, the Eq. 3.21 can be found.

$$\left[\frac{m}{\Delta t^2} + \frac{c}{2 \cdot \Delta t} \right] \cdot u_{i+1} + \left[k - \frac{2 \cdot m}{\Delta t^2} \right] \cdot u_i + \left[\frac{m}{\Delta t^2} - \frac{c}{2 \cdot \Delta t} \right] \cdot u_{i-1} = F(t_i) \quad (3.21)$$

The explicit solution of the equation is represented by the displacement of the system at time t_{i+1} using known displacement at previous steps (t_i and t_{i-1}). Using the displacement solution, the velocity and acceleration responses at referenced time

instant i can be evaluated using the Eq. 3.20. The initial conditions of the system ($t_i = 0$) and at time $t-1$ are required for the evaluation of the first displacement solution (u_1). In this case the $u-1$ value is not known since it does not have a physical meaning, but it can be mathematically evaluated by substitution of u_1 relation in the \dot{u}_i one obtained by the Eq. 3.22.

$$u_{-1} = u_0 - \Delta t \cdot \dot{u}_0 + \frac{\Delta t^2}{2} \cdot \ddot{u}_0 \quad (3.22)$$

where the acceleration at time $t_0 = 0$ is evaluated according to the equation of motion for the given time (Eq. 3.23).

$$m \cdot \ddot{u}_0 + c \cdot \dot{u}_0 + k \cdot u_0 = F(t_0) \quad (3.23)$$

For a dynamic system, the stability of the central difference method is satisfied according to the following equation (Eq. 3.24).

$$\frac{\Delta t}{T_n} \leq \frac{1}{\pi} \quad (3.24)$$

where T_n represents the fundamental period of the system. Let's consider the case of the elastic SDOF damped system subjected to a sinusoidal load proposed in Sect. 3.1. Since the system is initially at rest, the value of displacement at instant t_{-1} is equal to zero. Assuming $\Delta t = 0.1$ s and substituting the mass, spring and damping coefficient, the equation of motion can be written again (Eq. 3.25).

$$2.03 \cdot u_{i+1} - 3.85 \cdot u_i + 1.97 \cdot u_{i-1} = F(t_i) \cdot 10^{-3} \quad (3.25)$$

Thus, the displacement at time step t_{i+1} can be evaluated. Figure 3.19 shows the dynamic response of the system in terms of displacements, while in Table 3.2 the numerical results are summarized.

3.4.1.2 Runge-Kutta Method

In the Runge-Kutta approach, the solution at time $i+1$ is obtained by an approximate evaluation of the function values in a number of points (n) inside the interval (Epperson 2013). The accuracy of this method is directly proportional to the number of points that defines the order of the method. For a *fourth order method*, a balanced equation is used to achieve a good approximation (Eq. 3.26).

$$u_{i+1} = u_i + (c_1 \cdot k_1 + c_2 \cdot k_2 + c_3 \cdot k_3 + c_4 \cdot k_4) \cdot \Delta t \quad (3.26)$$

The term multiplied by the time interval defines the average slope of the function in the considered interval. In addition, k_i coefficients represent the increments obtained

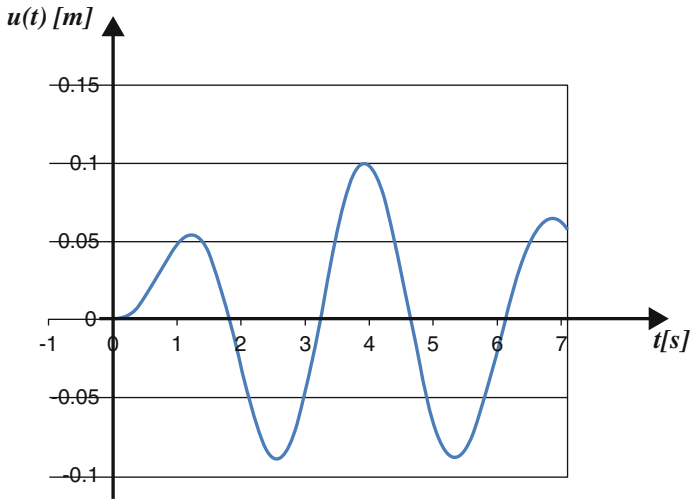


Fig. 3.19 Dynamic response of the system evaluated with central differences method for $\Delta t = 0.1$ s

Table 3.2 Numerical solutions obtained by the central differences method ($\Delta t = 0.1$ s)

i	t [s]	F(t) [N]	u(t) [m]	v(t) [m/s]	a(t) [m/s ²]
-1	0	0	0.0000	0.0000	0.0000
0	0	0	0.0000	0.0000	0.0000
1	0.1	0.99	0.0000	0.0024	0.0490
2	0.2	1.95	0.0005	0.0095	0.0911
3	0.3	2.82	0.0019	0.0201	0.1215
4	0.4	3.59	0.0045	0.0330	0.1365
5	0.5	4.21	0.0085	0.0465	0.1340
6	0.6	4.66	0.0138	0.0589	0.1133
7	0.7	4.93	0.0203	0.0683	0.0757
8	0.8	5.00	0.0275	0.0733	0.0238
9	0.9	4.87	0.0349	0.0726	-0.0383
10	1.0	4.55	0.0420	0.0654	-0.1055
11	1.1	4.04	0.0480	0.0515	-0.1720
12	1.2	3.38	0.0523	0.0313	-0.2319
13	1.3	2.58	0.0543	0.0057	-0.2796
14	1.4	1.67	0.0534	-0.0238	-0.3105
15	1.5	0.71	0.0495	-0.0553	-0.3209
...

as the product between the indicated interval (e.g. Δt) and an estimate of the function slope (Butcher 1963). To be more precise, these increments are assumed as described below:

- k_1 : based on the slope at time t_i by using $f_1 = f(t_i)$;

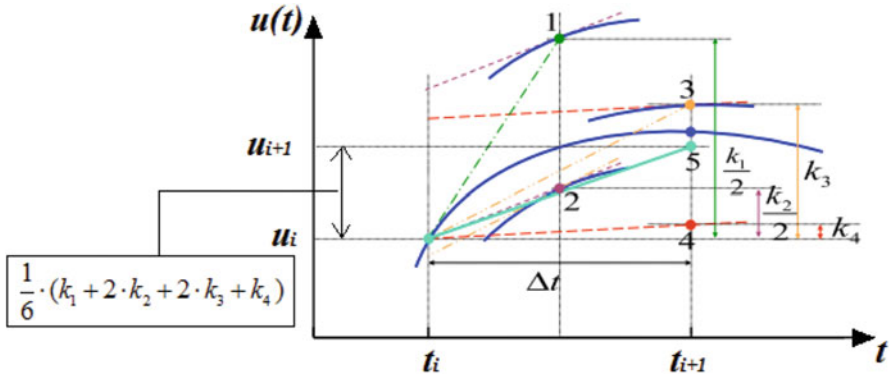


Fig. 3.20 Coefficients k_i identification and definition of the average slope

- k_2 : based on the slope at time $\frac{t_{i+1} + t_i}{2}$ by using the estimate $f_2 = f(t_i) + \frac{\Delta t}{2} \cdot k_1$;
- k_3 : based on the slope at time $\frac{t_{i+1} + t_i}{2}$ by using the estimate $f_3 = f(t_i) + \frac{\Delta t}{2} \cdot k_2$;
- k_4 : based on the slope at time t_{i+1} by using $f_4 = f(t_i) + \Delta t \cdot k_3$;

According to this definitions, the Eq. 3.27 defines the mathematical expression of the coefficient k_i .

$$\begin{cases} k_1 = f(t_i, u_i) = \left[\frac{du}{dt} \right] \text{for } : t = t_i; u = u_i \\ k_2 = f\left(t_i + \frac{\Delta t}{2}, u_i + k_1 \cdot \frac{\Delta t}{2}\right) = \left[\frac{du}{dt} \right] \text{for } : t = t_i + \frac{\Delta t}{2}; u = u_i + k_1 \cdot \frac{\Delta t}{2} \\ k_3 = f\left(t_i + \frac{\Delta t}{2}, u_i + k_2 \cdot \frac{\Delta t}{2}\right) = \left[\frac{du}{dt} \right] \text{for } : t = t_i + \frac{\Delta t}{2}; u = u_i + k_2 \cdot \frac{\Delta t}{2} \\ k_4 = f\left(t_i + \Delta t, u_i + k_3 \cdot \Delta t\right) = \left[\frac{du}{dt} \right] \text{for } : t = t_i + \Delta t; u = u_i + k_3 \cdot \Delta t \end{cases} \quad (3.27)$$

The definitions of the coefficients above reported are shown in Fig. 3.20.

Furthermore, the coefficients c_i are below reported (Eq. 3.28).

$$c_1 = c_4 = \frac{1}{6}; \quad c_2 = c_3 = \frac{1}{3} \quad (3.28)$$

Thus, the solution to the problem can be expressed as shown in Eq. 3.29.

$$u_{i+1} = u_i + \frac{1}{6} \cdot (k_1 + 2 \cdot k_2 + 2 \cdot k_3 + k_4) \cdot \Delta t \quad (3.29)$$

This method is explicit because the solution at time t_{i+1} depends on k_i coefficients that are based on the first derivative of the independent variable at time $t_i(\dot{u}(t_i))$. There is no specific method for choosing the time interval Δt . It must be not so large as to cause stability problems (e.g. stiff equations) nor too small because the numerical process could be impossible to solve. Since the dynamic motion is described by a second order differential equation, the Runge-Kutta method can

be applied by definition of an equivalent system of two linear ordinary first order differential equations (Eq. 3.30).

$$m \cdot \ddot{u} + c \cdot \dot{u} + k \cdot u = F(t) \rightarrow \begin{cases} \dot{u} = v \\ \dot{v} = \frac{1}{m} \cdot (F(t) - k \cdot u - c \cdot v) \end{cases} \quad (3.30)$$

The SDOF damped system used in the previous section is considered to evaluate the dynamic response with *fourth order Runge-Kutta method*. Since the equation of motion has to be decomposed into two ordinary differential equations, two sets of coefficients k_i have to be determined (Eq. 3.31).

$$\begin{cases} k_1(I) = v_i \\ k_2(I) = v_i + k_1(II) \cdot \frac{\Delta t}{2} \\ k_3(I) = v_i + k_2(II) \cdot \frac{\Delta t}{2} \\ k_4(I) = v_i + k_3(II) \cdot \Delta t \\ k_1(II) = \frac{1}{m} \cdot (F(t_i) - k \cdot u_i - c \cdot v_i) \\ k_2(II) = \frac{1}{m} \cdot \left[F\left(t_i + \frac{\Delta t}{2}\right) - k \cdot \left(u_i + k_1(I) \cdot \frac{\Delta t}{2}\right) - c \cdot \left(v_i + k_1(II) \cdot \frac{\Delta t}{2}\right) \right] \\ k_3(II) = \frac{1}{m} \cdot \left[F\left(t_i + \frac{\Delta t}{2}\right) - k \cdot \left(u_i + k_2(I) \cdot \frac{\Delta t}{2}\right) - c \cdot \left(v_i + k_2(II) \cdot \frac{\Delta t}{2}\right) \right] \\ k_4(II) = \frac{1}{m} \cdot [F(t_i + \Delta t) - k \cdot (u_i + k_3(I) \cdot \Delta t) - c \cdot (v_i + k_3(II) \cdot \Delta t)] \end{cases} \quad (3.31)$$

where v_i represents the velocity of the SDOF system mass at generic time t_i ($v_i = \dot{u}_i$). According to Runge-Kutta method, the displacement and velocity response will assume the following form (Eq. 3.32).

$$\begin{cases} u_{i+1} = u_i + \frac{1}{6} \cdot [k_1(I) + 2 \cdot k_2(I) + 2 \cdot k_3(I) + k_4(I)] \cdot \Delta t \\ \dot{u}_{i+1} = \dot{u}_i + \frac{1}{6} \cdot [k_1(II) + 2 \cdot k_2(II) + 2 \cdot k_3(II) + k_4(II)] \cdot \Delta t \\ \ddot{u}_{i+1} = \frac{1}{m} \cdot (F(t_i + \Delta t) - k \cdot u_{i+1} - c \cdot \dot{u}_{i+1}) \end{cases} \quad (3.32)$$

Figure 3.21 illustrates the displacements of the SDOF damped system analyzed.

In addition, some of the numerical values obtained are provided in the Table 3.3.

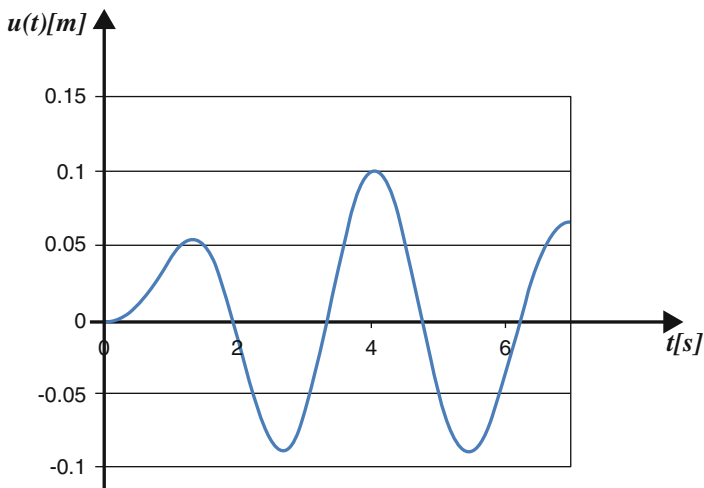


Fig. 3.21 Dynamic response of the system evaluated with fourth order Runge-Kutta method for $\Delta t = 0.1$ s

3.4.2 Implicit Methods

3.4.2.1 Newmark Method

The procedure proposed by Newmark in 1959 to evaluate the response of a system is one of the most commonly used methods. It is based on the two parameters β and γ , which represent the variation of acceleration within the specified time interval. The velocity and displacement of the system in step $i+1$ are given by the Eq. 3.33.

$$\begin{cases} \dot{u}_{i+1} = \dot{u}_i + [(1 - \gamma) \cdot \Delta t] \cdot \ddot{u}_i + \gamma \cdot \Delta t \cdot \ddot{u}_{i+1} \\ u_{i+1} = u_i + \Delta t \cdot \dot{u}_i + [(0.5 - \beta) \cdot \Delta t^2] \cdot \ddot{u}_i + \beta \cdot \Delta t^2 \cdot \ddot{u}_{i+1} \end{cases} \quad (3.33)$$

The physical parameter β is introduced to establish the acceleration model between two adjacent time intervals. At this purpose, if $\beta = 1/6$ the trend of the acceleration in the time interval is linear (*linear acceleration method*), while for $\beta = 1/4$ the acceleration is considered constant (*average acceleration method*). In addition, the typical value assumed by the parameter γ is $1/2$. The time stepping solution of the equation of motion can be obtained by substitution of the Eq. 3.33 in the equilibrium equation at time $i+1$ (Eq. 3.34).

$$\begin{aligned} m \cdot \ddot{u}_{i+1} + c \cdot (\dot{u}_i + (1 - \gamma) \cdot \Delta t \cdot \ddot{u}_i + \gamma \cdot \Delta t \cdot \ddot{u}_{i+1}) + \\ + k \cdot (u_i + \Delta t \cdot \dot{u}_i + (0.5 - \beta) \cdot \Delta t^2 \cdot \ddot{u}_i + \beta \cdot \Delta t^2 \cdot \ddot{u}_{i+1}) = F(t_{i+1}) \end{aligned} \quad (3.34)$$

Table 3.3 Numerical solutions obtained by 4th order Runge-Kutta method ($\Delta t = 0.1$ s)

k_1 (I)	k_2 (I)	k_3 (I)	k_4 (I)	k_1 (II)	k_2 (II)	k_3 (II)	k_4 (II)	t [s]	u(t) [m]	v(t) [m/s]	a(t) [m/s ²]
0	0	0	0	0	0	0	0	0	0	0	0
0.002	0.002	0.002	0.002	0.002	0.002	0.002	0.002	0.10	0.000	0.002	0.048
0.009	0.009	0.009	0.009	0.009	0.009	0.009	0.009	0.20	0.001	0.009	0.090
0.020	0.020	0.020	0.020	0.020	0.020	0.020	0.020	0.30	0.002	0.020	0.120
0.033	0.033	0.033	0.033	0.033	0.033	0.033	0.033	0.40	0.005	0.033	0.135
0.046	0.046	0.046	0.046	0.046	0.046	0.046	0.046	0.50	0.009	0.046	0.132
0.059	0.059	0.059	0.059	0.059	0.059	0.059	0.059	0.60	0.014	0.059	0.112
0.068	0.068	0.068	0.068	0.068	0.068	0.068	0.068	0.70	0.020	0.068	0.075
0.073	0.073	0.073	0.073	0.073	0.073	0.073	0.073	0.80	0.027	0.073	0.024
0.066	0.066	0.066	0.066	0.066	0.066	0.066	0.066	0.90	0.035	0.073	-0.038
0.052	0.052	0.052	0.052	0.052	0.052	0.052	0.052	1.00	0.042	0.066	-0.104
0.032	0.032	0.032	0.032	0.032	0.032	0.032	0.032	1.10	0.048	0.052	-0.170
0.006	0.006	0.006	0.006	0.006	0.006	0.006	0.006	1.20	0.052	0.032	-0.230
-0.023	-0.023	-0.023	-0.023	-0.023	-0.023	-0.023	-0.023	1.30	0.054	0.006	-0.277
-0.055	-0.055	-0.055	-0.055	-0.055	-0.055	-0.055	-0.055	1.40	0.053	-0.023	-0.308
...	1.50	0.049	-0.055	-0.319
...

Thus, the acceleration at time $i+1$ can be obtained from the known acceleration, velocity and displacement (Eq. 3.35).

$$\ddot{u}_{i+1} = \frac{\{F(t_{i+1}) - k \cdot u_i - (c + k \cdot \Delta t) \cdot \dot{u}_i - [c \cdot (1 - \gamma) + k \cdot (0.5 - \beta) \cdot \Delta t] \cdot \Delta t \cdot \ddot{u}_i\}}{[m + c \cdot \gamma \cdot \Delta t + k \cdot \beta \cdot \Delta t^2]} \quad (3.35)$$

The problem can be expressed in an alternative way in a more simple form. For this purpose, the problem is expressed in terms of increments of displacements, velocities and accelerations (Eq. 3.36).

$$\begin{cases} \Delta \ddot{u}_i = \ddot{u}_{i+1} - \ddot{u}_i \\ \Delta \dot{u}_i = \dot{u}_{i+1} - \dot{u}_i = \Delta t \cdot \ddot{u}_i + \gamma \cdot \Delta t \cdot \Delta \ddot{u}_i \\ \Delta u_i = u_{i+1} - u_i = \Delta t \cdot \dot{u}_i + \frac{\Delta t^2}{2} \cdot \ddot{u}_i + \beta \cdot \Delta t^2 \cdot \Delta \ddot{u}_i \end{cases} \quad (3.36)$$

The incremental displacement can be expressed as illustrated below (Eq. 3.37).

$$\Delta \ddot{u}_i = \frac{1}{\beta \cdot \Delta t^2} \Delta u_i - \frac{1}{\beta \cdot \Delta t} \cdot \dot{u}_i - \frac{1}{2 \cdot \beta} \cdot \ddot{u}_i \quad (3.37)$$

Composing the incremental displacement and velocity, the Eq. 3.38 is given.

$$\Delta \dot{u}_i = \frac{\gamma}{\beta \cdot \Delta t} \Delta u_i - \frac{\gamma}{\beta} \dot{u}_i + \Delta t \cdot \left(1 - \frac{\gamma}{2 \cdot \beta}\right) \cdot \ddot{u}_i \quad (3.38)$$

In addition, the equation of motion can be rewritten in the incremental form (Eq. 3.39).

$$m \cdot \Delta \ddot{u}_i + c \cdot \Delta \dot{u}_i + k \cdot \Delta u_i = \Delta F_i \quad (3.39)$$

Substituting Eqs. 3.37 and 3.38 into the incremental equation of motion, Δu_i can be evaluated as illustrated in Eq. 3.40.

$$\Delta u_i = \frac{\tilde{\Delta F}_i}{\tilde{k}} \rightarrow \begin{cases} \tilde{\Delta F}_i = \Delta F_i + \left(\frac{1}{\beta \cdot \Delta t} \cdot m + \frac{\gamma}{\beta} \cdot c\right) \dot{u}_i + \left(\frac{1}{2 \cdot \beta} \cdot m + \left(\frac{\gamma}{2 \cdot \beta} - 1\right) \cdot c\right) \cdot \ddot{u}_i \\ \tilde{k} = k + \frac{\gamma}{\beta \cdot \Delta t} \cdot c + \frac{1}{\beta \cdot \Delta t^2} \cdot m \end{cases} \quad (3.40)$$

From this value, the displacement at time t_{i+1} can be calculated ($u_{i+1} = u_i + \Delta u_i$). In addition, by applying the Eq. 3.38 the incremental velocity can be found to evaluate the velocity at time t_{i+1} ($\dot{u}_{i+1} = \dot{u}_i + \Delta \dot{u}_i$), while acceleration is usually evaluated directly at time t_{i+1} , according to the equation of motion (Eq. 3.41).

$$\ddot{u}_{i+1} = \frac{F(t_{i+1}) - c \cdot \dot{u}_{i+1} - k \cdot u_{i+1}}{m} \quad (3.41)$$

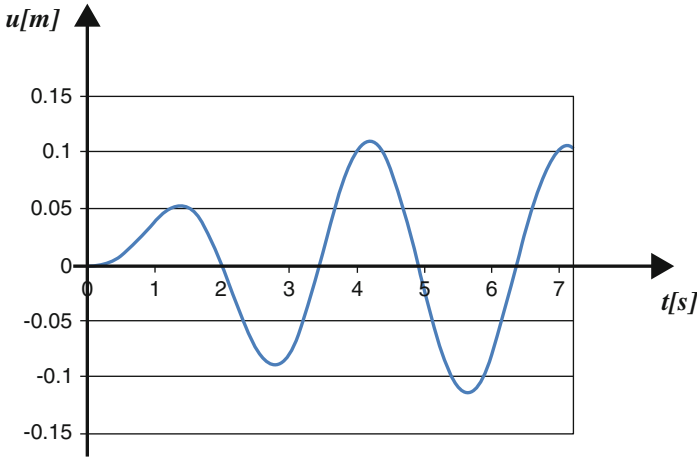


Fig. 3.22 Dynamic response of the system evaluated with Newmark (linear acceleration) method for $\Delta t = 0.1$ s

The dynamic response can be lead directly for elastic system because the stiffness term is independent from the displacement value (constant value). However, in the case of an inelastic system, the solution will be obtained by several iterations. The accuracy of the Newmark method is strictly related to the time interval, which also gives information about the stability of the procedure. In order to avoid stability problems, a maximum time interval value has to be fixed according to the vibrational period of the system. Equation 3.42 shows the relationships to be respected to ensure a stable mathematical procedure.

$$\frac{\Delta t}{T_n} \leq \frac{1}{\pi \cdot \sqrt{2 \cdot (\gamma - 2 \cdot \beta)}} \rightarrow \begin{cases} \frac{\Delta t}{T_n} \leq \infty \text{ for : average acceleration} \\ \frac{\Delta t}{T_n} \leq 0.55 \text{ for : linear acceleration} \end{cases} \quad (3.42)$$

Even in this case, the SDOF system proposed previously is considered to evaluate its dynamic response according to the linear acceleration (*l.a.*) model ($\beta = 1/6$). Figure 3.22 illustrates the dynamic response of the system, evaluated using the *linear acceleration model*.

Table 3.4 reports the numerical results obtained.

3.4.3 Comparison Between the Different Numerical Methods

In order to focus on the intrinsic errors of the numerical method proposed, Figs. 3.23, 3.24, and 3.25 illustrate the dynamic responses comparison between ana-

Table 3.4 Numerical solutions obtained by Newmark method according to linear acceleration model

t [s]	u(t) [m]	v(t) [m/s]	a(t) [m/s ²]
0	0	0	0
0.1	0.0001	0.0024	0.0484
0.2	0.0006	0.0087	0.0904
0.3	0.0019	0.0180	0.1216
0.4	0.0043	0.0294	0.1388
0.5	0.0079	0.0414	0.1398
0.6	0.0126	0.0526	0.1237
0.7	0.0184	0.0617	0.0913
0.8	0.0249	0.0672	0.0445
0.9	0.0318	0.0682	-0.0134
1	0.0384	0.0638	-0.0782
1.1	0.0443	0.0537	-0.1449
1.2	0.0489	0.0380	-0.2084
1.3	0.0517	0.0173	-0.2635
1.4	0.0522	-0.0075	-0.3053
1.5	0.0500	-0.0350	-0.3299
...

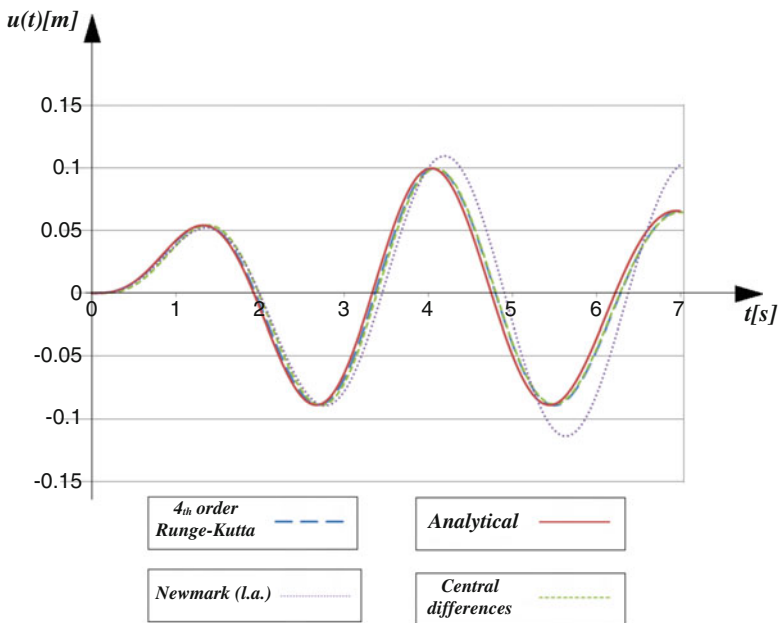


Fig. 3.23 Displacement responses evaluated according to analytical, central differences, 4th order Runge-Kutta and Newmark (linear acceleration) method ($\Delta t = 0.1$ s)

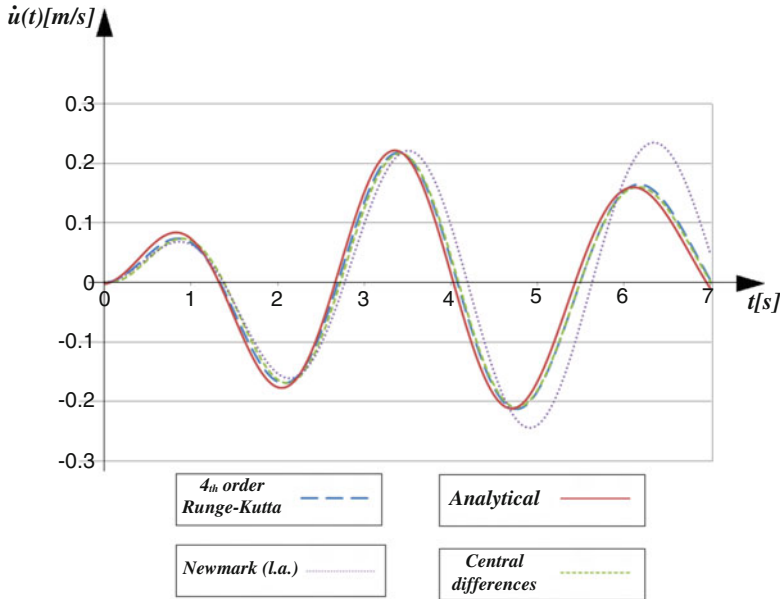


Fig. 3.24 Velocity responses evaluated according to analytical, central differences, 4th order Runge-Kutta and Newmark (linear acceleration) method ($\Delta t = 0.1$ s)

lytical, central differences 4th order Runge-Kutta and Newmark (linear acceleration) methods.

The 4th order Runge-Kutta method is accurate for every type of response but it has a greater computational charge, since it requires the definition of the average slope of the function in the time interval Δt for four points. The solutions obtained by Newmark method application have a good fit with the analytical trends in the initial part, but the errors increase with the time. Thus, Newmark's method can be affected by the propagation of round-off errors, depending on the time interval chosen. Observing the figure above, the central method results are perfectly in line with the analytical solution. This is not always a valid definition, since the results obtained by the central method are strongly dependent on the time interval. For this reason, every numerical method has been applied using a time interval of 0.5 s and considering the difference in terms of displacement. Figure 3.26 illustrates the comparison between the three new sets of solutions and the analytical one.

Comparing this figure with the Fig. 3.23 it is possible to observe that the central differences solution is strongly affected when the Newmark one has been slightly modified. Furthermore, the solution obtained by 4th order Runge-Kutta method has a trend almost equal to the first one. Thus, the Runge-Kutta method is less affected by the sampling interval than the other two methods. In addition, the Runge-Kutta method leads to an accurate response in terms of accelerations and velocity since it

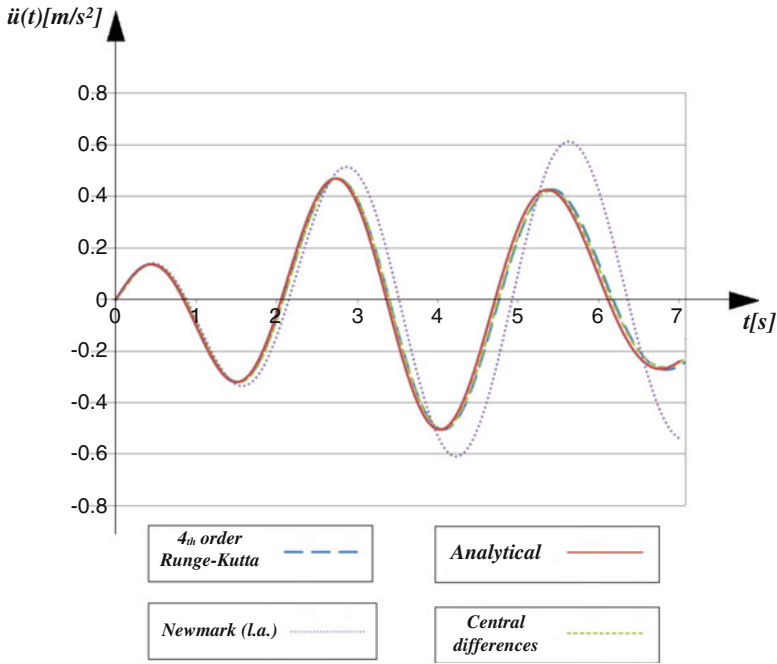


Fig. 3.25 Acceleration responses evaluated according to analytical, central differences, 4th order Runge-Kutta and Newmark (linear acceleration) method ($\Delta t = 0.1$ s)

has been developed to decrease the round-off errors for the derivatives of the main ODE. Table 3.5 resumes the main stability and accuracy aspects of each method explained.

3.4.4 Numerical Methods for Nonlinear Problems

The numerical methods represent an alternative way to solve any dynamic problem, especially for nonlinear systems (Kelley 2003). In these cases the analytical solutions can be challenging to obtain, while the simplified integral methods cannot be used since they are based on the superposition of the effects. Therefore, each of the previous numerical methods can be adapted to the nonlinear dynamic systems by modifying the stiffness coefficient in the equation of motion (Eq. 3.43).

$$m \cdot \ddot{u} + c \cdot \dot{u} + k(u) \cdot u = F(t) \tag{3.43}$$

The stiffness coefficient is not a constant, but it depends on the displacement of the system at the previous time step.



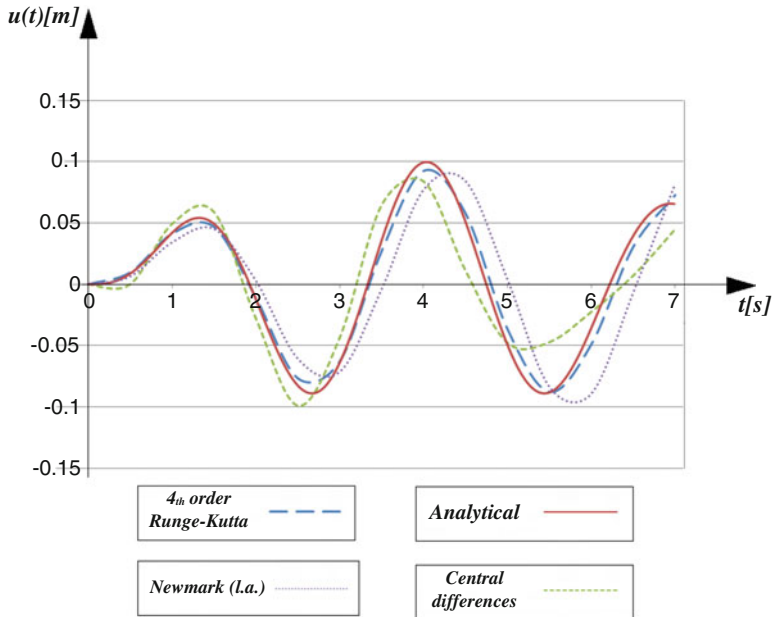


Fig. 3.26 Displacement responses evaluated according to analytical, central differences, 4th order Runge-Kutta and Newmark (linear acceleration) method ($\Delta t = 0.5$ s)

Table 3.5 Main characteristics of the numerical methods

Numerical method	Stability	Accuracy	Computational effort
Central differences	$\Delta t/T < 1/\pi$	Low-medium [f(Δt)]	Low
4th order Runge-Kutta	$\Delta t_{min} < \Delta t < \Delta t_{max}$	Good	Medium
Newmark (linear acceleration)	$\Delta t/T < 0.551$	Medium [f(Δt)]	Low

3.4.4.1 Central Difference Method

Starting from the considerations in Sect. 3.4.1.1, the equation of motion can be expressed as illustrated in Eq. 3.44.

$$\left[\frac{m}{\Delta t^2} + \frac{c}{2 \cdot \Delta t} \right] \cdot u_{i+1} + F_k(u_i) - \frac{2 \cdot m}{\Delta t^2} \cdot u_i + \left[\frac{m}{\Delta t^2} - \frac{c}{2 \cdot \Delta t} \right] \cdot u_{i-1} = F(t_i) \tag{3.44}$$

The stiffness force has been expressed in terms of the displacement at the previous step (u_i). This is a simplification of the problem that can lead to big round-off errors if the sampling time is not sufficiently small. In addition, when the velocity at time $i+1$ has an opposite sign of the velocity at time i , the systems is subjected to an unloading cycle starting in a generic instant of time within the specified interval. In other words, the chosen time interval is not capable of giving information about the actual point in which an elastic force with opposite sign of

the previous one arises in the system. Naturally, the numerical phenomenon just explained causes a propagation of errors especially if the external loads are very jagged. These aspects will be discussed in detail in the next paragraph, but for now it is sufficient to say that this type of error can be minimized using a variable Δt . The central difference method is not widely used in the dynamic applications because it is not very accurate.

3.4.4.2 Newmark Method

The application of Newmark method for nonlinear systems is common in the dynamic analysis since it is accurate and, at the same time, the requested computational effort is greater than the central differences method. As indicated in Sect. 2.5 for inelastic systems, Eqs. 3.40 and 3.41 are modified to obtain Eqs. 3.45 and 3.46.

$$\Delta u_i = \frac{\tilde{\Delta F}_i}{\tilde{k}} \rightarrow \begin{cases} \tilde{\Delta F}_i = \Delta F_i + \left(\frac{1}{\beta \cdot \Delta t} \cdot m + \frac{\gamma}{\beta} \cdot c\right) \dot{u}_i + \left(\frac{1}{2 \cdot \beta} \cdot m + \left(\frac{\gamma}{2 \cdot \beta} - 1\right) \cdot c\right) \cdot \ddot{u}_i \\ \tilde{k} = k(u_i) + \frac{\gamma}{\beta \cdot \Delta t} \cdot c + \frac{1}{\beta \cdot \Delta t^2} \cdot m \end{cases} \quad (3.45)$$

$$\ddot{u}_{i+1} = \frac{F(t_{i+1}) - c \cdot \dot{u}_{i+1} - k(u_i) \cdot u_{i+1}}{m} \quad (3.46)$$

It is possible to observe that for nonlinear systems, the stiffness contribution is not constant but instead depends on the displacement according to the F_k-u relation. The main problem is represented by the impossibility of using the real value of stiffness at time step $i+1$ since the displacement at this instant is the unknown of the equation. The problem can be solved according to two different ways, summarized below.

- (a) The secant stiffness can be assumed equal to the tangent one. Figure 3.27 illustrates the difference between the displacement evaluated with secant and tangent stiffness.

Fig. 3.27 Differences of displacements obtained with tangent and secant stiffness

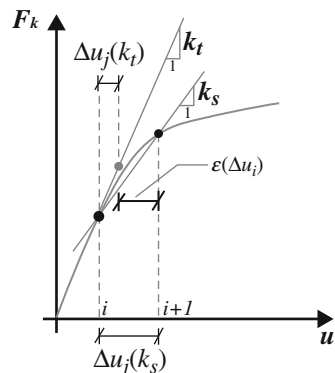
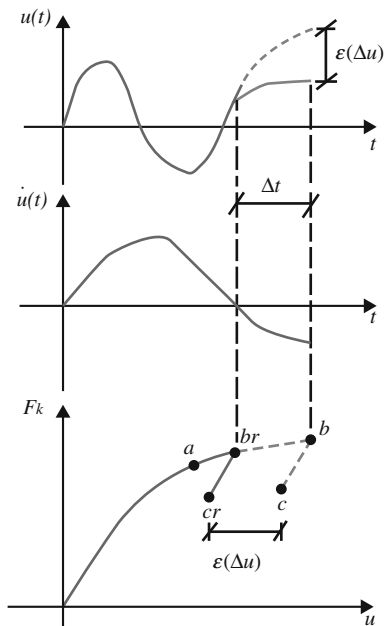


Fig. 3.28 Inaccuracy of the constant time interval

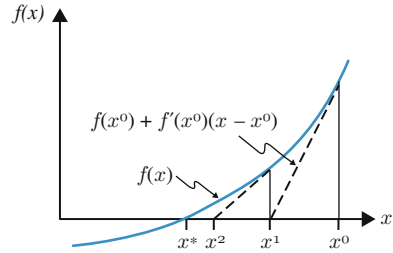


If the time interval is small enough, the displacement calculated according to tangent stiffness is no different from the displacement obtained by the use of secant stiffness. This is a simple approach for inelastic systems since the displacement increment can be found according to the responses and the tangent stiffness referenced at previous time step (*no iterative procedure*). The errors accumulated in the time domain with the approach based on the tangent stiffness can become significant and produce an inaccurate solution. An additional problem with this method is the incapability to adapt the real trend of F_{k-u} relation to a constant time interval. Suppose we have a displacement at time step i identified by “ a ”, and Δu_i is the displacement increment leading to point “ b ”. In addition, a negative velocity is assumed at time step $i+1$. This last aspect means that there will be a point between “ a ” and “ b ” for which the velocity is equal to zero. In other words, if the velocity is zero, the trend of F_{k-u} will be subjected to an unloading cycle in a point “ br ”. Applying the Newmark method again from the point “ b ” a further Δu_i is obtained by considering a negative stiffness coefficient that leads to the point “ c ”. If the numerical methods are applied from the real point “ br ”, the solution will lead to the point “ cr ” in the F_{k-u} diagram. Each consideration just discussed is represented in Fig. 3.28.

The term $\epsilon(\Delta u)$ represents the incremental displacement error due to the constant time interval chosen. Thus, the assumption of a constant Δt can lead to the overpass of an unloading branch of the force-displacement diagram with a decrease in the accuracy. This type of error can be eliminated through an iterative procedure based on the adjustment of the Δt such that leads to a velocity equal to zero at the time step $i+1$.

(b) The tangent stiffness is assumed after it is compared with the secant one through an iterative procedure.

Fig. 3.29 Identification of the solution of the function $f(x) = 0$ by means of different tangents



3.4.4.3 Newton Raphson Method

One of the most common iterative procedures is the *Newton-Raphson method* that is applied to evaluate the approximated solution of a generic function $f(x) = 0$. In a given interval $[x_a, x_b]$ the function is expressed in terms of the first derivatives of different points that represent the intersection between the tangents and the x-axis (Fig. 3.29).

Observing the figure above, the zero of the function can be found by tracing the tangents to the function for particular x^k values. Equation 3.47 illustrates the relationship between two adjacent x-coordinates for which the function has a zero value.

$$x^{k+1} = x^k - \left[\frac{df(x^k)}{dx} \right]^{-1} \cdot f(x^k) \text{ for } : k = 1, 2, \dots \tag{3.47}$$

The zero of the function (x^*) can be approximately evaluated by means of an iterative process that leads to the following conditions (Eq. 3.48).

$$x^{k+1} - x^k \approx 0 \rightarrow x^{k+1} = x^* \tag{3.48}$$

It is possible to demonstrate that an iterative sequence $x^{(k)}$ converging to the value x^* in quadratic way. Naturally, the iteration procedure is based on the assumption of an adequate initial point with value x_0 . In the dynamic applications, the *modified Newton-Raphson method* is applied to minimize the errors due to the variation of the stiffness by means of an iteration procedure that leads to have an incremental displacement equal to the real one minus a tolerance factor. Every ordinate step of the modified Newton-Raphson methods are described below.

- (I) The incremental dynamic response Δu_i is defined by using of the tangent stiffness at time step i ($k_i = k_t$) (Fig. 3.30).



Fig. 3.30 First step of the iterative procedure (Adapted from Chopra 2001)

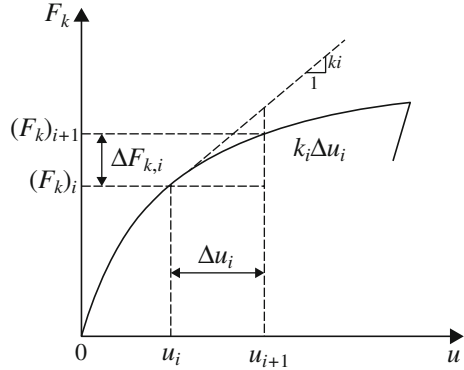
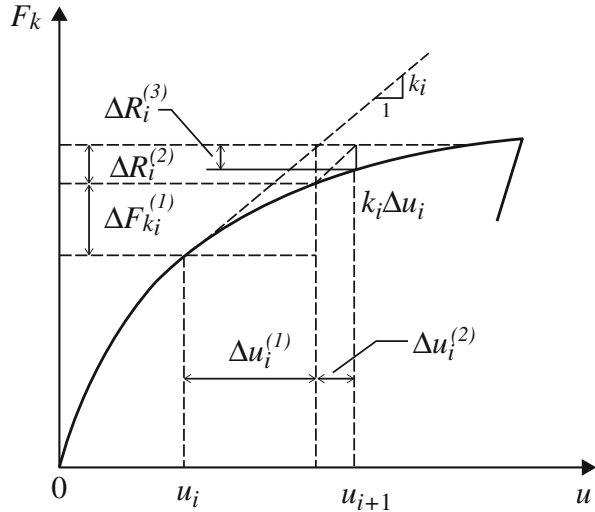


Fig. 3.31 Second step of the iterative procedure (Adapted from Chopra 2001)



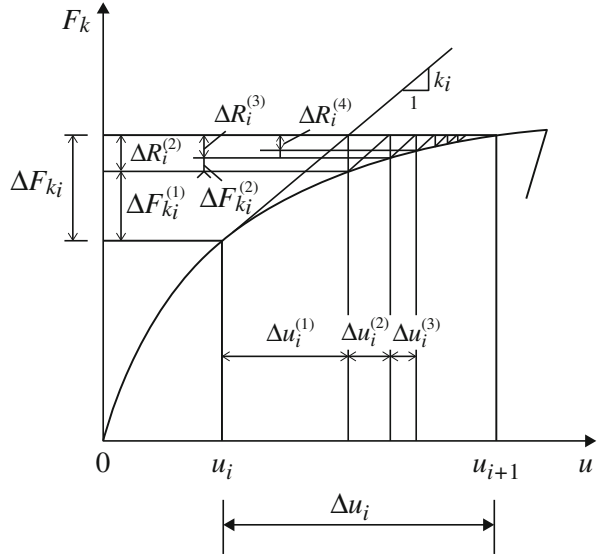
The real elastic force is different from the force found by multiplying the incremental displacement obtained and the tangent stiffness. This residual value is expressed by the term ΔR^{j+1} , where $j=1$. Generically, the residual elastic force is given by the Eq. 3.49.

$$\Delta R^{j+1} = k_i \cdot \Delta u_i - \Delta F_{k,i} \tag{3.49}$$

where j indicates the iterative step.

(II) A further incremental displacement due to the residual force is evaluated (Fig. 3.31).

Fig. 3.32 Last step of the iterative procedure (Adapted from Chopra 2001)



Equation 3.50 illustrates the additional incremental displacement.

$$\Delta u_i^{(j)} = \frac{\Delta R_i^{(j)}}{k_i} \tag{3.50}$$

(III) The iterative process will be stopped when the condition expressed in Eq. 3.51 is achieved.

$$\frac{\Delta u_i^{(n)}}{\sum_{j=1}^n \Delta u_i^{(j)}} \leq \epsilon_{toll} \tag{3.51}$$

where ϵ_{toll} indicates the allowable error and Fig. 3.32 shows all the iterations required to obtain the results reported in the equation above.

The value of the incremental displacement evaluated with the iterative approach of Newton-Raphson results are more accurate than the increment evaluated with no iterative method. Naturally, the same procedure will be applied for every time step in which the system exhibits nonlinear behavior. The proposed method is based on the definition of the displacement according to the initial tangent stiffness k_i . Alternatively, the iteration procedure can be applied by considering the tangent stiffness at each iterative step. This procedure leads to a faster convergence than the other one (Fig. 3.33).



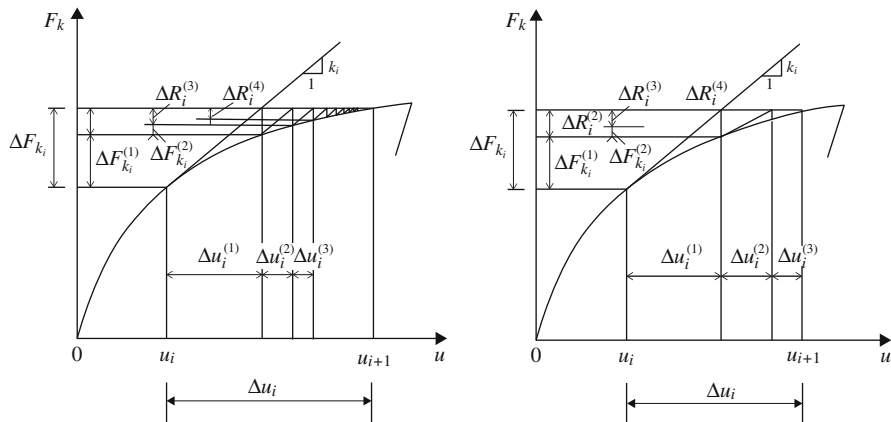


Fig. 3.33 Comparison between modified Newton-Raphson method for constant initial tangent stiffness and variable tangent stiffness (Adapted from Chopra 2001)

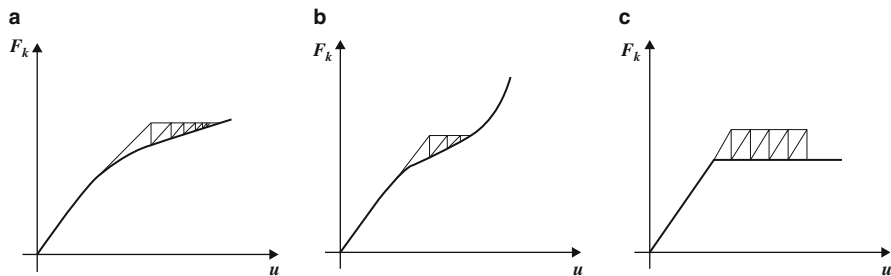


Fig. 3.34 F-u with medium hardening (a), with high hardening (b) and elasto-perfectly plastic mode (c)

The modified Newton-Raphson method quickly converges after a few iterations especially for the elasto-plastic model with moderate hardening. Its application can be inaccurate or impossible to achieve the convergence for high hardening behavior. Finally, the maximum tolerance ε_{tol} influences the iterative process when the function $F - u$ is not monotonically increasing (elasto-perfectly plastic model). The three aspects just discussed above are illustrated in Fig. 3.34.

Let's consider the same SDOF system subjected to the same sinusoidal load studied used in the previous paragraphs. The force-displacement relationship shown in Fig. 3.35 is assumed.

The figure above shows an elastic perfectly plastic model in which the dashed line represents the hypothetical unload path. The yielding point is characterized by the values reported in the Table 3.6.

The dynamic response has been evaluated by using a MATLAB code based on the adjustment of the time interval to take into account the signs of velocity and stiffness coefficient variations. Figure 3.36 illustrates the $u-t$ graph and also compares the

Fig. 3.35 F_k - u relation for the element composing the system

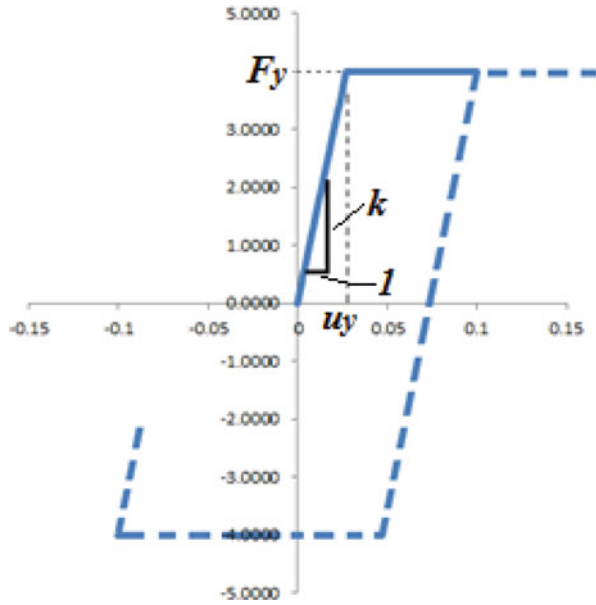


Table 3.6 Yielding force and displacement for the element composing the SDOF system

F_y [N]	u_y [m]
4	0.027

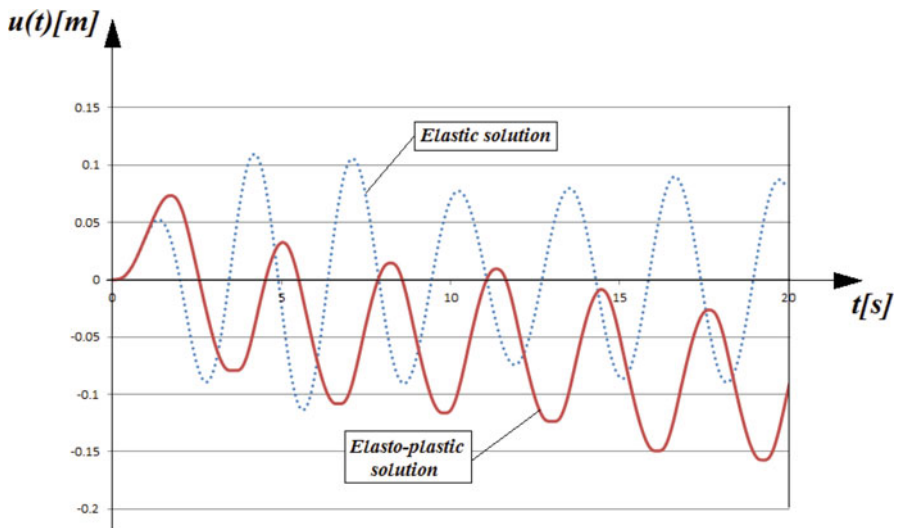


Fig. 3.36 Displacement response of SDOF system for elastic and elasto-perfectly plastic model

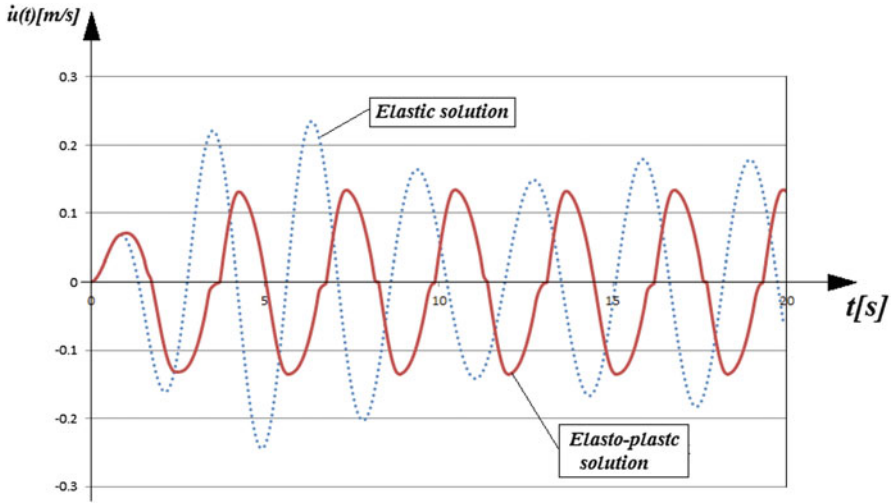


Fig. 3.37 Velocity response of SDOF system for elastic and elasto-perfectly plastic model

elastic and elasto-plastic response obtained according to the Newmark method and linear acceleration model with time step $\Delta t = 0.1$ s.

It is possible to observe how the plastic displacement (irreversible contribution) increases with the time causing the shifting of the mean displacement values line. At the same time, the amplitude of the displacement response decreases because the plastic dissipation is considered. In addition, considering the nonlinearity of the system, the dynamic response becomes more spread out over the time domain. In other words, the natural period of the SDOF system increases. Moreover, Figs. 3.37 and 3.38 illustrate the comparison between the velocity and acceleration responses of elastic and elasto-plastic models.

From the figure above, one can notice how the acceleration values for inelastic system decrease with respect to the elastic ones. This phenomenon is due to the further energy dissipation in the form of plastic deformation that leads to a decrease in the inertia force. Finally, Table 3.7 reports the obtained numerical values.

The differential equations describing the dynamic systems are each characterized by unique time constants. It is known that when the variability of these time constants is highly emphasized, the numerical evaluation of the differential equation becomes inaccurate. Mathematical problems affected by these phenomena are called stiff systems. Since in the nonlinear dynamic systems the stiffness parameter can assume a wide variety of values, the “mathematical stiffness” of the dynamic nonlinear systems is bigger than that of the elastic ones. In other words, the dynamic

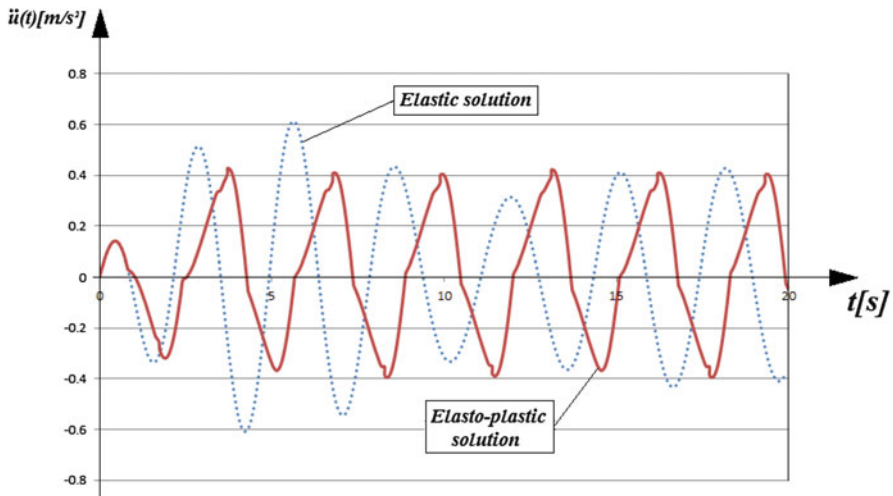


Fig. 3.38 Acceleration response of SDOF system for elastic and elasto-perfectly plastic model

response of an inelastic system evaluated numerically is strongly dependent on the chosen time step. In order to explain this aspect, Fig. 3.39 shows a comparison between the function $u-t$ obtained by the Newmark method for $\Delta t = 0.1$ s and $\Delta t = 0.025$ s.

Even with a smaller time step, the plastic deformations tend to shift the dynamic response leading to a mean displacement other than zero.

3.4.4.4 Runge-Kutta Method

The Runge-Kutta method can also be used for a nonlinear system in which the stiffness has to be expressed as a function of the displacement at the time t_{i+1} . Similar to the Newmark method, the problem can be solved iteratively taking into account the variation of the stiffness value according to the F_k-u law. As previously observed, the 4th order Runge-Kutta method is more stable than the other ones but it has a medium computational charge. Considering the previous numerical example, Fig. 3.40 illustrates the dynamic response evaluated by using the 4th order Runge-Kutta method by assuming $\Delta t = 0.025$ s. In this case, the solution has been obtained by applying a MATLAB code in which the time step value varies to take into account the stiffness changes more accurately.

Table 3.7 Numerical solution according to *Newmark linear acceleration method*

t [s]	u(t) [m]	v(t) [m/s]	a(t) [m/s ²]
0	0	0	0
0.10	0.0001	0.0024	0.0484
0.20	0.0006	0.0087	0.0904
0.30	0.0019	0.0180	0.1216
0.40	0.0043	0.0294	0.1388
0.50	0.0079	0.0414	0.1398
0.60	0.0126	0.0526	0.1237
0.70	0.0184	0.0617	0.0913
0.80	0.0249	0.0672	0.0445
0.83	0.0266	0.0680	0.0310
0.93	0.0335	0.0702	0.0211
1.03	0.0406	0.0711	0.0024
1.13	0.0477	0.0699	-0.0246
1.23	0.0545	0.0661	-0.0587
1.33	0.0608	0.0591	-0.0982
1.43	0.0662	0.0485	-0.1414
1.53	0.0703	0.0340	-0.1865
...
8.07	0.0128	0.0308	-0.3151
8.17	0.0144	0.0019	-0.3500
8.27	0.0144	0.0000	-0.3520
8.28	0.0144	-0.0009	-0.3871
8.38	0.0126	-0.0346	-0.3931
8.48	0.0074	-0.0671	-0.3657
8.58	-0.0009	-0.0957	-0.3069
8.68	-0.0117	-0.1178	-0.2209
8.78	-0.0243	-0.1315	-0.1138
8.88	-0.0378	-0.1353	0.0066
8.89	-0.0389	-0.1352	0.0165
8.99	-0.0523	-0.1324	0.0438
9.09	-0.0653	-0.1270	0.0779
9.19	-0.0775	-0.1183	0.1173
9.29	-0.0888	-0.1060	0.1603
9.39	-0.0986	-0.0900	0.2050
9.49	-0.1065	-0.0701	0.2495
9.59	-0.1124	-0.0465	0.2917
9.69	-0.1156	-0.0194	0.3299
9.79	-0.1162	-0.0047	0.3468
9.89	-0.1162	-0.0009	0.3700
9.89	-0.1162	0.0001	0.4000
9.99	-0.1144	0.0347	0.4027
10.09	-0.1092	0.0678	0.3710
...

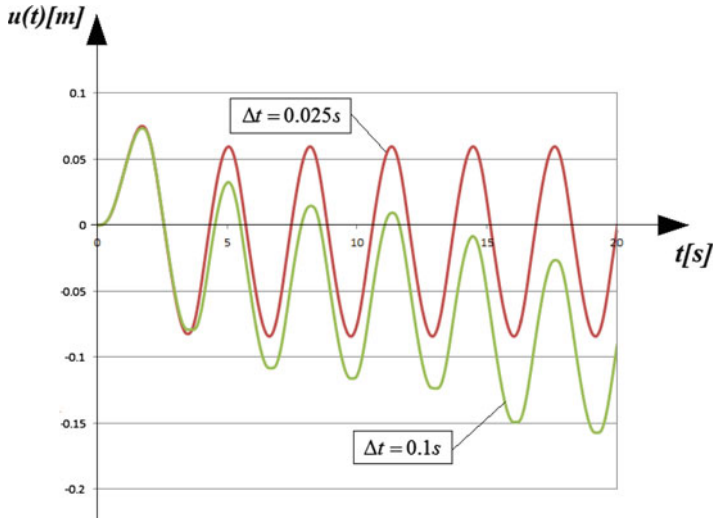


Fig. 3.39 Comparison between dynamic response according to Newmark with $\Delta t = 0.1$ s and $\Delta t = 0.025$ s

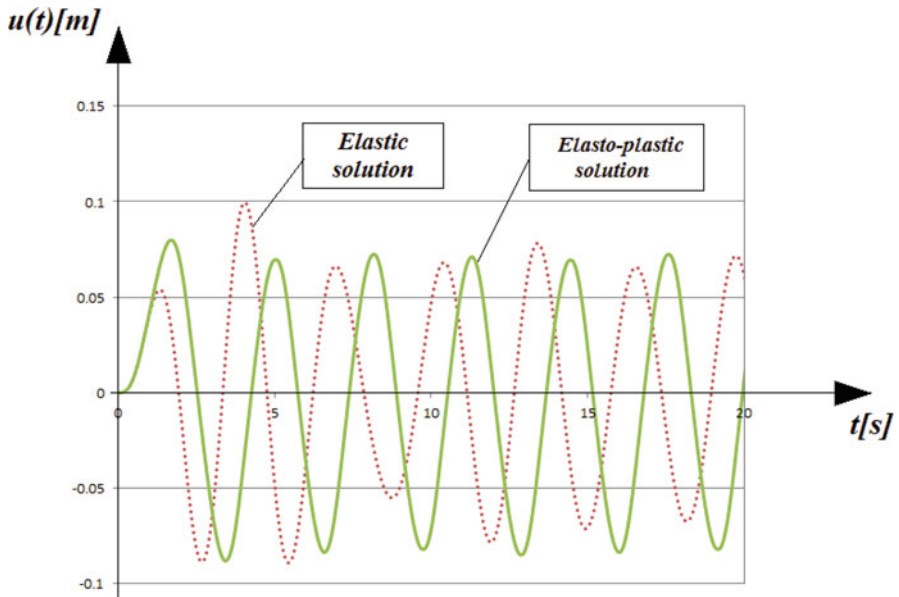


Fig. 3.40 Comparison between linear and nonlinear solutions obtained by 4th order Runge-Kutta method ($\Delta t = 0.025$ s)

References

- Brigham EO (1988) The fast fourier transform and its applications. Prentice-Hall, Englewood Cliffs
- Butcher JC (1963) Coefficients for the study of Runge-Kutta integration processes. J Aust Math Soc 3(2):185–201
- Carpinteri A (1998) Dinamica delle structure. Pitagora Editrice, Bologna
- Chopra AK (2001) Dynamics of structures: theory and applications to earthquake engineering, 2nd edn. Prentice-Hall, Upper Saddle River
- Epperson JF (2013) An introduction to numerical methods and analysis. Wiley, Hoboken
- Harris CM, Piersol AG (2002) Harris' shock and vibration handbook, vol 5. McGraw-Hill, New York
- Kelley CT (2003) Solving nonlinear equations with Newton's method. SIAM, Philadelphia
- Klaus-Jurgen B, Wilson Edward L (1976) Numerical methods in finite analysis [m]. Prentice-Hall, Englewood Cliffs
- Newmark NM (1959) A method of computation for structural dynamics. J Eng Mech Div 85(3): 67–94

Chapter 4

MDOF Systems



Abstract The chapter introduces the structural dynamic problem for structures discretized as systems with a finite number of degrees of freedom (Multi-Degree-of-freedom: MDOF). Distinction between shear-type frame and bending-type frame is provided. Modal analysis is introduced and the response of MDOF systems to both harmonic and earthquake excitations for undamped and damped systems. Finally the analysis of a 3D MDOF building is also provided.

4.1 Discretization

In many engineering applications, the real structures are considered discrete systems with a finite number of degrees of freedom (Multi-Degree-of-freedom: MDOF). This idealization is widely used for static problems (e.g. Finite Element Methods) and especially for dynamic applications in which the mass of the system can be associated to a few DOFs. Thus, the dynamic problem can be reduced to an algebraic system of equations whose solution is closer to the real one for a dense discretization. In dynamics of structures, the 2D multistory buildings are discretized as an assemblage of beam and column elements interconnected at nodal points where the DOFs are assumed located. In general, the weight of a multistory building can be assumed concentrated on each story since the beams and columns have a negligible mass with respect to the horizontal deck. Usually, the masses are lumped and considered in the middle of the roof level or on the connections between beams and columns. The discretization of the structure is carried out by individuating its nodes in which the kinematic variables are referred.

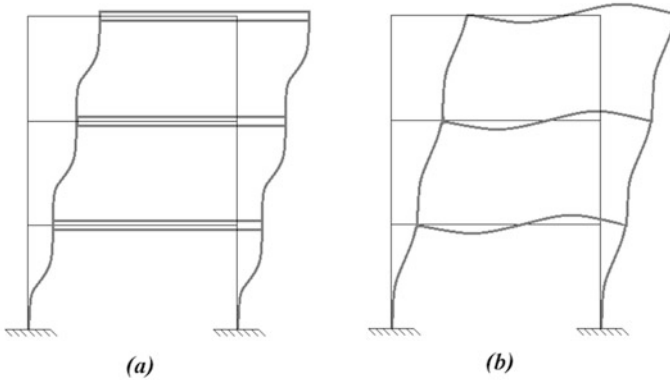


Fig. 4.1 2D three-story building shear type (a) and bending type (b)

4.2 Shear Type and Bending Type Frames

From the stiffness distribution on multistory buildings, some information can be detracted about the behavior of the structure towards to the dynamic excitation. For this reason, a 2D three-story building with inextensible elements is considered initially with infinitely rigid horizontal decks. Then the constraint of the horizontal element is released, by allowing flexural deformations. The first case for example applies to reinforced concrete buildings in which the horizontal decks are made of thick reinforced concrete plates or by a concrete and masonry flooring system. The large bending stiffness of the horizontal elements does not permit significant rotations in the beam-column connections. Therefore, the horizontal strength of the structure is described in terms of the lateral displacements only. In the dynamic analysis, the structures having the aforementioned characteristics are called shear type systems, since their global behavior is governed by the shear deformation. On the contrary, if the flooring system does not have a negligible flexibility, the rotational DOFs have to be considered in order to evaluate the global stiffness contribution (bending type systems). In Fig. 4.1 is shown the difference in terms of deformability between the shear and bending type buildings.

4.3 Mass, Stiffness and Damping Matrix

The inertia, stiffness and damping characteristics of MDOF systems are expressed in matrix form, where the generic influence component a_{ij} represents the j th force due to the imposition of a dual kinematic variable describing the i th DOF. First of all, the number of DOFs has to be evaluated according to the following expression valid for 2D systems (Eq. 4.1).

$$DOF = 3 \cdot N_n \quad (4.1)$$

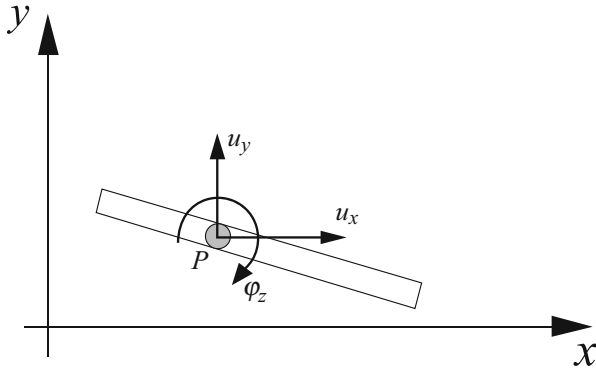


Fig. 4.2 Degree of freedom for a generic point P of a 2D system

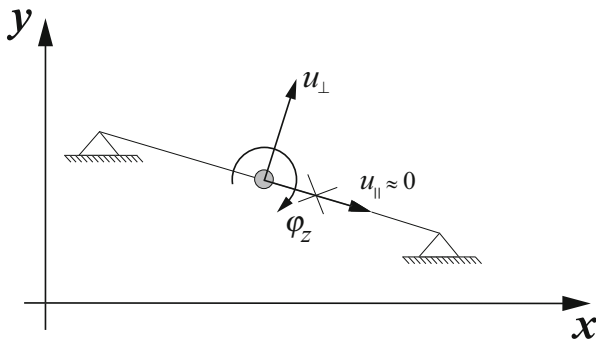


Fig. 4.3 Reduction of DOFs due to the inextensibility of the elements

where N_n represents the number of independent points of a physical system and the constant 3 defines its generic DOFs in a 2D X-Y plan (Fig. 4.2). Since in the structural analyses the axial stiffness is greater than the bending stiffness, the element composing a structural system can be assumed as rigid axially. This assumption leads to the reduction in the intrinsic DOF from three to two (Fig. 4.3). Considering a generic multi-story building, the number of DOFs is equal to the number of stories (N_f). In addition, for shear type systems the rotational DOFs in the beam-column nodes can be neglected ($\phi_z \approx 0$) and the problem is simplified further. Equations 4.2 give the number of DOFs for bending and shear type systems with external full restraint.

$$\begin{cases} DOF_{st} = N_f \rightarrow \text{shear type} \\ DOF_{bt} = N_f + N_n \rightarrow \text{bending type} \end{cases} \quad (4.2)$$

For example, in Fig. 4.1, the number of DOFs for bending and shear type system are given by Eq. 4.3.

$$\begin{cases} DOF_{st} = 3 \\ DOF_{bt} = 9 \end{cases} \quad (4.3)$$

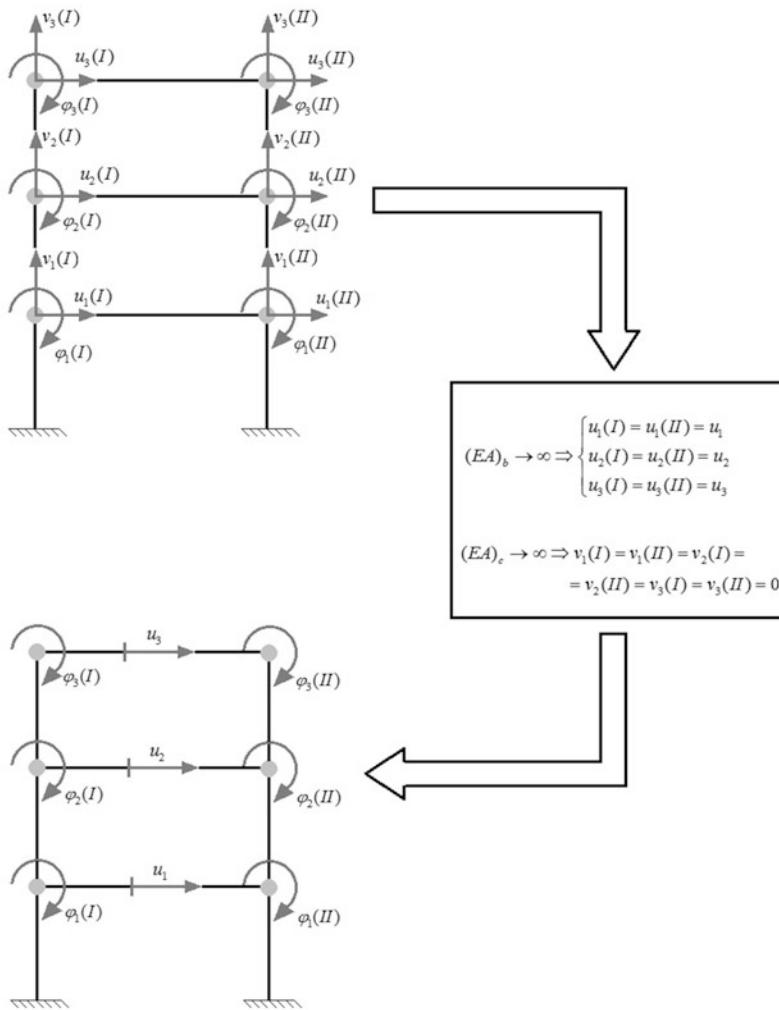


Fig. 4.4 Reduction of DOFs due to the internal rigid constraints of the element

In Fig. 4.4 is shown a generic bending moment frame in order to describe the reduction of the number of DOFs due to the axial rigidity of the beam (b) and column (c) elements. From Fig. 4.4, one can notice that all the vertical DOFs are equal to zero by effect of the infinite axial stiffness of the columns ($(EA)_c \rightarrow \infty$), while the inextensibility of the beams ($(EA)_b \rightarrow \infty$) causes an equal lateral displacement for every node located in the same story. After individuating the DOFs for the referenced structure, the mass, stiffness and damping matrix have to be evaluated.



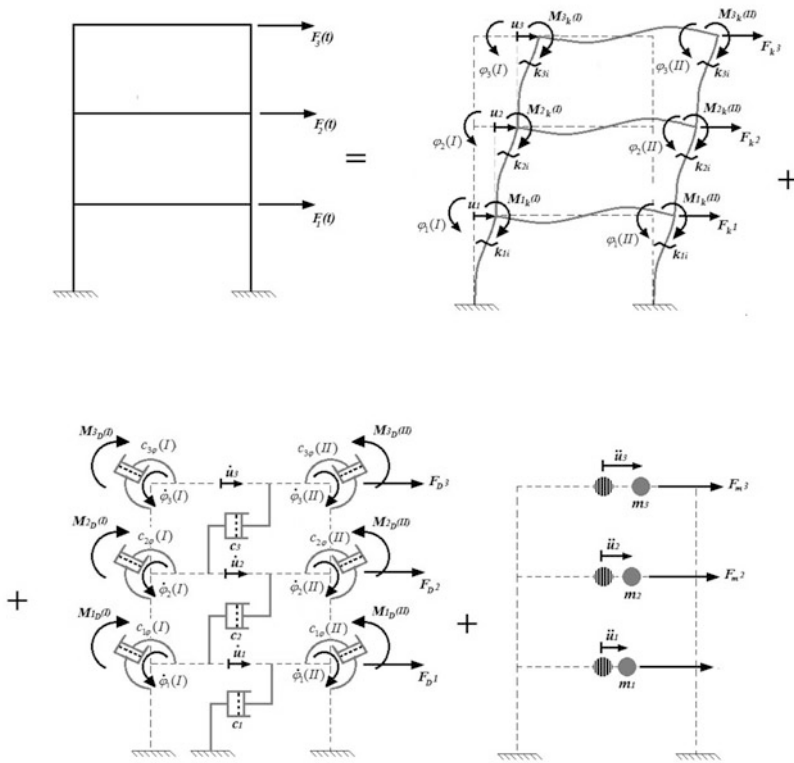


Fig. 4.5 Different contributions to the dynamic equilibrium for a three-story bending type system

4.3.1 Bending Type Frames

As discussed for SDOF systems, Fig. 4.5 graphically explains the generic dynamic problem for a bending type MDOF frame.

4.3.1.1 Stiffness Matrix

The stiffness matrix can be obtained according to the classical static methodologies. Each component k_{ij} represents the elastic force associated to the j th DOF that arises as an effect of the imposition of a unitary displacement expressed as i th DOF, while the displacement in all other DOFs are kept zero (Chopra 2017). Figure 4.6 describes all the elementary schemes assumed to define the elastic contributions associated to three-story systems.



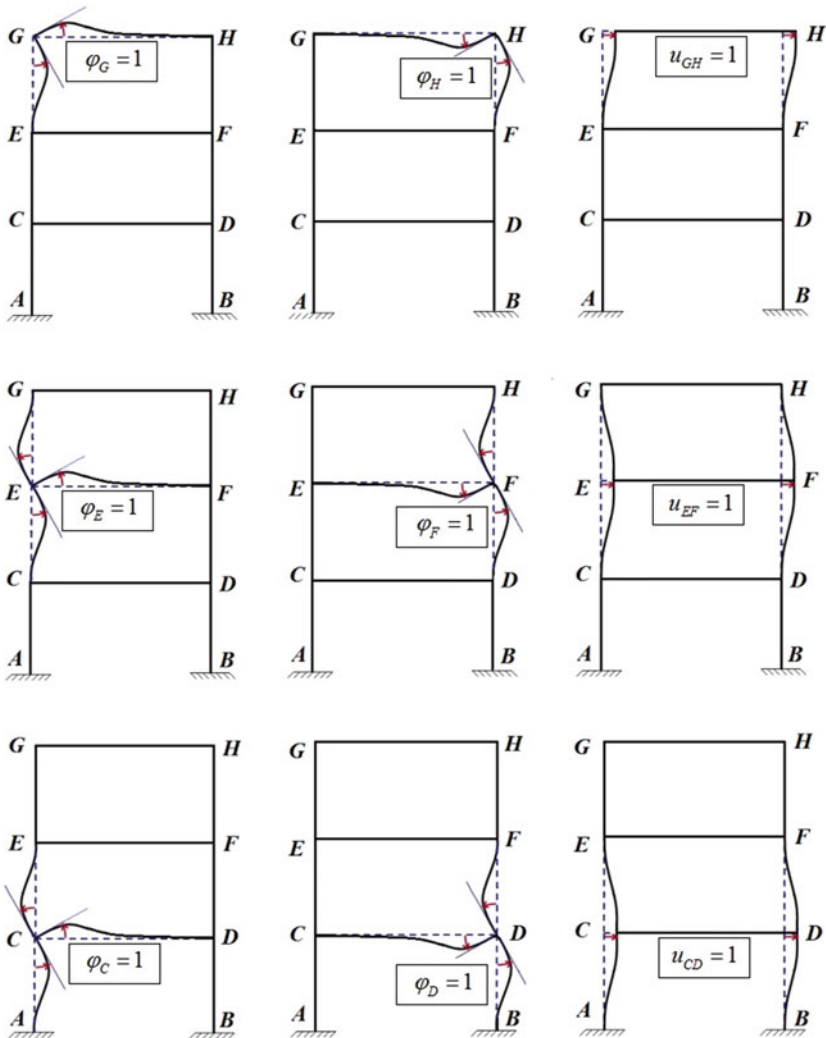


Fig. 4.6 Imposition of unitary displacements representing the DOFs of the system

When the unitary DOF is imposed, the remaining ones are kept at zero (fully restraint conditions). As known from the mechanics, from the imposition of a displacement in a node of the system (composed by a finite number of fully restraint elements) the elastic nodal reactions arise (McGuire et al. 2000). As example, Fig. 4.7 illustrates the elastic actions due to the DOFs referred to the third story. By imposition of the dual nodal equilibrium equations, the stiffness coefficients can be evaluated according to superposition of effects (Eq. 4.4).

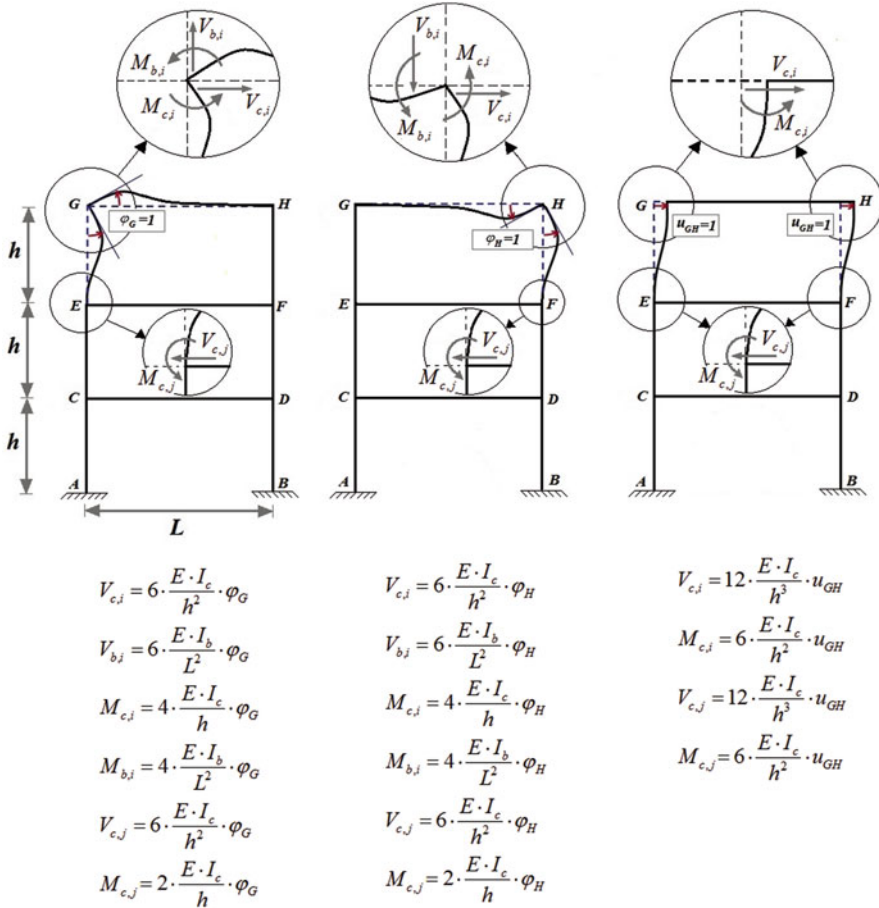


Fig. 4.7 Elastic forces arise from the DOFs associated to the third flooring system

$$\left\{ \begin{array}{l} \sum_C M_k = M_{C,k} \\ \sum_D M_k = M_{D,k} \\ \sum_{CD} F_{H,k} = F_{CD,k} \\ \sum_E M_k = M_{E,k} \\ \sum_F M_k = M_{F,k} \\ \sum_{EF} F_{H,k} = F_{EF,k} \\ \sum_G M_k = M_{G,k} \\ \sum_H M_k = M_{H,k} \\ \sum_{GH} F_{H,k} = F_{GH,k} \end{array} \right. \quad (4.4)$$

The previous system can be rewritten in matrix form as shown in the Eq. 4.5.

$$[k] \cdot \{\delta\} = \{F_k\} \quad (4.5)$$

where $[k]$ represents the stiffness matrix. The complete formulation for the analyzed three-story building is given in Eq. 4.6.

$$\begin{bmatrix} \left(\frac{8EI_c}{h} + \frac{4EI_b}{L}\right) & \frac{2EI_b}{L} & 0 & \frac{2EI_c}{h} & 0 & \frac{6EI_c}{h^2} & 0 & 0 & 0 \\ \frac{2EI_b}{L} & \left(\frac{8EI_c}{h} + \frac{4EI_b}{L}\right) & 0 & 0 & \frac{2EI_c}{h} & \frac{6EI_c}{h^2} & 0 & 0 & 0 \\ 0 & 0 & \frac{48EI_c}{h^3} & -\frac{6EI_c}{h^2} & -\frac{6EI_c}{h^2} & -\frac{24EI_c}{h^3} & 0 & 0 & 0 \\ \frac{2EI_c}{h} & 0 & -\frac{6EI_c}{h^2} & \left(\frac{8EI_c}{h} + \frac{4EI_b}{L}\right) & \frac{2EI_c}{h} & 0 & \frac{2EI_c}{h} & 0 & \frac{6EI_c}{h^2} \\ 0 & \frac{2EI_b}{h} & -\frac{6EI_c}{h^2} & \frac{2EI_b}{L} & \left(\frac{8EI_c}{h} + \frac{4EI_b}{L}\right) & 0 & 0 & \frac{2EI_c}{h} & \frac{6EI_c}{h^2} \\ \frac{6EI_c}{h^2} & \frac{6EI_c}{h^2} & -\frac{24EI_c}{h^3} & 0 & 0 & -\frac{6EI_c}{h^2} & -\frac{6EI_c}{h^2} & -\frac{24EI_c}{h^3} & -\frac{24EI_c}{h^3} \\ 0 & 0 & 0 & \frac{2EI_c}{h} & 0 & -\frac{6EI_c}{h^2} & \left(\frac{4EI_c}{h} + \frac{4EI_b}{L}\right) & \frac{2EI_b}{L} & \frac{6EI_c}{h^2} \\ 0 & 0 & 0 & 0 & \frac{2EI_c}{h} & -\frac{6EI_c}{h^2} & \frac{2EI_b}{L} & \left(\frac{4EI_c}{h} + \frac{4EI_b}{L}\right) & \frac{6EI_c}{h^2} \\ 0 & 0 & 0 & \frac{6EI_c}{h^2} & \frac{6EI_c}{h^2} & -\frac{24EI_c}{h^3} & \frac{6EI_c}{h^2} & \frac{6EI_c}{h^2} & \frac{24EI_c}{h^3} \end{bmatrix} \begin{Bmatrix} \varphi_C \\ \varphi_D \\ u_{CD} \\ \varphi_E \\ \varphi_F \\ u_{EF} \\ \varphi_G \\ \varphi_H \\ u_{GH} \end{Bmatrix} = \begin{Bmatrix} M_{C,k} \\ M_{D,k} \\ F_{CD,k} \\ M_{E,k} \\ M_{F,k} \\ F_{EF,k} \\ M_{G,k} \\ M_{H,k} \\ F_{GH,k} \end{Bmatrix} \quad (4.6)$$

The stiffness matrix is squared and symmetric and the diagonal terms represent the main elastic contributions of each DOFs (k_{ij} with $i=j$).

4.3.1.2 Damping Matrix

Similar to the stiffness matrix, the damping influence coefficient c_{ij} is evaluated by imposing a unit velocity along DOF I, while the velocity in all other DOFs are equal to zero. The compact matrix form of the damping forces is expressed in Eq. 4.7.

$$[c] \cdot \{\dot{\delta}\} = \{F_c\} \quad (4.7)$$

Assuming damping coefficients c_φ for the rotational DOFs and c_u for the linear DOFs, the damping matrix expression of the three-story bending type frame is given in Eq. 4.8.

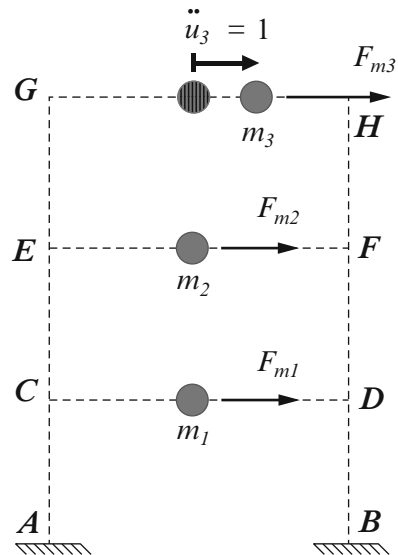
$$\begin{bmatrix} c_\varphi & 0 & 0 & 0 & 0 & 0 & 0 & 0 & 0 \\ 0 & c_\varphi & 0 & 0 & 0 & 0 & 0 & 0 & 0 \\ 0 & 0 & c_u & 0 & 0 & -c_u & 0 & 0 & 0 \\ 0 & 0 & 0 & c_\varphi & 0 & 0 & 0 & 0 & 0 \\ 0 & 0 & 0 & 0 & c_\varphi & 0 & 0 & 0 & 0 \\ 0 & 0 & -c_u & 0 & 0 & c_u & 0 & 0 & -c_u \\ 0 & 0 & 0 & 0 & 0 & 0 & c_\varphi & 0 & 0 \\ 0 & 0 & 0 & 0 & 0 & 0 & 0 & c_\varphi & 0 \\ 0 & 0 & 0 & 0 & 0 & -c_u & 0 & 0 & c_u \end{bmatrix} \begin{Bmatrix} \dot{\varphi}_C \\ \dot{\varphi}_D \\ \dot{u}_{CD} \\ \dot{\varphi}_E \\ \dot{\varphi}_F \\ \dot{u}_{EF} \\ \dot{\varphi}_G \\ \dot{\varphi}_H \\ \dot{u}_{GH} \end{Bmatrix} = \begin{Bmatrix} M_{c,C} \\ M_{c,D} \\ F_{c,CD} \\ M_{c,E} \\ M_{c,F} \\ F_{c,EF} \\ M_{c,G} \\ M_{c,H} \\ F_{c,GH} \end{Bmatrix} \tag{4.8}$$

Since the damping in the structure has been modeled with discrete dashpots, a unit rotational velocity imposed in a node does not lead a damping force in the other nodes. Different considerations can be made for the linear velocities since the associated dashpots are disposed as a continuous system, but even in this case, the damping matrix is symmetric.

4.3.1.3 Mass Matrix

The components of the mass matrix are defined by imposition of a unitary acceleration dual to the i th DOF and keeping the accelerations of the masses associated to the other DOFs at zero. Since the mass is considered concentrated in the middle of each story, the imposition of an acceleration on a mass cannot influence the motion of the other ones. For example, Fig. 4.8 illustrates the definition of the three components m_{ij} for the case in which the lateral acceleration is applied to the mass located to the third story.

Fig. 4.8 Definition of the m_{3j} mass matrix components



In this case, the mass components associated with the linear DOFs are given in the Eq. 4.9.

$$\begin{cases} m_{31} = F_{m1} = 0 \\ m_{32} = F_{m2} = 0 \\ m_{33} = F_{m1} = m_3 \cdot 1 \end{cases} \quad (4.9)$$

Even for the other two masses, the relative contributions can be simply evaluated by the imposition of a unitary acceleration on the first and second story, respectively. Since the DOF of the bending type frame is equal to nine, even the null inertia contributions due to rotations must be expressed. For this reason, the inertia forces for the MDOF system can be expressed as shown in the Eq. 4.10.

$$\begin{bmatrix} 0 & 0 & 0 & 0 & 0 & 0 & 0 & 0 & 0 \\ 0 & 0 & 0 & 0 & 0 & 0 & 0 & 0 & 0 \\ 0 & 0 & m_1 & 0 & 0 & 0 & 0 & 0 & 0 \\ 0 & 0 & 0 & 0 & 0 & 0 & 0 & 0 & 0 \\ 0 & 0 & 0 & 0 & 0 & 0 & 0 & 0 & 0 \\ 0 & 0 & 0 & 0 & 0 & m_2 & 0 & 0 & 0 \\ 0 & 0 & 0 & 0 & 0 & 0 & 0 & 0 & 0 \\ 0 & 0 & 0 & 0 & 0 & 0 & 0 & 0 & 0 \\ 0 & 0 & 0 & 0 & 0 & 0 & 0 & 0 & m_3 \end{bmatrix} \begin{Bmatrix} \ddot{\varphi}_C \\ \ddot{\varphi}_D \\ \ddot{u}_{CD} \\ \ddot{\varphi}_E \\ \ddot{\varphi}_F \\ \ddot{u}_{EF} \\ \ddot{\varphi}_G \\ \ddot{\varphi}_H \\ \ddot{u}_{GH} \end{Bmatrix} = \begin{Bmatrix} M_{m,C} \\ M_{m,D} \\ F_{m,CD} = F_{m1} \\ M_{m,E} \\ M_{m,F} \\ F_{m,EF} = F_{m2} \\ M_{m,G} \\ M_{m,H} \\ F_{m,GH} = F_{m3} \end{Bmatrix} \quad (4.10)$$

Only the direct components associated with the lateral displacement DOF are non-zero (diagonal matrix). The matrix form of the previous expression is given in Eq. 4.11.

$$[m] \cdot \{\ddot{\delta}\} = \{F_m\} \quad (4.11)$$

4.3.2 Shear Type Frames

In practical engineering applications, the multi-story buildings are considered a shear type system since the flooring systems are more rigid than the beams-columns system. As previously mentioned, the dynamic problem will be reduced because the rotational DOFs can be neglected. Considering the same three-story buildings, the inertia, stiffness and damping components can be deduced from the following scheme (Fig. 4.9) and the dynamic problem is reduced to a three DOFs system.

4.3.2.1 Stiffness Matrix

The influence stiffness components are evaluated in reference to the three elementary schemes illustrated in Fig. 4.10.

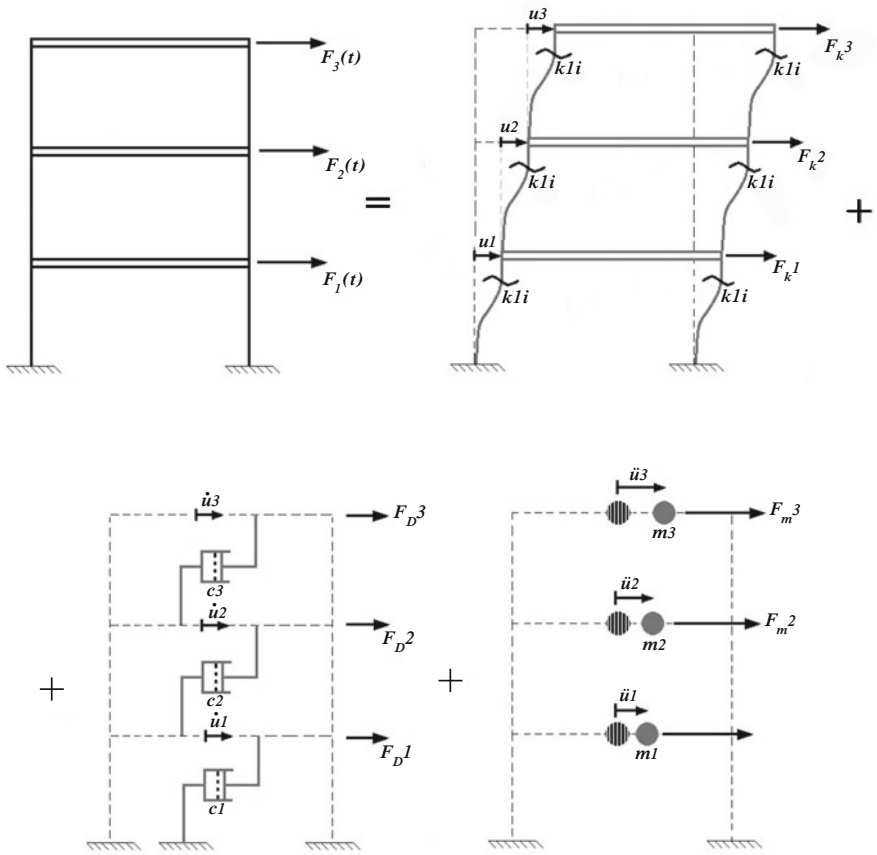


Fig. 4.9 Different contributions to the dynamic equilibrium for a three-story shear type system

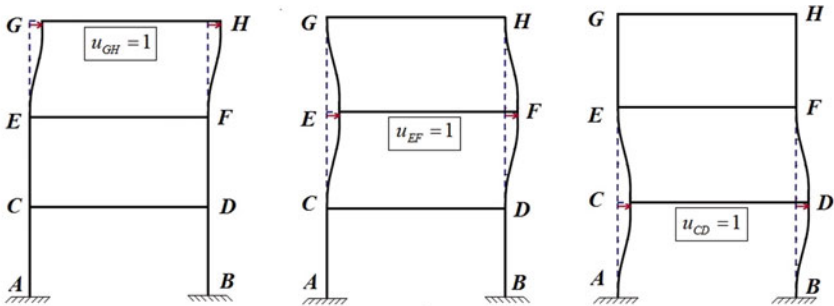


Fig. 4.10 Imposition of unitary displacements representing the DOFs of the system

Each DOF can be expressed as u_i notation, where i is the index of the story level (Eq. 4.12).

$$\begin{cases} u_{CD} = u_1 \\ u_{EF} = u_2 \\ u_{GH} = u_3 \end{cases} \quad (4.12)$$

Thus, the generic stiffness matrix of the MDOF system is given in Eq. 4.13.

$$\begin{bmatrix} (k_1 + k_2) & -k_2 & 0 \\ -k_2 & (k_2 + k_3) & -k_3 \\ 0 & -k_3 & k_3 \end{bmatrix} \begin{Bmatrix} u_1 \\ u_2 \\ u_3 \end{Bmatrix} = \begin{Bmatrix} F_{k,1} \\ F_{k,2} \\ F_{k,3} \end{Bmatrix} \quad (4.13)$$

where the generic influence stiffness coefficient k_i represents the direct elastic contribution associated with the i th DOF (Eq. 4.14)

$$k_i = k_{ii} = n_c \cdot \frac{12EI_c}{h^3} \quad (4.14)$$

In which n_c is the number of columns for the i th level (e.g. $n_c=2$ for each story in the MDOF analyzed). Finally, the elastic forces can be rewritten in Eq. 4.15

$$\frac{24EI_c}{h^3} \cdot \begin{bmatrix} 2 & -1 & 0 \\ -1 & 2 & -1 \\ 0 & -1 & 1 \end{bmatrix} \begin{Bmatrix} u_1 \\ u_2 \\ u_3 \end{Bmatrix} = \begin{Bmatrix} F_{k,1} \\ F_{k,2} \\ F_{k,3} \end{Bmatrix} \quad (4.15)$$

4.3.2.2 Damping Matrix

Assuming the same index notation used in the previous paragraph, the matrix form of damping forces is given by Eq. 4.16.

$$\begin{bmatrix} (c_1 + k_2) & -c_2 & 0 \\ -c_2 & (c_2 + c_3) & -c_3 \\ 0 & -c_3 & c_3 \end{bmatrix} \begin{Bmatrix} \dot{u}_1 \\ \dot{u}_2 \\ \dot{u}_3 \end{Bmatrix} = \begin{Bmatrix} F_{c,1} \\ F_{c,2} \\ F_{c,3} \end{Bmatrix} \quad (4.16)$$

4.3.2.3 Mass Matrix

Finally, the mass matrix is evaluated by remembering that each mass does not influence the other ones (lumped mass model). The inertia forces are expressed in the matrix Equation 4.17.

$$\begin{bmatrix} m_1 & 0 & 0 \\ 0 & m_2 & 0 \\ 0 & 0 & m_3 \end{bmatrix} \begin{Bmatrix} \ddot{u}_1 \\ \ddot{u}_2 \\ \ddot{u}_3 \end{Bmatrix} = \begin{Bmatrix} F_{m,1} \\ F_{m,2} \\ F_{m,3} \end{Bmatrix} \quad (4.17)$$

The diagonal mass matrix is composed as represented in the Eq. 4.18.

$$\begin{aligned} m_{ij} &= 0 \rightarrow \text{for } : i \neq j \\ m_{ij} &= m_i \rightarrow \text{for } : i = j \end{aligned} \quad (4.18)$$

4.4 Reduction of DOFs

The computational load required by a *bending type frame* is greater than the *shear type frame*. On the other hand, the DOF necessary for characterizing the dynamic behavior of a structure is generally less than the DOFs used to evaluate the static stresses and deformations. For example, for multi-story buildings, the predominant DOFs are the lateral displacements at each story. It is logical that the reduction in DOFs is for the case of the bending type systems for which the "static" DOFs include lateral displacement and nodal rotations. Generically, the total DOFs of the system can be reduced by applying the *condensation method*. At this purpose, one of the most commonly used approaches is the *Guyan reduction* (Guyan 1965) according to which the DOFs are divided into *master DOFs* and *slave DOFs*. For structural dynamic systems, the first ones are the lateral roof displacements, while the second ones include the nodal rotations. For the sake of simplicity, an undamped MDOF system is considered. The matrix form of the equation of motion has to be adjusted in order to divide the master DOFs (m) from the slave DOFs (s) (Eq. 4.19).

$$\begin{bmatrix} [M_{mm}] & [M_{ms}] \\ [M_{sm}] & [M_{ss}] \end{bmatrix} \begin{Bmatrix} \{\ddot{\delta}_m\} \\ \{\ddot{\delta}_s\} \end{Bmatrix} + \begin{bmatrix} [K_{mm}] & [K_{ms}] \\ [K_{sm}] & [K_{ss}] \end{bmatrix} \begin{Bmatrix} \{\delta_m\} \\ \{\delta_s\} \end{Bmatrix} = \begin{Bmatrix} \{F(t)_m\} \\ \{F(t)_s\} \end{Bmatrix} \quad (4.19)$$

This equation can be simplified by assuming that the inertial contributions associated with the slave DOFs are equal to zero.

$$[M_{ms}] = [M_{sm}] = [M_{ss}] = [0]$$

In addition, the external forces applied to the slave DOFs can be assumed negligible ($\{F(t)_s\} = \{0\}$). The system of the equations of motion can be rewritten in matrix format (Eq. 4.20).

$$\begin{bmatrix} [M_{mm}] & [0] \\ [0] & [0] \end{bmatrix} \begin{Bmatrix} \{\ddot{\delta}_m\} \\ \{\ddot{\delta}_s\} \end{Bmatrix} + \begin{bmatrix} [K_{mm}] & [K_{ms}] \\ [K_{sm}] & [K_{ss}] \end{bmatrix} \begin{Bmatrix} \{\delta_m\} \\ \{\delta_s\} \end{Bmatrix} = \begin{Bmatrix} \{F(t)_m\} \\ \{0\} \end{Bmatrix} \quad (4.20)$$

The vector of the slave DOFs δ_s can be obtained from the second row of the matrix given in Eq. 4.21.

$$co [K_{sm}] \{\delta_m\} + [K_{ss}] \{\delta_s\} = \{0\} \rightarrow \{\delta_s\} = -[K_{ss}]^{-1} [K_{sm}] \{\delta_m\} \quad (4.21)$$

Substituting the expression found in the first equation of motion, the Eq. 4.22 is given.

$$[M_{mm}] \{\ddot{\delta}_m\} + \left([K_{mm}] - [K_{ms}] [K_{ss}]^{-1} [K_{sm}] \right) \{\delta_m\} = \{F(t)_m\} \quad (4.22)$$

The equation of motion has been rewritten by referencing only the master DOFs and the Eq. 4.23 defines the reduced or condensed stiffness matrix $[K_R]$.

$$[K_R] = \left([K_{mm}] - [K_{ms}] [K_{ss}]^{-1} [K_{sm}] \right) \quad (4.23)$$

The dimension of this matrix is equal to the master DOFs. For the symmetry of the stiffness matrix, one can notice that $[K_{sm}] = [K_{sm}]^T$. In addition, the master mass matrix is represented by a diagonal matrix in which the non-zero contributions are equal to the masses concentrated at each story. As an example of a Guyan reduction application, let's consider the three-story bending type frame seen previously. Equation 4.24 represents the stiffness matrix reshaped in order to divide the master components (u_{CD} , u_{EF} , u_{GH}) from the slave ones (φ_C , φ_D , φ_E , φ_F , φ_G , φ_H).

$$\begin{bmatrix} \frac{48EI_c}{h^3} & -\frac{24EI_c}{h^3} & 0 & 0 & 0 & -\frac{6EI_c}{h^2} & -\frac{6EI_c}{h^2} & 0 & 0 \\ -\frac{24EI_c}{h^3} & \frac{48EI_c}{h^3} & -\frac{24EI_c}{h^3} & \frac{6EI_c}{h^2} & \frac{6EI_c}{h^2} & 0 & 0 & -\frac{6EI_c}{h^2} & -\frac{6EI_c}{h^2} \\ 0 & -\frac{24EI_c}{h^3} & \frac{24EI_c}{h^3} & 0 & 0 & \frac{6EI_c}{h^2} & \frac{6EI_c}{h^2} & \frac{6EI_c}{h^2} & \frac{6EI_c}{h^2} \\ 0 & \frac{6EI_c}{h^2} & 0 & \left(\frac{8EI_c}{h} + \frac{4EI_c}{L} \right) & \frac{2EI_c}{L} & \frac{2EI_c}{h} & 0 & 0 & 0 \\ 0 & \frac{6EI_c}{h^2} & 0 & \frac{2EI_c}{L} & \left(\frac{8EI_c}{h} + \frac{4EI_c}{L} \right) & 0 & \frac{2EI_c}{h} & 0 & 0 \\ -\frac{6EI_c}{h^2} & 0 & \frac{6EI_c}{h^2} & \frac{2EI_c}{h} & 0 & \left(\frac{8EI_c}{h} + \frac{4EI_c}{L} \right) & \frac{2EI_c}{L} & \frac{2EI_c}{h} & 0 \\ -\frac{6EI_c}{h^2} & 0 & \frac{6EI_c}{h^2} & 0 & \frac{2EI_c}{h} & \frac{2EI_c}{L} & \left(\frac{8EI_c}{h} + \frac{4EI_c}{L} \right) & 0 & \frac{2EI_c}{h} \\ 0 & -\frac{6EI_c}{h^2} & \frac{6EI_c}{h^2} & 0 & 0 & \frac{2EI_c}{h} & 0 & \left(\frac{4EI_c}{h} + \frac{4EI_c}{L} \right) & \frac{2EI_c}{L} \\ 0 & -\frac{6EI_c}{h^2} & \frac{6EI_c}{h^2} & 0 & 0 & 0 & \frac{2EI_c}{h} & \frac{2EI_c}{L} & \left(\frac{4EI_c}{h} + \frac{4EI_c}{L} \right) \end{bmatrix} \begin{Bmatrix} u_{CD} \\ u_{EF} \\ u_{GH} \\ \varphi_C \\ \varphi_D \\ \varphi_E \\ \varphi_F \\ \varphi_G \\ \varphi_H \end{Bmatrix} = \begin{Bmatrix} F_{CD,k} \\ F_{EF,k} \\ F_{GH,k} \\ M_{C,k} \\ M_{D,k} \\ M_{E,k} \\ M_{F,k} \\ M_{G,k} \\ M_{H,k} \end{Bmatrix} \quad (4.24)$$

The partitioned matrices represented in the Eqs. 4.25, 4.26 and 4.27 can be defined.

$$[K_{mm}] = \begin{bmatrix} \frac{48EI_c}{h^3} & -\frac{24EI_c}{h^3} & 0 \\ -\frac{24EI_c}{h^3} & \frac{48EI_c}{h^3} & -\frac{24EI_c}{h^3} \\ 0 & -\frac{24EI_c}{h^3} & \frac{24EI_c}{h^3} \end{bmatrix} \quad (4.25)$$

$$[K_{ms}] = [K_{sm}]^T = \begin{bmatrix} 0 & 0 & -\frac{6EI_c}{h^2} & -\frac{6EI_c}{h^2} & 0 & 0 \\ \frac{6EI_c}{h^2} & \frac{6EI_c}{h^2} & 0 & 0 & -\frac{6EI_c}{h^2} & -\frac{6EI_c}{h^2} \\ 0 & 0 & \frac{6EI_c}{h^2} & \frac{6EI_c}{h^2} & \frac{6EI_c}{h^2} & \frac{6EI_c}{h^2} \end{bmatrix} \quad (4.26)$$

$$[K_{ss}] = \begin{bmatrix} \left(\frac{8EI_c}{h} + \frac{4EI_b}{L}\right) & \frac{2EI_b}{L} & \frac{2EI_c}{h} & 0 & 0 & 0 \\ \frac{2EI_b}{L} & \left(\frac{8EI_c}{h} + \frac{4EI_b}{L}\right) & 0 & \frac{2EI_c}{h} & 0 & 0 \\ \frac{2EI_c}{h} & 0 & \left(\frac{8EI_c}{h} + \frac{4EI_b}{L}\right) & \frac{2EI_b}{L} & \frac{2EI_c}{h} & 0 \\ 0 & \frac{2EI_c}{h} & \frac{2EI_b}{L} & \left(\frac{8EI_c}{h} + \frac{4EI_b}{L}\right) & 0 & \frac{2EI_c}{h} \\ 0 & 0 & \frac{2EI_c}{h} & 0 & \left(\frac{4EI_c}{h} + \frac{4EI_b}{L}\right) & \frac{2EI_b}{L} \\ 0 & 0 & 0 & \frac{2EI_c}{h} & \frac{2EI_b}{L} & \left(\frac{4EI_c}{h} + \frac{4EI_b}{L}\right) \end{bmatrix} \quad (4.27)$$

It can be observed that the master stiffness matrix is coincident with the total stiffness matrix of the same MDOF system assumed as shear type. Anyway, the $[K_R]$ (3×3) reduced stiffness matrix is defined according to Eq. 4.23. Thus, the equation of motion for the bending type three-story frame is given by Eq. 4.28.

$$[M_m] \left\{ \dot{\delta}_m \right\} + [K_R] \left\{ \delta_m \right\} = \begin{bmatrix} m_1 & 0 & 0 \\ 0 & m_2 & 0 \\ 0 & 0 & m_3 \end{bmatrix} \begin{Bmatrix} \ddot{u}_1 \\ \ddot{u}_2 \\ \ddot{u}_3 \end{Bmatrix} + [K_R] \begin{Bmatrix} u_1 \\ u_2 \\ u_3 \end{Bmatrix} \quad (4.28)$$

4.5 Modal Analysis

The case of a MDOF system subjected to free vibration is analyzed here considering the generic scheme shown in Fig. 4.11. The dynamic problem is defined by means of a system of n equations of motion, in which n indicates the number of DOF of the system. In Eq. 4.29 the matrix form of the equation of motion for an undamped discrete system is reported (Chopra 2017).

$$[M] \cdot \{\ddot{u}(x, t)\} + [K] \cdot \{u(x, t)\} = \{0\} \quad (4.29)$$

Since the stiffness matrix is not diagonal, the differential equations are not independent from one another. In other words, each equation of motion contains more than one kinematic unknown. From a mathematical point of view, the solution of the dynamic differential system is complicated. In order to avoid a rigorous solution, a coordinate transformation can be applied (Eq. 4.30) (Bathe and Wilson 1976).

$$\{u(x, t)\} = [\phi(x)] \cdot \{q(t)\} \quad (4.30)$$

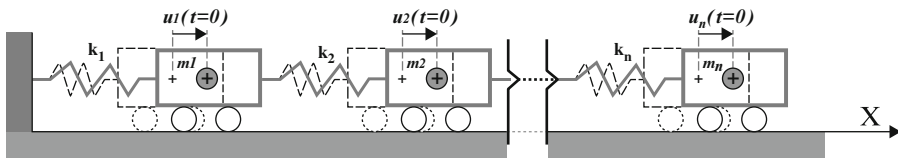


Fig. 4.11 Discrete model of MDOF undamped system



The independent variables of the system have been expressed as the multiplication between a spatial function $[\phi(x)]$ and a time function $\{q(t)\}$. Substituting the previous expression, Eq. 4.31 is given.

$$[M] \cdot [\phi] \cdot \{\ddot{q}(t)\} + [K] \cdot [\phi] \cdot \{q(t)\} = \{0\} \quad (4.31)$$

Since ϕ is time-independent, it is considered as a constant within the differential equations. The coordinate transformation approach has led to obtain an uncoupled system of equations. In fact, Eq. 4.29 assumes the typical form of the equations of motion for n independent SDOF systems for less than a constant ϕ . In reference to the characteristics just discussed, the main goal of the problem is to evaluate the component of the matrix spatial function $[\phi]$. Remembering the generic time solution for an undamped SDOF system (Eq. 4.32).

$$\begin{cases} q(t) = \frac{\dot{u}_0}{\omega} \cdot \sin(\omega \cdot t) + u_0 \cdot \cos(\omega \cdot t) \\ \ddot{q}(t) = -\omega^2 \left(\frac{\dot{u}_0}{\omega} \cdot \sin(\omega \cdot t) + u_0 \cdot \cos(\omega \cdot t) \right) \end{cases} \quad (4.32)$$

The equation of motion can be rewritten as given by the Eq. 4.33.

$$\begin{aligned} & -\omega^2 \cdot [M] \cdot [\phi] \cdot \left(\frac{\dot{u}_0}{\omega} \cdot \sin(\omega \cdot t) + u_0 \cdot \cos(\omega \cdot t) \right) + \\ & + [K] \cdot [\phi] \cdot \left(\frac{\dot{u}_0}{\omega} \cdot \sin(\omega \cdot t) + u_0 \cdot \cos(\omega \cdot t) \right) = \{0\} \end{aligned} \quad (4.33)$$

Thus, Eq. 4.34 is obtained.

$$([K] - \omega^2 \cdot [M]) \cdot [\phi] = \{0\} \quad (4.34)$$

It is important to emphasize again, from a mathematical point of view, that the initial equations of motion have been transformed into a homogeneous algebraic equation for n independent SDOF systems such that each of them is characterized by the scalar vector ϕ_i . The coefficients of the algebraic equations are given by the term $([K] - \omega^2 \cdot [M])$, while $[\phi]$ represents the unknown ones. In order to obtain a nontrivial solution ($[\phi] \neq [0]$), the coefficient must have a result that is exactly equal to zero (Eq. 4.35).

$$([K] - \omega^2 [M]) = \{0\} \quad (4.35)$$

This means setting the determinant of the coefficient matrix to zero. Thus, if the square of the angular frequency is replaced with the generic constant λ , the problem can be expressed by Eq. 4.36.

$$\det [[K] - \lambda \cdot [M]] = 0 \quad (4.36)$$

This is a typical eigenvalue problem (Kuttler 2007) in which the λ value represents the eigenvalue and each vector ϕ is the associated eigenvector. Naturally, the total number of eigenvalues and eigenvectors is equal to the number of DOF of the

system (n). Therefore, the null determinant condition corresponds to an n th order algebraic equation. In addition, since the stiffness and mass matrix are positive and symmetric, all the eigenvalues will be real and different from one another. The following steps define the procedure to be applied in order to evaluate all the eigenvectors.

- I. Definition of the eigenvalues. They represent the n roots of the algebraic equation associated to the condition of determinant equal to zero (Eq. 4.37).

$$\det [[K] - \lambda \cdot [M]] = \det \left[[M]^{-1} [K] - \lambda \cdot [I] \right] = 0 \quad (4.37)$$

Eq. 4.37 can be also expressed as

$$a_0 + a_1 \cdot \lambda + \dots + a_2 \cdot \lambda^2 + a_{n-1} \cdot \lambda^{n-1} + a_n \cdot \lambda^n = 0 \quad (4.38)$$

Thus the eigenvalues will be represented as given by the Eq. 4.39.

$$\lambda_i \text{ with } : i = 1, 2, \dots, n \rightarrow \lambda_1 < \lambda_2 < \dots < \lambda_n \quad (4.39)$$

- II. Evaluation of the i th eigenvector associated to the eigenvalue λ_i (Eq. 4.40).

$$([K] - \lambda_i \cdot [M]) \cdot \{\phi_i\} = \{0\} \rightarrow \{\phi_i\} = \begin{Bmatrix} \phi_{1i} \\ \phi_{2i} \\ \vdots \\ \phi_{ni} \end{Bmatrix} \quad (4.40)$$

When all the eigenvectors are defined, the scalar spatial matrix can be obtained (Eq. 4.41).

$$[\phi] = \left[\begin{array}{c} \begin{Bmatrix} \phi_{11} \\ \phi_{21} \\ \vdots \\ \phi_{n1} \end{Bmatrix} \\ \begin{Bmatrix} \phi_{12} \\ \phi_{22} \\ \vdots \\ \phi_{n2} \end{Bmatrix} \\ \begin{Bmatrix} \ddots \\ \ddots \\ \ddots \\ \ddots \end{Bmatrix} \\ \begin{Bmatrix} \phi_{1n} \\ \phi_{2n} \\ \vdots \\ \phi_{nn} \end{Bmatrix} \end{array} \right] = [\{\phi_1\} \{\phi_2\} \dots \{\phi_n\}] \quad (4.41)$$

It represents the eigenspace of the problem. The uncoupling of the equation of motions is due to the positivity and symmetry of the mass and stiffness matrix. From these characteristics, it is possible to demonstrate the orthogonal property of the eigenvectors. For this demonstration, a pair of different eigenvectors and their associated eigenvalues are considered. From the dynamic equilibrium equation the following system can be obtained (Eq. 4.42).

$$\begin{cases} [K] \{\phi_i\} = \omega_i^2 [M] \{\phi_i\} \\ [K] \{\phi_n\} = \omega_n^2 [M] \{\phi_n\} \end{cases} \quad (4.42)$$

Multiplying both of the terms of the two equations by the transposed eigenvector which is not associated with it, Eq. 4.43 is given.

$$\begin{cases} \{\phi_h\}^T [K] \{\phi_l\} = \omega_l^2 \{\phi_h\}^T [M] \{\phi_l\} \\ \{\phi_l\}^T [K] \{\phi_h\} = \omega_h^2 \{\phi_l\}^T [M] \{\phi_h\} \end{cases} \quad (4.43)$$

Transposing the second equation, for the symmetry of the mass and stiffness matrix it is possible to obtain Eq. 4.44.

$$\left(\{\phi_l\}^T [K] \{\phi_h\} \right)^T = \omega_h^2 \left(\{\phi_l\}^T [M] \{\phi_h\} \right)^T \rightarrow \{\phi_l\} [K] \{\phi_h\}^T = \omega_h^2 \{\phi_l\} [M] \{\phi_h\}^T \quad (4.44)$$

Thus the equation system can be rewritten (Eq. 4.45).

$$\begin{cases} \{\phi_h\}^T [K] \{\phi_l\} = \omega_l^2 \{\phi_h\}^T [M] \{\phi_l\} \\ \{\phi_h\}^T [K] \{\phi_l\} = \omega_h^2 \{\phi_h\}^T [M] \{\phi_l\} \end{cases} \quad (4.45)$$

Subtracting each term of the second equation from the related term of the first expression, the Eq. 4.46 is obtained.

$$(\omega_l^2 - \omega_h^2) \{\phi_h\}^T [M] \{\phi_l\} = 0 \quad (4.46)$$

Since all of the eigenvalues are real, positive and different from each other, the previous expression can be particularized as given in Eq. 4.47.

$$\{\phi_h\}^T [M] \{\phi_l\} = 0 \quad (4.47)$$

Substituting this expression into one of the equations reported before, the following relationship can be deduced (Eq. 4.48).

$$\{\phi_h\}^T [K] \{\phi_l\} = 0 \quad (4.48)$$

The two last equations demonstrate the orthogonality of the eigenvectors with respect to the mass and stiffness matrix. As given by the properties of algebra, if a square matrix is symmetric and the number of the associated eigenvalues is equal to the dimension of the matrix, it will be diagonalizable. The diagonalization of the matrix is obtained by as generically expressed in the Eq. 4.49.

$$[D] = [v]^T [A] [v] \quad (4.49)$$

where D indicates the diagonal matrix of the original matrix A, while v represents the eigenvectors matrix evaluated with referring to the matrix A. Using the same definition for the mass and stiffness matrix and for the *i*th eigenvector, Eq. 4.50 is given.

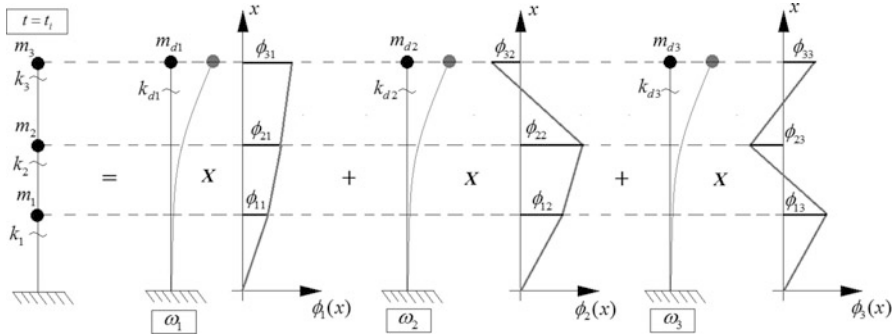


Fig. 4.12 Decomposition of the motion of a 3-DOF system for a given time instant

$$\begin{cases} [\phi_i]^T [K] [\phi_i] = [K_d] \\ [\phi_i]^T [M] [\phi_i] = [M_d] \end{cases} \quad (4.50)$$

where the diagonal matrices $[K_d]$ and $[M_d]$ are called *generalized modal stiffness matrix* and *generalized modal mass matrix*, respectively. The diagonal mass and stiffness matrices lead to obtain a decoupled dynamic equation system. Thus, the dynamic motion of the n -DOF system for a given time instant can be assumed to be the response of n independent system with equivalent mass Md_{ii} and stiffness Kd_{ii} . Each of these dynamic responses are characterized by a spatial shape function $\{\phi_i\}$. Figure 4.12 graphically focuses on this aspect for a generic 3-DOF system. In order to simplify the problem, the eigenvectors are considered normalized with respect to the mass. Naturally, the introduction of an arbitrary constant in a mathematical expression does not modify its solution. Thus, the constant Q_i associated with the i th eigenvector is introduced (Eq. 4.51).

$$Q_i = \frac{1}{\sqrt{\{\phi_i\}^T [M] \{\phi_i\}}} \quad (4.51)$$

The normalized i th eigenvector $\{\Psi_i\}$ is given by the Eq. 4.52.

$$\{\Psi_i\} = Q_i \cdot \{\phi_i\} \quad (4.52)$$

The mass and stiffness diagonal matrix can be rewritten by referring to the normalized eigenvectors (Eq. 4.53).

$$\begin{cases} [\Psi_i]^T [K] [\Psi_i] = [K_{d(\psi)}] \\ [\Psi_i]^T [M] [\Psi_i] = [M_{d(\psi)}] \end{cases} \quad (4.53)$$

The normalization with respect to the mass leads to obtaining a diagonal normalized mass matrix equal to the identity matrix (Eq. 4.54).

$$\{\Psi_i\}^T [M] \{\Psi_i\} = \frac{\{\phi_i\}^T [M] \{\phi_i\}}{\sqrt{(\{\phi_i\}^T [M] \{\phi_i\})^2}} = 1 \quad (4.54)$$

At the same time, it is easily demonstrated that the diagonal normalized stiffness matrix is composed of all the eigenvalues of the problem (Eq. 4.55).

$$\{\Psi_i\}^T [K] \{\Psi_i\} = \frac{\{\phi_i\}^T [K] \{\phi_i\}}{\sqrt{(\{\phi_i\}^T [M] \{\phi_i\})^2}} = \lambda_i = \omega_i^2 \quad (4.55)$$

This matrix obtained is called the *spectral matrix*. Generically, the normalized diagonal matrix can be expressed as given by the Eqs. 4.56 and 4.57.

$$[\bar{M}] = [I] = \begin{bmatrix} 1 & 0 & \cdots & 0 \\ 0 & 1 & \cdots & 0 \\ \vdots & \vdots & \ddots & \vdots \\ 0 & 0 & \cdots & 1 \end{bmatrix} \rightarrow \begin{cases} \bar{m}_{ij} = 1 \text{ for } i = j \\ \bar{m}_{ij} = 0 \text{ for } i \neq j \end{cases} \quad (4.56)$$

$$[\bar{K}] = [\Lambda] = \begin{bmatrix} \omega_1^2 & 0 & \cdots & 0 \\ 0 & \omega_2^2 & \cdots & 0 \\ \vdots & \vdots & \ddots & \vdots \\ 0 & 0 & \cdots & \omega_n^2 \end{bmatrix} \rightarrow \begin{cases} \bar{k}_{ij} \neq \omega_i^2 \text{ for } i = j \\ \bar{k}_{ij} = 0 \text{ for } i \neq j \end{cases} \quad (4.57)$$

Finally, the matrix form of the equations of motion can be rewritten as given by the Eq. 4.58.

$$[\bar{M}] \{\ddot{q}(t)\} + [\bar{K}] \{q(t)\} = \{0\} \quad (4.58)$$

Substituting the matrices with their components the Eq. 4.59 is obtained.

$$\begin{bmatrix} 1 & 0 & \cdots & 0 \\ 0 & 1 & \cdots & 0 \\ \vdots & \vdots & \ddots & \vdots \\ 0 & 0 & \cdots & 1 \end{bmatrix} \begin{Bmatrix} \ddot{q}_1(t) \\ \ddot{q}_2(t) \\ \vdots \\ \ddot{q}_n(t) \end{Bmatrix} + \begin{bmatrix} \omega_1^2 & 0 & \cdots & 0 \\ 0 & \omega_2^2 & \cdots & 0 \\ \vdots & \vdots & \ddots & \vdots \\ 0 & 0 & \cdots & \omega_n^2 \end{bmatrix} \begin{Bmatrix} q_1(t) \\ q_2(t) \\ \vdots \\ q_n(t) \end{Bmatrix} = \begin{Bmatrix} 0 \\ 0 \\ \vdots \\ 0 \end{Bmatrix} \quad (4.59)$$

It is important to point out some observations about the procedure just discussed. First of all, the eigenvalues of the problem represent the square of the angular *natural frequencies* ($\lambda_i = \omega_i^2$) for each of the independent SDOF systems (Blevins

2001). In addition, the generic eigenvector $\{\phi_i\}$ is a linearly independent vector that represents the *natural modes of vibration* of the MDOF system for a given natural frequency ω_i . Therefore, the generic free vibration motion of an undamped n-DOF system can be obtained by the superposition of n free oscillations with natural frequency ω_i ($i = 1, 2, \dots, n$) where each of them is associated with a given shape of the oscillation defined by means of $\{\phi_i\}$. Moreover, the matrix containing the natural mode of vibration is called the *modal matrix* where the generic component ϕ_{ij} represents the i th DOF of the system and j is the index associated with the natural frequency ω_j . Since the mathematical problem shown for the MDOF systems is based on the superposition of the effects, it is only valid for linear elastic models. In order to focus on the practical aspects of the free vibration MDOF system, it is important to characterize the problem in terms of vibrational modes response (time independent) and of dynamic response of the system (time dependent). These concepts will be discussed in detail in the following two paragraphs.

4.5.1 Vibrational Modes Response

The coordinate transformation imparted on the DOFs of the system has been used to uncouple the dynamic equilibrium equations. This has led to the evaluation of the dynamic response of the system for a given time instant by linear combination of the response of n equivalent SDOF systems characterized with different natural frequencies ω_i and spatial shapes $\{\phi_i\}$. These last ones represent the natural modes of vibration that give information about the deformed configurations of the MDOF system. Since the natural frequency of the system are increasing with the modes ($\omega_1 < \omega_2 < \dots < \omega_n$), it is possible to demonstrate that the associated natural modes have a number of sign inversions equal to $i-1$, where i represents the referenced mode. Figure 4.13 illustrates the aforementioned characteristics of a generic three DOFs system. As observed previously, the orthogonality of the modes means that each of them is independent of the others. Another physical implication of this property can be carried out in reference to the energetic content of the vibrational modes. For this reason, the mutual virtual work of l th and h th vibrational modes can be expressed by the Eq. 4.60.

$$\delta L_{h,l} = \{\delta\phi_h\}^T \cdot ([M] \{\delta\phi_l\} \ddot{q}_l + [K] \{\delta\phi_l\} q_l) \quad (4.60)$$

From the orthogonality of the modes, the following results are obtained (Eq. 4.61).

$$\delta L_{h,l} = \left(\{\delta\phi_h\}^T [M] \{\delta\phi_l\} \right) \ddot{q} + \left(\{\delta\phi_h\}^T [K] \{\delta\phi_l\} \right) q_l = 0 \quad (4.61)$$

This condition implies that the modes are energetically independent. The vibrational modes analysis is able to provide a lot of information about the MDOF system behavior. At the same time, it cannot represent the rigorous dynamic response of the system because this last one is necessarily dependent on the time.

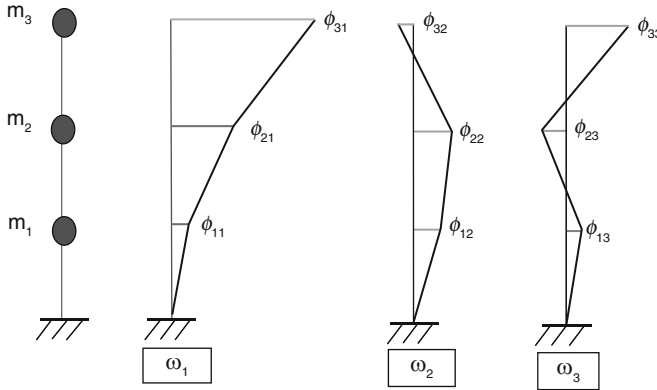


Fig. 4.13 Vibrational modes of a three DOFs system

4.5.2 Modal Expansion of Displacements

The complete dynamic characterization of the MDOF system can be obtained from the values of the DOFs (Fu and He 2001). Remembering the imposition carried out at the initial part of the Sect. 4.5, the displacement associated with the mass of the system can be evaluated (Eq. 4.62).

$$\{u(t)\} = [\phi(x)] \cdot \{q(t)\} \tag{4.62}$$

Vector $\{q(t)\}$ contains the time variable functions associated with each DOF. Thus, the $q_i(t)$ term represents a scalar factor of the given vibrational mode $\{\phi_i\}$ and it is called a *modal coordinate*. Since the modal coordinates are not space dependent, by using the Eq. 4.62 the shape of the displacement vector associated with a given mode i ($\{u_i(x,t)\}$) is proportional to the relative vibrational mode. Figure 4.14 illustrates the definition of each vector displacement contribution for the three MDOF seen before.

The dashed lines refer to the vibrational modes. Therefore, the linear combination between the modal coordinates and the vibrational modes lead to the evaluation of the dynamic response of the MDOF system (Eq. 4.63).

$$\{u(t)\} = \{\phi_1\} \cdot q_1(t) + \{\phi_2\} \cdot q_2(t) + \{\phi_3\} \cdot q_3(t) \tag{4.63}$$

Figure 4.15 illustrates the time evolution of the deformed shape for the three DOF system in reference to the three time steps. The dashed lines represent the displacement contributions for the three modes in each time step while the bold continuous lines are the dynamic displacement responses for each time step. If one vibrational mode is more dominant than the other ones ($\{q_i\} \gg \{q_h\}, \{q_l\}, \dots$) the dynamic response of the system is almost entirely due to this vibrational mode.



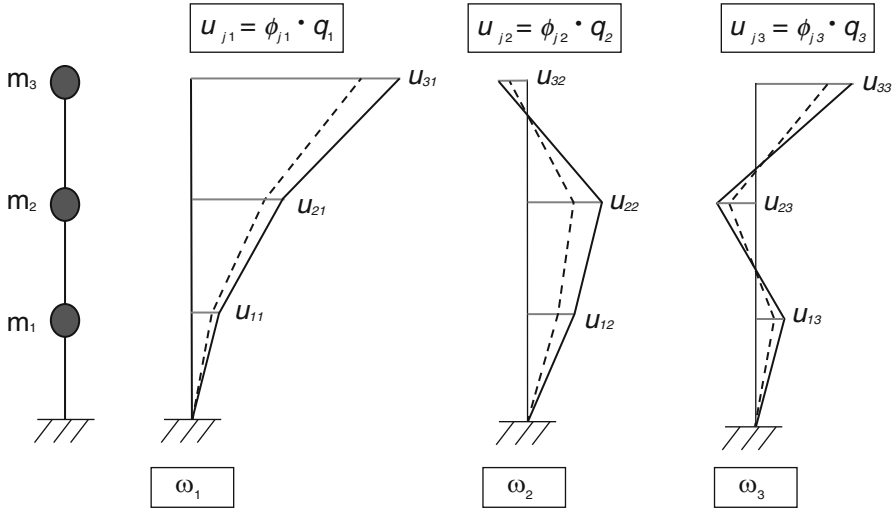


Fig. 4.14 Displacement contributions for each mode of a three DOFs system

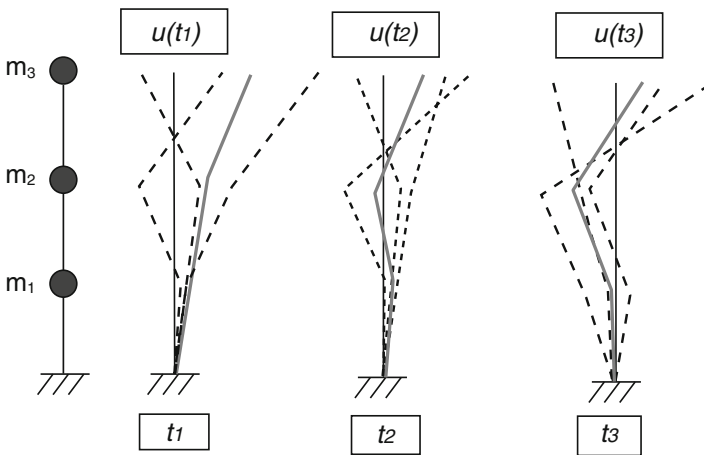
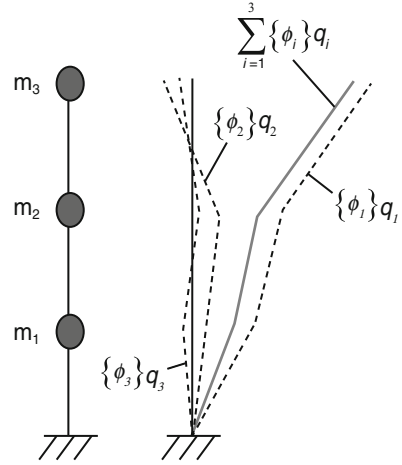


Fig. 4.15 Dynamic response of the three DOFs system for time step t_1 , t_2 and t_3

Figure 4.16 shows a generic example for a three MDOF system. As will be discussed in the next part of this chapter, the first modes are always predominant to the high modes for regular multi-story buildings.

Fig. 4.16 Predominant first mode for a three DOF system



4.5.3 Energetic Considerations

The kinematic and potential energy for the i th mode of a MDOF system can be defined as expressed in Eq. 4.64.

$$\begin{aligned}
 E_K &= \frac{1}{2} \{\ddot{u}_i\}^T [M] \{\ddot{u}_i\} = \frac{1}{2} \{\phi_i\}^T [M] \{\phi_i\} \cdot \ddot{q}_i^2 \\
 E_E &= \frac{1}{2} \{u_i\}^T [K] \{u_i\} = \frac{1}{2} \{\phi_i\}^T [K] \{\phi_i\} \cdot q_i^2
 \end{aligned}
 \tag{4.64}$$

One can notice how each of them is directly proportional to the product between the vibrational modes. This implies that the total energy of the system is distributed among each independent vibrational mode (Eq. 4.65).

$$(E_K + E_E) = \sum_{i=1}^n E(\{\phi_i\})
 \tag{4.65}$$

4.6 Free Vibrations

4.6.1 Undamped Systems

As obtained in the previous part, the dynamic solution of the equation of motion is defined by means of the vibrational modes and of the modal coordinates (Eq. 4.66) (Chopra 2017).

$$\{u(t)\} = [\phi(x)] \cdot \{q(t)\} = \sum_{i=1}^n \{\phi_i\} \cdot q_i \quad (4.66)$$

The vibrational modes are defined from the modal analysis of the system, while the modal coordinates can be obtained from the typical solutions of the SDOF by imposing the initial conditions. In reference to the case of SDOF undamped system subjected to free vibrations, the time dependent solution can be expressed in matrix form (Eq. 4.67).

$$q_i(t) = A_{1i} \cdot \sin(\omega_i \cdot t) + A_{2i} \cdot \cos(\omega_i \cdot t) \quad (4.67)$$

where the constants are expressed as vectors and can be evaluated by means of the initial conditions. Similarly to the SDOF case, the initial conditions are defined by means of the initial displacement and velocity values (Eq. 4.68).

$$\begin{aligned} \{u(t)\} &= \sum_{i=1}^n \{\phi_i\} \cdot (A_{1i} \cdot \sin(\omega_i \cdot t) + A_{2i} \cdot \cos(\omega_i \cdot t)) \\ \{\dot{u}(t)\} &= \sum_{i=1}^n \omega_i \cdot \{\phi_i\} \cdot (A_{1i} \cdot \cos(\omega_i \cdot t) - A_{2i} \cdot \sin(\omega_i \cdot t)) \end{aligned} \quad (4.68)$$

The values of each component of the displacement and velocity vector are imposed at time $t = 0$ (Eq. 4.69).

$$\begin{aligned} \{u(0)\} &= \{u_{0,i}\} = \sum_{i=1}^n \{\phi_i\} \cdot A_{2i} \\ \{\dot{u}(0)\} &= \{\dot{u}_{0,i}\} = \sum_{i=1}^n \omega_i \cdot \{\phi_i\} \cdot A_{1i} \end{aligned} \quad (4.69)$$

In other words, the following modal coordinates can be deduced at time $t = 0$ (Eq. 4.69).

$$\begin{aligned} q_i &= A_{2i} \\ \dot{q}_i &= \omega_i \cdot A_{1i} \end{aligned} \quad (4.70)$$

Finally, in the Eq. 4.71 the dynamic displacement response of the system is given.

$$\{u(t)\} = \sum_{i=1}^n \{\phi_i\} \cdot \left(q_i \cdot \cos(\omega_i \cdot t) + \frac{\dot{q}_i}{\omega_i} \cdot \sin(\omega_i \cdot t) \right) \quad (4.71)$$

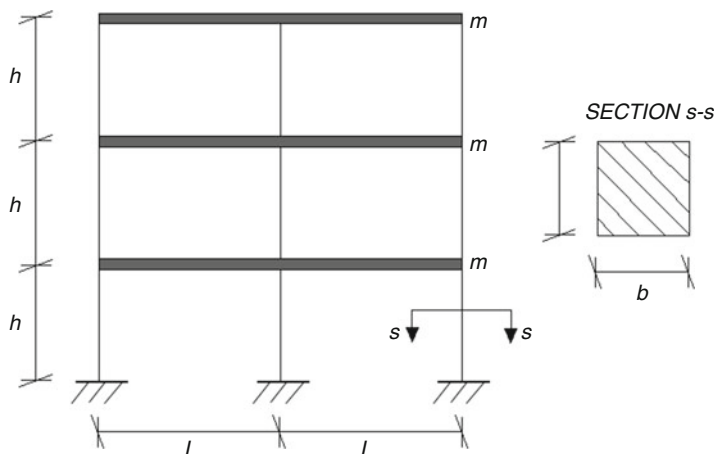


Fig. 4.17 Three-story shear type frame

Table 4.1 Geometric and mechanical characteristics of the frame

E [MPa]	b [m]	h [m]	L [m]	m [kg]
30,000	0.30	3.00	5.00	40,000

This expression is similar to the dynamic response obtained for the undamped SDOF system. In this case, the initial displacement and velocity are expressed in matrix form.

4.6.1.1 Numerical Example for Undamped System

Let's consider a three-story regular building illustrated in Fig. 4.17 for which each flooring system is considered infinitely rigid (shear type system). The geometric and mechanical characteristics of the model shown in Fig. 4.17 are reported in Table 4.1

The column elements are assumed with the same area defined by the cross section s-s. The mass and stiffness matrix are reported in the Eqs. 4.72 and 4.73.

$$[M] = m \cdot \begin{bmatrix} 1 & 0 & 0 \\ 0 & 1 & 0 \\ 0 & 0 & 1 \end{bmatrix} = 40,000 \cdot \begin{bmatrix} 1 & 0 & 0 \\ 0 & 1 & 0 \\ 0 & 0 & 1 \end{bmatrix} \text{ [kg]} \quad (4.72)$$

$$[K] = \frac{36EI_c}{h^3} \cdot \begin{bmatrix} 2 & -1 & 0 \\ -1 & 2 & -1 \\ 0 & -1 & 2 \end{bmatrix} = 2.7 \cdot 10^7 \cdot \begin{bmatrix} 2 & -1 & 0 \\ -1 & 2 & -1 \\ 0 & -1 & 2 \end{bmatrix} \text{ [N/m]} \quad (4.73)$$

The eigenvalues are defined by referring to Eq. 4.74.

$$\begin{aligned} \det \left[[M]^{-1} [K] - \lambda \cdot [I] \right] &= \det \left[0.675 \cdot 10^3 \cdot \begin{bmatrix} 2 & -1 & 0 \\ -1 & 2 & -1 \\ 0 & -1 & 1 \end{bmatrix} - \lambda \cdot \begin{bmatrix} 1 & 0 & 0 \\ 0 & 1 & 0 \\ 0 & 0 & 1 \end{bmatrix} \right] = \\ &= \det \begin{bmatrix} 1350 - \lambda & -675 & 0 \\ -675 & 1350 - \lambda & -675 \\ 0 & -675 & 675 - \lambda \end{bmatrix} = 0 \end{aligned} \quad (4.74)$$

From the condition reported above, the characteristic polynomial expressed in Eq. 4.75 is given.

$$\lambda^3 - 3.38 \cdot 10^3 \cdot \lambda^2 + 2.73 \cdot 10^6 \cdot \lambda - 0.31 \cdot 10^9 = 0 \quad (4.75)$$

The three roots of the polynomial are given by Eq. 4.76.

$$\lambda_1 = 133.69 \frac{\text{rad}}{\text{s}^2} \quad \lambda_2 = 1049.60 \frac{\text{rad}}{\text{s}^2} \quad \lambda_3 = 2191.71 \frac{\text{rad}}{\text{s}^2} \quad (4.76)$$

The natural frequency of the three modes can be evaluated (Eq. 4.77).

$$\omega_1 = 11.56 \frac{\text{rad}}{\text{s}} \quad \omega_2 = 32.40 \frac{\text{rad}}{\text{s}} \quad \omega_3 = 46.82 \frac{\text{rad}}{\text{s}} \quad (4.77)$$

Thus, the natural periods can be defined (Eq. 4.78).

$$T_1 = 0.54 \text{ s} \quad T_2 = 0.19 \text{ s} \quad T_3 = 0.13 \text{ s} \quad (4.78)$$

It is now possible to calculate the eigenvectors for each natural frequency as given by the Eq. 4.79.

$$\begin{aligned} \text{Mode1} \rightarrow & \begin{bmatrix} (1350 - 133.69) & -675 & 0 \\ -675 & (1350 - 133.69) & -675 \\ 0 & -675 & (675 - 133.69) \end{bmatrix} \begin{Bmatrix} \phi_{11} \\ \phi_{21} \\ \phi_{31} \end{Bmatrix} = \\ & = \begin{bmatrix} 1216.31 & -675 & 0 \\ -675 & 1216.31 & -675 \\ 0 & -675 & 541.31 \end{bmatrix} \begin{Bmatrix} \phi_{11} \\ \phi_{21} \\ \phi_{31} \end{Bmatrix} = \begin{Bmatrix} 0 \\ 0 \\ 0 \end{Bmatrix} \end{aligned}$$

$$\begin{aligned}
 \text{Mode2} &\rightarrow \begin{bmatrix} (1350 - 1049.60) & -675 & 0 \\ -675 & (1350 - 1049.60) & -675 \\ 0 & -675 & (675 - 1049.60) \end{bmatrix} \begin{Bmatrix} \phi_{12} \\ \phi_{22} \\ \phi_{32} \end{Bmatrix} = \\
 &= \begin{bmatrix} 300.40 & -675 & 0 \\ -675 & 300.40 & -675 \\ 0 & -675 & -374.60 \end{bmatrix} \begin{Bmatrix} \phi_{12} \\ \phi_{22} \\ \phi_{32} \end{Bmatrix} = \begin{Bmatrix} 0 \\ 0 \\ 0 \end{Bmatrix} \\
 \text{Mode3} &\rightarrow \begin{bmatrix} (1350 - 2191.71) & -675 & 0 \\ -675 & (1350 - 2191.71) & -675 \\ 0 & -675 & (675 - 2191.71) \end{bmatrix} \begin{Bmatrix} \phi_{13} \\ \phi_{23} \\ \phi_{33} \end{Bmatrix} = \\
 &= \begin{bmatrix} -841.71 & -675 & 0 \\ -675 & -841.71 & -675 \\ 0 & -675 & -1516.71 \end{bmatrix} \begin{Bmatrix} \phi_{13} \\ \phi_{23} \\ \phi_{33} \end{Bmatrix} = \begin{Bmatrix} 0 \\ 0 \\ 0 \end{Bmatrix}
 \end{aligned} \tag{4.79}$$

Usually, the eigenvectors are evaluated by setting the values of the referenced components to the top DOF of the frame equal to one. In other words, each eigenvectors is expressed as normalized to the top modal displacement. In the case study, the free vibrational modes are given by Eq. 4.80.

$$\phi = \left[\begin{Bmatrix} 0.45 \\ 0.80 \\ 1 \end{Bmatrix} \begin{Bmatrix} -1.25 \\ -0.55 \\ 1 \end{Bmatrix} \begin{Bmatrix} 1.80 \\ -2.25 \\ 1 \end{Bmatrix} \right] \tag{4.80}$$

It can be noticed that the second and third eigenvectors have one and two sign inversions, respectively. Figure 4.18 illustrates the vibrational modes, normalized with respect to the top modal displacement of the system. In addition, the mass normalized vibrational modes are given in Eq. 4.81.

$$\begin{cases} \text{Mode1} \rightarrow Q_1 = \frac{1}{\sqrt{\{\phi_1\}^T [M] \{\phi_1\}}} = 0.0037 \\ \text{Mode2} \rightarrow Q_2 = \frac{1}{\sqrt{\{\phi_2\}^T [M] \{\phi_2\}}} = 0.0030 \\ \text{Mode3} \rightarrow Q_3 = \frac{1}{\sqrt{\{\phi_3\}^T [M] \{\phi_3\}}} = 0.0016 \end{cases} \rightarrow \psi = 10^{-2} \cdot \begin{bmatrix} 0.16 & -0.37 & 0.30 \\ 0.30 & -0.16 & -0.37 \\ 0.37 & 0.30 & 0.16 \end{bmatrix} \tag{4.81}$$

Thus, the matrix form of the equation of motion is given by the Eq. 4.82.

$$\begin{bmatrix} 1 & 0 & 0 \\ 0 & 1 & 0 \\ 0 & 0 & 1 \end{bmatrix} \begin{Bmatrix} \ddot{q}_1(t) \\ \ddot{q}_2(t) \\ \ddot{q}_3(t) \end{Bmatrix} + \begin{bmatrix} 133.69 & 0 & 0 \\ 0 & 1049.60 & 0 \\ 0 & 0 & 2191.71 \end{bmatrix} \begin{Bmatrix} q_1(t) \\ q_2(t) \\ q_3(t) \end{Bmatrix} = \begin{Bmatrix} 0 \\ 0 \\ 0 \end{Bmatrix} \tag{4.82}$$

The solution of the dynamic equilibrium equations in terms of displacements at each story is evaluated as given by the Eq. 4.83.

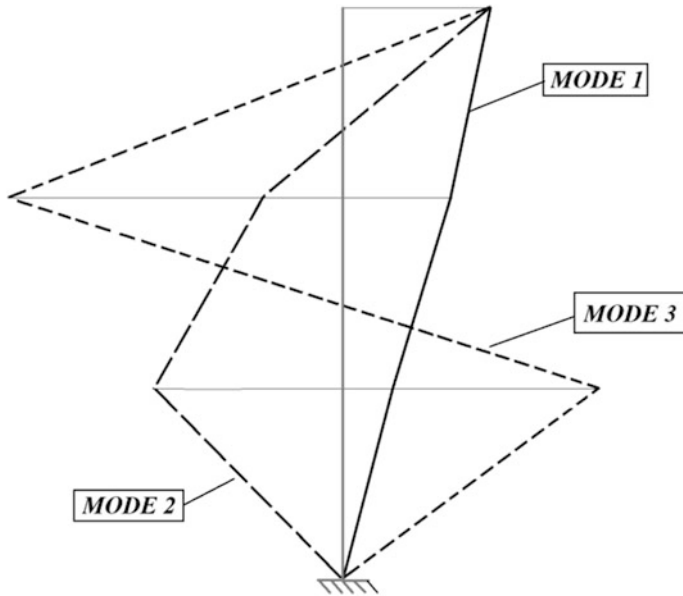


Fig. 4.18 Vibrational modes of the shear type frame normalized with respect to the top modal displacements

$$\{u(t)\} = \sum_{i=1}^n \{\phi_i\} \cdot \left(q_i \cdot \cos(\omega_i \cdot t) + \frac{\dot{q}_i}{\omega_i} \cdot \sin(\omega_i \cdot t) \right) \tag{4.83}$$

Rewriting the above expression in the form of a system, the Eq. 4.84 is given.

$$\begin{cases} \{u_1(t)\} = \begin{Bmatrix} \phi_{11} \\ \phi_{21} \\ \phi_{31} \end{Bmatrix} \cdot \left(q_1 \cdot \cos(\omega_1 \cdot t) + \frac{\dot{q}_1}{\omega_1} \cdot \sin(\omega_1 \cdot t) \right) \\ \{u_2(t)\} = \begin{Bmatrix} \phi_{12} \\ \phi_{22} \\ \phi_{32} \end{Bmatrix} \cdot \left(q_2 \cdot \cos(\omega_2 \cdot t) + \frac{\dot{q}_2}{\omega_2} \cdot \sin(\omega_2 \cdot t) \right) \\ \{u_3(t)\} = \begin{Bmatrix} \phi_{13} \\ \phi_{23} \\ \phi_{33} \end{Bmatrix} \cdot \left(q_3 \cdot \cos(\omega_3 \cdot t) + \frac{\dot{q}_3}{\omega_3} \cdot \sin(\omega_3 \cdot t) \right) \end{cases} \rightarrow \{u(t)\} = \{u_1(t)\} + \{u_2(t)\} + \{u_3(t)\} \tag{4.84}$$

Next, let's consider the initial displacement and velocity vector reported in the Eq. 4.85.

$$\begin{aligned} \{u_{0,i}\}^T &= \{0.1 \ 0.5 \ 1\} \text{ [m]} \\ \{\dot{u}_{0,i}\}^T &= \{0 \ 0 \ 0\} \text{ [m/s]} \end{aligned} \tag{4.85}$$

The modal coordinates at time $t = 0$ can be evaluated from the initial conditions (Eq. 4.86).

$$\begin{aligned} \{u_{0,i}\} &= \sum_{i=1}^3 \{\phi_i\} \cdot q_i \\ \{\dot{u}_{0,i}\} &= \sum_{i=1}^3 \{\phi_i\} \cdot \dot{q}_i \end{aligned} \quad (4.86)$$

Multiplying both sides by $\{\phi_i\}^T [M]$, Eq. 4.87 is obtained.

$$\begin{aligned} \{\phi_i\}^T [M] \{u_{0,i}\} &= \sum_{i=1}^3 \{\phi_i\}^T [M] \{\phi_i\} q_i \\ \{\phi_i\}^T [M] \{\dot{u}_{0,i}\} &= \sum_{i=1}^3 \{\phi_i\}^T [M] \{\phi_i\} \cdot \dot{q}_i \end{aligned} \quad (4.87)$$

where $\{\phi_i\}^T [M] \{\phi_i\}$ is a diagonal matrix and the modal coordinates can be deduced as given by Eq. 4.88.

$$\begin{aligned} q_i &= \frac{\{\phi_i\}^T [M] \{u_{0,i}\}}{\{\phi_i\}^T [M] \{\phi_i\}} \\ \dot{q}_i &= \frac{\{\phi_i\}^T [M] \{\dot{u}_{0,i}\}}{\{\phi_i\}^T [M] \{\phi_i\}} \end{aligned} \quad (4.88)$$

From this definition, the modal coordinates for the case study are evaluated and expressed in Eq. 4.89

$$\{q_i\} = \begin{Bmatrix} 0.7851 \\ 0.2088 \\ 0.0061 \end{Bmatrix} \quad \{\dot{q}_i\} = \begin{Bmatrix} 0 \\ 0 \\ 0 \end{Bmatrix} \quad (4.89)$$

Thus, the displacements are given by the Eq. 4.90.

$$\begin{cases} \{u_1(t)\} = \begin{Bmatrix} 0.45 \\ 0.80 \\ 1 \end{Bmatrix} \cdot 0.7851 \cdot \cos(11.56 \cdot t) \\ \{u_2(t)\} = \begin{Bmatrix} -1.258 \\ -0.55 \\ 1 \end{Bmatrix} \cdot 0.2088 \cdot \cos(32.40 \cdot t) \\ \{u_3(t)\} = \begin{Bmatrix} 1.8 \\ -2.25 \\ 1 \end{Bmatrix} \cdot 0.0061 \cdot \cos(46.82 \cdot t) \end{cases} \quad (4.90)$$

It is possible to observe how the modal became very small for higher modes. In other words, the amplitude contribution of the first mode is greater than the other ones ($q_1 > q_2 > q_3$). It is important to remember that the displacement values found

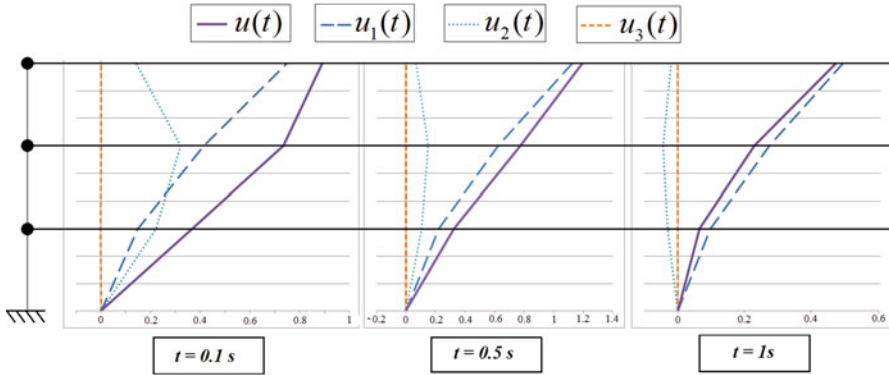


Fig. 4.19 Dynamic response of first mode, second mode, third mode and total of the three DOFs frame for $t = 0.1$ s, $t = 0.5$ s and $t = 1$ s

are in reference to the relative displacement for each DOF. Figure 4.19 illustrates the absolute displacements for each mode obtained for three different time instants. Then, Eq. 4.90 defines the total dynamic response.

$$\{u(t)\} = \{u_1(t)\} + \{u_2(t)\} + \{u_3(t)\} \tag{4.91}$$

Since the modal coordinates associated with the third mode are much smaller than the other ones, its contribution can be considered as null. In addition, one will notice that the first mode is the predominant one because the total dynamic response is very close to the first mode response. Even the second mode has little influence in the dynamic response. The dynamic response of the MDOF system is expressed as a linear combination of three periodic responses associated to its modes. This observation leads to evaluate the total displacement at a generic time as reported below (Eq. 4.92).

$$u(t) = \sum_{i=1}^3 u_i(t) \simeq A_{eq} \cdot \cos(\omega_{eq} \cdot t + \phi_{eq}) \tag{4.92}$$

where “e” identifies the equivalent characteristics of the periodic response. Thus, Eq. 4.92 can be rewritten as shown below (Eq. 4.93).

$$A_{eq} \cdot \cos(\omega_{eq} \cdot t + \phi_{eq}) \propto q_1 \cdot \cos(\omega_1 \cdot t + \phi_1) + q_2 \cdot \cos(\omega_2 \cdot t + \phi_2) + q_3 \cdot \cos(\omega_3 \cdot t + \phi_3) \tag{4.93}$$

For this case study, the phase lag is equal to zero. In addition, since the energy of a periodic signal is proportional to the square of its amplitude, the following energy balance equation can be written (Eq. 4.94).

$$A_{eq}^2 \propto q_1^2 + q_2^2 + q_3^2 \tag{4.94}$$

Substituting Eq. 4.94 in Eq. 4.93, the following Eq. 4.95 is given.

$$\cos(\omega_{eq} \cdot t) \approx \left(\frac{q_1 \cdot \cos(\omega_1 \cdot t) + q_2 \cdot \cos(\omega_2 \cdot t) + q_3 \cdot \cos(\omega_3 \cdot t)}{\sqrt{q_1^2 + q_2^2 + q_3^2}} \right) \quad (4.95)$$

Substituting the trigonometric terms with the associated 2nd order Taylor series terms centered in $x = 0$, Eq. 4.96 is given.

$$1 - \frac{(\omega_{eq} \cdot t)^2}{2} = \frac{q_1 + q_2 + q_3}{\sqrt{q_1^2 + q_2^2 + q_3^2}} - \left(\frac{q_1 \cdot \frac{(\omega_1 \cdot t)^2}{2} + q_2 \cdot \frac{(\omega_2 \cdot t)^2}{2} + q_3 \cdot \frac{(\omega_3 \cdot t)^2}{2}}{\sqrt{q_1^2 + q_2^2 + q_3^2}} \right) \quad (4.96)$$

Deriving twice with respect to the time variable, Eq. 4.97 is obtained.

$$\omega_{eq} = \frac{q_1 \cdot \omega_1 + q_2 \cdot \omega_2 + q_3 \cdot \omega_3}{\sqrt{q_1^2 + q_2^2 + q_3^2}} \quad (4.97)$$

Substituting the associated numerical values, the following result is obtained (Eq. 4.98).

$$\omega_{eq} = \frac{0.7851 \cdot 11.56 + 0.2088 \cdot 32.40 + 0.0061 \cdot 46.82}{\sqrt{0.7851^2 + 0.2088^2 + 0.0061^2}} = 19.85 \text{ rad/s} \quad (4.98)$$

This result confirms that the first mode is predominant in the dynamic response of the three DOF, but the second mode contributes as well.

4.6.2 Damped Systems

If the damping is considered, the equation of motion is rewritten in the following matrix form (Eq. 4.99).

$$[\phi_i]^T [M] [\phi_i] \{\ddot{q}(t)\} + [\phi_i]^T [C] [\phi_i] \{\dot{q}(t)\} + [\phi_i]^T [K] [\phi_i] \{q(t)\} = \{0\} \quad (4.99)$$

As previously observed, the matrices $[\phi_i]^T [M] [\phi_i]$ and are diagonalizable, but the term is not diagonal. The MDOF system cannot be solved as the superposition of n independent SDOF systems since the equations of motion are not uncoupled. When the damping matrix is diagonalizable, then it is called "classical damping matrix" and according to Rayleigh (Liu and Gorman 1995) it is obtained as the linear combination of stiffness and mass property of the system (Eq. 4.100).

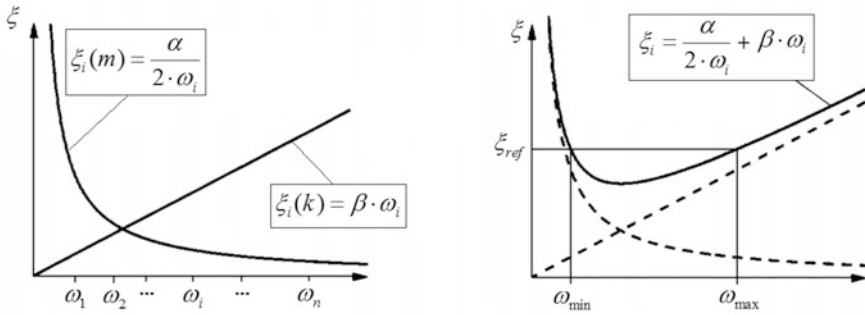


Fig. 4.20 Definition of the two control frequencies in the Rayleigh damping formulation (Chopra 2017)

$$[C] = \alpha [M] + \beta [K] \tag{4.100}$$

Multiplying both terms by the inverse mass matrix, the Eq. 4.101 is obtained.

$$2 \cdot \xi_i \cdot \omega_i = \alpha + \beta \cdot \omega_i^2 \rightarrow \xi_i = \frac{1}{2} \cdot \left(\frac{\alpha}{\omega_i} + \beta \cdot \omega_i \right) \tag{4.101}$$

The coefficients α and β depend on the damping ratio and on the natural frequency associated to the modes of the system. In practice, the damping ratio is assumed constant for every mode, while the maximum and minimum natural frequencies of interest are chosen. This damping evaluation depends on the pair of natural frequencies used. Figure 4.20 explains graphically the problem.

The control frequency values ω_{min} and ω_{max} must be chosen in order to consider all the predominant modes and to obtain reasonable damping ratio values. Usually, these parameters are defined as the predominant frequency ($\omega_{min}=\omega_1$) and the last frequency of interest for the system. According to this definition, the Eq. 4.102 shows the evaluation of the α and β coefficients.

$$\begin{cases} \alpha = 2 \cdot \xi \cdot \frac{\omega_{max} \cdot \omega_1}{(\omega_{max} + \omega_1)} \\ \beta = \frac{2 \cdot \xi}{(\omega_{max} + \omega_1)} \end{cases} \tag{4.102}$$

where ξ_{ref} is the referenced damping ratio experimentally deduced for the MDOF system. Thus, the classical damping matrix (or Rayleigh damping matrix) can be rewritten as given by Eq. 4.103.

$$[C] = \frac{2 \cdot \xi}{(\omega_{max} + \omega_1)} \cdot (\omega_{max} \cdot \omega_1 \cdot [M] + [K]) \tag{4.103}$$



Substituting this matrix in the Eq. 4.99 the dynamic equilibrium equations will be uncoupled and the solution can be easily obtained (Eq. 4.102).

$$[M_d] \{\ddot{q}(t)\} + [C_d] \{\dot{q}(t)\} + [K_d] \{q(t)\} = \{0\} \quad (4.104)$$

where $[C_d] = [\phi_i]^T [C] [\phi_i]$ is the diagonal damping matrix. According to this damping formulation, if the vibrational modes are normalized with respect to the mass, the equation of motion can be rewritten as given by Eq. 4.105.

$$[I] \{\ddot{q}(t)\} + 2 \cdot \xi_i \cdot \omega_i \cdot [I] \{\dot{q}(t)\} + [A] \{q(t)\} = \{0\} \quad (4.105)$$

4.6.2.1 Numerical Example for Damped System

For the case study described in Sect. 4.6.1.1, the first and second frequencies can be used as two control frequencies, assuming ζ_{ref} equal to 5%. Then, the following values of α and β are deduced (Eq. 4.106).

$$\begin{cases} \alpha = 2 \cdot 0.05 \cdot \frac{(32.40+11.56)}{(32.40+11.56)} = 0.8520 \\ \beta = \frac{2 \cdot 0.05}{(32.40+11.56)} = 0.0023 \end{cases} \quad (4.106)$$

Thus, the diagonal damping matrix is given by Eq. 4.107.

$$\begin{aligned} [C] &= 0.8520 \cdot 40,000 \cdot \begin{bmatrix} 1 & 0 & 0 \\ 0 & 1 & 0 \\ 0 & 0 & 1 \end{bmatrix} + 0.0023 \cdot 2.7 \cdot 10^7 \cdot \begin{bmatrix} 2 & -1 & 0 \\ -1 & 2 & -1 \\ 0 & -1 & 1 \end{bmatrix} \\ &= 6.14 \cdot 10^4 \cdot \begin{bmatrix} 2.55 & -1 & 0 \\ -1 & 2.55 & -1 \\ 0 & -1 & 1.55 \end{bmatrix} \end{aligned} \quad (4.107)$$

Equation 4.108 reports the diagonal damping matrix.

$$[C_d] = [\phi]^T [C] [\phi] = 10^4 \begin{bmatrix} 8.51 & 0 & 0 \\ 0 & 37.10 & 0 \\ 0 & 0 & 217.07 \end{bmatrix} \quad (4.108)$$

while the diagonal damping matrix normalized with respect to the mass is given by Eq. 4.109.

$$[C_d] = [\Psi]^T [C] [\Psi] = \begin{bmatrix} 1.16 & 0 & 0 \\ 0 & 3.34 & 0 \\ 0 & 0 & 5.56 \end{bmatrix} \quad (4.109)$$

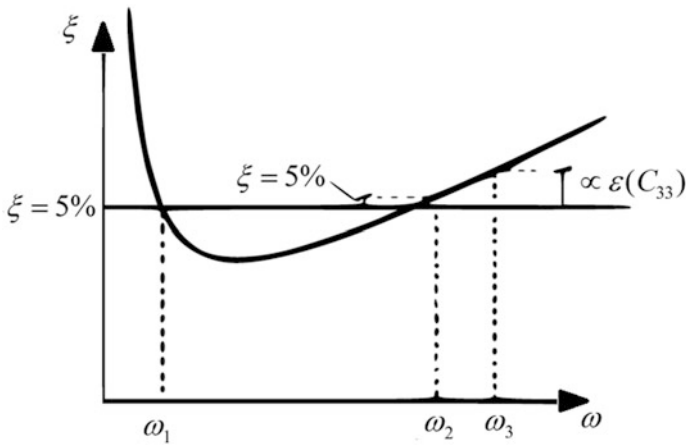


Fig. 4.21 Numerical errors in the definition of damping matrix coefficients

Comparing the results found with the ideal damping matrix composed by the terms $C_{ii} = 2 \cdot \xi_i \cdot \omega_i$, it is possible to evaluate the following percentage differences (Eq. 4.110).

$$\begin{aligned} \varepsilon(C_{11}) &= \frac{(1.16 - 1.15)}{1.15} = 0.87\% \\ \varepsilon(C_{22}) &= \frac{(3.34 - 3.24)}{3.24} = 3.08\% \\ \varepsilon(C_{33}) &= \frac{(5.56 - 4.68)}{4.68} = 18.80\% \end{aligned} \tag{4.110}$$

From this observation, one can find that the assumption of a constant damping ratio of 5% and control frequency lead to consistent result for the two first modes (Fig. 4.21). The evaluation of the modal coordinates will be dependent on the damping. In reference to the generic solution of a damped SDOF system, the Eq. 4.111 is given.

$$q_i(t) = e^{-\xi \cdot \omega_i \cdot t} \cdot \left\{ q_i \cdot \cos(\omega_{Di} \cdot t) + \frac{\dot{q}_i + \xi \cdot \omega_i \cdot q_{0i}}{\omega_{Di}} \cdot \sin(\omega_{Di} \cdot t) \right\} \tag{4.111}$$

In the Eq. 4.112 the dynamic displacement response of the system is given.

$$\{u(t)\} = \sum_{i=1}^n \{ \phi_i \} \cdot \left(e^{-\xi \cdot \omega_i \cdot t} \cdot \left\{ q_i \cdot \cos(\omega_{Di} \cdot t) + \frac{\dot{q}_i + \xi \cdot \omega_i \cdot q_i}{\omega_{Di}} \cdot \sin(\omega_{Di} \cdot t) \right\} \right) \tag{4.112}$$



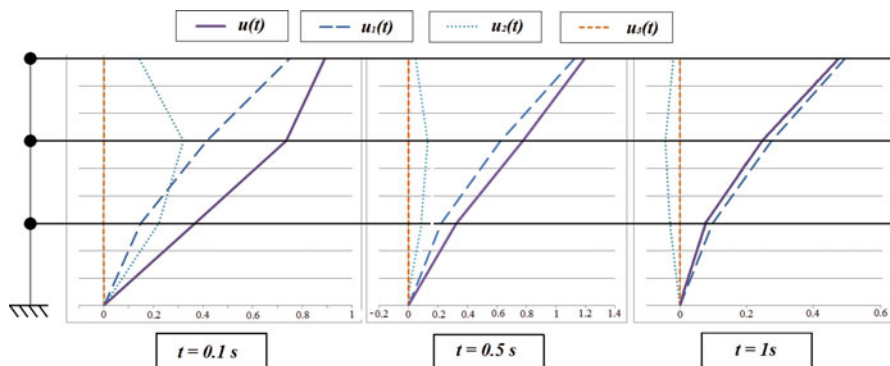


Fig. 4.22 Numerical errors in the definition of damping matrix coefficients

Considering the same structure and initial conditions of the previous paragraph and assuming $\xi = 5\% \rightarrow \omega_i \approx \omega_{D_i}$, the three components of dynamic response are expressed in the Eq. 4.113.

$$\begin{cases} \{u_1(t)\} = \{\phi_1\} \cdot e^{-\xi \cdot \omega_1 \cdot t} \cdot q_1 \cdot \{\cos(\omega_1 \cdot t) + \xi \cdot \sin(\omega_1 \cdot t)\} \\ \{u_2(t)\} = \{\phi_2\} \cdot e^{-\xi \cdot \omega_2 \cdot t} \cdot q_2 \cdot \{\cos(\omega_2 \cdot t) + \xi \cdot \sin(\omega_2 \cdot t)\} \\ \{u_3(t)\} = \{\phi_3\} \cdot e^{-\xi \cdot \omega_3 \cdot t} \cdot q_3 \cdot \{\cos(\omega_3 \cdot t) + \xi \cdot \sin(\omega_3 \cdot t)\} \end{cases} \quad (4.113)$$

Substituting the numerical values, Eq. 4.114 is obtained.

$$\begin{cases} \{u_1(t)\} = e^{-0.005 \cdot 11.56 \cdot t} \cdot \begin{Bmatrix} 0.45 \\ 0.80 \\ 1 \end{Bmatrix} \cdot 0.7851 \cdot (\cos(11.56 \cdot t) + 0.05 \cdot \sin(11.56 \cdot t)) \\ \{u_2(t)\} = e^{-0.005 \cdot 32.40 \cdot t} \cdot \begin{Bmatrix} -1.258 \\ -0.55 \\ 1 \end{Bmatrix} \cdot 0.2088 \cdot (\cos(32.40 \cdot t) + 0.05 \cdot \sin(32.40 \cdot t)) \\ \{u_3(t)\} = e^{-0.005 \cdot 46.82 \cdot t} \cdot \begin{Bmatrix} 1.8 \\ -2.25 \\ 1 \end{Bmatrix} \cdot 0.0061 \cdot (\cos(46.82 \cdot t) + 0.05 \cdot \sin(46.82 \cdot t)) \end{cases} \quad (4.114)$$

Then, Eq. 4.115 shows the total dynamic response in terms of displacements.

$$\{u(t)\} = \{u_1(t)\} + \{u_2(t)\} + \{u_3(t)\} \quad (4.115)$$

Since the decrease in the amplitude response is proportional to the terms $\xi \cdot \omega_i \cdot t$ the damping effects tend to further reduce the dynamic response of the higher modes ($\omega_1 < \omega_2 < \omega_3$) Fig. 4.22 illustrates the absolute displacements for each mode obtained for three different time instants. We can see that the contributions of

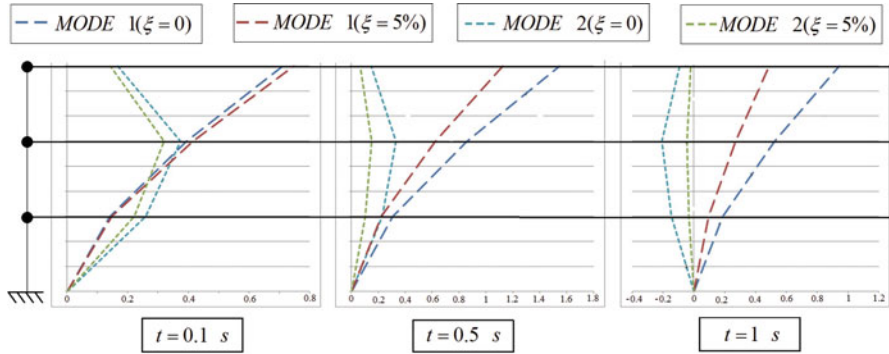


Fig. 4.23 Undamped and damped dynamic response of first and second mode of the three DOFs frame for $t = 0.1$ s, $t = 0.5$ s and $t = 0.1$ s

Table 4.2 Absolute percentage reduction of the dynamic response between undamped and damped case for the first and second modes

t = 0.1 s		t = 0.5 s		t = 1 s	
u [%]		u [%]		u [%]	
MODE 1	MODE 2	MODE 1	MODE 2	MODE 1	MODE 2
5.10	14.54	27.16	54.32	48.33	78.72

the second and third mode for $t = 15$ s is essentially equal to zero. The presence of damping in a MDOF system leads to a major predominance of the first mode over the undamped system case. In order to focus on the aforementioned issue, Fig. 4.23 is proposed referring to the total dynamic response of the system (Table 4.2).

4.7 Response to Harmonic Excitation

4.7.1 Undamped Systems

The dynamic response of an MDOF system to an external harmonic force can be derived by applying the procedure based on the modal analysis and on evaluations of the modal coordinates as explained in Sect. 4.6.1 with reference to the SDOF forced system. Suppose we consider the same 3-DOF shear type frame seen previously, in which the external forces are applied on the masses (Fig. 4.24).

The equation of motion can be expressed as reported in Eq. 4.116.

$$[\phi_i]^T [M] [\phi_i] \{\ddot{q}(t)\} + [\phi_i]^T [K] [\phi_i] \{q(t)\} = [\phi_i]^T \{F(t)\} \tag{4.116}$$

The external harmonic force vector is given by Eq. 4.117.



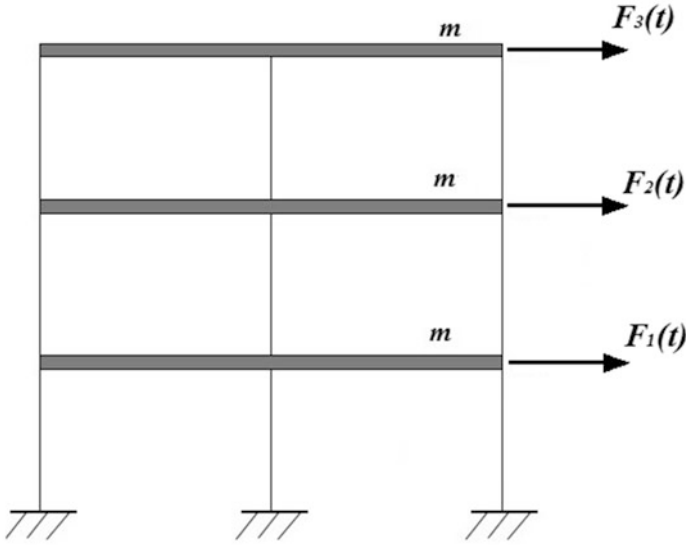


Fig. 4.24 Three DOFs shear type frame forced by harmonic excitations

$$\{F(t)\} = \begin{Bmatrix} F_1(t) \\ F_2(t) \\ F_3(t) \end{Bmatrix} = \begin{Bmatrix} F_{0,1} \cdot \sin(\omega_{f,1} \cdot t) \\ F_{0,2} \cdot \sin(\omega_{f,2} \cdot t) \\ F_{0,3} \cdot \sin(\omega_{f,3} \cdot t) \end{Bmatrix} \quad (4.117)$$

Similarly, to the free vibration case, the equations of motion can be interpreted as n uncoupled equations of SDOF systems in which $[M_d] = [\phi_i]^T [M] [\phi_i]$ and $[K_d] = [\phi_i]^T [K] [\phi_i]$ represent the equivalent independent mass and stiffness parameters for each SDOF system. In addition, $[\phi_i]^T \{F(t)\}$ indicates the force applied to the n SDOF equivalent systems. The dynamic response is governed by the steady state and free vibration solution. Since the external force is a harmonic function, the steady state response can be evaluated as expressed in Eq. 4.118.

$$\{u_{p,i}(t)\} = \{\phi_i\} \cdot \frac{F_{0,i}}{K_{d,ii} \cdot (1 - \beta_i^2)} \cdot \sin(\omega_{f,i} \cdot t) \quad (4.118)$$

Then, the modal coordinates are given by Eq. 4.119.

$$q_{p,i} = \frac{F_{0,i}}{K_{d,ii} \cdot (1 - \beta_i^2)} \cdot \sin(\omega_{f,i} \cdot t) \quad (4.119)$$

4.7.1.1 Numerical Example for Undamped System with Harmonic Excitation

For the case study, the dynamic steady state solution is evaluated as expressed by the Eq. 4.120.

$$\begin{aligned}
 u_{p,1DOF}(t) &= \phi_{11} \cdot \frac{1}{(1-\beta_1^2)} \cdot \frac{F_{0,1}}{K_{d,11}} \cdot \sin(\omega_{f,1} \cdot t) + \\
 &+ \phi_{12} \cdot \frac{1}{(1-\beta_2^2)} \cdot \frac{F_{0,1}}{K_{d,22}} \cdot \sin(\omega_{f,1} \cdot t) + \phi_{13} \cdot \frac{1}{(1-\beta_3^2)} \cdot \frac{F_{0,1}}{K_{d,33}} \cdot \sin(\omega_{f,1} \cdot t) \\
 u_{p,2DOF}(t) &= \phi_{21} \cdot \frac{1}{(1-\beta_1^2)} \cdot \frac{F_{0,2}}{K_{d,11}} \cdot \sin(\omega_{f,2} \cdot t) + \\
 &+ \phi_{22} \cdot \frac{1}{(1-\beta_2^2)} \cdot \frac{F_{0,2}}{K_{d,22}} \cdot \sin(\omega_{f,2} \cdot t) + \phi_{23} \cdot \frac{1}{(1-\beta_3^2)} \cdot \frac{F_{0,2}}{K_{d,33}} \cdot \sin(\omega_{f,2} \cdot t) \\
 u_{p,3DOF}(t) &= \phi_{31} \cdot \frac{1}{(1-\beta_1^2)} \cdot \frac{F_{0,3}}{K_{d,11}} \cdot \sin(\omega_{f,3} \cdot t) + \\
 &+ \phi_{32} \cdot \frac{1}{(1-\beta_2^2)} \cdot \frac{F_{0,3}}{K_{d,22}} \cdot \sin(\omega_{f,3} \cdot t) + \phi_{33} \cdot \frac{1}{(1-\beta_3^2)} \cdot \frac{F_{0,3}}{K_{d,33}} \cdot \sin(\omega_{f,3} \cdot t)
 \end{aligned} \tag{4.120}$$

The previous equations can be rewritten in order to define the dynamic amplification factor for each DOF by extrapolating the stiffness associated to the first mode ($K_{d,11}$) (Eq. 4.121).

$$\begin{aligned}
 u_{p,1DOF}(t) &= \frac{F_{0,1}}{K_{d,11}} \cdot \left\{ \begin{aligned} &\phi_{11} \cdot \frac{1}{(1-\beta_1^2)} \cdot \sin(\omega_{f,1} \cdot t) \\ &+ \phi_{12} \cdot \frac{1}{(1-\beta_2^2)} \cdot \frac{K_{d,11}}{K_{d,22}} \cdot \sin(\omega_{f,2} \cdot t) \\ &+ \phi_{13} \cdot \frac{1}{(1-\beta_3^2)} \cdot \frac{K_{d,11}}{K_{d,33}} \cdot \sin(\omega_{f,3} \cdot t) \end{aligned} \right\} \\
 u_{p,2DOF}(t) &= \frac{F_{0,2}}{K_{d,11}} \cdot \left\{ \begin{aligned} &\phi_{21} \cdot \frac{1}{(1-\beta_1^2)} \cdot \sin(\omega_{f,1} \cdot t) \\ &+ \phi_{22} \cdot \frac{1}{(1-\beta_2^2)} \cdot \frac{K_{d,11}}{K_{d,22}} \cdot \sin(\omega_{f,2} \cdot t) \\ &+ \phi_{23} \cdot \frac{1}{(1-\beta_3^2)} \cdot \frac{K_{d,11}}{K_{d,33}} \cdot \sin(\omega_{f,3} \cdot t) \end{aligned} \right\} \\
 u_{p,3DOF}(t) &= \frac{F_{0,3}}{K_{d,11}} \cdot \left\{ \begin{aligned} &\phi_{31} \cdot \frac{1}{(1-\beta_1^2)} \cdot \sin(\omega_{f,1} \cdot t) \\ &+ \phi_{32} \cdot \frac{1}{(1-\beta_2^2)} \cdot \frac{K_{d,11}}{K_{d,22}} \cdot \sin(\omega_{f,2} \cdot t) \\ &+ \phi_{33} \cdot \frac{1}{(1-\beta_3^2)} \cdot \frac{K_{d,11}}{K_{d,33}} \cdot \sin(\omega_{f,3} \cdot t) \end{aligned} \right\}
 \end{aligned} \tag{4.121}$$

For the sake of simplicity, the following relations are considered (Eq. 4.122).

$$\begin{aligned} F_0 &= F_{0,1} = F_{0,2} = F_{0,3} = 5000 \text{ kN} \\ \omega_f &= \omega_{f,1} = \omega_{f,2} = \omega_{f,3} = 9 \text{ rad/s} \end{aligned} \quad (4.122)$$

According to these conditions, Eq. 4.121 can be rewritten as expressed in Eq. 4.123.

$$\begin{aligned} u_{p,1DOF}(t) &= \frac{F_0}{K_{d,11}} \cdot \sin(\omega_f \cdot t) \cdot \left\{ \begin{aligned} &\phi_{11} \cdot \frac{1}{(1 - \beta_1^2)} \\ &+ \phi_{12} \cdot \frac{1}{(1 - \beta_2^2)} \cdot \frac{K_{d,11}}{K_{d,22}} \\ &+ \phi_{13} \cdot \frac{1}{(1 - \beta_3^2)} \cdot \frac{K_{d,11}}{K_{d,33}} \end{aligned} \right\} \\ u_{p,2DOF}(t) &= \frac{F_0}{K_{d,11}} \cdot \sin(\omega_f \cdot t) \cdot \left\{ \begin{aligned} &\phi_{21} \cdot \frac{1}{(1 - \beta_1^2)} \\ &+ \phi_{22} \cdot \frac{1}{(1 - \beta_2^2)} \cdot \frac{K_{d,11}}{K_{d,22}} \\ &+ \phi_{23} \cdot \frac{1}{(1 - \beta_3^2)} \cdot \frac{K_{d,11}}{K_{d,33}} \end{aligned} \right\} \\ u_{p,3DOF}(t) &= \frac{F_0}{K_{d,11}} \cdot \sin(\omega_f \cdot t) \cdot \left\{ \begin{aligned} &\phi_{31} \cdot \frac{1}{(1 - \beta_1^2)} \\ &+ \phi_{32} \cdot \frac{1}{(1 - \beta_2^2)} \cdot \frac{K_{d,11}}{K_{d,22}} \\ &+ \phi_{33} \cdot \frac{1}{(1 - \beta_3^2)} \cdot \frac{K_{d,11}}{K_{d,33}} \end{aligned} \right\} \end{aligned} \quad (4.123)$$

The terms in the brackets correspond to the dynamic amplification factor if the $K_{d,11}$ stiffness can be assumed as representative of the MDOF system stiffness. This assumption is accurate for regular MDOF structure for which the first mode is always predominant. Thus, from the Eq. 4.123, the following equivalent dynamic amplification factor can be deduced (Eq. 4.124).

$$\begin{aligned} |A_{1DOF}| &= \left\{ \phi_{11} \cdot \frac{1}{(1 - \beta_1^2)} + \phi_{12} \cdot \frac{1}{(1 - \beta_2^2)} \cdot \frac{K_{d,11}}{K_{d,22}} + \phi_{13} \cdot \frac{1}{(1 - \beta_3^2)} \cdot \frac{K_{d,11}}{K_{d,33}} \right\} \\ |A_{2DOF}| &= \left\{ \phi_{21} \cdot \frac{1}{(1 - \beta_1^2)} + \phi_{22} \cdot \frac{1}{(1 - \beta_2^2)} \cdot \frac{K_{d,11}}{K_{d,22}} + \phi_{23} \cdot \frac{1}{(1 - \beta_3^2)} \cdot \frac{K_{d,11}}{K_{d,33}} \right\} \\ |A_{3DOF}| &= \left\{ \phi_{31} \cdot \frac{1}{(1 - \beta_1^2)} + \phi_{32} \cdot \frac{1}{(1 - \beta_2^2)} \cdot \frac{K_{d,11}}{K_{d,22}} + \phi_{33} \cdot \frac{1}{(1 - \beta_3^2)} \cdot \frac{K_{d,11}}{K_{d,33}} \right\} \end{aligned} \quad (4.124)$$

Remembering that $|A_i| = \frac{1}{(1-\beta_i^2)}$, the previous relations can be rewritten and given by Eq. 4.125.

$$\begin{aligned} |A_{1DOF}| &= \left\{ \phi_{11} \cdot |A_1| + \phi_{12} \cdot |A_2| \cdot \frac{K_{d,11}}{K_{d,22}} + \phi_{13} \cdot |A_3| \cdot \frac{K_{d,11}}{K_{d,33}} \right\} \\ |A_{2DOF}| &= \left\{ \phi_{21} \cdot |A_1| + \phi_{22} \cdot |A_2| \cdot \frac{K_{d,11}}{K_{d,22}} + \phi_{23} \cdot |A_3| \cdot \frac{K_{d,11}}{K_{d,33}} \right\} \\ |A_{3DOF}| &= \left\{ \phi_{31} \cdot |A_1| + \phi_{32} \cdot |A_2| \cdot \frac{K_{d,11}}{K_{d,22}} + \phi_{33} \cdot |A_3| \cdot \frac{K_{d,11}}{K_{d,33}} \right\} \end{aligned} \quad (4.125)$$

In reference to the case study, the diagonal stiffness matrix is obtained in Eq. 4.126.

$$[K_d] = [\phi_i]^T [K] [\phi_i] = 10^7 \cdot \begin{bmatrix} 0.98 & 0 & 0 \\ 0 & 12.02 & 0 \\ 0 & 0 & 81.50 \end{bmatrix} [\text{N/m}] \quad (4.126)$$

Therefore, the amplification factors for each of the masses of the system given by Eq. 4.127 are obtained.

$$\begin{aligned} |A_{1DOF}| &= 1.23 \\ |A_{2DOF}| &= 3.21 \\ |A_{3DOF}| &= 4.38 \end{aligned} \quad (4.127)$$

The dynamic amplification for the masses located on the higher story of the frame is greater than the lower ones. In addition, it is noted that the resonance of the system can be achieved for the three cases with $\beta_i = 1$ $i = 1, 2, 3$. Generally, the amplification function for a MDOF system has a number of peaks equal to the number of DOFs, since each of them is associated with a vibrational mode. Observing Eq. 4.123, it is possible to observe that three resonance conditions can be reached ($\omega = \omega_1$, $\omega = \omega_2$ and $\omega = \omega_3$). Since the MDOF system is undamped, the displacements associated with the resonance conditions tend to be infinite (Fig. 4.25). The total dynamic response of the MDOF system is evaluated by means of the sum between the free vibrational and the steady state effects (Eq. 4.128).

$$\begin{aligned} \{u(t)\} &= \sum_{i=1}^3 \{\phi_i\} \cdot \left(\begin{aligned} &A_{1i} \cdot \sin(\omega_i \cdot t) + A_{2i} \cdot \cos(\omega_i \cdot t) \\ &+ \frac{F_{0,i}}{K_{d,ii} \cdot (1 - \beta_i^2)} \cdot \sin(\omega_{f,i} \cdot t) \end{aligned} \right) \\ \{u(t)\} &= \sum_{i=1}^3 \omega_i \cdot \{\phi_i\} \cdot \left(\begin{aligned} &A_{1i} \cdot \cos(\omega_i \cdot t) - A_{2i} \cdot \sin(\omega_i \cdot t) \\ &+ \beta_i \cdot \frac{F_{0,i}}{K_{d,ii} \cdot (1 - \beta_i^2)} \cdot \cos(\omega_{f,i} \cdot t) \end{aligned} \right) \end{aligned} \quad (4.128)$$

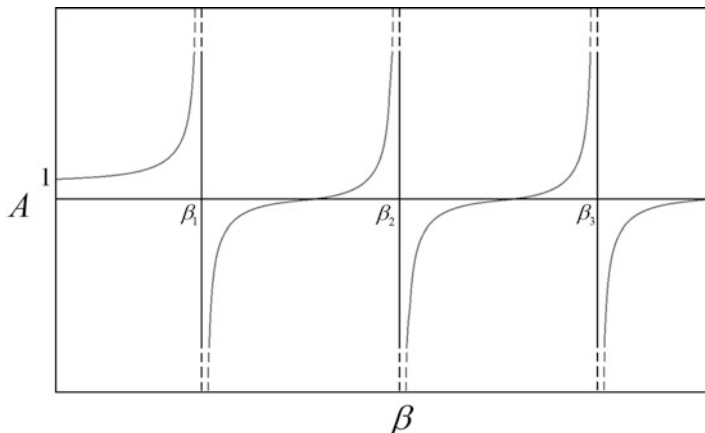


Fig. 4.25 Amplification function for the first DOF (u_1) of a three story shear type undamped building

Thus, the associated modal coordinates are given below (Eq. 4.129).

$$q_i(t) = A_{1,i} \cdot \sin(\omega_i \cdot t) + A_{2,i} \cdot \cos(\omega_i \cdot t) + \frac{F_{0,i}}{K_{d,ii} \cdot (1 - \beta_i^2)} \cdot \sin(\omega_{f,i} \cdot t) \quad (4.129)$$

Imposing the values of each component of the displacement and velocity vector at time $t = 0$ (Eq. 4.130).

$$\begin{aligned} \{u(0)\} &= \{u_{0,i}\} = \sum_{i=1}^n \{\phi_i\} \cdot A_{2i} \\ \{\dot{u}(0)\} &= \{\dot{u}_{0,i}\} = \sum_{i=1}^n \omega_i \cdot \{\phi_i\} \cdot \left(A_{1i} + \beta_i \cdot \frac{F_{0,i}}{[K_{d,ii}] \cdot (1 - \beta_i^2)} \right) \end{aligned} \quad (4.130)$$

The Eq. 4.131 is given.

$$\begin{aligned} q_i(t) &= A_{2i} \\ \dot{q}_i(t) &= \left(A_{1i} + \beta_i \cdot \frac{F_{0,i}}{[K_{d,ii}] \cdot (1 - \beta_i^2)} \right) \end{aligned} \quad (4.131)$$

The same initial conditions of the MDOF system of the previous paragraph are assumed (Eq. 4.132).

$$\begin{aligned}\{u_{0,i}\}^T &= \{0.1 \ 0.5 \ 1\} \text{ [m]} \\ \{\dot{u}_{0,i}\}^T &= \{0 \ 0 \ 0\} \text{ [m/s]}\end{aligned}\quad (4.132)$$

Multiplying both sides of the Eq. 4.129 by $\{\phi_i\}^T [M]$, the following relations are obtained (Eq. 4.133).

$$\begin{aligned}\{\phi_i\}^T [M] \{u_{0,i}\} &= \sum_{i=1}^3 \{\phi_i\}^T [M] \{q_i\} \\ \{\phi_i\}^T [M] \{\dot{u}_{0,i}\} &= \sum_{i=1}^3 \{\phi_i\}^T [M] \{\dot{q}_i\}\end{aligned}\quad (4.133)$$

From which the modal coordinates given by the Eq. 4.134 can be found.

$$\{q_i\} = \begin{Bmatrix} 0.7851 \\ 0.2088 \\ 0.0061 \end{Bmatrix} \quad \{\dot{q}_i\} = \begin{Bmatrix} 0 \\ 0 \\ 0 \end{Bmatrix}\quad (4.134)$$

The values of the constants are given in Eqs. (4.135) and (4.136).

$$\begin{aligned}\{A_{1i}\} &= \{\dot{q}_i\} - \beta_i \cdot \frac{\{\phi_i\} F_{0,i}}{[K_{d,i}] \cdot (1 - \beta_i^2)} = \\ &= \begin{Bmatrix} 0 \\ 0 \\ 0 \end{Bmatrix} - 10^{-3} \cdot \begin{Bmatrix} 5.4038 \\ 0.1315 \\ 0.0132 \end{Bmatrix} = -10^{-3} \cdot \begin{Bmatrix} 5.4038 \\ 0.1315 \\ 0.0132 \end{Bmatrix}\end{aligned}\quad (4.135)$$

$$\{A_{2i}\} = \{q_i\} = \begin{Bmatrix} 0.7851 \\ 0.2088 \\ 0.0061 \end{Bmatrix}\quad (4.136)$$

The frequency ratios are given by Eq. 4.137.

$$\begin{aligned}\beta_1 &= 0.7785 \\ \beta_2 &= 0.2778 \\ \beta_3 &= 0.1922\end{aligned}\quad (4.137)$$

Thus, dynamic response of the MDOF system can be rewritten as expressed below (Eq. 4.138).

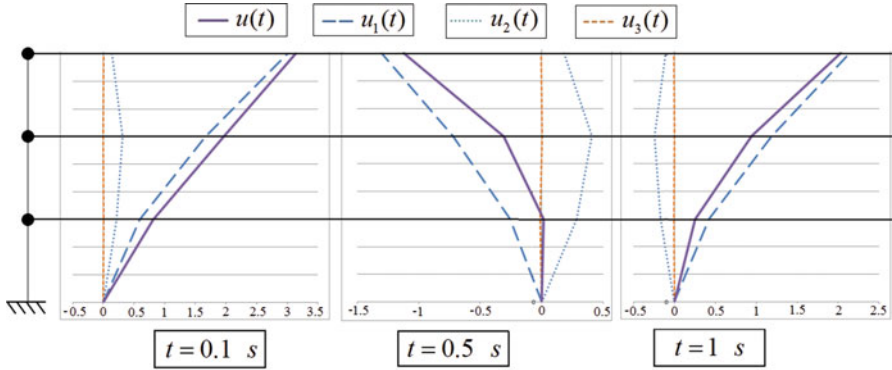


Fig. 4.26 Dynamic response of first mode, second mode, third mode and total of the three DOFs forced frame for $t = 0.1$ s, $t = 0.5$ s and $t = 1$ s

$$\begin{cases} \{u_1(t)\} = \begin{Bmatrix} 0.45 \\ 0.80 \\ 1 \end{Bmatrix} \cdot \begin{Bmatrix} 0.7851 \cdot \cos(11.56 \cdot t) \\ -10^{-3} \cdot 5.4038 \cdot 0.7785 \cdot \sin(11.56 \cdot t) \\ + \frac{5000000}{0.98 \cdot 10^7 \cdot (1 - 0.7785^2)} \cdot \sin(9 \cdot t) \end{Bmatrix} \\ \{u_2(t)\} = \begin{Bmatrix} -1.258 \\ -0.55 \\ 1 \end{Bmatrix} \cdot \begin{Bmatrix} 0.2088 \cdot \cos(32.40 \cdot t) \\ -10^{-3} \cdot 0.1315 \cdot 0.2778 \cdot \sin(32.40 \cdot t) \\ + \frac{5000000}{12.02 \cdot 10^7 \cdot (1 - 0.2778^2)} \cdot \sin(9 \cdot t) \end{Bmatrix} \\ \{u_3(t)\} = \begin{Bmatrix} 1.8 \\ -2.25 \\ 1 \end{Bmatrix} \cdot \begin{Bmatrix} 0.0061 \cdot \cos(46.82 \cdot t) \\ -10^{-3} \cdot 0.0133 \cdot 0.1922 \cdot \sin(46.82 \cdot t) \\ + \frac{5000000}{81.50 \cdot 10^7 \cdot (1 - 0.1922^2)} \cdot \sin(9 \cdot t) \end{Bmatrix} \end{cases} \quad (4.138)$$

Figure 4.26 shows the dynamic response evaluated at three different time instants. The presence of the external forces on the masses of the system leads to the modification of percentage contributions of the vibrational modes to the dynamic response. As seen in the previous paragraph, the dynamic response of the MDOF system can be expressed by the Eq. 4.139.

$$u(t) = \sum_{i=1}^3 u_i(t) \simeq A_{eq} \cdot \cos(\omega_{eq} \cdot t + \phi_{eq}) \quad (4.139)$$

The total dynamic response of the case study frame can be written as given by Eq. 4.140.

$$A_{eq} \cdot \cos(\omega_{eq} \cdot t + \phi_{eq}) \propto q_1 \cdot \cos(\omega_1 \cdot t + \phi_1) + q_2 \cdot \cos(\omega_2 \cdot t + \phi_2) + q_3 \cdot \cos(\omega_3 \cdot t + \phi_3) + \left(\frac{F_0}{k}\right)_{eq} \cdot |A_{eq}| \cdot \sin(\omega_{f,eq} \cdot t) \quad (4.140)$$

Introducing the constant $C = \left(\frac{F_0}{k}\right)_{eq} \cdot |A_{eq}|$ and since the energy of a periodic signal is proportional to the square of its amplitude, the following energy balance equation can be written (Eq. 4.141).

$$A_{eq}^2 \propto q_1^2 + q_2^2 + q_3^2 + C^2 \quad (4.141)$$

Substituting this expression into the previous relation, Eq. 4.142 is given.

$$\cos(\omega_{eq} \cdot t) \approx \left(\frac{q_1 \cdot \cos(\omega_1 \cdot t) + q_2 \cdot \cos(\omega_2 \cdot t) + q_3 \cdot \cos(\omega_3 \cdot t) + C \cdot \sin(\omega_{f,eq} \cdot t)}{\sqrt{q_1^2 + q_2^2 + q_3^2 + C^2}} \right) \quad (4.142)$$

Substituting the trigonometric terms with the associated 2nd order Taylor series centered in $x = 0$, Eq. 4.143 is given.

$$1 - \frac{(\omega_{eq} \cdot t)^2}{2} = \frac{q_1 + q_2 + q_3}{\sqrt{q_1^2 + q_2^2 + q_3^2 + C^2}} - \left(\frac{q_1 \cdot \frac{(\omega_1 \cdot t)^2}{2} + q_2 \cdot \frac{(\omega_2 \cdot t)^2}{2} + q_3 \cdot \frac{(\omega_3 \cdot t)^2}{2}}{\sqrt{q_1^2 + q_2^2 + q_3^2 + C^2}} \right) + C \cdot \frac{(\omega_{f,eq} \cdot t)}{\sqrt{q_1^2 + q_2^2 + q_3^2 + C^2}} \quad (4.143)$$

Deriving twice with respect to the time variable, Eq. 4.144 is obtained.

$$\omega_{eq} = \frac{q_1 \cdot \omega_1 + q_2 \cdot \omega_2 + q_3 \cdot \omega_3}{\sqrt{q_1^2 + q_2^2 + q_3^2 + C^2}} \quad (4.144)$$

It is possible to see that the constant C at denominator tends to reduce the natural equivalent frequency of the MDOF system subjected to external forces. This leads to obtaining a result closer to the first mode frequency ($\omega_1 = \min(\omega_i)$) and therefore its contribution for the total dynamic response is still more representative.

4.7.2 Viscously Damped Systems

Similar to previous case, Eq. 4.145 represents the dynamic equilibrium equation for a damped MDOF system.

$$[\phi_i]^T [M] [\phi_i] \{\ddot{q}(t)\} + [\phi_i]^T [C] [\phi_i] \{\dot{q}(t)\} + [\phi_i]^T [K] [\phi_i] \{q(t)\} = [\phi_i]^T \{F(t)\} \quad (4.145)$$

System of equations can be uncoupled only for classic damping matrix formulation. In this case, according to the results found for SDOF systems, the steady state

solution assumes the form reported in Eq. 4.146.

$$\{u_{p,i}(t)\} = \{\phi_i\} \cdot \frac{F_{0,i}}{K_{d,ii}} \cdot \frac{1}{(1-\beta_i^2)^2 + (2 \cdot \xi \cdot \beta_i)^2} \cdot \left[(1 - \beta_i^2) \cdot \sin(\omega_{f,i} \cdot t) - 2 \cdot \xi \cdot \beta_i \cdot \cos(\omega_{f,i} \cdot t) \right] \quad (4.146)$$

where the modal coordinates are given by Eq. 4.147.

$$q_{p,i} = \frac{F_{0,i}}{K_{d,ii}} \cdot \frac{1}{(1-\beta_i^2)^2 + (2 \cdot \xi \cdot \beta_i)^2} \cdot \left[(1 - \beta_i^2) \cdot \sin(\omega_{f,i} \cdot t) - 2 \cdot \xi \cdot \beta_i \cdot \cos(\omega_{f,i} \cdot t) \right] \quad (4.147)$$

In order to simplify the following dissertation, the terms reported in Eq. 4.148 are considered.

$$|A_i|^2 = \frac{1}{(1 - \beta_i^2)^2 + (2 \cdot \xi \cdot \beta_i)^2} \quad (4.148)$$

$$B_i = \left[(1 - \beta_i^2) \cdot \sin(\omega_{f,i} \cdot t) - 2 \cdot \xi \cdot \beta_i \cdot \cos(\omega_{f,i} \cdot t) \right]$$

For the case study, the dynamic steady state solution is evaluated as expressed by the Eq. 4.149.

$$\begin{aligned} u_{p,1DOF}(t) &= \phi_{11} \frac{F_{0,1}}{K_{d,11}} |A_1|^2 \cdot B_1 + \phi_{12} \cdot \frac{F_{0,1}}{K_{d,22}} \cdot |A_2|^2 \cdot B_2 + \phi_{13} \cdot \frac{F_{0,1}}{K_{d,33}} \cdot |A_3|^2 \cdot B_3 \\ u_{p,2DOF}(t) &= \phi_{21} \cdot \frac{F_{0,2}}{K_{d,11}} \cdot |A_1|^2 \cdot B_1 + \phi_{22} \cdot \frac{F_{0,2}}{K_{d,22}} \cdot |A_2|^2 \cdot B_2 + \phi_{23} \cdot \frac{F_{0,2}}{K_{d,33}} \cdot |A_3|^2 \cdot B_3 \\ u_{p,3DOF}(t) &= \phi_{31} \cdot \frac{F_{0,3}}{K_{d,11}} \cdot |A_1|^2 \cdot B_1 + \phi_{32} \cdot \frac{F_{0,3}}{K_{d,22}} \cdot |A_2|^2 \cdot B_2 + \phi_{33} \cdot \frac{F_{0,3}}{K_{d,33}} \cdot |A_3|^2 \cdot B_3 \end{aligned} \quad (4.149)$$

Since the damping ratio assumes a very small value, for the sake of simplicity the B_i coefficients can be assumed as reported in Eq. 4.150.

$$B_i \approx (1 - \beta_i^2) \cdot \sin(\omega_{f,i} \cdot t) \quad (4.150)$$

The previous equations can be rewritten in order to define the dynamic amplification factor for each DOF by explicating the stiffness associated to the first mode ($K_{d,11}$) (Eq. 4.151).

$$\begin{aligned}
 u_{p,1DOF}(t) &= \frac{F_{0,1}}{K_{d,11}} \cdot \sin(\omega_f \cdot t) \cdot (1 - \beta_1^2) \cdot \left\{ \begin{aligned} &\phi_{11} \cdot |A_1|^2 \\ &+ \phi_{12} \cdot \frac{K_{d,11}}{K_{d,22}} \cdot |A_2|^2 \cdot \frac{(1 - \beta_2^2)}{(1 - \beta_1^2)} \\ &+ \phi_{13} \cdot \frac{K_{d,11}}{K_{d,33}} \cdot |A_3|^2 \cdot \frac{(1 - \beta_3^2)}{(1 - \beta_1^2)} \end{aligned} \right\} \\
 u_{p,2DOF}(t) &= \frac{F_{0,2}}{K_{d,11}} \cdot \sin(\omega_f \cdot t) \cdot (1 - \beta_1^2) \cdot \left\{ \begin{aligned} &\phi_{21} \cdot |A_1|^2 \\ &+ \phi_{22} \cdot \frac{K_{d,11}}{K_{d,22}} \cdot |A_2|^2 \cdot \frac{(1 - \beta_2^2)}{(1 - \beta_1^2)} \\ &+ \phi_{23} \cdot \frac{K_{d,11}}{K_{d,33}} \cdot |A_3|^2 \cdot \frac{(1 - \beta_3^2)}{(1 - \beta_1^2)} \end{aligned} \right\} \\
 u_{p,3DOF}(t) &= \frac{F_{0,3}}{K_{d,11}} \cdot \sin(\omega_f \cdot t) \cdot (1 - \beta_1^2) \cdot \left\{ \begin{aligned} &\phi_{31} \cdot |A_1|^2 \\ &+ \phi_{32} \cdot \frac{K_{d,11}}{K_{d,22}} \cdot |A_2|^2 \cdot \frac{(1 - \beta_2^2)}{(1 - \beta_1^2)} \\ &+ \phi_{33} \cdot \frac{K_{d,11}}{K_{d,33}} \cdot |A_3|^2 \cdot \frac{(1 - \beta_3^2)}{(1 - \beta_1^2)} \end{aligned} \right\}
 \end{aligned} \tag{4.151}$$

Thus, the three dynamic amplification factors reported in Eq. 4.152 can be evaluated.

$$\begin{aligned}
 |A_{1DOF}| &= (1 - \beta_1^2) \cdot \left\{ \begin{aligned} &\phi_{11} \cdot |A_1|^2 + \phi_{12} \cdot \frac{K_{d,11}}{K_{d,22}} \cdot |A_2|^2 \cdot \frac{(1 - \beta_2^2)}{(1 - \beta_1^2)} \\ &+ \phi_{13} \cdot \frac{K_{d,11}}{K_{d,33}} \cdot |A_3|^2 \cdot \frac{(1 - \beta_3^2)}{(1 - \beta_1^2)} \end{aligned} \right\} \\
 |A_{2DOF}| &= (1 - \beta_1^2) \cdot \left\{ \begin{aligned} &\phi_{21} \cdot |A_1|^2 + \phi_{22} \cdot \frac{K_{d,11}}{K_{d,22}} \cdot |A_2|^2 \cdot \frac{(1 - \beta_2^2)}{(1 - \beta_1^2)} \\ &+ \phi_{23} \cdot \frac{K_{d,11}}{K_{d,33}} \cdot |A_3|^2 \cdot \frac{(1 - \beta_3^2)}{(1 - \beta_1^2)} \end{aligned} \right\} \\
 |A_{3DOF}| &= (1 - \beta_1^2) \cdot \left\{ \begin{aligned} &\phi_{31} \cdot |A_1|^2 + \phi_{32} \cdot \frac{K_{d,11}}{K_{d,22}} \cdot |A_2|^2 \cdot \frac{(1 - \beta_2^2)}{(1 - \beta_1^2)} \\ &+ \phi_{33} \cdot \frac{K_{d,11}}{K_{d,33}} \cdot |A_3|^2 \cdot \frac{(1 - \beta_3^2)}{(1 - \beta_1^2)} \end{aligned} \right\}
 \end{aligned} \tag{4.152}$$

For the analyzed case, the following values have been found (Eq. 4.153).

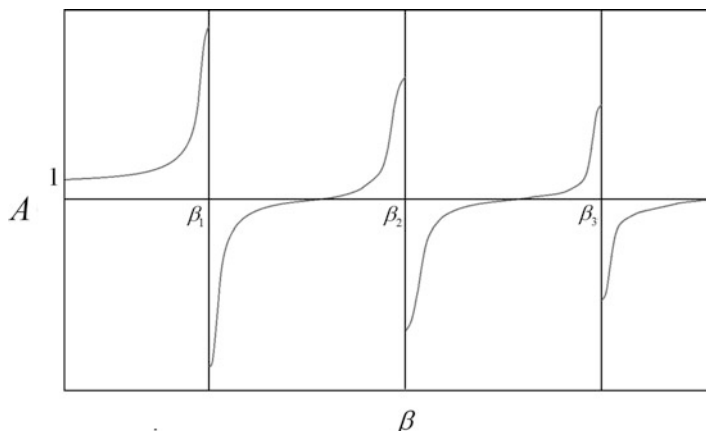


Fig. 4.27 Amplification function for the first DOF (u_1) of a three story shear type damped building

$$\begin{aligned}
 |A_{1DOF}| &= 1.18 \\
 |A_{2DOF}| &= 3.09 \\
 |A_{3DOF}| &= 4.21
 \end{aligned} \tag{4.153}$$

It can be observed that these values are less than the other ones evaluated for an undamped MDOF system. As we know, the damping on the structure leads to the dissipation of the free vibration response in a brief amount of time. For this reason, the total dynamic response of the system is practically governed by the steady state response.

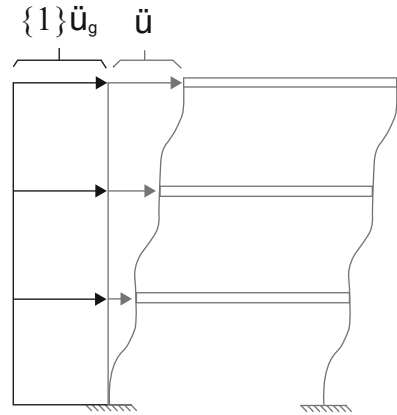
Generally, according to the considerations made for the amplification function of an undamped system, the introduction of damping in the system leads to obtain the resonance conditions, while the amplification factor is not infinite. Figure 4.27 refers to the amplification function for a generic 3-DOF damped system.

4.8 Earthquake Response

When the external forces applied on the masses of the MDOF system are due to the earthquake excitation, the vector $F(t)$ of equilibrium equations assumes the following form (Eq. 4.154).

$$\{F(t)\} = - \begin{bmatrix} m_1 & 0 & \cdots & 0 \\ 0 & m_2 & \cdots & 0 \\ \vdots & \vdots & \ddots & \vdots \\ 0 & 0 & \cdots & m_n \end{bmatrix} \cdot \begin{Bmatrix} \ddot{u}_g(t) \\ \ddot{u}_g(t) \\ \ddot{u}_g(t) \end{Bmatrix} = - \begin{bmatrix} m_1 & 0 & \cdots & 0 \\ 0 & m_2 & \cdots & 0 \\ \vdots & \vdots & \ddots & \vdots \\ 0 & 0 & \cdots & m_n \end{bmatrix} \cdot \begin{Bmatrix} 1 \\ 1 \\ \vdots \\ 1 \end{Bmatrix} \cdot \ddot{u}_g(t) \tag{4.154}$$

Fig. 4.28 Composition of lateral displacement components



The ground acceleration induces the inertial forces for each DOF of the system. As discussed in the paragraph for SDOF systems, the seismic excitation causes an acceleration at the base of the structure ($\ddot{u}_g(t)$) and a relative acceleration $\ddot{u}(t)$ that produces deformation on the structure. The first one causes a rigid motion of the system (Fig. 4.28). For a generic MDOF system the lateral components are expressed in a matrix called *Influence coefficient matrix*, composed of a number of columns equal to the base motion components and a number of rows equal to the DOFs.

Since only lateral displacements are usually generated by earthquake excitation the *Influence coefficient matrix* reduces to an *influence coefficient vector* of dimension $n \times 1$, where n is the number of DOFs. Thus, the equation of motion for a MDOF system classical damped subjected to earthquake excitation can be expressed as shown in Eq. 4.155.

$$[\phi_i]^T [M] [\phi_i] \{\ddot{q}(t)\} + [\phi_i]^T [C] [\phi_i] \{\dot{q}(t)\} + [\phi_i]^T [K] [\phi_i] \{q(t)\} = -[\phi_i]^T [M] \{1\} \ddot{u}_g \tag{4.155}$$

where $\{1\}$ represents the Influence coefficient vector and the right and left sides of the equation have been previously multiplied by $[\phi]^T$. Normalizing with respect to the mass, the equation of motion can be rewritten as shown in Eq. 4.156.

$$[I] \{\ddot{q}(t)\} + [\bar{C}] \{\dot{q}(t)\} + [A] \{q(t)\} = -\{g\} \ddot{u}_g \tag{4.156}$$

where the damping is defined according to Rayleighs formulation (Eq. 4.157).

$$[C] = \alpha [M] + \beta [K] \rightarrow \sum_{i=1}^n \{\Psi_i\}^T [C] \{\Psi_i\} = \sum_{i=1}^n \frac{\{\phi_i\}^T [C] \{\phi_i\}}{\sqrt{(\{\phi_i\}^T [M] \{\phi_i\})^2}} = [\bar{C}] \tag{4.157}$$

Vector $\{g\}$ contains the coefficients expressed by Eq. 4.158.

$$g_i = \frac{\{\phi_i\}^T [M] \{1\}}{\sqrt{\{\phi_i\}^T [M] \{\phi_i\}}} = \{\Psi_i\}^T [M] \{1\} \quad (4.158)$$

It represents the i th *modal participation factor* that indicates the contribution of the associated mode to the vibration of the system. This parameter is expressed in $[kg]^{1/2}$ unit measure and is very important since it provides information about the representativeness of the mode. As observed in the previous paragraph, the contribution of each mode decreases as the frequency of the modes increases. In other words, the absolute values of the modal participation factors are sorted as shown (Eq. 4.159).

$$|g_1| > |g_2| > \dots > |g_n| \quad (4.159)$$

This leads to have a low external seismic excitation for higher modes (Eq. 4.160).

$$|F(t)_1| > |F(t)_2| > \dots > |F(t)_n| \quad (4.160)$$

Similarly, the square of i th the modal participation factor g_i is called *modal mass* associated to the respective mode (Eq. 4.161).

$$m_{\text{mod},i} = g_i^2 = \frac{\left(\{\phi_i\}^T [M] \{1\}\right)^2}{\{\phi_i\}^T [M] \{\phi_i\}} = \left(\{\Psi_i\}^T [M] \{1\}\right)^2 \quad (4.161)$$

It represents the energetic contribution of the i th mode to the total dynamic response of the system. In other words, $m_{\text{mod},i}$ is the mass contribution of mode i and its unit of measure is $[kg]$. From this definition, it is found that the sum of the n -DOFs modal masses are equal to the total mass of the MDOF system (Eq. 4.162).

$$\sum_{i=1}^n m_{\text{mod},i} = \sum_{i=1}^n m_i \quad (4.162)$$

Thus the percentage contribution of each mode can be deduced according Eq. 4.163.

$$\% (m_{\text{mod},i}) = \frac{m_{\text{mod},i}}{\sum_{i=1}^n m_i} \quad (4.163)$$

Usually, when the accumulated percentage modal mass is greater than 90% it is possible to neglect the remaining vibrational modes. Different from the harmonic excitation case, the solution of the problem cannot be obtained in closed form. For this reason, the dynamic response of the MDOF system can be evaluated by means of two different approaches outlined below:

- I. numerical methods application;
- II. combinations of the modal displacements obtained from the elastic spectrum

The second approach is widely used because it uses a simple method to obtain the maximum dynamic response of a MDOF system subjected to a seismic excitation. It is based on the elastic acceleration spectrum definition in Sect. 12.3 that represents the maximum earthquake response of different SDOF systems. Usually, the acceleration responses of the system are evaluated for each vibrational mode ($S_a(\omega_i)$). In addition, the pseudo-velocity ($PS_v(\omega_i)$) and pseudo-displacement ($PS_d(\omega_i)$) response can be obtained from the acceleration responses (Eq. 4.164).

$$S_a(\omega_i) \rightarrow \begin{cases} PS_v(\omega_i) = \frac{S_a(\omega_i)}{\omega_i} \\ PS_d(\omega_i) = \frac{S_a(\omega_i)}{\omega_i^2} \end{cases} \quad (4.164)$$

Since this analysis is not capable of evaluating the time dependent dynamic response but only its maximum values, the modal coordinates can be expressed as given by Eq. 4.165.

$$q_{i,\max} = g_{m,i} \cdot S_d(\omega_i) \simeq g_{m,i} \cdot \frac{S_a(\omega_i)}{\omega_i^2} \quad (4.165)$$

where the modal coordinates are dependent on the modal participation factor because it can be seen as a scale factor of the dynamic response for the considered mode. According to the coordinate transformation and with the mass normalization, the maximum displacements for the i th mode are given by the Eq. 4.166.

$$\{u_{i,\max}\} = \{\Psi_i\} \cdot q_{i,\max} \simeq \{\phi_i\} \cdot g_{m,i} \cdot \frac{S_a(\omega_i)}{\omega_i^2} \quad (4.166)$$

Applying the same consideration for every vibrational mode, the following total maximum displacement matrix is evaluated (Eq. 4.167).

$$[u_{\max}] = [\Psi_i] \cdot \{q_{\max}\} = [\{u_{1,\max}\} \{u_{2,\max}\} \dots \{u_{n,\max}\}] \quad (4.167)$$

Each column vector represents the maximum dynamic displacement associated to every masses of the system for the vibrational mode i . The maximum total dynamic displacements have to be evaluated by means of modal combinations. For this purpose, three different modal combination approaches are proposed:

- (a) Square Root of Sum of Squares (SRSS)

$$u_{i,\max} = \sqrt{(\Psi_{i1} \cdot q_{1,\max})^2 + (\Psi_{i2} \cdot q_{2,\max})^2 + \dots + (\Psi_{in} \cdot q_{n,\max})^2} \quad (4.168)$$

This approach is used when the natural periods are clearly different from one another.

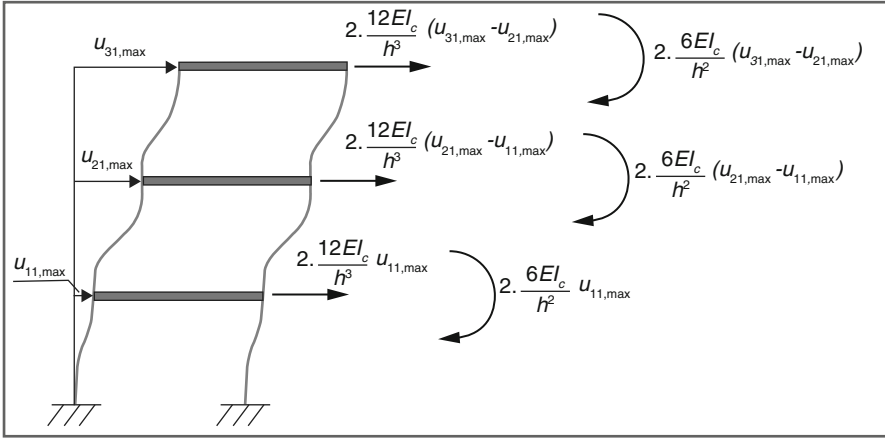


Fig. 4.29 Maximum elastic story forces for the first mode

(b) Complete Quadratic Combination (CQC)

$$u_{i,\max} = \sqrt{\sum_{j=1}^n \sum_{l=1}^n \rho_{ij} \cdot (\Psi_{il} \cdot q_{l,\max}) \cdot (\Psi_{ij} \cdot q_{j,\max})} \quad (4.169)$$

where ρ_{ij} represents the correlation coefficient between mode i and j and is defined by Eq. 4.170.

$$\rho_{ij} = \frac{8 \cdot \xi^2 \cdot (1 + \omega_i/\omega_j) \cdot (\omega_i/\omega_j)^{3/2}}{\left(1 - (\omega_i/\omega_j)^2\right)^2 + 4 \cdot \xi^2 \cdot (\omega_i/\omega_j) \cdot (1 + (\omega_i/\omega_j))^2} \quad (4.170)$$

In addition, the elastic internal actions can be evaluated for each mode by referring to the maximum displacement matrix.

4.8.1 Numerical Example

In Fig. 4.29 are shown the values of shear and bending moment for the first mode of a generic three DOFs shear type frame.

Thus, similarly to the maximum displacement, the maximum shear ($V_{i,\max}$) and bending moment ($M_{i,\max}$) for each mode can be defined (Eq. 4.171).

$$\begin{aligned} [V_{\max}] &= [\{V_{1,\max}\} \{V_{2,\max}\} \dots \{V_{n,\max}\}] \\ [M_{\max}] &= [\{M_{1,\max}\} \{M_{2,\max}\} \dots \{M_{n,\max}\}] \end{aligned} \quad (4.171)$$

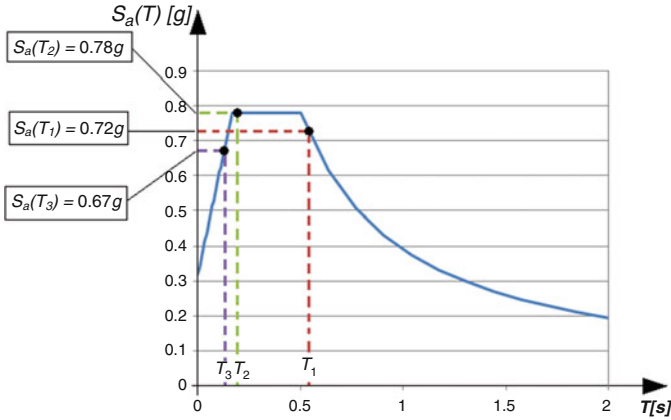


Fig. 4.30 Elastic acceleration response spectrum and modal accelerations

The total maximum shear and bending moment at each story is evaluated by SRSS (Eq. 4.172) or CQC (Eq. 4.173) combination

$$\begin{cases} V_{i,\max} = \sqrt{V_{i1,\max}^2 + V_{i2,\max}^2 + \dots + V_{in,\max}^2} \\ M_{i,\max} = \sqrt{M_{i1,\max}^2 + M_{i2,\max}^2 + \dots + M_{in,\max}^2} \end{cases} \quad (4.172)$$

$$\begin{cases} V_{i,\max} = \sqrt{\sum_{j=1}^n \sum_{i=1}^n \rho_{ij} \cdot (V_{i,\max}) \cdot (V_{j,\max})} \\ M_{\max} = \sqrt{\sum_{j=1}^n \sum_{i=1}^n \rho_{ij} \cdot (M_{i,\max}) \cdot (M_{j,\max})} \end{cases} \quad (4.173)$$

Suppose we consider the three DOF shear type frame analyzed previously, for which the vibrational modes and the natural period have been calculated (Eq. 4.174).

$$T_1 = 0.54 \text{ s} \quad T_2 = 0.19 \text{ s} \quad T_3 = 0.13 \text{ s} \quad (4.174)$$

Figure 4.30 illustrates the considered elastic response spectra with the definition of the three values of acceleration $S_a(T_i)$. The modal participation factor of the normalized modes are evaluated in Eq. 4.175.



$$\begin{aligned}
 g_{m,1} &= \frac{\{0.45 \ 0.80 \ 1\} \cdot 40,000 \cdot \begin{bmatrix} 1 & 0 & 0 \\ 0 & 1 & 0 \\ 0 & 0 & 1 \end{bmatrix} \begin{Bmatrix} 1 \\ 1 \\ 1 \end{Bmatrix}}{\sqrt{\{0.45 \ 0.80 \ 1\} \cdot 40,000 \cdot \begin{bmatrix} 1 & 0 & 0 \\ 0 & 1 & 0 \\ 0 & 0 & 1 \end{bmatrix} \begin{Bmatrix} 0.45 \\ 0.80 \\ 1 \end{Bmatrix}}} = 331.19 \text{ [kg}^{1/2}\text{]} \\
 g_{m,2} &= \frac{\{-1.25 \ -0.55 \ 1\} \cdot 40,000 \cdot \begin{bmatrix} 1 & 0 & 0 \\ 0 & 1 & 0 \\ 0 & 0 & 1 \end{bmatrix} \begin{Bmatrix} 1 \\ 1 \\ 1 \end{Bmatrix}}{\sqrt{\{-1.25 \ -0.55 \ 1\} \cdot 40,000 \cdot \begin{bmatrix} 1 & 0 & 0 \\ 0 & 1 & 0 \\ 0 & 0 & 1 \end{bmatrix} \begin{Bmatrix} -1.25 \\ -0.55 \\ 1 \end{Bmatrix}}} = -94.79 \text{ [kg}^{1/2}\text{]} \\
 g_{m,3} &= \frac{\{-2.25 \ 1.80 \ 1\} \cdot 40,000 \cdot \begin{bmatrix} 1 & 0 & 0 \\ 0 & 1 & 0 \\ 0 & 0 & 1 \end{bmatrix} \begin{Bmatrix} 1 \\ 1 \\ 1 \end{Bmatrix}}{\sqrt{\{-2.25 \ 1.80 \ 1\} \cdot 40,000 \cdot \begin{bmatrix} 1 & 0 & 0 \\ 0 & 1 & 0 \\ 0 & 0 & 1 \end{bmatrix} \begin{Bmatrix} -2.25 \\ 1.80 \\ 1 \end{Bmatrix}}} = 36.40 \text{ [kg}^{1/2}\text{]}
 \end{aligned} \tag{4.175}$$

Then the modal masses reported in Eq. 4.176 can be determined.

$$\begin{aligned}
 m_{\text{mod},1} &= g_{m,1}^2 = 109690 \text{ [kg]} \\
 m_{\text{mod},2} &= g_{m,2}^2 = 8985 \text{ [kg]} \\
 m_{\text{mod},3} &= g_{m,3}^2 = 1325 \text{ [kg]}
 \end{aligned} \tag{4.176}$$

The sum of the three modal masses is equal to the total mass of the frame. In addition, the following percentage mass contributions for each mode are evaluated (Eq. 4.177).

$$\begin{aligned}
 \% (m_{\text{mod},1}) &= 91.4\% \\
 \% (m_{\text{mod},2}) &= 7.5\% \\
 \% (m_{\text{mod},3}) &= 1.1\%
 \end{aligned} \tag{4.177}$$

It is evident that the first mode is predominant in the dynamic response of the system. However, in this example, all of the three modes will be considered. According to the modal participation factors calculated, the maximum modal coordinates are evaluated and expressed by Eq. 4.178.

$$\begin{aligned}
 q_{1,\max} &= 331.19 \cdot \frac{0.72 \cdot 9.81}{(11.56)^2} = 17.51 \\
 q_{2,\max} &= -94.79 \cdot \frac{0.78 \cdot 9.81}{(32.40)^2} = -0.70 \\
 q_{3,\max} &= 36.40 \cdot \frac{0.67 \cdot 9.81}{(46.82)^2} = 0.11
 \end{aligned} \tag{4.178}$$

Now, the three maximum modal displacement vectors can be obtained (Eq. 4.179).

$$\begin{aligned}
 \{u_{1,\max}\} &= \frac{\begin{Bmatrix} 0.45 \\ 0.80 \\ 1 \end{Bmatrix}}{\sqrt{\{0.45 \ 0.80 \ 1\} \cdot 40,000 \cdot \begin{bmatrix} 1 & 0 & 0 \\ 0 & 1 & 0 \\ 0 & 0 & 1 \end{bmatrix} \begin{Bmatrix} 0.45 \\ 0.80 \\ 1 \end{Bmatrix}}} \cdot 17.51 = 10^{-2} \cdot \begin{Bmatrix} 2.870 \\ 5.170 \\ 6.450 \end{Bmatrix} \\
 \{u_{2,\max}\} &= \frac{\begin{Bmatrix} -1.25 \\ -0.55 \\ 1 \end{Bmatrix}}{\sqrt{\{-1.25 \ -0.55 \ 1\} \cdot 40,000 \cdot \begin{bmatrix} 1 & 0 & 0 \\ 0 & 1 & 0 \\ 0 & 0 & 1 \end{bmatrix} \begin{Bmatrix} -1.25 \\ -0.55 \\ 1 \end{Bmatrix}}} \cdot (-0.69) = 10^{-2} \cdot \begin{Bmatrix} 0.260 \\ 0.110 \\ -0.210 \end{Bmatrix} \\
 \{u_{3,\max}\} &= \frac{\begin{Bmatrix} -2.25 \\ 1.80 \\ 1 \end{Bmatrix}}{\sqrt{\{-2.25 \ 1.80 \ 1\} \cdot 40,000 \cdot \begin{bmatrix} 1 & 0 & 0 \\ 0 & 1 & 0 \\ 0 & 0 & 1 \end{bmatrix} \begin{Bmatrix} -2.25 \\ 1.80 \\ 1 \end{Bmatrix}}} \cdot 0.11 = 10^{-2} \cdot \begin{Bmatrix} -0.041 \\ 0.032 \\ 0.018 \end{Bmatrix}
 \end{aligned} \tag{4.179}$$

Inputting the just evaluated terms into the maximum displacement matrix, Eq. 4.180 is given.

$$[u_{\max}] = 10^{-2} \cdot \begin{Bmatrix} 2.870 & 0.260 & -0.041 \\ 5.170 & 0.110 & 0.032 \\ 6.450 & -0.210 & 0.018 \end{Bmatrix} \tag{4.180}$$

The maximum shear and bending moments at each story are expressed by Eq. 4.181.

$$\begin{cases} V_{i3,\max} = 3 \cdot \frac{12EI_c}{h^3} \cdot (u_{3i,\max} - u_{2i,\max}) \\ V_{i2,\max} = 3 \cdot \frac{12EI_c}{h^3} \cdot (u_{2i,\max} - u_{1i,\max}) \\ V_{i1,\max} = 3 \cdot \frac{12EI_c}{h^3} \cdot u_{1i,\max} \end{cases} \begin{cases} M_{i3,\max} = 3 \cdot \frac{6EI_c}{h^2} \cdot (u_{3i,\max} - u_{2i,\max}) \\ M_{i2,\max} = 3 \cdot \frac{6EI_c}{h^2} \cdot (u_{2i,\max} - u_{1i,\max}) \\ M_{i1,\max} = 3 \cdot \frac{6EI_c}{h^2} \cdot u_{1i,\max} \end{cases} \quad (4.181)$$

Thus the following numerical value can be found (Eq. 4.182).

$$\begin{aligned} [M_{\max}] &= \begin{Bmatrix} 581.20 & 52.65 & -8.30 \\ 465.75 & -30.40 & 14.80 \\ 259.20 & -64.80 & -2.85 \end{Bmatrix} \text{ [kN} \cdot \text{m]} \\ [V_{\max}] &= \begin{Bmatrix} 1162.4 & 105.3 & -16.6 \\ 931.5 & -60.8 & 29.6 \\ 518.4 & -129.6 & -5.7 \end{Bmatrix} \text{ [kN]} \end{aligned} \quad (4.182)$$

In order to obtain a single solution in terms of maximum displacements and internal actions, the SRSS modal combination is used. Thus, the kinematic and static solutions are reported in Eq. 4.183.

$$\begin{aligned} \{u_{\max}\}^T &= 10^{-2} \{2.88 \ 5.17 \ 6.45\} \text{ [m]} \\ \{M_{\max}\}^T &= \{538.60 \ 466.95 \ 267.20\} \text{ [kN} \cdot \text{m]} \\ \{V_{\max}\}^T &= \{1167.2 \ 933.9 \ 534.4\} \text{ [kN]} \end{aligned} \quad (4.183)$$

It is possible to see that the total dynamic response in terms of internal actions and displacements is very close to the first mode results. In addition, the sum of the internal action represents the total base reaction. For this reason, the base shear is given by Eq. 4.184.

$$V_{b,\max} = 2635.60 \text{ kN} \quad (4.184)$$

Figure 4.31 illustrates the deformed shape and internal actions diagrams for the three DOFs shear type frame analyzed.

4.9 3D MDOF Multistory Buildings

Since the DOFs of the spatial structure are greater than the associated 2D one, the computational effort is increased. In this paragraph, the stiffness and mass assembly methodologies will be discussed for typical regular multistory buildings having three DOFs (Fig. 4.32).

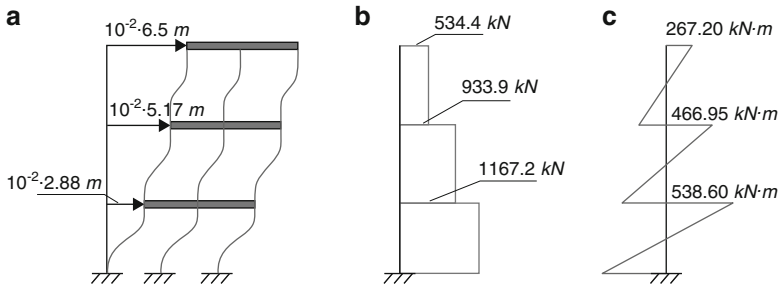


Fig. 4.31 Deformed shape (a), total shear diagram (b) and total bending moment (c) in terms of maximum values

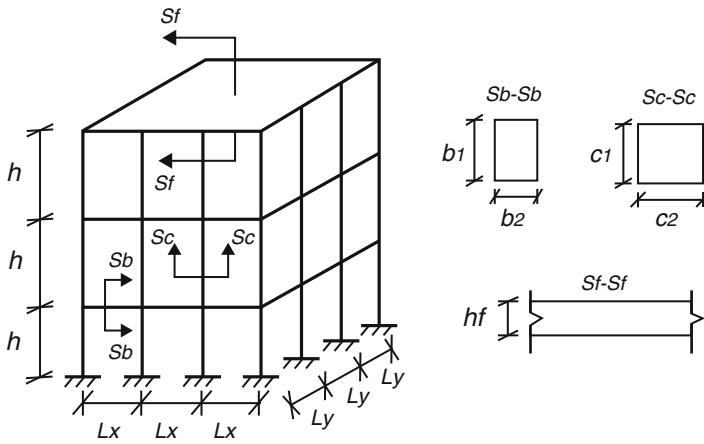


Fig. 4.32 3D three-story buildings

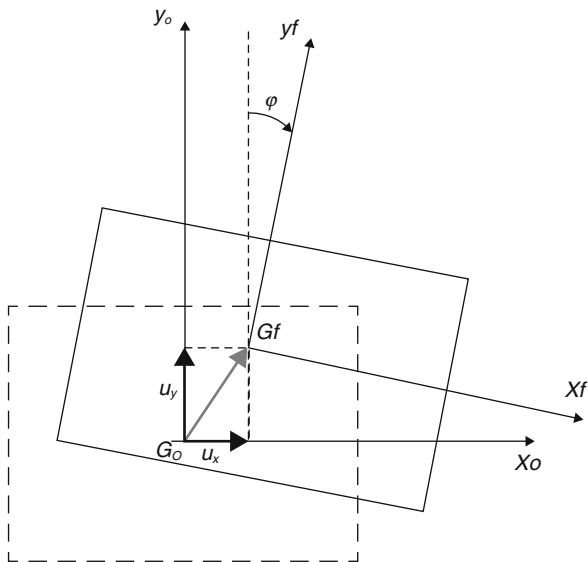
Assuming that every beam and column has respectively the same cross section $sb-sb$ and $sc-sc$ indicated on the figure reported above, it is possible to define the following inertia moments (Eq. 4.185).

$$\begin{aligned}
 \text{beam} &\rightarrow I_b = \frac{b_2 \cdot b_1^3}{12} \\
 \text{column} &\rightarrow I_c = \frac{c_2 \cdot c_1^3}{12}
 \end{aligned}
 \tag{4.185}$$

In addition, an elastic modulus is assumed for every frame element. According to the lumped masses model, each mass is supposed concentrated in the gravitational center of the associated flooring system. For the case study, the masses of the MDOF frame are evaluated as expressed in Eq. 4.186.



Fig. 4.33 DOFs for each flooring system



$$\begin{cases} m_1 = \rho_c \cdot [(16 \cdot h \cdot c_1 \cdot c_2) + h_f (3 \cdot L_x \cdot 3 \cdot L_y)] \\ m_2 = \rho_c \cdot [(16 \cdot h \cdot c_1 \cdot c_2) + h_f (3 \cdot L_x \cdot 3 \cdot L_y)] \\ m_3 = \rho_c \cdot [(16 \cdot \frac{h}{2} \cdot c_1 \cdot c_2) + h_f (3 \cdot L_x \cdot 3 \cdot L_y)] \end{cases} \quad (4.186)$$

where ρ_c is the mass per unit volume of the elements. In practical applications, the mass contribution associated with the columns is neglected since it is less than the flooring system (Eq. 4.187).

$$m_1 = m_2 = m_3 = 9 \cdot \rho_c \cdot h_f \cdot L_x \cdot L_y \quad (4.187)$$

According to the assumption of rigid flooring system and axially rigid elements, the DOFs of the system are reported in Eq. 4.188.

$$DOFs = 3 \cdot n_f = 3 \cdot 3 = 9 \quad (4.188)$$

where n_f represents the number of flooring system of the MDOS structure, while 3 indicates the generic DOFs for each mass that are illustrated in Fig. 4.33.

The generic motion of the point P located on the rigid deck can be described by Eq. 4.189.

$$\begin{cases} u_{x,P} = u_x + \phi \cdot \Delta y_P \\ u_{y,P} = u_y - \phi \cdot \Delta x_P \end{cases} \quad (4.189)$$

Therefore, the dynamic equilibrium equations have been expressed for the x and y direction and for the rotation φ . Equation 4.190 is formed to represent the equilibrium system of equations for the undamped three-story frame in free vibrations conditions.

$$\begin{cases} (x) \rightarrow [M_x]\{\dot{u}_x\} + [M_x \cdot \Delta y]\{\dot{\varphi}\} + [K_x]\{u_x\} + [K_x \cdot \Delta y]\{\varphi\} = \{0\} \\ (y) \rightarrow [M_y]\{\dot{u}_y\} - [M_y \cdot \Delta x]\{\dot{\varphi}\} + [K_y]\{u_y\} - [K_y \cdot \Delta x]\{\varphi\} = \{0\} \\ (\varphi) \rightarrow [M_x \cdot \Delta y]\{\dot{u}_x\} + [M_y \cdot \Delta x]\{\dot{u}_y\} + [M_\varphi]\{\dot{\varphi}\} + [K_\varphi]\{\varphi\} = \{0\} \end{cases} \quad (4.190)$$

Defining the DOFs vectors expressed by Eq. 4.191, the three system equations can be condensed in matrix format as shown by Eq. 4.192.

$$\{u\}^T = \left\{ \{u_x\}^T \{u_y\}^T \{\varphi\}^T \right\} \quad (4.191)$$

$$\begin{aligned} & \begin{bmatrix} [M_x] & [0] & [M_x \cdot \Delta y] \\ [0] & [M_y] & -[M_y \cdot \Delta x] \\ [M_x \cdot \Delta y] & -[M_y \cdot \Delta x] & [M_\varphi] \end{bmatrix} \begin{Bmatrix} \{u_x\} \\ \{u_y\} \\ \{\varphi\} \end{Bmatrix} + \\ & + \begin{bmatrix} [K_x] & [0] & [K_x \cdot \Delta y] \\ [0] & [K_y] & -[K_y \cdot \Delta x] \\ [K_x \cdot \Delta y] & -[K_y \cdot \Delta x] & [K_\varphi] \end{bmatrix} \begin{Bmatrix} \{u_x\} \\ \{u_y\} \\ \{\varphi\} \end{Bmatrix} = \begin{Bmatrix} \{0\} \\ \{0\} \\ \{0\} \end{Bmatrix} \quad (4.192) \end{aligned}$$

The reduced mass and stiffness matrix can be rewritten as given by Eq. 4.193.

$$\begin{aligned} [M_{xx}] &= [M_x]; [M_{yy}] = [M_y]; [M_{x\varphi}] = [M_x \cdot \Delta y]; [M_{y\varphi}] = -[M_y \cdot \Delta x]; [M_{\varphi\varphi}] = [M_\varphi] \\ [K_{xx}] &= [K_x]; [K_{yy}] = [K_y]; [K_{x\varphi}] = [K_x \cdot \Delta y]; [K_{y\varphi}] = -[K_y \cdot \Delta x]; [K_{\varphi\varphi}] = [K_\varphi] \end{aligned} \quad (4.193)$$

This notation is more applicable than the first one since the principal mass and stiffness contribution (diagonal terms) are expressed with a double equal index. It is important to observe that each submatrix has $n_f \times n_f$ dimensions, where n_f represents the number of flooring systems, while the compact matrix dimension is $n \times n$ where n is the total number of DOFs.

The stiffness and mass components denoted with index “ $\varphi\varphi$ ” describe the pure torsional property of the frame that provides the torsional moment to the columns of the frame. Generally, the torsional moments are lower than the bending moment due to the $\{u_x\}$ and $\{u_y\}$ DOFs. Another interesting observation can be made related to the components of the mass and stiffness submatrices expressed by the indices “ $x\varphi$ ” and “ $y\varphi$ ”. They cause additional shear forces on the columns and are called torsional effects. It can be observed that these effects increase with the terms Δy_i and Δx_i that represent the offset between the gravitational center and the referenced

center of the i th story in the y and x direction, respectively. In structural engineering applications, the stiffness center is considered as a reference point for each flooring system. In Eq. 4.194 every mass submatrix is defined for the analyzed frame.

$$[M_{xx}] = [M_{yy}] = \begin{bmatrix} m_1 & 0 & 0 \\ 0 & m_2 & 0 \\ 0 & 0 & m_3 \end{bmatrix}; [M_{\varphi\varphi}] = \begin{bmatrix} I_{o,1} & 0 & 0 \\ 0 & I_{o,2} & 0 \\ 0 & 0 & I_{o,3} \end{bmatrix}$$

$$[M_{x\varphi}] = \begin{bmatrix} m_1 \cdot \Delta y_1 & 0 & 0 \\ 0 & m_2 \cdot \Delta y_2 & 0 \\ 0 & 0 & m_3 \cdot \Delta y_3 \end{bmatrix}; [M_{y\varphi}] = \begin{bmatrix} -m_1 \cdot \Delta x_1 & 0 & 0 \\ 0 & -m_2 \cdot \Delta x_2 & 0 \\ 0 & 0 & -m_3 \cdot \Delta x_3 \end{bmatrix} \quad (4.194)$$

In the previous equation the terms $I_{o,i}$ represent the polar inertia moment with the pole corresponding to the gravitational center of the i th story. For the case study, the three inertial moments are given by Eq. 4.195.

$$I_{o,1} = I_{o,2} = I_{o,3} = (I_{x_o-x_o} + I_{y_o-y_o}) =$$

$$= \rho_c \cdot \left[\frac{3 \cdot L_x \cdot (3 \cdot L_y)^3}{12} + \frac{3 \cdot L_y \cdot (3 \cdot L_x)^3}{12} \right] = \rho_c \cdot \frac{81}{12} \cdot [L_x \cdot (L_y)^3 + L_y \cdot (L_x)^3] \quad (4.195)$$

Since the mass and the stiffness are uniformly distributed over each story, the offset in the x and y direction is always equal to zero ($\{\Delta y\} = \{\Delta x\} = \{0\}$). This property leads to the following associated matrices (Eq. 4.196).

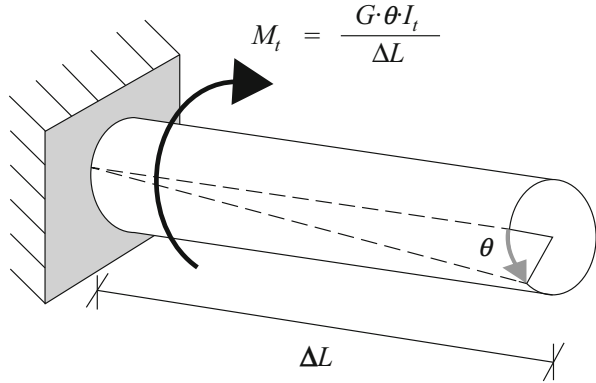
$$[M_{x\varphi}] = [M_{y\varphi}] = [K_{x\varphi}] = [K_{y\varphi}] = \begin{bmatrix} 0 & 0 & 0 \\ 0 & 0 & 0 \\ 0 & 0 & 0 \end{bmatrix} \quad (4.196)$$

Regarding the $[K_{xx}]$ and $[K_{yy}]$ stiffness submatrices, Eq. 4.197 is given,

$$[K_{xx}] = [K_{yy}] = 16 \cdot \begin{bmatrix} \frac{24EI_c}{h^3} & -\frac{12EI_c}{h^3} & 0 \\ -\frac{12EI_c}{h^3} & \frac{24EI_c}{h^3} & -\frac{12EI_c}{h^3} \\ 0 & -\frac{12EI_c}{h^3} & \frac{12EI_c}{h^3} \end{bmatrix} \quad (4.197)$$

where 16 is the number of columns that contributes to the lateral stiffness. The components due to the pure torsional effects are based on the torsional stiffness of the columns (Fig. 4.34), where G defines the shear elastic modulus and I_t represents the torsional inertia of the element. For a full section of mono-dimensional elements the inertial moment can be expressed as reported in Eq. 4.198.

Fig. 4.34 Torsional effects on a generic mono-dimensional element



$$I_t = \int (x^2 + y^2) \cdot dA = I_o = I_{x_o-x_o} + I_{y_o-y_o} \tag{4.198}$$

The inertial moment is equal to the polar inertia of the cross section, in which the referenced pole is coincident with the mass center. According to the previous properties, the pure torsional stiffness submatrix is given by Eq. 4.199.

$$[K_{\varphi\varphi}] = 16 \cdot \begin{bmatrix} \frac{2G I_{t,c}}{h} & -\frac{G I_{t,c}}{h} & 0 \\ -\frac{G I_{t,c}}{h} & \frac{2G I_{t,c}}{h} & -\frac{G I_{t,c}}{h} \\ 0 & -\frac{G I_{t,c}}{h} & \frac{2G I_{t,c}}{h} \end{bmatrix} \tag{4.199}$$

In which the index “c” of the torsional inertia indicates the columns.

Therefore, the equation of motion for the 3D three-story building can be rewritten (Eq. 4.200).

$$\begin{bmatrix} m_1 & 0 & 0 & 0 & 0 & 0 & 0 & 0 & 0 \\ & m_2 & 0 & 0 & 0 & 0 & 0 & 0 & 0 \\ & & m_3 & 0 & 0 & 0 & 0 & 0 & 0 \\ & & & m_4 & 0 & 0 & 0 & 0 & 0 \\ & & & & m_5 & 0 & 0 & 0 & 0 \\ & & & & & m_6 & 0 & 0 & 0 \\ & & & & & & m_7 & 0 & 0 \\ S & Y & M & M. & & & & m_8 & 0 \\ & & & & & & & & m_9 \end{bmatrix} \begin{Bmatrix} u_{x,1} \\ u_{x,2} \\ u_{x,3} \\ u_{y,1} \\ u_{y,2} \\ u_{y,3} \\ \dot{\varphi}_1 \\ \dot{\varphi}_2 \\ \dot{\varphi}_3 \end{Bmatrix} +$$



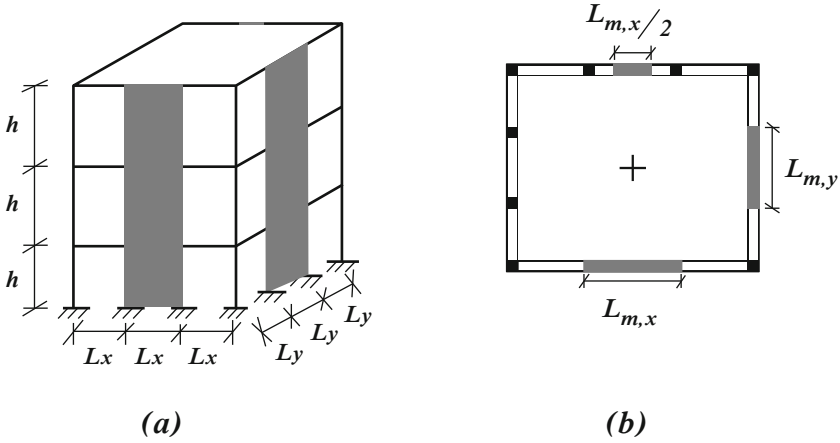


Fig. 4.35 3D view (a) and plan (b) of the three-story building with four shear walls

$$\begin{aligned}
 & +16 \begin{bmatrix} 24 \frac{EI_c}{h^3} & -12 \frac{EI_c}{h^3} & 0 & 0 & 0 & 0 & 0 & 0 & 0 & 0 \\ & 24 \frac{EI_c}{h^3} & -12 \frac{EI_c}{h^3} & 0 & 0 & 0 & 0 & 0 & 0 & 0 \\ & & 12 \frac{EI_c}{h^3} & 0 & 0 & 0 & 0 & 0 & 0 & 0 \\ & & & 24 \frac{EI_c}{h^3} & -12 \frac{EI_c}{h^3} & 0 & 0 & 0 & 0 & 0 \\ & & & & 24 \frac{EI_c}{h^3} & -12 \frac{EI_c}{h^3} & 0 & 0 & 0 & 0 \\ & & & & & -12 \frac{EI_c}{h^3} & -12 \frac{EI_c}{h^3} & 0 & 0 & 0 \\ & & & & & & 2 \frac{GI_{t,c}}{h} & -\frac{GI_{t,c}}{h} & 0 & 0 \\ & & & & & & & 2 \frac{GI_{t,c}}{h} & -\frac{GI_{t,c}}{h} & 0 \\ & & & & & & & & \frac{GI_{t,c}}{h} & 0 \end{bmatrix} \begin{Bmatrix} \dot{u}_{x,1} \\ \dot{u}_{x,2} \\ \dot{u}_{x,3} \\ \dot{u}_{y,1} \\ \dot{u}_{y,2} \\ \dot{u}_{y,3} \\ \dot{\phi}_1 \\ \dot{\phi}_2 \\ \dot{\phi}_3 \end{Bmatrix} = \begin{Bmatrix} 0 \\ 0 \\ 0 \\ 0 \\ 0 \\ 0 \\ 0 \\ 0 \\ 0 \end{Bmatrix} \\
 & \qquad \qquad \qquad S \qquad Y \qquad M \qquad M.
 \end{aligned} \tag{4.200}$$

Now, the same structure is considered but with additional shear walls that cause an offset between stiffness and mass center in each story (Fig. 4.35).

For the sake of simplicity, the columns are assumed to have a square shape ($c_1 = c_2 = c$). Every shear wall is extended for the whole height of the building, thus the offset between stiffness and mass center will be equal at each story. The stiffness center of a flooring system is evaluated according to the static model shown in Fig. 4.36.



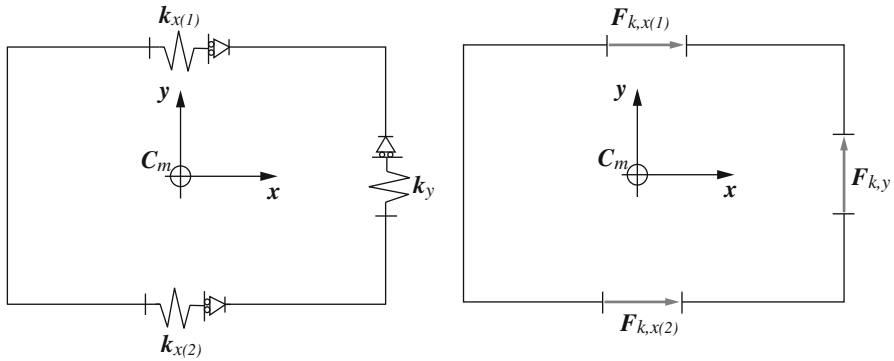
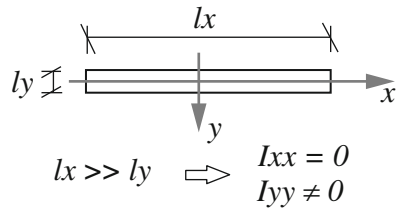


Fig. 4.36 Equivalent simplified flooring system

Fig. 4.37 Simplified model of shear wall



where the generic elastic reaction is given by Eq. 4.201.

$$F_{k,i} = k_i \cdot u_i \tag{4.201}$$

Thus, the absorbed action of a shear wall is proportional to its stiffness. For this reason, it is useful to define a physical model in order to evaluate the stiffness of each shear wall.

First, the x-y reference system has its origin coincident with the mass center (C_m). The generic shear wall provides a stiffness contribution along its axis that is in the direction along which the associated inertia moment is prevalent (Fig. 4.37).

Considering a flexural behavior for a shear wall and imposing the associated unitary displacement at given story (Fig. 4.38), the stiffness contribution can be evaluated with respect to the geometric characteristics of the walls.

Thus, Eq. 4.202 specifies the three stiffness components,

$$k_{x(1),i} = 3 \cdot \frac{EI_{m,yy}}{H_i^3} = \frac{E}{H_i^3} \cdot \frac{c \cdot \left(\frac{L_{m,y}}{2}\right)^3}{4} = \frac{E}{H_i^3} \cdot \frac{c \cdot (L_{m,y})^3}{32}$$

$$k_{x(2),i} = 3 \cdot \frac{EI_{m,yy}}{H_i^3} = \frac{E}{H_i^3} \cdot \frac{c \cdot (L_{m,y})^3}{4}$$

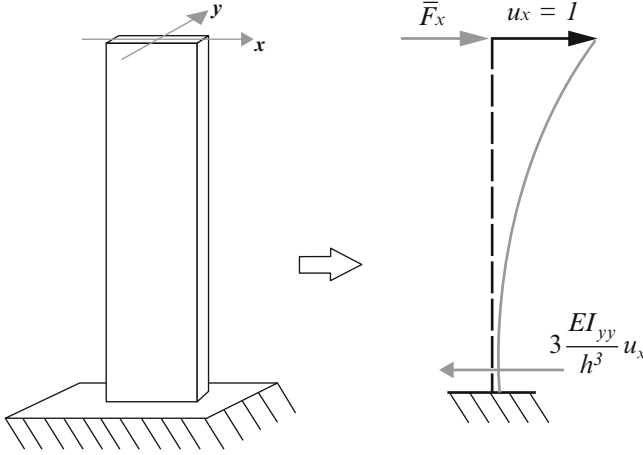


Fig. 4.38 Static scheme for a bending resisting wall

$$k_{y,i} = 3 \cdot \frac{EI_{m,xx}}{H_i^3} = \frac{E}{H_i^3} \cdot \frac{c \cdot (L_{m,x})^3}{4} \quad (4.202)$$

where the index “i” refers to the *i*th story. Since the dimensions of the cross section of the columns are smaller than the shear walls, they are neglected in the stiffness center definition.

From the stiffness of each component, it is possible to define the center of stiffness of the flooring systems (Eq. 4.203) using the scheme shown in Fig. 4.39.

$$\left\{ \begin{array}{l} Y_k = \frac{S_{k_x}}{\sum K_{x,i}} = \frac{\left[\frac{E}{H_i^3} \cdot \frac{c \cdot (L_{m,y})^3}{4} \right] \cdot 0 + \left[\frac{E}{H_i^3} \cdot \frac{c \cdot (L_{m,y})^3}{32} \right] \cdot 3L_y}{\frac{9}{32} \cdot \left[\frac{E}{H_i^3} \cdot c \cdot (L_{m,y})^3 \right]} = \frac{L_y}{3} \\ X_k = \frac{S_{k_y}}{\sum K_y} = \frac{\left[\frac{E}{H_i^3} \cdot \frac{c \cdot (L_{m,x})^3}{4} \right] \cdot 3L_x}{\left[\frac{E}{H_i^3} \cdot \frac{c \cdot (L_{m,x})^3}{4} \right]} = 3L_x \end{array} \right. \quad (4.203)$$

The terms Δx and Δy represent the offsets between the mass and stiffness center. In the analyzed case they are given by Eq. 4.204.

$$\begin{aligned} \Delta x &= 3L_x - \frac{3}{2}L_x = \frac{3}{2}L_x \\ \Delta y &= -\frac{3}{2}L_y + \frac{1}{3}L_y = -\frac{7}{6}L_y \end{aligned} \quad (4.204)$$

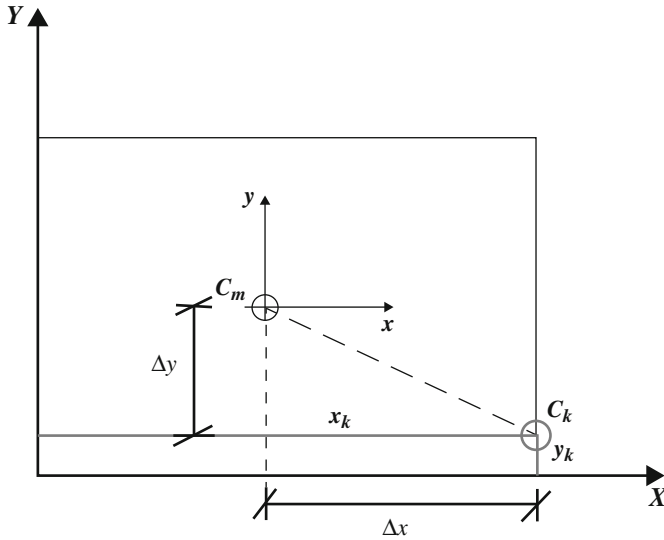


Fig. 4.39 Definition of the stiffness center

Now it is possible to evaluate the components of the mass (Eq. 4.205) and stiffness (Eq. 4.206) submatrices associated to the mixed index “ φx ” and “ φy ”.

$$[M_{x\varphi}] = -\frac{7}{6}L_y \cdot \begin{bmatrix} m_1 & 0 & 0 \\ 0 & m_2 & 0 \\ 0 & 0 & m_3 \end{bmatrix}; [M_{y\varphi}] = \frac{3}{2}L_x \cdot \begin{bmatrix} -m_1 & 0 & 0 \\ 0 & -m_2 & 0 \\ 0 & 0 & -m_3 \end{bmatrix} \quad (4.205)$$

$$[K_{x\varphi}] = -\frac{7}{6}L_y \cdot \begin{bmatrix} \frac{24EI_c}{h^3} & -\frac{12EI_c}{h^3} & 0 \\ -\frac{12EI_c}{h^3} & \frac{24EI_c}{h^3} & -\frac{12EI_c}{h^3} \\ 0 & -\frac{12EI_c}{h^3} & \frac{12EI_c}{h^3} \end{bmatrix}; \quad (4.206)$$

$$[K_{y\varphi}] = +\frac{3}{2}L_x \cdot \begin{bmatrix} \frac{24EI_c}{h^3} & -\frac{12EI_c}{h^3} & 0 \\ -\frac{12EI_c}{h^3} & \frac{24EI_c}{h^3} & -\frac{12EI_c}{h^3} \\ 0 & -\frac{12EI_c}{h^3} & \frac{12EI_c}{h^3} \end{bmatrix}$$

References

- Bathe KJ, Wilson EL (1976) Numerical methods in finite element analysis, vol 197. Prentice-Hall, Englewood Cliffs
- Blevins R (2001) Formulas for natural frequency and mode shape. Krieger Publishing Company, Malabar
- Chopra AK (2017) Dynamics of structures: theory and applications to earthquake engineering, 5th edn. Pearson Education, Inc., Hoboken, 960 pp
- Fu ZF, He J (2001) Modal analysis. Butterworth-Heinemann, Oxford/Boston
- Guyan RJ (1965) Reduction of stiffness and mass matrices. AIAA J 3(2):380
- Kuttler K (2007) An introduction to linear algebra. Brigham Young University, Provo
- Liu M, Gorman DG (1995) Formulation of rayleigh damping and its extensions. Comput Struct 57(2):277–285
- McGuire W, Gallagher RH, Ziemian RD (2000) Matrix structural analysis. Wiley, New York

Chapter 5

Energy Dissipation



Abstract The chapter introduces the energy balance equation of a generic system. Attention is given to damping energy and plastic energy (Vakakis et al., *Nonlinear targeted energy transfer in mechanical and structural systems*, vol 156. Springer, Dordrecht, 2008). Two methods are introduced to estimate the damping on the structural systems through experimental techniques: the Logarithmic Decrement Analysis (LDA) and the Half-Power Method (HPM). The ductility factor and the equal displacement criteria is also introduced.

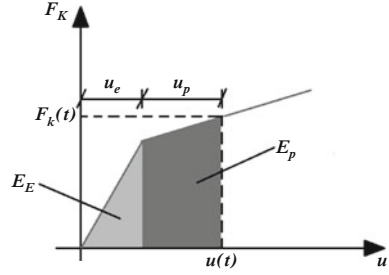
5.1 Energy Balance Equation

The input energy of a generic inelastic system is mainly dissipated by damping and plastic deformation phenomena, while the remaining part is transformed in kinematic and potential energy. Equation 5.1 defines the integral expression of the dynamic equilibrium of a generic system.

$$\int_0^u m \cdot \ddot{u}(t) \cdot du + \int_0^u c \cdot \dot{u}(t) \cdot du + \int_0^u k(u, \dot{u}) \cdot u(t) \cdot du = \int_0^u F(t) \cdot du \quad (5.1)$$

The term on the right side is the input energy E_I . The first integral on the left associated to the inertia force defines the kinetic energy E_K associated with the mass of the system. The second integral associated with the damping coefficient gives information about the energy dissipated by the viscous damping phenomena (E_D). Finally, the third term on the left side represents the deformation energy that can be decomposed into the elastic component E_E (conservative contribution) and the

Fig. 5.1 Elastic and plastic deformation energy contributions



plastic component E_P (irreversible contribution). The recoverable and irreversible deformation energy contributions are explicitly expressed in Eq. 5.2.

$$\begin{cases} E_E = \int_0^{u_e} k_e \cdot u(t) \cdot du \\ E_P = \int_0^{u_p} k_p \cdot u(t) \cdot du \end{cases} \quad (5.2)$$

Figure 5.1 illustrates the two forms of energy just discussed for a generic elastic model with hardening.

Accounting for the previous considerations, the energy balance equation can be rewritten (Eq. 5.3).

$$E_K + E_D + E_E + E_P = E_I \quad (5.3)$$

Assuming an undamped elastic system and expressing the energy equilibrium in incremental form, the equation reported above assumes the same expression as that of the conservation energy law (Eq. 5.4).

$$\Delta E_K + \Delta E_E = \Delta E_I \quad (5.4)$$

When an earthquake excitation is considered, the input energy can be evaluated as shown in the Eq. 5.5.

$$E_I = \int_0^u F(t) \cdot du = - \int_0^u m \cdot \ddot{u}_g(t) \cdot du \quad (5.5)$$

In this case, it is important to notice that the damping, kinetic and deformation energy values depend on the relative displacement of the system from the ground,

while the input energy relates to the ground acceleration (Uang and Bertero 1990). The energy balance equation during an earthquake excitation is useful to understand the dynamic effects on the system through the energy interaction. Considering the input energy a constant value, the amplitude of the motion (in terms of displacements) increases if the dissipation phenomena are negligible (Eq. 5.6).

$$\int_0^u m \cdot \ddot{u}(t) \cdot du + \int_0^{u_e} k_e \cdot u(t) \cdot du + \int_0^u c \cdot \dot{u}(t) \cdot du + \int_0^{u_p} k_p \cdot u(t) \cdot du = \int_0^u F(t) \cdot du \quad (5.6)$$

Remembering that the recoverable energy of a periodic excitation is directly proportional to the square of amplitude response (A), the equation above can be rewritten in the following form (Eq. 5.7).

$$\int_0^u F(t) \cdot du \propto A^2 \quad (5.7)$$

Thus, for a conservative system the amplitude of the response is maximized. If the dissipation phenomena are considered, the previous expression can be rewritten (Eq. 5.8).

$$\int_0^u F(t) \cdot du - \int_0^{u_p} k_p \cdot u(t) \cdot du - \int_0^u c \cdot \dot{u}(t) \cdot du \propto A^2 \quad (5.8)$$

In this case, the amplitude of the dynamic response decreases. This result is very important since it is the basis of the active provisions used for the structures in order to limit their amplitude response. On the other hand, the reduction of the response amplitude due to the dissipation phenomena can lead to an excessive amount of plastic deformation, causing the damage or even the collapse of the structure.

5.2 Damping Energy

As mentioned in Sect. 1.5, the energy dissipated by means of hysteretic process is approximately described by the viscous damping ratio ξ . It has been observed that this term depends on the frequency excitation and on the strain energy (elastic characteristics) (Zahrah and Hall 1984). Experimental tests are conducted to measure the damping property of a system by considering a frequency harmonic excitation equal to the natural frequency ($\beta = 1$). This approach leads to obtaining an exact measure of damping for the resonance conditions and overestimated

damping ratio values for the other conditions. Thus, the energy dissipated by equivalent viscous damping for a generic load path is reported in Eq. 5.9.

$$E_D = \int_0^{u_f} 2 \cdot \xi_{(\beta=1)} \cdot m \cdot \omega \cdot \dot{u}(t) \cdot du \quad (5.9)$$

Please note that the damping ratio is a constant in the integral expression since it is experimentally defined. In addition, by observing Eq. 5.9 one can notice that the dissipated energy is evaluated as a percentage (ξ) of the total hysteretic energy for the load path.

5.2.1 Logarithmic Decrement Analysis (LDA)

Mass and stiffness of a dynamic system can be determined by its physical characteristics, while an estimate of damping resistance can be obtained by experimental measurements of the response of the structure to a given excitation. For this reason, the experimental techniques used to estimate damping ratio are based on the free vibration or on forced vibration response.

According to the first technique, damping effects for the free vibration decay of underdamped systems (Sect. 2.1.1.2) can be defined by means of the Logarithmic Decrement Analysis (LDA) (Inman 2014) of the displacement response (Helmholtz 1962) given by Eq. 5.10.

$$\delta = 2\pi\xi \frac{\omega}{\omega_D} \quad (5.10)$$

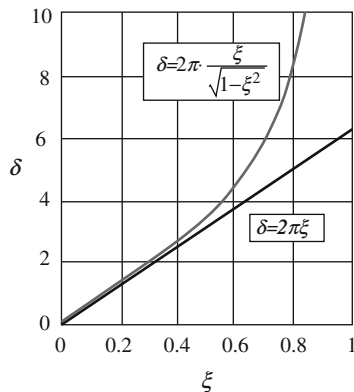
Generally, the natural damped frequency $\omega_D = \omega \cdot \sqrt{1 - \xi^2}$ can be assumed equal to the natural frequency, leading to the following expression of the logarithmic decrement (Eq. 5.11).

$$\delta = 2\pi\xi \quad (5.11)$$

Figure 5.2 illustrates the different values assumed by logarithmic decrement by referring to Eqs. 5.10 and 5.11.

For a damping ratio greater than 0.4–0.5 the differences between the two decrement values cannot be neglected. In these cases, the damped natural period is evaluated from the free vibration record by measuring the time required to complete one cycle of vibration. In the practical applications, since the accelerations are

Fig. 5.2 Comparison between logarithmic decrement for $\omega_D = \omega$ and $\omega_D = \omega \cdot \sqrt{1 - \xi^2}$ (Chopra 2017)



easier to measure than the displacement, the decrement can be expressed in terms of accelerations (Eq. 5.12).

$$\delta = \ln \left(\frac{\dot{u}_n}{\dot{u}_{n+1}} \right) \cdot 2\pi\xi \frac{\omega}{\omega_D} \quad (5.12)$$

Thus, the decrement, together with the damped and the natural periods are estimated experimentally from the acceleration response of the system. Starting from these values, the damping ratio can be evaluated (Eq. 5.13).

$$\xi = \frac{\delta}{\sqrt{4\pi^2 + \delta^2}} \quad (5.13)$$

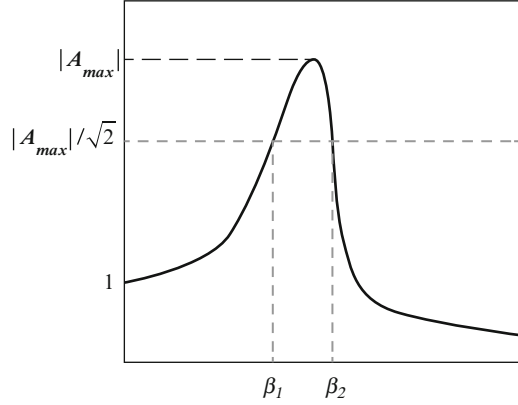
As stated above, the damping ratio can even be estimated from the experimental tests on forced systems. Usually, the experimental methods used are based on the definition of the maximum applied force in resonance conditions or on the detection of the specific representative bandwidth for the amplification phenomena. In the first methodology, the system is subjected to a harmonic excitation having a frequency equal to the natural frequency of the system ($\beta = 1$). As known, the dynamic response of the system is maximum and it is detected by Eq. 5.14.

$$u_{max} = \frac{F_0}{k} \cdot \frac{1}{\sqrt{(1 - \beta^2)^2 + (2 \cdot \xi \cdot \beta)^2}} \quad (5.14)$$

By experimental testing, it is possible to measure the maximum dynamic displacement u_{max} , while F_0 represents the amplitude of the external excitation. For resonance conditions, Eq. 5.15 is given.

$$\xi = \frac{1}{2 \cdot k} \cdot \frac{F_0}{u_{max}} \quad (5.15)$$

Fig. 5.3 Half power method



5.2.2 Half-Power Method (HPM)

The damping ratio on a structure can be estimated using the Half-Power Method (HPM) (Badsar et al. 2010) based on the definition of the frequency ratio values for an amplification factor equal to $|A_{max}|/\sqrt{2}$ (Fig. 5.3).

The experimental method is called half power since the square of the referenced amplitude is equal to 50% of the maximum power. According to the amplitude factor definition, Eq. 5.16 represents the values of β_1 and β_2 .

$$\beta^4 - 2 \cdot (1 - 2 \cdot \xi^2) \cdot \beta^2 + 1 - \frac{2}{|A_{max}|^2} = 0 \rightarrow \beta_{1,2}^2 = (1 - 2 \cdot \xi^2) \pm 2 \cdot \xi \cdot \sqrt{1 - \xi^2} \quad (5.16)$$

For small values of damping, the previous expression can be rewritten (Eq. 5.17).

$$\beta_{1,2} = \sqrt{1 \pm 2 \cdot \xi} \quad (5.17)$$

Since the dynamic response of the system is measured in the frequency domain, the damping ratio is defined by means of the previous expression (Eq. 5.18).

$$\xi = \frac{1}{2} \cdot (\beta_2 - \beta_1) \quad (5.18)$$

5.3 Plastic Energy

The capacity of a structural system to dissipate energy in the form of plastic energy is described by the *ductility factor* (Lee et al. 1999) given by Eq. 5.19.

$$\mu = \frac{\delta_u}{\delta_y} \quad (5.19)$$

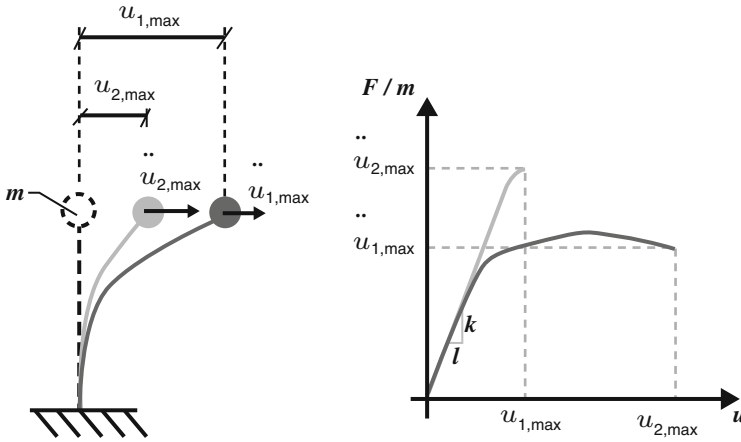


Fig. 5.4 Comparison between resistant and ductile system

It represents the ratio between the maximum tolerable displacement δ_u and the yielding displacement δ_y . Naturally, systems with high values of ductility factor are able to dissipate plastic energy leading to a decrease of the action absorbed. This concept is focused by Fig. 5.4 where a comparison between a resistant and ductile system is given.

The maximum displacement of the resistant system is less than the ductile one. At the same time, since the stiffness of the first system does not decrease, the action applied to the mass is greater than the ductile element. In reference to the ductile system, the energetic equilibrium at a generic state in which $u > u_y$, is given by Eq. 5.20.

$$E(t) = E_M + E_E + E_P = \int_0^u m \cdot \ddot{u}(t) \cdot du + k_e \cdot \frac{u_y^2}{2} + \int_0^u k(u(t)) \cdot (u(t) - u_y) \cdot du \tag{5.20}$$

The two last terms of the right side of the equation represent the deformation energy that has been divided into the elastic and plastic components. Suppose we compare the response of the system with the infinitely elastic and elasto-plastic models (Fig. 5.5).

The following parameter is introduced (Eq. 5.21).

$$q = \frac{F_e}{F_y} \tag{5.21}$$

where F_e identifies the generic elastic action, while F_y is the yielding force. Coefficient q is called *over strength factor* or *strength reduction factor*. It is used in the design application in order to reduce the elastic action on a structure due to the



Fig. 5.5 Infinitely elastic and elasto-plastic models

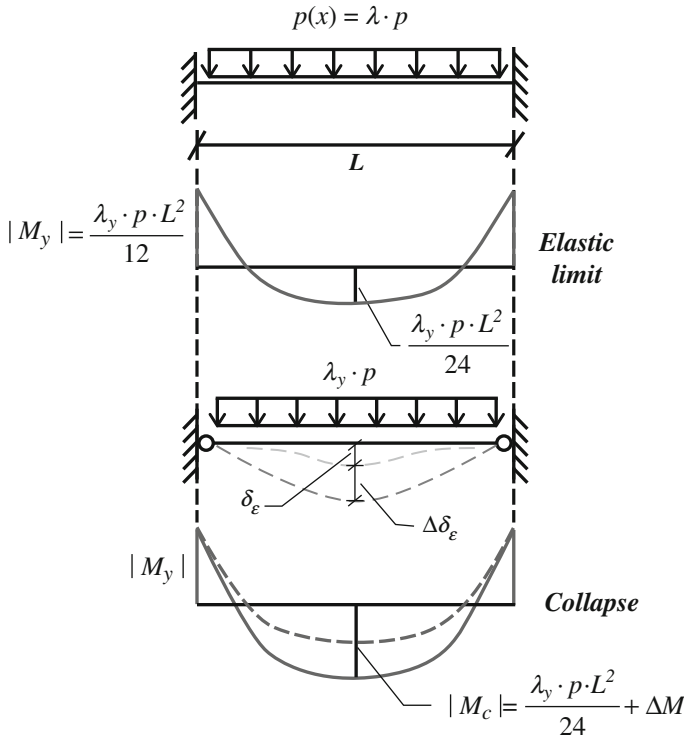
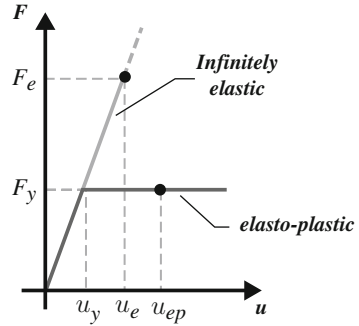


Fig. 5.6 Limit analysis of a fully restrained beam

plastic dissipation. The over strength factor is influenced by the ductility property of the structure (Baker et al. 1980). In order to address more thoroughly the problem, the fully restrained beam is considered subjected to a uniformly distributed static load (Fig. 5.6).

Referencing the Figure reported above, it is possible to observe that after reaching the elastic limit the internal actions are redistributed. The collapse conditions of



a structural system reported in Fig. 5.4 is evaluated according to the upper bound theorem, considering an elastic perfectly plastic model (Eq. 5.22).

$$\lambda_c = \frac{16 \cdot M_y}{p \cdot L^2} \tag{5.22}$$

Thus, the collapse load for elastic perfectly plastic model ($p_{ep,(c)}$) is given by Eq. 5.23,

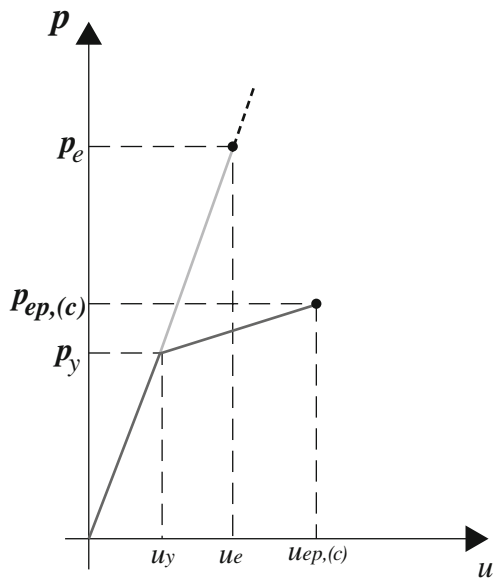
$$p_{ep,(c)} = \frac{16 \cdot M_y}{L^2} \tag{5.23}$$

where M_y is the bending moment value causing the plasticization of the cross section. Considering a constant rectangular section of the beam with dimensions $b \times h$, the M_y value is given by Eq. 5.24,

$$M_y = 6 \cdot \frac{f_y}{b \cdot h^2} \tag{5.24}$$

where f_y represents the yielding tension of the material constituting the beam. Generally the structural system is able to carry a greater load than the yielding load of the external cross sections (p_y). Figure 5.7 graphically explains this aspect through a comparison between the elasto-plastic model and the infinitely elastic one.

Fig. 5.7 Comparison between the elasto-plastic and infinitely elastic load evolution



By imposing the two deformation works, it is possible to obtain the relationship between the two load values (Eq. 5.25).

$$\frac{p_e^2}{p_y^2} = \left(\frac{p_{ep.(c)}}{p_y} \cdot (\mu - 1) + \mu \right) \quad (5.25)$$

Remembering that the ratio between p_e and p_y is the structure factor, Eq. 5.26 is given.

$$q = \sqrt{\left(\frac{p_{ep.(c)}}{p_y} \cdot (\mu - 1) + \mu \right)} \quad (5.26)$$

Substituting the value of $p_{ep.(c)}$ obtained before and assuming $p_y = \frac{12 \cdot M_y}{L^2}$ (according to the static equilibrium in the external cross sections), the over strength factor assumes the expression reported in Eq. 5.27.

$$q = \sqrt{\left(\frac{4}{3} \cdot \mu - \frac{1}{3} \right)} \quad (5.27)$$

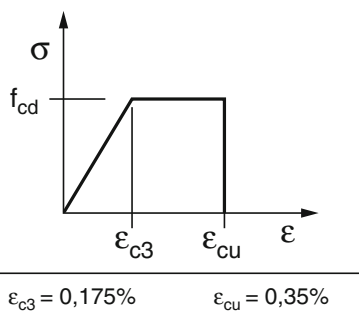
From this equation it is possible to observe how the over strength factor depends on ductility of the element. Suppose we have a concrete element and according to the elastic perfectly plastic model proposed by NTC08 (Fig. 5.8) it is possible to specify the ductility factor (Eq. 5.28).

$$\mu = \frac{\varepsilon_{cu}}{\varepsilon_{c3}} = \frac{3.50}{1.75} = 2 \quad (5.28)$$

Equation 5.29 provides the value of the over strength factor in the static case.

$$q = 1.29 \quad (5.29)$$

Fig. 5.8 Stress-deformation model for concrete (Adapted from Fig. 4.1.1 – NTC08)



Naturally, for assembled elements, the definition of the collapse load becomes very difficult since the interaction between the systems has to be considered. In dynamic cases, the procedure used to determine the over strength factor cannot be defined with incremental static analysis since the response of the system is not governed by a quasi-static loading process. For a generic system, the over strength factor will be defined as maximum acceleration reduction, since the applied force is variable over time. For this purpose, the maximum elastic dynamic response of a structural system is described by means of the elastic spectra in which for every natural period the maximum acceleration acting on the system is reported. In Sect. 12.2, the elastic spectrum for a generic dynamic excitation will be discussed in detail. Now it is generically introduced in order to explain how the maximum dynamic response of a system depends on it. In addition, the acceleration reduction on an elasto-plastic system is defined according to three criteria based on the period value (Leelataviwat et al. 2009). According to the results of numerical investigations, the following criteria are proposed:

- *Equal displacement criterion.* It is valid for high value of vibrational period ($T > 0.5$ s).

According to Fig. 5.9a, the structure period is defined by Eq. 5.30.

$$q = \frac{u_{max}}{u_y} = \mu \tag{5.30}$$

- *Equal energy criterion.* It describes the acceleration reduction for medium period ($0.1s < T < 0.5$ s).

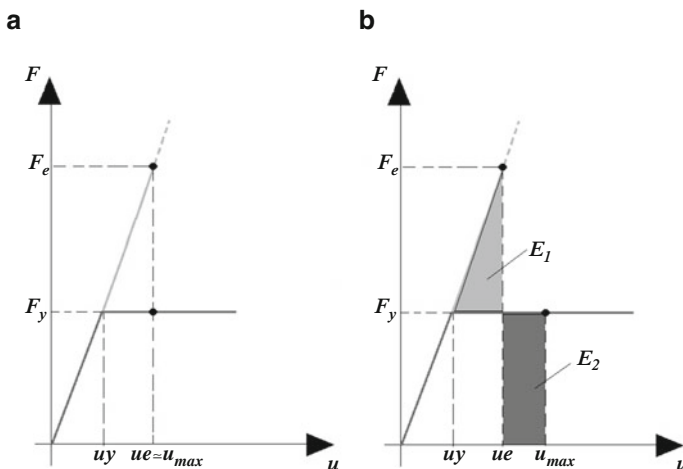


Fig. 5.9 Equal displacement criterion (a) and equal energy criterion (b)



Referencing Fig. 5.9b, the following energy equilibrium expression is obtained (Eq. 5.31).

$$E_1 = E_2 \rightarrow (F_e - F_y) \cdot \frac{(u_e - u_y)}{2} = F_y \cdot (u_{\max} - u_e) \quad (5.31)$$

Equation 5.32 reports the structure factor deduced from the previous expression.

$$q = \sqrt{2 \cdot \mu - 1} \quad (5.32)$$

- *Equal acceleration criterion.* It is valid for low value of vibrational period ($T < 0.1$ s).

For equal acceleration criterion there is no a reduction, then the over strength factor is equal to one (Eq. 5.33).

$$q = 1 \quad (5.33)$$

It is possible to observe how the structure factor depends on the ductility property of the system.

References

- Badsar S, Schevenels M, Haegeman W, Degrande G (2010) Determination of the material damping ratio in the soil from SASW tests using the half-power bandwidth method. *Geophys J Int* 182(3):1493–1508
- Baker J, Baker L, Heyman, J (1980) *Plastic design of frames I fundamentals*, vol 1. UP Archive
- Chopra AK (2017) *Dynamics of structures: theory and applications to earthquake engineering*, 5th edn. Pearson Education, Inc., Hoboken, 960 pp
- Helmholtz HV (1962) *Helmholtz's treatise on physiological optics*. Dover, New York, p 42
- Inman DJ (2014) *Engineering vibration*. Pearson, Boston
- Lee LH, Han SW, Oh YH (1999) Determination of ductility factor considering different hysteretic models. *Earthq Eng Struct Dyn* 28(9):957–977
- Leelataviwat S, Saewon W, Goel SC (2009) Application of energy balance concept in seismic evaluation of structures. *J Struct Eng* 135(2):113–121
- Uang CM, Bertero VV (1990) Evaluation of seismic energy in structures. *Earthq Eng Struct Dyn* 19(1):77–90
- Vakakis AF, Gendelman OV, Bergman LA, McFarland DM, Kerschen G, Lee YS (2008) *Nonlinear targeted energy transfer in mechanical and structural systems*, vol 156. Springer, Dordrecht
- Zahrah TF, Hall WJ (1984) Earthquake energy absorption in SDOF structures. *J Struct Eng* 110(8):1757–1772

Chapter 6

Distributed Mass and Elasticity Systems



Abstract Typical problems of discretized systems (e.g. lumped mass systems) have been analyzed in the previous chapters. In some real cases, the simplified approach of lumped masses is not feasible, then an infinite number of DOFs have to be considered in the analyses. The dynamic problem of systems with distributed mass and elasticity are formulated in this chapter. A Simple structure is considered in order to provide the closed form solution for both free vibrations and forced system analyses.

6.1 Introduction

Many structural systems can be discretized as lumped mass physical models (e.g. multistory buildings) since they are composed of massless flexible elements and infinite rigid diaphragms in which the mass is concentrated. When a structure has an almost uniform distributed mass and stiffness (Stokey 1988), the idealization of the lumped masses cannot be used. In these cases, the problem becomes more complex because the DOFs are infinite. In the following section, the generic undamped beam element with distributed mass and elasticity will be studied (Fig. 6.1).

In order to write the dynamic equilibrium with respect to the vertical direction (Eq. 6.1), let's consider the differential element of the beam in Fig. 6.1.

$$\frac{dV}{dx} \cdot dx = p(x, t) - m(x) \cdot \frac{d^2u}{dt^2} \quad (6.1)$$

If the rotational inertia contribution is neglected, the rotational equilibrium equation is similar to the static equilibrium equation and the following relation can be deduced (Eq. 6.2).

$$V = \frac{dM}{dx} \quad (6.2)$$

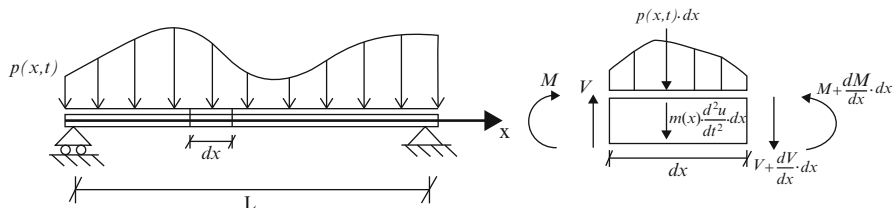


Fig. 6.1 Elementary scheme of distributed mass and elasticity beam

In addition, if the shear deformation is assumed equal to zero (Bernoulli beam element) and the flexural stiffness is constant, it is possible to define Eq. 6.3.

$$M = EI \cdot \frac{d^2 u}{dx^2} \quad (6.3)$$

According to Eqs. 6.2 and 6.3, the equilibrium dynamic equation can be rewritten as given by Eq. 6.4 (Truesdell 1984).

$$m(x) \cdot \frac{d^2 u}{dt^2} + EI \cdot \frac{d^4 u}{dx^4} = p(x, t) \quad (6.4)$$

6.2 Vibrational Modes Analysis

Starting from Eq. 6.4, in the free vibration case ($q(x, t) = 0$) it is possible to apply the coordinate transformation similarly to the MDOFs systems case. In this case the equilibrium equation can be expressed as shown in Eq. 6.5.

$$m(x) \cdot \phi(x) \cdot \ddot{q}(t) + EI \cdot \phi^{IV}(x) \cdot q(t) = 0 \quad (6.5)$$

Dividing by the term $m(x) \cdot \phi(x)$, the ratio between $\ddot{q}(t)$ and $q(t)$ is defined (Eq. 6.6).

$$\frac{\ddot{q}(t)}{q(t)} = -\frac{EI \cdot \phi^{IV}(x)}{m(x) \cdot \phi(x)} = -\omega^2 \quad (6.6)$$

Thus, the equation of motion can be rewritten in the form given by Eq. 6.7.

$$EI \cdot \phi^{IV}(x) - \omega^2 \cdot m(x) \cdot \phi(x) = 0 \quad (6.7)$$

It is noticeable that the system is characterized by an infinite number of natural vibrations and modal deformed shape. Supposing the mass as the constant ($m(x) = m$), the equation becomes as expressed below (Eq. 6.8).

$$\phi^{IV}(x) - \beta^4 \cdot \phi(x) = 0 \rightarrow \beta^4 = \omega^2 \cdot \frac{m}{EI} \quad (6.8)$$

Since it is a 4th order differential equation with constant coefficients, the general solution can be given by Eq. 6.9.

$$\phi(x) = C_1 \cdot \sin(\beta \cdot x) + C_2 \cdot \cos(\beta \cdot x) + C_3 \sinh(\beta \cdot x) + C_4 \cosh(\beta \cdot x) \quad (6.9)$$

Thus, the complete dynamic solution is given by Eq. 6.10

$$u(x, t) = q(t) \cdot [C_1 \cdot \sin(\beta \cdot x) + C_2 \cdot \cos(\beta \cdot x) + C_3 \sinh(\beta \cdot x) + C_4 \cosh(\beta \cdot x)] \quad (6.10)$$

The application of the boundary conditions leads to evaluation of the four constants (C_1, C_2, C_3 and C_4). The parameters are obtained as the nontrivial solution of the equation reported above. Finally, the natural frequencies are calculated and from their values, the modal deformed shape will be obtained. Lets consider the simple cantilever element shown in Fig. 6.2 for which the boundary conditions expressed in Eq. 6.11 are defined.

$$\begin{cases} u(0) = 0 \\ \frac{du}{dx}(0) = 0 \\ V(L) = 0 \\ M(L) = 0 \end{cases} \rightarrow \begin{cases} \phi(0) = 0 \\ \frac{d\phi}{dx}(0) = 0 \\ \frac{d^3\phi}{dx^3}(L) = 0 \\ \frac{d^2\phi}{dx^2}(L) = 0 \end{cases} \quad (6.11)$$

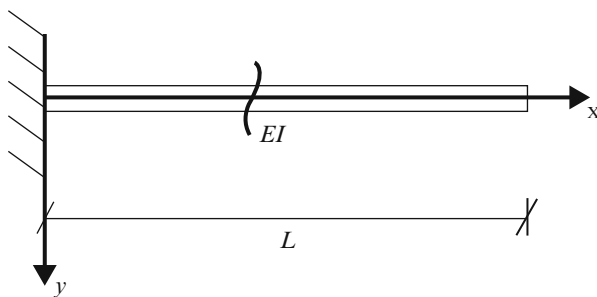


Fig. 6.2 Cantilever beam with distributed mass and elasticity

By including the boundary conditions reported above, the Eq. 6.12 is obtained.

$$\begin{cases} C_2 + C_4 = 0 \\ \beta \cdot (C_1 + C_3) = 0 \\ C_1 \cdot (\sin(\beta \cdot L) + \sinh(\beta \cdot L)) + C_2 \cdot (\cos(\beta \cdot L) + \cosh(\beta \cdot L)) = 0 \\ C_1 \cdot (\cos(\beta \cdot L) + \cosh(\beta \cdot L)) - C_2 \cdot (\sin(\beta \cdot L) - \sinh(\beta \cdot L)) = 0 \end{cases} \quad (6.12)$$

The two first equations define simple relations between the constants, while the last two equations can be written in the following system form (Eq. 6.13).

$$\begin{bmatrix} \sin(\beta \cdot L) + \sinh(\beta \cdot L) & \cos(\beta \cdot L) + \cosh(\beta \cdot L) \\ \cos(\beta \cdot L) + \cosh(\beta \cdot L) & -\sin(\beta \cdot L) + \sinh(\beta \cdot L) \end{bmatrix} \begin{Bmatrix} C_1 \\ C_2 \end{Bmatrix} = \begin{Bmatrix} 0 \\ 0 \end{Bmatrix} \quad (6.13)$$

Naturally, the problem is solved as nontrivial solution by imposing the determinant of the coefficients matrix to be equal to zero, whence the following characteristic equation is obtained (Eq. 6.14).

$$1 + \cos(\beta \cdot L) \cdot \cosh(\beta \cdot L) = 0 \quad (6.14)$$

Since it is not possible to find a simple mathematical solution from Eq. 6.14, the Eq. 6.15 represents the first three numerical solution values.

$$\beta_1 = \frac{1.875}{L}; \beta_2 = \frac{4.694}{L} \beta_3 = \frac{7.855}{L} \dots \quad (6.15)$$

Thus, the natural frequencies can be evaluated (Eq. 6.16).

$$\omega_1 = 3.52 \cdot \sqrt{\frac{EI}{m \cdot L^4}} \quad \omega_2 = 22.03 \cdot \sqrt{\frac{EI}{m \cdot L^4}} \quad \omega_3 = 61.70 \cdot \sqrt{\frac{EI}{m \cdot L^4}} \dots \quad (6.16)$$

Substituting the generic i th- β coefficient in the Eq. 6.9 and imposing the two boundary conditions, Eq. 6.17 depending on the arbitrary coefficient C_1 (or C_2) is obtained.

$$\phi_i(x) = C_1 \cdot \left[\cosh(\beta_i \cdot x) - \cos(\beta_i \cdot x) - \frac{\cosh(\beta_i \cdot x) + \cos(\beta_i \cdot x)}{\sinh(\beta_i \cdot x) + \sin(\beta_i \cdot x)} \cdot (\sinh(\beta_i \cdot x) - \sin(\beta_i \cdot x)) \right] \quad (6.17)$$

Figure 6.3 illustrates the first three vibrational modes of the cantilever beam considered.

Similar to the case of the lumped mass system, the dynamic response of the beam can be obtained as a linear combination of the modes (Eq. 6.18),

$$u(x, t) = \sum_{i=1}^{\infty} \phi_i(x) \cdot q_i(t) \quad (6.18)$$

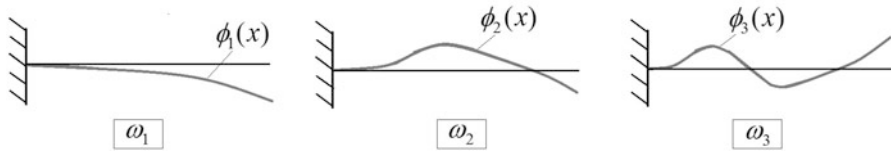


Fig. 6.3 First three vibrational modes of the cantilever beam

where $q_i(t)$ represents the modal coordinates associated with the vibrational mode i . From this definition, according to the force-displacement relations, the bending moment and shear functions can be evaluated (Eq. 6.19).

$$\begin{aligned} M(x, t) &= - \sum_{i=1}^{\infty} EI \cdot \phi_i''(x) \cdot q_i(t) \\ V(x, t) &= - \sum_{i=1}^{\infty} EI \cdot \phi_i'''(x) \cdot q_i(t) \end{aligned} \quad (6.19)$$

6.3 Vibrational Modes Analysis of Forced Systems

For a generic forced system, the dynamic equilibrium equation can be expressed by Eq. 6.20.

$$\sum_{i=1}^{\infty} m(x) \cdot \phi_i(x) \cdot \ddot{q}_i(t) + EI \cdot \sum_{i=1}^{\infty} \phi_i^{IV}(x) \cdot q_i(t) = F(x, t) \quad (6.20)$$

Multiplying both terms in Eq. 6.20 by the generic modal function and then integrating over the total length of the element, the following equation is obtained.

$$\ddot{q}_i(t) \cdot \int_0^L m(x) \cdot (\phi_i(x))^2 \cdot dx + EI \cdot q_i(t) \cdot \int_0^L \phi_i(x) \cdot \phi_i^{IV}(x) \cdot dx = \int_0^L F(x, t) \cdot \phi_i(x) \cdot dx \quad (6.21)$$

All the terms where $\phi_h(x)$ and $\phi_i(x)$ appear with $h \neq i$ are equal to zero according to the orthogonality of the modes. Thus, the dynamic equilibrium equation can be rewritten in terms of generalized characteristics in Eq. 6.22,

$$\ddot{q}_i(t) \cdot M_i + q_i(t) \cdot K_i = F_i \quad (6.22)$$

where the coefficients expressed with n index represent the generalized mass, stiffness and force for the generic mode i of the system. Equation 6.23 defines their mathematical expressions,

$$\begin{aligned} M_i &= \int_0^L m(x) \cdot (\phi_i(x))^2 \cdot dx \\ K_i &= \int_0^L EI(x) \cdot (\phi_i''(x))^2 \cdot dx \\ F_i &= \int_0^L F(x, t) \cdot \phi_i(x) \cdot dx \end{aligned} \quad (6.23)$$

where the term K_i has been rewritten by applying the integration by part. The associated natural frequency is obtained by the ratio between the generalized stiffness and mass (Eq. 6.24).

$$\frac{K_i}{M_i} = \omega_i^2 \quad (6.24)$$

The expression of the equation of motion in terms of generalized characteristics defines a generic formulation of the problem. Thus, the dynamic solution (in terms of displacements and internal actions) will be evaluated by means of the linear combination of infinite modes. It is important to remember that each of them represents a generalized and independent SDOF system. In addition, if the external excitation is due to an earthquake, the generalized force is given by Eq. 6.25.

$$F_i = -\ddot{u}_g(t) \cdot \int_0^L m(x) \cdot \phi_i(x) \cdot dx \quad (6.25)$$

References

- Stokey WF (1988) Vibration of systems having distributed mass and elasticity. In: Harris CM (ed) Shock and vibration handbook, chapter 7. McGraw-Hill, New York
 Truesdell C (1984) Timoshenko's history of strength of materials (1953). Springer, New York

Chapter 7

Generalized SDOF Systems



Abstract The chapter introduces the concept of generalized systems. A brief introduction of the Lagrangian approach applied to the mechanical systems is provided. Furthermore, some numerical examples are reported (system with distributed mass and elasticity, system with distributed elasticity and lumped mass, and general systems).

7.1 Lagrangian Approach

In the previous chapter, the generalized characteristics of a system have been introduced. They represent the parameters (mass, stiffness and force) associated with a specific vibrational mode of the system. The name generalized comes from the Lagrangian mechanics (Lagrange 1811) where the univocal state of a physical system is expressed by the generalized coordinates (Batchelor 2000). Consider a mechanical system having n DOFs described in a generic reference system with order m and coordinates x . Every variable x can be expressed in terms of a generalized variable q_i (Eq. 7.1).

$$\begin{cases} X_1 = f(q_1, q_2, \dots, q_n) \\ X_2 = f(q_1, q_2, \dots, q_n) \\ \dots \\ X_m = f(q_1, q_2, \dots, q_n) \end{cases} \quad (7.1)$$

The number of generalized coordinates is equal to the number of DOFs of the system. In addition, it can be observed that each generalized coordinate is linearly independent from the others, therefore they only depend on the time ($q = q(t)$). From this property, Eq. 7.2 can be obtained.

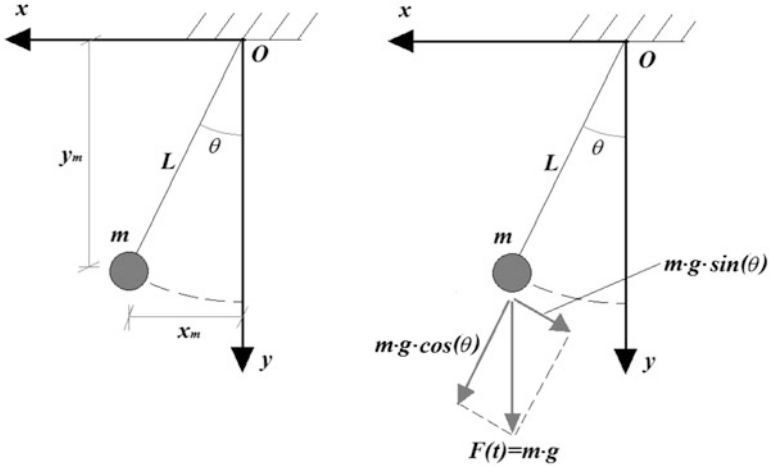


Fig. 7.1 Pendulum system

$$\frac{dx_j(t)}{dt} = \sum_{i=1}^n \frac{dx_j}{dq_i} \cdot \frac{dq_i}{dt} = \sum_{i=1}^n \frac{dx_j}{dq_i} \cdot \dot{q}_i \quad (7.2)$$

As an example, let's consider the pendulum illustrated in Fig. 7.1, for which the generic position is defined by means of the coordinates x_m and y_m of the mass.

The motion of the mass is described by the variable θ that is the generalized coordinate of the system (DOFs = 1). Equation 7.3 can be derived.

$$\begin{cases} x_m = L \cdot \sin(\theta) \\ y_m = L \cdot \cos(\theta) \end{cases} \quad (7.3)$$

The first equation is identically satisfied while the second one is reported below (Eq. 7.4),

$$m \cdot \ddot{y}_m + m \cdot g \cdot \cos^2(\theta) = m \cdot g \quad (7.4)$$

where, the acceleration \ddot{y}_m can be expressed as given by Eq. 7.5.

$$\ddot{y}_m = \frac{d}{dt} \left(\frac{dy_m}{d\theta} \cdot \dot{\theta} \right) = \frac{dy_m}{d\theta} \cdot \ddot{\theta} = -L \cdot \sin(\theta) \cdot \ddot{\theta} \quad (7.5)$$

Thus, the equilibrium dynamic equation is expressed as given by Eq. 7.6,

$$-m \cdot L \cdot \sin(\theta) \cdot \ddot{\theta} + m \cdot g \cdot \cos^2(\theta) = m \cdot g \quad (7.6)$$

while the angular acceleration is given by Eq. 7.7.

$$\ddot{\theta} = -\frac{g \cdot (1 - \cos^2(\theta))}{L \cdot \sin(\theta)} = -\frac{g}{L} \cdot \sin(\theta) \quad (7.7)$$

The same result can be obtained if the equation of motion is written directly in terms of (Eq. 7.8).

$$I_o \cdot \ddot{\theta} + m \cdot g \cdot \cos^2(\theta) = m \cdot g \quad (7.8)$$

Where I_o represents the polar inertia mass with respect to the pole O (Eq. 7.9).

$$I_o = m \cdot L^2 \quad (7.9)$$

Thus, Eq. 7.10 is obtained.

$$m \cdot L^2 \cdot \ddot{\theta} + m \cdot g \cdot \sin(\theta) \cdot L = 0 \rightarrow \ddot{\theta} = -\frac{g}{L} \cdot \sin(\theta) \quad (7.10)$$

7.2 Approximated Solution

For a complex system with distributed mass, the dynamic solution can be obtained as a linear combination of infinite vibrational modes. In order to simplify the problem, it is possible to pass from an infinite DOFs system to a generalized SDOF system. This procedure comes from the possibility of describing a generic body motion through few simplified generalized coordinates. Even the shape functions have to be defined in order to obtain the dynamic response. These shape functions have to be evaluated by modal analysis, but they can be approximatively assumed according to some considerations. Naturally this approach gives exact results for systems composed by rigid bodies (univocal shape function), but it is approximate for flexible systems. As an example, let's consider the following rigid body (Fig. 7.2).

The generalized coordinate has been expressed as $q_v(t)$. The displacement function $v(x)$ is expressed as reported in Eq. 7.11.

$$v(x) = \phi(x) \cdot q_v(t) \quad (7.11)$$

The definition of the shape function $\phi(x)$ is required to obtain the dynamic solution for the considered system. Since the body is a rigid bar, it is possible to select the following exact expression of the shape function (Eq. 7.12).

$$\phi(x) = \frac{x}{L} \quad (7.12)$$

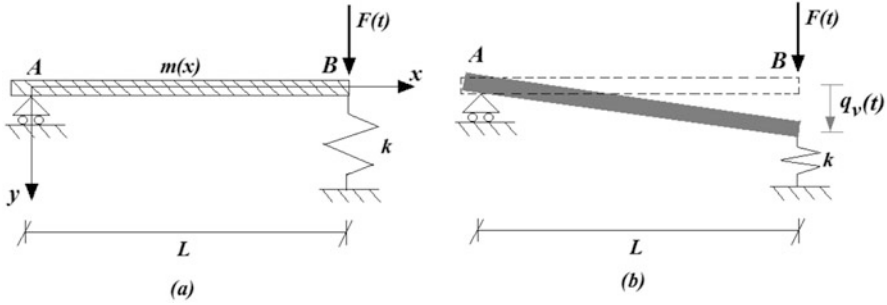


Fig. 7.2 Rigid body subjected to an external dynamic force (a) and the imposition of the generalized coordinate (b)

The dynamic response of the rigid body is given by Eq. 7.13.

$$v(x) = \frac{x}{L} \cdot q_v(t) \quad (7.13)$$

The associated equation of motion can be derived (Eq. 7.14).

$$m_{(b)} \cdot \frac{x}{L} \cdot \ddot{q}_v(t) + k_{(b)} \cdot \frac{x}{L} \cdot q_v(t) = F(t)_{(b)} \quad (7.14)$$

The mass, stiffness and external force coefficients have to be defined. Since the equation of motion has been written with reference to the generalized coordinate assumed for the point B, according to the definition of the mass and stiffness property the following values are deduced (Eq. 7.15).

$$\begin{aligned} k_{(b)} &= k \\ m_{(b)} &= \frac{m}{3} \end{aligned} \quad (7.15)$$

Figure 7.3 graphically explains the definitions of the previous coefficients. Therefore, the equation of motion is given below (Eq. 7.16).

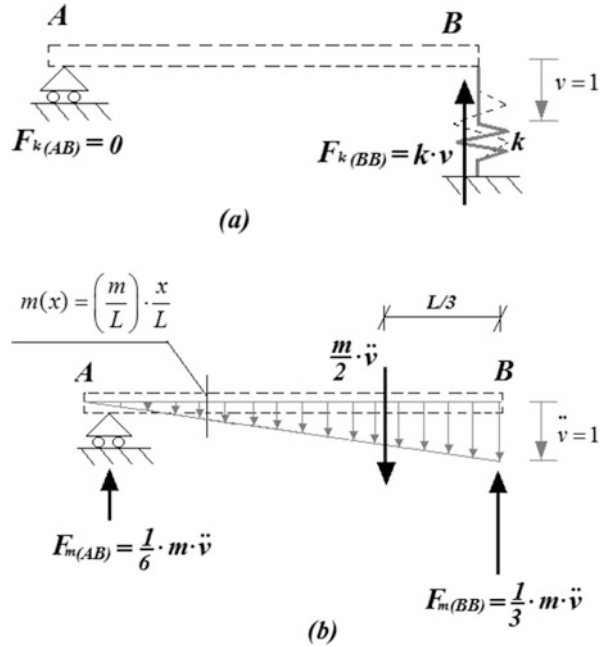
$$\frac{1}{3} \cdot m \cdot \frac{x}{L} \cdot \ddot{q}_v(t) + k \cdot \frac{x}{L} \cdot q_v(t) = F(t) \quad (7.16)$$

7.2.1 Example 1: System with Distributed Mass and Elasticity

Let's consider the cantilever beam analyzed in Chap. 8 for which the generalized coordinate is applied at the free point of the element (Fig. 7.4). In this case, the definition of a shape function is not exact, because it depends on

(continued)

Fig. 7.3 Definition of the stiffness (a) and mass (b) coefficients for the generalized system



an infinite number of modes. Since it is known that the first mode is always predominant for uniformly distributed mass and stiffness systems, the shape function can be assumed equal to the first vibrational mode. For the cantilever beam, it was observed that the mathematical expression of the vibrational modes is complex and has to be solved numerically.

Generally, the shape function is chosen in order to respect the boundary conditions and the real elastic behavior. For this purpose, the shape function of the cantilever beam can be deduced as flexural deformed shape due to a unitary force applied to the free node (Eq. 7.17).

$$\phi(x) = \frac{x^2}{2 \cdot L^2} \cdot \left(3 - \frac{x}{L}\right) \tag{7.17}$$

This expression is externally and internally compatible since it is defined from the static analysis by imposing the given boundary conditions. According

(continued)



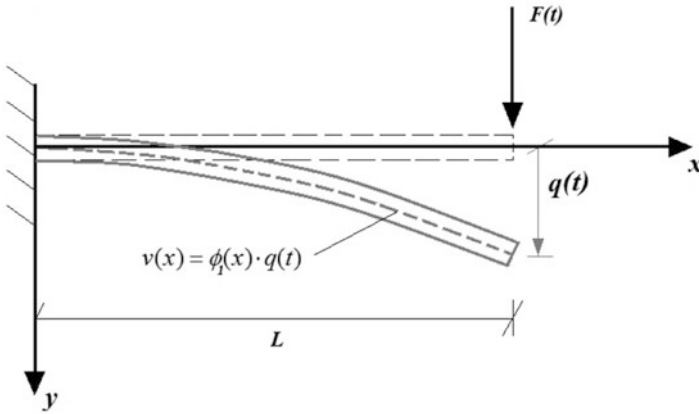


Fig. 7.4 Generalized cantilever system

to the Eq. 7.22, the equation of motion is expressed in terms of generalized characteristics (Eq. 7.18).

$$\tilde{m} \cdot \ddot{q}(t) + \tilde{k} \cdot q(t) = F(t) \quad (7.18)$$

Thus, the generalized mass, stiffness and force can be evaluated (Eq. 7.19).

$$\begin{aligned} \tilde{m} &= 0.24 \cdot m \\ \tilde{k} &= 3 \frac{EI}{L^3} \\ \tilde{F} &= 0.38 \cdot F(t) \end{aligned} \quad (7.19)$$

A uniformly distributed load was assumed and thus Eq. 7.20 is given.

$$0.24 \cdot m \cdot \ddot{q}(t) + 3 \cdot \frac{EI}{L^3} \cdot q(t) = 0.38 \cdot p(t) \cdot L \quad (7.20)$$

In addition, the natural frequency of the generalized system can be deduced (Eq. 7.21).

Table 7.1 Geometric and mechanical properties for the cantilever beam

E[MPa]	L[m]	b[m]	h[m]	p[kg/m ³]
20,000	5.00	0.2	0.5	2500

$$\tilde{\omega} = \sqrt{\frac{\tilde{k}}{\tilde{m}}} = \frac{3.53}{L} \cdot \sqrt{\frac{EI}{m \cdot L}} \quad (7.21)$$

According to Eq. 7.19, the internal moment and shear are shown in Eq. (7.22).

$$\begin{aligned} M(x) &= -EI \cdot \phi''(x) \cdot q(t) = -3 \cdot \frac{EI}{L^2} \cdot \left(1 - \frac{x}{L}\right) \cdot q(t) \\ V(x) &= -EI \cdot \phi'''(x) \cdot q(t) = -3 \cdot \frac{EI}{L^3} \cdot q(t) \end{aligned} \quad (7.22)$$

Let's consider a numerical example. In Table 7.1 the geometric and mechanical characteristics are summarized.

Moreover b and h represent the dimensions of the cross section for the cantilever beam. Thus, with respect to the main central axis for which the inertia moment is maximum, the generalized properties can be evaluated as given by Eq. 7.23.

$$\begin{cases} \tilde{m} = 0.24 \cdot \rho \cdot L \cdot h \cdot b = 240 \text{ Kg} \\ \tilde{k} = 3 \cdot \frac{EI}{L^3} = 3 \cdot \frac{E \cdot \frac{b \cdot h^3}{12}}{L^3} = 512,000 \text{ N/m} \end{cases} \quad (7.23)$$

Natural frequency and period are calculated and reported in Eq. 7.24.

$$\tilde{\omega} = 46.19 \text{ rad/s} \rightarrow \tilde{T} = 0.14 \text{ s} \quad (7.24)$$

7.2.2 Example 2: System with Distributed Elasticity and Lumped Mass

Let's consider now the three DOF system studied in Sect. 4.6.1 (Fig. 4.17). The three multistory shear type buildings are considered as a lumped mass system, but in this case it will be treated as a generalized system. The top displacement is chosen as generalized coordinate ($q(t)=q_3(t)$). Since the system has an almost regular uniformly distributed mass and stiffness, the first mode will be predominant. For this reason, it can be used as shape function (Eq. 7.25).

$$\phi^T = \phi_1^T = (0.45, 0.80, 1) \quad (7.25)$$

In this case, the integral expressions are substituted by the series relations (Eq. 7.26).

$$\begin{cases} \tilde{m} = \sum_{i=1}^{n=3} m_i \cdot (\phi_{1i})^2 \\ \tilde{k} = \sum_{i=1}^{n=3} k_i \cdot (\phi_{1(i)} - \phi_{1(i-1)})^2 \\ \tilde{F} = \sum_{i=1}^{n=3} F_i(t) \cdot \phi_{1i} \end{cases} \quad (7.26)$$

Thus, the generalized mass, stiffness and force are evaluated for the case study (Eq. 7.27).

$$\begin{cases} \tilde{m} = m \cdot (0.45^2 + 0.35^2 + 1^2) = 1.84 \cdot m = 73,700 \text{ kg} \\ \tilde{k} = 36 \cdot \frac{EI_c}{h^3} \cdot (0.45^2 + 0.35^2 + 0.2^2) = 13.14 \cdot \frac{EI_c}{h^3} = 9.86 \cdot 10^3 \text{ N/m} \\ \tilde{F} = F(t) \cdot (0.45 + 0.80 + 1) = 2.25 \cdot F(t) \end{cases} \quad (7.27)$$

The natural frequency can be calculated (Eq. 7.28).

$$\tilde{\omega} = 11.56 \text{ rad/s} \rightarrow \tilde{T} = 0.54 \text{ s} \quad (7.28)$$

Obviously, the same natural frequency and period that is associated with the first mode has been obtained. Suppose we consider the same structure subjected to an earthquake excitation: now the generalized problem will be solved considering as shape function a linear combination of the three modes with participating mass normalized with respect to the maximum value as coefficients (Eq. 7.29).

$$\phi = \phi_1 \cdot g_1 + \phi_2 \cdot g_2 + \phi_3 \cdot g_3 \quad (7.29)$$

Normalizing with respect to the component associated to the top DOF, Eq. 7.30 is obtained.

$$\phi = \phi_1 \cdot g_1 + \phi_2 \cdot g_2 + \phi_3 \cdot g_3 \quad (7.30)$$

Thus, the generalized properties can be evaluated (Eq. 7.31).

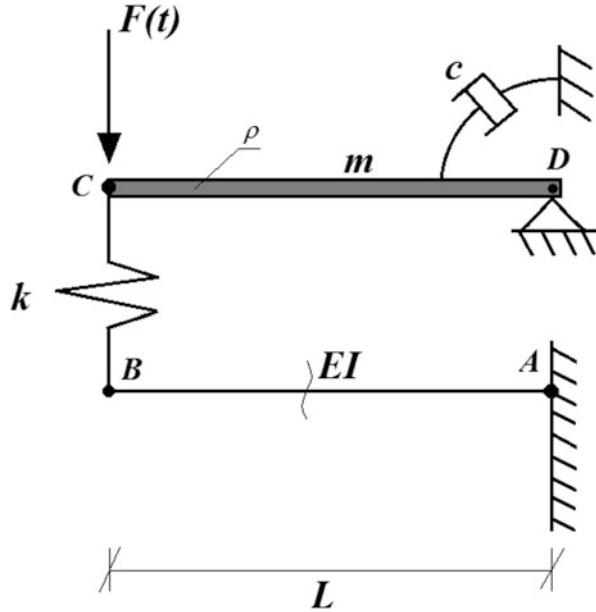
$$\begin{cases} \tilde{m} = 3.42 \cdot m = 738,000 \text{ kg} \\ \tilde{k} = 36 \cdot \frac{EI_c}{h^3} = 67.26 \cdot \frac{EI_c}{h^3} = 5.05 \cdot 10^7 \text{ N/m} \\ \tilde{F} = -3.16 \cdot \ddot{U}_g \cdot m \end{cases} \quad (7.31)$$

The natural generalized frequency and period are given by Eq. 7.32.

$$\tilde{\omega} = 19.20 \text{ rad/s} \rightarrow \tilde{T} = 0.33 \text{ s} \quad (7.32)$$

In this case the generalized problem gives the exact solution since the shape function has been evaluated with respect to the real contribution of each mode.

Fig. 7.5 Dynamic complex system



7.2.3 Example 3: General Systems

In this paragraph a complex MDOF system will be analyzed with the generalized approach (Fig. 7.5).

The problem is solved by assuming the vertical time displacement of point B as a generalized coordinate. The first problem is represented by the shape functions for the rigid and flexible body

Figure 7.6 illustrates a compatible deformed configuration for the system, in which the term ρ represents the mass per surface of the square element.

The unknown generalized coordinates q_1 and $q_1 I$ are defined by the imposition of equilibrium equations for the two bodies (Eq. 7.33).

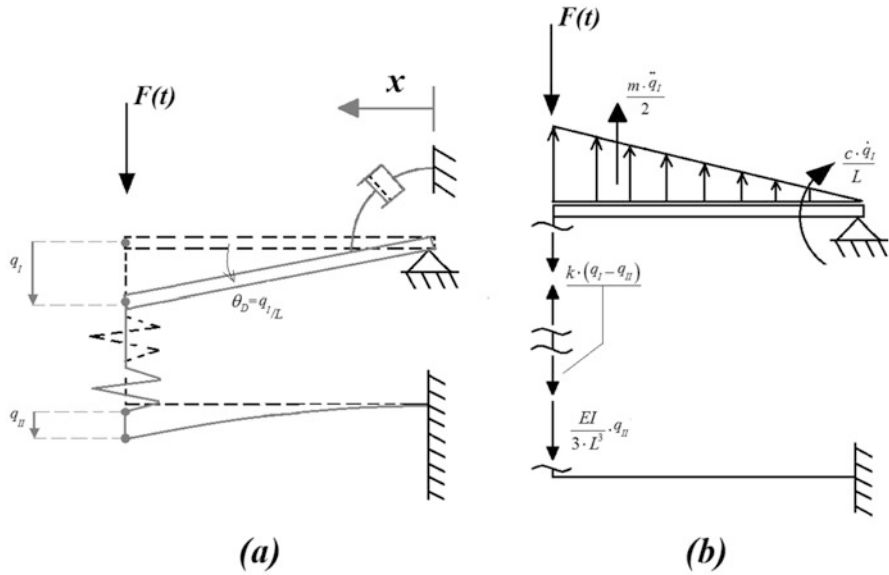


Fig. 7.6 Compatible deformation (a) and internal actions (b)

$$\begin{cases} (I) \Sigma M_D = 0 \rightarrow c \cdot \frac{\dot{q}_I}{L} - k \cdot (q_I - q_{II}) \cdot L + \frac{2}{3} \cdot m \cdot \ddot{q}_I \cdot L - F(t) \cdot L = 0 \\ (II) \Sigma F_v = 0 \rightarrow k \cdot (q_I - q_{II}) + \frac{EI}{3 \cdot L^3} \cdot q_{II} = 0 \end{cases} \quad (7.33)$$

From the second equation, it is possible to evaluate the following relationships (Eq. 7.34).

$$q_I = q_{II} \left(1 - \frac{EI}{3 \cdot k \cdot L^3} \right) \quad (7.34)$$

Substituting this definition into the first equation, the following result is obtained (Eq. 7.35).

$$\ddot{q}_{II} \cdot \frac{2}{3} \cdot m \cdot L \cdot \left(1 - \frac{EI}{3 \cdot k \cdot L^3} \right) + \dot{q}_{II} \cdot \frac{c}{L} \cdot \left(1 - \frac{EI}{3 \cdot k \cdot L^3} \right) + q_{II} \cdot \frac{EI}{3 \cdot L^2} = F(t) \cdot L \quad (7.35)$$

From this equation, it is possible to define the generalized mass, stiffness and damping (Eq. 7.36).

$$\begin{cases} \tilde{m} = \frac{2}{3} \cdot m \cdot \left(1 - \frac{EI}{3 \cdot k \cdot L^3}\right) \\ \tilde{c} = \frac{c}{L^2} \cdot \left(1 - \frac{EI}{3 \cdot k \cdot L^3}\right) \\ \tilde{k} = \frac{EI}{3 \cdot L^3} \end{cases} \quad (7.36)$$

Finally, the equation of motion is given (Eq. 7.37).

$$\tilde{m} \cdot \ddot{q}_{II} + \tilde{c} \cdot \dot{q}_{II} + \tilde{k} \cdot q_{II} = F(t) \quad (7.37)$$

References

- Batchelor GK (2000) An introduction to fluid dynamics. Cambridge University Press, Cambridge
 Lagrange JL (1811) Mécanique analytique, nouvelle édition, orig. 1788 (Paris: Courcier)

Part II
Introduction to Earthquake Engineering

Chapter 8

Seismology and Earthquakes



Abstract The chapter provides a large overview on seismology. The earthquake genesis, waves propagation and attenuation relationships are discussed. From the engineering point of view, the characterization of an earthquake is a key point. Thus, a detailed description of the ground motion and seismological parameters is provided.

8.1 Basic Concepts of Seismology

8.1.1 Earthquake Genesis

8.1.1.1 Internal Structure of the Earth

The earth's structure is composed of five layers with different mechanical and physical characteristics. The outermost layer is called the crust and has a thickness of 25–40 km below the continents and of 5 km beneath the oceans. The earth's crust is composed of resistant material such as basaltic and granitic rock. Under the crust, the mantle layer is extended for 2850 km and can be divided into upper mantle and lower mantle. In this layer, high temperatures are achieved (2250 °C in average) and the materials have a viscous semi-molten behavior. Thus, the mantle's materials behave like a solid if they are subjected to impulsive stress and like a fluid when they are subjected to static stress. A further internal layer with 2260 km of thickness is called the outer core and it is at liquid state. The innermost layer is the inner core (solid core), which is dense and subjected to very high pressure at 2760 °C. Figure 8.1 illustrates the internal composition of the earth.

8.1.1.2 Plate Tectonics

In 1915 Wegener introduced the continental drift theory according to which the continents were places with respect to each other. Wegener believed that over

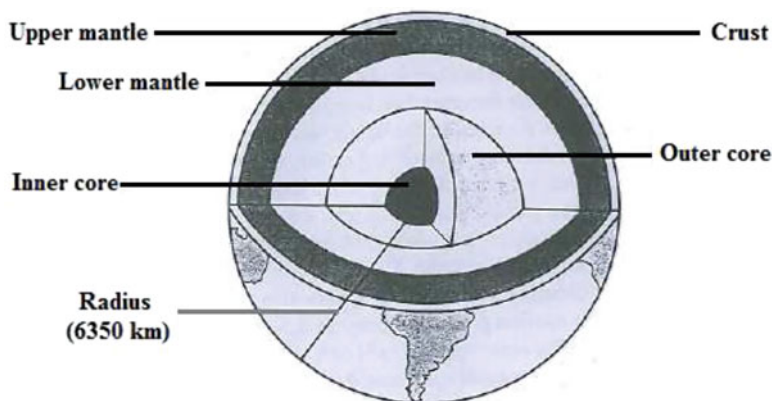


Fig. 8.1 Internal structure of the earth



Fig. 8.2 Pangea continent (Wegener's theory of continental drift)

200 million years ago the earth had only one large continent called Pangea (Fig. 8.2). This region broke into different pieces that slowly drifted until the current continental configuration.

The theory of continental drift was widely accepted after 1960 when the current seismographs and new techniques were used in order to investigate the ocean floor. These searches lead to evidence of historical movement of the continents according to the Wegener's theory that suggested images of massive continents pushing through the seas and across the ocean floor. From this scientific background, a modern theory of plate tectonics evolved, according to which the earth's surface is divided into a number of large and massive blocks called plates that are subjected to relative movements. Figure 8.3 shows the six major tectonic plates and the fourteen subcontinental plates.

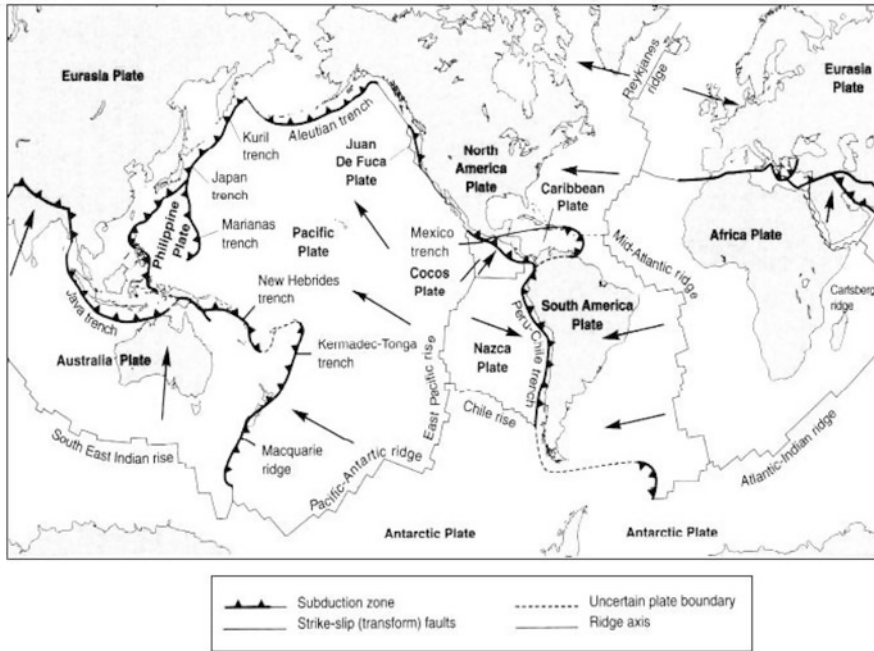


Fig. 8.3 Major tectonic plates (Fowler 1990)

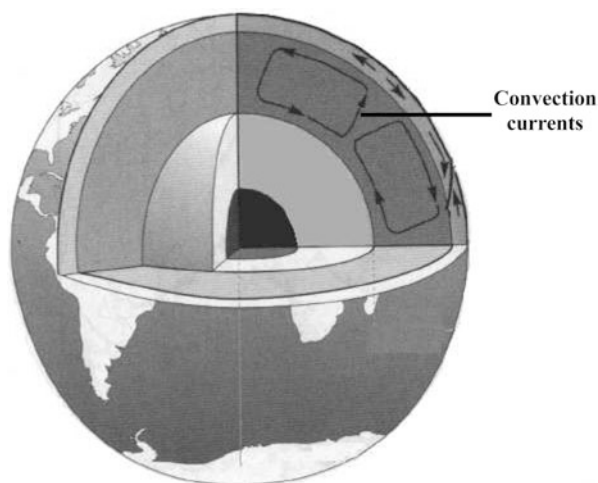
Smaller micro-plates are individuated near to the major plate boundaries. Since the tectonic plates move relatively to one another, the quite slow deformation between plates occurs only in narrow zones in proximity of their boundaries. The result of a rapid relative deformation (called seismic deformation) is the earthquake, while if it occurs slowly and continuously it is called aseismic deformation. The earthquake epicenter map representative of the worldwide seismicity confirms the hypothesis of tectonic deformation located close to its boundary (Fig. 8.4).

The cause of the movement can be found in a thermo-mechanical equilibrium of the earth's materials. In fact, the upper part of the mantle is in contact with the cooler portion of the crust while the lower portion is located near to the hot outer core. The temperature differences inside the mantle produce a variation of material's density that leads to an unstable situation in which the denser material sinks under the action of gravity, while the less dense material tends to rise up. This movement continuously occurs since the cooler material gradually becomes less dense and vice versa for the warmer materials. Thus, convection currents occur inside the mantle (Fig. 8.5) and they lead to the movement of the plate tectonics.



Fig. 8.4 Worldwide seismic activity (Bolt 1988)

Fig. 8.5 Convection currents in the mantle (Noson et al. 1988)



Since the masses of the movable block are extremely wide, the plate's movement produces a very large driving force. The nature of the earthquakes depends on the plate boundaries, which can be divided into three different types:

- *Spreading ridges*

When two adjacent plates move in opposite directions, the molten rock (magma) coming from the upper mantle rises to the surface becoming solid because of the temperature reduction. Thus, the accumulated solidified mantle material grows over the years and it shapes the spreading ridge. This type of

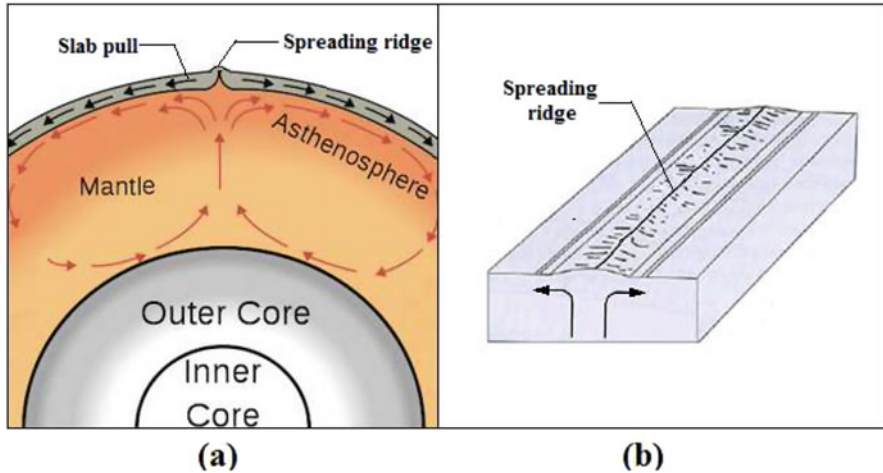


Fig. 8.6 Spreading ridge boundary in an earth's cross section (a) and in a 3D view (b)

boundary plate is located in the oceanic zone, where the crust is not very thick. Thus, usually these are called oceanic spreading ridge. Another phenomenon termed *ridge push* or *slab pull* contributes to the movement of plates. It is caused by the fact that the density of the oceanic crust is greater than the one of lower mantle, which is capable of creating a traction force downward. Figure 8.6 illustrates the spreading ridge with referring to slab pull phenomenon. The thin crust located in the vicinity of the spreading ridge is formed by the slow upward movement of magma or by means of the quick ejection of magma during the seismic activity.

- Subduction zones

According to the constancy of the earth's mass, the creation of new plate material at spreading ridges must be balanced by the consumption of plate material at other locations that are called subduction zones. In this part of the earth, one plate moves downward, under the other one. Since the oceanic crust is colder and denser than the continental one, generally it sinks under the continental crust (Fig. 8.7).

- Transform faults (strike-slip)

When the plates move each other without creating or consuming crust portion, the associated plate boundary is called a transform fault. The tangential movement along the transform fault is the main cause of earthquakes. Generally they are located orthogonally to two oceanic ridges and they are characterized by scarps or depressions (Fig. 8.8).

The arrows on Fig. 8.8 represent the movement direction along the transform fault (grey arrows) and along the ridge crests (black arrows). From these movements, it is possible to identify two crust zones that move between one

Fig. 8.7 Subduction zone between oceanic and continental crust

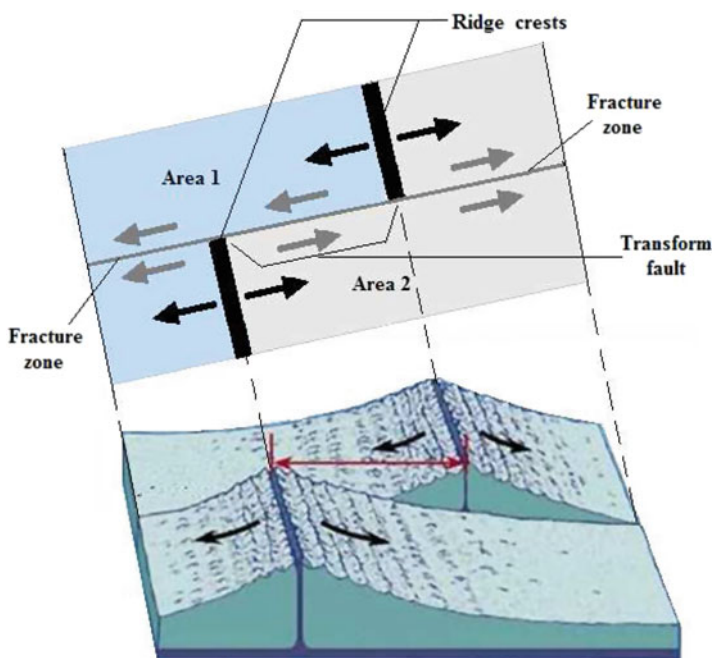
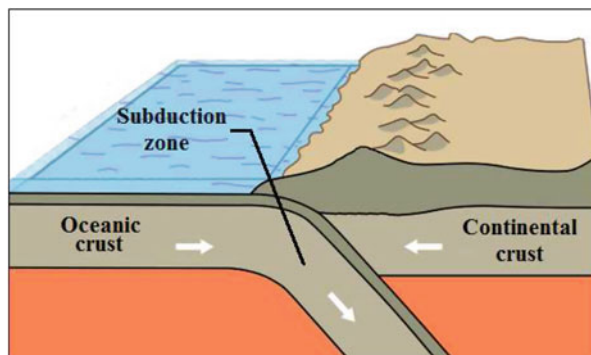


Fig. 8.8 Transform fault (strike-slip)

another (Area 1 and Area 2). The main example of a transform fault (strike-slip) is San Andreas fault that connects the East Pacific ridge (Mexico) with the Juan de Fuca ridge (Washington State).

8.1.1.3 Faults

In some regions, plate boundaries are not easily distinguishable since they are spread out with the edges of the plates broken to form micro-plates inside the main larger

plates. The local fractured portion of the crust is called the fault and along it is where movement occurs. The length of a fault varies from several meters to hundreds of kilometers and its depth can extend up to ten kilometers. In many cases, the fault rupture does not reach the earth's surface or is otherwise extended along a notable length on the surface. The presence of a depth or superficial fault does not mean that in that region an earthquake will occur. In other words, it is important to detect if a fault can be considered active or inactive. For this purpose, the most common criterion is the one proposed by Slemmons (1977), which determines an active fault by referencing the elapsed period of time since the most recent fault movement. According to this definition, some scientific authorities use different time periods ranging between 35,000 years and 100,000 years. The active faults confined within the earth's crust are generically called seismogenic faults. In addition, the fault generating movement near or on the topographic surface are called capable faults. A generic fault is described by means of *geometric* and *kinematic* parameters that will be discussed in Sect. 8.1.2.

8.1.1.4 Elastic Rebound Theory

As discussed in the previous paragraphs, in most cases the relative plate movements occur near the boundary zones. During the movement process, elastic strain energy is stored in the materials as shear stresses on the fault plane that separates the plates. When shear stress reaches the shear strength of the fault material, the accumulated strain energy is released, leading to the material failure, following the elastic rebound theory (Reid 1911). Of course, the mechanical characteristics of the rock materials affect the failure process. For ductile and weak rocks, only little strain energy is stored and when it is released slowly it causes aseismic movement. On the contrary, a sudden failure process is activated for strong and brittle materials (Fig. 8.9). In this case, part of the released energy is dissipated thermally, while the remaining part generates stress waves that are felt as earthquakes.

After the release of energy, a fault dislocation occurs since one portion moves relatively to the other. The three representative steps describing the elastic rebound theory are shown in Fig. 8.10.

Faults are not uniform and therefore both strong and weak zones can exist over the surface. In fact, the rupture surface manifests some irregular strong zones due to the asperity that influences the total contact area between the two surfaces of the faults. Obviously, if a surface has a wide presence of asperities, the shear stress is concentrated on a large area, but in the opposite case the shear stress is applied to a small amount of asperities (Fig. 8.11).

From Fig. 8.11a it is possible to notice how the shear stress is almost uniformly distributed since the asperity is widely located on the rupture surface. The asperity model was proposed by Kanamori (1977) to explain the earthquake genesis mechanism. According to this model, the release of energy is governed by the distribution of the asperities. The shear strength can be achieved only for one asperity or for a set of them, causing its failure and a redistribution of the stress on the weak zones. This

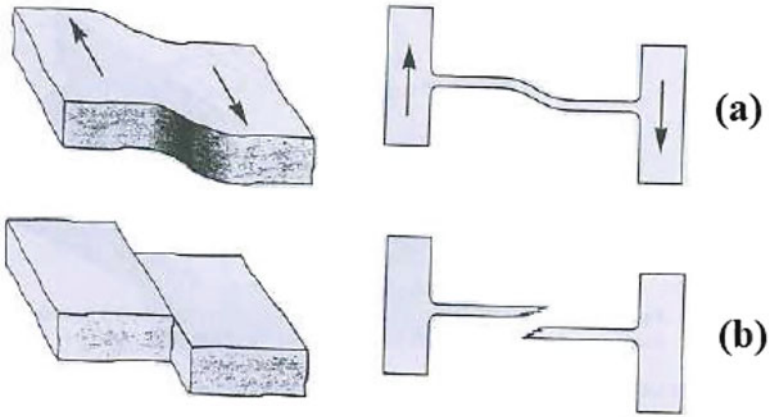


Fig. 8.9 Effects of energy release on ductile and weak material (a) and in strong and brittle material (b)

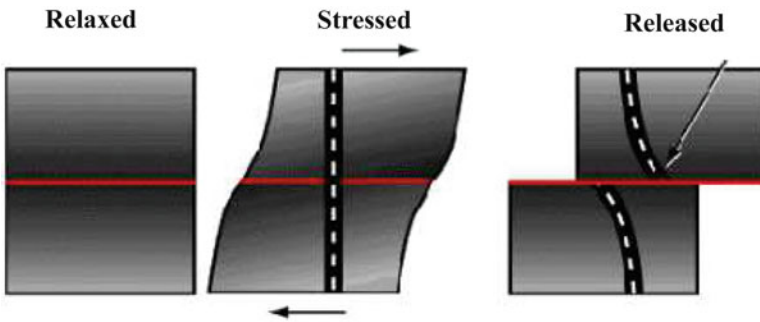


Fig. 8.10 Three steps described by elastic rebound theory

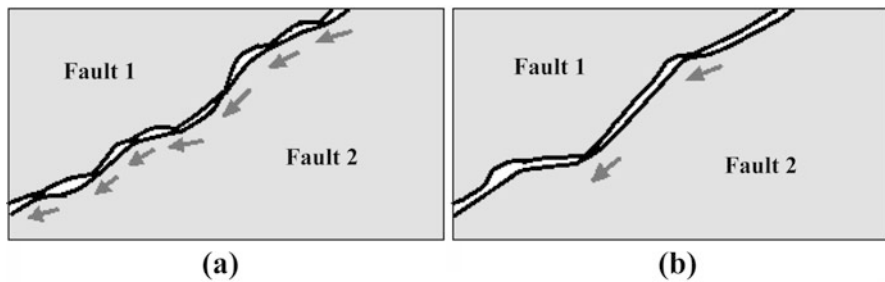


Fig. 8.11 Surface with diffused asperity (a) and with modest asperity (b)

process produces feeble wave propagation on the surface, called fore-shocks. When the shear strength is reached for the resistant part of the rupture surface, the sudden release of energy occurs in terms of main-shock. Another model complementary to the previous one was proposed by Aki (1984) (Barriers model) and it is based on the assumption of an inhomogeneous stress distribution along the fault surface. The failure phenomenon is governed by particular zones called barriers, in which stress intensification can occur. Thus, the fracture process starts from the weakest zones and propagates towards the barriers. When shear resistance is reached on the weak zones, the release of energy leads to the main shock. Progressively the stress on the fault surface adjusts to the new uniform distribution, causing the aftershocks.

8.1.1.5 Seismic Gap

According to the elastic rebound theory, the occurrence of an earthquake depends on the energy heap process. Thus, the probability of the occurrence of an earthquake on a particular fault segment is related to the elapsed period, since the last earthquake has occurred. In addition, the released energy is another important parameter in the prediction of the earthquake occurrence. By considering the fault movement and the historical earthquakes along a fault, it is possible to estimate gaps in seismic activity for the analyzed fault segment. It is also possible not having a gap for a zone in which wide earthquakes have occurred, because the considered segment fault has been affected by an aseismic motion.

8.1.2 Seismological Parameters

A seismic event is described by means of three acceleration history components (NS, WE and UD) which define the accelerations trend in the time domain for a seismic station. The acceleration history on the earth's surface is recorded by a seismograph. It is composed by a simple pendulum joined with a recording system (Fig. 8.12).

When a seismic event occurs, the associated wave causes the movement of the support system. The different stiffness and mass characteristics between pendulum and support causes a relative motion (ground motion) recorded on the rotating drum by means of a little pen installed on the pendulum. Figure 8.13 illustrates a generic ground motion record on a seismic station. The figure shows the different waves contributions to the motion (P-waves, S-waves and surface waves). The wave characteristics will be discussed in detail in Sect. 8.1.3.

From this figure, it can be observed that the first part of the acceleration time history is caused by the P-waves. After a time interval, the S-waves and surface waves occur. This aspect is related to the different velocity values of accelerations

Fig. 8.12 Simple scheme of pendulum seismograph

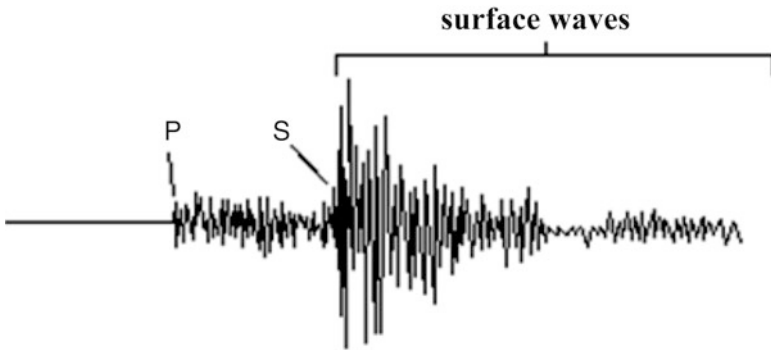
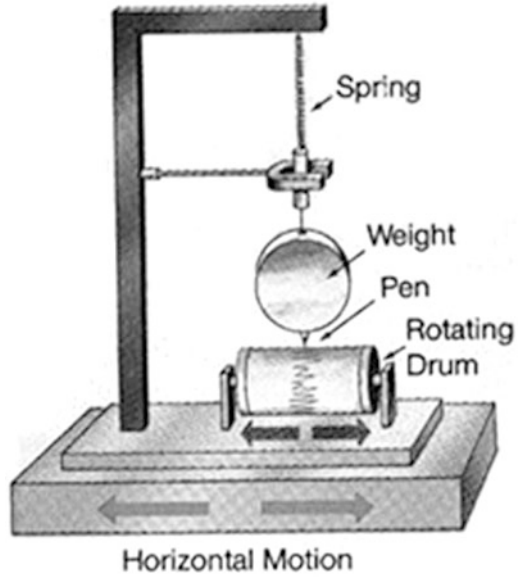


Fig. 8.13 Typical seismic accelerations record

(Eq. 8.1), while the delay between arrival of S-waves (ΔT_{ps}) depends on the distance between the seismic station and the hypocenter.

$$V_P > V_S > V_R \tag{8.1}$$

where V_P , V_S and V_R represent the velocity of P-waves, S-waves and Rayleigh waves, respectively. The time interval ΔT_{PS} can be used to estimate the epicentral distance (R_{epi}) with respect to the seismic station (Eq. 8.2).

$$R_{epi} = \frac{V_P V_S}{V_P - V_S} \Delta T_{PS} \tag{8.2}$$

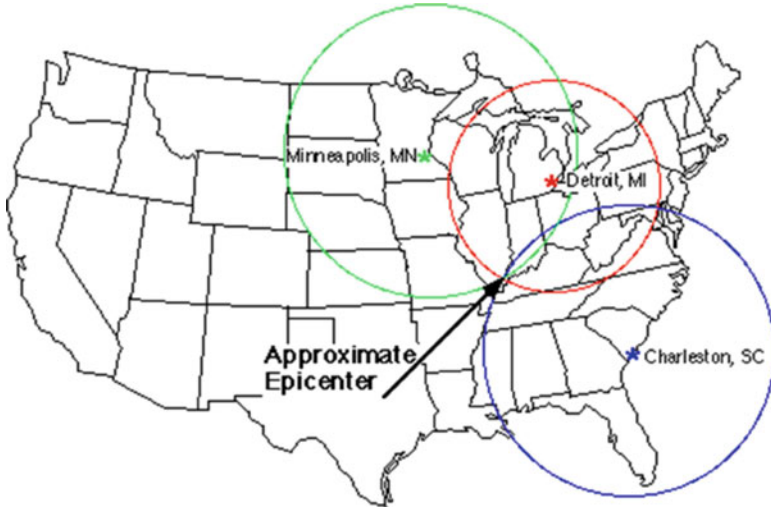


Fig. 8.14 Example of evaluation of approximated epicenter

The localization of the epicenter allows the evaluation of the epicentral distance for three different seismic stations and defines the intersection among the three respective circles with radius equal to its own value of distance (Fig. 8.14).

The acceleration time histories give local information on the earthquake, but they cannot characterize the seismic source. One of the most important parameters describing a seismic event is its intensity. It can be based on the seismic effects (qualitative approach) or on the instrumental measures (quantitative approach). In the first case, the seismic intensity is deduced by referring to the building damages, loss of human life, geomorphological variations and so on. One of the most used macro-seismic scales was proposed by Mercalli, Cancani, and Sieberg in 1930. It is based on the definition of 12 intensity degrees describing a typical recorded effect (Fig. 8.15).

However, this scale is not objective and cannot be used as a source parameter. A quantitative approach is preferred for defining the earthquake scenario. Taking into account the geometric and energetic characteristics of the earthquake source, it is possible to define the seismic intensity by means of a parameter called *magnitude* (M). In 1930 Richter et al. (1990) proposed a parameter called *local magnitude* (M_L) based on the instrumental measures on the ground surface. Analytically, the local magnitude is defined as the logarithmic difference between a reference amplitude (A_0) and a measured peak amplitude (A) for a specific distance (Eq. 8.3).

$$M_L = \log(A) - \log(A_0) \quad (8.3)$$

The term (A_0) represents the maximum amplitude for a Wood-Anderson seismograph 100 km far from the epicenter. Moreover, the moment magnitude (M_W) is

Fig. 8.15
Mercalli-Cancani-Sieberg
scale

I	Detected only by sensitive instruments
II	Felt by few persons at rest, especially on upper floors; delicately suspended objects may swing
III	Felt noticeably indoors, but not always recognized as earthquake; standing autos rock slightly, vibration like passing truck
IV	Felt indoors by many, outdoors by few, at night some may awaken; dishes, windows, doors disturbed; autos rock noticeably
V	Felt by most people; some breakage of dishes, windows, and plaster; disturbance of tall objects
VI	Felt by all, many frightened and run outdoors; falling plaster and chimneys, damage small
VII	Everybody runs outdoors; damage to buildings varies depending on quality of construction; noticed by drivers of autos
VIII	Panel walls thrown out of frames; fall of walls, monuments, chimneys; sand and mud ejected; drivers of autos disturbed
IX	Buildings shifted off foundations, cracked, thrown out of plumb; ground cracked; underground pipes broken
X	Most masonry and frame structures destroyed; ground cracked, rails bent, landslides
XI	Few structures remain standing; bridges destroyed, fissures in ground, pipes broken, landslides, rails bent
XII	Damage total; waves seen on ground surface, lines of sight and level distorted, objects thrown up in air

used to describe the energy release during the seismic event by means of the seismic moment (M_0) and is expressed in Eq. 8.4

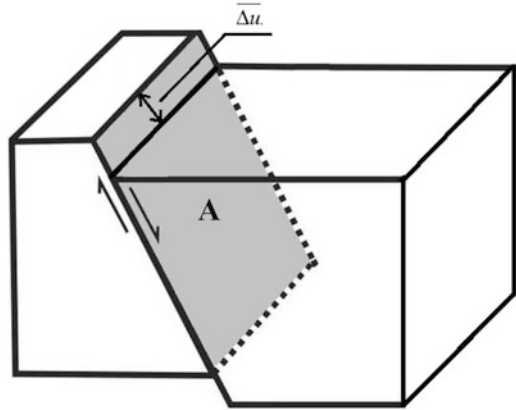
$$M_W = \frac{2}{3} \log(M_0) - \text{cost.} \quad (8.4)$$

where *cost.* is a constant equal to 6 for moment magnitude expressed in $N \cdot m$ or 10.7 for moment magnitude expressed in $\text{dyne} \cdot \text{cm}$. The energy release in the event is defined by means of M_0 and is proportional to the crustal characteristics for the rupture plane as shown in the Eq. 8.5.

$$M_0 = G \bar{\Delta} u A \quad (8.5)$$

where G is the shear modulus of the crustal material, A represents the rupture area and $\bar{\Delta} u$ is the mean value of the coseismic sliding along the rupture plane (Fig. 8.16).

Fig. 8.16 Area of the rupture plane (A) and coseismic sliding ($\overline{\Delta u}$) in a normal-fault



Two other magnitude scales are used to provide information about the body wave magnitude (M_b) and the surface wave magnitude (M_S). The expression of the aforementioned parameters (Eqs. 8.6 and 8.7) are reported and discussed below

$$M_b = \log\left(\frac{A}{T_b}\right) + \text{corr}(D, h) \quad (8.6)$$

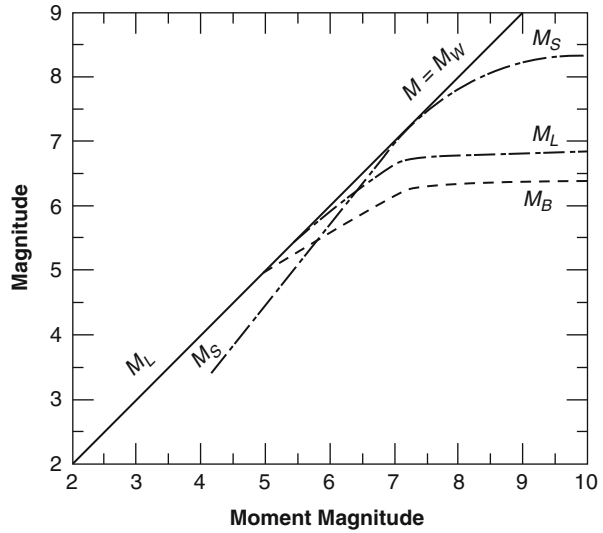
$$M_S = \log\left(\frac{A}{T_S}\right) + \text{corr}(D, h) \quad (8.7)$$

where A represents the amplitude of the ground motion and T_b and T_S are the period of the body-wave and of the surface-wave, respectively. It can be observed that the first term of the two equations is proportional to the energy of an oscillator by means of the ratio between amplitude and period. The term indicated with $\text{corr}(D, h)$ is a correction to be applied in order to take into account the waves attenuation phenomena proportionally to the fault depth (h) and to the distance (D) between station and epicenter. In Fig. 8.17 the comparisons between the above discussed types of magnitude scales and the moment magnitude are reported to emphasize the differences in the range of high values of magnitude. In fact, it is possible to observe that the moment magnitude is the unique parameter that does not suffer from saturation, while the other ones reach the saturation for values of magnitude greater than 5–6. This problem is due to the incapability of the seismographs to record the long period fluctuations generated by the earthquakes with high energy.

The release energy during a seismic event is one of the interesting parameters to be estimated. It considers a generic particle subjected to a harmonic excitation with amplitude A and period T . For a particle with distance d from the source of the excitation, its total energy (E) can be written as in the Eq. 8.8.

$$\log(E) = \log(F(d, \rho, V)) + \log\left(\frac{A}{T}\right) \quad (8.8)$$

Fig. 8.17 Comparisons between moment magnitude (M_W) and the other scale magnitude



where the function $F(d, \rho, V)$ depends on the distance (d), the density of the perturbed element (ρ) and on the propagation velocity (V). Since the amplitude A is strongly dependent on the seismic intensity, a correlation between energy and magnitude of the seismic event has been observed experimentally. Gutenberg and Richter proposed an empirical relationship between magnitude M_S and energy E (Eq. 8.9).

$$\log(E) = 11.8 + 1.5M_d \quad (8.9)$$

This relationship suggests that for a unitary magnitude, there is a corresponding release of energy equal to 30. Thus, the seismic energy increases exponentially with the magnitude. Furthermore, Gutenberg and Richter also provided a relationship between the magnitude of a seismic event and its frequency of occurrence λ (Eq. 8.10).

$$\log(\lambda) = a - bM \quad (8.10)$$

where the parameters a and b have to be calibrated for the available seismic data of the region of interest. The term λ defines the number of events with magnitude greater than M for a given time interval. The complete characterization of the expected effects in a surface site depends on the intensity and geometric parameters expressed in terms of distances. For this reason, several distance parameters can be considered and they are illustrated in Fig. 8.18 in the case of normal-fault.

where R_{jb} is the horizontal distance on the surface projection of the rupture plane (Joyner-Boore distance or fault-distance), R_{epi} defines the epicentral distance and

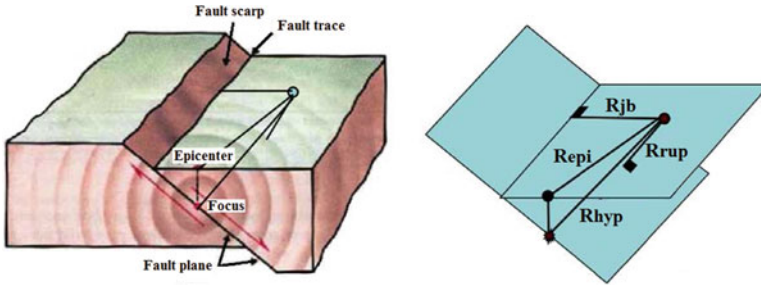


Fig. 8.18 Distance parameters

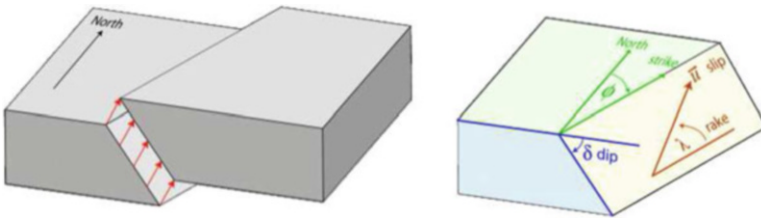


Fig. 8.19 Fault-plane parameters (Courtesy of the INGV 2013)

R_{hyp} represents the hypocentral distance. The R_{rup} distance parameter is the closest distance to the rupture plane and it describes the radiation of seismic waves better than the other ones. According to the theory of the elastic rebound, earthquake generation is due to a sudden release of the elastic energy through a sliding surface called *fault*. The geometric parameters that describe the fault are the orientation (strike) and the slope (dip) of the fault-plane and the direction of the sliding through the fault (slip) and they define the focal mechanism, also called fault-plane solution (Fig. 8.19).

The type of movement occurring on a fault is determined by the direction of the strike and dip. Even if the bidirectional movement occurs, one component of it is always predominant. For this reason, the fault movements are divided into:

- *Dip slip movement*

The primary movement occurs in the direction of the dip. This type of movement is further divided by a function of the direction of the movement and dip angle. Usually this classification is led by referring to the relative movement between the hanging wall and foot wall (Fig. 8.20).

The first one is the rock portion above the fault plane, while the second one represents the rock part located under the fault plane. A *Normal fault* is detected when the foot wall moves over the hanging wall and a tensile stress is generated in the crust. On the contrary, when the foot wall moves under the hanging wall a

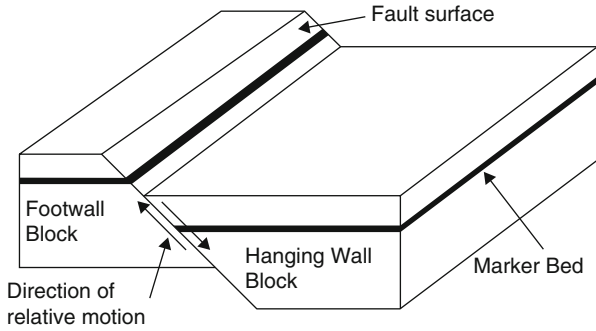


Fig. 8.20 Fault terminology

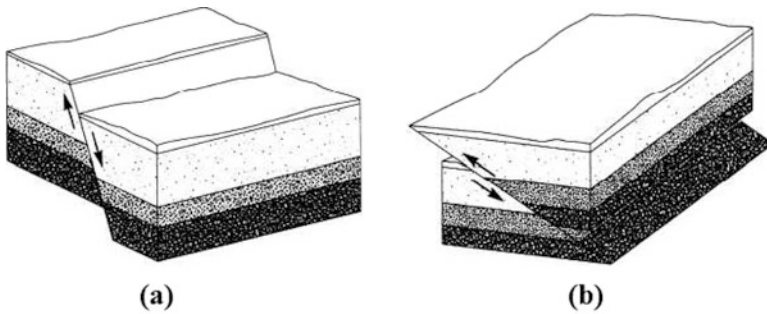
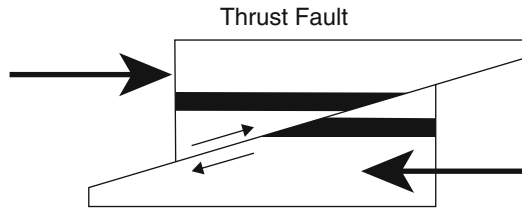


Fig. 8.21 Normal fault (a) and reverse fault (b)

Fig. 8.22 Thrust Fault (dip angle less than 30°)



reverse fault is identified. If the fault plane has a small dip angle, a special type of reverse fault is identified with the name of *thrust fault*. Figure 8.21 illustrates an example of normal and reverse fault.

- *Strike slip movement*

The movement occurs parallel to the strike and the associated *strike-slip* fault plane is usually close to being vertical (Fig. 8.23). Depending on the relative direction of movement, it is possible to have a *right lateral* and *left strike-slip fault*. The individuation of the movement direction is led by observing the other side displacement direction of the fault (Fig. 8.23).

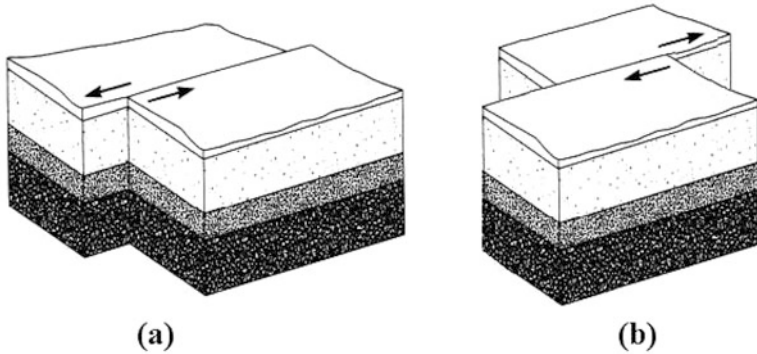


Fig. 8.23 Left lateral (a) and right lateral strike-slip (b)

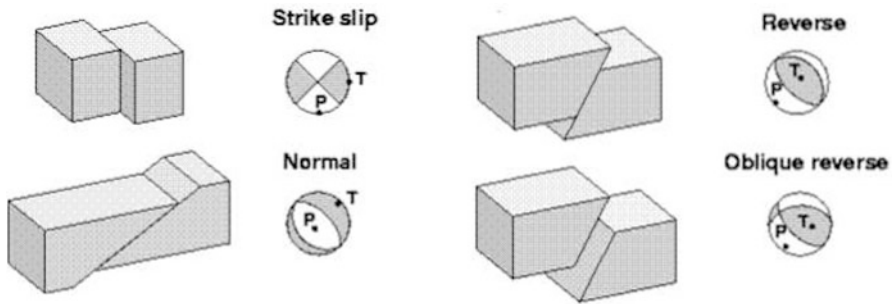


Fig. 8.24 Focal mechanism and related fault types (USGS 2008)

In addition, *oblique fault* movement occurs when it is characterized by both dip-slip and strike-slip components.

Furthermore, the focal mechanisms are represented by means of white and grey geographic oriented spheres (“beach balls”) containing the hypocenter, in which the fault plane and the auxiliary plane (orthogonal to the fault plane) are used in order to define the compressed (white zones) and tied zones (grey zones). The focal mechanism is provided to understand the fault movement which is often used in the attenuation models as the source-site parameter. For this reason, four different fault mechanisms can be identified: strike slip (left-lateral or right-lateral), normal, reverse and oblique reverse (Fig. 8.24).

8.1.3 Waves Propagation

The motion on the earth’s surface due to sudden release of energy from the seismic source is controlled by the elastic wave propagation in the soil. This type of physical

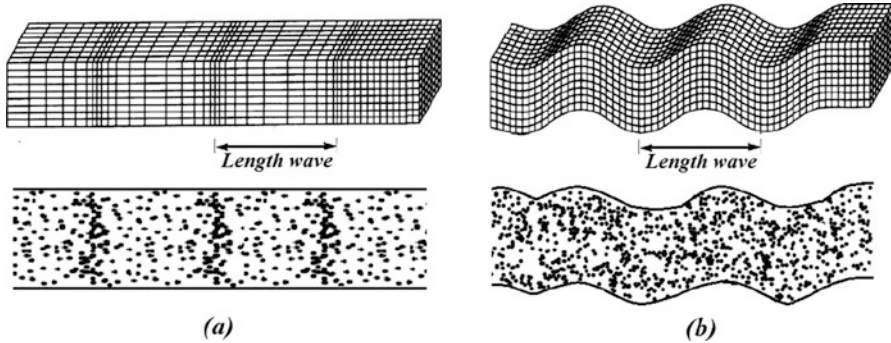


Fig. 8.25 P-waves (a) and S-waves (b) in an elastic 1D element (Bolt 1988)

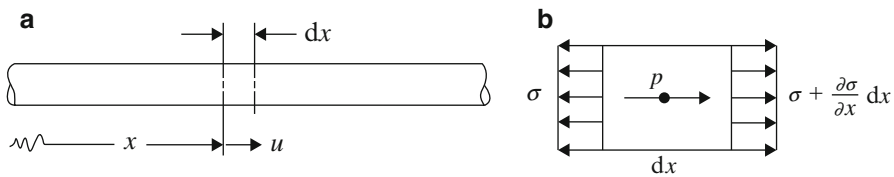


Fig. 8.26 Mono-dimensional elastic body (a) and stress state for dx length element (b)

mechanism is such that only the energy is transferred by the waves through the elastic body (mass or volume waves). The waves are divided into two types:

- *P-waves (compression waves)*
- *S-waves (distortion waves)*

The wave propagation causes the particle oscillation in the same direction through compression and expansion steps. The *P-waves* lead to volume variation but not shape modification of the elastic body. For the *S-waves* the fluctuation of the body's particles occurs perpendicularly to the wave direction. In this case the volume of the body became constant but the shape change (distortion) (Fig. 8.25).

The wave length is one of the characteristics of the propagation in the time domain and it defines the distance between two deformed zones next to each other. D'Alembert was the first scientist who studied the problem of the elastic wave propagation in a mono-dimensional body. In reference to a generic P-waves propagation, Equation describes the equilibrium, kinematic compatibility and elastic relationship for the bar shown in Fig. 8.26.

$$\begin{cases} \frac{d\sigma}{dx} + p = \rho \frac{\partial^2 u}{\partial t^2} \\ \epsilon = \frac{du}{dx} \\ \sigma = E\epsilon \end{cases} \quad (8.11)$$

where ρ is the density of the element and q is its weight expressed in reference to the unitary length. Neglecting the own weight of the element, setting the ratio $\sqrt{\frac{E}{\rho}}$ and considering the Eq. 8.11, the following equation of motion can be obtained (Eq. 8.12)

$$\frac{\partial^2 u}{\partial x^2} = \frac{1}{V^2} \frac{\partial^2 u}{\partial t^2} \quad (8.12)$$

where the term V represents the propagation wave velocity, and u is the displacement of the material point of the elastic element. V defines the velocity of the perturbation, while $\frac{\partial u}{\partial t}$ is the velocity of the actual particle of the body. The equation of motion obtained can be particularized for P-waves or S-waves by fixing the corrected quantity and boundary conditions. In Eq. 8.13 the expressions of the wave propagation velocities are reported for three significant theoretical cases.

$$\begin{cases} V_P = \sqrt{\frac{E}{\rho}} \\ V_S = \sqrt{\frac{G}{\rho}} \\ V_{P,c} = \sqrt{\frac{M}{\rho}} \end{cases} \quad (8.13)$$

V_P and V_S refer to the propagation of P-waves and S-waves, respectively. The $V_{P,c}$ term represents the perturbation velocity for P-waves in the case of lateral constraints applied in the bar. In the last case, the elastic coefficient M can be defined as in Eq. 8.14.

$$M = \frac{1 - \nu}{(1 + \nu)(1 - 2\nu)} \quad (8.14)$$

The volume waves propagation occurs in the different soil layers of the earth's crust and are controlled by the geometric optics laws. The different stiffness characteristics of two adjacent soil layers leads to refraction and reflection of the waves. Since the stiffness of the soil is increasing with the depth, in the real cases the local direction of propagation (seismic ray) is represented by a curve having its tangent vertical for the soil surface (vertical seismic rays) as shown in Fig. 8.27.

This phenomenon leads to the direction of attention only to S-waves on the surface, since they produce the horizontal shaking on the structures. The earth's surface can be seen as an irregularity in the wave propagation. When the elastic waves achieve the surface they are transformed into surface waves. The two main types of surface waves are:

- Rayleigh waves
- Love waves

Fig. 8.27 Vertical seismic rays on the surface

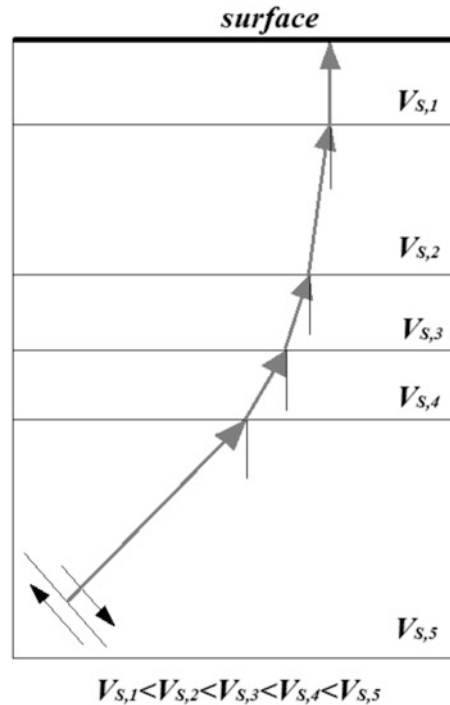
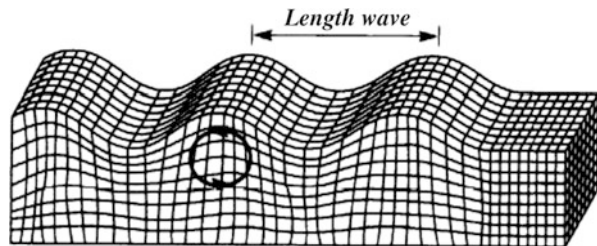


Fig. 8.28 Rayleigh waves (Bolt 1988)



In the first case, the particle oscillation occurs in a vertical plane containing the direction of propagation. Each particle of the elastic element is subjected to an elliptical motion as shown in the Fig. 8.28.

For the Love wave the oscillation of the particles occurs in the plane parallel to the surface plane (Fig. 8.29). The perturbation velocity depends on the frequency of excitation, but its value can be assumed equal to 90% of the S-waves velocity.

One of the most interesting phenomena of wave propagation is represented by the *geometric attenuation* of motion with the distance due to the energy dispersion in the space. Naturally, this aspect is inversely proportional to the distance between the seismic source and the local surface point. Furthermore, the attenuation phenomenon is also related to the shape of the wavefront which defines the envelope of the perturbed points at the same time. This characteristic depends on the waves

Fig. 8.29 Love waves (Bolt 1988)

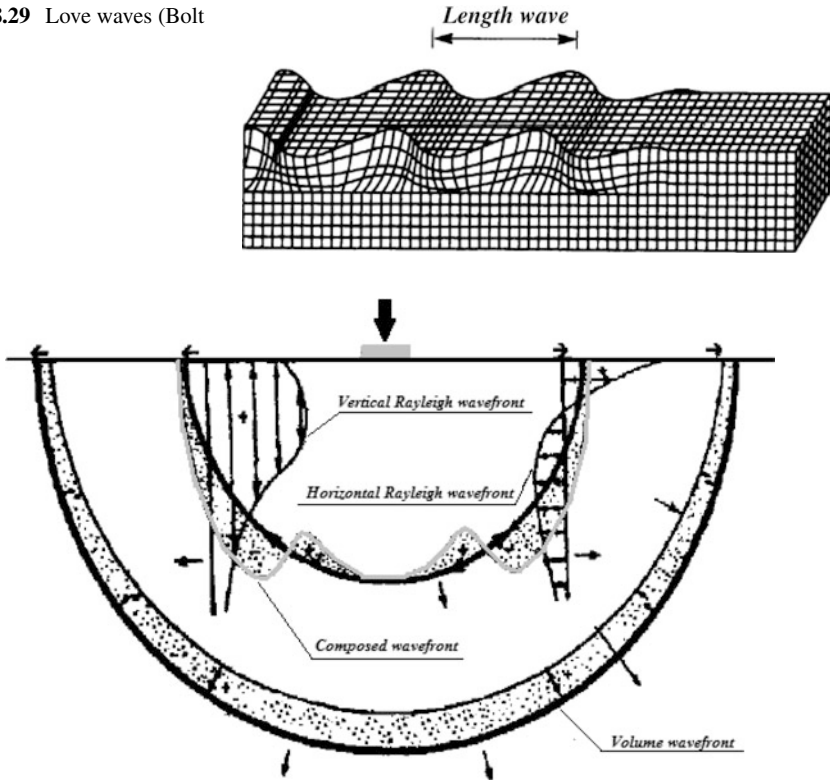


Fig. 8.30 Wavefronts for Rayleigh waves and volume waves generated by the impulsive load on surface (Woods 1968)

type. For this reason, Fig. 8.30 illustrates the typical wavefront of *volume waves* and *Rayleigh waves* induced by an impulse applied on the soil surface.

The wavefront of the Rayleigh waves is described by a cylinder shape, while a spherical shape is observed for wavefront volume. Thus, considering r as distance between the source of the perturbation and the generic point, the geometric attenuation proportional factor is given by the ratio $\frac{1}{r^n}$. As observed about the wavefront shape, the exponent n is equal to $\frac{1}{2}$ for Rayleigh waves and is equal to 1 for volume waves. Furthermore, it was observed that the transported energy of the Rayleigh waves is about 67% of the total energy, while the remaining part is associated with volume waves (26% for S-waves and 7% for P-waves). The inelastic behavior of the soil causes dissipation with consequentially further attenuation of the motion on the surface (*intrinsic attenuation*). In the practical soil dynamic applications, the soil behavior is approximated by means of a viscous-elastic model in which the original elastic characteristics are modified in the complex associated parameters. Since the ground motion due to earthquakes can be described by an

exponential equation, the generic dynamic displacement on the surface can be expressed as in Eq. 8.15.

$$u(x, t) = u_0 \cdot e^{\alpha_s x} \cdot e^{-i\omega(\frac{x}{V_s} - t)} \quad (8.15)$$

where the first exponential term indicates the intrinsic attenuation by means of the α_s term (Eq. 8.16) which is related to the soil thickness and the rupture depth (R_{rup}). Both exponential parameters are inversely proportional to the distance x , so that these contributions give information about the geometric attenuation.

$$\alpha_s = \frac{\omega D}{V_s} \quad (8.16)$$

where D measures the soil viscous damping. For shallow earthquakes, the attenuation phenomenon is predominant with respect to the attenuation due to the energy dissipation in the perturbed soil.

8.1.4 Attenuation Relationship

One of the goals of seismology is to predict the ground motion in a specific site at a given epicentral distance (R_{epi}) for a given earthquake. At this purpose, different mathematical attenuation laws are proposed to estimate a specific ground motion parameter, considering a wide set of seismic events characterizing the seismic zone. The attenuation relationships define the exceedance probability for a given ground motion parameter (Y) with respect to a parameter y^* for a given magnitude (M) and distance (R) (Eq. 8.17)

$$P[Y > y^* | M, R] = 1 - F_Y(y^*) \quad (8.17)$$

Figure 8.31 illustrates a generic attenuation curve for the parameter Y with the related probability distribution.

Many attenuation models have been proposed to predict the value of the considered ground motion parameter and each of them is calibrated with respect to a specific geographic zone. However, modern GMPE mainly uses the moment magnitude (M_W) and the closest distance to the rupture plane (R_{RUP}) as magnitude and distance parameter in equation.

The main GMPEs will be discussed next. A common engineering application of the GMPE focuses on the spectral acceleration prediction at different periods. For this purpose, many attenuation models have been developed such as Ambraseys et al. (1996) GMPE which is valid for European sites.

$$\log S_a(T_i) = C_1' + C_2 M + C_4 \log R + C_A S_A + C_S S_S \quad (8.18)$$

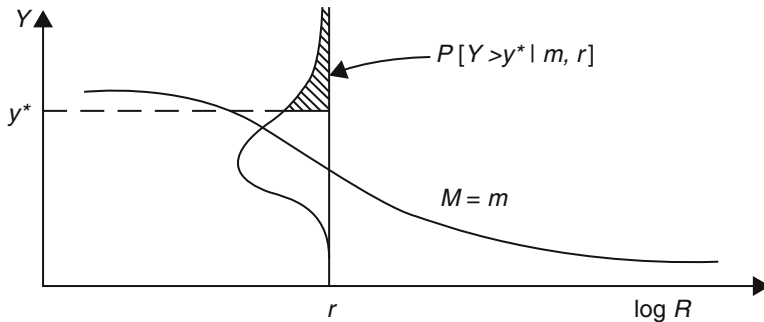


Fig. 8.31 Attenuation curve for Y parameter

where C_1' , C_2 , C_4 , C_A and C_S are the site-dependent coefficients, determined using 416 records in Europe and adjacent regions, while M and R are the magnitude and fault distance, respectively. The parameters S_A and S_S refer to the site conditions (stiff or soft soil). The equation is recommended for a magnitude range between 4.0 and 7.5 and for source distances of up to 200 km (Ambraseys et al. 1996). The output are the spectral ordinates ($S_a(T_i)$), damped at 5%, in a period range of 0.1–2 s. The Campbell and Bozorgnia (2008) and Boore and Atkinson (2008) GMPEs (Eqs. 8.19 and 8.20) have been derived by empirical regression of part of PEER database and they define the spectral ordinates with 5% of damping for periods from 0.01 to 10 s.

$$\ln(S_a(T_i)) = F_M(M) + F_D(R_{JB}, M) + F_S(V_{S30}, R_{JB}, M) \tag{8.19}$$

The attenuation relationship of Boore-Atkinson is obtained as the sum of three contributions: F_M is the magnitude scaling, F_D represents the distance function and F_S is the site amplification coefficient. The main input parameters are the Joiner-Boore distance (R_{JB}), the moment magnitude (M) and the average shear wave velocity in a depth of 30 m (V_{S30}). The site amplification term is obtained by summing a linear contribution (F_{LIN}) and a nonlinear contribution (F_{NL}). The Boore-Atkinson attenuation model is applicable for a magnitude range 5–8 and Joyner-Boore distance less than 200 km.

$$\ln S_a(T_i) = (f_{mag} + f_{dis} + f_{ftt} + f_{hng} + f_{site} + f_{sed}) + \ln(S_a(T_i)_{Comp/GM}) \tag{8.20}$$

The last term of the Campbell and Bozorgnia predictive equation is the adjustment to the median model represented by the sum of the six terms: magnitude term (f_{mag}), distance term (f_{dis}), style of faulting term (f_{ftt}), hanging wall term (f_{hng}), shallow site response term (f_{site}) and deep site response term (f_{sed}). This model can be applied for a magnitude greater than 4 and less than 8 and for a distance ranging from 0 to 200 km. In addition, the Campbell-Bozorgnia model can be assumed valid for western United States sites and in other similarly tectonically active regions. For



each GMPE discussed, the total aleatory standard deviation is defined as the sum of two terms (Eq. 8.21).

$$\sigma_{\tau} = \sqrt{\sigma^2 + \tau^2} \quad (8.21)$$

where the σ^2 term represents the *intra-event variance* and τ^2 parameter is the *inter-event variance*. The intra-event component describes the dispersion degree for a single ground motion, instead the dispersion between an event and the mean of all the events is called inter-event term.

8.2 Ground Motion Parameters

The ground motion parameters describe the motion on the ground, so they assumed a certain importance in the engineering applications. Since these parameters characterize the motion trend, they are also called waveform parameters. They can be divided into three different categories based on the given information:

1. peak parameters;
2. frequency content and energetic parameters;
3. time parameters.

It is important to define each of them to obtain a complete characterization of the ground motion.

8.2.1 Peak Parameters

The peak parameters refer to the maximum values of the ground motion time history. The most common peak value is the Peak Ground Acceleration (PGA), which identifies the maximum value of the recorded acceleration time history. From this peak value, the Peak Ground Velocity (PGV) and the Peak Ground Displacement (PGD) can be obtained by a single and a double integration of the acceleration in the time domain, respectively. Figure 8.32 illustrates the three aforementioned parameters for a record of Northridge earthquake (1/17/1994).

8.2.2 Frequency and Energetic Content

8.2.2.1 Theoretical Background

Every ground motion recorded is represented as an irregular acceleration history in the time domain. Anyway, it is possible to decompose any periodic function into

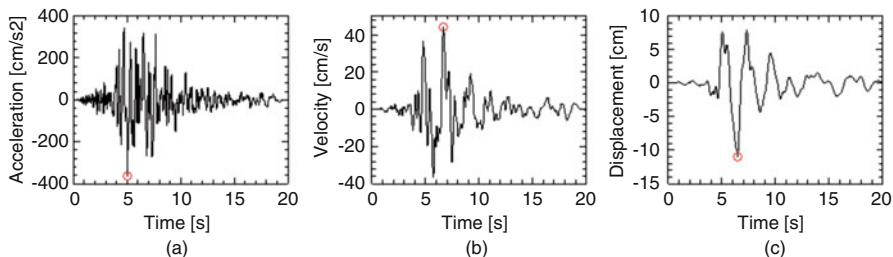


Fig. 8.32 PGA (a) PGV (b) and PGD (c) for the Northridge earthquake (1/17/94, 12:31, Canyon Country – W Lost Canyon)

a linear combination of infinite harmonic functions with given frequency (f) and phase (φ). This approach was proposed by Fourier in early nineteenth century and it provides the generic time contribution of the periodic function as shown in the Eq. 8.22

$$F(t) = \frac{1}{2}a_0 + \sum_{n=1}^{\infty} c_n \sin(\omega_n t + \phi_n) \quad (8.22)$$

where a_0 is the constant of the series (Eq. 8.23), while c_n represents the amplitude associated to the harmonic part of the previous expression.

$$a_0 = \frac{1}{T_i} + \int_0^{T_i} F(t) dt \quad (8.23)$$

where T_i indicates the characteristic period of the function $F(t)$. Introducing the following expressions reported in the Eq. 8.24, the Fourier series can be rewritten as indicated in the Eq. 8.25.

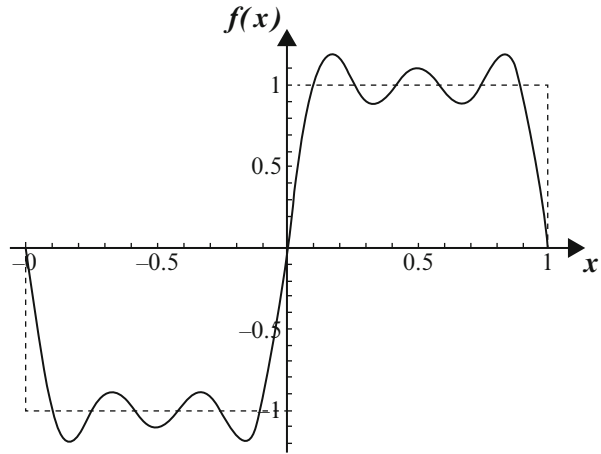
$$\begin{cases} c_n = \sqrt{a_n^2 + b_n^2} \\ \phi_n = \arctan\left(\frac{a_n}{b_n}\right) \end{cases} \quad (8.24)$$

$$F(t) = \frac{1}{2}a_0 + \sum_{n=1}^{\infty} a_n \cos\left(\frac{2 \cdot \pi \cdot n}{T_i} \cdot t\right) + b_n \sin\left(\frac{2 \cdot \pi \cdot n}{T_i} \cdot t\right) \quad (8.25)$$

Instead Eq. 8.26 defines the values of the coefficients a and b .

$$\begin{cases} a_n = \frac{2}{T_i} \int_0^{T_i} F(t) \cdot \cos\left(\frac{2 \cdot \pi \cdot n}{T_i} \cdot t \cdot dt\right) \\ b_n = \frac{2}{T_i} \int_0^{T_i} F(t) \cdot \sin\left(\frac{2 \cdot \pi \cdot n}{T_i} \cdot t \cdot dt\right) \end{cases} \quad (8.26)$$

Fig. 8.33 Example of Fourier-series for $n = 4$



Let's consider the case of square wave with absolute value of amplitude equal to 1 (Fig. 8.33). Only four harmonic contributions will be considered ($n = 4$).

The approximation of the method improves as the number of selected harmonic functions increases. It has been shown that, for a unique representation of the signal in the frequency domain, both amplitude and phase information should be provided for each frequency component. The first one give information about the energy contribution, while the second part represents the shift of the regular function in the time. The representation of the periodic functions in the frequency domain is very useful for many engineering applications. For this purpose, the Fourier transform is used to obtain the periodic function in terms of amplitude (A) or phase (φ) with referring to the frequency contributions. Equation 8.27 shows the mathematical expression of the Fourier transform, while the Fig. 8.34 illustrates the general scheme used to switch from the periodic function in the time domain to the frequency domain.

$$F(\omega) = \int_{-\infty}^{\infty} F(t) \cdot e^{-i\omega t} dt \quad (8.27)$$

In order to use Eq. 8.27 with sampled digital data, it is necessary to convert the Fourier transform in discrete form. The Fast Fourier Transform (FFT) is the most efficient algorithm used in the engineering applications that can be applied for a periodic function sampled in N points at fixed time range Δt (Eq. 8.28).

$$F(k\omega) = \Delta t \sum_{n=0}^{N-1} F(n\Delta t) \cdot e^{-ik\omega \Delta t} \quad (8.28)$$

As for the Fourier transform, the second half of the results obtained with the FFT are symmetrically equal to the first half one. One immediate advantage of the

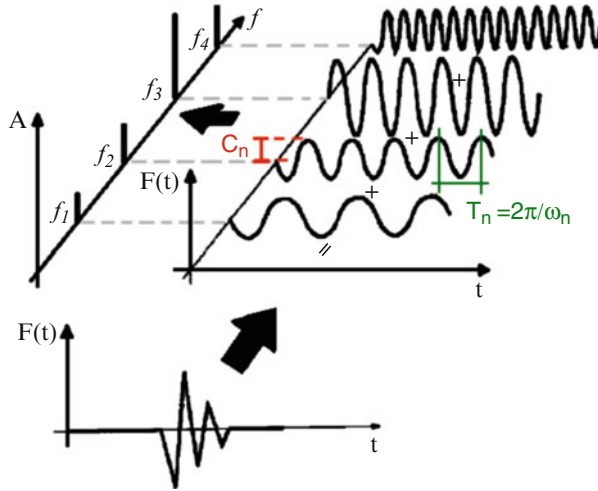


Fig. 8.34 From time domain to frequency domain

Fourier transform is that complex differential operations in the time domain are converted into simpler algebraic operations in the frequency domain. This permits the reduction of the computational load. Similarly, the inverse operation applied by the Fourier transform makes it very easy to return to the time domain, starting from the frequency domain. The mathematical instrument allowing the operation just discussed is called the Inverse Fourier Transform. Equations 8.29 and 8.30 illustrate the inverse Fourier transform in the continuum and in the discrete domain, respectively.

$$F(t) = \int_{-\infty}^{+\infty} F(\omega) \cdot e^{i2\pi\omega t} d\omega \tag{8.29}$$

$$F(kt) = \Delta\omega \sum_{n=0}^{N-1} F(n\Delta\omega) \cdot e^{ik\Delta\omega\Delta t} \tag{8.30}$$

The following Table 8.1 summarizes the main Fourier transform properties.

Table 8.1 Main Fourier transform properties

Symmetry	$ F(-\omega) = F^*(\omega) $
Linearity	$k_1F_1(t) + k_2F_2(t) \leftrightarrow k_1F_1(\omega) + k_2F_2(\omega)$
Scaling	$Z(t) = F(kt) \leftrightarrow Z(\omega) = \frac{F(\frac{\omega}{k})}{ k }$
Shifting	$F(t - t_0) \leftrightarrow e^{-i\omega t_0} F(\omega)$
Differentiability	$\frac{dF(t)}{dt} \leftrightarrow i\omega F(\omega)$
Integration	$\int_{-\infty}^t F(t)dt \leftrightarrow \frac{1}{i\omega} F(\omega) + \pi F(0)\delta(\omega)$

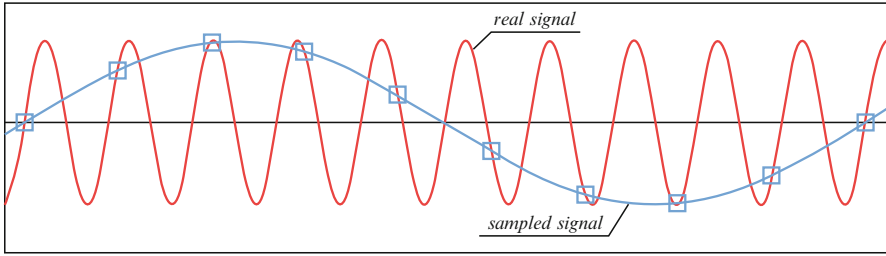


Fig. 8.35 Real signal vs sampled signal

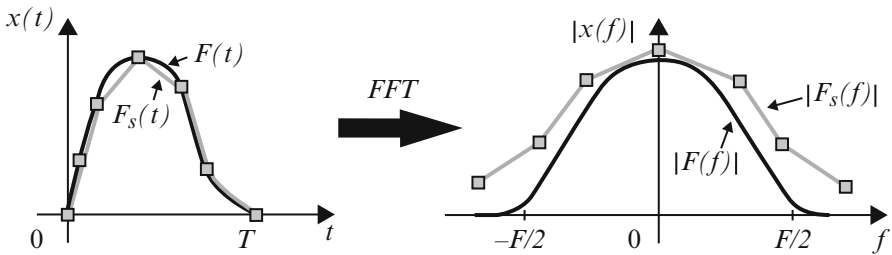


Fig. 8.36 Aliasing distortion observed in the amplitude Fourier spectrum

Recalling that the primary purpose of digital Fourier analysis is to obtain a discrete approximation of the continuum periodic function, the signal sampling operation is essential in order to obtain consistent results. In Fig. 8.35 the real periodic signal is compared with the same sampled signal.

The figure above shows an incorrect sampling procedure because the sampling interval (Δt) is very high with respect to the frequency of the real signal. This phenomenon is called Aliasing distortion in the frequency domain and it can be explained by referencing a generic case shown in Fig. 8.36. In the time interval $[0, T]$, the sampled function $F_s(t)$ can be assumed equal to the real signal $F(t)$. However, $F_s(n \cdot \Delta \omega)$ is only approximately equal to the real function $F(n \cdot \Delta \omega)$ in the frequency interval $[0, F]$.

In order to avoid the aliasing phenomenon, the minimum sampling frequency (Δf) has to be equal to two times the maximum frequency deduced from the Fourier spectrum ($F/2$ in the previous example). This last parameter is called Nyquist frequency and is expressed in the Eq. 8.31.

$$f_N = \frac{1}{2} \Delta f = \frac{1}{2 \Delta t} \tag{8.31}$$

If a filter is applied before signal sampling in order to remove all the contributions associated with a frequency greater than the Nyquist one, the aliasing phenomenon would not occur (anti-aliasing filter). One of the advantages of the frequency domain



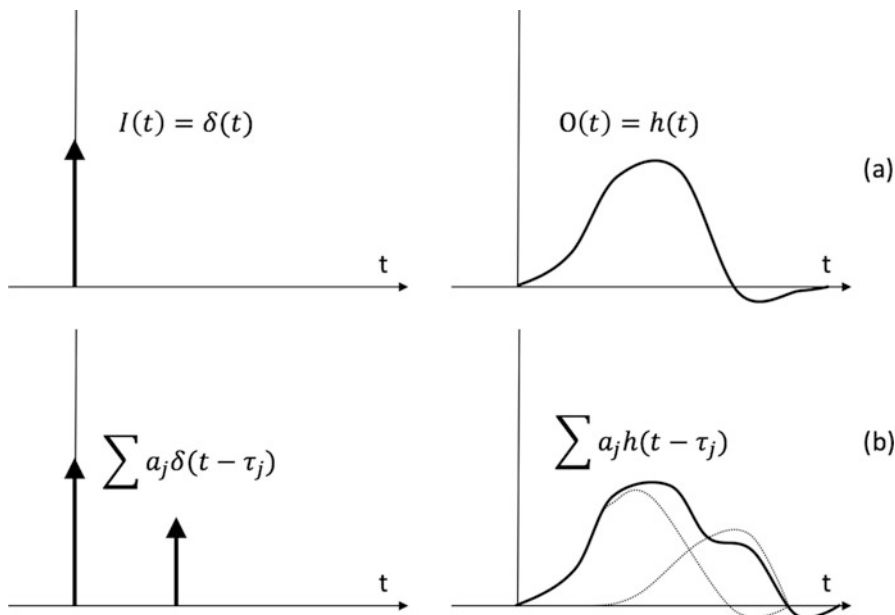


Fig. 8.37 Response to a elementary impulse (a) and to two elementary impulses (b)

approach is to remove fixed contributions of the decomposed harmonic signals or, in other words, it is possible to remove the unwanted frequencies. The procedure just discussed is called signal filtering and is based on the modification of the frequency content of the input signal by application of filters. They are considered as dynamic systems capable of transmitting only the energy contained in a specific bandwidth. In order to understand the filtering signal concepts, the dynamic response of a physical system is discussed below. Considering a physical system in which an impulsive signal $\delta(t)$ is applied, the response of the system $h(t)$ can be assumed as a periodic function. If the given system is linear and time-invariant, by applying several elementary impulses, the response is given by the sum of each elementary response (Fig. 8.37).

The terms $I(t)$ and $O(t)$ refer to the system input and output, respectively. The time τ_j refers to the instant in which the j th elementary impulse is applied. Each generic periodic input function ($I(t)$) can be seen as sum of several elementary impulses occurring in different time instants (τ). Thus, the dynamic response of the system ($O(t)$) can be assumed as expressed in Eq. 8.32.

$$O(t) = \int_{-\infty}^{+\infty} I(\tau)h(t - \tau)d\tau \tag{8.32}$$

Fig. 8.38 Logical scheme of linear physical system

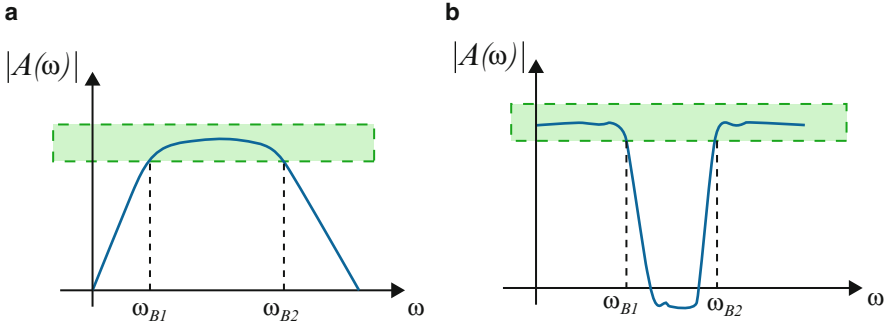
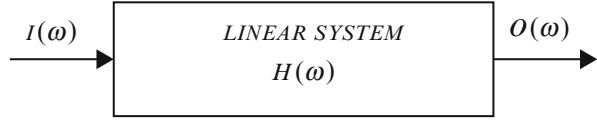


Fig. 8.39 Band-pass filter (a) and band-eliminate filter (b)

This expression is called the convolution product between the function $I(t)$ and $h(t)$. Using the Fourier transform leads to the estimation of the output response in the frequency domain (Eq. 8.33).

$$O(\omega) = \int_{-\infty}^{+\infty} I(\tau) [h(t - \tau) \cdot e^{i\omega t} dt] d\tau = H(\omega) \int_{-\infty}^{+\infty} I(\tau) \cdot e^{i\omega t} d\tau = H(\omega)I(\omega) \tag{8.33}$$

The dynamic response in the frequency domain ($O(\omega)$) is given by the product between the input $I(\omega)$ and the parameter $H(\omega)$, called transfer function. For a linear system, it represents the algebraic relationship between the input and output of the system (Fig. 8.38).

The transfer function $H(\omega)$ depends on the dynamic characteristics of the system. In other words, the transfer function can be compared to a special filter that modifies the frequency content of the input signal. Generally, the filter used to modify the signal characteristics is capable of eliminating a given band-frequency and leaving another one unchanged. Thus, the filter used in signal processing can be divided into two different types:

1. band-pass filter;
2. band-eliminate filter.

In the first case all the contributions due to the frequencies outside the band are eliminated, while in the second case, they remain constant (Fig. 8.39).

If the passing band is associated with a high frequency value, the associated filter is called *high-pass*. On the contrary, when the low frequency remains constant, the filter is called *low-pass*.



8.2.2.2 Filtering

Many engineering applications are based on seismic signals such as acceleration time history. However, often the respective velocity and displacement time histories obtained by integration methods might be affected by some errors (e.g. permanent drifts) due to low frequencies components in the signal. In this case, filtering operations became the primary means for correcting the ground motion records. The Butterworth filter is one of the most used filters in the seismic applications and it is a band-pass filter that passes frequencies within a certain range and rejects frequencies outside that range.

$$|H(\omega)| = \frac{1}{\sqrt{1 + \left(\frac{\omega}{\omega_c}\right)^2 N}} \tag{8.34}$$

Equation 8.34 shows the amplitude response of a Butterworth filter, where ω is the generic angular frequency, ω_c represents the cutoff frequency and n is the order of the filter. Low frequency operation can cause the loss of important physical information related to the soil permanent displacement. In addition, the cut of the high frequency field is necessary for removing the pseudo-horizontal part of the associated elastic spectrum. For the reasons just mentioned, setting the three Butterworth parameters case by case is reasonable and guarantees more adaptability in the signal analysis operations. The accuracy of band-pass filtering is proportional to the order of the filter ($n_1 < n_2 < n_3$), in fact, as shown in the Fig. 8.40, with the increase of the filter order, the filter shape becomes very close to the ideal band-pass filter.

The application of the specific filtering process for uncorrected records is necessary for removing the linear drift in the displacement histories, obtained by means of the double integration of the acceleration recorded history. This process is called baseline correction and consists of reporting the mean value of the recorded acceleration to the null value (Fig. 8.41).

In Fig. 8.42 the differences between the baseline *uncorrected* and *corrected* displacement histories for the Emilia earthquake (station of Modena and North-South component, 2012) are shown.

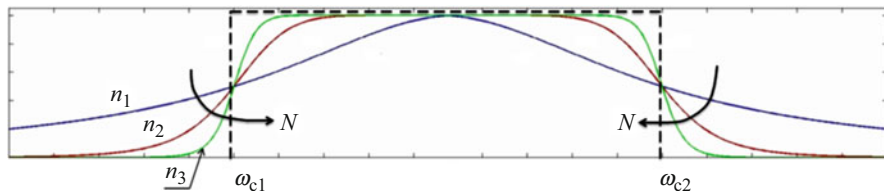


Fig. 8.40 Three different orders of Butterworth filter and ideal band-pass filter

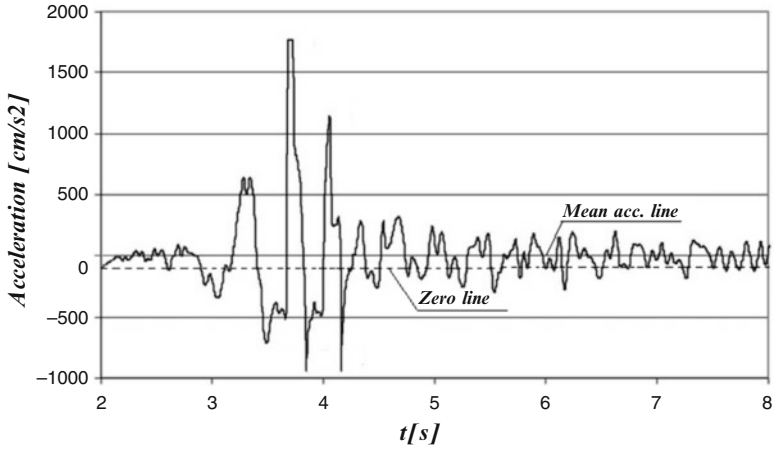
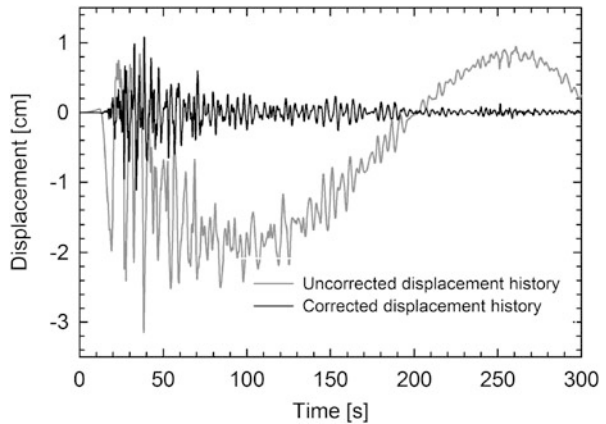


Fig. 8.41 Baseline correction to be applied for removing the difference between mean acceleration line and zero line

Fig. 8.42 Displacement history for uncorrected and corrected record (Emilia earthquake, 05/20/2012)



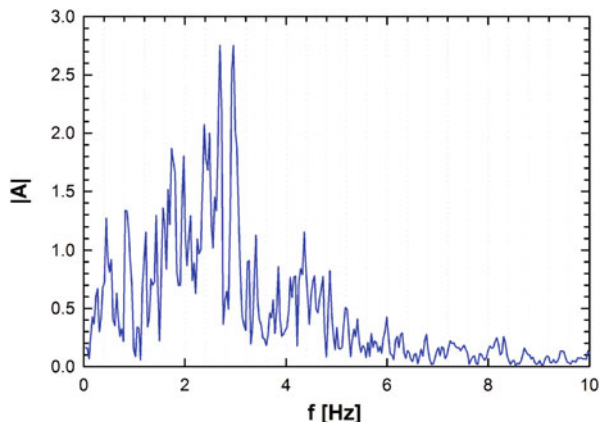
It can be observed that the baseline correction is an essential process for removing the displacement and velocity drifts.

8.2.2.3 Frequency Content

The frequency content of a seismic record gives information about its predominant frequency band (Δf_p) and the distribution of amplitude or phase contributions in the frequency interval $[f_{min}, f_{max}]$. In the practice of earthquake engineering applications, the frequency content of a record is expressed only in terms of



Fig. 8.43 Amplitude Fourier spectrum for Kozani-Prefecture record (Kozani mainshock, 13/05/1999)



amplitude Fourier spectrum, because it is directly related to the energy of the record. For example, in the Fig. 8.43 the Fourier amplitude spectrum of Kozani mainshock earthquake is reported.

From Fig. 8.43 it is possible to see that the maximum amplitude contribution is given by the frequency of 3 Hz, while after 5 Hz the frequency content became very poor. The individuation of the predominant frequency band is a simple procedure and it is essential to identify the possible resonance phenomena with respect to a given structure.

8.2.2.4 Energy Content

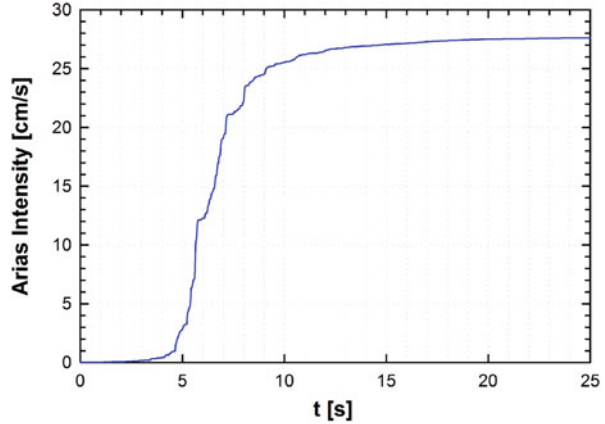
An efficient measure of a seismic event in terms of dissipated energy of a structure subjected to the earthquake excitation has been given by Arias in 1970. The Arias Intensity (I_A) is an integral parameter based on the accumulated energy in a SDOF system with damping and vibrational frequency ω (Eq. 8.35).

$$I_A = \frac{\pi}{2g} \int_0^{t_e} a(t)^2 dt \quad (8.35)$$

The Arias intensity is expressed as a velocity (cm/s), it is defined in the direction of the motion and it's proportional to the square of the accelerations in the interval $[0, t_e]$, where t_e indicates the duration of the recorded earthquake record. The definition of I_A for each time instant of the referring interval represents the cumulative energy trend in the time domain (Fig. 8.44).

Figure 8.44 can provide information about the real duration of the earthquake (see also Sect. 8.2.3). It can be noted that the greatest intensity gradient is located in the interval $[5, 10]$ Hz.

Fig. 8.44 Arias intensity trend for Kozani-Prefecture record (Kozani mainshock, 13/05/1999)



8.2.3 Duration

As discussed in the previous paragraph, the Arias intensity provides information about the real duration of the earthquake. This parameter is very important, because it controls the damage level of a structure excited in the horizontal plan. In fact, it has been experimentally observed that a seismic event with high value of PGA and short duration leads to less level of damage than an event with low value of PGA and long duration. The duration of an earthquake can be defined from the recorded acceleration time history by means of two proposed methods:

1. *significant duration approach*;
2. *bracketed duration approach*.

The first one is the most used in the practical applications and it considers the duration as time range in which 90% of the total energy is registered (Trifunac and Brady 1975). Thus, this definition shows the direct link between the Arias intensity (energy content) and the duration of the seismic event. Figure 8.45 highlights the definition of effective duration.

The *significant duration* is defined for the time value associated with Arias intensity greater than 5% and lesser than 90%. Page et al. (1972) proposed the definition of *bracketed duration* as the time range between the first and last peak acceleration value greater than 0.05 g (Fig. 8.46).

Another parameter is represented by the *peak acceleration time* (T_p) which defines the time instant related to the peak acceleration.

Fig. 8.45 Significant duration definition for Kozani-Prefecture record (Kozani mainshock, 13/05/1999)

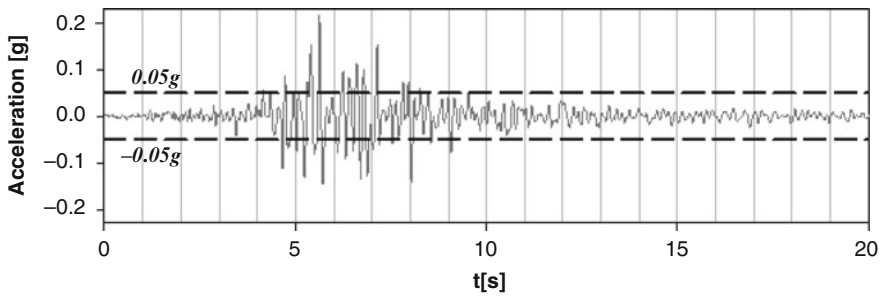
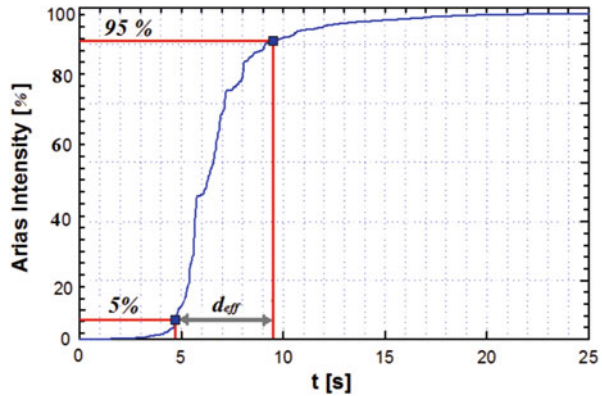


Fig. 8.46 Bracketed duration definition for Kozani-Prefecture record (Kozani mainshock, 13/05/1999)

8.2.4 Other Parameters

In structural and geotechnical engineering the parameters providing information about the frequency content, the duration and the peak values simultaneously are widely used. The most important set of data is the set of Root Mean Square (RMS) parameters, that provide information about both the frequency content and the amplitude characteristics related to the accelerations, velocities and displacements (a_{RMS} , v_{RMS} and d_{RMS}). The expressions of RMS parameters are mathematically similar and the acceleration RMS is reported in Eq. 8.36.

$$a_{RMS} = \sqrt{\frac{1}{T_d} \int_0^{T_d} a(t)^2 dt} \tag{8.36}$$

where T_d is the duration of the motion, while $a(t)$ represents the acceleration corrected history. In Table 8.2 all the main properties of the ground motion (waveform parameters) are summarized.



Table 8.2 Waveform parameters

Amplitude paramaters	Time paramaters	RMS paramaters	Energy and frequency paramaters
PGA	Duration [T_d]	a_{RMS}	Arias intensity [I_a]
PGV	Peak acceleration time [T_p]	v_{RMS}	Fourier transform [$F(\omega)$]
PGD		d_{RMS}	

References

- Aki K (1984) Asperities, barriers, characteristic earthquakes and strong motion prediction. *J Geophys Res.* <https://doi.org/10.1029/JB089iB07p05867>
- Ambraseys NN, Simpson KA, Bommer J (1996) Prediction of horizontal response spectra in Europe. *Earthq Eng Struct Dyn* 25(4):371–400
- Bolt B (1988) *Earthquakes*. W. H. Freeman and Company, San Francisco
- Boore DM, Atkinson GM (2008) Ground-motion prediction equations for the average horizontal component of PGA, PGV, and 5 between 0.01 s and 10.0 s. *Earthq Spectra* 24(1):99–138. <https://doi.org/10.1193/1.2830434>
- Campbell KW, Bozorgnia Y (2008) NGA ground motion model for the geometric mean horizontal component of PGA, PGV, PGD and 5 spectra for periods ranging from 0.01 to 10 s. *Earthq Spectra* 24(1):139–171. <https://doi.org/10.1193/1.2857546>
- Fowler C (1990) *The solid earth*. Cambridge University Press, Cambridge
- INGV (2013) The national institute of geophysics and vulcanology. Available at: <http://www.ingv.it/en/>
- Kanamori H (1977) The energy release in great earthquakes. *J Geophys Res* 82:2981–2987
- Noson L, Qamar A, Thorsen G (1988) Washington state earthquake hazards. Report, Washington Division of Geology and Earth Resources Information Circular 85
- Page R, Boore D, WB J, Coulter H (1972) Ground motion values for use in seismic design of the trans-alaska pipeline systems. Report, USGS
- Reid H (1911) The mechanics of the earthquake, the California earthquake of 18 Apr 1906. Report, Report of the State Investigation Commission
- Richter PJ, Nims DK, Kelly JM, Kallembach R (1990) The EDR-energy dissipating restraint. A new device for mitigation of seismic effects. In: Proceedings of the 1990 SEAOC convention, vol 1, pp 377–401
- Slemmons MD (1977) Vicksburg, miss.: U.S. army engineer waterways experiment station, soils and pavements laboratory. Report, Washington Division of Geology and Earth Resources Information Circular 85
- Trifunac M, Brady A (1975) On the correlation of seismic intensity scales with the peaks of recorded strong ground motion. *Bull Seismol Soc Am* 65(1):139–162
- USGS (2008) The 2008 U.S. geological survey national seismic hazard maps. <http://earthquake.usgs.gov/research/hazmaps/>
- Woods R (1968) Screening of surface waves in soils. *J Soil Mech Found Div ASCE* 94:951–979

Chapter 9

Major Seismic Events That Occurred in Italy and in the World




Abstract The chapter introduces the major historical seismic events occurred in Italy and in the world. The main seismological and general information are listed for each seismic event (e.g. magnitude, fault type, etc.).


9.1 Introduction


In this chapter is presented a classification of the 10 strongest earthquakes that occurred in Italy in the past 150 years (INGV 2013) and in the World from 1960 until today (USGS 2008, Oceanic and Administration 2015). Each earthquake is described with a table reporting the following information:


- date and location of the event;
- magnitude;
- fault type;
- fault rupture length;
- estimated damages;
- peak ground acceleration (PGA);
- comments;


9.2 Earthquakes Occurred in Italy in the Past 150 Years


(1) 1908/12/28 Messina and Reggio Calabria	
Magnitude:	7.2.
Fault type:	normal fault.
Breaking fault length:	40 km.
Estimated damages:	120,000 victims, more than 40,000 collapsed buildings.
Peak ground acceleration:	0.27 g.
Comments:	<p>A tsunami with wave height of 10 m caused thousands of victims, completing and aggravating the devastation and destruction of the earthquake (Farrell et al. 2015). In about 80 towns of the provinces of Messina and Reggio Calabria, extensive damages hit from 70 to 100% of buildings. The earthquake with the following tsunami and fire destroyed completely the building stock of Messina. In Calabria the earthquake had destructive effects in a wider area than in Sicily. After this event, in Italy started the study of the effects of earthquakes and a seismic zones classification was issued.</p> <div style="text-align: center;">  </div> <p style="text-align: center;">Fig. 9.1</p>


(2) 1905/09/08 Nicastro, Calabria	
Magnitude:	7.1.
Fault type:	normal fault.
Breaking fault length:	30 km.
Estimated damages:	557 victims, serious damages to the surrounding towns.
Peak ground acceleration:	about 0.3 g.
Comments:	<p>The earthquake struck with destructive effects the region of the Gulf of St. Eufemia. 13 towns were almost completely destroyed and more than 100 were seriously damaged in the provinces of Cosenza, Catanzaro, Vibo Valentia (Stanley et al. 2014) and Reggio Calabria. These effects were worsened by the state of the building stock, characterized by poor construction techniques. The shock was followed by a tsunami which raised the sea level of 1,3 meters, submerging the coast that goes from Vibo Marina to Tropea.</p> <div style="text-align: center;">  </div> <p style="text-align: center;">Fig. 9.2</p>


(3) 1915/01/13 Avezzano, Abruzzo	
Magnitude:	7.0.
Fault type:	normal fault.
Breaking fault length:	about 30 km.
Estimated damages:	more than 30,000 victims.
Peak ground acceleration:	about 0.4 g.
Comments:	<p>The town of Avezzano was literally toppled from the shaking: 96% of its population died and it lost its most important monuments. Only one high-rise building remained standing. These damages were attributed to the length of the shock, over 1 min, and the enormous amount of power released during the tremor. Damage of the earthquake was distributed throughout a wide area in central and southern Italy. The main shock was felt in Rome where light damages to historic building occurred.</p>  <p style="text-align: center;">Fig. 9.3</p>

(4) 1980/11/23 Irpinia, Campania e Basilicata	
Magnitude:	6.9.
Fault type:	normal fault.
Breaking fault length:	about 30 km.
Estimated damages:	almost 3000 victims and 300,000 buildings seriously damaged.
Peak ground acceleration:	0.38 g.
Comments:	<p>The quake had devastating effects in a wide area of the Southern Apennines, especially in the region called Irpinia and in the adjacent areas in the provinces of Salerno and Potenza. 14,000 houses at least were seriously damaged in the epicentral area alone (Valensise 1993). Many collapses occurred in Naples affecting many old houses made in tuff and many damaged or decaying buildings. 506 towns in the eight affected provinces were damaged.</p>  <p style="text-align: center;">Fig. 9.4</p>

(5) 1930/07/23 Irpinia, Campania and Basilicata	
Magnitude:	6.7.
Fault type:	normal fault.
Breaking fault length:	about 30 km.
Estimated damages:	1400 victims, 3000 collapsed buildings.
Peak ground acceleration:	about 0.27 g.
Comments:	<p>The earthquake was especially destructive in Aquilonia and Lacedonia, where about 70% of buildings collapsed completely. Most of these were built with river stones and poor quality mortar. The quake was affected in a wide territory between Campania, Apulia and Basilicata for an estimated total area of 36,000 km². Collapses and deep lesions were found in 68 countries of the provinces of Avellino, Potenza, Foggia, Benevento and Salerno. Many of historical value buildings such as churches and old castles were destroyed.</p> <div style="text-align: center;">  </div> <p style="text-align: center;">Fig. 9.5</p>

(6) 1920/09/07 Garfagnana, Tuscany	
Magnitude:	6.5.
Fault type:	inverse fault.
Breaking fault length:	not found.
Estimated damages:	171 victims, 650 injured people.
Peak ground acceleration:	0.2 g.
Comments:	<p>Fivizzano was destroyed, and with it part of the regions of Lunigiana and Garfagnana. The area of damage was extensive, including the coasts of Liguria, the Versilia, the mountainous areas of Parma, Modena, the provinces of Pistoia and Pisa. The quake was felt from the French Riviera to the Friuli and, on the south, in the whole of Tuscany, Umbria and Marche. According to surveys, most of the damages was due to the poor quality of the mortars used in the masonry houses.</p> <div style="text-align: center;">  </div> <p style="text-align: center;">Fig. 9.6</p>

(7) 2016/10/30 Norcia, Umbria	
Magnitude:	6.5.
Fault type:	normal fault.
Breaking fault length:	15 km
Estimated damages:	several collapsed buildings.
Peak ground acceleration:	0.48 g
Comments:	<p>the earthquake was felt in almost all the Italian country and even in some parts of Austria. It was a shallow quake as its depth was between 5 and 9 km, and was the mainshock of a seismic sequence started on August 24th. It did not cause casualties but the buildings suffered huge damages. More than half of the houses of Castelluccio di Norcia were destroyed. Also important historical monuments collapsed, such as the San Benedetto basilica and the Santa Maria Argentea cathedral in Norcia. Significant hydro-geological effects were also generated and the two edges of the fault are clearly visible as there is a difference in level up to 70 cm.</p>  <p style="text-align: center;">Fig. 9.7</p>

(8) 1976/05/06 Tolmezzo, Friuli Venezia Giulia	
Magnitude:	6.4.
Fault type:	normal fault.
Breaking fault length:	about 20 km.
Estimated damages:	989 victims, more than 45,000 homeless.
Peak ground acceleration:	0.35 g.
Comments:	<p>The earthquake lasted 50 s. The seismic event, combined with the morphology of the ground, generated numerous landslides which damaged many roads hampering rescue efforts. The towns affected by the greatest losses were 41; those seriously damaged were 45. Collapses occurred across the border with Austria and in the territory of Slovenia. After the main event, the most violent aftershocks occurred more than 4 months later, on 11 and 15 September.</p>  <p style="text-align: center;">Fig. 9.8</p>


(9) 1968/01/15 Belice, Sicily	
Magnitude:	6.4.
Fault type:	normla fault.
Breaking fault length:	40 km.
Estimated damages:	about 300 victims, 70,000 homeless.
Peak ground acceleration:	0.12 g.
Comments:	<p>Belice's valley was considered, until the earthquake of 1968, one of the so-called "non-seismic areas" and consequently built with crumbling structures, consisting of caves and huts used as houses. Several settlements in Trapani's province were totally destroyed by the shaking and different roads suffered disruptions hampering rescue efforts.</p> 

Fig. 9.9





(10) 2009/04/06 Lâquila, Abruzzo	
Magnitude:	6.3.
Fault type:	normal fault.
Breaking fault length:	25 km.
Estimated damages:	308 victims, 1500 injured people, 10,000 million euros in damages.
Peak ground acceleration:	0.3 g.
Comments:	<p>The fault located near the settlement of Paganica was the one considered responsible for the earthquake (Chiarabba et al. 2009). It was clearly felt throughout central Italy down to Naples and the main shock was followed by dozens of aftershocks. In this event public, private, artistic and architectural building stock was damaged as well as many infrastructures. In the only city of L'Aquila lived over 55% of the population directly affected by the earthquake.</p> 


Fig. 9.10


9.3 Earthquakes Occurred in the World from 1960 to the Present Day


(1) 1960/05/22 Valdivia, Chile	
Magnitude:	9.5.
Fault type:	thrust fault (subduction of the Nazca plate beneath the South American plate).
Breaking fault length:	1000 km.
Estimated damages:	5700 victims, 2 million homeless, about 1000 million dollars in damages.
Peak ground acceleration:	0.29 g.
Comments:	<p>The earthquake generated one of the most destructive Pacific tsunamis with waves high up to 25 m. It reached the coastline of Chile within 10 to 15 min killing at least 200 people, sinking all the boats, and inundating half a kilometer inland (Cifuentes 1989). It was particularly destructive even in the Hawaiian Islands and in Japan, where it arrived about 15 h later. In addition to the tsunami there were other geologic phenomena like extensive subsidence, alteration of the shoreline and of local flooding. After the main shock, the Cordón Caulle volcano erupted for 47 h.</p> <div style="text-align: center;">  </div> <p style="text-align: center;">Fig. 9.11</p>


(2) 1964/03/28 Prince William Sound, Alaska	
Magnitude:	9.2.
Fault type:	thrust fault (subduction of the Pacific plate beneath the North American plate).
Breaking fault length:	700 km.
Estimated damages:	about 130 victims, more than 310 million dollars in damages.
Peak ground acceleration:	0.44 g.
Comments:	<p>The earthquake caused vertical displacements which ranged from about 12 m of uplift to 2,3 meters of subsidence relative to sea level (Plafker 1965). The zone of subsidence covered about approximately 285.000 km². A Pacific-wide tsunami was generated which was destructive in Western Canada, Oregon, California and the Hawaiian islands, killing about 110 people. There were 52 larger aftershocks, the first 11 of which, with magnitude greater than 6,0 on the Richter scale, occurred in the first day.</p> <div style="text-align: center;">  </div> <p style="text-align: center;">Fig. 9.12</p>


(3) 2004/12/26 Off the west coast of Northern Sumatra, Indonesia	
Magnitude:	9.1.
Fault type:	Thrust fault (subduction of the Indian plate beneath the Burma plate).
Breaking fault length:	about 1500 km.
Estimated damages:	about 230,000 victims.
Peak ground acceleration:	0.25 g.
Comments:	<p>The hypocentre of the main earthquake was in the Indian Ocean, just north of Simeulue Island, at a depth of 50 km below the mean sea level. The earthquake generated the greatest fault rupture of any recorded earthquake, spanning a distance of about 1500 km. The whole rupture lasted 10 min (Lay et al. 2005). Along the plate boundary there were displacements up to 20 m that generated a devastating tsunami. It struck Sumatra in 15 min, Thailand in half an hour, India in two hours with no possibility to alert the people since there were no sensors able to predict the propagation of the tsunami.</p> <div style="text-align: center;">  </div> <p style="text-align: center;">Fig. 9.13</p>


(4) 2010/02/27 Offshore Maule, Chile	
Magnitude:	8.8.
Fault type:	thrust fault (subduction of the Nazca plate beneath the South American plate).
Breaking fault length:	more than 500 km.
Estimated damages:	500 victims at least, 500,000 seriously damaged buildings.
Peak ground acceleration:	about 0.3 g.
Comments:	<p>This earthquake occurred at the boundary between the Nazca and South American tectonic plates. The two plates are converging at a rate of 70 mm per year. From 1973 in this area there were at least 13 quakes with a magnitude higher than 7.0. A tsunami was generated but it caused few damages.</p> <div style="text-align: center;">  </div> <p style="text-align: center;">Fig. 9.14</p>


(5) 2005/03/28 Northern Sumatra, Indonesia	
Magnitude:	8.7.
Fault type:	thrust fault (subduction of the Indian plate beneath the Burma plate).
Breaking fault length:	300 km.
Estimated damages:	1300 victims.
Peak ground acceleration:	about 0.3 g.
Comments:	<p>The Indian plate is moving in a northeastward direction at about 5 to 5,5 cm per year relative to the Burma plate. The rupture started off the western coast of North Sumatra near Nias Island and progressed in a southeast direction along a preexisting major fault. Nias Island had the hardest losses both in terms of deaths and damages to the buildings. A tsunami with wave height up to 3 m occurred along the Indonesian coast but the population was informed and had time to escape.</p>  <p style="text-align: center;">Fig. 9.15</p>

(6) 1965/02/04 Rat Islands, Alaska	
Magnitude:	8.7.
Fault type:	thrust fault (subduction of the Pacific plate beneath the North American plate).
Breaking fault length:	600 km.
Estimated damages:	130 victims.
Peak ground acceleration:	not found.
Comments:	<p>This region, where the Pacific and North American plates are forced directly into one another, is one of the world's most active seismic zones. Only 9 deaths were due to the earthquake, the others were caused by the tsunami generated after the main shock.</p> <div style="text-align: center;">  <p style="font-size: small; text-align: center;">Anchorage Museum of History & Art - L. Strong & Archibald</p> </div> <p style="text-align: center;">Fig. 9.16</p>

(7) 2007/09/12 Southern Sumatra, Indonesia	
Magnitude:	8.5.
Fault type:	thrust fault (subduction of the Australian Plate beneath and the Sunda plate).
Breaking fault length:	350 km.
Estimated damages:	25 victims, 160 injured people, 50,000 seriously damaged buildings.
Peak ground acceleration:	0.2 g.
Comments:	<p>At the location of these earthquakes, the Australia plate moves northeast with respect to the Sunda plate at a velocity of about 60 mm/year. After the first, and largest, shock, the Pacific Tsunami Warning Centre issued a tsunami alert for the Indian Ocean basin. A tsunami approximately 1 m high was reported at Padang, Indonesia.</p> <div style="text-align: center;">  </div> <p style="text-align: center;">Fig. 9.17</p>

(8) 1963/10/13 Kuril Islands, Russia	
Magnitude:	8.5.
Fault type:	thrust fault.
Breaking fault length:	245 km.
Estimated damages:	1 injured person, 2 destroyed docks.
Peak ground acceleration:	about 0.1 g.
Comments:	<p>In the region of the earthquake’s epicenter, the Pacific plate moves northwest with respect to the Okhotsk plate with a velocity of about 90 mm/year, and becomes progressively deeper to the northwest, remaining seismically active to a depth of 680 km. The earthquake generated a tsunami with a maximum wave height of 5 m.</p> <div style="text-align: center;">  <p>Fig. 9.18</p> </div>

(9) 2001/06/23 Off the coast of Peru	
Magnitude:	8.4.
Fault type:	thrust fault(subduction of the Nazca plate beneath the South American plate).
Breaking fault length:	150 km.
Estimated damages:	about 100 victims, 2600 injured people, more than 25,000 collapsed buildings.
Peak ground acceleration:	0.44 g.
Comments:	<p>The epicenter of the quake was off the coast, just north of the town of Ocona in Southern Peru. The motions were so strong that even in Peru's capital, Lima (600 km away), homes collapsed and injured several people. 25 people at least died because of the tsunami generated by the earthquake.</p> <div style="text-align: center;">  </div> <p style="text-align: center;">Fig. 9.19</p>

(10) 2003/09/25 Hokkaido, Japan	
Magnitude:	8.3.
Fault type:	thrust fault.
Breaking fault length:	about 100 km.
Estimated damages:	about 700 injured people, 90 million dollars in damages.
Peak ground acceleration:	about 0.2 g.
Comments:	<p>The hypocenter of the earthquake was off the coast at a depth of about 30 km. Damages were restricted to the coastal area and nobody died. However the quake generated landslides and a tsunami with 4 m wave height.</p> <div style="text-align: center;">  </div> <p style="text-align: center;">Fig. 9.20</p>

References

- Chiarabba C, Amato A, Anselmi M, Baccheschi P, Bianchi I, Cattaneo M, Cecere G, Chiaraluce L, Ciaccio MG, De Gori P, De Luca G (2009) The 2009 L'Aquila (central Italy) MW6.3 earthquake: main shock and aftershocks. *Geophys Res Lett* 36(18):6. <http://doi.org/10.1029/2009GL039627>
- Cifuentes IL (1989) The 1960 Chilean earthquakes. *J Geophys Res Solid Earth* 94(B1):665–680
- Farrell EJ, Ellis JT, Hickey KR (2015) Tsunami case studies
- INGV (2013) The national institute of geophysics and vulcanology. Available at: <http://www.ingv.it/en/>
- Lay T, Kanamori H, Ammon CJ, Nettles M, Ward SN, Aster RC, Beck SL, Bilek SL, Brudzinski MR, Butler R, et al (2005) The great Sumatra-Andaman earthquake of 26 December 2004. *Science* 308(5725):1127–1133
- Oceanic N, Administration A (2015) Global significant earthquake database, 2150 bc to present

- Plafker G (1965) Tectonic deformation associated with the 1964 Alaska earthquake. *Science* 148(3678):1675–1687
- Stanley JD, Bernasconi MP, Nickerson GA (2014) Large scarps and massive slide on the Briatico–Bivona shelf, Calabria, Italy: potential link with the destructive September 1905 earthquake. *J Coast Res* 30(2):215–227
- USGS (2008) The 2008 U.S. geological survey national seismic hazard maps: <http://earthquake.usgs.gov/research/hazmaps/>
- Valensise G (1993) Summary of contributions on the 23 November 1980, Irpinia earthquake

Chapter 10

Seismic Hazard Analysis



Abstract The chapter introduces the analyses used to estimate the seismic hazard at a specific site. A brief introduction and definition of risk is given. The Deterministic Seismic Hazard Analysis (DSHA) and the Probabilistic Seismic Hazard Analysis (DSHA) are discussed.

10.1 Introduction

All the seismological considerations given in Chap. 8 can be used to produce the models used for the seismic hazard estimation at a specific site. This procedure represents the first step in earthquake engineering, because each hazard level is associated with a seismic action to be considered for the structures. The seismological models are based on the macro-division of the region of interest. The fundamental equation of seismic risk is the following (Eq. 10.1).

$$R = H \times D \times L \quad (10.1)$$

where (H) is the hazard, (D) is the vulnerability and (L) is the exposure. The seismic hazard H represents the probability of occurrence of a given seismic event. The vulnerability D represents the probability of being in a given damage state. The exposure L is a parameter related to the density of the population and the built environment in general. In Fig. 10.1 are shown some examples of the Italian maps referred to the hazard, the vulnerability and the exposure.

In general, the hazard H is defined as the probability of having a certain ground motion parameter value in a given observation period. The methodologies used to evaluate the seismic hazard can be grouped in deterministic-based or probabilistic-based and they are described in detail in the following paragraphs.

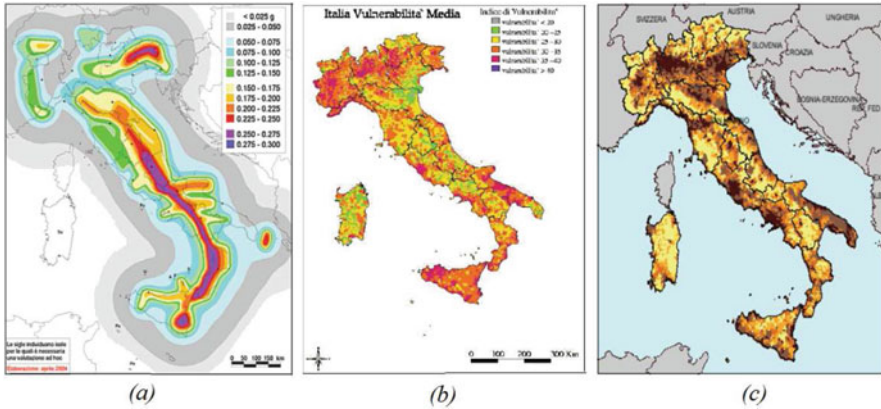


Fig. 10.1 Hazard map (a), vulnerability map (b) and exposure map (c) for Italy

10.2 Deterministic Seismic Hazard Analysis (DSHA)

This is the first approach used in earthquake engineering and it is structured into 5 different steps reported below.

- **Step 1:** identification of all the seismic sources capable of producing an effect on the site of interest.

In order to identify all the possible potential sources, the seismogenetic-source map is defined. It contains the seismogenetic zones identified in the region of interest. For the Italian sites, the ZS9 map (Fig. 10.2) has been defined and thus provides information about the expected seismic source mechanism for each uniform zone in which the Italian territory is divided (macro-seismic division).

The seismo-genetic map can be found online at the link:

<http://www.arcgis.com/home/webmap/viewer.html?webmap=8c5d55e0d3b34ea78346e802fd4f6d73>

In addition, the INGV provides the Database of Individual Seismogenic Sources (DISS), available to the link:

<http://diss.rm.ingv.it/diss/KML-HTMLoptions.html> (Basili et al. 2008). Each of the zones is characterized by the effective depth (Z_{eff}), the maximum magnitude (M_{max}) and the fault type. As an example, let's consider the zone 929 (Tirrenic Calabria) (Fig. 10.3).

Figure 10.4 shows a screenshot of DISS for the North-Calabrian sites from which it is possible to notice the different geometric fault contributions.

- **Step 2:** Evaluation of the maximum expected magnitude from the seismological and historical data.

The mean number of possible seismic events with magnitude greater than a given limit m in a given period (λ_m) are estimated by using the recurrence law (Gutenberg-Richter law) (Eq. 10.2). As seen in Sect. 10.2, this relationship

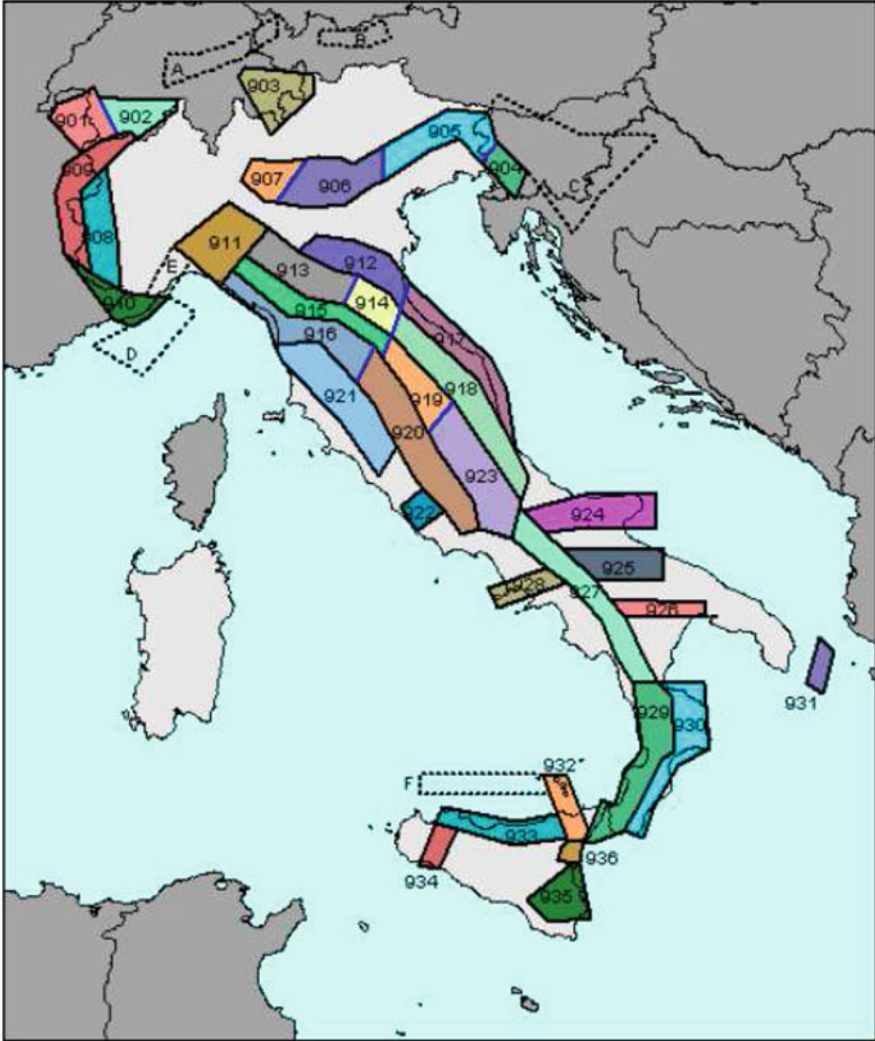


Fig. 10.2 ZS9 map (Meletti and Valensise 2004)

is expressed in semi-logarithmic scale by a linear function, where the two parameters have to be calibrated by referring to the historical data. In the Fig. 10.5 two examples are reported.

$$\log(\lambda_m) = a - bM \tag{10.2}$$

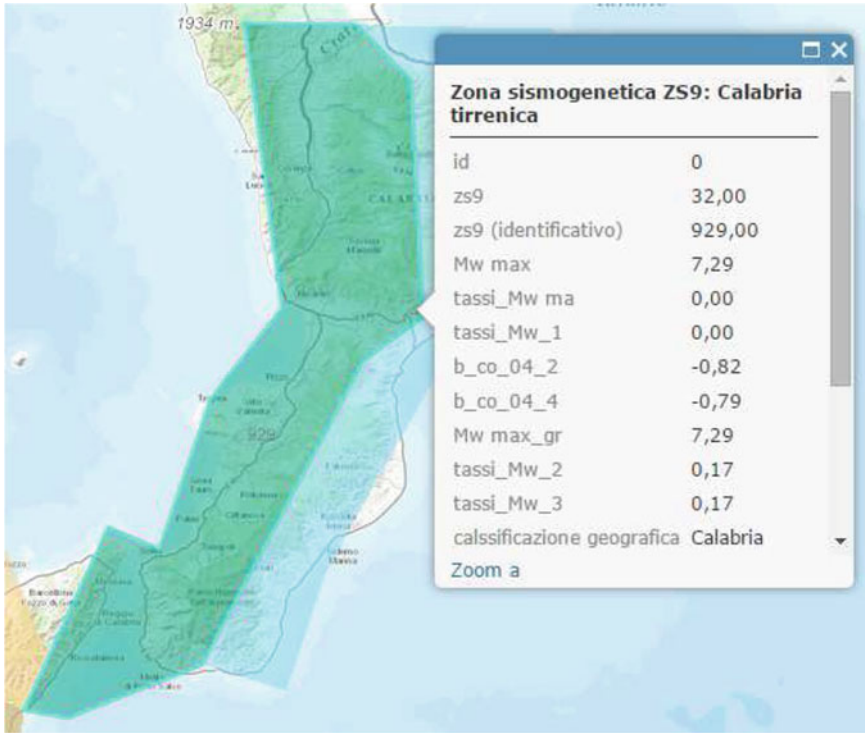


Fig. 10.3 Seismo-genetic information about zone 929

Fig. 10.4 Screenshot of results obtained in the DISS (Basili et al. 2008)

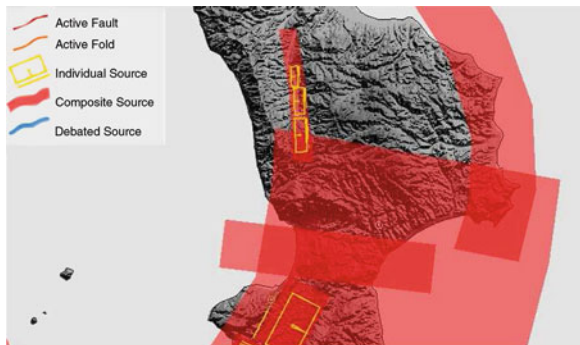


Fig. 10.5 Gutenberg-Richter laws for two different sites with data coming from Esteva, 1970 (Kramer 1996)

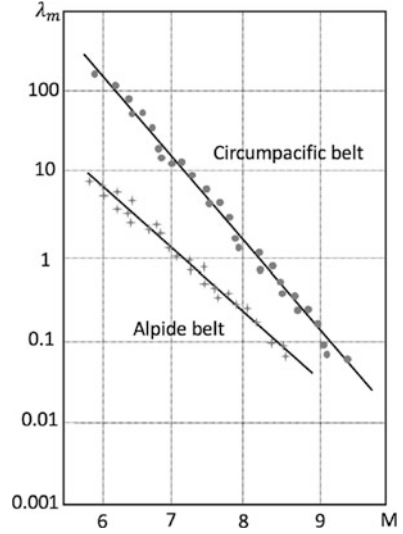
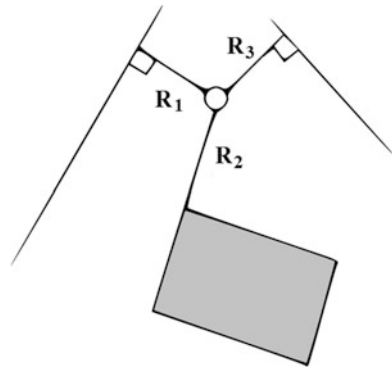


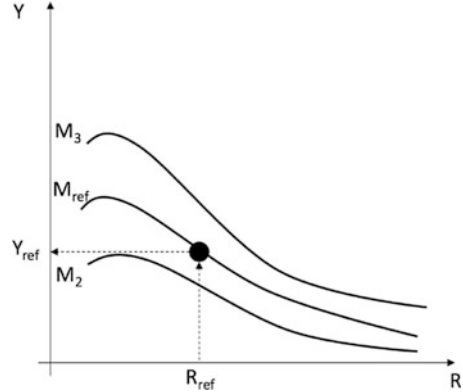
Fig. 10.6 Example of source-site distance definition



The inverse of the λ_m parameter represents the mean return period $T_{(R,m)}$. After estimating the parameters a and b , it is possible to define the maximum magnitude associated with a given return period, or, in other words, for a given exceedance probability.

- **Step 3:** Definition of the source-site distances (R) (Fig. 10.6).
- **Step 4:** Estimation of the expected effect on the site by means of a given attenuation model. The main parameters characterizing the attenuation phenomena are the magnitude $M_{(ref)}$ (defined in Step 2) and the source-site distance $R_{(ref)}$ (defined in Step 3). A large variety of attenuation laws based on other seismogenetic parameters are proposed in the Sect. 8.1.4.

Fig. 10.7 Example of motion parameter estimation from the attenuation curves



- **Step 5:** Selection of the control earthquake in terms of ground motion parameters. Starting from the given attenuation model, the parameter $M_{(ref)}$ and $R_{(ref)}$ it is possible to evaluate the ground motion parameter controlling the hazard at the site.

Figure 10.7 represents the estimation process of the motion parameter (Y_{ref}) starting from the attenuation curves.

Figure 10.8 displays all the discussed steps to be followed in the DSHA.

The main limitations of the DSHA are listed below:

- Uncertainty of the recurrence model and attenuation model. The consistency of the parameters defined by the two models depends on the number of past seismic events considered in the analysis.
- Overestimation of the expected ground motion parameter coming from the choice of the source-site distances. Since the seismo-genetic zones are wide, if the site is inside a specific zone, it is suggested to consider it a null distance. This leads to obtain the estimated effects greater than the real ones.

10.3 Probabilistic Seismic Hazard Analysis (PSHA)

The Probabilistic Seismic Hazard Analysis (PSHA) was proposed by Cornell (1968), who recognized the need for seismic hazard to be based on a method which properly accounted for the intrinsic uncertainties associated with the earthquake. The hazard parameter $P(Y > \bar{Y})$ defines the exceedance probability of a given parameter \bar{Y} with respect to the corresponding threshold value. The model for the occurrence of ground motions at a specific site for specified level of magnitude is assumed to be that of a Poisson process. One of the property of the Poisson process is that it's memoryless, so every event is independent from the other within a given period range. In addition, this is a stationary approach because the probability is the same for any constant time interval. Considering a time interval VR , the probability

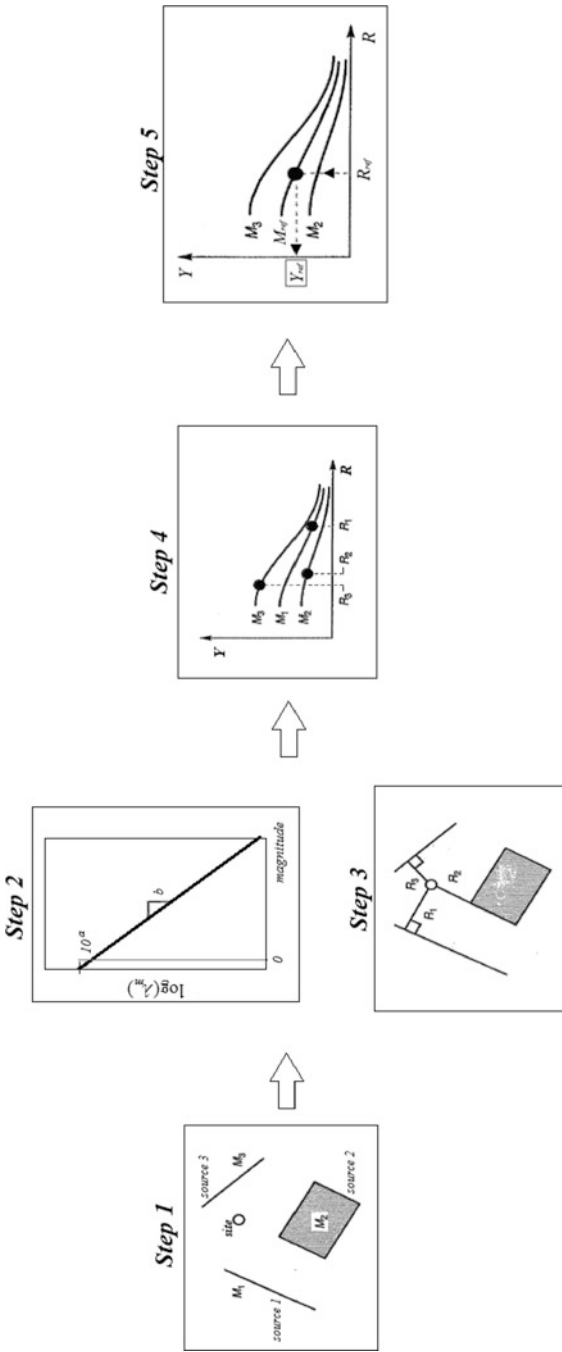
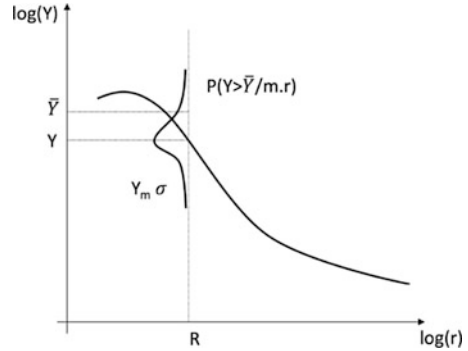


Fig. 10.8 Logical scheme of the steps for the DSHA

Fig. 10.9 Exceedance probability conditioned by the magnitude m and source-site distance r



of having at least one seismic event with magnitude greater than the limit m , is reported in Eq. 10.3.

$$P(N \geq 1) = 1 - e^{-\lambda V_R} \quad (10.3)$$

where λ is the mean annual seismic frequency with a given magnitude, while its inverse value represents the return period T_R . In addition, the natural uncertainty associated with the variability of the parameters of the model (source-site distance, magnitude and other seismological parameters) is accounted for by considering the parameters as random variables, whose discrete values are assigned weights reflecting their likelihood. Thus, the referenced magnitude ($M_{(ref)}$) and source-site distance of interest ($R_{(ref)}$) are expressed in terms of probability density function $f_M(m)$ and $f_R(r)$ respectively. Then, the probability defining the seismic hazard at the site is defined in Eq. 10.4.

$$P(Y > \bar{Y}) = \iint_{m,r} P(Y > \bar{Y}/m, r) \cdot f_M(m) \cdot f_R(r) \cdot dm \cdot dr \quad (10.4)$$

where $P(Y > \bar{Y})$ is the conditional probability of having a hazard parameter Y greater than the limit \bar{Y} , for an event with a magnitude m and source-site distance r . In other words, the attenuation effects are considered as stochastic variables normally distributed. Thus, if Y_m indicates the mean hazard parameter and σ is the standard deviation of the normal distribution, the given seismological parameters are used to estimate the desired probability (Fig. 10.9).

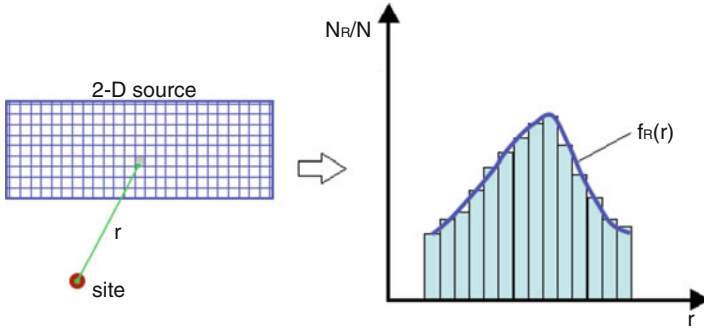


Fig. 10.10 Definition of the probability density function of source-site distance

The probability density functions (*pdf*) associated with the magnitude and distance definitions take into account the power and the spatial uncertainty, respectively. The impossibility of defining the geometry of a spatial seismic source with high-quality accuracy leads to consider the distance R as a stochastic variable. The pdf of source-site distance $f_R(r)$ can be defined by considering a uniform seismic event distribution on the source zone. This assumption leads to the definition of the frequency histograms and the corresponding *pdf* (Fig. 10.10).

As shown in the previous paragraph, in order to take into account the variability of the intensity of the seismic events in the given period of interest, the Gutenberg-Richter law is used. In this case, the pdf associated with the magnitude can be evaluated using Eq. 10.5,

$$f_M(m) = \int_{m_0}^{m_1} \frac{b \cdot e^{-b(m-m_0)}}{1 - e^{-b(m_1-m_0)}} dm \tag{10.5}$$

where m_0 and m_1 define the minimum and maximum magnitude thresholds, while b is the coefficient obtained from the regression of the historic data. The steps followed in the PSHA are the same of the DSHA, only the parameters definition is different. Figure 10.11 illustrates all the ordered steps used in the PSHA.

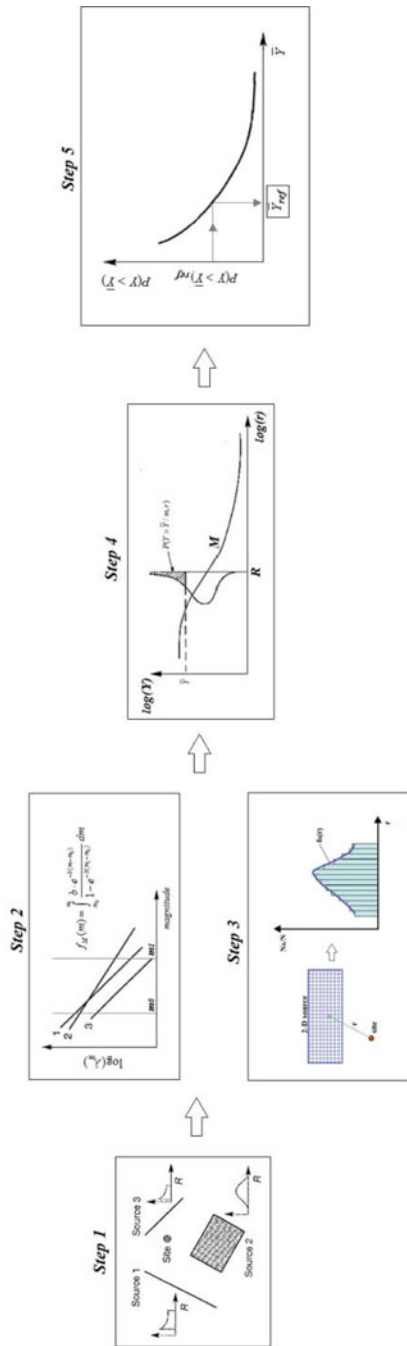


Fig. 10.11 Logical scheme of the steps for the PSHA

References

- Basili R, Valensise G, Vannoli P, Burrato P, Fracassi U, Mariano S, Tiberti MM, Boschi E (2008) The database of individual seismogenic sources (DISS), version 3: summarizing 20 years of research on Italy's earthquake geology. *Tectonophysics* 453(1):20–43
- Cornell CA (1968) Engineering seismic risk analysis. *Bull Seismol Soc Am* 58(5):1583–1606
- Kramer SL (1996) Geotechnical earthquake engineering. Prentice-Hall civil engineering and engineering mechanics series. Prentice Hall, Upper Saddle River
- Meletti C, Valensise G (2004) Zonazione sismogenetica ZS9 – App.2 al Rapporto Conclusivo. Gruppo di Lavoro MPS (2004) Redazione della mappa di pericolosità sismica prevista dall'Ordinanza PCM 3274

Chapter 11

Earthquake Prediction



Abstract The chapter introduces some of seismic prediction methods proposed in the last 50 years. Having in mind the physical and statistical limits in earthquake predictability, the earthquake prediction methods are impartially reported in this chapter.

11.1 Introduction

Although many researchers still concentrate their efforts on assigning probability values, it is well known that making quantitative probabilistic claims, particularly for large and sporadic events, requires a long series of recurrences, which cannot be obtained at local scale from the existing earthquakes catalogs.

The operational and decision-making problems related to earthquake forecast/prediction and seismic hazard assessment are nowadays a matter of significant debate, due to the unsatisfactory global performance of Probabilistic Seismic Hazard Assessment at the occurrence of most of the recent destructive earthquakes. Based on the available data and current knowledge of seismic process, earthquakes cannot be predicted precisely. There are, in fact, several elements that limit the accuracy of the predictions. From a physical point of view, an earthquake involves a fault segment with finite dimensions; therefore, location uncertainty will be at least equal to the seismic source size (e.g. several hundred km in the case of 2011 Tohoku earthquake). Moreover, although many researchers still concentrate their efforts on assigning probability values, it is well known that making quantitative probabilistic claims, particularly for large and sporadic events, requires a long series of recurrences, which cannot be obtained at local scale from the existing catalogs of earthquakes. Having in mind the physical and statistical limits in earthquake predictability, it still appears a reasonable task to provide improving space-time constraints about impending strong earthquakes.

11.2 General Aspects

The United States National Research Council, Panel on Earthquake Prediction of the Committee on Seismology suggested the following consensus definition (1976, p. 7): “An earthquake prediction must specify the expected magnitude range, the geographical area within which it will occur, and the time interval when it will happen with sufficient precision so that the ultimate success or failure of the prediction can readily be judged. Only by careful recording and analysis of failures as well as successes can the eventual success of the total effort be evaluated and future directions charted.”

The ICEF Report (IR) attempts to enrich this definition with the following distinction of prediction and forecast: “A prediction is defined as a deterministic statement that a future earthquake will or will not occur in a particular geographic region, time window, and magnitude range, whereas a forecast gives a probability (greater than zero but less than one) that such an event will occur.” (IR, p. 319).

Earthquake prediction is a branch of seismology and it is usually defined as *the specification of the time, location, and magnitude of future earthquakes within stated limits* (Geller 1997). Prediction procedures have to be reliable and accurate in order to justify the costs of actions to be done. The possibility to establish scientific methods for predicting seismic events has been always a hot topic. While some scientists still believe that prediction might be possible, many others now claim that earthquake prediction is inherently impossible. In 1997, Geller claimed that *the results in non-linear dynamics are consistent with the idea that earthquakes are inherently (or effectively) unpredictable due to highly sensitive non-linear dependence on the initial conditions*. Nowadays, the systematic instrumentation of large regions allows the acquisition of large data sets. Thus, some scientists are confident that earthquake prediction will be possible in the near future. In 1980, Aki said: *I believe it is possible to develop in the next decade a quantitative scale which measures the gradation of concerns about the earthquake occurrence on the basis of observed data on precursory phenomena*. In the 1980s, the scientific research was focusing on empirical analysis trying to identify distinctive precursors for earthquakes or some geophysical trends or patterns in seismicity that might have preceded an earthquake. The basic idea of the empirical methods is the observation of a precursor that would allow alarms to be issued with high reliability and accuracy. Earthquake precursors can be defined as anomalous phenomena (seismological, geodetic, hydrological, geochemical, electromagnetic, animal behavior and so on). The main problem is that there are not objective definitions and quantitative physical mechanisms associated to these anomalies. In 1982, Raleigh et al. *claim that reliance on empirically established precursory phenomena will still be necessary until a better formulation of a theoretical model is possible. Both as a means of developing the observational basis for better models and collecting data which will have value as precursory signals, an extensive network for closely monitoring and for analyzing strain and seismicity data in real time is imperative*. In 2011, the International Commission on Earthquake

Forecasting for Civil Protection (ICEF) reviewed some precursor methods including changes in strain rates, seismic wave speeds, and electrical conductivity; variations of radon concentrations in groundwater, soil, and air; fluctuations in groundwater levels; electromagnetic variations near and above Earth's surface; thermal anomalies; anomalous animal behavior; and seismicity patterns. The conclusions of the Commission are summarized in the next paragraphs.

11.3 Prediction Methods

The ICEF has reviewed the knowledge about earthquake predictability and its current implementation in prediction and forecasting methods. Since any information about the future occurrence of earthquakes contains large uncertainties, it can be evaluated and provided in terms of probabilities on various time scales and ranges (long or short terms). Obviously, the capabilities of earthquake forecasting will benefit from investments in observational technologies and data collection programs. The most widely-used long-term (years to decades) models used in seismic hazard assessment assume earthquakes happen randomly in time, while short-term (month or lesser) models are not able to predict large earthquakes. The most promising approach seems nowadays related to predictions at the intermediate term time scale (months to years). According to the last aspect, the search for diagnostic precursors has not yet produced a successful short-term prediction scheme.

The four main precursors used in prediction models are:

- animal behavior
- changes in V_p/V_s
- radon emission
- electromagnetic variation
- anomalous variations in seismic activity

11.3.1 *Animal Behavior*

Abnormal animal behavior is the oldest and most consistently reported short-term earthquake pre-cursor (Lott et al. 1981). When animals showed an unusual behavior before a seismic event, it has been suggested they are sensitive to the P-wave. Thus, they are not able to predict the earthquake at long-term, but only the imminent arrival of S-waves. From the same study, it has also been suggested that unusual animal behaviors can be displayed some hours or days before the main seismic shock (fore-shock activity) even for imperceptible magnitude by humans. Statistically, an unusual animal behavior before the earthquake has been observed in one case over 5 for the case of similar earthquakes. This trend can be explained by the

Fig. 11.1 Anomalous behavior of toads in China before Sichuan earthquake (2008)



flashbulb memories] that are memories for the circumstances in which one first learned of a very surprising and consequential (or emotionally arousing) event (Brown and Kulik 1977). An example of this anomalous behavior has been observed in China (Mianzhu) just few hours before Sichuan earthquake (2008, May 12th) when thousands of toads appeared in the streets (Fig. 11.1).

11.3.2 Changes in VP/VS

Small-scale laboratory experiments have shown that the ratio between the P-wave and the S-wave velocity changes when the rock is near the point of fracturing. This breakthrough was made by Russian seismologists observing such changes in the region of a subsequent earthquake (Hammond 1973) as effect of dilatancy. In 1973, Whitcomb studied a velocity anomaly beneath the Transverse Ranges in southern California (Fig. 11.2).

After the first coherent and positive results, additional studies on quarry blasts observed no variation in the velocity ratio. Later in 1997, Lindh et al. (1978) claimed an alternative explanation for the velocity anomalies which were *caused by differences in the depth and magnitude of the source earthquakes during the “anomalous” periods and were unrelated to any premonitory material property changes.*

Fig. 11.2 V_p and V_s data variation during 1971 San Fernando earthquake in southern California (Whitcomb et al. 1973)

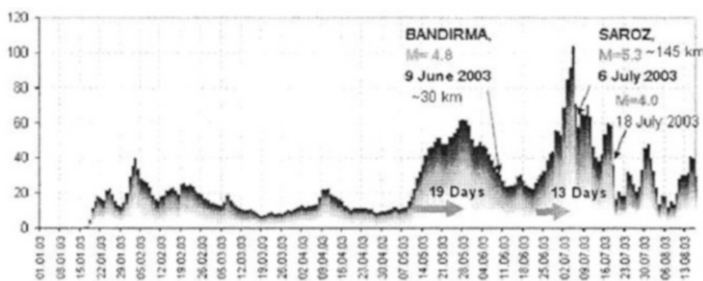
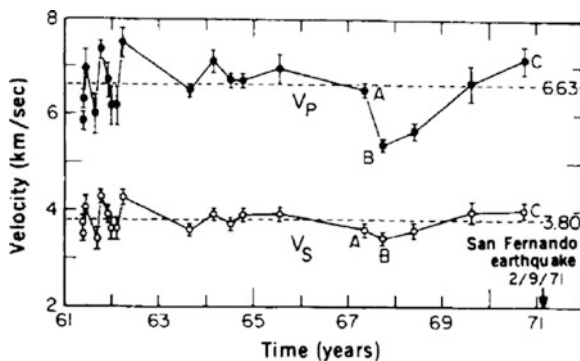


Fig. 11.3 Daily radon concentration in the Marmara region (Turkey, 2003)

11.3.3 Radon Emission

Small amounts of radon, different from the atmospheric gases, are contained into uranium-bearing rocks. This gas is a product of radioactive decay of radio and it is not uniformly distributed on the Earth. Radon is almost no soluble in water, is highly volatile and it diffuses through soils and rocks. Some researches on radon concentration in ground water claimed that this gas could be considered as an earthquake precursor. After Taskent earthquake (1966–1967), large radon concentrations were recorded in wells located in the region near the epicenter. Right before the 2003 earthquakes in Turkey, radon flux variations were observed right before the main shocks with peaks of radon concentrations just right before the shake followed by a rapid decrease (Fig. 11.3).

Furthermore, laboratory experiments showed that radon emission increases significantly during rock fracturing, since the pre-seismic stresses fracture the rock and cause the release of the gas in the atmosphere and in the ground water. Even for soft soils, the vertical raising (up and down) of the soil during a foreshock can produce variations of the radon concentration. Recently Cicerone et al. (2009) collected up to 125 variations of radon concentration, associated with 86 earthquakes. According



to ICEF, these anomalies have been rarely recorded by more than one or two instruments, and often at distant sites but not at sites closer to the epicenter, therefore the correlation is not really significant.

11.3.4 Electromagnetic Variations

Several measurements of the electro magnetic signal (Seismic Electrical Signals, SES) caused by stress and strain variation due to pre-seismic activities have been observed in the past (Park 1996). So, the collected data has allowed researchers to do statistical analysis in order to consider these variations as earthquake precursors.

In 1981, professors P. Varotsos, K. Alexopoulos and K. Nomicos (VAN group) (Varotsos et al. 1981) claimed that by measuring geoelectric voltage it is possible to predict earthquakes of magnitude larger than 2.8 within the Greece territory at least 7 h before the main shock. In 1986, the same research group downsized the dimensions of the predicted parameters. An interesting result was observed in 2006, when a SES variation was recorded almost simultaneously with East Kythira earthquake (Fig. 11.4).

The analysis of the wave propagation of SES in the Earth's crust (Bernard and Le Mouel 1996) proofed the physical impossibility for signals with the amplitude reported by the VAN method to be transmitted over several hundred kilometers from the epicenter to the monitoring station. Later, the VAN method was criticized as statistically inconsistent because 74% of the seismic events in the considered catalog were false while 14% had uncertain correlation.

In the same year, the Journal Geophysical Research Letters presented a debate on the statistical significance of the VAN method. The largest part of reviewers

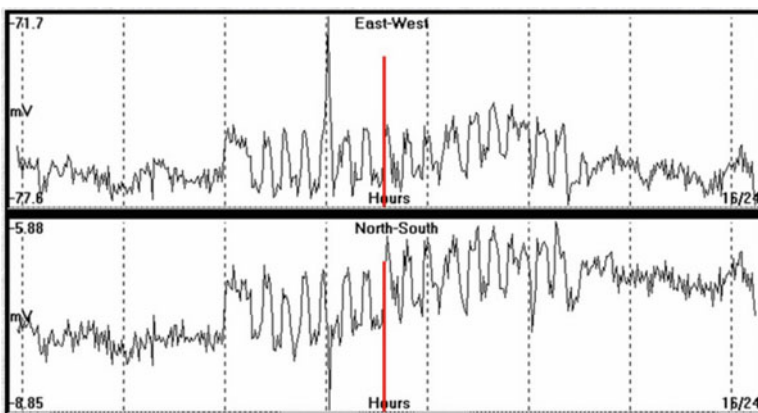


Fig. 11.4 Seismic Electrical Signals recorded in Greece almost concurrently with East Kythira earthquake (2006)

claimed that VAN method was statistically insignificant. Following this debate, the VAN method has been further modified in 2001 to take into account the time series analysis.

11.3.5 Precursory Seismicity Patterns

Currently the catalogues of earthquakes represent the most widely available geophysical data, collected systematically for quite a prolonged period of time; that is why most of the proposed methods for earthquake prediction are based on specific changes of background seismicity. Even if the ultimate validation of precursors may come only from the tests in forward predictions, the availability of earthquake catalogues allows for a formal analysis of possible anomalies in seismic activity, which may precede the strong events. Several possible scenarios of precursory seismic activity have been proposed; nevertheless, only a few formally defined algorithms allow for a systematic monitoring of seismicity, as well as for a widespread testing of their performances. Nowadays, one of the most promising approaches is represented by the intermediate-term middle-range earthquake predictions (i.e. with a characteristic alarm-time from a few months to a few years and a space uncertainty of hundreds of kilometers) based on the detection of formally defined variations in the background seismicity that precedes large earthquakes in a predefined area. In fact, the formal analysis of the seismic flow evidenced that specific patterns in the events below some magnitude threshold, M_0 , may prelude to an incumbent strong event, with magnitude above the same threshold M_0 . An essential step, when analyzing premonitory seismicity patterns, consists in the definition of the area where precursors have to be searched, the area of investigation, which increases with the size of the events to be predicted.

11.4 Earthquake Prediction and Time-Dependent Seismic Hazard Scenarios

Recently the research group from the University of Trieste (<http://www.geoscienze.units.it/>) developed an integrated neo-deterministic approach for seismic hazard assessment that combine different pattern recognition techniques, designed for the space-time identification of strong earthquakes, with algorithms for the realistic modeling of seismic ground motion. The integrated approach allows for time dependent definition of the seismic input through the routine updating of earthquake predictions.

11.4.1 Algorithms for Intermediate-Term Middle Range Earthquake Prediction

Different methods have been developed during the last decades, which permit to identify the areas characterized by an increased probability of strong earthquakes occurrence, based on a quantitative analysis of seismicity at the middle-range intermediate-term space-time scale. In this section we consider two algorithms, namely CN (Keilis-Borok and Rotwain 1990) and M8 algorithms (Keilis-Borok and Rotwain 1990), that are based on a multiple set of premonitory patterns and have been designed following the general concepts of pattern recognition. Quantification of the seismicity patterns is obtained through a set of empirical functions of seismicity, each representing a reproducible precursor, whose definition has been guided by the theory of complex system and laboratory experiments on rocks fracturing. Specifically, the functions, which are evaluated on the sequence of the main shocks occurred within the analyzed region, account for increased space-time clustering of moderate size earthquakes, as well as for specific changes in seismic activity, including anomalous activation and quiescence.

The results of the global real-time experimental testing of M8 and CN algorithms allowed for a statistical assessment of their predictive capability (e.g. Kossobokov 2013), as confirmed by ICEF Report (Jordan et al. 2011). These indicate the possibility of practical earthquake forecasting, although with limited accuracy (i.e. with a characteristic alarm-time ranging from a few months to a few years and a space uncertainty of hundred kilometers). The recent M8.3 earthquake, which struck Chile on September 16 2015 (Fig. 11.5), scores amongst the successful predictions in the M8 on-going real-time experiment for the great (M8.0+) and major (M7.5+) earthquakes worldwide (see <http://mitp.ru/en/default.html>).

These methodologies are applied and routinely tested (since 2003) also in the Italian region and its surroundings (Peresan et al. 2011). Actually, Italy is the only region of moderate seismic activity where the two algorithms CN and M8S (i.e. a stabilized variant of M8) are applied simultaneously for the routine intermediate-term middle-range earthquake prediction of earthquakes with magnitude larger than a given threshold (namely 5.4 and 5.6 for CN algorithm, and 5.5 for M8S algorithm). The routinely updated results and a complete archive of predictions are made available on-line via the following website: (<http://www.geoscienze.units.it/esperimento-di-previsione-dei-terremoti-mt.html>).

The results obtained so far evidenced the high confidence level (above 97%) of the issued predictions by real-time monitoring (Peresan et al. 2005). The probability gain associated with CN and M8S predictions for the Italian territory can be grossly estimated between 2 and 4, in good agreement with the independent estimates by ICEF (Jordan et al. 2011). Noticeably, these conclusions are based rigorously on the results from real-time prospective testing of the considered prediction algorithms, and thus reflect their effective predictive capability.

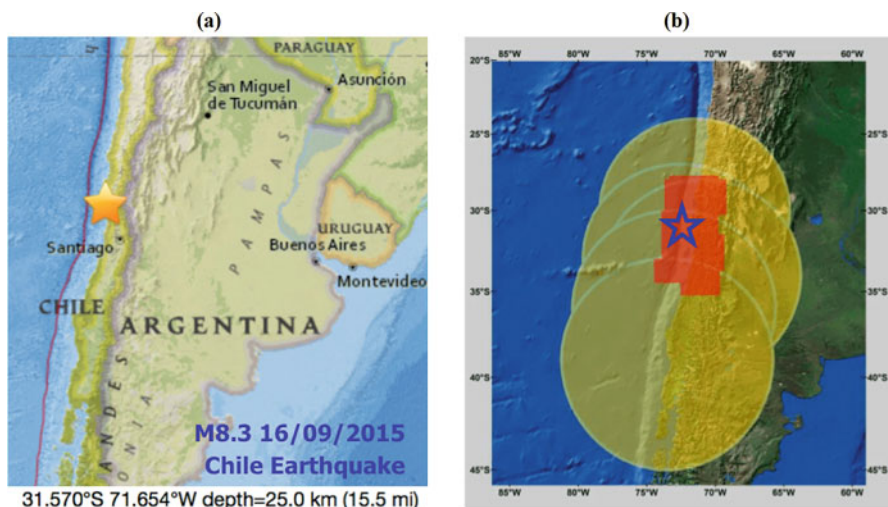


Fig. 11.5 Prediction of the M8.3 Chile earthquake (a) Map of the epicenter as reported by USGS (<http://earthquake.usgs.gov>) and (b) map of ongoing alarms at the time of the earthquake occurrence, as identified by M8 algorithm (yellow circles) and, in second approximation, by MSC algorithm (red area), (<http://www.mitp.ru/en/index.html>)

11.4.2 *Neo-Deterministic Time-Dependent Seismic Hazard Scenarios for the Italian Territory*

An operational integrated procedure for seismic hazard assessment has been developed that allows for the definition of time-dependent scenarios of ground shaking, through the routine updating of earthquake predictions, performed by means of CN and M8S algorithms. Accordingly, a set of neo-deterministic scenarios of ground motion at bedrock, proper for the time interval when a strong event is likely to occur within the alerted areas, can be defined based on the calculation of realistic synthetic seismograms, as described in detail in Peresan et al. (2005).

Following the procedure for the neo-deterministic seismic zoning, NDSHA (Panza et al. 2014), ground motion is defined by full waveforms modeling, starting from the available information on the Earth structure, seismic sources, and the level of seismicity of the investigated area. Seismic sources considered for ground motion modeling are defined based on the largest events reported in the earthquake catalogue, as well as incorporating the additional information about the possible location of strong earthquakes provided by the morphostructural analysis, active fault studies and other geophysical indicators (including Earth Observations, like GPS), thus filling in gaps in known seismicity.

The time-dependent ground motion scenarios for the Italian territory are routinely updated every two months since 2006. A strong earthquake ($M_w = 6.1$)

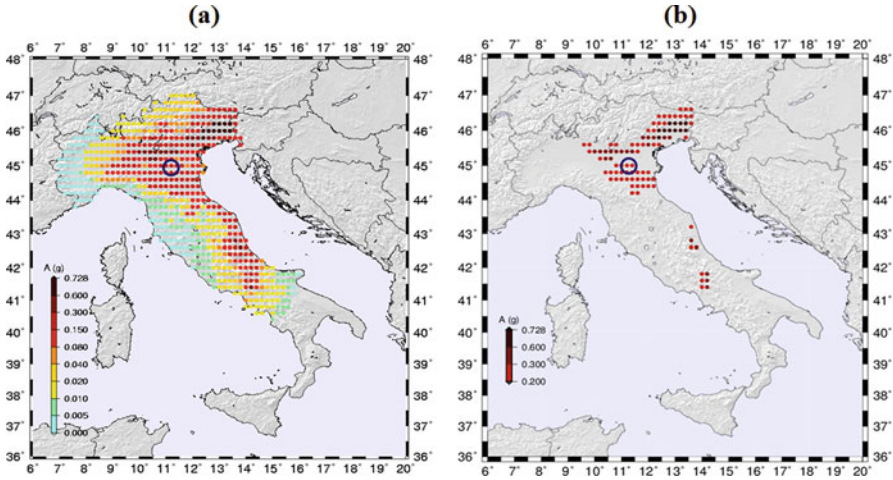


Fig. 11.6 Time-dependent scenarios of ground shaking, associated to an alarm declared by CN algorithm for the period 1 March 1 May 2012: (a) Peak Ground Acceleration map, computed considering simultaneously all of the possible sources within the alarmed area and for frequencies up to 10 Hz; (b) same as map (a), but for $A > 0.2$ g. The circle evidences the area within 30 km distance from the epicenter of the Emilia earthquake (After Peresan et al. 2012).

hit the Emilia region, Northern Italy, on 20th May 2012. The time-dependent ground shaking scenario associated to CN Northern region defined for the period 1 March 2012 1 May 2012, correctly predicted the ground shaking, as large as 0.25 g, recorded for this earthquake (Fig. 11.6). Notably, the ground shaking for this earthquake systematically exceeded the values expected at the bedrock in the area according to current Italian seismic regulation (i.e. $PGA < 0.175$ g), which is based on a classical PSHA map (Gruppo di Lavoro 2004). Since the time NDSHA time-dependent scenarios are regularly computed, namely starting on 2006, this is the second large earthquake that struck the Italian territory, along with L'Aquila earthquake ($M = 6.3$, 2009). In both cases the method correctly predicted the observed ground motion, although L'Aquila earthquake scores as a failure in the earthquake prediction experiment, because the epicenter was located about 10 km outside the alarmed territory (Peresan et al. 2005).

The provided examples of the existing operational practice in predicting seismic ground shaking are perfectly in line, or even anticipating, the guidelines and recommendations given in the Report of the International Commission on Earthquake Forecasting (Jordan et al. 2011). The results acquired in the prospective application of the time-dependent NDSHA approach provide information that can be useful to assign unbiased priorities for timely mitigation actions. As an example, for sites where large ground shaking values (e.g. greater than 0.2 g) are estimated at bedrock (Fig. 11.6), further investigations can be performed taking into account the local soil conditions, to assess the performances of relevant structures, such as historical and strategic buildings (e.g. following the procedures described at: [المنارة للاستشارات](http://www.provincia.trieste.it/opencms/opencms/it/attivita-servizi/cantieri-</p>
</div>
<div data-bbox=)

della-provincia/immobili/Programma_verifiche_sismiche/ in addition to natural low key actions as described in Kantorovich and Keilis-Borok 1991).

11.5 Notable Predictions

The scientific or quasi-scientific basis for earthquake prediction methods derived from important studies carried out before some earthquakes. In the following part, they are discussed in order to explain the statistical and scientific observations based-on some precursors.

11.5.1 Haicheng (China, 1975)

On 4 February 1975 a 7.3 magnitude earthquakes occurred in China. Its epicenter was located near to the small town of Haicheng (Fig. 11.7).

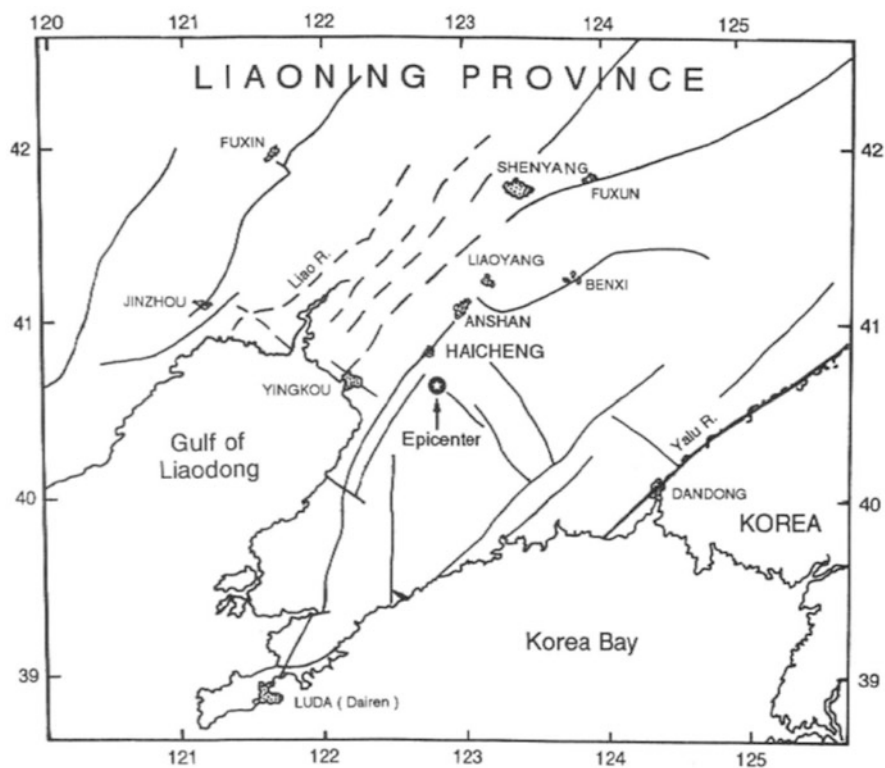


Fig. 11.7 Haicheng area and major faults in Liaoning Province

The fore-shock sequence recorded in the days before the main shock was recurring. The first seismic activity was on February 1 with a magnitude of about 0.5, while 2 days later more than eight tiny shocks were detected. Twenty four hours before the earthquake the fore-shock sequence began more intense and the number of recorded shocks were about 20. Few hours before the earthquake the fore-shock activity continued with a frequency of five shocks/hour (the largest one was with $M = 4.7$). The intense and repetitive fore-shock activity had led to successfully predict the main shock which occurred at 19:36 CST. Local politicians ordered the evacuation the day before the earthquake took place, and saved many lives. Since 1971, vertical fault creep measurements had been conducted across the right-lateral Jinzhou fault. The measurements showed that the elevation offset was constant in the first 20 months, then increased in the second half of 1973 and finally reversed the direction on October 1974. This trend was opposite with respect to the usual observations in the region (geodetically measured in 1971), so this phenomenon was considered an anomaly. In December 1974, a group of seismologists developed a synthetic short-term prediction for small earthquakes in the region according to the studies conducted in the Dandong zone. Two days after, an earthquake swarm with maximum magnitude of 4.8 occurred between the north zone of Dandong and Haicheng. Later on, the earthquake swarm was recognized as correlated with the water movements in Qinwo Reservoir.

Haicheng earthquake was also a notable case of animal anomalous behavior. It was shown experimentally an increase of 2 in the ground temperature that has interrupted the hibernation of the snakes. More than 20 snakes were found frozen to death in the evening because they have been fooled by the warm weather. Also other types of anomalous animal behavior was observed continuously especially in the rural areas (Fig. 11.8).

11.5.2 *Parkfield (USA, 1985–1993)*

Various earthquakes occurred near the town of Parkfield in California and they have been studied by geologists who installed an elaborate array of seismometers, creep meters, strain meters, and other instruments since 1985. Already since 1857, five moderate earthquakes occurred in the Parkfield section of the San Andreas Fault. In Fig. 11.9 is shown the epicenter distribution of the earthquakes in the period 1975–1984.

The typical earthquakes in the region have similar faulting mechanism, magnitude, rupture length, location, and, in some cases, the same epicenter and direction of rupture propagation as earlier shocks. The earthquakes in 1979 at Coyote Lake and in 1984 at Morgan Hill (magnitude 6) are examples of characteristic earthquakes, apparently repeating the shocks in 1897 and 1911.

In 1985, Bakun and Lindh (1985) Lindh proposed to model the process of the characteristic earthquakes on Parkfield region, assuming a deterministic recurrence law for the earthquakes. Later Bakun (1988) observed a recurrence of shocks

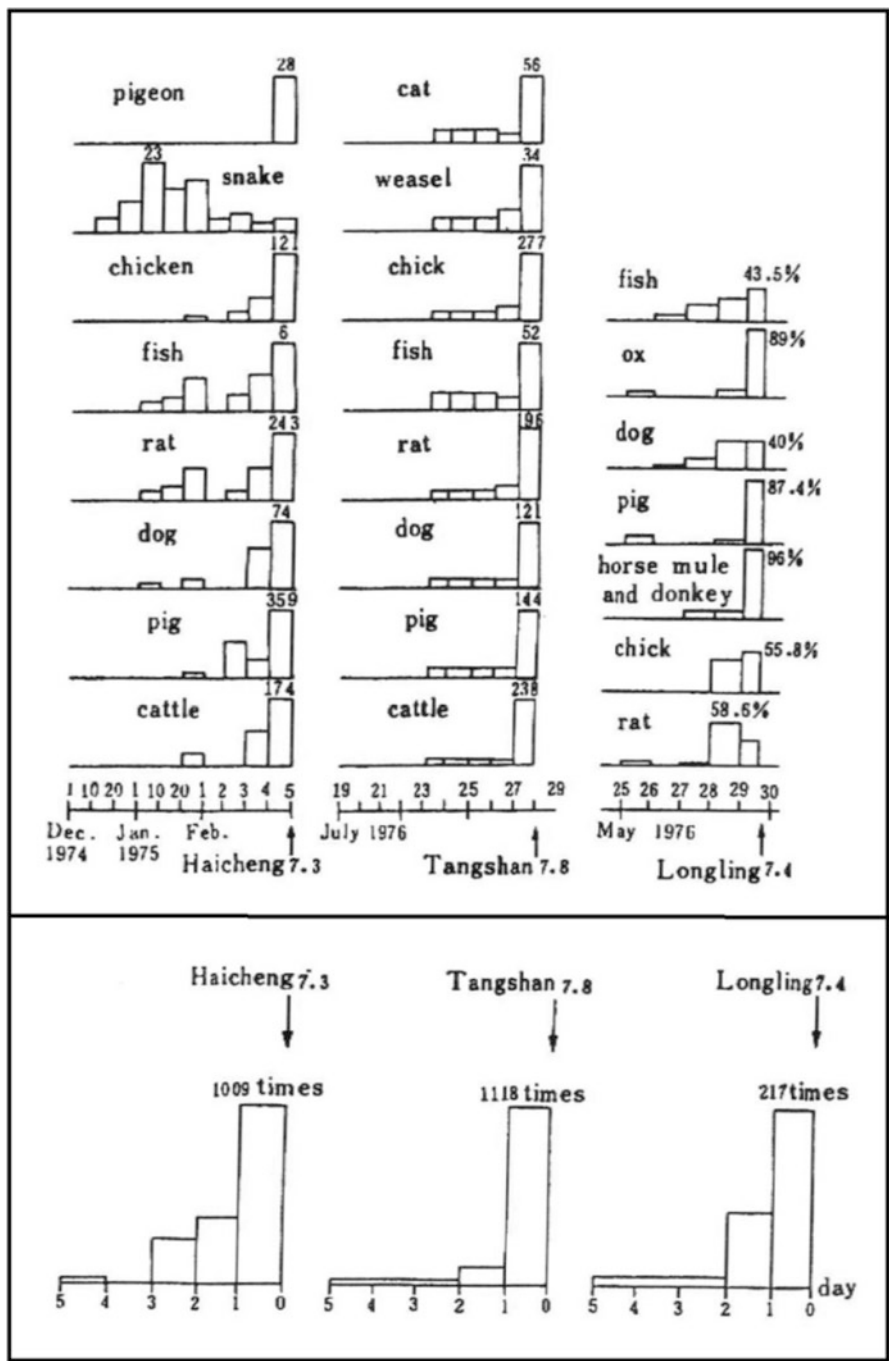


Fig. 11.8 Animal precursors observed in Chinese earthquake

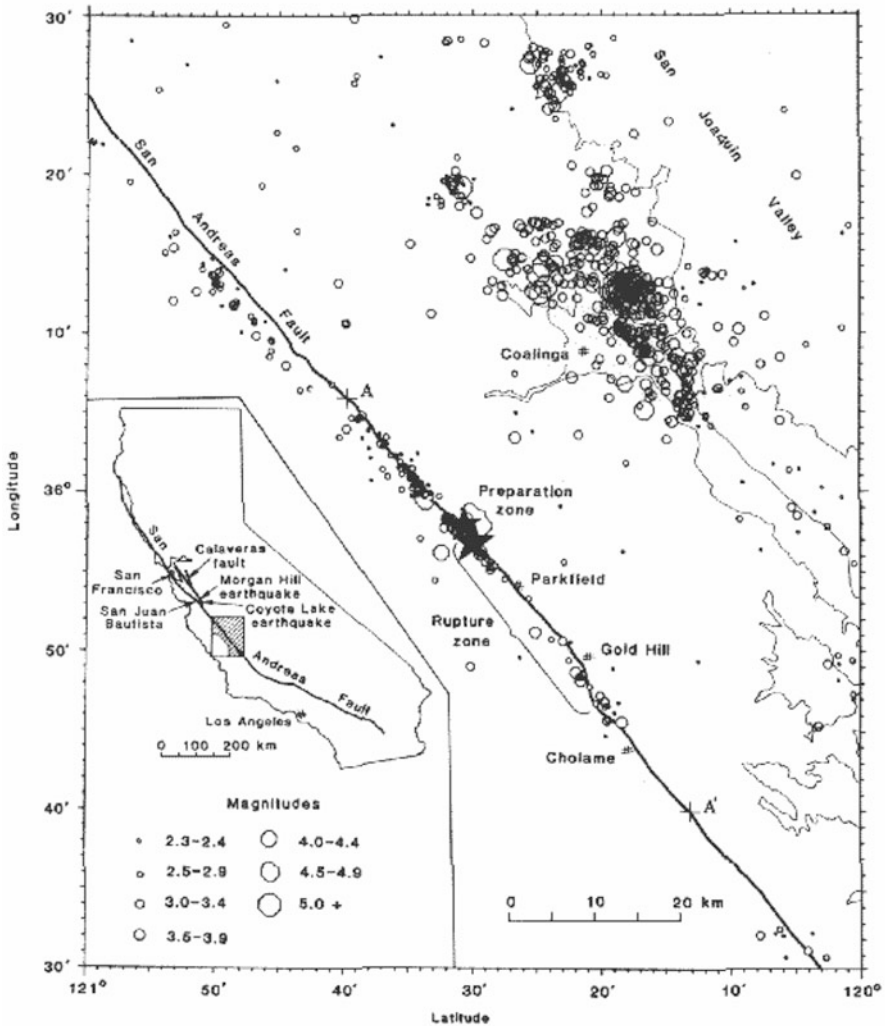


Fig. 11.9 Map of earthquake epicenters (1975–1984) relative to the trace of the San Andreas fault (bold line) and the epicenters of the fore-shock (ML 5.1) and the main shock in 1966 (small and large stars, respectively, near the center of the map) (Courtesy of USGS 2008)

with magnitude 6 every 21–22 years, having the same epicenter and rupture area. Figure 11.10 illustrates the Parkfield recurrence model considering the earthquake sequences in 1881, 1901, 1922, 1934, and 1966.

According to this model the prediction (with 95% of confidence) of the next earthquake (with magnitude 6) would hit around 1988, or 1993 but this prediction was unsuccessful. Only on October 20th 1992, an earthquake of magnitude 4.7



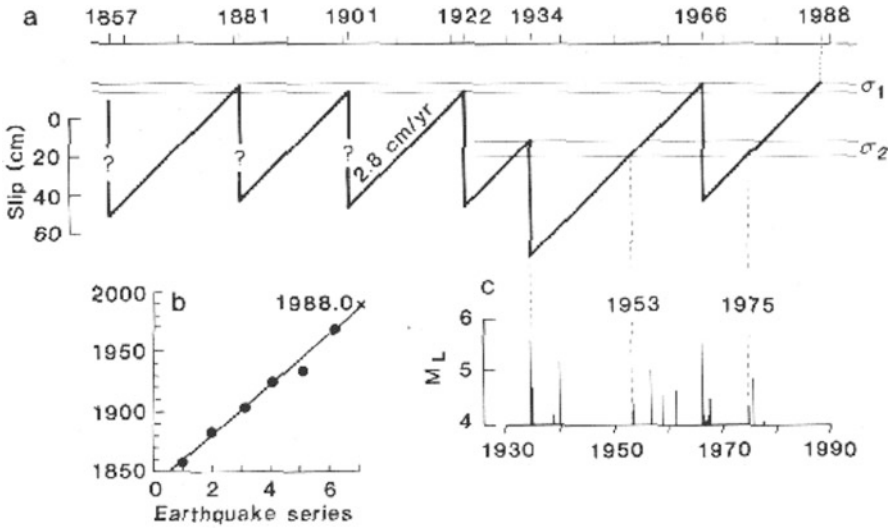


Fig. 11.10 The Parkfield recurrence model (Courtesy of USGS 2008)

occurred near Parkfield (California) and an alert was broadcast in five different counties. After this shock, none of the earthquakes predicted by the model happened.

11.5.3 Loma Prieta (USA, 1989)

On October 17th 1989, a 6.9 moment magnitude earthquake with epicenter in the Santa Cruz Mountains caused significant damage in the San Francisco Bay area. One year later, in 1990 USGS claimed that this earthquake was an anticipated event. According to USGS, *the Loma Prieta earthquake demonstrated that meaningful predictions can be made of potential damage patterns and that, at least in well-studied areas, long-term forecasts can be made for future earthquake locations and magnitudes. Such forecasts can serve as a basis for action to reduce the threat major earthquakes pose to the United States.*

Lindh et al. (1978) claimed that the southernmost part of the rupture zone of the 1906 San Francisco earthquake had slipped much less than the points to the north, and thus had a high probability of rupturing within the next few decades. In addition, some anomalous not quantitative phenomena were observed but not strictly correlated to the earthquake. For example, Silver and Valettsilver (1992) observed variations in the period of eruption of a geyser. Harris (1998) reviewed some scientific forecasts, but none of these could be rigorously tested.

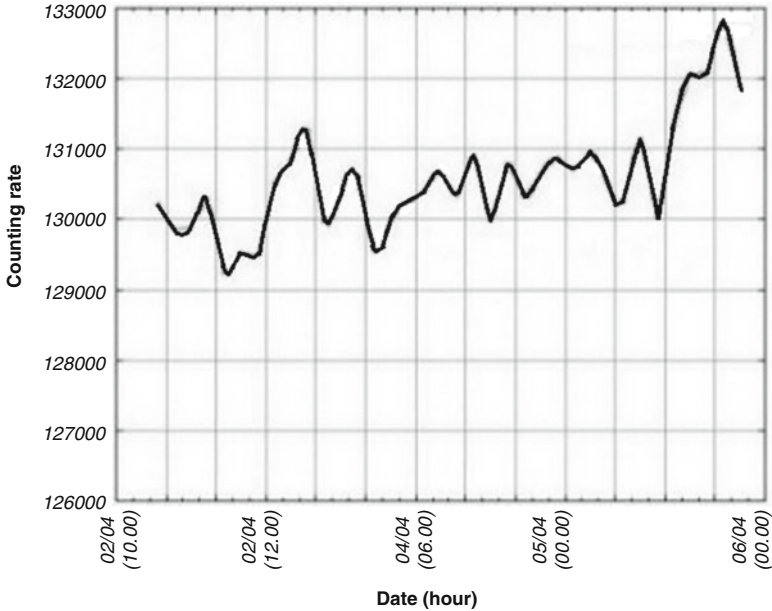


Fig. 11.11 Trend of radon level from May 2nd to May 6th in L'Aquila region (2009)

11.5.4 L'Aquila (Italy, 2009)

On April 6th 2009, an earthquake with magnitude 6.3 occurred in the Abruzzo region of Central Italy. Many damages have been recorded in the city of L'Aquila and its surrounding area. On December 2008, low-level swarm earthquakes occurred in the Abruzzo region and on March 30th, L'Aquila was struck by a shock with magnitude 4. Three days before, the seismologist Giampaolo Giuliani predicted an earthquake within 24h and a day later he made a second prediction about a catastrophic earthquake in the range of 6–24 h. The city of Sulmona was evacuated, but the earthquake did not occur. These predictions were based-on the anomalies in the radon emission, that Giuliani monitored using instruments designed and built in the Physic Lab under the Gran Sasso Mountain.

Some hours before LAquila seismic event of April 6th, Giuliani recorded an increase of radon level (Fig. 11.11).

He tried to alert the public, but he was unsuccessful. After the main seismic shock of April 6th, the debate about the radon emission as earthquake precursor started. Dr. Marzocchi (Chief scientist of INGV) examined two documents containing examples of radon concentrations measured by Giuliani. He focused on the problem of having many peaks in the radon measurements in a very short time period. In addition, there was no correlation between the size of the peaks and the magnitudes of the subsequent quakes. For the mentioned reasons, the recorded radon levels used by Giuliani as earthquake precursors were not considered scientifically significant.

Other scientists also claimed that there is no connection between the radon emission and the earthquakes, thus the radon emission cannot be considered as an earthquake precursor.

Recently in 2013, Pitari et al. (2014) concluded that *no evidence has been found on the deterministic character of the observed radon emission changes to forecast the location and timing of the earthquakes, or that seismic activity before a major event does necessarily produce significant radon increases in the atmosphere boundary layer.*

References

- Bakun WH, Lindh AG (1985) The parkfield, California, prediction experiment. *Earthq Prediction Res* 3(3–4):285–304
- Bernard P, Le Mouel J (1996) On electrotelluric signals. A critical review of VAN, pp 118–152
- Brown R, Kulik J (1977) Flashbulb memories. *Cognition* 5(1):73–99
- Cicerone RD, Ebel JE, Britton J (2009) A systematic compilation of earthquake precursors. *Tectonophysics* 476(3):371–396
- Geller RJ (1997) Earthquake prediction: a critical review. *Geophys J Int* 131(3):425–450
- Hammond AL (1973) Earthquake predictions: breakthrough in theoretical insight? *Science (NY)* 180(4088):851
- Harris RA (1998) Forecasts of the 1989 Loma Prieta, California, earthquake. *Bull Seismol Soc Am* 88(4):898–916
- Jordan T, Chen YT, Gasparini P, Madariaga R, Main I, Marzocchi W, Papadopoulos G, Yamaoka K, Zschau J (2011) Operational earthquake forecasting: state of knowledge and guidelines for implementation. *Ann Geophys*
- Kantorovich L, Keilis-Borok V (1991) Earthquake prediction and decision-making: social, economic and civil protection aspects. In: *International conference on earthquake prediction: state-of-the-art*, pp 586–593
- Keilis-Borok V, Rotwain I (1990) Diagnosis of time of increased probability of strong earthquakes in different regions of the world: algorithm CN. *Phys Earth Planet Inter* 61(1–2):57–72
- Kossobokov VG (2013) Earthquake prediction: 20 years of global experiment. *Nat Hazards* 69(2):1155–1177
- Gruppo di Lavoro MP (2004) Redazione della mappa di pericolosità sismica prevista dall'Ordinanza PCM 3274 del 20 marzo 2003. Rapporto Conclusivo per il Dipartimento della Protezione Civile, INGV, Milano-Roma, 5 Apr 2004
- Lindh A, Lockner D, Lee W (1978) Velocity anomalies: an alternative explanation. *Bull Seismol Soc Am* 68(3):721–734
- Lott DF, Hart BL, Howell MW (1981) Retrospective studies of unusual animal behavior as an earthquake predictor. *Geophys Res Lett* 8(12):1203–1206
- Panza G, Peresan A, Magrin A (2014) Neo-deterministic seismic hazard scenarios for friuli venezia giulia and surrounding areas. Report, ISPRA– Istituto Superiore per la Protezione e la Ricerca Ambientale – Servizio Geologico d'Italia
- Park SK (1996) Precursors to earthquakes: seismoelectromagnetic signals. *Surv Geophys* 17(4):493–516
- Peresan A, Kossobokov V, Romashkova L, Panza G (2005) Intermediate-term middle-range earthquake predictions in Italy: a review. *Earth-Sci Rev* 69(1):97–132
- Peresan A, Zuccolo E, Vaccari F, Gorshkov A, Panza GF (2011) Neo-deterministic seismic hazard and pattern recognition techniques: time-dependent scenarios for North-Eastern Italy. *Pure Appl Geophys* 168(3–4):583–607

- Peresan A, Kossobokov VG, Panza GF (2012) Operational earthquake forecast/prediction. *Rendiconti Lincei-Scienze Fisiche E Naturali* 23(2):131–138
- Pitari G, Coppari E, De Luca N, Di Carlo P (2014) Observations and box model analysis of radon-222 in the atmospheric surface layer at Laquila, Italy: March 2009 case study. *Environ Earth Sci* 71(5):2353–2359
- Silver PG, Valettsilver NJ (1992) Detection of hydrothermal precursors to large northern California earthquakes. *Science* 257(5075):1363–1368
- USGS (2008) The 2008 U.S. geological survey national seismic hazard maps. <http://earthquake.usgs.gov/research/hazmaps/>
- Varotsos P, Alexopoulos K, Nomicos K (1981) Seven-hour precursors to earthquakes determined from telluric currents. *Praktika Acad Athens* 56:417–433
- Whitcomb JH, Garmany JD, Anderson DL (1973) Earthquake prediction – variation of seismic velocities before San Francisco earthquake. *Science* 180(4086):632–635

Chapter 12

Seismic Input



Abstract The chapter introduces the main concepts of the seismic input definition according to the seismic codes. In particular, the Italian (NTC-08, Nuove Norme Tecniche per le Costruzioni. Gazzetta Ufficiale della Repubblica Italiana, 2008) and European (1998-1 E, Design of structures for earthquake resistance Part 1: general rules, seismic actions and rules for buildings. European Committee for Standardization, 2004) standards are discussed in detail. Furthermore, the Response Spectrum method and the use of time histories as seismic input are analyzed.

12.1 Introduction

Nowadays, all the main seismic standards are structural and performance based. This aspect can be observed in the definition of different particular conditions (LS). Each of them is characterized by different hazard levels, or rather, several exceedance probabilities P_{VR} in a given reference period V_R . This approach leads to approximately removing the time unpredictability of the seismic excitation, but its spatial and quantity prediction remains the main problem.

In practice, the seismic action at a given limit state can be evaluated with simplified methods or according to more rigorous methodologies, depending on the type and importance of the structure to be designed.

For ordinary structures like residential multistory buildings, the seismic action can be defined using a given response spectra. If T_{ref} is the period of interest of the structure, the $S_a (T = T_{ref})$ will be the spectral acceleration to be used in the analyses. This simplified method is based on the response of a SDOF system to a seismic excitation, so it can be used for regular and small size structures.

In the remaining cases, the seismic input has to be defined by referring to the complete acceleration histories expected on the structures.

12.2 Brief History of Italian Seismic Standards

The first European seismic standards were released after the Calabrian earthquake in 1783 during the Bourbon Kingdom of Naples. They included design rules for reconstructions which were valid in the Reggio Calabria region. After 1859 Norcia earthquake, the Pontifical seismic standards were released and they included obligatory technical rules aimed at the reconstruction of the civil buildings and factories. Nevertheless, the first seismic standards of the Italian Reign were released with the R.D.(Royal Decree) *n*^o 193/1908 after the catastrophic Reggio Calabria and Messina earthquake of 1908. Since the seismic engineering knowledge was not yet developed, these rules included some empirical prescriptions for both existing and new buildings. Additional new rules were released after the earthquakes which occurred in Marsica (1915/01/13 and 1930/11/01), Irpinia (1930/07/24 and 1962/08/21) and Belice (1968/01/15), to modify and integrate the existing ones. All of these regulations are considered to be the *first generation seismic standards*. It is interesting to notice the evolution of the seismic zonation of the Italian territory after the occurrence of the catastrophic events. In 1909 only the Calabrian and Messina zones were considered to be seismic regions. After Marsica earthquake (1915), Abruzzo and nearby areas were added as Italian seismic zones. In 1927 two categories of seismic zones (I and II) were introduced and they were modified again after the Irpinia and Belice events.

The *second generation seismic standards* were released in 1974 with the law *n*^o 64 of 1974/02/02 in which the first earthquake engineering concepts and knowledge were adopted. This standard was valid for different types of structures, such as masonry buildings, bridges etc., and they followed the first seismic analyses developed in the United States. The technical standards mainly refer to the maximum height, the minimum distances between two buildings and the vertical and horizontal actions to be considered in the design of the structural elements (using an equivalent static model). After the Friuli earthquake (1975/05/06), a new provision was released to add part of Friuli Region as a seismic zone. Only after the Irpinia earthquake (1980/11/23) two D.M.(Decrees of the Ministry) were issued that introduced an additional seismic zone III (low seismicity zone) and also included other Italian areas in the seismic classification. One of the most important regulations is D.M. 1996/01/16 (“*Norme tecniche per le costruzioni in zona sismica*”) in which structural analysis, execution and inspection standards for reinforced concrete, pre-stressed concrete and steel structures are contained. In addition, for the first time the Limit State (LS) was proposed even if the procedures are essentially based on the Allowable Stress Design method (ASD). The D.M. 1996 was important because the prescriptive approach used before was switched into a performance based approach.

The following standards are considered as *third generation rules*. The O.P.C.M. 3274/2003 was promulgated after the seismic event of San Giuliano di Puglia, which had a broad impact on the media. In this decree, the standardization task passed from the Ministry of Public Works (LL.MM.) to the Civil Protection

(National Emergency Authority of Italy). The general criteria for classifying the whole national territory according to seismic hazard was decided. The entire Italian geographical area was divided into four seismic zones. The complete and definitive version of the O.P.C.M. was published on May 10, 2005 according to the European Community prescriptions contained in Eurocode 8 (EC8). Furthermore, in 2005 the D.M. “*Norme tecniche per le costruzioni*” was issued in which all the prescriptions in terms of safety (including the seismic standards of the previous O.P.C.M.) are contained. Finally, in 2008/01/14 the latest D.M. with the title “*Applicazione delle nuove norme tecniche per le costruzioni (NTC2008)*” was published on the G.U. replacing the previous D.M. of 2005. In 2009, the *Circolare esplicativa n° 617* was added to the 2008/01/14 D.M.. In addition, with NTC2008, the technical standards pass from the Allowable-Stress Design method (ASD) to the Limit State Design method (LSD).

12.3 Elastic Response Spectra

The time-response of a structure for a generic earthquake is difficult to determine, as a high computational charge is requested and, at the same time, it identifies an inefficient engineering representation. The prediction of the maximum seismic action on the structure is obtained with more simple calculation procedures giving the most unfavorable structural response. In order to apply these concepts to any structure, the response spectra methodology is applied, in which the relationship between the maximum response of the structure (in terms of accelerations, velocities and displacements) and its fundamental period is calculated for a given strong motion. In fact, a generic structure can be described by stiffness and mass characteristics, which give information about the fundamental vibration frequency (ω_0) and then the fundamental period (T_0). Figure 12.1 schematically illustrates the elastic response spectra definition.

Fig. 12.1 Scheme of the definition of the elastic acceleration response spectra for a given strong motion

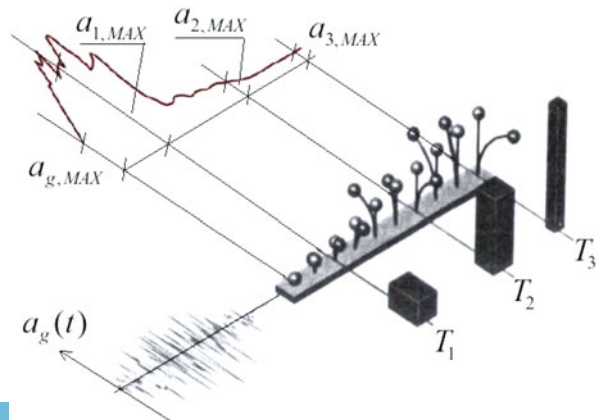


Figure 12.1 shows a series of structures approximately represented by a number of oscillators characterized by their own natural period (T_i). For each of them the maximum acceleration due to the strong motion ($a_g(t)$) is calculated and reported in the ordinates axis. The first oscillator is characterized by an infinite stiffness, or, in other words, it identifies the soil response. Thus, the maximum value of acceleration corresponding to the first oscillator ($a_{g,MAX}$) represents the peak ground acceleration, since it is defined as the maximum acceleration of the ground motion. The procedure just discussed can be carried out by numerical integration of the dynamic equation for each oscillator in the elastic field (Eq. 12.1).

$$m\ddot{u} + c\dot{u} + ku = -m\ddot{u}_g \quad (12.1)$$

where m , c and k represent the mass, the viscous damping and the stiffness of the oscillator, respectively, while u is the displacement at a generic time instant and \ddot{u}_g is the seismic acceleration applied at the base of the SDOF element. This procedure leads to building the elastic displacement response spectra (S_d), but observing the dynamic equation it is possible to deduce a simple relationship between the accelerations and the displacements in the ideal case of undamped system (Eq. 12.2).

$$\ddot{U} = \frac{k}{m}u = \omega^2u \quad (12.2)$$

where \ddot{U} is the absolute acceleration and ω is the angular frequency. Similarly, the expression reported above can be adopted in terms of maximum values (Eq. 12.3).

$$S_a(\omega) = \omega^2 S_d(\omega) \quad (12.3)$$

where $S_a(\omega)$ defines the generic spectral ordinates of the acceleration response. This formulation is correct for undamped structures, but, since this is only an ideal case, it is commonly called pseudo-acceleration response spectrum. In addition, the pseudo-velocity response spectrum can be obtained by referring to the Duhamel integral (Eq. 12.4) which can be used in order to solve the dynamic problem.

$$u(t) = \frac{1}{\omega_D} \int_0^t \ddot{u}_g(\tau) e^{-\xi\omega(t-\tau)} \sin \omega_D(t-\tau) d\tau \quad (12.4)$$

For an under-damped system, the natural angular frequency ω can be assumed equal to the damped angular frequency ω_D , then the argument of the integral is almost coincident with the velocity at time t . In terms of maximum values, the relationship between the displacements and velocities can be written as shown in Eq. 12.5.

$$S_v(\omega) \cong \omega S_d(\omega) \quad (12.5)$$

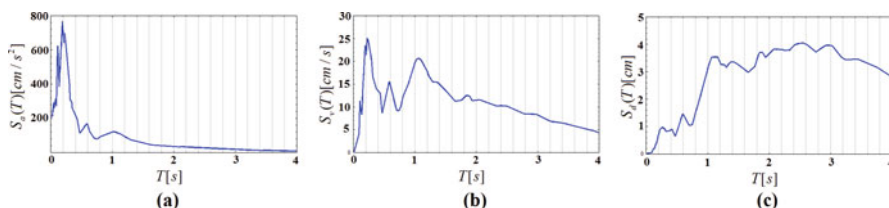


Fig. 12.2 Acceleration (a), velocity (b) and displacement (c) response spectra for Kozani-Prefecture record (Kozani mainshock, 13/05/1999)

where $S_v(\omega)$ represents the pseudo-velocity spectral ordinate. The accuracy of the S_v and S_a expression is inversely proportional to the damping of the structure. Figure 12.2 shows all the spectra obtained from OPENSIGNAL 4.0 (Cimellaro and Marasco 2015) for the corrected record of Kozani-Prefecture ($f_{(min)} = 0.25$ Hz, $f_{(max)} = 25$ Hz, $n = 4$).

Alternatively, the acceleration, velocity and displacement spectra can be evaluated with classical methods of solution of equations of motion.

12.4 Uniform Hazard Spectrum (UHS)

The UHS is a response spectrum in which every spectral acceleration has the same return period. UHS is always associated to a given hazard level and exceedance probability. It is determined by enveloping the results of the PSHA. The interactive hazard maps provide the spectral accelerations in ten period values for ten different exceedance probability (from 2% to 81%). In Fig. 12.3 the uniform hazard spectra, related to the median level (50 percentile), is obtained by the interactive maps for the southern Italian site of Soveria Mannelli (16.3859 longitude, 39.0969 latitude, close to Lamezia Terme).

The UHS is evaluated by enveloping the response spectrum associated to different earthquakes scenario at a given site that provide distinct contributions to the UHS as it was observed by Reiter (1991). According to him the contribution to the hazard can be classified into two categories of earthquakes: the small nearby earthquakes influence mainly the small periods of the spectrum, while large distant earthquakes have a greater contribution in the hazard definition for large periods (Fig. 12.4).

The idea behind the UHS is to design a building with the same risk level, which means considering ground motions parameters with equal exceedance probability independent from the period of the structure and from the specific seismic event.

For this reason, the Uniform Hazard Spectrum is an efficient way of representing the seismic hazards at a given site, but at the same time, the spectral values at each period cannot occur in a single ground motion record. In other words, the amplitude

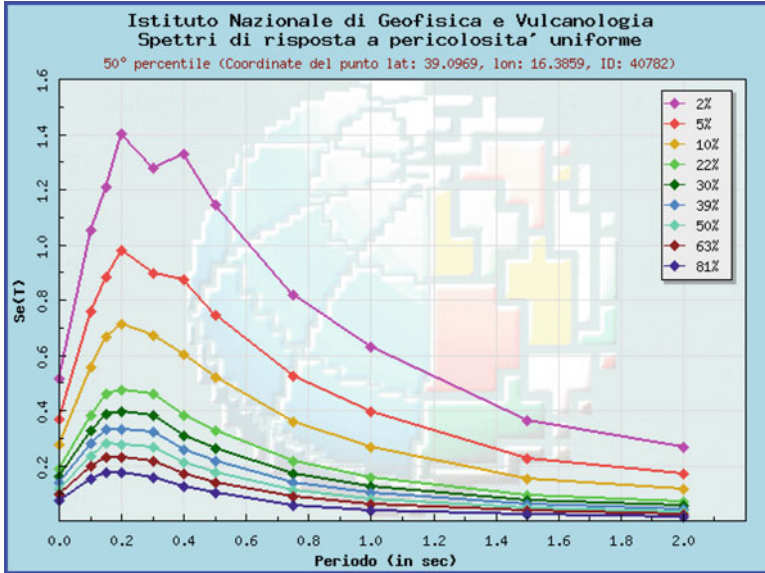


Fig. 12.3 Uniform hazard spectra for a southern Italy site of Soveria Mannelli

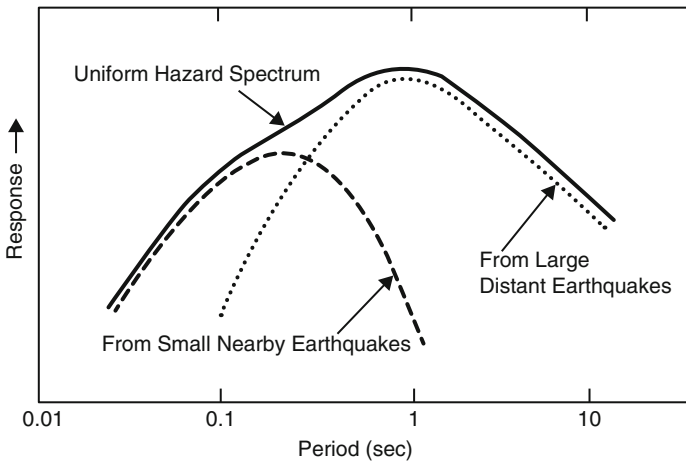


Fig. 12.4 Scheme of UHS with the two earthquake contributions

of a single ground motion is not equally spaced-out from the UHS over all periods. Thus, the uniform hazard spectrum is not very representative as a target spectrum for a single individual ground motion. The lack of correlation between the UHS and a single seismic event with given magnitude M and epicentral distance R_{epi} can be

solved using the hazard deaggregation. This process leads to the evaluation of the effective contribution in the hazard analysis of each pair $M - R_{epi}$ (Eq. 12.6).

$$\lambda_m(m_j, r_j) \approx P(m_j = M) \cdot P(r_j = R_{epi}) \cdot \sum_{i=j}^{N_s} v_i \cdot P(Y > \bar{Y}/m_j, r_j) \quad (12.6)$$

where λ_i is the contribution of the $M - R_{epi}$ pair for a given mean annual exceedance probability λ_m . The expression reported above represents the inverse process used for evaluating the hazard in the PSHA. Thus, from the all magnitude and epicentral distance values found, the preponderant pair can be defined in the hazard analysis. The S1 project of INGV (Barani et al. 2009) also provides the deaggregation study for every grid point and in Fig. 12.5 is shown an example of the deaggregation results for a specific site. The deaggregation parameters can be used for several purposes including the ground motion selection (Cimellaro et al. 2011; Cimellaro 2013).

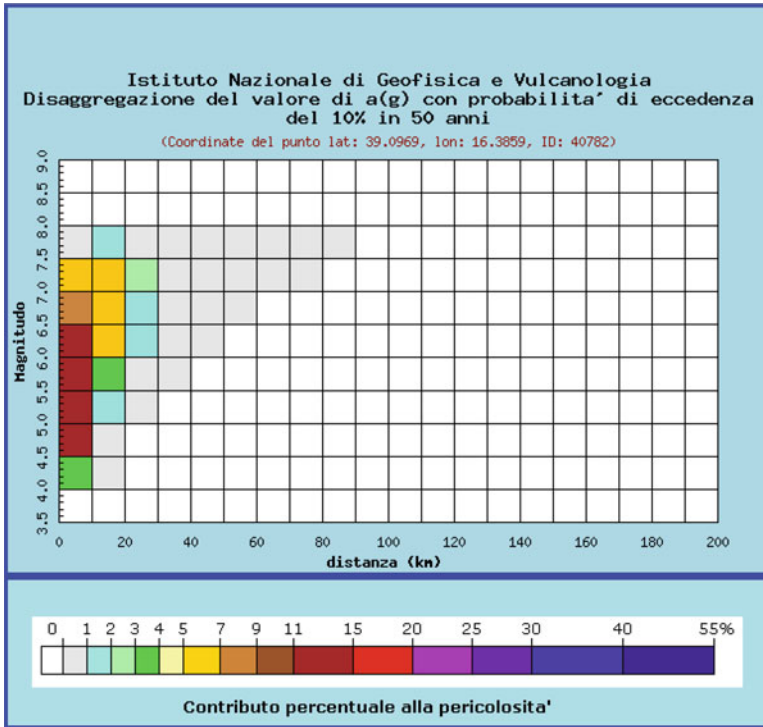


Fig. 12.5 Deaggregation hazard contributions for a southern Italy site of Soveria Mannelli

12.5 Design Response Spectrum (DS)

The Design Response Spectra (DS) change worldwide according to the codes (e.g. Uniform Building Code, Eurocode 8, and International Building Code, Italian code etc). This section will focus on the description of the Italian Design Spectrum according to NTC08 (2008) and EC8 (1998-1 2004).

12.5.1 Design Response Spectrum According to NTC08 and EC8

In all the International, European and National standards, the hazard definition refers to the PSHA, because this approach is capable of providing the seismic design parameters for different measures of performance level of the structures (Limit States (LS)) (Cimellaro and Reinhorn 2011). Each of them is defined through the exceedance probability P_{VR} in a given period V_R . The choice of the period of interest is associated to the requested structural durability and to its importance. In other words, the V_R parameter represents the period (expressed in years) in which the structure maintains its functionality (design life of the structure). In the Italian standards, this parameter is expressed (Eq. 12.7) by the product between the design life of the structure (V_N) and a coefficient depending on the importance class defined in the section 2.4.2 of NTC 2008 reported in Table 12.1.

$$V_R = V_N \cdot C_U \quad (12.7)$$

In the European standards the *classes of importance* are summarized in Table 12.2.

As discussed, the probabilistic approach refers to a Poissonian model, in which the parameters above are expressed as shown in the Eq. 12.8.

$$T_R = -\frac{V_R}{\ln(1 - P_{VR})} \quad (12.8)$$

where T_R is the return period. In all the technique standards, two different categories of LS are identified: *Serviceability Limit State* (SLS) and *Ultimate Limit State* (ULS). SLS indicates the particular conditions after which there is loss of functionality for the structure, while the ULS are those associated with collapse

Table 12.1 Classes of importance and related coefficients for the European standards (EN1 1998-1)

Importance class	I	II	III	IV
Coefficient C_u	0.7	1.0	1.5	2.0

Table 12.2 Classes of importance and related coefficients for the European standards (EN1 1998-1)

Importance class	Buildings	Important factor γ_t
I	Buildings of minor importance for public safety, e.g. agricultural buildings, etc.	0.8
II	Ordinary buildings, not belonging in the other categories	1.0
III	Buildings whose seismic resistance is of importance in view or the consequences associated with a collapse, e.g., schools, assembly halls, cultural institutions etc.	1.2
IV	Importance for civil protection, e.g. hospital, fire stations, power plants, etc. importance for civil protection, e.g. hospital, fire stations,	1.4

Table 12.3 Limit states and related exceedance probabilities in 50 years according to the Italian seismic standard

Limit state (LS)		Exceedance probability
Serviceability limit state	OLS (SLO)	81%
	DLS (SLD)	63%
Ultimate limit state	SLS (SLV)	10%
	CLS (SLC)	5%

or with other forms of structural failure which might endanger the safety of the people (Cimellaro and Reinhorn 2011). In the NTC 2008, four different LS are fixed: *Operational Limit State* (OLS), *Damage Limit State* (DLS), *life Safety Limit State* (SLS) and *Collapse prevention Limit State* (CLS), which are reported in Table 12.3 for a period of 50 years.

The described approach is *performance – based*, since the new constructions must be designed according to different structural behavioral conditions occurring over its entire life. The seismic actions to be used for a given LS are defined with respect to the hazard at the referenced site. The seismic hazard is expressed in terms of maximum expected ground acceleration (a_g) in free field condition on horizontal and rigid site surface, and in terms of elastic horizontal and vertical spectral acceleration for the same conditions. INGV provides the hazard map of Italy, in which the maximum ground accelerations corresponding to a exceedance probability of 10% in 50 years are defined with respect to 50th percentile (Fig. 12.6). Furthermore, the trends of the maximum ground accelerations with the exceedance probability are called hazard curves. They are provided for different values of accuracy (16th, 50th and 84th) in order to understand the dispersion measure. Four different seismic zones are identified depending on the a_g value. (Table 12.4).

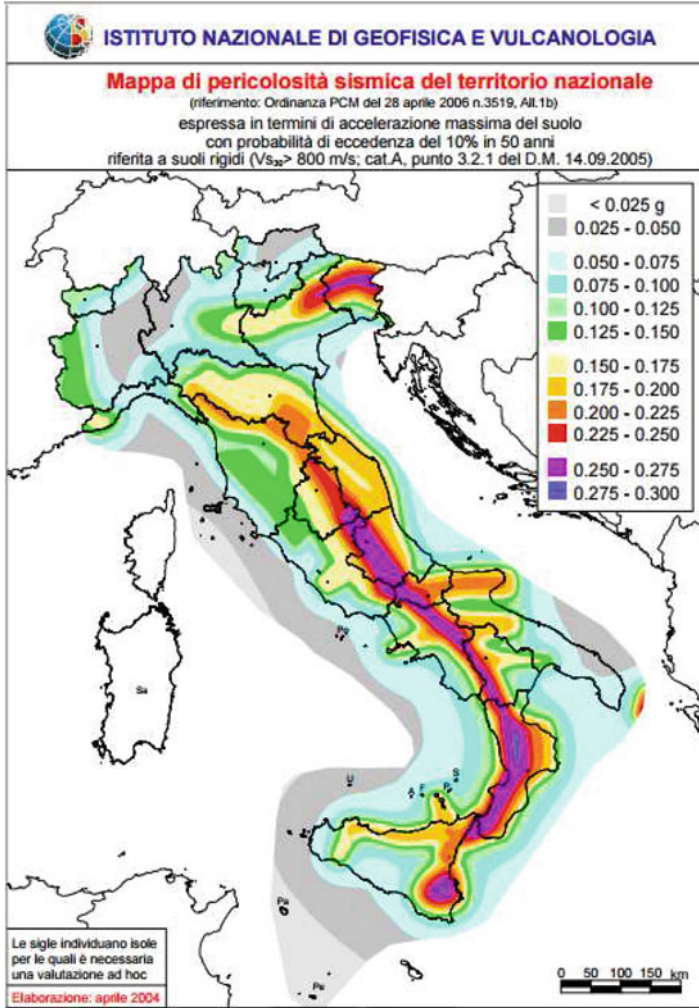


Fig. 12.6 Italian hazard map

Table 12.4 Italian seismic zone

Seismic zone	a_g [g] PVR = 10% in 50 years
1	$a_g > 0.25$
2	$0.15 < a_g \leq 0.25$
3	$0.05 < a_g \leq 0.15$
4	$a_g \leq 0.05$

On the other hand, the spectral shapes are defined in terms of:

- Maximum ground acceleration a_g
- Maximum amplitude factor for horizontal acceleration spectrum F_0
- Initial period value of constant velocity range T_C^*

The parameters mentioned above have been evaluated for nine different values of return period (30, 50, 72, 101, 140, 201, 475, 975 and 2475 years), or rather for nine values of exceedance probability. These parameters are reported in the Annex B of the NTC08 for all the points of the national grid. Furthermore, for different T_R values than the ones proposed, the referenced a_g , F_0 and T_C^* coefficients can be evaluated with a logarithmic interpolation. In addition, if the site is not located in the referenced grid point, the associated hazard parameters have to be assumed according to bilinear interpolation of the coefficients associated to the four closer grid points. The interactive hazard data are provided by the INGV in the S1 project and they are available at the link: <http://esse1-gis.mi.ingv.it>.

12.5.1.1 How to Build the Design Response Spectrum According to NTC08

The mathematical expressions of the DS proposed in NTC08 is calibrated using three coefficients a_g , F_0 and TC_* that modify the shape and the amplitude of the spectrum at a given site.

Since the three coefficients refer to the condition of flat and rigid surface, additional parameters are used to take into account the amplification phenomena due to the *stratigraphy effects and topographic effects*. The real soil stiffness induces an amplification of the ground motion that depends on the shear wave velocity measured 30 m deep (V_{S30}). This coefficient is assumed to be equivalent to the stiffness index of the soil. For this reason, the NTC08 proposes to group five different soil categories (Table 12.2.II NTC08). Seed et al. (1976) observed from more than 100 acceleration spectra that the real stratigraphy of the soil leads to the two effects discussed below:

- *amplification of the maximum accelerations;*
- *shifting towards greater periods.*

Figure 12.7 shows the mean elastic acceleration response spectra analyzed by Seed et al. (1976) for four soil categories normalized to the peak ground accelerations.

The above discussed effects and observations should be included using two coefficients S_S and S_δ related to the soil categories. The first one represents the accelerations amplifications, while the second term refers to the spectrum shifting.

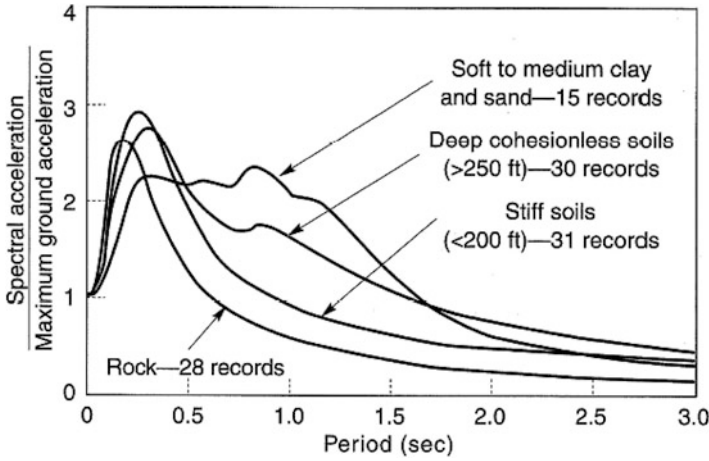


Fig. 12.7 Mean elastic acceleration spectra normalized to the PGA for four soil categories

Table 12.5 Stratigraphy amplification coefficients (Table 3.2. V NTC08).

Soil category	S_S	C_C
A	1.00	1.00
B	$1.00 \leq 1.40 - 0.40 \cdot F_o \cdot \frac{a_g}{g} \leq 1.20$	$1.10 \cdot (T_C^*)^{-0.20}$
C	$1.00 \leq 1.70 - 0.60 \cdot F_o \cdot \frac{a_g}{g} \leq 1.50$	$1.05 \cdot (T_C^*)^{-0.33}$
D	$0.90 \leq 2.40 - 1.50 \cdot F_o \cdot \frac{a_g}{g} \leq 1.80$	$1.25 \cdot (T_C^*)^{-0.50}$
E	$1.00 \leq 2.00 - 1.10 \cdot F_o \cdot \frac{a_g}{g} \leq 1.60$	$1.15 \cdot (T_C^*)^{-0.40}$

Table 12.6 Topography amplification coefficient (Table 12.2. VI NTC08)

Topographic category	Structure location	S_T
T1	–	1.0
T2	At the top of the cliff	1.2
T3	At the ridge of the relief	1.2
T4	At the ridge of the relief	1.4

12.5.1.2 Horizontal Design Spectrum

For the horizontal spectral acceleration components the S_S and C_C coefficients are reported in Table 12.5.

Furthermore, the European and National standards define two categories S1 and S2 referring to liquefaction susceptible soils.

The amplification phenomena due to the site topography is considered by means of a coefficient S_T shown in Table 12.6.

Thus, the total amplification is expressed with the coefficient $S = S_S \cdot S_T$. The definition of the design horizontal response spectrum is carried out considering four

Table 12.7 Referring periods and damping ratio for the NTC08

$T_B[s]$	$T_C[s]$	$T_D[s]$	$\eta[\%]$
$T_C/3$	$C_C T_C^*$	$4 \frac{a_g}{g} + 1.6$	$\sqrt{\frac{10}{2 + \xi}} \geq 0.55$

Table 12.8 Coefficients for T_1 horizontal spectrum (Table 3.2 EC8)

Soil category	S	T(s)	T(s)	T(s)
A	1.0	0.15	0.4	2.0
B	1.2	0.15	0.5	2.0
C	1.15	0.20	0.6	2.0
D	1.35	0.20	0.8	2.0
E	1.4	0.15	0.5	2.0

Table 12.9 Coefficients for T_2 horizontal spectrum (Table 3.3 EC8)

Soil category	S	T(s)	T(s)	T(s)
A	1.0	0.05	0.25	1.2
B	1.35	0.05	0.25	1.2
C	1.5	0.10	0.25	1.2
D	1.8	0.10	0.30	1.2
E	1.6	0.05	0.25	1.2

period ranges identified by the period T_B (initial value of constant acceleration range), T_C (initial value of constant velocity range), and T_D (initial value of constant displacement range) with a fixed damping ratio (η). Table 12.7 reports the aforementioned period parameters and the damping ratio expression.

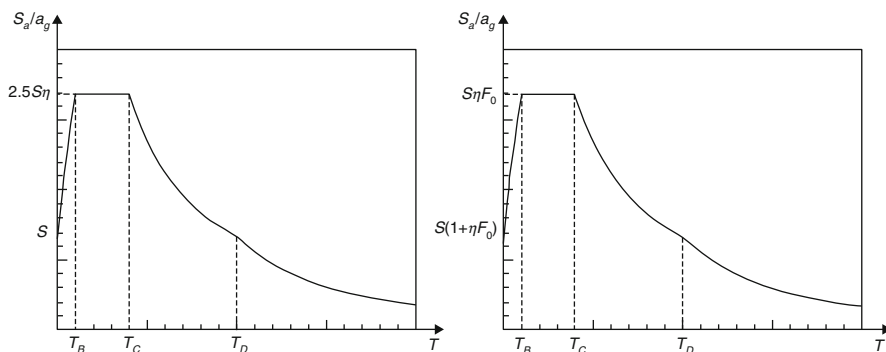
where ξ is the equivalent viscous damping ratio of the structure expressed in percentage. The equations of the Italian design horizontal spectrum (Eq. 12.9), expressed for different period ranges, are reported below.

$$\begin{aligned}
 0 \leq T < T_B : S_a(T) &= a_g \cdot S \cdot \eta \cdot F_O \cdot \left[\frac{T}{T_B} + \frac{1}{\eta \cdot F_O} \left(1 - \frac{T}{T_B} \right) \right] \\
 T_B \leq T < T_C : S_a(T) &= a_g \cdot S \cdot \eta \cdot F_O \\
 T_C \leq T < T_D : S_a(T) &= a_g \cdot S \cdot \eta \cdot F_O \cdot \left[\frac{T_C}{T} \right] \\
 T_D \leq T : S_a(T) &= a_g \cdot S \cdot \eta \cdot F_O \cdot \left[\frac{T_C T_D}{T^2} \right]
 \end{aligned} \tag{12.9}$$

The same methodology is suggested by the European standards (EC8), except for the set of hazard parameters. In fact in the EC8, only the maximum horizontal acceleration for a ground type A(a_g) must be taken into account for the design spectrum evaluation. The three period values must be assumed according to the National standards, but if the real stratigraphy of the soil is not known it is possible to consider two types of spectra (T_1 and T_2) for which the soil coefficient and the referenced period values are indicated (Tables 12.8 and 12.9).

Table 12.10 Topography amplification coefficient (Annex A EN-5:2004)

Topographic conditions (average slope, angle 15°)		
	Ridges with crest width significantly less than the base width (b)	Presence of a loose surface layer (c)
Isolated cliffs and slopes (a)		
$S_T \geq 1.2$	$1.2 \leq S_T \leq 1.4$	$S_T \geq 0.2 \min(S_T(a)S_T(b))$

**Fig. 12.8** Comparison between DS according to NTC08 and EC8

The importance class of the building is considered increasing or decreasing the ground acceleration value (a_{gR}) as expressed in Eq. 12.10.

$$a_g = a_{gR} \gamma_I \quad (12.10)$$

In addition, for important structures (γ_I) the topographic amplification effects should be taken into account as suggested in the EN-5:2004 (Table 12.10).

The complete formulation of the design horizontal spectrum according to EC8 is expressed in the Eqs. 12.11.

$$\begin{aligned}
 0 \leq T \leq T_B : S_a(T) &= a_g \cdot S \cdot \left[1 + \frac{T}{T_B} (\eta \cdot 2.5 - 1) \right] \\
 T_B \leq T \leq T_C : S_a(T) &= a_g \cdot S \cdot \eta \cdot 2.5 \\
 T_C \leq T \leq T_D : S_a(T) &= a_g \cdot S \cdot \eta \cdot 2.5 \cdot \left[\frac{T_C}{T} \right] \\
 T_D \leq T : S_a(T) &= a_g \cdot S \cdot \eta \cdot 2.5 \cdot \left[\frac{T_C T_D}{T^2} \right]
 \end{aligned} \quad (12.11)$$

Finally, a comparison between the horizontal DS obtained according to Italian and European rules is reported in the Fig. 12.8.

Table 12.11 Period coefficients for NTC08 (Table 12.2, VII)

Soil category	S_S	T_B	T_C	T_D
A,B,C,D,E	1.0	0.05 s	0.15 s	1.0 s

Table 12.12 Period coefficients for EC8 (Table 12.4.)

Spectrum	a_{vg}/a_g	$T_B(s)$	$T_C(s)$	$T_D(s)$
Tipo 1	0.90	0.05	0.15	1.0
Tipo 2	0.45	0.05	0.15	1.0

12.5.1.3 Vertical Design Spectrum

The vertical spectral components are also defined in three period ranges. In this case the suggested values of characteristic periods and amplification coefficients are defined independently from the soil categories. Tables 12.11 and 12.12 show the T_B , T_C and T_D values proposed by NTC08 and EC8, respectively.

NTC08 defines a coefficient F_V as maximum amplitude factor for vertical acceleration (Eq. 12.12), while EC8 indicate the acceleration ratio a_{vg}/a_g . For both of them the stratigraphic amplification coefficient is equal to the unit ($SS = 1$) but for NTC08 the topography amplification coefficient ST is the same of the horizontal components.

$$F_V = 1.35 \cdot F_O \cdot \left(\frac{a_g}{g} \right)^{0.5} \quad (12.12)$$

By means of Eqs. 12.13 and 12.14 the vertical DS can be defined according to NTC08 and EC8, respectively.

$$\begin{aligned}
 0 \leq T < T_B : S_{ve}(T) &= a_g \cdot S \cdot \eta \cdot F_V \cdot \left[\frac{T}{T_B} + \frac{1}{\eta \cdot F_V} \left(1 - \frac{T}{T_B} \right) \right] \\
 T_B \leq T < T_C : S_{ve}(T) &= a_g \cdot S \cdot \eta \cdot F_V \\
 T_C \leq T < T_D : S_{ve}(T) &= a_g \cdot S \cdot \eta \cdot F_V \cdot \left[\frac{T_C}{T} \right] \\
 T_D \leq T : S_{ve}(T) &= a_g \cdot S \cdot \eta \cdot F_V \cdot \left[\frac{T_C T_D}{T^2} \right]
 \end{aligned} \quad (12.13)$$

$$\begin{aligned}
 0 \leq T \leq T_B : S_{ve}(T) &= a_{vg} \cdot \left[1 + \frac{T}{T_B} (\eta \cdot 3 - 1) \right] \\
 T_B \leq T \leq T_C : S_{ve}(T) &= a_{vg} \cdot S \cdot \eta \cdot 3 \\
 T_C \leq T \leq T_D : S_{ve}(T) &= a_{vg} \cdot S \cdot \eta \cdot 3 \cdot \left[\frac{T_C}{T} \right] \\
 T_D \leq T : S_{ve}(T) &= a_{vg} \cdot S \cdot \eta \cdot 3 \cdot \left[\frac{T_C T_D}{T^2} \right]
 \end{aligned} \quad (12.14)$$

Both the European and National standards provide some limitations in the use of the horizontal and the vertical DS as target for the seismic input:

- DS can be evaluated with $S_a(T)$ mathematical expressions for period range lesser than 4 s;
- For S1 and S2 soil categories the S , T_B , T_C and T_D coefficients must be defined by means of specific researches;
- For ULS the DS can be reduced proportionally to a parameters q considering the dissipation capacity of structures. The EC8 defines this parameter as behavior coefficient, while in the NTC08 it is called structural factor. Moreover, the minimum design acceleration threshold must be equal to 0.2 g. Naturally, for SLS q must be set equal to 1 since the structure is in the elastic field.

12.5.2 Conditional Mean Spectrum (CMS)

The shape of a uniform hazard spectrum (UHS) has been criticized to be unrealistic for a site where the spectral ordinates of the UHS at different periods are governed by different scenario events and conservative for long-return-period earthquake shaking. This limitation has led to the development of the Conditional Mean Spectrum (CMS) which is obtained by conditioning on a spectral acceleration related to one period. The deaggregation parameters (M , R and ε), obtained from the PSHA as mean values are depending on the period of interest and are used to calculate the predicted mean and standard deviation of the logarithmic spectral acceleration values using the selected ground motion prediction equation (GMPE).

Knowing the GMPE, the CMS can be calculated as the sum of two contributions: the first one is the logarithmic spectral acceleration ($\log(S_a(T_{ref}))$) and the second part is obtained as the product between the conditional mean ε value, for the period of interest (T_{ref}), the standard deviation of logarithmic distribution ($\sigma_{\log(S_a)}$) and the correlation coefficient ($\rho(T_i, T_{ref})$) (Eq. 12.15). Analytically the logarithmic spectral acceleration is given by

$$\log(S_a(T_i)) / \log(S_a(T_{ref})) = \log(S_a(T_{ref})) + \rho(T_i, T_{ref}) \varepsilon(T_{ref}) \sigma_{\log(S_a)}(T_i) \quad (12.15)$$

The parameter ε is a measure of the difference between the logarithmic spectral acceleration of a record and the mean or median logarithmic spectral demand predicted, while the correlation coefficient defines the linear correlation between a pair of ε associated to two different periods. Figure 12.9a shows an example of ε -defined for a period of interest of 1 s, while Fig. 12.9b illustrates the line of best fit for $\varepsilon(T_i = 2 \text{ s})$ and referring $\varepsilon(T_{ref} = 1 \text{ s}) = 2$, obtained for a large suite of ground motions in the NGA database (Baker 2011). The slope of the previously mentioned line represents the correlation coefficient for the two ε values ($\rho(T_i, T_{ref})$).

Recently this method starts to be adopted also in Europe, therefore a new correlation equation has been developed for the European sites analyzing 595 strong

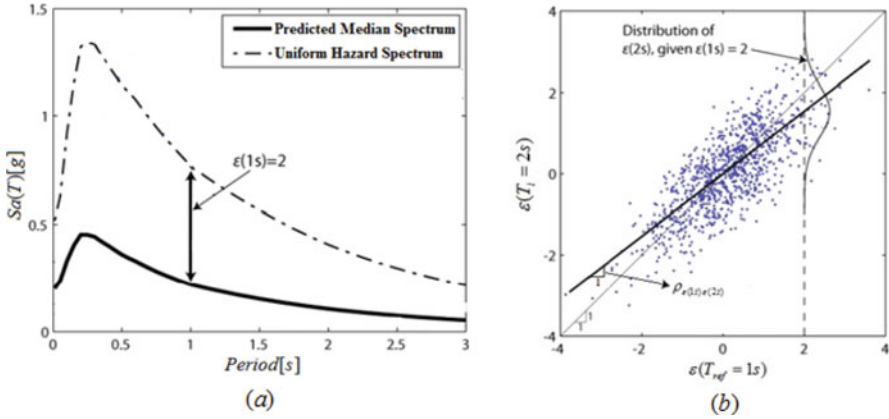


Fig. 12.9 Example of ε -definition for period of 1 s (a) and correlation coefficient for $\varepsilon(T = 1\text{ s})$ and $\varepsilon(T = 2\text{ s})$ (b).

motion records and considering the Ambraseys Ground-Motion Prediction Equation (GMPE) to evaluate the ε (Cimellaro 2013) (Eq. 12.16).

$$\rho_{\varepsilon(T_1)\varepsilon(T_2)} = 1 - \left(\frac{A_0 + A_2 \log T_{min} + A_4 (\log(T_{max}))^2}{1 + A_1 \log T_{max} + A_3 (\log(T_{min}))^2} \right) \ln \left(\frac{T_{min}}{T_{max}} \right) \quad (12.16)$$

where $T_{min} = \min(T_1, T_2)$, $T_{max} = \max(T_1, T_2)$, while A_0, A_1, A_2, A_3, A_4 are the model parameters. Similar analytical predictive equations were proposed by Chiou and Youngs (2008) (Equation) in which the parameters of the model have been modified to adjust to European strong motion.

$$\rho_{\varepsilon(T_1)\varepsilon(T_2)} = \begin{cases} C_2 \rightarrow & \text{if } T_{max} < A_1 \\ C_1 \rightarrow & \text{if } T_{min} < A_1 \\ \min(C_2, C_4) & \text{if } T_{max} < A_2 \\ C_4 \rightarrow & \text{else} \end{cases} \quad (12.17)$$

where $T_{min} = \min(T_1, T_2)$, $T_{max} = \max(T_1, T_2)$ while A_1, A_2, A_4 are the coefficients and they are determined as a function of seven model parameters ($A_0, A_1, A_2, A_3, A_4, A_5, A_6$ and A_7).

Previously Baker and Cornell (2006) proposed a correlation model for the California sites valid for a low period range of 0.05–5 s (Eq. 12.18), while later Baker and Jayaram (2008) have proposed a redefined correlation model suitable over the 0.01–10 s period range.

$$\rho_{\varepsilon(T_1)\varepsilon(T_2)} = 1 - \cos \left(\frac{\pi}{2} - \left(A_0 - A_1 \cdot I_{T_{min} < A_2} \ln \frac{T_{min}}{A_2} \right) \right) \ln \left(\frac{T_{min}}{T_{max}} \right) \quad (12.18)$$



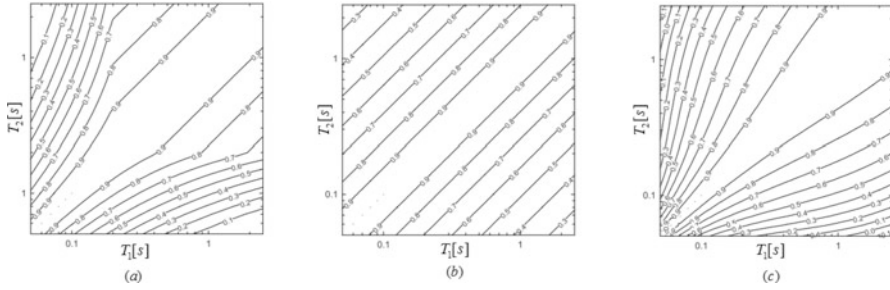


Fig. 12.10 Contours of the predicted horizontal correlation coefficients of response spectra versus natural vibration periods T_1 and T_2 for Ambraseys (2005) GMPE, using Baker and Cornell (a), Chiou and Youngs (b) and Cimellaro (c)

where $T_{min} = \min(T_1, T_2)$, $T_{max} = \max(T_1, T_2)$, $(T_{min} < A_2)$ is a step function equal to 1 if $T_{min} < A_2$ and equal to 0 otherwise and A_0, A_1 and A_2 are the parameters of the model.

Figure 12.10 shows the contours of the predicted horizontal correlation coefficients of the response spectra discussed above versus natural vibration periods T_i and T_j for the 2005 Ambraseys GMPE (Cimellaro and De Stefano 2010).

Contours of the predicted horizontal correlation coefficients of response spectra versus natural vibration periods T_1 and T_2 for Ambraseys (2005) GMPE, using Baker and Cornell (a), Chiou and Youngs (b) and Cimellaro (c).

12.6 Use of Acceleration Time Histories

According to NTC8, the use of acceleration time histories is allowed for particular structural and geotechnical systems. Each of them must be applied simultaneously in the two horizontal directions (X and Y) and in the vertical direction (Z). The three acceleration time histories in the three directions define an acceleration group. EC8 fixes the minimum number of acceleration groups to three, but for detailed analyses it is suggested to use seven groups of acceleration histories. The seismic standards allow the use of three types of accelerograms:

- *real ground motions* (from strong motion databases);
- *real ground motions* (from strong motion databases);
- *synthetic ground motions* (generated from theoretical seismological models).

Only the first category can be used in dynamic geotechnical applications. A common goal of the artificial and real accelerograms is the compatibility with the target spectra in the given period of interest. EC8 and NTC08 do not establish any rigid range of period for real ground motions. On the contrary, the maximum and minimum values of period are given for artificial accelerograms (Tables 12.13 and 12.14).

Table 12.13 Referring period intervals for NTC08

Ultimate Limit State (ULS)	Service Limit State (SLS)
$\max[(0.15s - 2.0s); (0.15s - 2.0T_{ref})]$	$\max[(0.15s - 2.0s); (0.15s - 1.5T_{ref})]$

Table 12.14 Reference period interval for EC8

$$\frac{0.2T_{ref} - 2.0T_{ref}}{}$$

The accelerograms can be selected to be spectrum compatible with the target spectrum, so that the mean acceleration response spectrum of the set has a dispersion of 10% in the period range of interest.

In addition, the set of accelerograms to be selected must be consistent with the geological characteristics of the site. The simulated *synthetic ground motions* can be evaluated from theoretical seismological models of seismic fault rupture by means of dynamic or kinematic models. Using this procedure it is not possible to have consistent results for frequency values greater than 5 Hz. On the other hand, the artificial accelerograms do not have a reasonable amplitude, frequency content and duration, since they are estimated from stochastic approaches.

These observations led to prefer the real ground motion records because they are realistic and they have the best correlation between the spatial components. Furthermore, nowadays the availability of a wide strong motion databases has led to prefer real ground motion records in the analysis using advanced ground motion selection methods.

12.6.1 Ground Motion Selection and Modification

It is important to mention that the general characteristics of the earthquake ground motion set depends on the specific goals of the analyses to be performed. In fact the Performance Assessment of Buildings (Applied_Technology_Council 2011) define three selection methodologies depending on the performance assessment of buildings:

- *Intensity-based assessment;*
- *Scenario-based assessment;*
- *Time-based assessment.*

These methodologies include the development of a target response spectrum, the selection of an appropriate suite of earthquake ground motions and the scaling procedure for consistency with the target spectrum. The scaling procedure is necessary for modifying the record and match the target spectrum for the period of interest.

The first step in the ground motion selection procedure is defining the target spectrum according to the type of assessment (Table 12.15).

Table 12.15 Target spectrum used in the performance analyses (ATC-58-1, 2012)

Intensity-based assessment	Scenario-based assessment	Time-based assessment
Any spectrum consistent with site geologic characteristics	Spectrum deriving with an appropriate GMPE	One spectrum for each seismic hazard interval used in the analysis

Once the target spectrum has been defined, the ground motion selection is carried out to obtain a set of ground motions that will produce unbiased estimates of median structural response with non linear response history analyses (NRHA) or other specific analyses. In other words, the ground motion selection is applied to obtain an estimate of the structural dynamic response as accurate as possible. In order to simplify the spectral matching procedure, three different approaches are proposed:

- *scaling in time domain* (simple amplitude scaling for a specific period value);
- *Frequency content modification*;
- *Adding wavelets functions in the record in the time domain.*

The *frequency content modification* is the basic procedure for generating artificial accelerograms matching the target spectrum, but also the third approach is used to obtain artificial time histories which are spectrum compatible.

12.6.1.1 Real Ground Motion Records

In this paragraph specific selection and modification procedures won't be discussed, but instead the focus will be on the general characteristics of all methodologies currently available. First of all, it is suggested to select real acceleration time histories coming from different seismic stations and for different events. As discussed previously, the consistency with a target spectrum and with the seismological characteristics of the site are the first steps in the selection and scaling procedure.

Thus, the ground motions are selected by means of several matching target spectrum shape-based criteria and source and waveform-based criteria from the available database. In literature are available several ground motion selection and modification procedures. Each of them is based on the same logical steps to be followed (Fig. 12.11).

The amplitude-based modification procedures in the time domain are based on the definition of a scale factor SF which depends on the spectral acceleration of the target spectrum ($S_{a, target}(T_{ref})$) (Eq. 12.19).

$$SF = \frac{S_{a, target}(T_{ref})}{S_{a, gm}(T_{ref})} \quad (12.19)$$

where $S_{a, gm}(T_{ref})$ represents the spectral acceleration at the same period of the considered ground motion. Usually, for building structures the period of interest

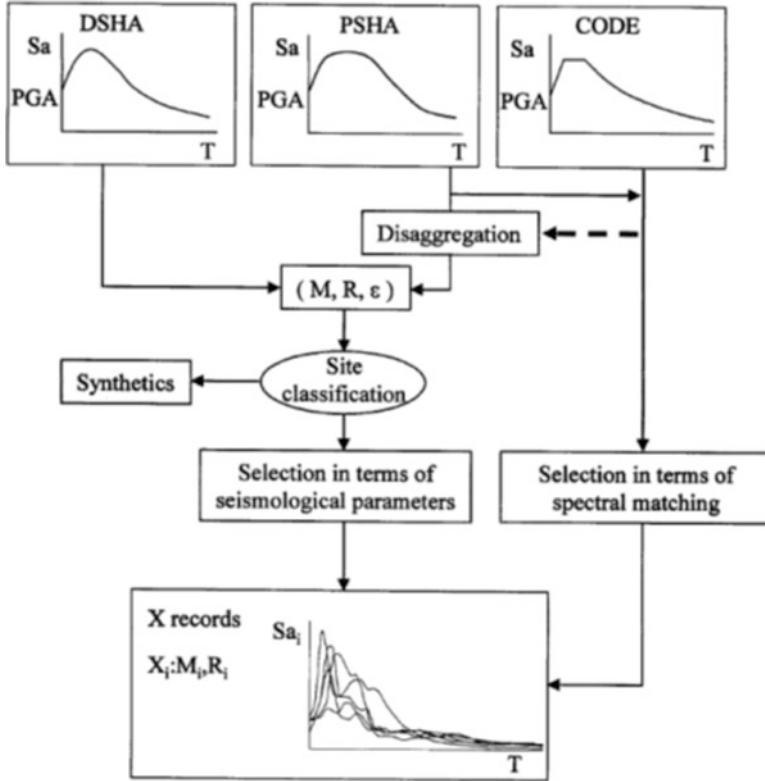


Fig. 12.11 Overview of the options available for selecting and scaling real accelerograms (Adapted from Bommer and Acevedo 2004)

T_{ref} is assumed equal to the fundamental period of the structure (first vibrational mode) (Fig. 12.12a). For geotechnical systems the period of interest $T_{ref} = 0$ which means to use the PGA as target acceleration (Fig. 12.12b).

Despite the large availability of strong motion databases, finding real ground motions with similar seismological characteristics (fault mechanism, epicentral distance, rupture depth etc.), site category (depending on V_{S30}) and adequate mean spectral compatibility, might not be enough. This observation has led proposing new approaches based on the generation of artificial or synthetic ground motion records.

12.6.1.2 Artificial Seismic Records

Artificial accelerograms are obtained through numerical simulations starting from a target spectrum. A commonly used method adjusts the Fourier amplitude spectrum iteratively, based on the ratio of the target response spectrum to the time history response spectrum, while keeping the Fourier phase of the reference time history



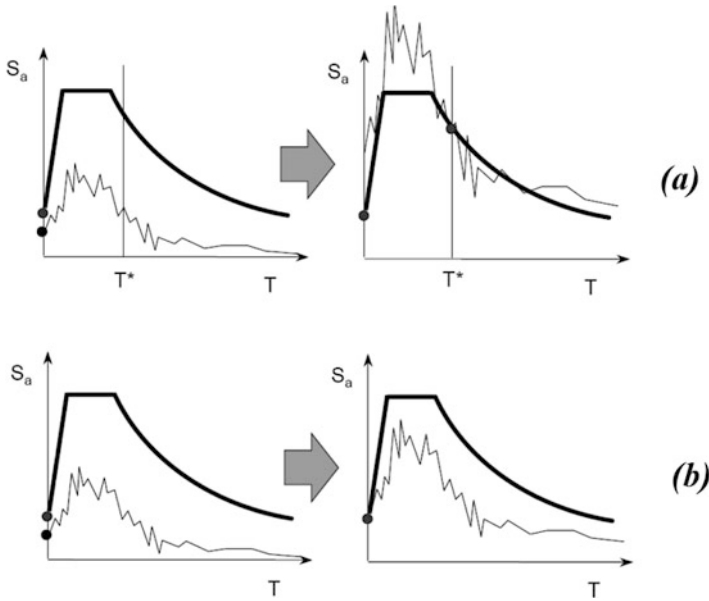
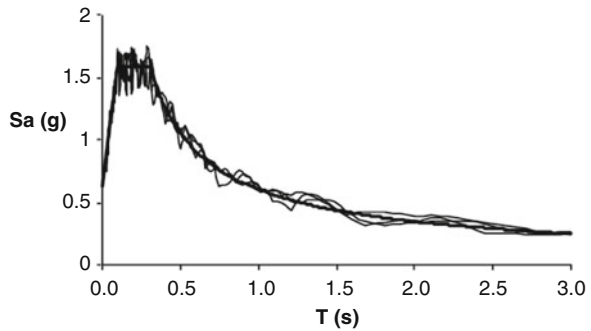


Fig. 12.12 Scaling procedure to match spectral acceleration at some period (a) or at PGA (b)

Fig. 12.13 Example of SIMQKE results in terms of spectrum-compatibility



fixed (code BELFAGOR and SIMQKE, Gasparini and Vanmarcke (1976)). In other words this is an iterative procedure through which the frequency content of the record is modified step by step (Fig. 12.13).

The thick black spectrum defines the target spectrum, while the other lines represent all the compatible modified records (artificial accelerograms). This approach can alter the non-stationary character of the time history, if the shape of the Fourier amplitude spectrum is changed significantly.

An alternative approach for spectral matching adjusts the time history in the time domain by adding wavelets to the selected ground motion record (Lilhanand

and Tseng 1988; code RSPMATCH Abrahamson 1998). While this procedure is more complicated than the frequency domain approach, it has good convergence properties and in most cases preserves the nonstationary characteristics of the ground motion. The ground motion records developed with this procedure are often referred to as intelligent artificial accelerograms.

12.6.1.3 Synthetic Seismic Records

The synthetic procedures are based on the *empirical* or *physical* methods for the generation of the ground motions. The empirical methods can be carried out using the attenuation relationships, while the physical methods include dynamic and kinematic models.

Dynamic models rigorously take into account the causative forces resulting in earthquakes and are based on the dynamics of the fault rupture, which involves specifying the forces (tectonic stresses) that drive the process and the forces (such as friction and asperities on the fault) that resist the rupture propagation. Mechanics and equations of motion are then used to define the rupture process and the resulting ground motion. Such techniques are highly complex, require very intensive calculations and also require the specification of many geophysical parameters that are generally unavailable and unpredictable for future earthquakes. Hence, they have been very infrequently used to generate motions for engineering purposes. The main application of dynamic fault models has been to interpret the rupture history of previous earthquakes in order to better understand the processes of generation and propagation.

Kinematic fault models (Hartzell et al. 1976) are more widely used to generate synthetic ground motions. The model characterizes the rupture process in terms of the displacement (slip function) of the fault as a function of time and location. The response at a site can then be calculated using mathematical forms called Greens functions¹ that represent the ground motion at the site deriving from an instantaneous unit pulse displacement at a particular point on the fault. They simulate the propagation of seismic waves from the fault to the observation point, taking into account the effect of the intervening geologic structure. Calculating Greens functions represents the largest portion of kinematics modeling computations. A common practice that has come into use, to overcome the lack of strong motion recordings, is the use of weak motion recordings from small earthquakes as empirical Greens functions. The two components necessary for fully defining the motion are, therefore, the Greens functions and the distribution in time and space of the individual point ruptures that make up the complete fault rupture. Of course, it is impossible to predict in both time and space the rupture propagation for future earthquakes, so a degree of randomness is usually introduced into the summation of the sub-events in order to represent the heterogeneity of real fault ruptures typical of large earthquakes.

12.6.2 Available Databases for Signal Processing and Ground Motion Selection

All the ground motions are recorded and collected in the database in order to be available for any seismic analysis. Three of the most useful strong motion databases are the Italian ACcelerometric Archive (ITACA), the European Strong Motion Database (ESMD) and the Pacific Earthquake Engineering Research database (PEER) for Italian sites, European sites and world sites, respectively. From ITACA and from ESMD one can obtain the acceleration time histories (corrected and uncorrected) and additional information about any recorded ground motion in zip files after registration in the official site (<http://itaca.mi.ingv.it/ItacaNet/> for ITACA and www.isesd.hi.is/ for ESMD). The PEER ground motions are freely available at the link: <http://ngawest2.berkeley.edu/>. Figures 12.14, 12.15 and 12.16 show the screenshots related the databases just mentioned and they also illustrate the differences between the internet graphical user interfaces.

For a single event the East-West (E-W), the North-South (N-S) and the Vertical (V) components are given for the three databases. In addition, Fault-Normal (FN)

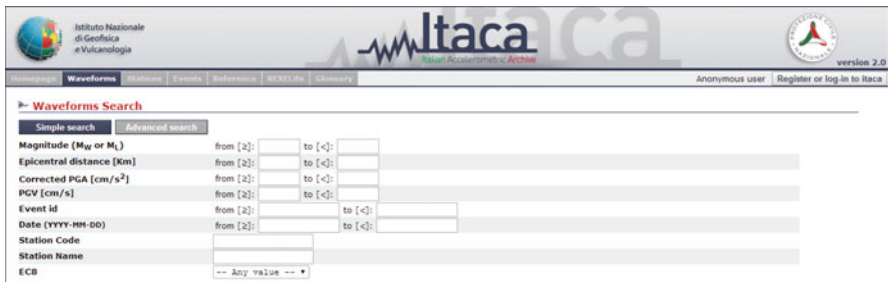


Fig. 12.14 Screenshot of the ITACA internet GUI

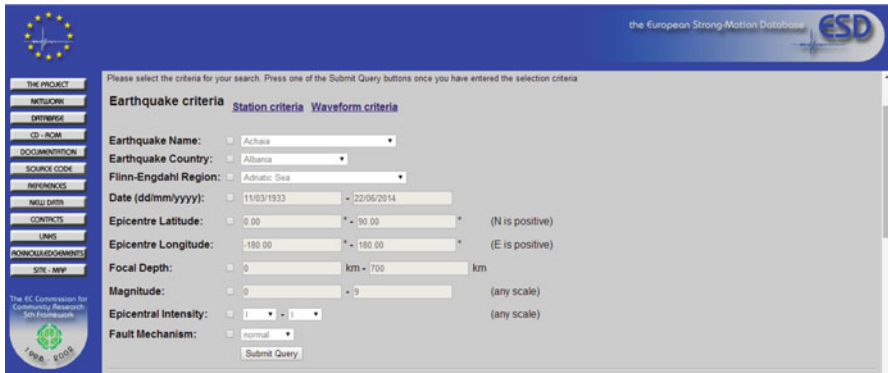


Fig. 12.15 Screenshot of the ESMD internet GUI



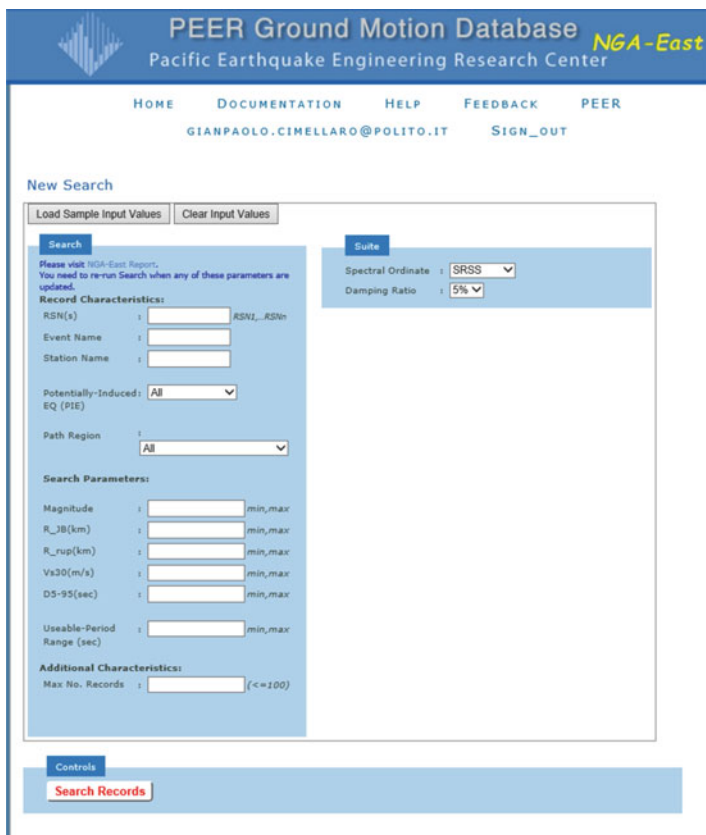
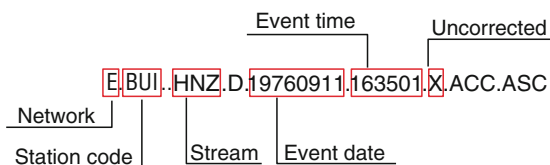


Fig. 12.16 Screenshot of the PEER internet GUI

Fig. 12.17 Format of the output uncorrected record name (ITACA)



and Fault-Parallel (FP) components of the shaking are available for the latest version of the PEER database. The Italian and European strong motion database provide uncorrected and corrected (with default Butterworth filter and baseline correction) acceleration histories. In order to explain the main differences between the output file formats, a Friuli earthquake record was selected from the three database and the main format name differences are summarized in Figs. 12.17, 12.18 and 12.19.

In each database it is possible to perform any research using the station criteria or the waveform criteria.



Fig. 12.18 Format of the output uncorrected record name (ESMD)

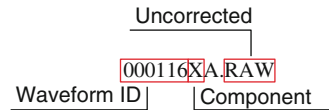
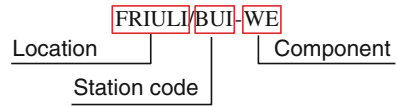


Fig. 12.19 Format of the output record name (PEER)



References

- 1998-1 E (2004) Design of structures for earthquake resistance Part 1: general rules, seismic actions and rules for buildings. European Committee for Standardization
- Abrahamson N (1998) Non-stationary spectral matching program RSPMatch. Report PG&E Internal Report, University of California
- Applied_Technology_Council (2011) Draft guidelines for seismic performance assessment of buildings volume 1 – methodology atc-58-1_draft_75 Applied Technology Council (ATC-58 Project), 201 Redwood Shores Parkway, Suite 240
- Baker JW (2011) Conditional mean spectrum: tool for ground-motion selection. *J Struct Eng ASCE* 137(3):322–331
- Baker JW, Cornell A (2006) Correlation of response spectra values for multi-component ground motions. *Bull Seismol Soc Am* 96:215–227
- Baker JW, Jayaram N (2008) Correlation of spectral acceleration values from NGA ground motion models. *Earthq Spectra* 24(1):299–317
- Barani S, Spallarossa D, Bazzurro P (2009) Disaggregation of probabilistic ground-motion hazard in Italy. *Bull Seismol Soc Am* 99(5):2638–2661
- Bommer JJ, Acevedo AB (2004) The use of real earthquake accelerograms as input to dynamic analysis. *J Earthq Eng* 8(1):43–91
- Chiou BSJ, Youngs RR (2008) An NGA model for the average horizontal component of peak ground motion and response spectra. *Earthq Spectra* 24(1):173–215
- Cimellaro GP (2013) Correlation in spectral accelerations for earthquakes in Europe. *Earthq Eng Struct Dyn* 42(4):623–633. <https://doi.org/10.1002/eqe.2248>
- Cimellaro GP, De Stefano A (2010) Correlation in spectral accelerations of European ground motion records. In: Proceedings of 9NCEE, Toronto
- Cimellaro GP, Marasco S (2015) A computer-based environment for processing and selection of seismic ground motion records: opensignal. *Front Built Environ* 1:17
- Cimellaro G, Reinhorn AM (2011) Multidimensional performance limit state for hazard fragility functions. *J Eng Mech, ASCE* 137(1):47–60. [https://doi.org/10.1061/\(ASCE\)EM.1943-7889.0000201](https://doi.org/10.1061/(ASCE)EM.1943-7889.0000201)
- Cimellaro GP, Reinhorn AM, D'Ambrisi A, De Stefano M (2011) Fragility analysis and seismic record selection. *J Struct Eng, ASCE* 137(3):379–390
- Gasparini DA, Vanmarcke EH (1976) Simulated earthquake motions compatible with prescribed response spectra. Report, Massachusetts Institute of Technology, Cambridge
- Hartzell S, Frazier GA, Brune JN (1976) 3-dimensional earthquake modeling by summation of greens functions with an application to August 2, 1975 anza earthquake. *Trans Am Geophys Union* 57(12):953–953

- Lilhanand K, Tseng WS (1988) Development and application of realistic earthquake time histories compatible with multiple-damping design spectra. *Development* 3:7–8
- NTC-08 (2008) Nuove Norme Tecniche per le Costruzioni. *Gazzetta Ufficiale della Repubblica Italiana*
- Reiter L (1991) *Earthquake hazard analysis: issues and insights*. Columbia University Press, New York
- Seed HB, Ugas C, Lysmer J (1976) Site-dependent spectra for earthquake-resistant design. *Bull Seismol Soc Am* 66(1):221–243

Chapter 13

Opensignal



Abstract The chapter illustrates the capabilities of the OPENSIGNAL computer-based platform environment (Cimellaro GP, Marasco S, *Frontiers in Built Environment* 1:17, 2015) for processing and selecting the seismic input to be used in the seismic analyses. All the features and the software components are explained in detail and an illustrative application is reported.

13.1 Introduction

The use of ground motion data has been growing worldwide due to the large availability of ground motion records and increased interest from the earthquake engineering community in using nonlinear response history analysis in seismic analysis and design. In particular, the selection and processing of earthquake records plays a key role in seismic risk assessment of buildings and structures in general. A computer-based platform OPENSIGNAL¹ has been developed (Cimellaro and Marasco 2015) for the analysis, processing and selection of ground motion records from the main international databases (ESMD, PEER, ITACA, Chilean database) using different search criteria. The main advantage and unique quality of the platform is that it allows spectral matching selection using different target spectra rather than the UHS such as the Conditional Mean Spectra (CMS) or any other user-defined target spectra (Cimellaro et al. 2011). In particular, the computer environment allows building the Conditional Mean Spectra on the Italian national territory. Furthermore, the proposed platform combines the functionalities of different software, such as multi record processing and also allows exporting the selected records in different formats (e.g. excel, txt) using a simple graphical interface. The computer-based platform is freely available for the general public at the following website: <http://areweb.polito.it/ricerca/ICRED/Software/OpenSignal.php>

13.2 State of Art

Nowadays, the state-of-practice in earthquake engineering design has progressively moved toward the use of dynamic elastic and even nonlinear time history analysis with respect to response spectrum analysis, because of the exponential increment of computational power. All these methods require the selection of a proper suite of earthquake ground motions as prerequisite in order to be reliable. In fact, among all possible sources of uncertainty (e.g. structural material properties, modeling approximations, design and analysis assumptions etc.) the selection of earthquake ground motion has the highest effect on the variability of the structural response. The selection of earthquake records in most seismic design codes are based on parameters obtained by disaggregated seismic hazard maps at a specific site such as the magnitude, M , and the source-to-site distance, R , but other parameters can also be used such as the *soil type*, the *source mechanism*, the *duration* etc. Other parameters can also be used based on intensity measures such as the peak ground acceleration (pga), the spectral acceleration at the fundamental period of the structure $S_d(T_1)$ etc. Other selection criteria are based on spectral matching to a specific target spectrum, such as a design code spectrum evaluated by referring to seismic scenario determined by a ground motion prediction equation (GMPE), a uniform hazard spectrum (UHS), a conditional mean spectrum (CMS), etc. Using design code spectrum and UHS might cause over-softening and over-damping during the analysis; therefore, a matching procedure based on the conditional mean spectrum leads to more consistent results. Several alternatives and more advanced methods are available in literature (see review in Cimellaro and De Stefano 2010).

A large number of computer programs, public and commercial, are available at the ORFEUS (Observatories and Research Facilities for European Seismology) data center (<http://www.orfeus-eu.org/software.html>). Most existing public signal processing software are developed to analyze single seismic earthquake records at a time (e.g. Seismosignal – available at <http://www.seismosoft.com/en/seismosignal.aspx>). For multiple records analysis commercial software such as BISPEC (Hachem 2008) (<http://www.ce.memphis.edu/7137/PDFs/BispecHelpManual.pdf>) is needed, but they have the inconvenience that they are not freely available in the market. Furthermore, most of these programs can be used after the earthquake records are selected, but they are not able to guide you through the ground motion selection process from a given database, thus is one example of how they do not provide users with the ability to perform all of these functions in an integrated fashion.

Recently Katsanos and Sextos (2013) developed a Matlab-based software environment which integrates finite element analysis with earthquake records selection which works with the PEER database. However signal processing, soil response analysis and the possibility of using new target spectra such as the Conditional Mean Spectra is not included in the program. Consequently, there is a need for a specific platform that combines all of these functionalities together. The computer-based platform OPENSIGNAL, which can read data in a large variety of file formats from the most common ground motion databases, is freely available for the general public (available at <http://areeweb.polito.it/ricerca/ICRED/Software/OpenSignal.php>). In

fact, the platform can be used to automatically select seismic records from several databases such as the PEER-NGA strong motion database (PEER – <http://ngawest2.berkeley.edu/>), the European Strong-Motion database (ESMD – http://www.isesd.hi.is/ESD_Local/frameset.htm) and from ITalian ACcelerometric Archive (ITACA – <http://itaca.mi.ingv.it>), but it also allows manual reading of seismic records by selecting the free format. It is composed of several interactive graphical interfaces that integrate the most common signal-processing and selection criteria techniques used in earthquake engineering. For example, it allows processing multiple ground motion records simultaneously, filtering the unwanted frequency contents, carrying out spectral analysis, soil response analyses etc. Finally, all processed data and records can be exported into other common formats such as MS Excel, txt, etc.

The goal of OPENSIGNAL is to provide users with the latest techniques on ground motion selection and processing, while simultaneously providing utilities for file management, import and export of data, unit conversion, and other time-consuming tasks for earthquake engineering professionals, students and researchers.

13.3 Structure of the Software

The software architecture of OPENSIGNAL is based on three main windows that provide tools, which corresponds to the same logical process that is usually followed by each designer to select “reliable” earthquake records:

1. *Signal processing analysis;*
2. *Seismic record selection;*
3. *Site response analysis.*

(i) *Signal Processing* is designed for a user who has his own input data and needs to process it; (ii) *Seismic records selection* window supplies the instruments for obtaining both response spectra and time-histories; (iii) *Site Response Analysis* concerns the analysis of the amplification effects at a given site due to the soil stratigraphy.

The main graphical interface of the program is shown in Fig. 13.1.

Each part of the computer environment has been implemented in MATLAB and has a graphical user interface that is simple and intuitive to be used. Each toolbox can be used following the sequence shown in Fig. 13.1 or independently. In the next paragraphs, each part of the platform is described in detail.

13.4 Strong Motion Databases

The proposed framework retrieves records from the PEER-NGA strong motion database (PEER – available at <http://ngawest2.berkeley.edu/>), the European strong motion database (ESMD – available at <http://goo.gl/hkUKDG>), the ITalian

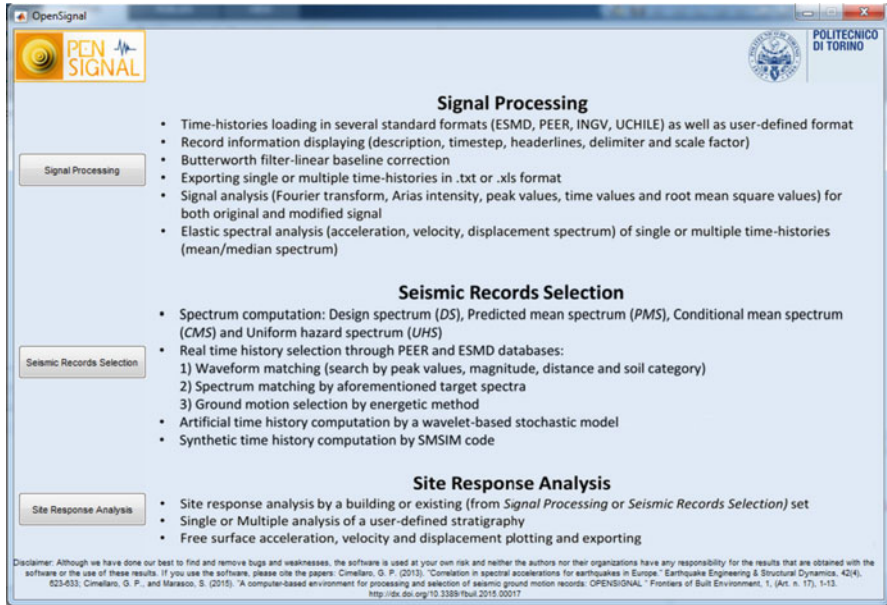


Fig. 13.1 Main graphical interface of the software

ACcelerometric Archive (ITACA available at <http://itaca.mi.ingv.it>), and the Chilean ground motion database (records from 1994 to 2010 are available at <http://terremotos.ing.uchile.cl/>). Additional Chilean records related to the 1985 earthquake are available at <http://goo.gl/JeowCW>, while the raw data (uncorrected) of the records of the 2014 Iquique earthquake are available at <http://www.sismologia.cl/>. Furthermore, the software also allows manual reading of the seismic records selecting the free format, if the file format is different from the three databases mentioned above.

13.5 Signal Processing and Filtering

Figure 13.2 shows the main user dialog window of “signal processing” tool. Signal processing allows the user to open raw data obtained from the main source databases from all over the world and calculate the principal seismic parameters, such as Arias Intensity, Fourier Transform as well as the file information (i.e event description, sampling interval, etc.). In the Input Data (upper left), the records are uploaded and read automatically for the selected ground motion databases (PEER, ESMD, ITACA and UCHILE) or using the option free format. The signal processing module (Fig. 13.2) allows the correction of the ground motion records with the Butterworth

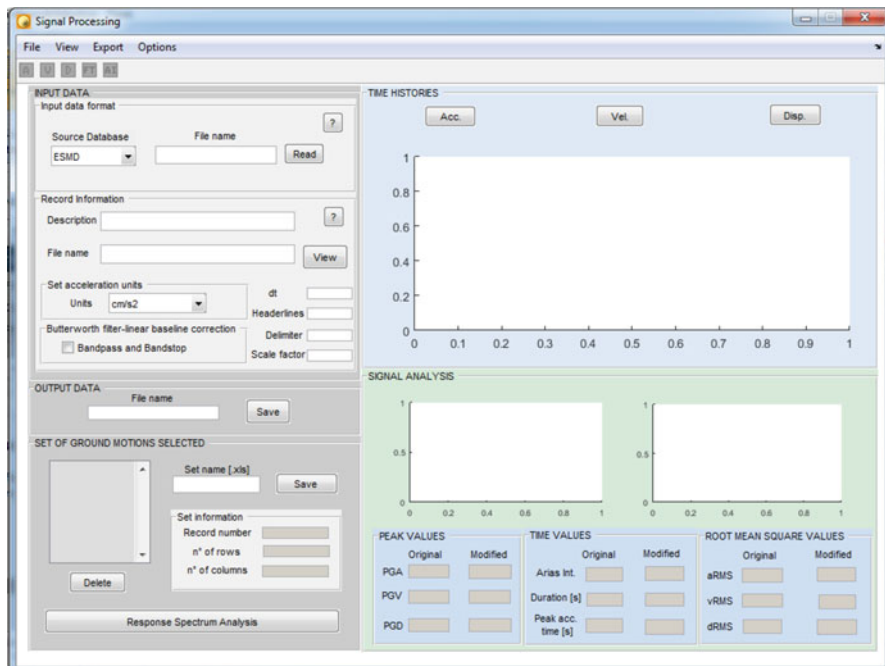


Fig. 13.2 User dialog window for “Signal Processing”

filter by modifying the default set up values ($f_{min} = 0.25$ Hz, $f_{max} = 25$ Hz, $n = 4$) if needed. It is also possible to scale the acceleration history selected by setting the scale factor. The effect of the filter is shown in the Time Histories visualization panel in which the accelerations, velocities and displacements records, both filtered and unfiltered are displayed. In the *Signal Processing window* (Fig. 13.2) the main parameters of the earthquake records (e.g. peak ground acceleration, velocity and displacement, duration, etc.) both peak and root mean square values are calculated and saved for both filtered and unfiltered data. The Arias Intensity and the Fourier Transform graph are plotted as well. All processed data and records can be saved in both *xls* and *txt* format using the saving input data block (bottom-left in Fig. 13.2). Then the set of records created can be processed in the spectral analysis dialog window (Fig. 13.3).

13.5.1 Response Spectra Analysis

Signal Processing tool contains a powerful tool, the *Response Spectrum Analysis*, which permits simultaneous Spectrum Analysis of different time-histories. Starting

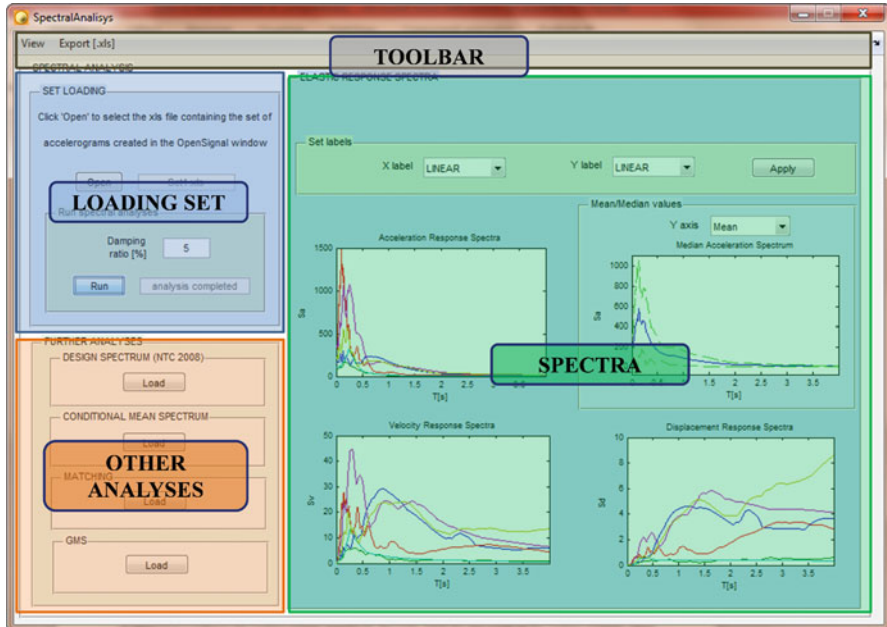


Fig. 13.3 User dialog window for Spectral analysis

from the set of ground motions selected and filtered, the Elastic Response Spectra (acceleration, velocity, displacement etc.) can be computed for a given value of damping ratio. Furthermore, the mean and median acceleration response spectra of the uploaded set of records with the associated range of dispersion ($\pm\sigma$) can also be evaluated and plotted using log and semi-log scales.

Different types of target spectrum can be defined in the framework. The Design Spectrum (DS) can be evaluated according to the Italian seismic standards, the NTC 2008 for any point in the Italian territory, once the parameters are defined (e.g. nominal life, soil category, damping ratio, over strength factor q to describe the inelastic behavior, etc.). Additionally the DS according to the European seismic standard, EC8, and to the US standards can be evaluated inserting the proper parameters. Furthermore, the platform allows the evaluation for a given probability of exceedance of the Uniform Hazard Spectrum (UHS), and the Predicted Mean Spectrum (PMS) using four different ground motion prediction equations (GMPE) which are currently available: Ambraseys et al. (1996), Campbell and Bozorgnia (2008), Boore and Atkinson (2008), Iyengar et al. (2010) and Contreras and Boroschek (2012). However, the real novelty of the proposed system architecture is that it allows evaluation of the Conditional Mean Spectrum (CMS) on the entire Italian territory (Cimellaro 2013).

13.6 Seismic Records Selection

Ground motion selection is applied in order to obtain a set of motions that are usually used in dynamic elastic and even nonlinear response history analysis. The *Seismic Records Selection* module is shown in Fig. 13.4 where after selecting the ground motion database to be used for the search (e.g. PEER or ESMD), the waveform (left in Fig. 13.4) or spectral criteria (right in Fig. 13.4) can be used. The *Seismic Records Selection* tool shown in Fig. 13.4 has a layout perceived in two main panels, *Spectrum panel* and *Time-History panel*. The first one provides the computation of the most used Spectra (i.e Design Spectrum, Conditional Mean Spectrum, Predicted Mean Spectrum, Uniform Hazard Spectrum). The second one is subdivided in three sections: Real, Artificial and Synthetic Time-History. In particular, Artificial and Synthetic Time-history panels allow generating new input data using the SMSIM code (Boore 2003) and a wavelet-based stochastic model (Yamamoto 2011). The Real Time-History panel allows finding earthquake records in the main databases (e.g. PEER or ESMD) by peak values, magnitude and soil category (waveform matching), by spectrum matching or energetic methods.

13.6.1 Real Time History Selection

13.6.1.1 Waveform and Spectral Matching

The waveform matching can be obtained selecting some specific parameters obtained by the disaggregated seismic hazard maps at a specific site such as the moment magnitude, M_w , the fault distance or Joyner-Boore distance (R or R_{JB} ,

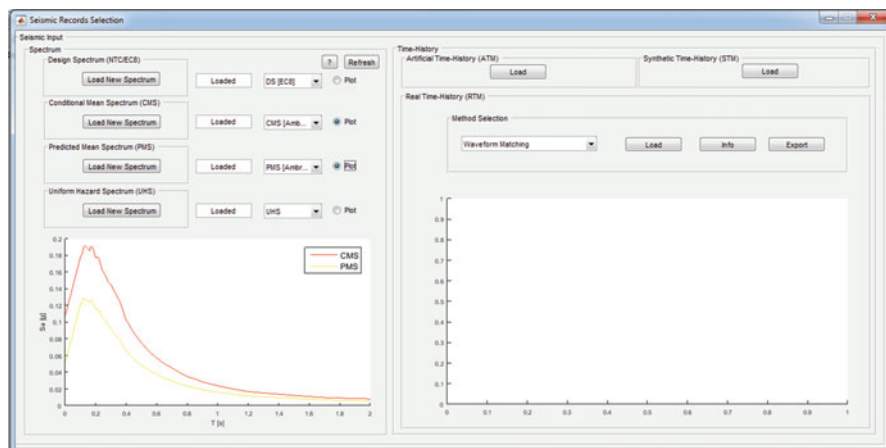


Fig. 13.4 User dialog window for Seismic Records Selection

expressed in km), the fault mechanism, the soil type according to EC8 and US standards and the waveform parameters (e.g. Peak Ground Acceleration, Peak Ground Velocity, Peak Ground Displacement). In the search with the Spectral Matching block, the first step is the definition of the type of matching to be carried out. There are three currently available options: (i) Single period, (ii) Multi periods (up to three values) and (iii) Mean Deviation. A selected percentage error is defined in all cases to vary the number of earthquakes selected. The second step is the selection of the Target Spectrum among the CMS, the DS, the UHS, the PMS or any User Defined (UDS) response spectrum. After the selection of the target spectrum, the search of the records between the ground motion databases available in the computer environment is performed. Both horizontal and vertical components of ground motion can be considered for ESMD, while the geometric mean components are used for PEER. Then the records found can be preselected in a table and visually inspected comparing both response spectra and other data (e.g. location) and only after this further check the records can be downloaded and saved.

13.6.1.2 Energetic Method

A novel Ground Motion Selection and Modification (GMSM) procedure is also implemented in the software for minimizing the dispersion of the Engineering Demand Parameters (EDP) and enhancing the accuracy in the prediction of dynamic structural response (*energetic method*). The new selection and scaling procedure emerges from comparing a set of horizontal ground motions at various ranges of frequency and then obtaining a set of ground motions with similar seismic severity by matching the target spectrum at the period of interest T_{ref} . Furthermore, the selected motions are scaled in order to have an equivalent Housner intensity in the period range $0.2T_{ref} - 2T_{ref}$ comparable with the target spectrum one. The horizontal components for every band of frequency is obtained using a specific index that depends on the energy-frequency trend's shape as well as on its scattering degree around the mean value (Marasco and Cimellaro 2017). This allows obtaining a set of spectrum-compatible records with almost identical severity and low dispersion of the structural response parameters. The methodology has been tested showing a significant effectiveness in terms of low variability of parameters and accuracy in preserving the median demand for a given hazard scenario. This new software component is able to select and modify ground motion records coming from PEER and ESMD database and setting magnitude and epicenter distance ranges, by imposition of a given reference period. Then, seven groups of records (in both horizontal direction) can be derived and used in the time history analyses. The proposed GMSM procedure is available both for structural and geotechnical applications. The *Energetic method dialog box* is shown on Fig. 13.5.

As a result, this new energetic proposed approach allows to select a representative set of ground motion according to the spectrum-compatibility criterion, to the frequency content representativeness and to the consistency of the expected structural damage for the given hazard scenario.

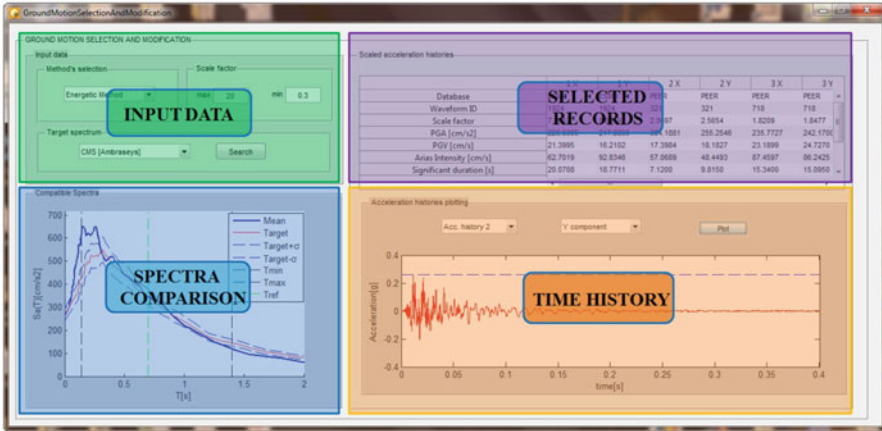


Fig. 13.5 User dialog window for energy-based GSM procedure

13.6.2 Artificial Time-History Selection

The decomposition of ground motion time-histories into wavelet packets and the reconstruction of time-histories from wavelet packets has been applied in the creation of a stochastic ground-motion model (Yamamoto and Baker 2013). The wavelet packet is defined as in the Eq. 13.1.

$$c_{j,k}^i = \int_{-\infty}^{\infty} x(t) \psi_{j,k}^i(t) dt \tag{13.1}$$

Exploiting two groups of wavelet packets, 13 parameters quantify time and frequency characteristics of the acceleration time histories. Such parameters are predicted as a function of four predictor variables: the moment magnitude (M_w), the hypocentral distance (R_{hyp}), rupture distance (R_{rup}), and average shear-wave velocity within 30 m depth (V_{s30}). In turn, the predictor variables are obtained by a two-stage regression analysis. In Yamamoto and Baker (2013) it has been proposed a range of values that provides a good match from the GMPEs; those values are reported and recommended inside the code. As in synthetic time-histories, the generation of independent time-histories is unlimited and the signal processing is analogous (Fig. 13.6).

13.6.3 Synthetic Time-History Selection

OPENSIGNAL allows the creation of synthetic time-histories exploiting the physic concepts implemented in SMSIM code (Boore 2003) where the total spectrum of the motion at a site can be divided into contributions from earthquake source, path (P),

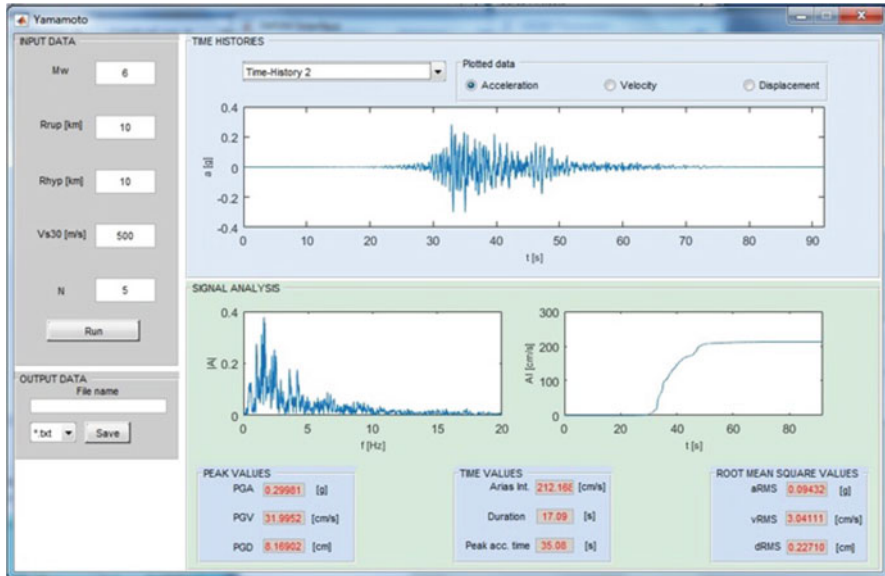


Fig. 13.6 Window of generation of artificial time-histories. Synthetic time-histories share a coincident layout with few differences in the INPUT DATA panel

and site. The shape and amplitude of the source spectrum are function of earthquake size; it is overall defined by three elements: a constant value (C), the seismic moment (M_0) and the displacement source spectrum ($S(M_0, f)$). The constant C is computed (Eq. 13.2) according to the radiation pattern (R_{rp}), the partition of total shear-wave energy into horizontal components (V), a reference distance (R_0), the effect of the free surface (F), the soil density (ρ_s) and the shear wave velocity (β_s) in the vicinity of source. The soil density and the shear wave velocity are set by the user; R_{rp} is set to 0.55, V to 1/2, R_0 to 1, and F to 2.

$$C = \frac{R_{rp}VF}{4\pi\rho_s\beta_s^3R_0} \tag{13.2}$$

Different formulations of displacement source spectrum exist in literature; in OPENSIGNAL is possible to choose between a singular corner frequency or a double corner frequency. In the first case the only input is the stress drop ($\delta\sigma$) while the user selects the ratio of both corner frequencies as well as the stress drop in the second case. The variability of the stress drop can be formulated by the reference magnitude of the stress drop and the derivative of it in the log space. The path contribution is split in the geometric spreading ($Z(R)$) and attenuation ($Q(f)$) as given in Eq. 13.3.

$$P(R, f) = Z(R) \exp\left(\frac{\pi fR}{Q(f)}c_q\right) \tag{13.3}$$

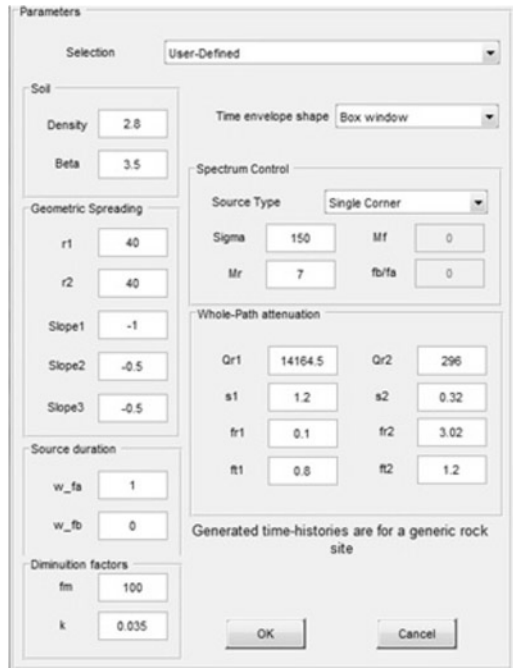
where c_q is the seismic velocity used in the determination of $Q(f)$. The geometric spreading in OPENSIGNAL is defined by means of five parameters, in order to create a series of three linear straight lines with slope (p_1, p_2, p_3) with in the range among (R_1, R_2) . The attenuation contribute is represented by three piecewise-continuous line segments specified by 8 parameters: the slopes of first (s_1) and third lines (s_2) that have values (Q_{r1}) and (Q_{r2}) at frequencies (f_{r1}) and (f_{r2}) , the transition frequencies (f_{t1}) and (f_{t2}) . The site effect is generally formulated as the product of an amplification effect and diminution effect. OPENSIGNAL provides a formulation for a generic rock site amplification, by recommending a proper local site analysis to take into account the amplification of soil. The diminution factor describes the path-independent loss of high frequency by applying two filters (Eq. 13.4).

$$D(f) = \frac{\exp(-\pi k_0 f)}{\sqrt{1 + \left(\frac{f}{f_{max}}\right)^8}} \tag{13.4}$$

The user defines a proper value of (k_0) and (f_{max}) . All the parameters are set in a proper window (Fig. 13.7) where the user can choose the time envelope shape.

An arbitrary number of independent time-histories can be generated by multiplying the normalized amplitude spectrum of white-noise with the computed spectrum. The total duration of the white-noise is set according as Eq. 13.5.

Fig. 13.7 Required parameters for generation of synthetic time-histories



$$D_{tot} = 2 \left(0.05R + \frac{1}{f_a} \right) \tag{13.5}$$

The time envelope shape is scaled according to the source duration weight (w_a, w_b). For each time-history, several parameters are computed and displayed (e.g. velocity, displacement, Fourier amplitude, Arias intensity).

13.7 Approximated Site Response Analysis

The CMS and the UHS are usually used as target spectra in order to perform the selection procedure discussed previously. Since the two spectra just mentioned are obtained for the condition of rigid and flat surface, the selection procedure does not lead to a representative set of acceleration histories. In real cases, the soil parameters affect the seismic response of a geotechnical system, because the soil filters the seismic input, so specific frequencies may be amplified while others may not. Thus, the soil surface seismic response is not coincident with the assumption of rigid and flat surface (bedrock). In order to take into account the local site effects of the ground motion propagation a special OPENSIGNAL component is implemented (Fig. 13.8). A new set of accelerograms or an existing one can be used as input motion at bedrock. For this reason, it is possible to select the acceleration histories selected in the *Matching* procedure (Import set in Fig. 13.8). This software component performs the soil response analysis by using a time domain solution of the dynamic equations with the implicit method of Newmark based on the Eqs. 13.6 and 13.7.



Fig. 13.8 User dialog window for site response analysis



$$\dot{u}_{i+1} = \dot{u}_i + [(1 - \gamma)\Delta t]\ddot{u}_i + (\gamma\Delta t)\ddot{u}_{i+1} \tag{13.6}$$

$$u_{i+1} = u_i + (\Delta t)\dot{u}_i + [(\frac{1}{2} - \beta)\Delta t^2]\ddot{u}_i + (\beta\Delta t^2)\ddot{u}_{i+1} \tag{13.7}$$

where Δt defines the time step, u , \dot{u} and \ddot{u} represent the displacement, velocity and acceleration of the system, respectively. These ones are determined at the time $i+1$ starting from the known values at time i . The parameters β and γ define the variation of the acceleration over a time step and in the present work they have been set equal to $\beta = \frac{1}{4}$ and $\gamma = \frac{1}{2}$ (average acceleration method). The layered soil column is idealized as a multi-degree of freedom system with lumped parameters (spring-dashpot system Fig. 13.9) and the seismic excitation is imposed at the base of the physical model (bedrock) as an acceleration history. The equations of motion can be expressed in the following matrix form Eq. 13.8.

$$[M] \{\ddot{u}\} + [C] \{\dot{u}\} + [K] \{u\} = -[M] [I] \{\ddot{u}_g\} \tag{13.8}$$

where $[M]$, $[C]$ and $[K]$ are the mass matrix, viscous damping matrix and stiffness matrix respectively, while \ddot{u} , \dot{u} and u define the vectors of the absolute nodal accelerations, velocities and displacements respectively. The term $\{I\} \ddot{u}_g$ represents the earthquake load, where each component of the vector I is equal to the unit value. In a nonlinear formulation the energy of the system is dissipated through the hysteretic loading-unloading cycle, thus, the viscous damping matrix may be defined in order to simulate the mentioned process of dissipation. In addition, in the time domain analyses, the damping depends on the frequencies. One of the most common and simplified methods used to compute the damping matrix is the Rayleigh formulation (RF), where the damping is assumed to be proportional to

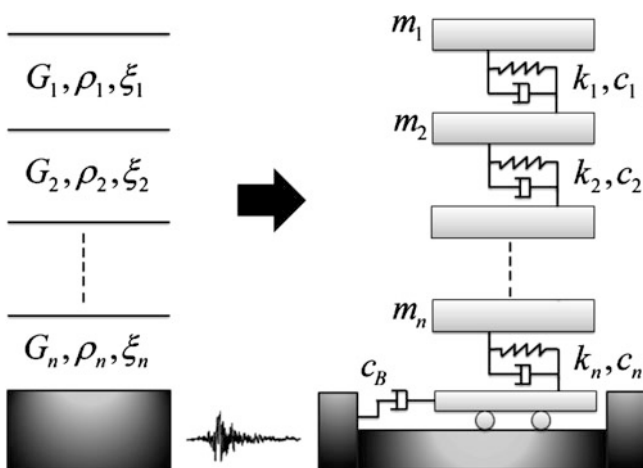


Fig. 13.9 Multi degree of freedom system with excitation at the base

the mass matrix and to the stiffness matrix (Eq. 13.9) by means of two coefficients a_0 and a_1 frequency dependent (Eq. 13.10 and 13.11).

$$[C] = a_0 [M] + a_1 [K] \quad (13.9)$$

$$a_0 = \xi \frac{4\pi(f_0 f_1)}{f_0 + f_1} \quad (13.10)$$

$$a_1 = \xi \frac{1}{\pi(f_0 + f_1)} \quad (13.11)$$

where ξ is the damping ratio of the soil system and f_0 and f_1 are the two control frequencies. The main approximation of this procedure consists in the underestimation of the damping at frequencies between f_0 and f_1 , and the overestimation of the damping at frequencies lower than f_0 and higher than f_0 . Thus, the selection of the two control frequencies is very important in order to obtain good results. For this purpose, OPENSIGNAL performs the dynamic analysis calculating the damping matrix according to Hudson et al. (1994) in which f_0 is the fundamental frequency of the soil column and f_1 represents the predominant frequency of the ground motion. In addition, OPENSIGNAL takes into account the variation of damping ratio among the layers of soil calculating the damping matrix as an ensemble of damping element matrices (Eq. 13.12).

$$[C] = \frac{4\pi(f_0 f_1)}{f_0 + f_1} \begin{bmatrix} \xi_1 m_1 & 0 & \dots & 0 \\ 0 & \xi_2 m_2 & 0 & 0 \\ \dots & 0 & \dots & \dots \\ 0 & 0 & \dots & \xi_n m_n \end{bmatrix} + \frac{1}{\pi(f_0 + f_1)} \begin{bmatrix} \xi_1 k_1 & -\xi_1 k_1 & \dots & 0 \\ -\xi_1 k_1 & \xi_1 k_1 + \xi_2 k_2 & -\xi_2 k_2 & \dots \\ \dots & -\xi_2 k_2 & \dots & -\xi_{n-1} k_{n-1} \\ 0 & \dots & -\xi_{n-1} k_{n-1} & \xi_{n-1} k_{n-1} + \xi_n k_n \end{bmatrix} \quad (13.12)$$

OPENSIGNAL uses a hybrid method in which the hysteretic behaviour of the soil is approximated using the shear modulus degradation curve ($G-\gamma$) and the damping ratio curve ($\xi-\gamma$). For this reason, the clay, the sand and the rock degradation curves are available in OPENSIGNAL according with the default curves available in EERA (Bardet et al. 2000).

This approach allows approximating the real soil behavior, by assuming that the shear modulus and the damping ratio vary with the shear strain amplitude (equivalent linear model). The nodal displacements and the shear deformations related to the relative displacements are calculated for a generic time using the Newmark method. These values will be considered to upload the shear modulus and the damping ratio used in the following instant to define the new stiffness

Table 13.1 OPENSIGNAL soil response analysis vs EERA

Feature	OPENSIGNAL	EERA
Discretization	Lumped mass	Continuous layers
Type of solution	Time domain	Frequency domain
Type of analysis	Step by step integration	Transfer function
Soil model	$G(\gamma)$ and $D(\gamma)$ curves	$G(\gamma)$ and $D(\gamma)$ curves
Damping model	Rayleigh formulation (RF)	Kelvin-Voigt model
Nonlinearity	Solution with parameters uploading at every step	Iterative approximation of equivalent linear response

and damping matrix. The main approximation is due to the nonlinear behavior of the soil and the inconsistency of the soil parameters determination in the large shear strain range, because in this field the real stiffness and damping depend on the number of loading-unloading cycles. Nevertheless, it was observed that in the medium deformation range the nonlinear behavior of the soil is not significantly influenced by the load path. The comparison between the method implemented in OPENSIGNAL and the one implemented in EERA is shown in Table 13.1. The proposed hybrid method can lead to inaccurate solutions for seismic records with high amplitude, because they generate wide shear deformations in the soil column and, as mentioned before, in the large strain range it is necessary to consider the real ($\tau - \gamma$) trend in order to appreciate the nonlinear soil phenomena. Thus, in this case, it is necessary to adopt a specific nonlinear soil response analysis software. In addition, since the proposed method carries out the RF to define the damping in each step, the solution is strictly dependent upon the f_0/f_1 ratio. For this reason, at high values of the frequency ratio the RF leads to an underestimated damping, then the calculated solution is greater than the real one.

13.8 Case Study

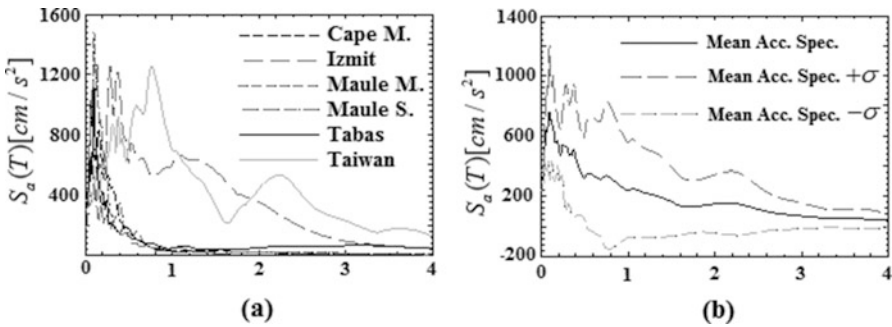
As an illustrative example to show the capabilities of the computer-based platform environment, six ground motion records have been chosen to test the record processing tool, while a set of deaggregation parameters has been identified to test the record selection criteria tool. The first dialog window of the computer environment focuses on the ground motion signal processing, using filters to process the signals and evaluate the elastic response spectrum.

The platform allows automatic reading of the accelerograms from these databases and plotting the main related information. In particular, the records can be selected from the PEER strong motion database (PEER), the European Strong Motion Database (ESMD), the Italian Accelerometric Archive version 2.0 (ITACA) and the University of Chile database (UCHILE).

As an illustrative example, six records, from UCHILE, ESMD and PEER database have been selected and listed in Table 13.2. The associated acceleration

Table 13.2 Six ground motion records from UCHILE, ESMD and PEER database

Database	Station ID	Event ID	Earthquake name	Date	PGA [cm/s ²]	ML/W	R [km]
UCHILE	S/N 6735	Matanzas	Maule	27/02/2010	311.15	8.8	-
UCHILE	S/N 935	Santiago Centro	Maule	27/02/2010	186.87	8.8	-
ESMD	553	472	Izmit	17/08/1999	319.29	7.6	12.00
ESMD	54	87	Tabas	16/09/1978	319.85	7.3	12.00
PEER	89324	P0810	Cape Mendocino	25/04/1922	360.22	7.1	18.50
PEER	CHY006	P1120	Taiwan	20/09/1999	362.74	7.3	14.93

**Fig. 13.10** Elastic acceleration response spectra (a) and mean acceleration response spectrum (b)

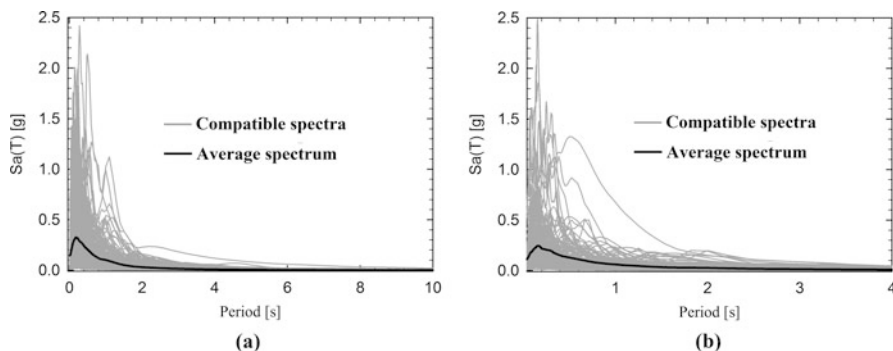
elastic response spectra damped at 5% are shown in Fig. 13.10. The six uncorrected records have values of PGA between 186.87 cm/s^2 and 362.74 cm/s^2 and local/moment magnitude between 7.1 and 8.8. Every uncorrected record in Table 13.2 has been filtered with a Butterworth filter having $f_{min} = 0.25 \text{ Hz}$, $f_{max} = 25 \text{ Hz}$ and $n = 4$. The filtered set of records is then used for the response spectral analysis. In Fig. 13.13 the acceleration elastic response spectra of the ground motion set in Table 13.2 with a damping ratio equal to 5% are shown. After uploading the records, OPENSIGNAL allows the evaluation of main signal parameters divided into three main categories:

- Peak values: PGA , PGV and PGD ;
- Time values: *Arias intensity*, *Duration*, *Peak acceleration time*;
- Root mean square values: a_{RMS} , v_{RMS} , d_{RMS} .

The parameters are calculated for both the unfiltered (*Original*) and filtered (*Modified*) records. As example, the time histories of *Maule* earthquake are considered and the relative signal parameters are summarized in Table 13.3. The selection criteria of the ground motion records follow two different approaches: *waveform matching* and *spectral matching*. OPENSIGNAL enables the selection procedure

Table 13.3 Signal properties of the unfiltered vs. filtered records (Maule earthquake Matanzas S/N 6736)

	PGA [cm/s ²]	PGV [cm/s]	PGD [cm]	I_a [cm/s]	Duration [s]	Peak acc. Time [s]	a_{RMS}	v_{RMS}	d_{RMS}
Unfiltered	333.8	48.0	-	707.8	33.85	41.3	64.1	14.4	-
Filtered	311.2	47.0	30.7	665.0	33.75	41.38	62.4	7.8	8.8

**Fig. 13.11** Waveform matching for the PEER database (a) and ESMD (b)

to perform, starting from the European database (ESMD) and the international database (PEER). The selection procedure can be carried out by choosing between the horizontal and the vertical components of ground motion for the ESMD, while the geometrical horizontal mean values are considered for the selection of the acceleration history in the PEER database.

The selection procedure based on *waveform matching* is based on the source and site characteristics such as the *Moment Magnitude* (M_w), the *fault distance* or *Joyner-Boore distance* (R_{JB}) and the *soil category*, or on the waveform characteristics such as the *peak ground acceleration* (PGA), the *peak ground velocity* (PGV) and the *peak ground displacement* (PGD). For example, in Fig. 13.11 the response spectra of the ground motions selected from the PEER (Fig. 13.11a) and the ESMD (Fig. 13.11b) respectively are shown, considering a range of moment magnitude of 3–6.5 and the fault distance of 10–50 km. Several techniques have been developed for selecting a reliable set of earthquake records to be used in the dynamic structural analysis. One selection criteria is based on the spectral matching for a specific target spectrum. Thus, the definition of a target spectrum represents the preliminary phase of the spectral matching, and for this purpose, OPENSIGNAL allows choosing between five different spectra:

1. Design Spectrum (DS) according to NTC2008, EC8 and FEMA 302;
2. Uniform Hazard Spectrum (UHS);

3. Predicted Mean Spectrum (PMS) according to Ambraseys et al. (1996), Campbell and Bozorgnia (2008), Boore and Atkinson (2008), Iyengar et al. (2010), Contreras and Boroschek (2012), GMPE;
4. Conditional Mean Spectrum (CMS);
5. User Defined Spectrum (UDS).

As an example, the three deaggregation parameters have been chosen to define the CMS which will be used as target spectrum in order to perform the spectral matching (Table 13.4). The Conditional Mean Spectrum (CMS) has been defined for the period of 0.2 s and for a probability of exceedance of 10% in 50 years. The CMS has been built taking into account the deaggregation values associated with the reference period using the Boore and Atkinson (2008) GMPE. In OPENSIGNAL three different approaches for spectral matching are available:

- *Single period approach;*
- *Multi period approach;*
- *Mean deviation approach.*

OPENSIGNAL can use any of the matching procedures mentioned above, by selecting the tolerance in term of percentage error for the first two approaches or in term of mean deviation for the latter one. The search can be performed for the X, Y or Z components for both the ESMD and PEER records. In Table 13.5 the parameters used for the matching criteria for both the ESMD and PEER database are summarized, while the results are shown in Fig. 13.12.

Table 13.4 Mean deaggregation values chosen

M	R [km]	ϵ	$V_{S,30}$ [m/s]	Fault
7.85	34.55	0.97	350	Normal

Table 13.5 Spectral matching parameters

Database	Matching criteria	Component	% error	Ti [s]
ESMD	Single period	Y-component	10	0.2
PEER	Single period	Y-component	10	0.2

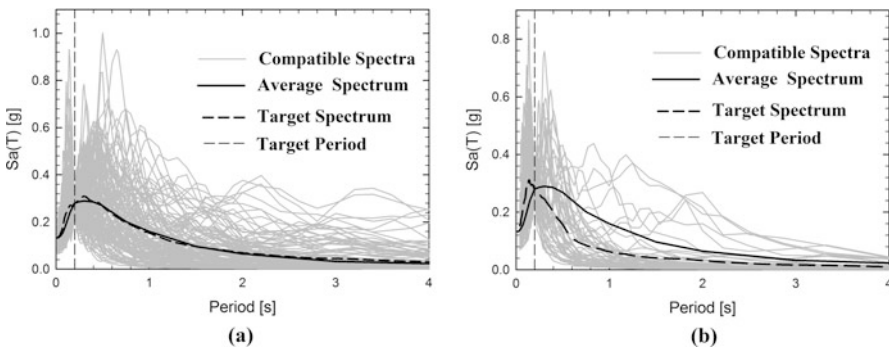


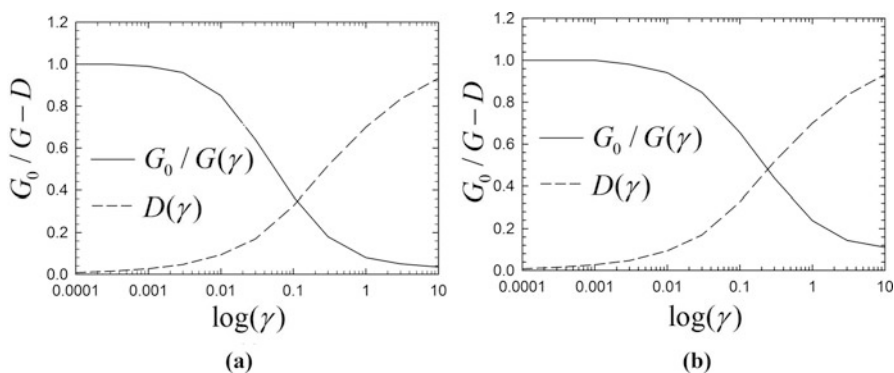
Fig. 13.12 Single period matching with conditional mean spectrum as target spectrum, for the (a) PEER database and (b) ESMD

Table 13.6 Ground motion characteristics

Station ID	Event name	Date	ML
TLM1	Friuli	05/06/1976	4.5
CSC	Val Nerina	09/19/1979	5.5

Table 13.7 Geotechnical soil characteristics

Layer	Soil	Thickness [m]	Shear wave velocity [m/s]	Initial shear modulus [MPa]	Initial damping ratio [%]	Unit weight [kg/m ³]
1	Sand	6.5	136.21	37.18	0.24	2004.08
2	Sand	5.0	176.15	62.19	0.24	2004.08
3	Clay	9.0	404.46	348.35	0.24	2129.46
4	Sand	8.0	225.52	101.93	0.24	2004.08
5	Clay	6.0	275.84	162.03	0.24	2129.46
6	Sand	8.0	207.46	86.26	0.24	2004.08

**Fig. 13.13** Shear modulus degradation curve and damping ratio curve for sand (a) and clay (b)

As a practical example of Soil response analysis, two different ground motions with medium intensity have been considered and their main characteristics are illustrated in Table 13.6. The stratigraphic characteristics of the soil column chosen in the application are reported in Table 13.7 in which layer 1 defines the soil surface while the layer 6 is located above the bedrock.

Figure 13.13 illustrates the $(G_0/G-\gamma)$ and $(\xi-\gamma)$ curves used in the application.

The accuracy of the numerical solution depends on the number of sublayers, or rather on the degree of freedom. Since the generic half earthquake wave length should be described by at least 3–4 points for each layer, the thickness to be assigned to the single layer should not be greater than the ratio between the shear wave

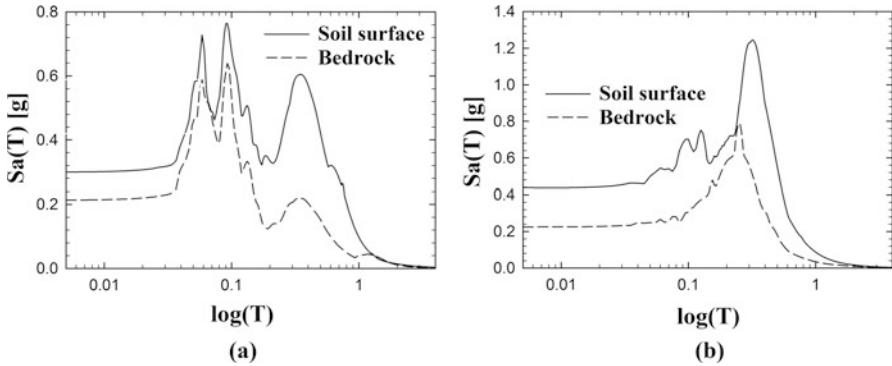


Fig. 13.14 Val Nerina earthquake (a) and Friuli earthquake (b) comparisons between bedrock and soil surface results

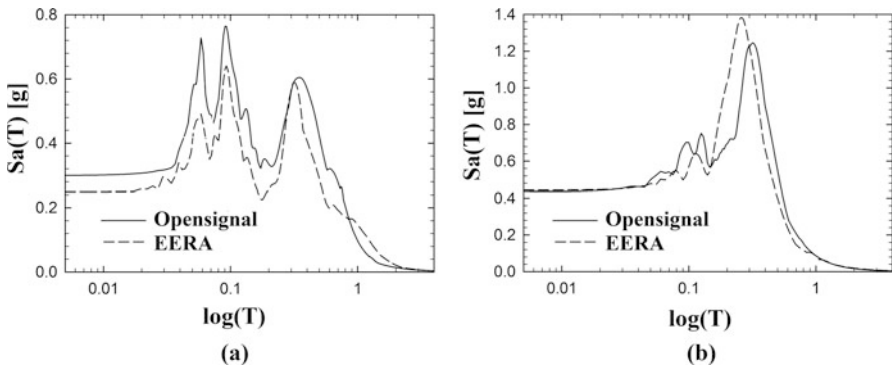


Fig. 13.15 Val Nerina earthquake (a) and Friuli earthquake (b) comparisons between EERA and OPENSIGNAL results

velocity (V_s) and six times the height of the predominant seismic frequency (f_{max}). In order to satisfy the previous conditions (Eq. 13.13), OPENSIGNAL performs a preliminary division of the soil column.

$$h_{max} \cong \frac{V_s}{7f_{max}} \tag{13.13}$$

The amplification phenomena are emphasized in Fig. 13.14 in which the spectrum on bedrock is compared with the spectrum on the soil surface. Finally, the results obtained with OPENSIGNAL and EERA are compared in Fig. 13.15.

References

- Ambraseys NN, Simpson KA, Bommer J (1996) Prediction of horizontal response spectra in Europe. *Earthq Eng Struct Dyn* 25(4):371–400
- Bardet J, Ichii K, Lin C (2000) EERA: a computer program for equivalent-linear earthquake site response analyses of layered soil deposits. University of Southern California, Department of Civil Engineering
- Boore DM (2003) Simulation of ground motion using the stochastic method. In: *Seismic motion, lithospheric structures, earthquake and volcanic sources: the Keiiti Aki volume*. Birkhäuser, Basel, pp 635–676
- Boore DM, Atkinson GM (2008) Ground-motion prediction equations for the average horizontal component of pga, pgv, and 5between 0.01 and 10.0 s. *Earthq Spectra* 24(1):99–138. <https://doi.org/10.1193/1.2830434>
- Campbell KW, Bozorgnia Y (2008) Nga ground motion model for the geometric mean horizontal component of pga, pgv, pgd and 5spectra for periods ranging from 0.01 to 10 s. *Earthq Spectra* 24(1):139–171. <https://doi.org/10.1193/1.2857546>
- Cimellaro GP (2013) Correlation in spectral accelerations for earthquakes in europe. *Earthq Eng Struct Dyn* 42(4):623–633. <https://doi.org/10.1002/eqe.2248>
- Cimellaro GP, De Stefano A (2010) Correlation in spectral accelerations of European ground motion records. In: *Proceedings of 9NCEE, Toronto*
- Cimellaro GP, Marasco S (2015) A computer-based environment for processing and selection of seismic ground motion records: Opensignal. *Front Built Environ* 1:17
- Cimellaro GP, Reinhorn AM, D'Ambrisi A, De Stefano M (2011) Fragility analysis and seismic record selection. *J Struct Eng, ASCE* 137(3):379–390
- Contreras V, Boroschek R (2012) Strong ground motion attenuation relations for chilean subduction zone interface earthquakes. In: *Proceedings of 15WCEE, Lisbon*
- Hachem MM (2004) Bispec: a nonlinear spectral analysis program that performs bi-direction dynamic time-history analysis of pendulum system. University of California at Berkeley. Available online at <http://www.ce.berkeley.edu/~hachem/bispec/>
- Hudson M, Idriss I, Beikae M (1994) Users manual for quad4m: a computer program to evaluate the seismic response of soil structures using finite element procedures and incorporating a compliant base. University of California, Davis
- Iyengar R, Chadha R, Balaji Rao K, Raghukanth S (2010) Development of probabilistic seismic hazard map of india. Report on the National Disaster Management Authority, Government of India, India
- Katsanos EI, Sextos AG (2013) Issars: an integrated software environment for structure-specific earthquake ground motion selection. *Adv Eng Softw* 58:70–85
- Marasco S, Cimellaro GP (2017) A new energetic based ground motion selection and modification algorithm. In: *Proceedings of 16th World Conference on Earthquake Engineering, 16WCEE, Paper N 1645, 9th to 13th Jan 2017, International Association on Earthquake Engineering*
- Yamamoto Y (2011) Stochastic model for earthquake ground motion using wavelet packets. Ph.D. thesis, Department of Civil and Environmental Engineering, Stanford University, Stanford, 295 p
- Yamamoto Y, Baker JW (2013) Stochastic model for earthquake ground motion using wavelet packets. *Bull Seismol Soc Am* 103(6):3044–3056

Chapter 14

Methods of Analysis



Abstract The chapter analyzes the structural seismic analysis methods. The four common analysis method are illustrated (Linear static, linear dynamic, nonlinear static, and nonlinear dynamic analyses). Additionally, the direct displacement-based seismic design procedure is discussed in detail.

14.1 Introduction

The methods of analysis for multistory buildings are based on static or dynamic approaches. Since the earthquake excitation is a dynamic action, the second procedure is more conservative and accurate than the first one. In addition, both analysis procedures can be applied by including mechanical nonlinearities (nonlinear methods) or by neglecting them (linear methods). The choice of the methodology to be used depends on the degree of accuracy of the problem and on the geometric configuration system. For this reason, static analyses can be applied for buildings having a regular mass and stiffness distribution in elevation and in plan. In these cases the dynamic action due to an earthquake is assumed to have a pseudo-static force configuration. The dynamic analyses are able to take into account the time variation of the system response but they request a higher computational effort.

The linear analyses can be used for both non-dissipative systems and dissipative ones with low plasticity, however in this last case the results might be too conservative. From this definition, it is clear that the reliability of the linear methods depends on the distribution of the plastic dissipation elements (*ductility request distribution*). In addition to that, if the stiffness and mass distribution of the elements of the building is not uniform, the linear analyses lead to results which are not comparable with the nonlinear ones. Either way, the linear analyses for dissipative systems leads obtaining actions greater than the effective one. For this reason, when the linear analysis is used for dissipative system, it is necessary to reduce the forces deduced from the design elastic spectrum by means of the over-strength factor q discussed in Sect. 5.2. The NTC08 (2008) approach is based on the definition of a constant value of q for all period values of the design spectrum greater than

T_B . The value of the over-strength factor needs to be selected as function of the ductility characteristics of the system and it is used for the two directions of the seismic excitation. NTC08 proposes the expression given by Eq. 14.1 for over-strength factor definition to be used for horizontal elastic seismic actions.

$$q = q_0 \cdot K_R \quad (14.1)$$

where q_0 represents the maximum value of over-strength factor that depends on the expected ductility, structural typology and on the α_u/α_1 ratio. The term α_u represents the initial seismic action value causing the formation of a number of plastic hinges that lead to an unstable configuration, while α_1 is the value associated with the first flexural plasticization on the more heavily stressed elements. The coefficient K_R takes into account the regularity and it assumes a value equal to 1 for regular structures and 0.8 for structures with irregularity in elevation. The values assumed for q_0 and α_u/α_1 coefficients are reported in paragraph 7.4.3.2 of NTC08.

Instead for vertical seismic actions, the suggested value of the over-strength factor is 1.5. The reduction of the seismic design actions due to dissipative effects has to be used only for Ultimate Limit State (ULS) design or verification methods. Figure 14.1 illustrates an example of scale reduction for a generic elastic design spectrum that defines the seismic input for the structure.

The linear analyses where the elastic forces are reduced due to the presence of dissipative systems are not able to take into account the modifications in the struc-

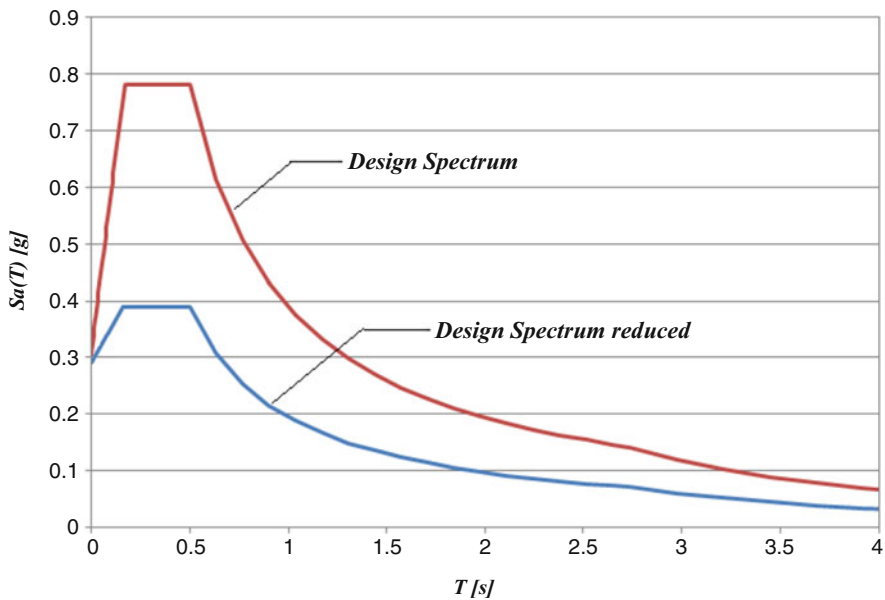


Fig. 14.1 Reduction of the design spectral accelerations

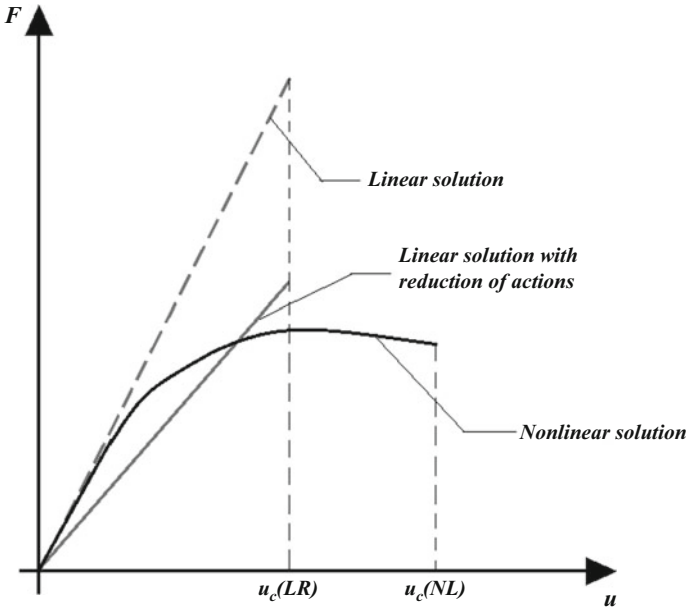


Fig. 14.2 Comparison between nonlinear and linear with force reduction behavior

tural response due to the damage increments (progressive plastic hinges formation). In other words, it is not possible to consider the redistribution of the internal forces inside the structural elements of the system. Figure 14.2 schematically illustrates the F - u relationship obtained for a generic dissipative structure assuming a linear (with force reduction) or nonlinear behavior.

The values of $u_{c(NL)}$ and $u_{c(LR)}$ represent the collapse displacement (ultimate capacity) obtained for nonlinear solution and linear with force reduction solution, respectively. It is possible to observe how the ultimate capacity of the system evaluated with the two methods, can be significantly different.

In order to obtain a more accurate response at ULS, the nonlinear procedures must be used. These methods request a wide computational effort, since they are based on the redefinition of the stiffness characteristics after the formation of a plastic hinge. NTC08 does not give enough information about the applications of nonlinear methodologies, while more information is given in Chapter 4 of the EC8 (1998-1 (2004)).

Usually, for *new buildings* the linear dynamic analysis is most commonly used because it allows designing the structural elements. For *existing buildings* instead it is necessary to assess the safety of the structures through a nonlinear dynamic analysis since the nonlinear effects have to be necessarily considered to achieve an accurate response. In the following paragraphs, the four analysis methods listed in NTC2008 will be discussed in detail.

14.2 Linear Static Analysis

As mentioned in Part I, the effects of the higher modes of a regular structure can be neglected since the first mode is predominant. In these cases, both for the dissipative and the non-dissipative systems, the seismic action can be modeled with a pseudo-static equivalent distribution. Since the masses of a multistory building are practically concentrated on the stories, the seismic action is composed of equivalent inertia static forces applied on each flooring system. NTC08 proposes the following criteria to be satisfied in order to use the linear static analysis:

- regular mass and stiffness distribution along the vertical direction;
- the fundamental period of the structure (T_1) has to respect the condition given in Eq. (14.2).

$$T_1 \leq \min(2.5 \cdot T_C, T_D) \quad (14.2)$$

According to NTC08, the fundamental period of the structure can be estimated by referring to the height of the structure and structural typology (Eq. 14.3).

$$T_1 = C_1 \cdot H^{3/4} \quad (14.3)$$

where the coefficient C_1 depends on the structural typology (Table 14.1) while H represents the height of the structure expressed in meters (measured from the foundation level).

The equivalent static inertial forces (F_i) applied at each story mass are evaluated according to Eq. 14.4, in which the distribution is assumed proportional to the first vibrational mode.

$$F_i = \frac{F_h \cdot z_i \cdot W_i}{\sum_j z_j \cdot W_j} \quad (14.4)$$

where:

- W_i and W_j represent the i th and j th mass;
- z_i and z_j are the height of mass i and j measured from the foundation level;
- F_h is the base shear deduced by the design spectral acceleration at period of interest ($S_d(T_1)$).

In Eq. 14.5 the base shear is given:

$$F_h = S_d(T_1) \cdot \frac{W}{g} \cdot \lambda \quad (14.5)$$

Table 14.1 Coefficient C_1 according to NTC08

Steel structures	Reinforced concrete structures	Other type structures
0.085	0.075	0.05

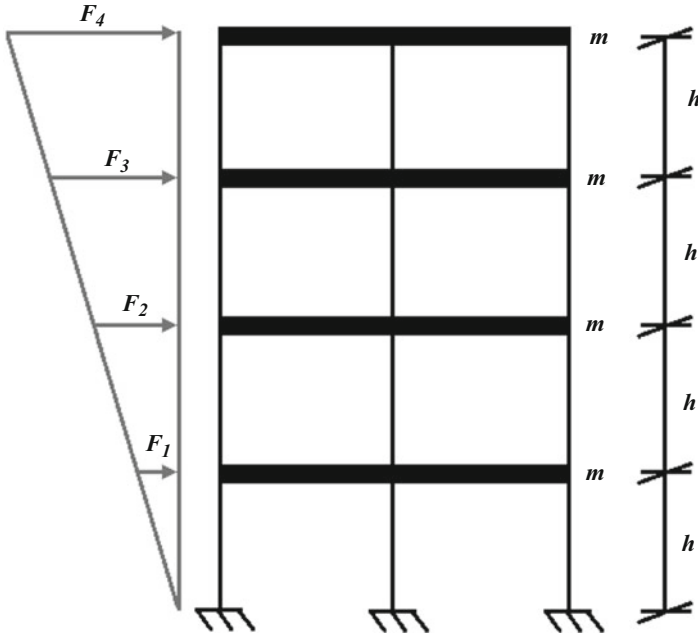


Fig. 14.3 Equivalent static forces distribution for a four story regular building

in which W indicates the total mass of the structure, g is the gravitational acceleration and λ represents a coefficient equal to 0.85 for structures with a number of stories greater than 2 and with $T_1 < 2T_C$, or equal to 1 otherwise. Naturally, the dissipative effects on the structure are taken into account by reducing the elastic design spectrum with an over-strength factor. Figure 14.3 illustrates a generic example of an equivalent static force distribution for a regular multistory building.

Considering the multistory building displayed in Fig. 14.3, the associated static equivalent forces applied at each story are given by Eq. 14.6.

$$\begin{aligned}
 F_1 &= S_d(T_1) \cdot 4 \cdot m \cdot \lambda \cdot \frac{(m \cdot g) \cdot h}{30 \cdot (m \cdot g) \cdot h} = \frac{1}{30} \cdot S_d(T_1) \cdot m \cdot \lambda \\
 F_2 &= S_d(T_1) \cdot 4 \cdot m \cdot \lambda \cdot \frac{(m \cdot g) \cdot 2 \cdot h}{30 \cdot (m \cdot g) \cdot h} = \frac{1}{15} \cdot S_d(T_1) \cdot m \cdot \lambda \\
 F_3 &= S_d(T_1) \cdot 4 \cdot m \cdot \lambda \cdot \frac{(m \cdot g) \cdot 3 \cdot h}{30 \cdot (m \cdot g) \cdot h} = \frac{1}{10} \cdot S_d(T_1) \cdot m \cdot \lambda \\
 F_4 &= S_d(T_1) \cdot 4 \cdot m \cdot \lambda \cdot \frac{(m \cdot g) \cdot 4 \cdot h}{30 \cdot (m \cdot g) \cdot h} = \frac{2}{15} \cdot S_d(T_1) \cdot m \cdot \lambda
 \end{aligned} \tag{14.6}$$

Due to the direction and center of the mass location (accidental eccentricity) unpredictability, the NTC-08 (2008) prescribes the use of different seismic load combinations to assess the response of the structure subjected to the earthquake excitation.

1. Accidental eccentricity is introduced in order to take into account the uncertainty in the location of the center of mass. The NTC-08 (2008) considers an accidental

eccentricity of 5% of the orthogonal structure's dimension in each direction. The application of the static forces with a certain center of the mass offset induces torque moments (moment in the X-Y plan) that have to be considered in the analyses.

2. Seismic action direction is not known, then the horizontal forces have to be applied considering both negative and positive direction.
3. Predominant direction of the earthquake unknown. At this purpose the NTC-08 (2008) provides to evaluate the seismic response of the structure in both horizontal directions as given by the Eq. 14.7

$$\begin{cases} E_x + 0.3 \cdot E_y + 0.3 \cdot E_z \\ E_y + 0.3 \cdot E_x + 0.3 \cdot E_z \end{cases} \quad (14.7)$$

where E_x , E_y , and E_z represent the seismic actions in X, Y, and Z directions, respectively. Since the simultaneous application of the maximum seismic actions in the horizontal directions is unlikely, the coefficient 0.3 is considered to reduce the maximum seismic action value in one of these directions. The Table 14.2 illustrates the total number of combinations to be considered in the linear static analysis.

The evaluation of the internal stress and strain on the structure have to be carried out considering the most critical seismic combination case which is given by the envelope of the 32 combinations.

14.3 Linear Dynamic Analysis

The seismic effects on a multistory building can be defined by using the modal analysis and the response spectrum that was discussed in detail in *Part 1*. This approach is widely used for its simplicity because it combines the responses associated to the different modes. The design spectrum at a given site is used for the definition of the seismic action. For ULS verification the dissipative effects are taken into account by scaling the design spectrum by the over-strength factor. According to NTC08, the effects of the seismic actions can be obtained using the Complete Quadratic Combination (CQC) approach (Kiureghian and Nakamura 1993). In this case, the participating mass of the mode must be greater than 5% in order to be considered representative. In addition, the total participating mass of the selected modes must be greater than 85%. The modal combination produces a single, positive result for each direction of acceleration. These values for a given response quantity are combined to produce a single positive result. This allows to neglect the direction uncertainty of the seismic excitation. Anyway, due to the bi-directionality of the seismic excitation and the uncertainty in the center of the mass location 8 different seismic combination (Table 14.3) have to be considered.

Also in the case of linear dynamic analysis, the results are assumed as envelope of the 8 different seismic combinations.

Table 14.2 Seismic load combinations for linear static analysis

Principal seismic action	Sign	Eccentricity	Secondary seismic action	Eccentricity	Combination
Ex	+	ey	0.3 Ey	ex	1
				ex	2
			0.3 Ey	ex	3
				ex	4
		ey	0.3 Ey	ex	5
				ex	6
			0.3 Ey	ex	7
				ex	8
	-	ey	0.3 Ey	ex	9
				ex	10
			0.3 Ey	ex	11
				ex	12
		ey	0.3 Ey	ex	13
				ex	14
			0.3 Ey	ex	15
				ex	16
Ey	+	ex	0.3 Ex	ey	17
				ey	18
			0.3 Ex	ey	19
				ey	20
		ex	0.3 Ex	ey	21
				ey	22
			0.3 Ex	ey	23
				ey	24
	-	ex	0.3 Ex	ey	25
				ey	26
			0.3 Ex	ey	27
				ey	28
		ex	0.3 Ex	ey	29
				ey	30
			0.3 Ex	ey	31
				ey	32

14.4 Nonlinear Static Analysis: Pushover

This simplified nonlinear method is used to estimate the seismic vulnerability of a structural system and is based on the concept of structural performance (Fajfar 2002). The analysis is also called *pushover analysis* since the structure is subjected to horizontal loads of distributed static inertial forces that increase monotonically leading to a plastic hinge formation and also to a stress redistribution. In other words, the pushover analysis is a simplified tool that permits the estimation of the *capacity* of a structure subjected to a given external lateral load (*demand*).

Table 14.3 Seismic load combinations for linear dynamic analysis

Principal seismic action	Sign	Eccentricity	Secondary seismic action	Eccentricity	Combination
Ex	+	ey	0.3 Ey	ex	1
				ex	2
		ey	0.3 Ey	ex	3
				ex	4
Ey	+	ex	0.3 Ex	ey	5
				ey	6
		ex	0.3 Ex	ey	7
				ey	8

The seismic demand is determined by means of the elastic design spectrum and it represents the maximum acceleration expected on the structure according to the hazard level of the considered site. The structural capacity is considered in terms of displacements of a representative point of the structure called the *control point*. Usually, the *control point* corresponds to the center of mass of the upper story of the multistory building. Since a monotonic equivalent static distribution is applied to the structure, the control displacement parameter (δ) will vary with a control force parameter that usually is the building base shear (F_b). Thus, the function $F_b - \delta$ defines the capacity of the structure subjected to a given equivalent static distribution and it is called *capacity curve* or *pushover curve*.

Figure 14.4 shows the evolution of the structural response when the intensity vector of the static equivalent forces increase: the number of plastic hinges (Megson 2005) that are formed after the elastic threshold increase up to the collapse of the element. This method can assess different parameters such as the total global displacement, the interstory drift, the deformation and the stresses in the structural elements considering the inelastic behavior of the different members. The main problems of the method are due to the choice of the static force distribution shape and to the typology of load application. Regarding the latter aspect, the pushover analysis can be carried out in force or displacement control. The second procedure is more efficient than the first one since it is possible to observe the softening portion of the capacity curve. Nevertheless, the pushover procedure based on the application of a monotonic force distribution is more useful, because it is based on the assumption of a force distribution compatible with the inertia effects induced by the earthquake excitation. For this reason, EC8 recommends the application of two different vertical force distributions for multistory buildings:

- *uniform distribution based on the lateral forces* proportional to the mass neglecting the height of the system (uniform acceleration response).
- *distribution proportional to the first mode* deduced from linear dynamic analysis or proportional to the lateral inertia forces defined from the linear static analysis.

According to NTC08, at least two lateral forces distributions must be considered. One coming from the principal distribution (*Group 1*) and the other from the secondary distribution (*Group 2*). The definitions of the two mentioned distributions are reported below:

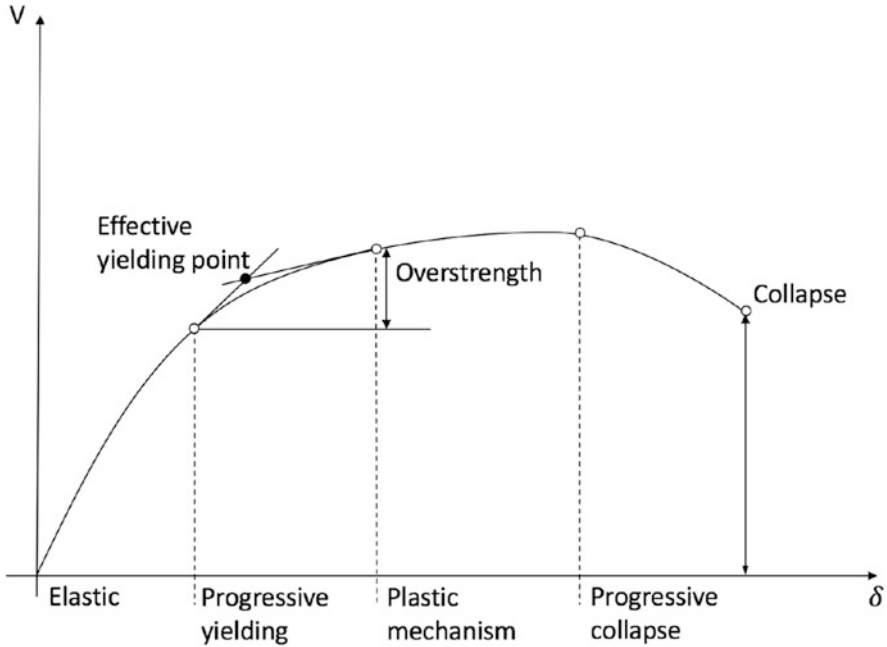


Fig. 14.4 Capacity curve or pushover curve (Adapted from Filiatrault and Christopoulos (2006))

(I) Group 1

- distribution proportional to the lateral inertia forces deduced by the linear static analysis. The mass participating factor of the fundamental mode in the considered direction should not be less than 75% [Ia];
- distribution proportional to the first vibrational mode in the considered direction. The mass participating factor of the fundamental mode in the considered direction should not be less than 75% [Ib];
- distribution proportional to the total shear at each story deduced by linear dynamic analysis. The fundamental period of the structure must be greater than T_C [Ic];

(II) Group 2

- uniform distribution along the whole height of the structure [IIa];
- adaptive distribution changing with the increase of the control displacement due to the hinges plasticization [IIb];

The generic mathematical form of the force distribution is given by Eq. 14.8:

$$\{F\} = \lambda(t) \cdot \{\phi\} \quad (14.8)$$

Table 14.4 Lateral force distributions according to NTC08

Group 1		
I_a	I_b	I_c
$\{F\} = \lambda(t) \cdot \{m\}^T \{\phi_1\}_{norm}$	$\{F\} = \lambda(t) \cdot \{F_i\}_{norm}$	$\{F\} = \lambda(t) \cdot \{V_{b,i}\}_{norm}$
Group 2		
II_a	II_b	
$\{F\} = \lambda(t) \cdot \{m\}^T \{I\}$	$\{F\} = \lambda(t) \cdot \{F_i(\delta_i)\}_{norm}$	

where $\lambda(t)$ is the scalar multiplier that identifies the time variability of the force distribution and $\{\phi\}$ is the vector that represents the shape function assigned to the distribution.

Table 14.4 reports the different forces distribution of Group 1 and 2 for a generic regular multistory building.

The force distribution vectors $\{F\}$ have been expressed by using an initial shape function normalized with respect to the force on top of the multistory building. The terms used in the expressions are below explained:

- $\{m\}^T \{\phi_1\}$: force distribution proportional to first vibrational mode $\{\phi_1\}$;
- $\{F_i\}$: lateral forces vector obtained according to Eq. 14.4;
- $\{V_{b,i}\}$: shear force vector deduced by the shear forces at each story;
- $\{m\}^T \{I\}$: force distribution to the mass (constant accelerations);
- $\{F_i(\delta_i)\}$: adaptive lateral forces vector. It is expressed as function of the displacement vector δ_i .

The pushover procedure can adopt a lateral force distribution proportional to the first vibrational mode, called *unimodal distribution* when the structure is regular both in plant and along the height, so the contribution of the higher modes on the structural response can be neglected. Instead when the higher modes can not be neglected a *multimodal distribution* can be applied by considering the lateral force distribution as a linear combination of the predominant modes (Paraskeva and Kappos 2010, Chopra and Goel 2002).

Some considerations need to be done about the evolution of the monotonic force distribution. Usually the increments of the forces are independent from the deformation level reached on the structure (*non-adaptive method*). On the contrary, the force distribution can be applied to take into account the effective deformation level of the structure that produces a redistribution of the forces, according to the new values of stiffness (*adaptive methods*) (Kalkan and Kunnath 2006). These methods are used for irregular structures, since the response is influenced by more than one mode.

Table 14.5 summarizes all the possible approaches to be used for the pushover analyses. The generic shape function has been expressed as $\{\phi\}$:

The term c_j represents the combination mode coefficient. Different multimodal models are proposed, but one of the most used ones is obtained by the *SRSS* combination of the static equivalent forces corresponding to the selected modes (Eq. 14.9).

$$\{\phi\} = \sqrt{\sum_{j=1}^N (g_j \cdot \{\phi\}_j)^2} \tag{14.9}$$

where g_j represents the modal participating factor associated to the mode $\{\phi\}_j$. Assuming the generic vector $\{\phi\}$ to be a shape function of the force distribution, Fig. 14.5 illustrates a capacity curve of a multistory building.

According to the previous considerations, the generic force applied on story i at time t_k is given by Eq. 14.10:

$$F_i(t_k) = \lambda(t_k) \cdot F_{i,initial} = F_{i,(k-1)} + \Delta F_{i,(k)} \tag{14.10}$$

When the pushover operates in force control, the variation ΔF_j is constant for all the time steps. From Fig. 14.5, it is possible to observe four different characteristic

Table 14.5 Different approaches for pushover analyses

	Non-adaptive	Adaptive
Unimodal	$\{F\} = \cos t \ \forall t$ $\{\phi\} = \{\phi\}_j \ j = 1$	$\{F\} = \{F(\delta_i)\} \ \forall t$ $\{\phi\} = \{\phi\}_j \ j = 1$
Multimodal	$\{F\} = \cos t \ \forall t$ $\{\phi\} = \sum_{j=1}^N c_j \cdot \{\phi\}_j$	$\{F\} = \{F(\delta_i)\} \ \forall t$ $\{\phi\} = \sum_{j=1}^N c_j \cdot \{\phi\}_j$

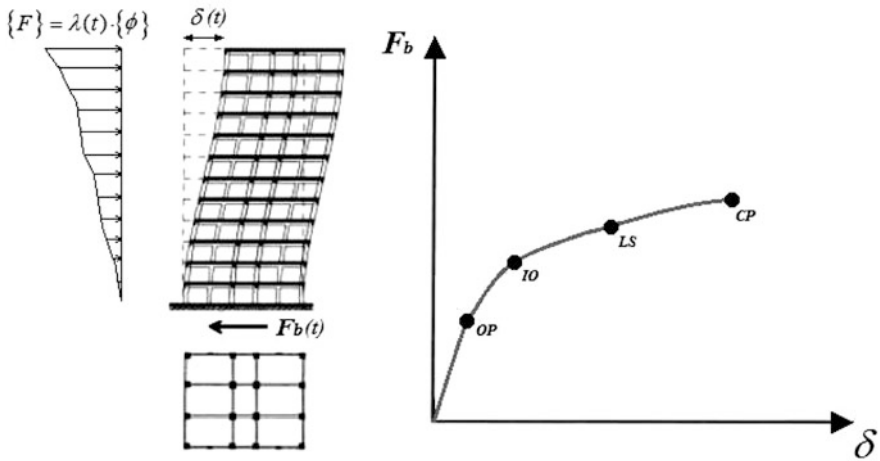


Fig. 14.5 Capacity curve for a multistory building subjected to a force distribution proportional to



points of the capacity curve that refer to a specific seismic limit condition (318 2014):

- *OP: Operational Performance;*
- *IO: Immediate Occupancy;*
- *LS: Life Safety;*
- *CP: Collapse Prevention.*

The main goal of a pushover analysis is to monitor the *performance point* (PP) of the structure subjected to an earthquake excitation. This point is representative of the pair $F_b - \delta$ that is reached under seismic excitation. The performance point of the structure is obtained by comparing the *capacity curve* with the *demand curve*. The demand of the system is expressed in terms of design response spectrum that represents the maximum response of an equivalent SDOF system. For consistency with the problem, the capacity curve has to be adapted for an equivalent SDOF system by means of the equivalent mass m^* and the definition of the transformation coefficient (Eq. 14.11).

$$\Gamma = \frac{m^*}{\sum_{h=1}^{DOFs} m_h \cdot \phi_h^2} = \frac{\sum_{h=1}^{DOFs} m_h \cdot \phi_h}{\sum_{h=1}^{DOFs} m_h \cdot \phi_h^2} \quad (14.11)$$

Thus, the equivalent base shear (F_b^*) and the top displacement (δ^*) can be obtained using Eq. 14.12.

$$F_b^* = \frac{F_b}{\Gamma} \quad \delta^* = \frac{\delta}{\Gamma} \quad (14.12)$$

Finally, the evaluation of the performance point can be determined with two methods:

- Capacity Spectrum Method (CSM);
- N2 method.

It is important to specify some aspects of the pushover analysis. First of all, the assumption of a non-adaptive force distribution can lead to inconsistent results for irregular structures (e.g. predominance of higher modes) or for high dissipation systems. In fact, the redistribution of the internal forces due to the plasticization of some elements' cross sections can vary the force applied at each story. In addition, since the pushover analysis is applied to estimate the performance of a 2D structure in a given horizontal direction, the torsional effects are not considered, or they are evaluated by comparing the effects of two analyses in the two horizontal directions (Cimellaro and Marasco 2014). Even in this case, the torsional effects are evaluated with an inconsistent procedure. Naturally this limit is amplified for a system having irregular plan in which the torsional effects cannot be neglected (Fajfar et al. 2005).

14.4.1 Capacity Spectrum Analysis Method

Mahaney et al. (1993) were the first to propose and develop the capacity spectrum analysis method (CSM), which is a graphic method that allows a visual evolution of how the structure will perform when subject to earthquake ground motion. The first thing to do is to convert the seismic demand curve and the capacity curve in the respective spectra with the relationship between the spectral acceleration S_a and the spectral displacement S_d as:

$$S_d = \frac{1}{4\pi^2} S_a T^2 \quad (14.13)$$

To transform the capacity curve is important that the behavior of the structure is equal as a single-degree-of-freedom system. To ensure the equality between the kinetics energy of the structure and the one of the equivalent single-degree-of-freedom system, the transformation coefficient Γ and the mass coefficient α_1 are used:

$$\begin{aligned} S_a &= \frac{F_b}{W\alpha_1} \\ S_d &= \frac{\delta}{\Gamma\phi} \end{aligned} \quad (14.14)$$

where F_b is the base shear of the target displacement, W is the total mass of the building, δ is the top displacement and ϕ is the modal shape. According to the displacement rule, an initial estimate of the performance point is made as an elastic structure displacement with the same initial stiffness:

$$d_i^0 = d_e \quad (14.15)$$

This establishes an equivalent bilinear capacity representation until the performance point, which is necessary to estimate quickly the equivalent damping and the consequent reduction of the spectral demand. When a structure enters in the nonlinear range during a seismic event it is subjected to damping which is assumed to be a combination of viscous damping and hysteretic damping. The equivalent viscous damping is therefore associated with a specific maximum displacement and is estimated using the equation:

$$\beta_{eq} = \beta_0 + 0.05 \quad (14.16)$$

where β_0 is the hysteretic damping, bound to the energy dissipation of the structure, while 0.05 is the viscous damping of the structure, considered equal to 5% for a concrete building.

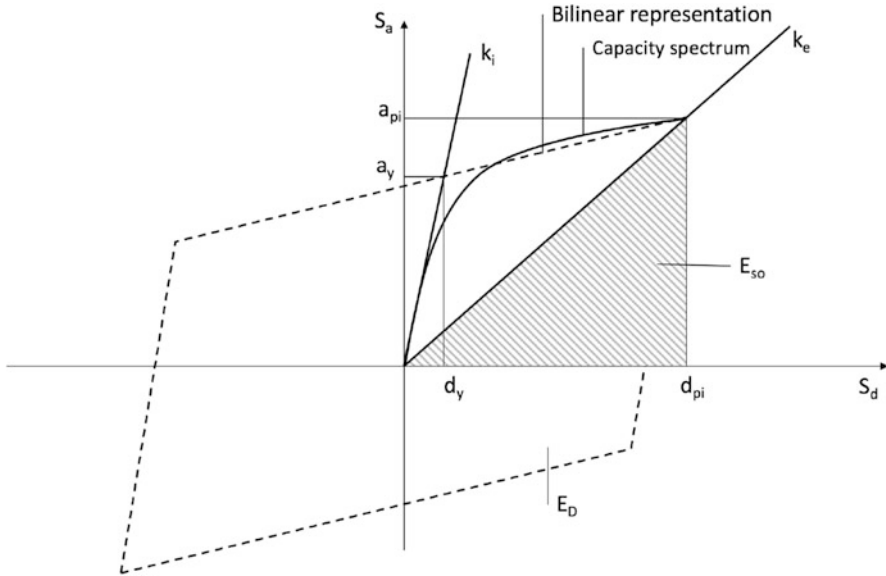


Fig. 14.6 Estimation of equivalent viscous damping

Figure 14.6 shows this estimation; d_{pi} and a_{pi} are the coordinates of the maximum displacement and the maximum acceleration expected, d_y and a_y are the yielding displacements and accelerations. The hysteretic damping can be estimated as:

$$\beta_0 = \frac{1}{4\pi} \frac{E_D}{E_{S0}} \quad (14.17)$$

where E_D and E_{S0} are respectively the dissipated hysterical and elastic energy that is returned during the cycling.

$$\begin{aligned} E_D &= 4(a_y d_{pi} - a_{pi} d_y) \\ E_{S0} &= \frac{1}{2} a_{pi} d_{pi} \end{aligned} \quad (14.18)$$

Equation 14.19 describes the equivalent viscous damping and it's calculated using the 4 critical points of the bilinear representation of the capacity spectrum:

$$\beta_{eq} = \frac{4(a_y d_{pi} - a_{pi} d_y)}{4\pi a_{pi} d_{pi}} + 5 = \frac{63.7(a_y d_{pi} - a_{pi} d_y)}{a_{pi} d_{pi}} + 5 \quad (14.19)$$

The hysteretic cycling tends to overlook the actual value of the equivalent viscous damping because the effects like pinching are not considered; for this reason it's possible to use the k factor as:

$$\beta_{eq} = \frac{63.7k (a_y d_{pi} - a_{pi} d_y)}{a_{pi} d_{pi}} + 5 \quad (14.20)$$

k depends on the structural behavior of the building and it's function of the resisting seismic system and of the duration of the seismic ground motion. In the ATC40 report, three types of structural behaviors are considered:

- type A: structure with hysterical cycling wide and stable;
- type B: structure with a moderate reduction of the hysterical cycling area;
- type C: structure with a considerable reduction of the hysterical cycling area.

The response spectrum is reduced using the equivalent damping as follows:

$$\eta = \sqrt{\frac{10}{5 + \beta_{eq}}} \quad (14.21)$$

The intersection point of the reduced demand spectrum with the capacity spectrum is determined. The intersection stops when the nonlinear displacement d_i given by the intersection of the two curves converges at the value of the displacement used to estimate the equivalent damping.

14.4.2 N2 Method

The N2 method is a variation of the CSM based on inelastic spectra (Fajfar and Fischinger 1988). This methodology is based on the fact that the response of a MDOF systems is equivalent to the one of a SDOF system with an appropriate hysterical characteristic. The acronym N2 indicates that it is a nonlinear method (N) that combines the pushover analysis of a MDOF model with the response spectrum analysis of an equivalent SDOF system that has a capacity represented by a bilinear curve (2). Furthermore, the methodology uses an inelastic spectrum for the representation of the demand. The pushover analysis is performed to define the capacity curve $F_b - \delta$. Consequently, the structure is modeled as a SDOF system and it is assumed that the displacement shape $\{\phi\}$ is constant. The modal participation factor Γ controls the transformation from MDOF to SDOF model and vice-versa and it is defined as:

$$\Gamma = \frac{\phi^T M \tau}{\phi^T M \phi} \quad (14.22)$$

where τ is the dragging vector corresponding to the system direction. The maximum resistance of the equivalent system F_{bu}^* is identified as:

$$F_{bu}^* = \frac{V_{bu}}{\Gamma} \quad (14.23)$$

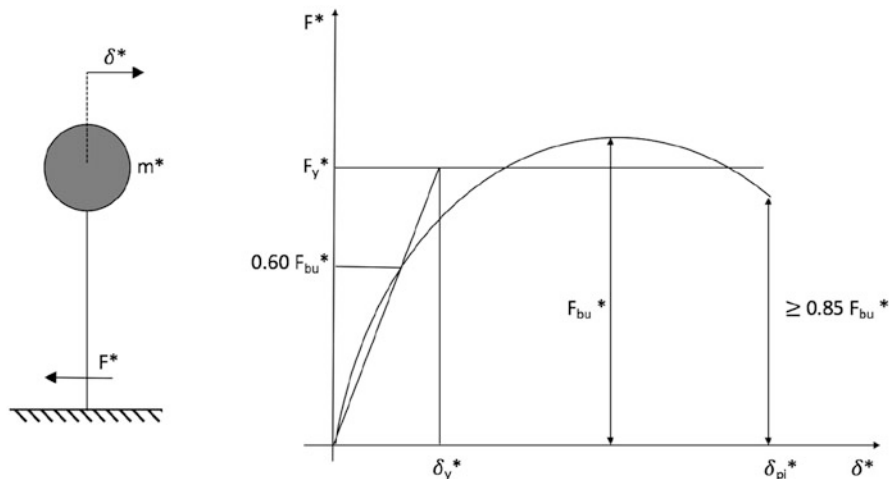


Fig. 14.7 System and equivalent bilinear diagram (Mezzina et al. 2011)

The maximum resistance value of the real structure is V_{bu} while the maximum resistance of the equivalent system is F_{bu} . Thus it's possible to identify the elastic stretch to the point $0.6 \cdot F_{bu}^*$ as the Fig. 14.7 shows.

The plasticization force F_y^* imposes the equality between the area under the bilinear curve and the capacity curve, multiplying it to the maximum displacement ϕ_u^* that corresponds to a resistance reduction $\leq 0.15F_{bu}^*$. The elastic period of the idealized bilinear system T^* can be determined as:

$$T^* = 2\pi \sqrt{\frac{m^*}{k^*}} \tag{14.24}$$

If the period of the SDOF is $T^* \leq T_C$, the maximum displacement d_{max}^* that the inelastic system can obtain is equal to the one of an elastic system (rule of the equal displacement).

$$\phi_{max}^* = \phi_{e,max} = S_{De}(T^*) \tag{14.25}$$

If the period of the SDOF is $T^* < T_C$, the response of the inelastic system is higher than the response of the elastic system (Eq. 14.26).

$$\phi_{max} = \frac{1}{R_\mu} \cdot \left[1 + (R_\mu - 1) \cdot \frac{T_C}{T^*} \right] \tag{14.26}$$

where R_μ represents the reduction factor, defined as

$$\begin{cases} R_\mu = 1 + (\mu - 1) \cdot \frac{T_C}{T^*} & \text{for } : T^* < T_C \\ R_\mu = \mu & \text{for } : T^* \geq T_C \end{cases} \tag{14.27}$$

When the maximum displacement is defined, it is possible to compute the effective displacement of the MDOF system as:

$$\phi_{max} = \Gamma d_{max}^* \quad (14.28)$$

After the estimation of the control point, it is possible to know the deformation configuration and, consequently, the verification of the building through the control of the displacement of the ductile elements and the resistance of the fragile elements. Overall, eight pushover analyses must be done: two towards the principal directions (X and Y) for two verse and two different load distributions.

14.5 Direct Displacement-Based Seismic Design Procedure

The seismic design of a structure is based on a specific target displacement for a specific seismic hazard level. This concept is at the base of the direct-displacement method and it was introduced by Priestley and Kowalsky (2000). The structure is modeled like a single-degree-of-freedom system and the global behavior of the structure at the target displacement is represented to the total equivalent viscous damping and the equivalent elastic lateral stiffness properties. Summing the assumed internal viscous damping and the equivalent viscous damping provided by the hysterical response of the structure it is possible to obtain the total viscous damping. Figure 14.8 shows the flowchart of the process.

- **Step 1** The first thing to do is to define the target displacement δ_t and relying on the first mode response, so it is possible to obtain the relationship:

$$\delta_t = \frac{\Delta_r}{\alpha_1 A_r^1} \quad (14.29)$$

Δ_{r1} is the maximum roof lateral displacement, α_1 is the first modal participation factor and Δ_r is the roof component of the fundamental mode shape. It possible to define the seismic hazard associated at the target displacement in terms of design relative displacement response; this can be obtained using the code design spectral acceleration of the seismic zone S_{ACode} and transform them in the corresponding spectral displacement value such as:

$$S_{DCode} = \frac{T_{eff}^2}{4\pi^2} S_{ACode} \quad (14.30)$$

where T_{eff} is the effective elastic secant period of the building. Equation 14.30 is not accurate for structures with long period, so in this case the EC8 method is suggested. When the design has a different performance level than the life safety limit state, the spectral displacement, according with 356 (2000), is approximated as follows:

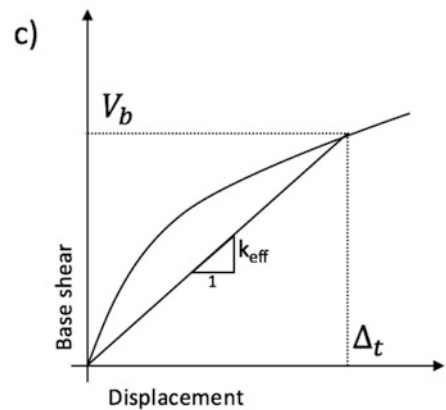
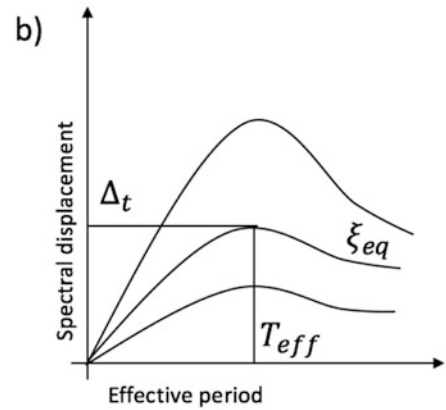
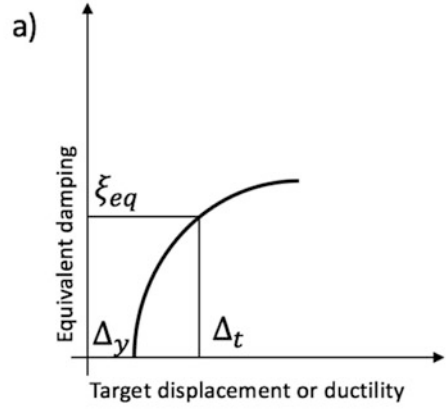
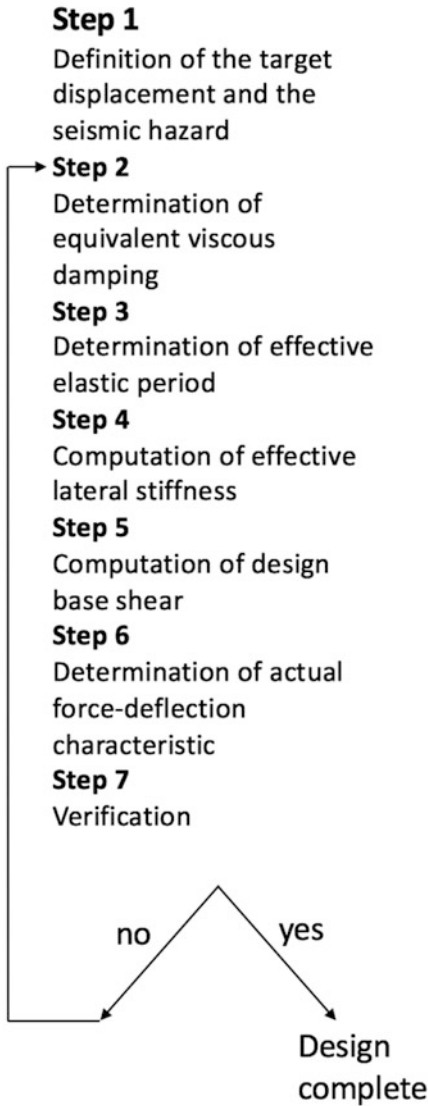


Fig. 14.8 Flowchart of direct-displacement seismic design adapted from Filiatrault and Christopoulos (2006)

$$S_{DT_r} = \left(\frac{T_r}{475} \right)^n S_{DCode} \quad (14.31)$$

where T_r is the mean return period of the ground motion and n is a power factor that depends on the site.

- **Step 2** The equivalent viscous damping ratio is obtained by:

$$\xi_{eq} = \frac{E_{D\Delta_t}}{2\pi k_{eff} \Delta_t^2} \quad (14.32)$$

where $E_{D\Delta_t}$ is the energy dissipated per cycle at the target displacement Δ_t and k_{eff} is the effective secant lateral stiffness of the structure. In order to model the nonstructural elements and/or the rest of the structure it is possible to increment the value of ξ_{eq} with a small amount of damping. Figure 14.8a shows the relationship between the equivalent damping value and the nonlinear characteristics of the structure. It's possible to define the characteristics of the structure as the maximum displacement of the system with continuous nonlinear hysteretic relations.

- **Step 3** The effective elastic period of the building ξ_{eff} is determined as in Fig. 14.8b after the calculation of the target displacement and the equivalent viscous damping.
- **Step 4** The computation of the effective lateral stiffness, considering the structure as a SDOF, is given by:

$$k_{eff} = \frac{4\pi^2 W_{eff}}{g T_{eff}^2} \quad (14.33)$$

where W_{eff} is the effective seismic weight applied to the structure.

- **Step 5** The computation of the design base shear is given by:

$$V_b = k_{eff} \Delta_t \quad (14.34)$$

The structural elements are designed so that the capacity of the system is equal to the base shear.

When the yield displacement of the structure is defined, the equivalent base shear that is derived from the design base shear is used to provide a conventional load and resistance design.

- **Step 6** It is possible to calculate the correct value of the equivalent viscous damping ξ_{eq} and compare this value with the assumed value ξ_{eq} to define the actual force-deflection characteristic of the structure.
- **Step 7**

$$\xi_{eq} = \xi_{eq} \quad (14.35)$$

If the upper relationship in Eq. 14.35 is verified, the direct displacement-base seismic design procedure is complete. If not, the value of the equivalent damping is changed and the process restarts from Step 2.

If the relationship between the equivalent damping and the global inelastic deformation of the system is known, it possible to avoid the complete assessment of the cyclic nonlinear characteristics of the structure.

14.6 Nonlinear Dynamic Analysis

The most accurate response of a system subjected to a seismic excitation is obtained through the integration of the nonlinear equations of motion. This method considers the nonlinearities and the variation of the response in the time domain. It is used in particular cases when the structures need to be designed with a high safety level (strategic buildings) or in the cases in which the ductility request is very high. The nonlinear dynamic analyses are also necessary for base-isolated or strongly irregular structures. However, in these cases the seismic action is modeled using acceleration time-history in the two horizontal (Fig. 14.9) and in the vertical direction.

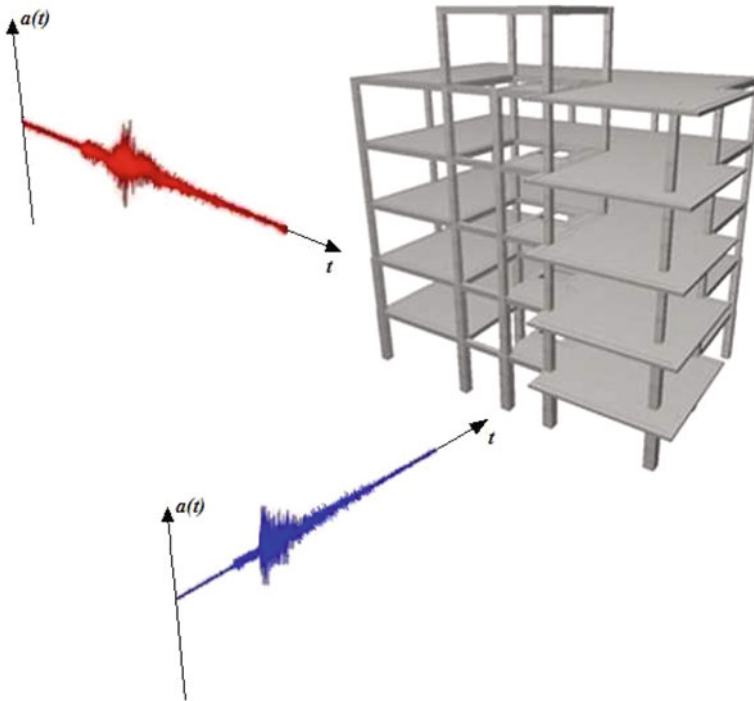


Fig. 14.9 Horizontal base seismic excitations in X and Y directions

According to EC8, if the groups of accelerations used in the analyses are less than seven, the maximum response from the nonlinear response history analysis must be considered. Instead when the earthquake records is equal or greater than seven, the final response can be obtained as an average of the nonlinear dynamic responses.

References

- 1998-1 E (2004) Design of structures for earthquake resistance Part 1: general rules, seismic actions and rules for buildings. European Committee for Standardization
- 318 AC (2014) Building code requirements for structural concrete
- 356 FEMAF (2000) Prestandard and commentary for the seismic rehabilitation of buildings
- Chopra AK, Goel RK (2002) A modal pushover analysis procedure for estimating seismic demands for buildings. *Earthq Eng Struct Dyn* 31(3):561–582
- Cimellaro GP, Marasco S (2014) Opensignal: a software framework for earthquake record processing and selection
- Fajfar P (2002) Structural analysis in earthquake engineering breakthrough of simplified non-linear methods. In: 12th European conference on earthquake engineering, London
- Fajfar P, Fischinger M (1988) N2-A method for non-linear seismic analysis of regular buildings. In: Proceedings of the ninth world conference in earthquake engineering, vol 5, pp 111–116
- Fajfar P, Marušić D, Peruš I (2005) Torsional effects in the pushover-based seismic analysis of buildings. *J Earthq Eng* 9(06):831–854
- Filiatrault A, Christopoulos C (2006) Principles of passive supplemental damping and seismic isolation. IUSS Press, Pavia
- Kalkan E, Kunnath SK (2006) Adaptive modal combination procedure for nonlinear static analysis of building structures. *J Struct Eng* 132(11):1721–1731
- Kiureghian AD, Nakamura Y (1993) CQC modal combination rule for high-frequency modes. *Earthq Eng Struct Dyn* 22(11):943–956
- Mahaney JA, Paret TF, Kehoe BE, Freeman SA, Consortium UCUSE, et al (1993) The capacity spectrum method for evaluating structural response during the loma prieta earthquake. US Central United States Earthquake Consortium (CUSEC), pp 501–510
- Megson T (2005) Structural and stress analysis, 2nd edn. Butterworth-Heinemann, pp xi–xii
- Mezzina M, Raffaele D, Uva G, Carano GC (2011) Progettazione sismo-resistente di edifici in cemento armato. CittàStudi Edizioni
- NTC-08 (2008) Nuove Norme Tecniche per le Costruzioni. Gazzetta Ufficiale della Repubblica Italiana
- Paraskeva TS, Kappos AJ (2010) Further development of a multimodal pushover analysis procedure for seismic assessment of bridges. *Earthq Eng Struct Dyn* 39(2):211–222
- Priestley M, Kowalsky M (2000) Direct displacement-based seismic design of concrete buildings. *Bull N Z Natl Soc Earthq Eng* 33(4):421–444

Part III
Seismic Design of Buildings

Chapter 15

Capacity Design



Abstract This chapter introduces the basic concept of the Capacity Design. The ordered steps to be followed in the seismic design of buildings are summarized according to the European standards.

15.1 Introduction

The Capacity Design is the sum of rules that have to be followed when designing structural elements exposed to seismic actions (Paulay and Priestley 1992). The brittle failure of structural elements must be avoided to allow a global ductile behavior for the construction, which is influenced by the behavior of the structural elements and their connections. In Capacity Design, bending mechanisms (ductile mechanism) are prioritized over shear mechanisms (brittle mechanisms). Figure 15.1 shows a bending failure mechanism (Fig. 15.1a) and a shear failure mechanism (Fig. 15.1b) of a beam.

The main concept of the Capacity Design philosophy can be schematically expressed by Fig. 15.2.

The chain is composed by some brittle links and a ductile link in the middle. When a tensile force is applied in the chain, the ductile link stretches by yielding before breaking while the brittle links do not yield. The failure will occur in the chain system when the weakest link breaks. If the ductile link is the weakest one, the global load capacity is less than the case in which the brittle links are the weakest elements. Nevertheless, the chain will show larger final elongation than the brittle failure case. In fact, when the global failure is brittle, the chain will fail suddenly and show limited final elongation. In a structural system, the ductile failure mechanism allows to have large deformations and therefore a greater energy dissipation. According to the chain example, it is necessary to make the ductile element the weakest one, to guarantee a ductile behaviour.

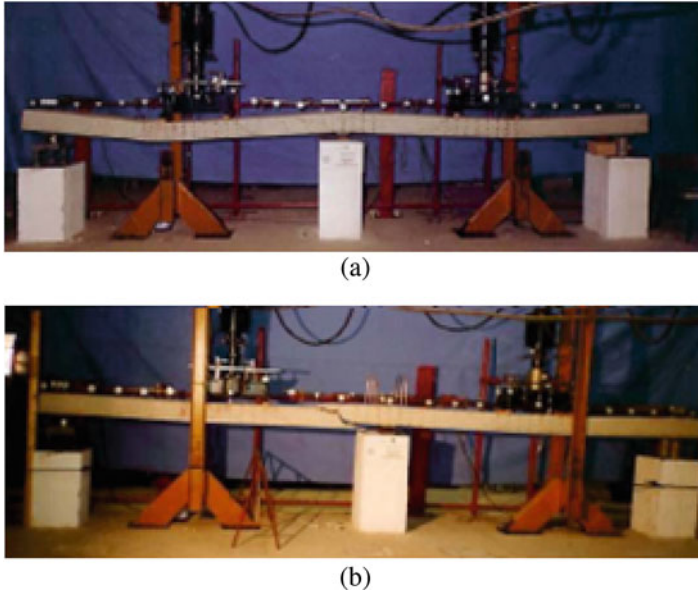


Fig. 15.1 (a) Bending failure mechanism; (b) Shear failure mechanism of a beam

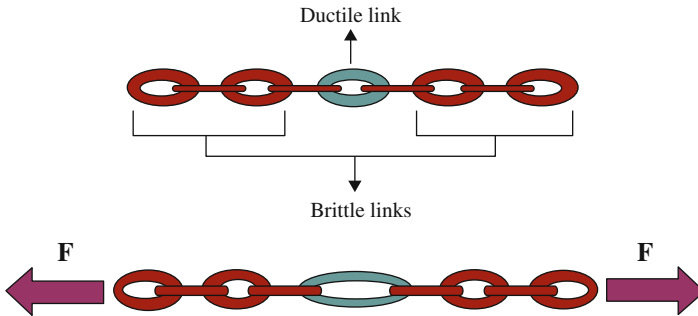


Fig. 15.2 Capacity design philosophy explained by the chain scheme (George and Varghese 2012)

15.2 Capacity Design of a Multi-story Building

Several research on seismic resistance of structures has attracted increasing attention worldwide due to the economic and social implications of inadequate seismic design. In major earthquakes, the insufficient seismic resistance of columns has been recognized as the most likely reason of collapse for concrete frame structures. This can lead to both loss of life and economic losses (Liu 2013). The current methodology focuses on the dissipation of the seismic energy through large inelastic deformations of structures. Modern design codes (such as Committee et al. 2008,

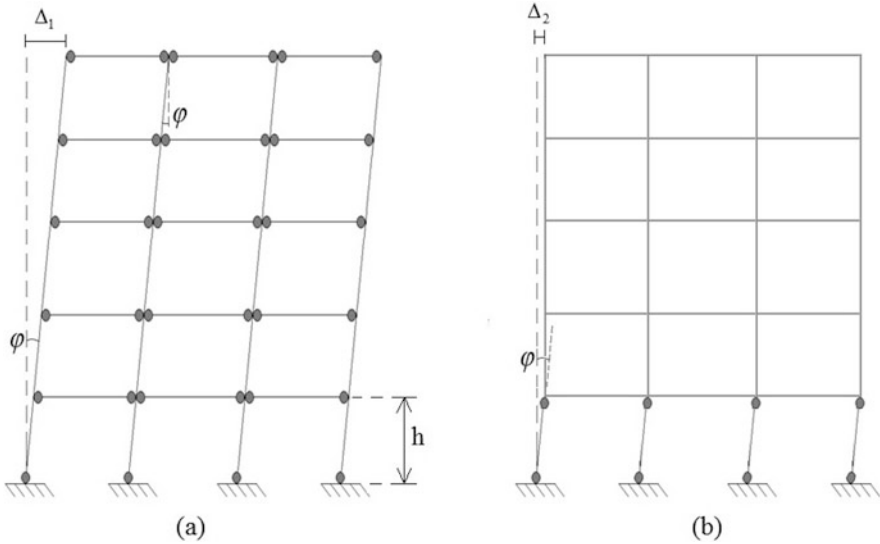


Fig. 15.3 Frame with strong columns and weak beams (a) and frame without strong columns and weak beams (b)

NZS 2006, 1998-1 2004, and NTC-08 2008) aim to develop yielding in beams rather than in columns by adopting the *strong column-weak beam* philosophy. The global seismic capacity of a concrete frame system is strictly dependent on the columns resistance which carry the lateral forces induced by the earthquake. The beams carry the vertical load which distribute in the columns as axial load. the seismic excitation induces additional internal actions on the beams. When collapse occurs on a beam or on several beams, a residual resistance to lateral actions is provided by the columns. Then, in structure with strong columns and weak beams, the yielding occurs before in the beams and the global capacity is guaranteed by the columns. This concept is similar to the chain scheme aforementioned, where the beams represent the ductile links which allow to dissipate seismic energy primarily in well-confined beam plastic hinges and the columns remain in the elastic field. Figure 15.3a illustrates a common behaviour of a frame with strong columns and weak beams, while Fig. 15.3b depicts the case of frame without strong columns and weak beams.

The frame without strong columns and weak beams (*Case B*) has a top displacement less than the one associated with the frame having strong columns and weak beams (*Case A*). It is interesting to formulate the expression used to calculate the collapse multiplier related to the two analyzed cases. According to the limit analysis of structures, the value of collapse multiplier (λ) identifies the coefficient to be multiplied by the elastic limit force of the system (F_y). This values is associated with the lateral resultant force which causes the plastic hinge formation at the base of the column and at both extreme points of the column, respectively for

Case A and *Case B*. Using the *upper bound limit theorem* two collapse multipliers can be evaluated using the kinematic approach by normalizing the internal work (work due to the internal stresses on the elements) with respect to the external work. Equation 15.1 shows the mathematical expression of the collapse multipliers for the two considered cases:

$$\begin{cases} \lambda_1 = \frac{n_c \cdot M_{y,c} + 2 \cdot n_{span} \cdot n_{story} \cdot M_{y,b}}{F_{y,1} \cdot z_R} \\ \lambda_2 = \frac{2 \cdot n_c \cdot M_{y,c}}{F_{y,2} \cdot z_R} \end{cases} \quad (15.1)$$

where $M_{y,c}$ and $M_{y,b}$ are the yield bending moment of the columns and the beams, respectively, n_c is the number of columns, while n_{story} and n_{span} are the number of story and span of the frame, respectively. $F_{y,1}$ and $F_{y,2}$ identify the resultant lateral forces causing the occurrence of the elastic limit shear force for *Case A* and *Case B*, respectively. Finally, z_R is the distance between the application of the resultant force's axis and the base level. It is possible to observe how the internal energy of the system (dissipated energy) in *Case A* is larger than *Case B*. Considering the columns with the same dimensions for both cases, the values $F_{y,2}$ is greater than $F_{y,1}$. In fact, in *Case A* the redistribution of the actions due to the formation of plastic hinges in the beams, increase the internal stress in the column which reaches the plastic deformation for load forces magnitude less than *Case B*. Figure 15.4 depicts a qualitative comparison between the global capacity curve obtained for the two cases.

Capacity Design rules are applied to ensure an adequate energy dissipation within the structural system subjected to a seismic excitation by designing a frame with strong columns and weak beams. Furthermore, the damage caused by an earthquake to a column should be limited to avoid any partial or total collapse. The beam-column joint are crucial zones for transferring the loads between the connecting elements. Past earthquakes have induced the collapse of many frame buildings due

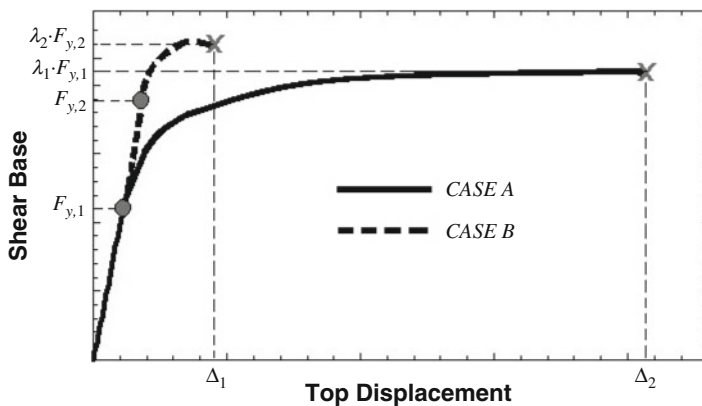


Fig. 15.4 Comparison of global capacity curves for *Case A* and *Case B*

to the relevant shear stresses in the beam-column joints (Uma and Jain 2006). The basic requirements is that the joint must be stronger than the other structural members and should always keep an elastic behavior since the recovery can be expensive and difficult.

15.3 Design Approach by Codes

The Capacity Design procedure is applied to establish the element hierarchy in the structure, by ensuring that the strength of the columns is higher than the beams while the beam-column joint is the stronger frame element. The global ductility of a structure is also increased by avoiding brittle mechanisms induced by shear stress and allowing the ductile mechanism due to bending. Similarly to the chains example, the local failure bending mechanisms must occur before the shear failure mechanisms. Figure 15.5 shows the schematic ordered strength hierarchy to be followed in the Capacity Design approach.

According to the strength hierarchy above discussed, the Capacity Design rules are listed below:

1. Design the beams for bending;
2. Design the beams for shear;
3. Design the columns for bending;
4. Design the columns for shear;
5. Design the beam-column joint.

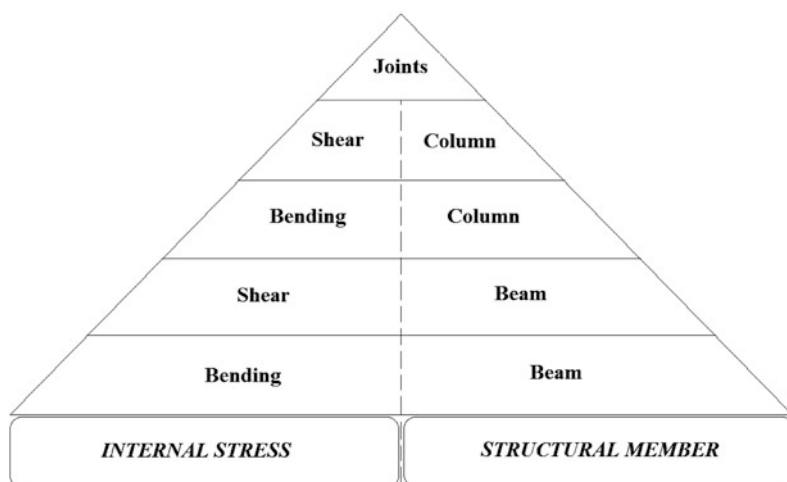


Fig. 15.5 Strength hierarchy in the capacity design approach

The Low Ductility Class (DCL) and the High Ductility Class (DCH) are provided by EC8 (1998-1 (2004)) to ensure a certain ductility level to structures under seismic actions. According to the Capacity Design rules, the design value of the seismic action (A_C) is obtained by multiplying the actions derived from the analysis (A_R) by a factor (γ_{Rd}) (Eq. 15.2). This factor accounts for the over strength of the concrete element due to the steel strain hardening and the concrete confinement. This factor is 1.3 in case of DCH and 1.1 in case of DCL.

$$A_C = \gamma_{RD} \cdot A_R \quad (15.2)$$

15.3.1 Design of Beams for Bending

The design values of the bending moment of the beams are obtained from the seismic analysis of the structure. The resisting bending moment for a beam (MC) is given by Eq. 15.3.

$$M_c = \gamma_{Rd} \cdot M_r \quad (15.3)$$

15.3.2 Design of Beams for Shear

The shear in the beam is calculated by imposing a static equilibrium. Since the seismic action is a cyclic load, the sign of the bending moment at both ends of the section can be positive or negative. In addition, the live vertical loads could increase or decrease the shear reactions on the beam, thus the shear is calculated considering the most critical load combination given by only the permanent loads (G_k) or the permanent and the live loads (Q_k) (Fig. 15.6).

The resisting shear (VC) of the beam is given by Eq. 15.4.

$$V_C = \max \left(\gamma_{Rd} \cdot \frac{M_{RA}^{\pm} + M_{RB}^{\pm}}{l} \pm \frac{G_k \cdot l}{2}; \gamma_{Rd} \cdot \frac{M_{RA}^{\pm} + M_{RB}^{\pm}}{l} \pm \frac{G_k \cdot l + 0.3 \cdot Q_k \cdot l}{2} \right) \quad (15.4)$$

where M_{RA} and M_{RB} are the resisting bending moments at the ends of the beam section (corresponding to the plastic hinge formation) and l is the length of the beam.

15.3.3 Design of Columns in Bending

Brittle failure in columns is prevented by increasing the design bending moment of an over-strength factor. The design bending moment in the columns is determined

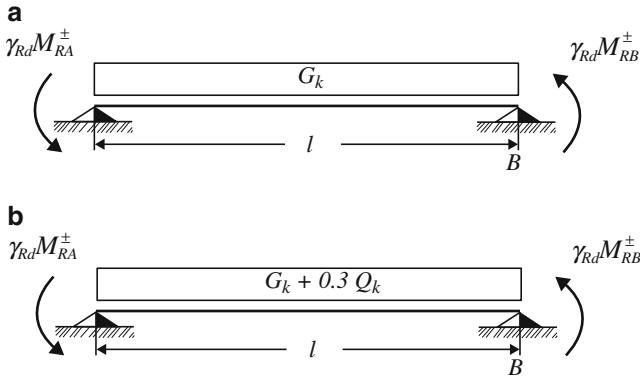


Fig. 15.6 The seismic load combination with permanent loads (a) and with permanent and live loads (b)

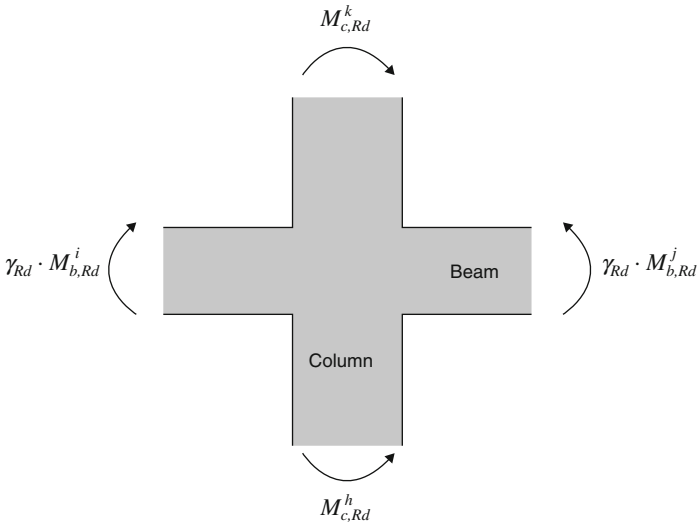


Fig. 15.7 Beam-column joint actions

using the equilibrium relationships at the beam-column joint. The moments coming from the beams are the plastic moments, which correspond to the formation of plastic hinges in the beams. The only unknown will be the column design bending moment. Figure 15.7 depicts the statical configuration of a generic beam-column joint.

The resisting bending moment of the column ($M_{c,Rd}$) should satisfy the expression below (Eq. 15.5).

$$\sum M_{c,Rd} \geq \gamma_{Rd} \cdot \sum M_{b,Rd} \tag{15.5}$$

where $M_{b,Rd}$ represents the bending moments corresponding to the formation of the plastic hinges in the beams. The resisting bending moment in the columns are obtained by multiplying the design bending moment derived from the structural analysis ($M_{c,Ed}$) by the amplification factor (α) given in Eq. 15.6.

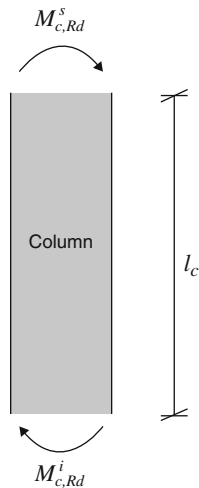
$$\alpha = \gamma_{Rd} \cdot \left| \frac{\sum M_{b,Rd}}{\sum M_{c,Ed}} \right| \quad (15.6)$$

15.3.4 Design of Columns in Shear

The design values of the shear force are determined following the Capacity Design rules considering that the columns are subjected to end moments corresponding to plastic hinge formation (Fig. 15.8). So the design shear of the column ($V_{C,Rd}$) is given by Eq. 15.7

$$V_{C,Rd} = \gamma_{Rd} \cdot \frac{M_{c,Rd}^s + M_{c,Rd}^i}{l_c} \quad (15.7)$$

Fig. 15.8 Column subjected to plastic moments



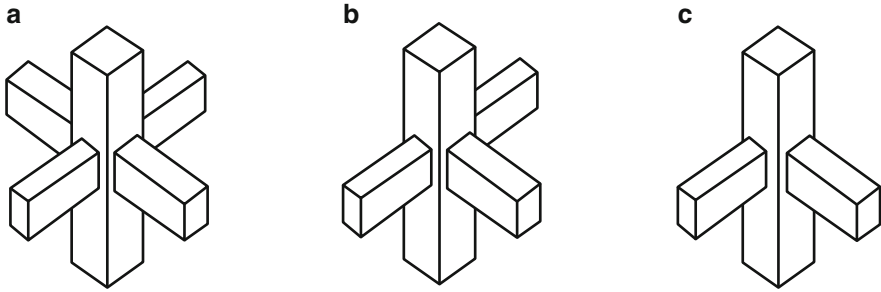


Fig. 15.9 Fully confined joint (a) and partially confined joint (b) (c)

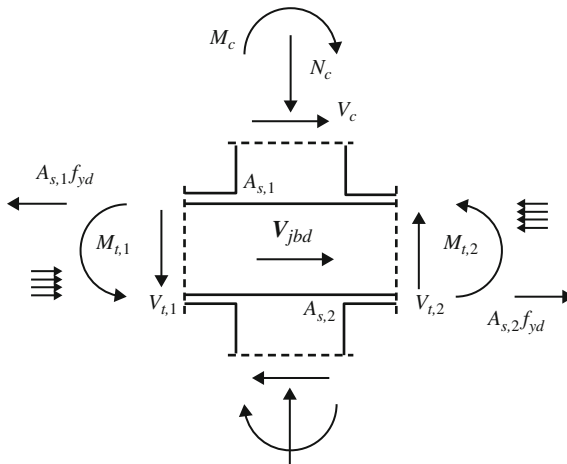


Fig. 15.10 Static configuration of the beam-column joint

15.3.5 Beam-Column Joint

The beam-column joint should prevent any failure of the adjacent beams and columns. The joint is classified as fully confined (Fig. 15.9a) or partially confined (Figs. 15.9b and c) depends on the numbers of adjacent beams.

The confinement of the column plays a key role for the resistance and the ductility of the joint. Considering the static scheme illustrated in Fig. 15.10, the resisting shear (V_{jbd}) is given by Eq. 15.8.

$$\begin{aligned}
 V_{jbd} &= \gamma_{Rd} \cdot (A_{S1} + A_{S2}) \cdot f_{yd} - V_C \text{ internal joint} \\
 V_{jbd} &= \gamma_{Rd} \cdot A_{S1} \cdot f_{yd} - V_C \text{ external joint}
 \end{aligned}
 \tag{15.8}$$

The shear strength of the beam-column joint can be evaluated according the model proposed by Paulay et al. (1978) which considers the total shear within the joint core as carried by:

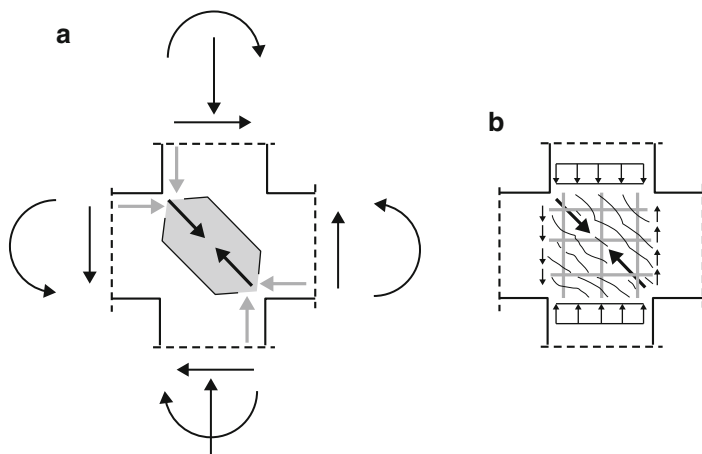


Fig. 15.11 Strut mechanism (a) and truss mechanism (b)

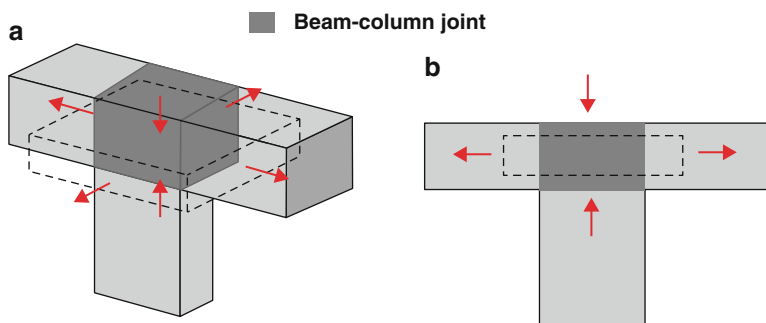


Fig. 15.12 Transversal strain in transversal direction for 3D joint (a) and 2D joint (b)

1. Diagonal concrete strut;
2. idealized truss (consisting in horizontal hoops, inclined and vertical reinforcement bars between the cracks).

Figure 15.11 shows the model proposed by Paulay et al. (1978) which illustrates the two separated contributions of shear within the joint.

The joint has to support the strut mechanism providing adequate transversal reinforcement which enhances the truss mechanism in the joint core. The main key parameter is the compressive strength of the diagonal concrete strut. The compressive strength of the concrete is affected by the tensile strains in the transverse direction (both considering the 2D and 3D model of the joint as shown in Fig. 15.12).

So the 1998-1 (2004) suggests a reduction factor η to be applied to the design compressive strength of the concrete (15.9).

$$\eta = 0.6 \cdot 1 - \frac{f_{ck}}{250} \quad (15.9)$$

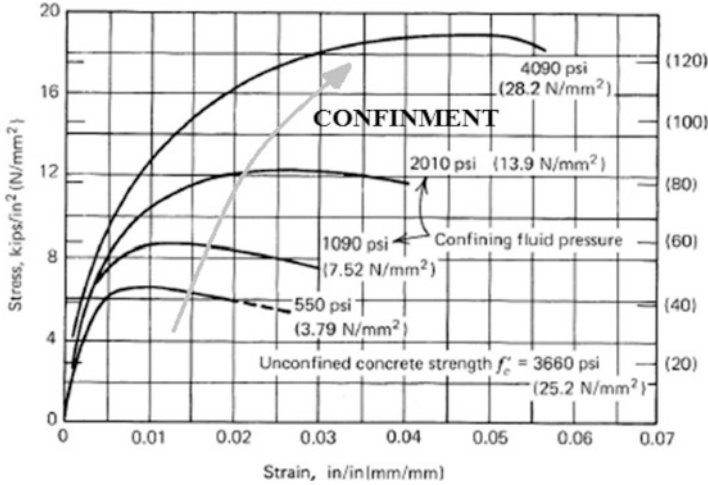


Fig. 15.13 Effect of confinement on the concrete (Park and Paulay 1975)

Recent studies have also demonstrated that critical situations can occur when the axial load acting on the column is large. In this case, the diagonal compression failure of strut can occur before the diagonal tensile cracking in the joint. The 1998-1 (2004) provides the following coefficients to reduce the total shear capacity (15.10)

$$\sqrt{1 - \frac{v_d}{\eta}} \tag{15.10}$$

where the parameter v_d represents the normalized axial load acting on the joint.

The presence of stirrups increases the confinement of the concrete (Mander et al. 1988) and therefore its compressive strength and ductility (Fig. 15.13).

The arrangement of the stirrups along the element and in the cross section influences the local stress-strain capacity of concrete. Figure 15.14 illustrates the effect of confinement in terms of confining forces considering different stirrups arrangements.

Considering the beam-column joint,

The local tensile stress (σ_ξ) in the beam-column joint should be less than the tensile strength of concrete, to avoid a brittle failure of the joint. This result can be obtained by adding stirrups in the columns (Fig. 15.15) that reduce the tensile stress in the concrete.

The corresponding tensile stresses acting on the concrete with and without stirrups are given by Eq. 15.11.

$$\begin{cases} \sigma_\xi = \sqrt{\left(\frac{\sigma}{2}\right)^2 + \tau^2} - \frac{\sigma}{2} \text{ without stirrups} \\ \sigma_\xi = \sqrt{\left(\frac{\sigma - \sigma_c}{2}\right)^2 + \tau^2} - \frac{\sigma - \sigma_c}{2} \text{ with stirrups} \end{cases} \tag{15.11}$$

where σ_c represents the confining stress induced by the stirrups.

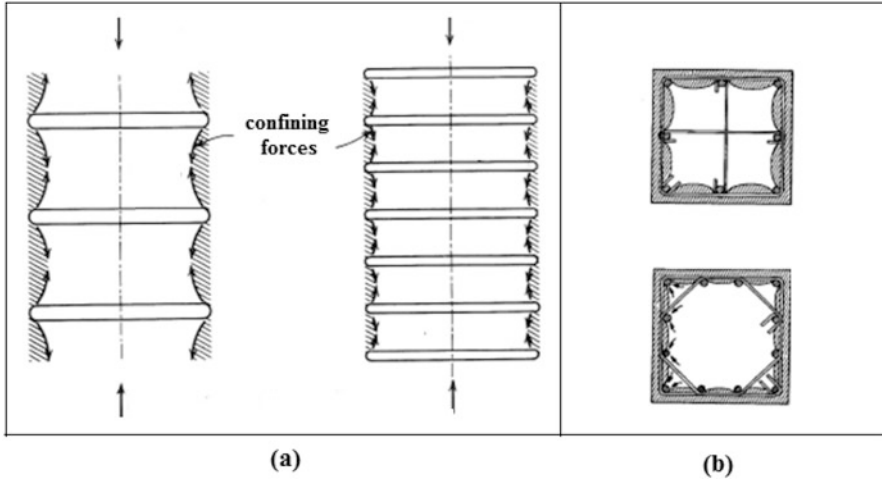


Fig. 15.14 Effect of confinement in terms of confining forces for a column along its height (a) and cross section (b) (Park and Paulay 1975)

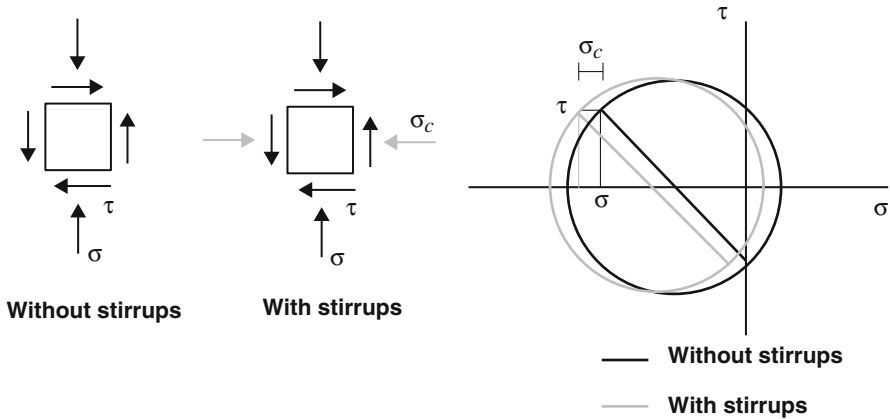


Fig. 15.15 Comparison of the internal plane stress between a confined and an unconfined beam-column joint

References

1998-1 E (2004) Design of structures for earthquake resistance Part 1: general rules, seismic actions and rules for buildings. European Committee for Standardization
 Committee A, Institute AC, for Standardization IO (2008) Building code requirements for structural concrete (ACI 318-08) and commentary. American Concrete Institute
 George SS, Varghese V (2012) General concepts of capacity based design. Int J Innov Technol Explor Eng (IJITEE) 1(2):211–215. ISSN:2278–3075
 Liu J (2013) Seismic behaviour of reinforced concrete columns. Ph.D thesis

- Mander JB, Priestley MJ, Park R (1988) Theoretical stress-strain model for confined concrete. *J Struct Eng* 114(8):1804–1826
- NTC-08 (2008) Nuove Norme Tecniche per le Costruzioni. *Gazzetta Ufficiale della Repubblica Italiana*
- NZS (2006) 3101. Code of practice and commentary for the design of concrete structures NZS-3101 82
- Park R, Paulay T (1975) Reinforced concrete structures. Wiley, New York
- Paulay T, Priestley MN (1992) Seismic design of reinforced concrete and masonry buildings. Wiley, New York
- Paulay T, Park R, Priestley M (1978) Reinforced concrete beam-column joints under seismic actions. *ACI J Proc* 75:585–593
- Uma S, Jain SK (2006) Seismic design of beam-column joints in RC moment resisting frames—review of codes. *Struct Eng Mech* 23(5):579

Chapter 16

Seismic Modeling of Infill Walls



Abstract This chapter analyzes the seismic modeling of infill walls. the first part of the chapter describes the main parameters of the infill walls which influences the displacement capacity of a frame system. the failure mechanism are also discussed considering the presence of the surrounding frame. a large variety of analytical models which take into account the presence of infill walls are detailed listed and explained. finally, the mechanisms of crisis of masonry panels (both in-plane and out of plane) are summarized.

16.1 Introduction

Infill walls and dividers made with light masonry bricks and bricklayers are commonly used in buildings whose skeleton consists of steel frames. They are known for their peculiar behavior compared to bare frames, and their influence on the seismic response of the building can either be positive or a negative. They can compensate with its own strength for the increase of inertial force, but on the other hand they can also represent a factor of great uncertainty that could invalidate the measures adopted to control the resistant mechanism.

Concerning the use of infill walls in new constructions, there are two main points of view: one claims that in order to prevent the alteration of the behavior expected at the design stage, the infilled frames must be disconnected from the structural skeleton; the other empathizes the role of infill walls as a second line of defense against severe seismic events, thus underlining the importance of making the infill frame collaborative with the load-bearing structure.

Overall, when applying one approach or another, it is essential to know the parameters that influence the properties of infill walls and the mechanisms of failure that affect them.

16.2 Influential Parameters

16.2.1 Strength of the Masonry Infill

The strength of the masonry infill is influenced by the properties of the mortar and the bricks, and a strong masonry is given by a better quality to the constitutive materials although this does not increase necessarily the lateral strength of the infilled frame as premature failure of the frame may occur when the masonry is excessively strong. Instead of hollow bricks, solid bricks are preferred as they show a higher compressive strength (Bin 2006).

16.2.2 Characteristics of the Reinforced Concrete Frame

The characteristics of the reinforced concrete frame which can influence the response of infilled frames are the concrete and steel area and the amount of longitudinal and transverse reinforcement. As observed in 1958 by Benjamin and Williams (Benjamin and Williams 1958), in the uncracked stage the variation of concrete and steel area does not influence the stiffness, while the resistance of the frame to bending moment, axial force and shear are relevant. As for the amount of longitudinal reinforcement, experiments run by Fiorato et al. (1970), by Valiasis (1989), Gavrilovic and Sendova (1992), and Ishibashi et al. (1992), show that it increases significantly the attainable ductility of the frame structure. If sufficient transverse reinforcement is provided, the infilled frame can sustain large deformations without a brittle shear failure.

16.2.3 Relative Stiffness

Between 1966 and 1969 in “A method for analysis of infilled frames”, Smith and Carter (1969) defined a dimensionless parameter λ_h to express the relative stiffness between the infill panel and the surrounding frame:

$$\lambda_h = \sqrt[4]{\frac{E_m t \sin(2\theta)}{4E_c I_c H_m}} \quad (16.1)$$

where:

- t = thickness of the masonry panel
- h_m = height of the masonry panel respectively
- θ = inclination of the diagonal of the panel
- E_m = modulus of elasticity of the masonry

- E_c = modulus of elasticity of the concrete
- I_c = moment of inertia of the columns.

The frame is much stiffer than the infill panel for small values of λ_h .

16.2.4 Gaps Between Infills and Surrounding Frame

Gaps between the masonry panel and the surrounding frame can be vertical or horizontal. Horizontal gaps between the panel and beam can generally influence the structure. Vertical gaps between the columns and the masonry can be negligible when they assume low values, because they close rapidly when the lateral force is applied. On the contrary, when large gaps are considered, the response of the structure is significantly influenced.

16.2.5 Openings

The amount of influence from openings – windows and doors is quite difficult to define. According to a research of Mallick and Garg (1971), the openings reduce the stiffness and the strength of the structure, especially when they are placed on the loaded corners.

16.3 Mechanisms of Failure

The failure mechanisms affecting the components of the infilled frames are named failure modes, and they are generally divided into failure modes of (i) infills (Sect. 16.3.1) and (ii) surrounding reinforced concrete frames (Sect. 16.3.2).

16.3.1 Failure Modes of Infills

The failure modes of infills are shown in Fig. 16.2 and they are of three types:

- **Compression failure**, which can occur following two mechanisms:
 - *Crushing of the loaded corner (Fig. 16.1)*: it takes place when lateral loading causes a biaxial compression stress in the area close to the loaded corners.
 - *Compressive failure of the diagonal strut (Fig. 16.3)*: it takes place when, as the tensile stress along the diagonal is relieved, the masonry between the cracks behave like small prisms loaded axially.

Fig. 16.1 Compressive failure due to crushing of the loaded corners

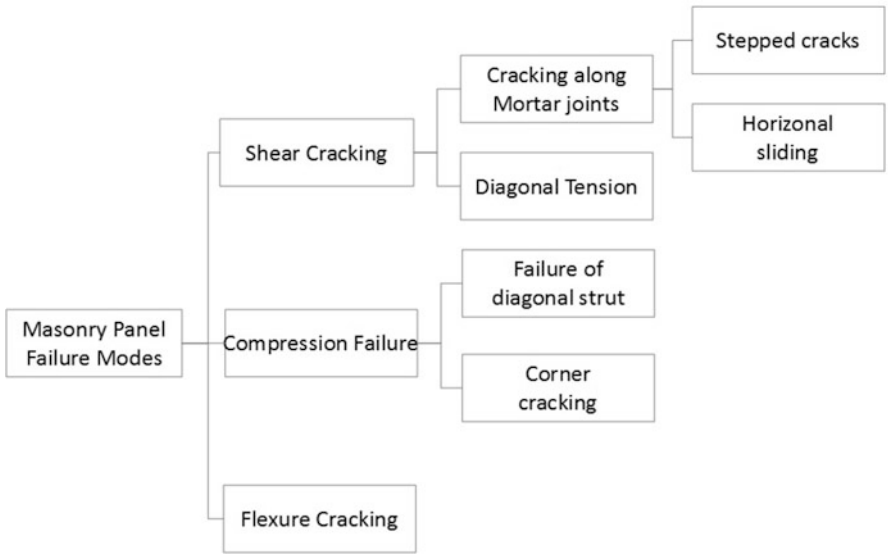
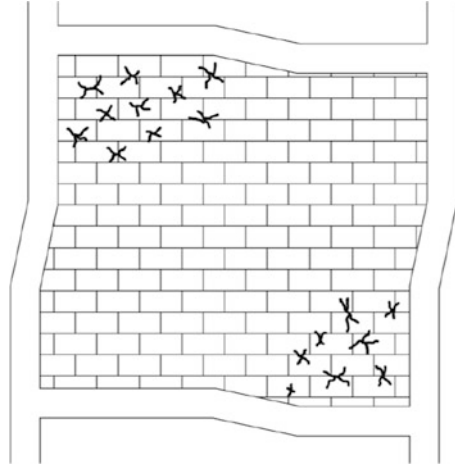
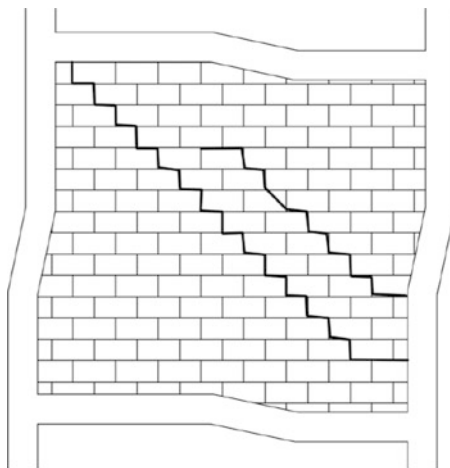


Fig. 16.2 Failure modes

- **Shear cracking**, which is the most common type of failure and it depends on shear and normal stress. When subjected to lateral forces, the stress along the diagonal is represented by the ratio of normal stress f_n and shear stress τ , which is equal to the ratio of the height of the masonry panel h_m and the length of masonry panel L_m . The combination of the two parameters can produce the following three mechanisms:

$$\frac{f_n}{\tau} = \frac{h_m}{L_m} = \text{aspect ratio} \tag{16.2}$$

Fig. 16.3 Shear cracking with stepped cracks



- *Stepped cracking along the mortar joints* (Fig. 16.4): it is the most common type of failure and it occurs when the shear stress predominates over the normal stress (low to medium aspect ratio) or when the mortar joints are weaker than the masonry units. In that case cracking usually occurs by debonding along the mortar joints.
- *Horizontal sliding along the mortar joints*: it happens when the formation of a horizontal crack causes the panel fails by shear (Fig. 16.5). The formation of the horizontal crack could be facilitated by the relative dimension of the masonry units and the infill panel, and it could form when the following equation is satisfied:

$$\frac{h_m}{L_m} < \frac{2b}{d} \quad (16.3)$$

where d and b are the length and height of masonry unit. Fiorato et al. (1970) reported this type of failure in tests of infilled reinforced concrete frames, and tests results indicate that the major crack usually starts a few courses below the upper loaded corner, it continues diagonally downwards to approximately the center of the panel, and then it propagates horizontally.

- *Cracking due to diagonal tension*: it occurs when the normal stress predominated over the shear stress (medium to high aspect ratio) and when in comparison with the masonry, the mortar joints are stronger.
- **Flexural cracking**, which can occur when the columns of the frame are weak and flexure effects are predominating, such as in multistory infilled frames. In these cases, as reported by Leuchars and Scrivener (1976), flexure cracks can open due to the low tensile strength of the masonry in the tensile side of the panel.

Fig. 16.4 Shear cracking with horizontal sliding

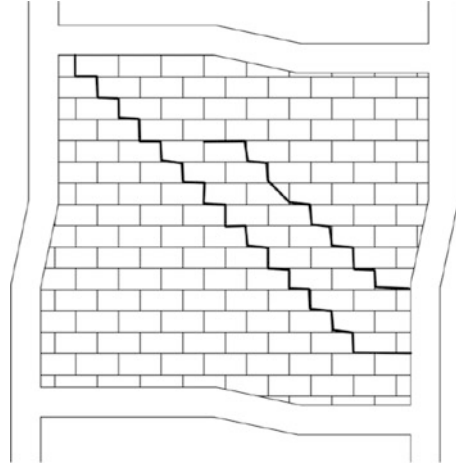
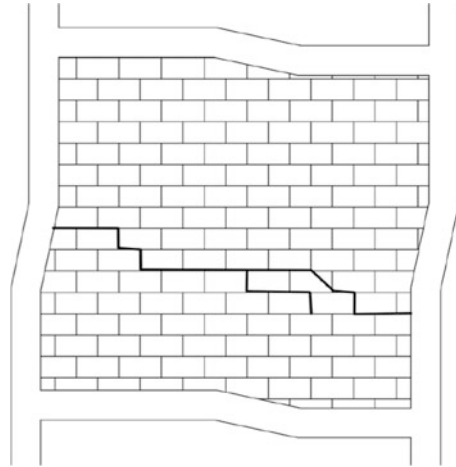


Fig. 16.5 Shear cracking due to diagonal tension



16.3.2 Failure Modes of Surrounding Reinforced Concrete Frames

The failure modes of surrounding reinforced concrete (Fig. 16.6) are of two types:

- **Flexure collapse mechanism**, which happens when, in a multistory frame, at the ends of the columns a flexure plastic hinge occurs, leading to a collapse after the failure of the panel (Fig. 16.7). Plastic hinges can also occur at the end and the middle height of the columns when sliding shear takes places in the masonry panel. The deformation capacity of the frame depends on the deformation of plastic hinges after they are formed. Thus, within the hinge region the inelastic deformation capacity should be guaranteed.

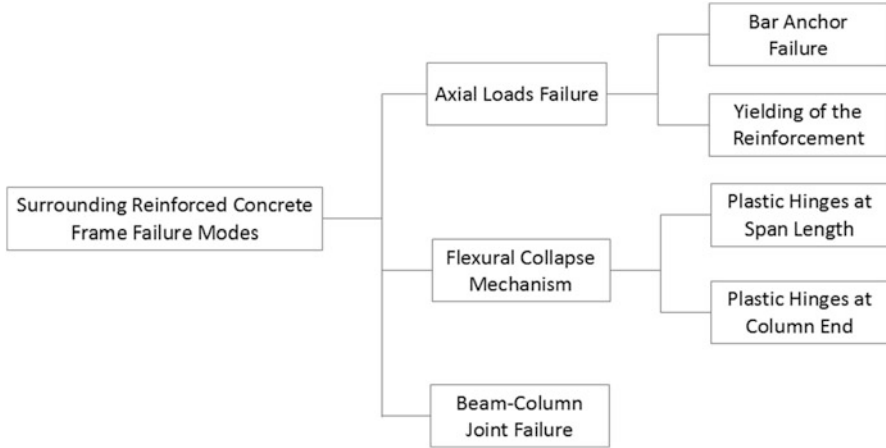
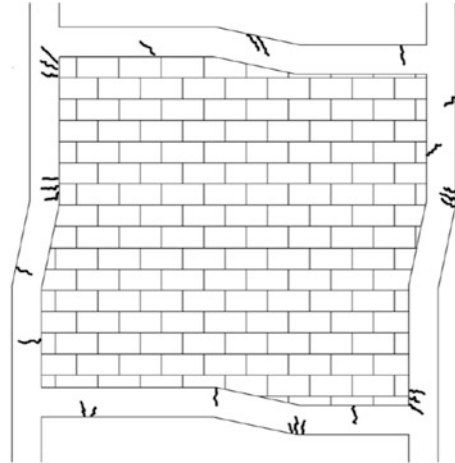


Fig. 16.6 Failure modes for surrounding reinforced concrete frame

Fig. 16.7 Flexure collapse mechanism with plastic hinges at member ends



- **Axial loads failure**, which can occur when the columns undergo a severe cyclic loading, thus leading to a compressive failure. In fact the columns subjected to tension and axial forces can yield and the reinforced concrete members can crack with the increment of the lateral forces.

This type of failure can occur in the following three modes:

- *Tension failure with yield of longitudinal reinforcement*: it may happen in infilled frames due to tensile strains. This produces a large elongation of the columns, which may lead to a loss of compatibility between the frame and the panels because of the distinct difference of the structural properties.

Fig. 16.8 Shear failure of the columns

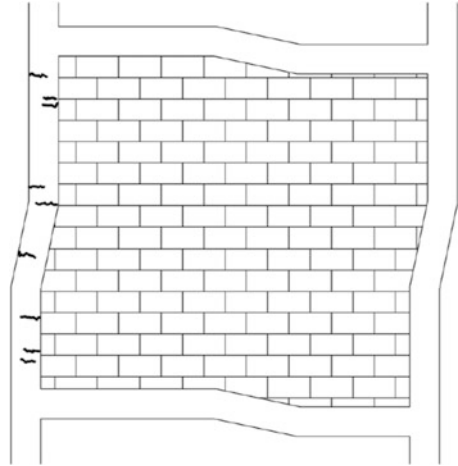
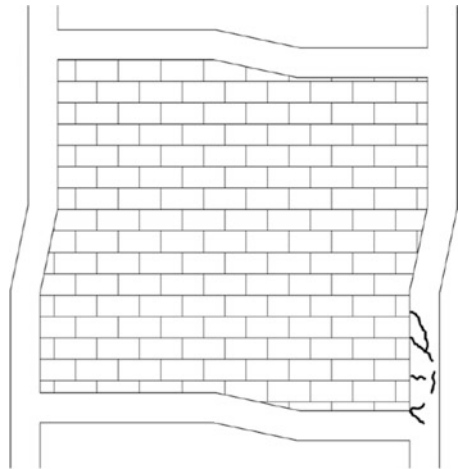


Fig. 16.9 Beam-column joint failure



- *Bar anchorage failure*: it is caused by slipping of the longitudinal reinforcement of the tension column, and it can be avoided by providing an adequate development length for the longitudinal bars.
- *Shear failure of the columns*: it happens when shear forces resulting from the composite interaction with the infill panels cause the failure of the columns. It can be avoided by providing adequate amount of transverse reinforcement and shear length of the concrete (Fig. 16.8).
- *Beam-column joint failure*: it occurs when high normal and tangential stresses develop along the contact lengths in the zones close to the stressed corners, causing large shear forces and bending moments (Fig. 16.9).

16.4 Existing Analytical Models

Due to the nonlinear inelastic behavior, both materially and geometrically, infilled frames are complex structural types which require sophisticated computational techniques to be correctly considered in the modeling. For this reason there are different techniques proposed in the literature for the in-plane analysis of the strength and stiffness of masonry infilled frames. These analytical models can be divided in two categories:

- **Local or micro-models**, which focus on the infill behavior specifically. The most common micro-model is the finite element analysis, first applied by Mallick and Severn (1967), which is advantageous as it describes the behavior of infilled frames in their various parts, indicating the local effects related to cracking, crushing, and contact interaction. However, this type of model also implies a greater computation effort, and with the improvement of computer capabilities and the development of the finite element method, these types of model have been discarded.
- **Simplified or macro-models**, which are the models based on a physical understanding of the behavior of the infill panel as a whole, and they are particularly useful in developing design equations. Some macro-models were developed to evaluate the stiffness of the structure assuming elastic behavior (Smolira 1973; Leuchars and Scrivener 1976; Liauw and Lee 1977), or to investigate the global response of infilled frame structures (Moroni et al. 1996), or to describe the influence of masonry panels on infilled frames. The latter purpose was achieved through the diagonal strut concept, which was first proposed in the tests conducted by Polliakov (1963), and it was further developed by Holmes (1961) and Smith and Carter (1969). It was later reported by Mallick and Severn (1967), Klinger and Bertero (1976), and many others afterwards.

As reported by Tucker (2007), the existing analytical models have been divided in *stiffness* (Sect. 16.4.1) and *strength* (Sect. 16.4.2) methods and they will be presented in chronological order in the following paragraphs.

16.4.1 Stiffness Methods

The object of the majority of the researches was the calculation of the width of the equivalent diagonal strut, after which, since the stiffness of a system is based on the elastic shortening of the diagonal strut, it becomes easy to determine it through a simple braced frame analysis.

16.4.1.1 Polyakov, 1956

Polliakov (1963) was the first to recognize that the most accurate representation of the stiffness of the masonry infilled structure is that of a braced frame with the masonry replaced by an equivalent diagonal strut. For his research he used a steel four-hinged frame, while most of the following researchers used fixed-based frames. For this reason his specific method has the merit to be the first one, but it became obsolete.

16.4.1.2 Holmes, 1961

Holmes's (Holmes 1961) merit is to have extended Polyakov's (Polliakov 1963) equivalent diagonal strut representation to infill structures. He obtained the following equation for the horizontal deflection of the infilled frame at failure:

$$S_H = e'_{cd} \cos \alpha \quad (16.4)$$

where S_H is the horizontal deflection (mm), e'_c is the strain in the infill at the moment of failure (mm/mm), d is the diagonal length of infill (mm) and α is the angle of the strut with the horizontal (degrees).

Another equation presented by Holmes is the one for the calculation of the horizontal load which causes crushing failure in the corner regions:

$$H = \frac{24EIe'_{cd}}{h^3(1 + \frac{I}{I_0} \cot \alpha) \cos \alpha} + A_{fc} \cos \alpha \quad (16.5)$$

where H is the horizontal shear force at failure (kN), E is Young's modulus of the column (kN/mm^2), I is the moment of inertia of the column (mm^4), I_0 is the moment of inertia of the beam (mm^4), h is the height of the frame (mm).

16.4.1.3 Stafford-Smith and Carter, 1969

In the equation developed by Smith and Carter (1969), he calculated α , the length of contact between the infill and the frame, as follows:

$$\frac{\alpha}{h} = \frac{\pi}{2\lambda h} \quad (16.6)$$

where α is the length of contact (mm), h is the height of the column between centerlines of beams (mm) and λ is the characteristic stiffness parameter (mm^{-1}). In particular, λh is a nondimensional expression for the relative stiffness of the frame to the infill, where λ is defined as:

$$\lambda = \sqrt[4]{\frac{E_t t \sin 2\theta}{4EIh'}} \quad (16.7)$$

where E_t is Young's modulus of infill (kN/mm^2), t is the thickness of the infill (mm), θ is the slope of infill diagonal to the horizontal (degrees), h' is the height of the infill (mm). Another equation that was attributed to Smith and Carter (1969) by Al-Nimry et al. (2014) is:

$$a = \frac{\pi}{2\lambda} \quad (16.8)$$

where a is the width of the equivalent strut (mm).

16.4.1.4 Fiorato, Sozen and Gamble, 1970

Fiorato et al. (1970) calculated the lateral stiffness as follows:

$$K_b = \frac{1}{\frac{1}{K_{sh}} + \frac{1}{K_{fl}}} \quad (16.9)$$

$$K_{sh} = \frac{A_w G_w}{h_w} \quad (16.10)$$

$$K_{fl} = \frac{3E_c I}{h^3} \quad (16.11)$$

where K_b is the lateral stiffness (kN/mm), K_{sh} is the shear stiffness of a cantilever composite beam (kN/mm), K_{fl} is the flexural stiffness of a cantilever composite beam (kN/mm), A_w is the cross-sectional area of the wall (mm^2), G_w is the infill shearing modulus (kN/mm^2), h_w is the height of the infill (mm) and E_c is the modulus of elasticity of the concrete (or frame) (kN/mm^2). Moreover Fiorato et al. (1970) calculated also G_w , the infill shearing modulus, using the linear shear strain measurements from the wall, obtaining:

$$G_w = \frac{kV}{A_w \varepsilon_{xy}} \quad (16.12)$$

where k is the coefficient depending on the shape of the cross section, V is the total shear force on the structure (kN), A_w is the cross-sectional area of the wall (mm^2), ε_{xy} is the shearing strain in the wall calculated from the linear strain measurements.

16.4.1.5 Mainstone, 1971

Mainstone (1971) used the relative stiffness parameter, λ for the experimental testing of small scale micro-concrete infill and scaled brick masonry, obtaining two sets of equations based on the value of the product λh : one set was for the brick

infill, the other for the concrete infill. Equations 16.13 and 16.14 are for λ_h values between four and five, while Eqs. 16.15 and 16.16 are for λ_h values that are higher than five.

$$\frac{w'_{eK}}{w'} = 0.175(\lambda_h h)^{-0.4} \quad \text{brick} \quad (16.13)$$

$$\frac{w'_{eK}}{w'} = 0.115(\lambda_h h)^{-0.4} \quad \text{concrete} \quad (16.14)$$

$$\frac{w'_{eK}}{w'} = 0.16(\lambda_h h)^{-0.3} \quad \text{brick} \quad (16.15)$$

$$\frac{w'_{eK}}{w'} = 0.11(\lambda_h h)^{-0.3} \quad \text{concrete} \quad (16.16)$$

where w'_{eK} is the effective width of infill considered as a single diagonal strut for stiffness (mm), w' is the diagonal length of the infill (mm) and λ_h is the relative stiffness parameter (mm^{-1}).

16.4.1.6 Liauw and Kwan, 1984

The width of the diagonal strut, w , was calculated by Kwan and Liauw (1984) as follows:

$$w = \frac{0.95h \cos \theta}{\sqrt{\lambda_h}} \quad (16.17)$$

where h is the story height (mm). Kwan and Liauw (1984) also worked on a finite element analysis that neglected friction, and their conclusion was that there is an upper limit to the width of the diagonal strut even for very stiff frames with flexible infill. They suggested to use smaller values from the Eq. 16.17 to calculate the width of the strut, such as 0.86 or even 0.45 instead of 0.95.

16.4.1.7 Decanini and Fantin, 1986

Based on results obtained from framed masonry tested under lateral forces, Decanini and Fantin (1986) proposed two sets of equations considering different states of the masonry infill.

For *uncracked panels*:

$$b_w = \left(\frac{0.748}{\lambda_h} + 0.085 \right) d_m, \quad \text{if } \lambda_h \leq 7.85 \quad (16.18)$$

$$b_w = \left(\frac{0.383}{\lambda_h} + 0.130 \right) d_m, \quad \text{if } \lambda_h \leq 7.85 \quad (16.19)$$

For *cracked panels*:

$$b_w = \left(\frac{0.707}{\lambda_h} + 0.010 \right) d_m, \quad \text{if } \lambda_h \leq 7.85 \quad (16.20)$$

$$b_w = \left(\frac{0.470}{\lambda_h} + 0.040 \right) d_m, \quad \text{if } \lambda_h \leq 7.85 \quad (16.21)$$

where d_m is the diagonal length of infill (mm).

16.4.1.8 Moghaddam and Dowling, 1988

Moghaddam and Dowling (1988) suggested that a simple percentage of the length of the diagonal could be used as the width of the strut, and calculated as follows:

$$w = \frac{d}{6} \quad (16.22)$$

16.4.1.9 Eurocode 8, 1988

The EC8 (1998-1 2004) stated that the width of the diagonal strut can be calculated using equations from literature, and that in order to give the effects of local thrusts on the beams and columns a requirement is to include three diagonal struts in the analysis. The equation suggested in the Eurocode 8 is:

$$b_w = 0.15d \quad (16.23)$$

where b_w is the width of the equivalent strut (mm).

16.4.1.10 Duranni and Luo, 1994

Luo et al. (1994) studies Mainstone's (Mainstone 1971) work and modified it, using the effective width factor to describe the stiffness of the infill and calculate the effective width of the equivalent diagonal strut as follows:

$$w_c = \gamma d \sin(2\theta) \quad (16.24)$$

$$\gamma = 0.32 \sqrt{\sin 2\theta} \left(\frac{H^4 E_t t}{m E_c I_c b} \right)^{-0.1} \quad (16.25)$$

$$m = 6 \left(1 + \frac{6\alpha \tan \left(\frac{E_b I_b H}{E_c I_c L} \right)}{\pi} \right) \quad (16.26)$$

where w_c is the width of the equivalent strut (mm), γ is the effective width factor, E_i is the modulus of elasticity of the masonry infill material (kN/mm^2), m is the dimensionless parameter relating the ratio of beam to column stiffness, I_c is the moment of inertia of the confining column (mm^4), E_b is the modulus of elasticity of the confining beam (kN/mm^2), I_b is the moment of inertia of the confining beam (mm^4), L is the length of the infill (mm).

16.4.1.11 Bennet, Flanagan, Adham, Fished and Tenbus, 1996

Bennett et al. (1996) calculated the width of the equivalent strut, w , as follows:

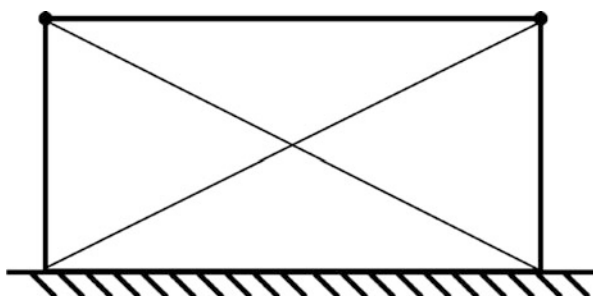
$$w = \frac{\pi}{C\lambda\cos\theta} \quad (16.27)$$

where C is the empirical constant based on infill damage.

16.4.1.12 Crisafulli, 1997

Initially the concept of the equivalent strut model was one diagonal strut that connected two opposite corners of the infill panel (Fig. 16.10). Two struts in each diagonal were planned in order to represent the cyclic behavior, and they only resisted compression stresses (Crisafulli 1997). Since the single diagonal strut model doesn't describe the local effects resulting from the interaction between the infill panel and the surrounding frame, and as a result the bending moments and shear forces are not realistic nor the location of potential plastic hinges can be adequately predicted, the model was modified by Crisafulli (1997) as in Fig. 16.11. The diagonal strut is characterized geometrically by its length, thickness and width (often defined respectively d_w , t_w and b_w), which can be seen instead in Fig. 16.12.

Fig. 16.10 The initial concept of equivalent strut model



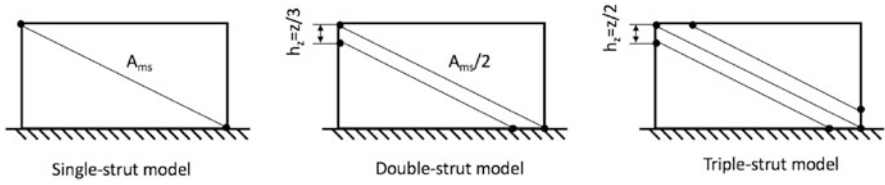


Fig. 16.11 Modified strut models (Adapted from Crisafulli 1997)

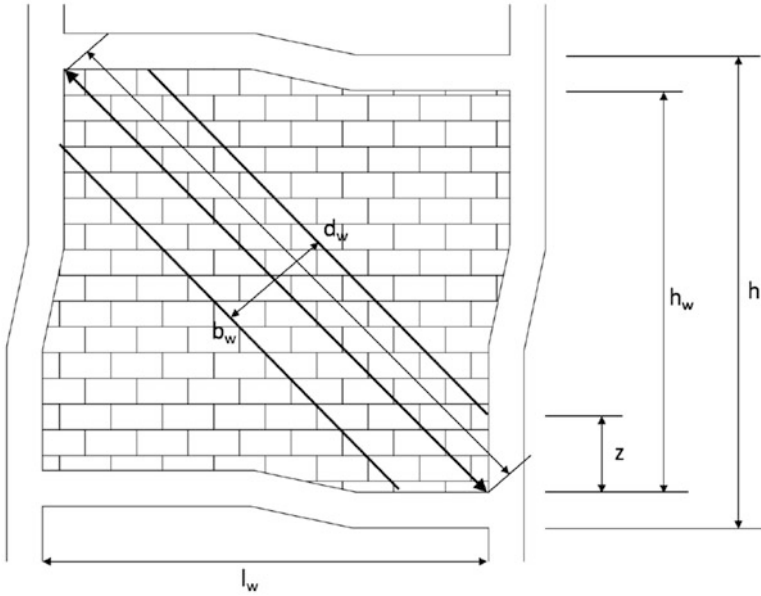


Fig. 16.12 Geometric characteristics of the diagonal strut

16.4.1.13 Al-Chaar, 2002

Al-Chaar et al. (2002) calculated the stiffness of masonry infilled frames as follows:

$$a = 0.0835CD \left(1 + \frac{2.574}{\lambda_t H} \right) \quad \frac{1}{h} \geq 1.5 \tag{16.28}$$

$$C = -0.3905 \left(\frac{l}{h} \right) + 1.7829 \tag{16.29}$$

$$a = 0.0835D \left(1 + \frac{6.027}{\lambda_t H} \right) \quad \frac{1}{h} \geq 1.0 \tag{16.30}$$



where a is the equivalent width of infill strut in the elastic range (mm), C is the multiplication factor that accounts for aspect ratio and D is the diagonal length infill (mm). Linear interpolation is required for aspect ratios ($\frac{1}{h}$) between 1.0 and 1.5.

16.4.1.14 El-Dakhakhni, Egaaly and Hamid, 2003

For El-Dakhakhni et al. (2003) a three-strut model better represented the actual distribution of forces from the infill to the frame, and they calculated the total strut area by multiplying the width by the infill thickness.

$$w = \frac{(1 - \alpha_c)\alpha_{ch}}{\cos\theta} \quad (16.31)$$

$$\alpha_{ch} = \sqrt{\frac{2(M_{pj} + 0.2M_{pc})}{t'_{m=0}}} \leq 0.4h \quad (16.32)$$

where a_c is the ratio between the column contact length and its height, M_{pk} is the minimum of the column's, the beam's or the connection's plastic moment capacity, referred to as the plastic moment capacity of the joint ($kN - mm$), M_{pc} is the column plastic moment capacity ($kN - mm$), $t'_{m=0}$ is the masonry strength parallel to bed joints (kN/mm^2). The strut area is split among three struts and the beam contact length needed to analyze the infilled frames is:

$$\alpha_{bl} = \sqrt{\frac{2(M_{pj} + 0.2M_{pb})}{t'_{m=90}}} \leq 0.4l \quad (16.33)$$

where a_b is the ratio between the beam contact length and its span, M_{pb} is the beam's plastic moment capacity ($kN - mm$) and $t'_{m=90}$ is the masonry strength perpendicular to bed joints (kN/mm^2).

16.4.2 Strength Methods

Strength methods until now have been based on several design philosophies and failure modes, such as the equivalent diagonal strut or the shear friction within the masonry or a plastic analysis that includes frame contributions. Some methods are for the capacity to the first crack loads, others for the ultimate load capacity, and a few include both capacities.

16.4.2.1 Mainstone, 1971

Mainstone (1971) calculated the composite strength of the frame-infill system as follows:

$$H = H_F + H_I \quad (16.34)$$

$$HI = R'_c \cos \theta \quad (16.35)$$

$$R'_c = f'_c - cw'_{cc}t \quad (16.36)$$

where H is the horizontal racking strength of the infilled frame (kN), H_f is the horizontal racking strength of the frame without the infill (kN), H_I is the nominal horizontal racking strength of the infill (kN), R'_c is the nominal diagonal load on the infill (kN), f'_c is the crushing strength of the material of the infill (kN/mm²), w'_{cc} is the effective width of infill considered as a single diagonal strut at ultimate strength (mm).

16.4.2.2 Klingner and Bertero, 1976

Klinger and Bertero (1976) calculated the axial force in the strut (kN) as follows:

$$S = \frac{EA}{L}v \quad (16.37)$$

where A is the cross-sectional area of the strut (mm²) and v is the axial deformation in the strut (mm). The product between the width of the strut calculated above and the panel's thickness allows to calculate the cross-sectional area of the strut. Instead, the strength envelope curve is calculated as follows:

$$S = Af_c(e^{\gamma v}) \quad (16.38)$$

where f_c is the compressive strength of the infill material (kN/mm²) and γ is the strength degradation parameter, equal to 1 for all analysis. The tensile capacity was taken as zero from a practicality standpoint.

16.4.2.3 Wood, 1978

Wood (1978) calculated the ultimate collapse load by examining the composite shear mode of failure with equal plastic moments M_p in the beam and columns.

$$F = \frac{4M_p}{H} + \frac{1}{2}\sigma_c B t_w \quad (16.39)$$

where F is the horizontal collapse load of composite panel (kN), σ_c is the compressive principle stress in wall (kN/mm^2), B is the length of the panel and t_w is the wall's thickness. Wood also considered a shear rotation failure mode to calculate the horizontal collapse load while taking into account the difference in rotation of the infill and the frame as follows:

$$F = \frac{2(M_p + M_e)}{H} + \sqrt{(C - C^2)}\sigma_c t_w B \quad (16.40)$$

where M_p is the plastic moment in beams and columns ($kN - mm$) and M_e is the beam end moment, not plastic ($kN - mm$), C is the ratio of horizontal wall stress to crushing stress taken as $1/2$.

16.4.2.4 Rosenblueth, 1980

Rosenblueth (1980) presented two equations for the strength of a typical infilled frame, one for sliding shear failure (Eq. 16.41) and one for compression failure of the diagonal strut (Eq. 16.42).

$$R_s = \left(0.9 + 0.3 \frac{l}{h}\right) f_{bs} h t \quad (16.41)$$

where R_s is the diagonal strut force when sliding initiate (kN) and f_{bs} is the shear bond strength (kN/mm^2).

$$R_c = \frac{2}{3} \alpha f'_m \sec \theta \quad (16.42)$$

where R_c is the diagonal strut force at compression failure (kN), α is the contact length between panel and the column (mm), f'_m is the compressive strength of the masonry (kN/mm^2).

16.4.2.5 Kwan and Liauw, 1984

Kwan and Liauw (1984) presented equations for the following four failure modes:

- Mode 1: corner crushing with failure in columns and infill-beam connections (Eq. 16.43);
- Mode 2: corner crushing with failure in beams and infill-column connections (Eq. 16.44);
- Mode 3: diagonal crushing with failure in infill-beam connection (Eq. 16.45);
- Mode 4: diagonal crushing with failure in infill-column connection (Eq. 16.46).

The corresponding equations are the following:

$$H_u = \sigma_c th \sqrt{\frac{2(M_{pj} + M_{pb})}{\sigma_c th^2}} \quad (16.43)$$

$$H_u = \frac{\sigma_c th}{\tan\theta} \sqrt{\frac{2(M_{pj} + M_{pb})}{\sigma_c th^2}} \quad (16.44)$$

$$H_u = \frac{4M_{pj}}{h} + \frac{\sigma_c th}{6} \quad (16.45)$$

$$H_u = \frac{4M_{pj}}{h} + \frac{\sigma_c th}{6 \tan^2\theta} \quad (16.46)$$

where H_u is the collapse shear (kN), σ_c is the crushing stress of the panel's material (kN/mm²), M_{pj} is the joint plastic moment capacity (kN-mm) and M_{pb} is the beam plastic moment capacity (kN-mm).

16.4.2.6 Stafford Smith and Coull, 1991

Smith et al. (1991) calculated the horizontal shear load as follows:

$$Q'_c = f'_m \alpha t \quad (16.47)$$

where Q'_c is the ultimate horizontal shear. However Smith et al. (1991) noticed that Eq. 16.47 overestimated the real values of the experimental data. Thus they modified the equation as follow:

$$Q'_c = 1.12 \left(\frac{4EI}{E_m th^3} \right)^{0.22} f'_m ht \cos^2\theta \quad (16.48)$$

where E_m is the modulus of elasticity of the masonry infill material (kN/mm²). Smith et al. (1991) furthermore calculated the allowable horizontal shear force based on shear failure, Q_s , as follows:

$$Q_s = \frac{f_{bs} Lt}{1.43 - \mu \left(\frac{0.8h}{L} - 0.2 \right)} \quad (16.49)$$

where f_{bs} is the bond shear strength (kN/mm²) and μ is the coefficient of internal friction. The maximum allowable horizontal shear force is:

$$Q_s \leq 0.7 L t f_{s, max} \quad (16.50)$$

where $f_{s\max}$ is the maximum allowable shear stress (kN/mm^2). The horizontal shear based on diagonal tensile failure, Q_d is:

$$Q_d = 1.7Ltf_t \quad (16.51)$$

where f_t is the allowable flexural tensile stress (kN/mm^2).

16.4.2.7 Flanagan, 1994

Flanagan and Bennett (1999b) calculated the ultimate capacity of an infilled frame, P_u , as follows:

$$P_u = \frac{6EI}{h^3}\delta + Af'_{m\cos\theta} \quad (16.52)$$

where δ is the column in-plane displacement taken at beam centerline (mm).

16.4.2.8 Mehrabi, Shing, Schuller and Noland, 1996

Mehrabi et al. (1996) calculated the sliding shear strength, F_w , as follows:

$$F_w = 0.345A_w + 0.9P_w \quad (16.53)$$

where A_w is the horizontal cross-sectional area of the infill (mm^2) and P_w is the vertical load acting on the infill (kN).

16.4.2.9 Galanti, Scarpas and Vrouwenvelder, 1998

Galanti et al. (1970) calculated the ultimate strength of the diagonal strut, F_D , as follows:

$$F_D = f_{wc}b_w t_w \sqrt{1 + a_s^2} \quad (16.54)$$

where f_{wc} is the compressive strength of the masonry (kN/mm^2), b_w is the width of the equivalent strut (mm), a_s is the wall aspect ratio. The maximum sliding shear, F_S , is calculated as follows:

$$F_S = \tau_m l_w t_w \quad (16.55)$$

where τ_m is the shear strength of mortar material and l_w is the wall's length.

16.4.2.10 Flanagan and Bennett, 1999

Flanagan and Bennett (1999a) calculated the cracking strength, H_{cr} , as follows:

$$H_{cr} = \frac{K_{cr} L t \sqrt{f'_m}}{1000} \quad (16.56)$$

where K_{cr} is an empirical constant. Based on testing of structural clay tile, a mean value of 0.066 is recommended for K_{cr} . The corner crushing strength, H_{ult} was calculated by Flanagan and Bennett (1999a) as follows:

$$H_{ult} = \frac{K_{ult} t f'_m}{1000} \quad (16.57)$$

where K_{ult} is an empirical constant.

References

- 1998-1 E (2004) Design of structures for earthquake resistance Part 1: general rules, seismic actions and rules for buildings. European Committee for Standardization
- Al-Chaar G, Issa M, Sweeney S (2002) Behavior of masonry-infilled nonductile reinforced concrete frames. *J Struct Eng* 128(8):1055–1063
- Al-Nimry H, Resheidat M, Al-Jamal M (2014) Ambient vibration testing of low and medium rise infilled RC frame buildings in Jordan. *Soil Dyn Earthq Eng* 59:21–29
- Benjamin J, Williams H (1958) The Behavior of one-story brick shear walls. *J Struct Eng Div. In: Proceedings of the American Society of Civil Engineers, American Society of Civil Engineers, New York*
- Bennett R, Fischer W, Flanagan R, Tenbus M (1996) Evaluation and analysis of the performance of masonry infills during the northridge earthquake. *Journal article, Oak Ridge National Lab., Oak Ridge*
- Bin Z (2006) Parametric study on the influence of infills on the displacement capacity of reinforced concrete frames for earthquake loss estimation. In: *European school for advanced studies in reduction of seismic Ris, Rel Rui Pinho*
- Crisafulli FJ (1997) Seismic behaviour of reinforced concrete structures with masonry infills. Ph.D. Thesis, Department of Civil Engineering, University of Canterbury, 404 p
- Decanini L, Fantin G (1986) Modelos simplificados de la mampostería incluida en porticos. *Características de stiffnessy resistencia lateral en estado limite Jornadas Argentinas de Ingeniería Estructural* 2:817–836
- El-Dakhkhni WW, Elgaaly M, Hamid AA (2003) Three-strut model for concrete masonry-infilled steel frames. *J Struct Eng* 129(2):177–185
- Fiorato AE, Sozen MA, Gamble WL (1970) An investigation of the interaction of reinforced concrete frames with masonry filler walls. Report, University of Illinois Engineering Experiment Station. College of Engineering. University of Illinois at Urbana-Champaign.
- Flanagan RD, Bennett RM (1999a) Arching of masonry infilled frames: Comparison of analytical methods. *Pract Period Struct Des Constr* 4(3):105–110
- Flanagan RD, Bennett RM (1999b) In-plane behavior of structural clay tile infilled frames. *J Struct Eng* 125(6):590–599

- Galanti FM, Scarpas A, Vrouwenvelder AC (1970) Calibration of a numerical model for the simulation of masonry under earthquake loading. *WIT Trans Built Environ* 32:395-405. ISSN:1743-3509
- Gavrilovic P, Sendova V (1992) Experimental and analytical studies of infill walls in reinforced concrete structures. In: Tenth world conference earthquake engineering, Madrid
- Holmes M (1961) Steel frames with brickwork and concrete infilling. *Proc Inst Civ Eng* 19(4):473-478
- Ishibashi K, Meli R, Alcocer S, Leon F, Sanchez T (1992) Experimental study on earthquake-resistant design of confined masonry structures. In: Proceedings of the tenth world conference on earthquake engineering, Madrid, pp 3469-3474
- Klinger R, Bertero V (1976) Infilled frames in earthquake resistant construction. Rep. EERC 76-32. Earthquake Engineering Research Center, University of California, Berkeley
- Kwan KH, Liauw TC (1984) Nonlinear analysis of integral infilled frames. *Eng Struct* 6(3):223-231
- Leuchars J, Scrivener J (1976) Masonry infill panels subjected to cyclic in-plane loading. *Bull N Z Soc Earthq Eng* 9(2):122-131
- Liauw T, Lee S (1977) On the behaviour and the analysis of multi-storey infilled frames subjected to lateral loading. *Proc Inst Civ Eng* 63(3):641-656
- Luo Y, Durrani A, Conte J (1994) Equivalent frame analysis of flat plate buildings for seismic loading. *J Struct Eng* 120(7):2137-2155
- Mainstone RJ (1971) Summary of paper 7360. on the stiffness and strengths of infilled frames. *Proc Inst Civ Eng* 49(2):230
- Mallick D, Garg R (1971) Effect of openings on the lateral stiffness of infilled frames. *Proc Inst Civ Eng* 49(2):193-209
- Mallick D, Severn R (1967) The behaviour of infilled frames under static loading. *Proc Inst Civ Eng* 38(4):639-656
- Mehrabi AB, Benson Shing P, Schuller MP, Noland JL (1996) Experimental evaluation of masonry-infilled rc frames. *J Struct Eng* 122(3):228-237
- Moghaddam H, Dowling PJ (1988) Earthquake resistant design of brick infilled frames. *Brick and Block Masonry*(8th IBMAC) London 2:774-784. Elsevier Applied Science
- Moroni MO, Astroza M, Gómez J, Guzmán R (1996) Establishing rw and cd factors for confined masonry buildings. *J Struct Eng* 122(10):1208-1215
- Polliakov SV (1963) Masonry in framed buildings: an investigation into the strength and stiffness of masonry infilling. National Lending Library for Science and Technology, Boston Spa
- Rosenblueth E (1980) Design Of earthquake resistant structures. Pentech Press, Plymouth
- Smith BS, Carter C (1969) A method of analysis for infilled frames. *Proc Inst Civ Eng* 44(1):31-48
- Smith BS, Coull A, Stafford-Smith BS (1991) Tall building structures: analysis and design, vol 5. Wiley, New York
- Smolira M (1973) Analysis of infilled shear walls. *Proc Inst Civ Eng* 55(4):895-912
- Tucker C (2007) Predicting the in-plane capacity of masonry infilled frames: a dissertation presented to the faculty of the graduate school. Tennessee Technological University
- Valiasis T (1989) Experimental investigation of the behaviour of r/c frames filled with masonry panels and subjected cyclic horizontal load-analytical modelling of the masonry panel. Phd thesis, Ph.D. thesis (in Greek), Aristotle University of Thessaloniki, Thessaloniki
- Wood R (1978) Plasticity, composite action and collapse design of unreinforced shear wall panels in frames. *Proc Inst Civ Eng* 65(2):381-411

Chapter 17

Passive Energy Dissipating Systems



Abstract This chapter introduces the different passive strategies used to protect the structure from seismic actions. The types of passive energy dissipation are illustrated. Furthermore, a large variety of passive energy dissipating systems are analyzed in detail.

17.1 Introduction

The principal scope of the seismic design is to avoid the catastrophic failure and loss of life with the design of functional structure that can resist at earthquake. Some strategic structures such as hospitals, police stations and the major infrastructure are design with a high performance level to resist at catastrophic events in order to remain functional after a seismic event. Different strategies can be used to protect the structure from seismic actions (Fig. 17.1)

- Seismic Isolation (Chap. 19);
- Passive Damping;
- Semi-Active and Active Systems;
- Smart Materials.

Damper devices are systems that dissipate energy during a seismic action, differently to seismic isolation system that reduces the seismic actions on the structure (Soong and Cimellaro 2009). The dissipation of energy does not have any effect on structure, which is protected by a high stiffness bracing system to remain in the elastic field. The main purpose is “braking rather than breaking”. In other words, the forces acting on the main structure is reduced, rather than letting the whole seismic action act on the structural elements causing unrepairable damages.

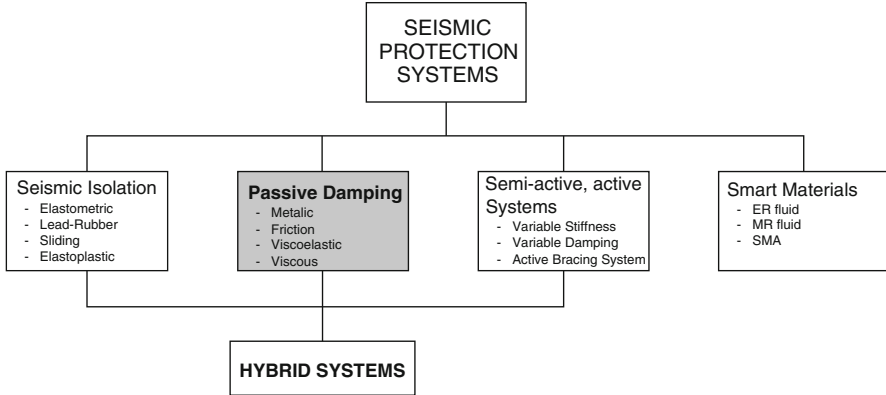


Fig. 17.1 Seismic protection system

17.2 Energy Balance Equation

The equation of a nonlinear Multi-Degree-of-Freedom (MDOF) system excited at the base by a horizontal acceleration time history, is given by

$$[M]\{\ddot{u}(t)\} + [C]\{\dot{u}(t)\} + \{F_r(t)\} = -[M]\{r\}\ddot{u}_g(t) + \{F_s\} \quad (17.1)$$

where $[M]$ and $[C]$ are the global mass and viscous damping, respectively; $\{\ddot{u}(t)\}$, $\{\dot{u}(t)\}$ and $\{u(t)\}$ are respectively the vector of global acceleration, velocity and displacement relative to the moving base at time t . $\{F_r\}$ is the vector of restoring forces at time t due to the hysteresis, while $\{F_s(t)\}$ is the vector of global static loads applied to the structure. $\{r\}$ is the vector coupling the directions of ground motion with the directions of the DOFs of the structure, and $\ddot{u}(t)$ is the horizontal acceleration of the ground at time t . Considering an increment of global structural displacement $\{du\}$, the energy formulation can be obtained by integrating the work done by each component of Eq. 17.1.

$$\begin{aligned} \int \{du\}^T [M] \{\ddot{u}(t)\} + \int \{du\}^T [C] \{\dot{u}(t)\} + \int \{du\}^T \{F_r(t)\} &= \\ = - \int \{du\}^T [M] \{r\} \ddot{u}_g(t) + \int \{du\}^T \{F_s\} & \end{aligned} \quad (17.2)$$

The incremental displacement and velocity can be expressed in the following form

$$\begin{aligned} \{du(t)\} &= \{\dot{u}(t)\}dt \\ \{d\dot{u}(t)\} &= \{\ddot{u}(t)\}dt \end{aligned} \quad (17.3)$$

Then, substituting the aforementioned expressions in the mass and damping terms, the following relationships are given

$$\begin{aligned}\int \{du\}^T [M] \{\ddot{u}(t)\} &= \int \{\dot{u}\}^T [M] \{\ddot{u}(t)\} dt = \int \{\dot{u}\}^T [M] \{d\dot{u}(t)\} \\ \int \{du\}^T [C] \{\dot{u}(t)\} &= \int \{\dot{u}\}^T [C] \{\dot{u}(t)\} dt = \int \{\dot{u}\}^T [C] \{du(t)\}\end{aligned}\quad (17.4)$$

Substituting the terms derived in Eq. 17.4, the energy balance equation can be rewritten as follow

$$\begin{aligned}\int \{\dot{u}(t)\}^T [M] \{d\ddot{u}(t)\} + \int \{\dot{u}(t)\}^T [C] \{du(t)\} + \int \{du\}^T \{F_r(t)\} &= \\ = - \int \{du\}^T [M] \{r\} \ddot{u}_g(t) + \int \{du\}^T \{F_s\}\end{aligned}\quad (17.5)$$

The energy balance equation can be redefined in the following form

$$E_K(t) + E_D(t) + E_{EH}(t) = E'_I(t) + E_{st}(t) \quad (17.6)$$

where $E'_K(t)$ is the relative kinetic energy, $E_D(t)$ is the energy dissipated by viscous damping, $E_{EH}(t)$ is the absorbed energy (due to both elastic and plastic deformation), $E'_I(t)$ is the relative input energy and $E_{st}(t)$ is the work done by static loads applied before and maintained during the seismic excitation. Equation 17.7 resumes all the energy components of Eq. 17.6.

$$\begin{aligned}E'_K(t) &= \frac{1}{2} \{\dot{u}(t)\}^T [M] \{d\dot{u}(t)\} \\ E_D(t) &= \int \{\dot{u}(t)\}^T [C] \{du(t)\} \\ E_{EH}(t) &= \int \{du(t)\}^T \{F_r(t)\} \\ E'_I(t) &= - \int \{du(t)\}^T [M] \{r\} \ddot{u}(t) \\ E_{st}(t) &= \int \{du(t)\}^T \{F_s\}\end{aligned}\quad (17.7)$$

The equation of the absorbed energy term $E_{EH}(t)$ can be written as follow

$$E_{EH}(t) = E_E(t) + E_H(t) \quad (17.8)$$

where E_E is the recoverable elastic strain energy and E_H is the energy dissipated through hysteretic damping. Then, the fluctuations of the term E_{EH} is affected by the hysteresis model defined through the elasto-plastic force-displacement hysteretic relation for a given DOF.

The energy balance equation (Eq. 17.6) can be also expressed in terms of absolute energy as follow

$$E_K^a(t) + E_D(t) + E_{EH}(t) = E_I^a + E_{st}(t) \quad (17.9)$$

where E_K^a is the absolute kinetic energy and E_I^a is the absolute input energy. When a dissipating system is included, the Eq. 17.9 is modified with a new term E_{SD} , that represents the supplemental damping in the system. Considering this last parameter, the absolute energy balance equation is obtained.

$$E_K^a(t) + E_D(t) + E_{EH}(t) + E_{SD}(t) = E_I^a + E_{st}(t) \quad (17.10)$$

A passive energy dissipating system has to be capable to absorb a certain amount of energy that is not necessary equal to the maximum requested energy dissipation by dampers. Then, it is useful to define a new term associated with the vibrational energy E_V which corresponds to the portion of input energy at time t that is not dissipated by viscous damping or through supplementing damping systems. According to this definition it is clear that the vibrational energy is associated with the amount of absolute energy which can potentially cause damage on the structure and it is equal to the sum of the absolute kinetic energy and the absorbed energy.

$$E_V(t) = E_K^a(t) + E_{EH}(t) \quad (17.11)$$

Thus, Eq. 17.10 becomes

$$E_V(t) = E_I^a(t) - E_{SD}(t) - E_D(t) \quad (17.12)$$

It is possible to notice that maximizing the dissipated energy (by viscous damping and supplemental dampers) does not necessary leads to minimize the vibrational energy over time since the input energy can significantly vary. Then, the optimum passive energy dissipation system design must take into account the characteristics of the motion (Cimellaro et al. 2009; Cimellaro and De Stefano 2010).

17.3 Types of Passive Energy Dissipating System

In literature the dampers devices are grouped as follows:

- *Displacement-activated dampers:*
 - Metallic dampers;
 - Friction dampers;
 - Self-Centering Systems.

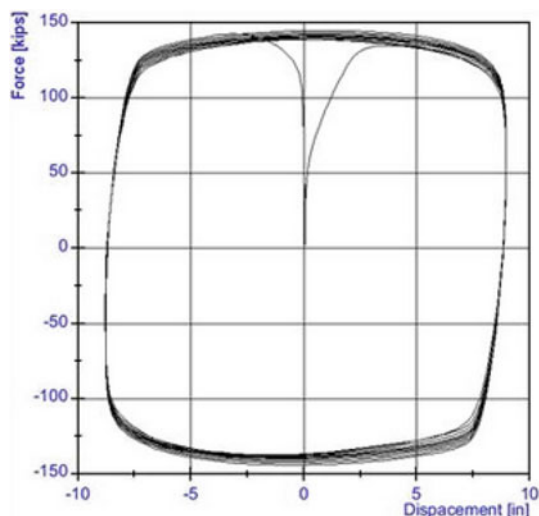


Fig. 17.2 Example of cyclic deformation for a *displacement-activated damper*

- *Velocity-activated dampers:*

- Viscous dampers;
- Viscoelastic dampers.

In the next sections each type of passive energy dissipating system will be described in detail.

17.3.1 *Displacement-Activated Dampers*

The cyclic response of displacement-activated dampers depend on relative displacement at the end points of the device, while the energy dissipation is due to the plastic deformation of the device. The displacement-activated dampers have a stable hysteretic behavior (Fig. 17.2). On the contrary, fatigue failure mechanism may occur for elevated number of cyclic deformation. In addition, they are highly sensitive to the temperature variations, and in case of negative thermal gradient these devices behave as a brittle material.

Different types of displacement-activated systems are described in detail in the next paragraph.

17.3.1.1 *Metallic Dampers*

Metallic dampers are generally made of thin plates where the plastic deformations are uniformly distributed (Hoehler and Stanton 2006). Different types of materials such as steel, lead, and shape memory alloy are usually used as metallic dampers

Fig. 17.3 Cyclic stress-strain hysteresis of a steel element

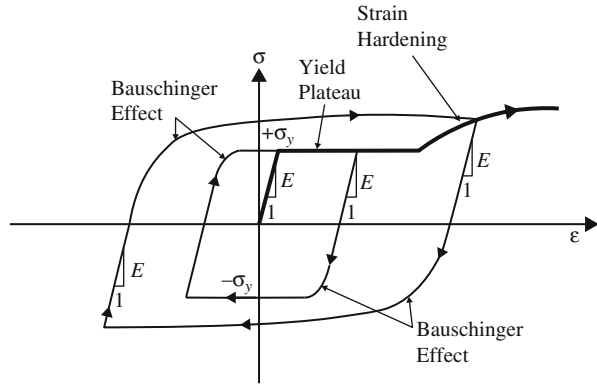
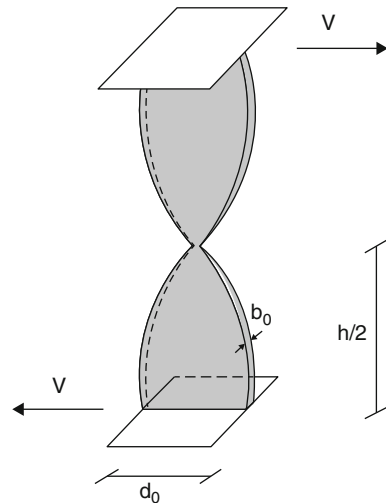


Fig. 17.4 Single steel plate damper



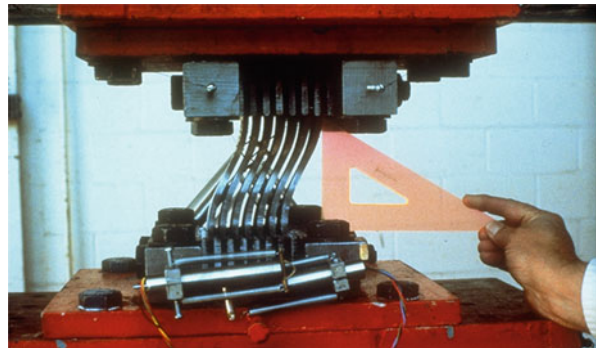
(Roh et al. 2011). According to the specification of these materials, the cyclic stress-strain behavior of the dampers is different. Figure 17.3 depicts an example of a cyclic stress-strain hysteresis for the steel element. Metallic dampers can be used as part of chevron bracing systems. In these cases, the yielding devices dissipate energy through the relative horizontal displacement between the chevron's top and the floor level. In order to maximize the energy dissipation, it is desirable that the plastic moments in the different sections are reached simultaneously (Fig. 17.4). Metallic plate where d_0 is smaller than b_0 are usually selected to minimize the local buckling effects (see Fig. 17.4). Some examples of typical metallic dampers are listed and discussed below.

- The *Added Damping Added Stiffness* (ADAS) system, originally manufactured by Bechtel Corporation, incorporates several interconnected yielding plates in series (Fig. 17.5). The ADAS elements (Scholl 1990) are usually capable to



Fig. 17.5 Example of ADAS dampers

Fig. 17.6 Deformation in an ADAS system



(a)

(b)

Fig. 17.7 ADAS system implementation in Wells Fargo building, San Francisco **(a)** Izazaga building, Mexico City **(b)**

sustain 100 loading cycles at three times the measured yielding displacement without any sign of degradation. In addition they can be safely designed for 10 times the yielding displacement (Fig. 17.6). Figure 17.7 shows some examples of ADAS system implementation.

Fig. 17.8 Example of TADAS system (Tsai et al. 1993)

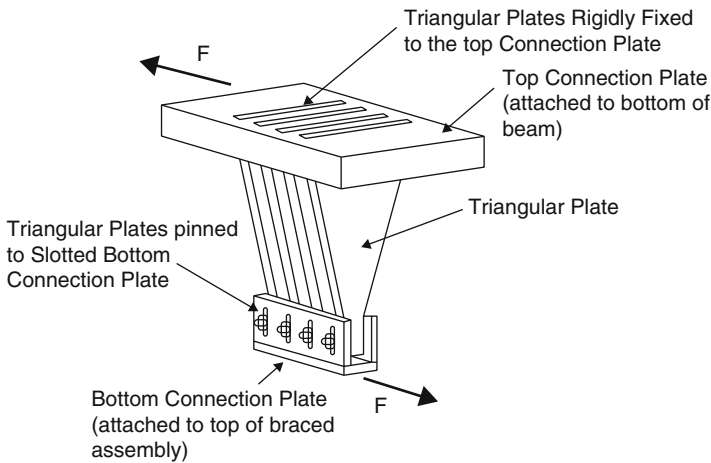
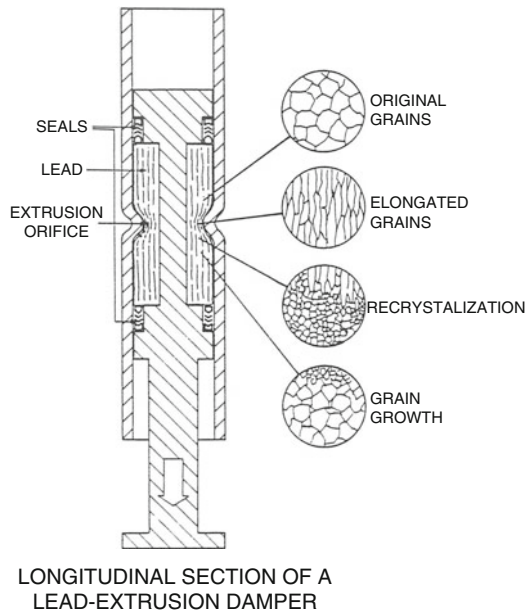


Fig. 17.9 Geometric scheme of TADAS system

- The *Triangular Added Damping Added Stiffness* (TADAS) system was developed by Tsai et al. (1993). It consists in a variation of ADAS system using triangular metallic plate dampers. The triangular plates are rigidly welded to a top plate and simply connected to a slotted base. The TADAS systems are not affected by gravity loads because of the slotted holes in the base plate, and no rotational restraint are required at the top of the brace connection assemblage. On the other hand, the construction is more complicated and a careful welding procedure is required. Figure 17.8 illustrates a geometric scheme of TADAS system (Fig. 17.9).

Fig. 17.10 Scheme of LED system



- The *Lead Extrusion Devices* (LED) were developed in the mid-1970s in New Zealand (Robinson and Tucker 1976). These devices take advantage of extrusion of lead through orifices within a cylindrical chamber (Fig. 17.10). The LED devices have a stable hysteretic behavior, and the fatigue failure is avoided for elevated number of cyclic deformation. In addition, the sensitiveness to a thermal gradient is low. The toxicity of lead represents the main disadvantage. The constricted tube and bulged shaft configurations of LED system are available (Fig. 17.11). Figure 17.12 illustrates an examples of LED system implementation.
- The *Buckling restrain braces* (BRB) were originally manufactured by Nippon Steel Corporation in Japan. They are composed of a steel core plate encased in a steel tube filled with concrete. The steel core carries the axial load while the outer tube, via the concrete, provides lateral support to the core and prevents global buckling (Fig. 17.13) (Tsai and Chih-Yu 2013). A thin layer of lubricating material is located at the concrete interface. Contrarily to the other metallic dampers, the BRB devices have a stable hysteretic behavior (Fig. 17.14). An example of BRB dampers implementation is illustrated in Fig. 17.15.

17.3.1.2 Friction Dampers

The friction dampers are devices that dissipate energy due to friction between two sliding surfaces. Originally, they were based on the vehicle braking system (Pall et al. 1980). Generally, the friction dampers have the following characteristics:

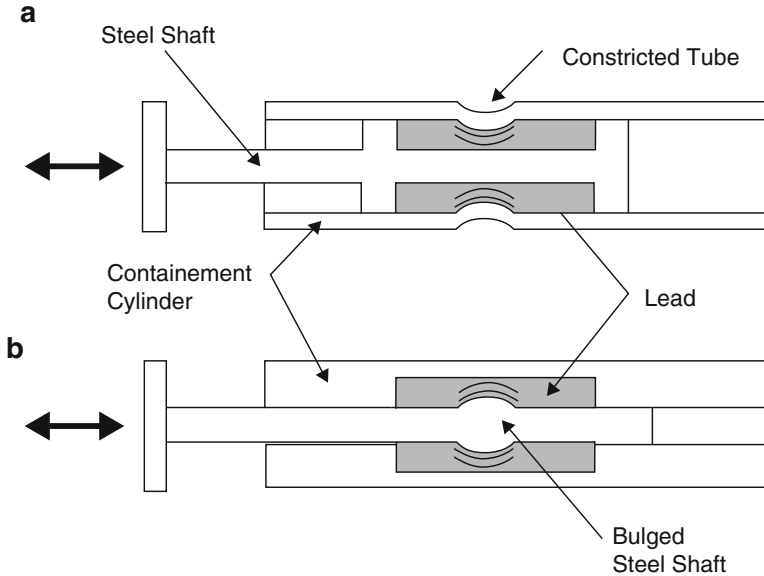
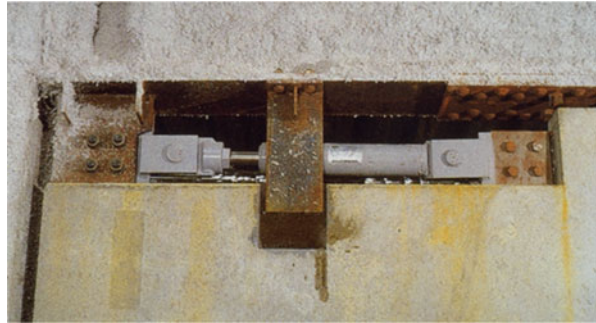


Fig. 17.11 Constricted tube configuration (a) and bulged shaft configuration (b)

Fig. 17.12 LED system implementation in Central Police Station in Wellington, New Zealand



1. Total friction force is independent of area of contact;
2. Friction force is proportional to the normal force acting on the sliding interface;
3. For low relative velocities, the friction force and sliding velocity are mutually independent.

As an advantage, the friction dampers behavior is independent of the intensity of load, frequency, and number of cycles. On the contrary, the behavior of these devices is strictly dependent on the mechanical configuration and on the materials used for the sliding surfaces. Different configurations of friction dampers can be used:

- In the configuration proposed by Pall et al. (1980) (Pall friction dampers), a friction damper is located on the X-braces joint (Fig. 17.16). The X-braces are

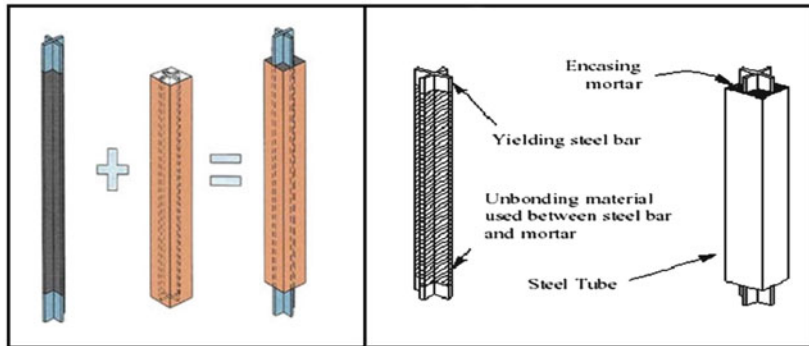


Fig. 17.13 Scheme of BRB

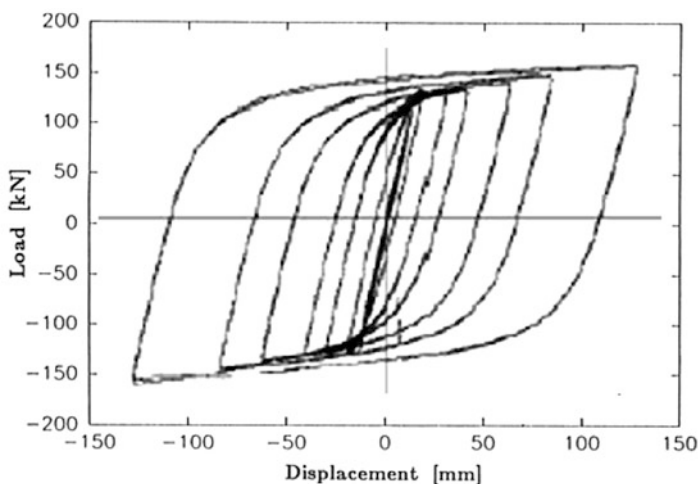


Fig. 17.14 Cyclic stress-strain hysteresis of BRB damper

connected by means of a flexible frame and they are subjected to tensile stress. An example of the Pall friction dampers is shown in Fig. 17.17.

- The Sumimoto friction damper is composed by a piston covered by a breaking copper bearing that slides within a steel cylinder (Aiken and Kelly 1990) (Fig. 17.18). Figure 17.19 illustrates an example of the installation of Sumimoto friction dampers.
- The Slotted Bolted Connections dampers are made of plates having slots in which the bolts slide (Fig. 17.20). The interacting surface is steel/steel or steel/brass (Fitzgerald et al. 1989). Figure 17.21 illustrates two installation details of the slotted-bolted-connections dampers.
- In the Energy Dissipating Restraint configuration, the friction forces arise along the interface between a steel cylinder wall and bronze friction wedges (Fig. 17.22). An additional stiffness is provided by a helical steel (Richter et al. 1990).



Fig. 17.15 Example of BRB dampers implementation

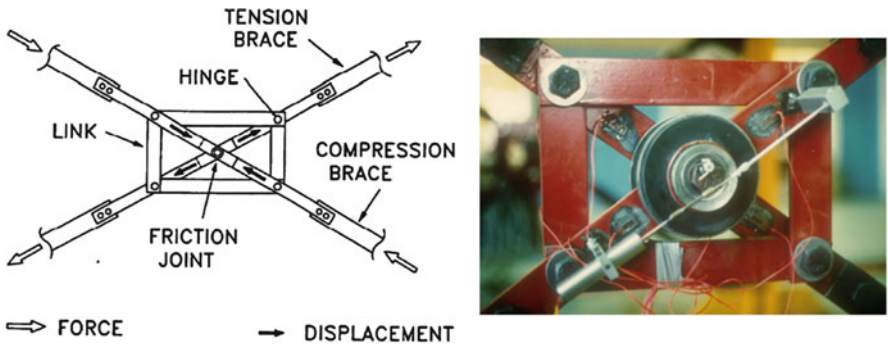


Fig. 17.16 Pall friction damper

17.3.1.3 Shape Memory Alloy Dampers

The shape memory alloy devices are made of shape memory alloy wires. While in the steel elements, the hysteretic behavior is due to a dislocation mechanism, in the case of shape memory alloys the hysteretic behavior is caused by a phase transformation (from martensite to austenite). Figure 17.23 shows the cyclic stress-strain relationship for these devices. These devices are able to limit the residual deformations with a consequent stability of deformation cycles. In addition, they resist the fatigue for reduced number of cycles, and they have a low sensitivity to thermal gradients. On the contrary, the shape memory alloy dampers do not reach high stiffness and their costs are elevated (Song et al. 2006). The Nickel-Titanium (NiTi) is the most widely used shape memory alloy since it has a very high fatigue life (100,000 cycles under cyclic strain $\max = 0.02$ according to Funakubo



Fig. 17.17 Pall friction dampers installation at the Concordia University library building, Montreal

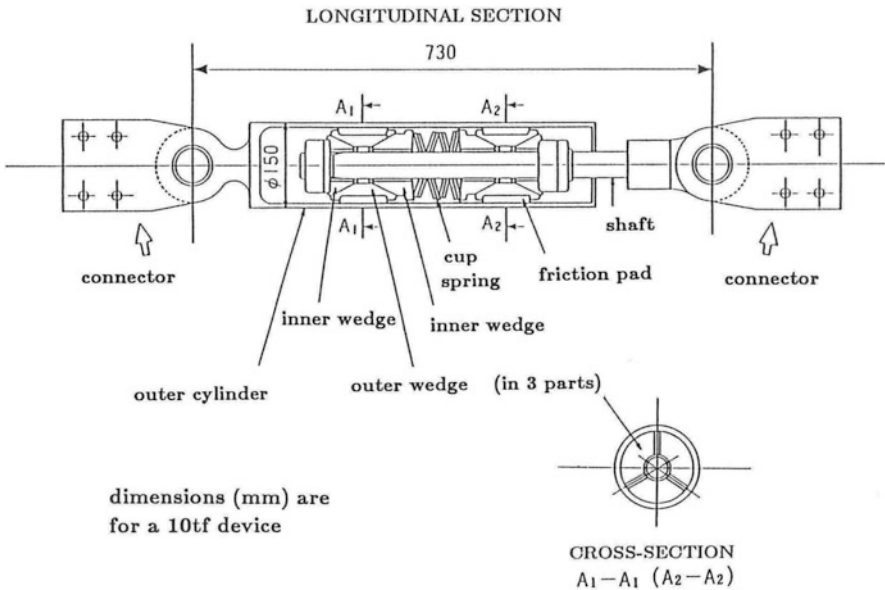


Fig. 17.18 Scheme of the Sumimoto friction damper (Constantinou and Symans 1992)

and Sakamoto 1987). The NiTi shape memory alloy has a large recoverable strain without residual deformation, a self-centering ability, and an excellent corrosion resistance. According to the characteristics above mentioned, the shape memory alloys are integrated in the brace system and they are called Reusable Hysteretic Damping Brace (RHDB) (Zhu and Zhang 2007). Figure 17.24 shows an example of RHDB configuration. Simulation and test on RHDB systems have shown a different behavior for the pre-tensioned and the un-pre-tensioned braces (Fig. 17.25). In order to enhance the behavior of these devices, the combined effects of the un-pre-tensioned and pre-tensioned RHDB can be used (Fig. 17.26).

Fig. 17.19 Sumimoto friction dampers installation at Asahi building in Tokyo, Japan

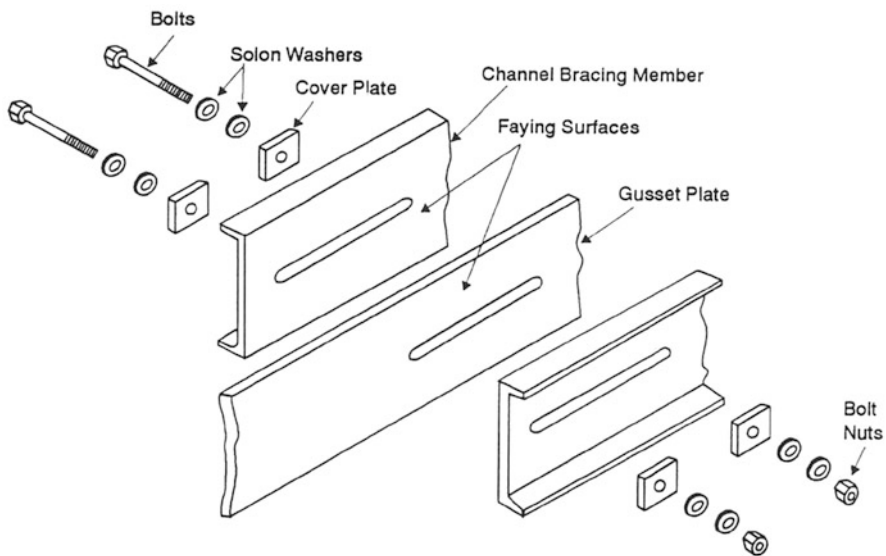


Fig. 17.20 Detailed view of the slotted bolted connections

17.3.1.4 Self-Centering Systems

The cost associated with the loss of business operation and the damage to structural and non-structural components following a moderately strong earthquake can be significant. Thus, most structural systems are designed to respond beyond the elastic limit with a consistent energy dissipation. In order to reduce or eliminate the cumulative damage to the main structural elements, the self-centering devices are used. These devices allow the structural system to return to its original position

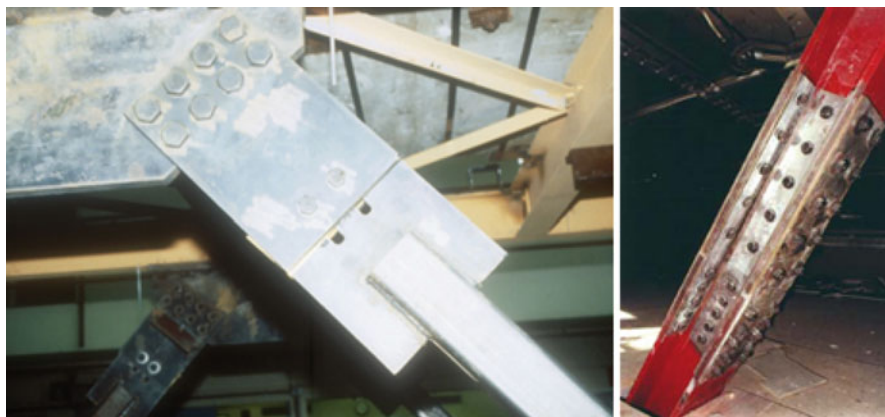


Fig. 17.21 Details of the slotted bolted connections dampers (Fitzgerald et al. 1989)

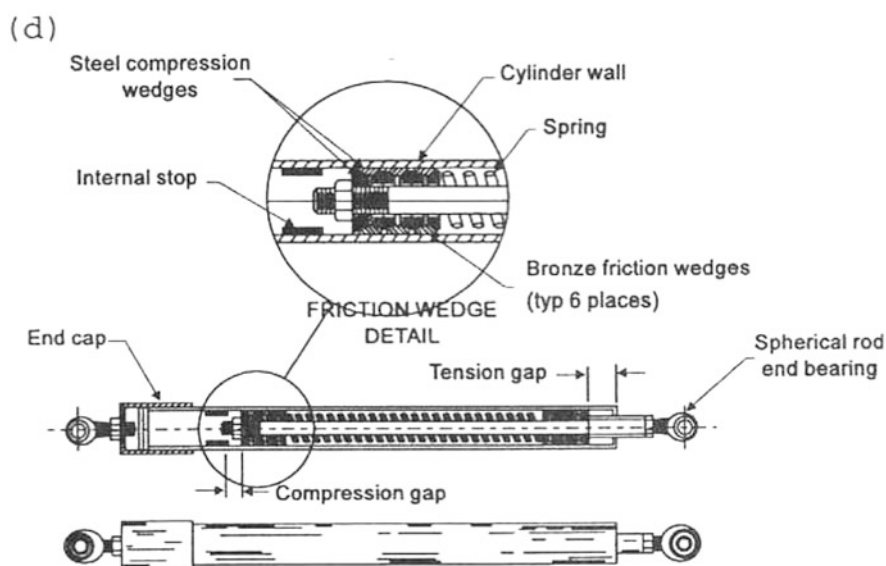


Fig. 17.22 Scheme of the energy dissipating restraint damper

after an earthquake. Figure 17.27 illustrates the characteristic flag-shaped seismic response of a self centering system.

Different self centering devices are provided for reinforced concrete and steel building frames. For steel moment resisting frames, a hybrid post-tensioned connection can be used (Ricles et al. 2001). This connection consists of high strength steel strands that run along side the web of the beam and then is anchored in the exterior column flange at the end of the frame. The seat and the top angles are bolted to both the column and the beam. The shear resistance is provided

Fig. 17.23 Cyclic stress-strain relationship for shape memory alloy dampers

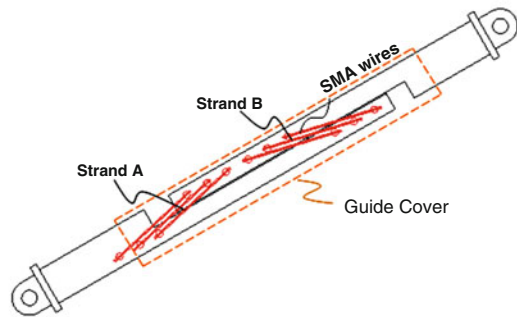
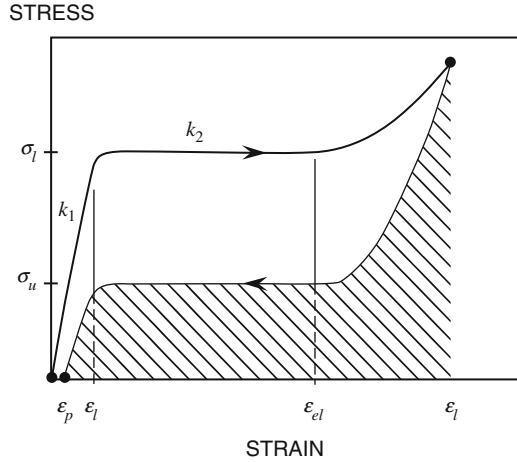


Fig. 17.24 RHDB configuration

by a combination of friction at the beam-column interface and also by the steel angles (Fig. 17.28). After major earthquakes, only the steel angles would need to be replaced. A Post-Tensioned Energy Dissipating (PTED) steel frame concept was proposed by Christopoulos and Filiatrault (2003). The post-tensioning force is applied at each floor by high strength bars located at mid-depth of the beam, and symmetrically placed energy-dissipating bars are also included at each connection (Fig. 17.29).

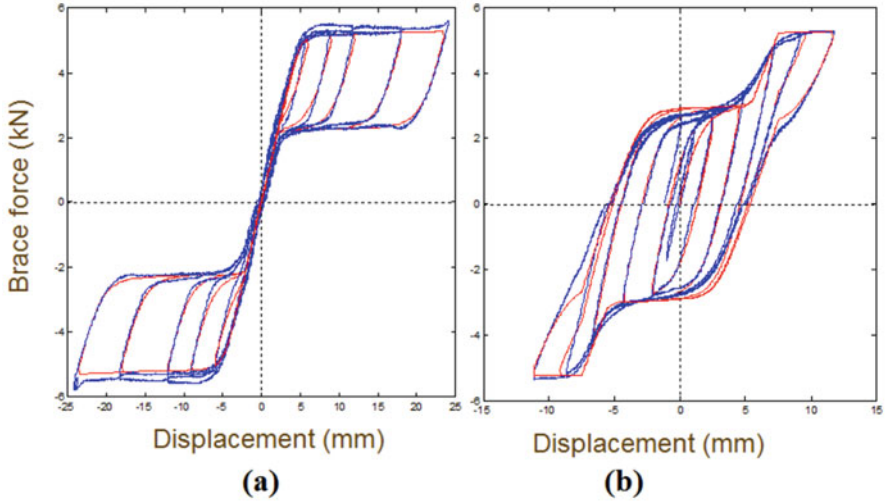


Fig. 17.25 Test and simulation results for the un-pretensioned (a) and the pretensioned (b) RHDB

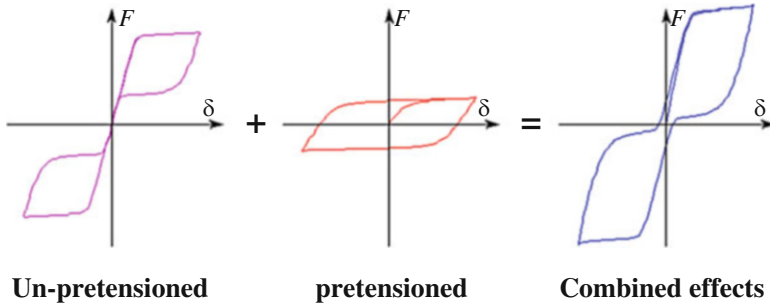


Fig. 17.26 Combination of the effects of un-pretensioned and pretensioned RHDB

17.3.2 Viscous and Viscoelastic Dampers

Viscous and viscoelastic dampers dissipate energy by transforming the mechanical energy into heat. This device consists of a container with a liquid that passes through holes due to the movement of a piston. The main advantages are the low sensibility to the variation of frequency and the phase shift between the force and the displacement. The disadvantages are the sensibility to temperature variations, the large dimensions, and the cost.

Viscoelastic dampers are made of a solid element or a fluid element. Solid devices are made of polymeric or vitreous materials which dissipate energy when a shear force is applied on them. The main disadvantages of solid viscoelastic dampers are the high sensibility to variation of temperature and difficulty to have high stiffness.



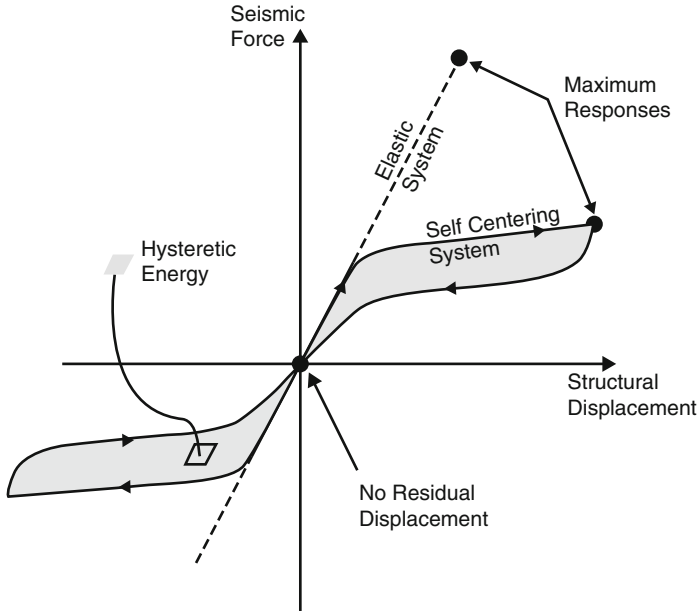


Fig. 17.27 Cyclic stress-strain relationship for self centering systems (Filiatrault et al. 2004)

Viscoelastic dampers have hysteretic behavior and their simplest representation is the model kelvin solid (Chawla and Meyers 1999), assuming that it is of a unit height and a unit area. The displacement is expressed in terms of strains and the force in terms of stress.

Considering Fig. 17.30, by applying equilibrium

$$\tau_e(t) + \tau_c(t) = \tau_s(t) \tag{17.13}$$

where $\tau_e(t)$ is the shear stress carried by an elastic component and $\tau_c(t)$ is the shear stress carried by a viscous component. Shear strain compatibility implicates

$$\gamma_e(t) = \gamma_c(t) = \gamma_s(t) \tag{17.14}$$

where $\gamma_e(t)$ is the elastic shear strain and $\gamma_c(t)$ is the viscous shear strain. Differentiating Eq. 17.14 gives the shear strain rate, and by replacing the constitutive relationship of the elastic and the viscous components the following equation is obtained

$$\frac{\dot{\tau}_e(t)}{G_e} = \frac{\tau_c}{G_c} = \dot{\gamma}_s(t) \tag{17.15}$$

Equations 17.13 and 17.15 lead to the shear constitutive relationship for Kelvin solid

$$\tau_s(t) = G_e \gamma_s(t) + G_c \dot{\gamma}_s(t) \tag{17.16}$$



Fig. 17.28 Hybrid post-tensioned connection developed by Ricles et al. (2001) (Filiatrault et al. 2004)

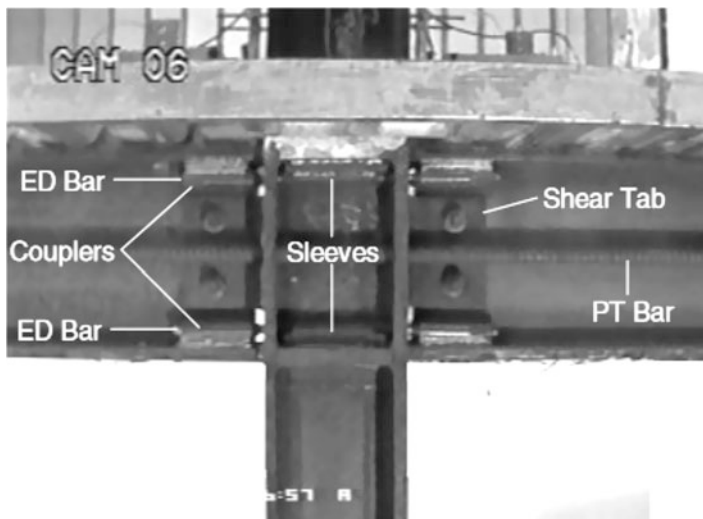
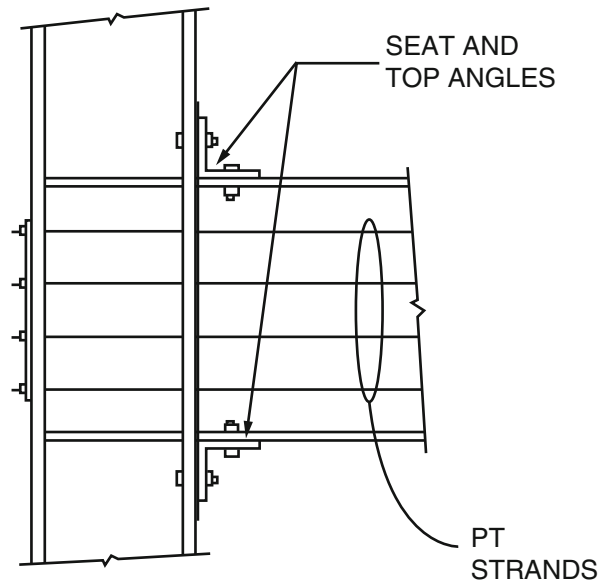


Fig. 17.29 PTED steel frame system

Assuming a shear thickness h and a shear area A_s for the viscoelastic material, Eq. 17.16 leads to a force-displacement relationship

$$F(t) = \bar{k} u(t) + \bar{c} \dot{u}(t) \tag{17.17}$$

with $\bar{k} = \frac{G_e A_s}{h}$ and $\bar{c} = \frac{G_c A_s}{h}$.

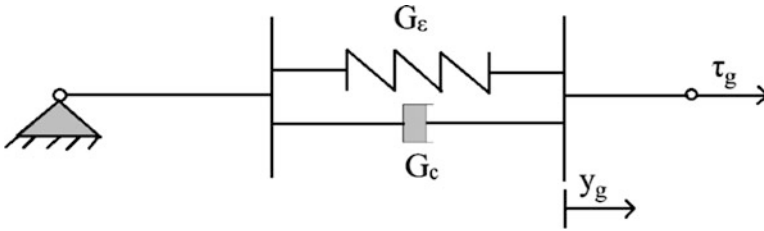


Fig. 17.30 Kelvin solid model

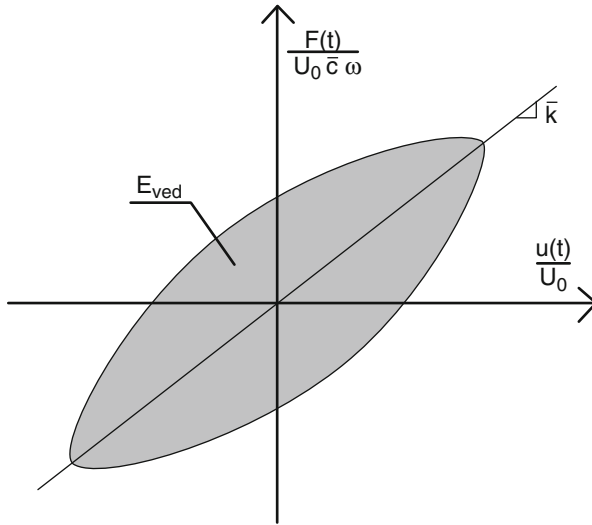


Fig. 17.31 Force-displacement relationship of Kelvin Solid

If the Kelvin element is subjected to a time-varying axial displacement $u(t) = U_0 \sin \omega t$, where U_0 is the displacement amplitude between the ends of the element and ω is the forcing frequency (Fig. 17.31). The axial forces induced in viscoelastic damper is given by Eq. 17.18

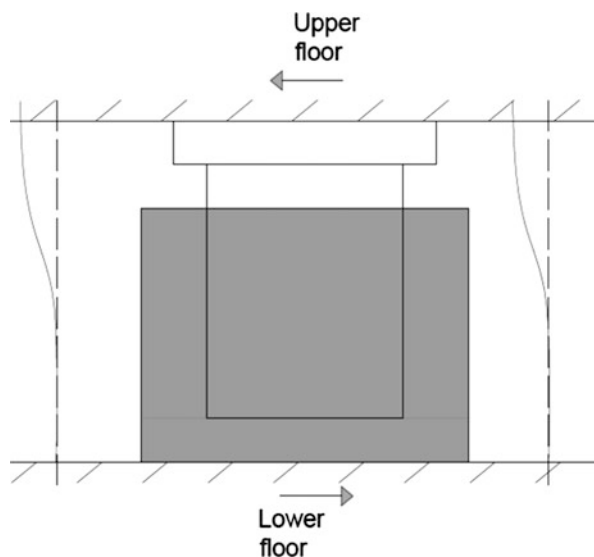
$$\frac{F(t)}{U_0 \bar{c} \omega} = \frac{\bar{k}}{\tau \omega} \left(\frac{u(t)}{U_0} \right) \pm \sqrt{1 - \left(\frac{u(t)}{U_0} \right)^2} \tag{17.18}$$

The energy dissipated E_{ved} by Kelvin solid in each cycle is given by Eq. 17.19, which represents the area under the force-displacement relationship.

$$E_{ved} = \bar{c} \pi \omega U_0^2 \tag{17.19}$$



Fig. 17.32 Viscous Wall Damper



This relationship reveals the material properties of Kelvin solid, in particular the damping

$$\bar{c} = \frac{E_{ved}}{\pi \omega U_0^2} \quad (17.20)$$

The viscous characteristics can be evaluated through the displacement controlled sinusoidal tests at various excitation frequencies.

17.3.2.1 Viscous Wall Dampers

A structural implementation of viscous dampers are Viscous Wall Dampers (Fig. 17.32), which is made of a steel box filled with viscous fluid with a vane dipped in it. The box is connected to the lower floor, while the steel plate is connected to the upper floor. During seismic actions, the relative movement causes the plate to move through the viscous fluid. In addition, the damping depends on the displacement and the velocity of the motion. Viscous walls can be constructed with one vane (Fig. 17.33a) or two vanes (Fig. 17.33b).

17.4 Mechanical Model of Dampers

Dampers are considered energy dissipating devices and they are classified into two categories:

- Displacement-activated dampers;
- Velocity-activated dampers.

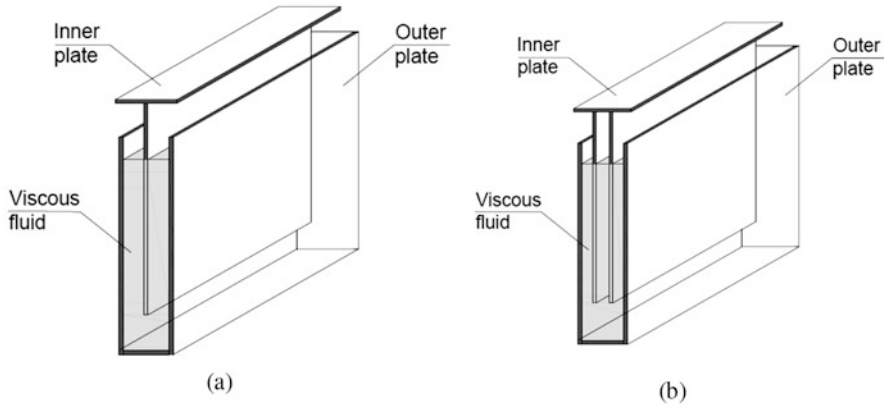


Fig. 17.33 Viscous wall with one vane (a) and two vanes (b)

The cyclical response of displacement activated dampers is captured by monitoring the relative displacement of the device's extremities. This kind of devices is characterized by a hysteretic bilinear or trilinear behavior. This type of dampers can be further divided into:

- Elasto-plastic dampers (EP), which is characterized by the elastic stiffness, hardening factor, and ductility;
- Friction damper (FR), which is characterized by its scrolling force.

As for the velocity-activated dampers, the cyclical response is controlled by the relative velocity of the device's extremities and the excitation frequency. Two types of dampers can be classified under this category:

- Linear viscous damper (VL), which is governed by its viscous coefficient;
- Linear elastic viscous dampers, characterized by its elastic stiffness and loss factor.

The mechanical models of the four types of dampers discussed above are presented in Fig. 17.34.

17.5 Characteristics of the Braces

Generally, the dampers are characterized by the following characteristics:

- Reduce the displacement;
 - Increase the energy dissipation;
 - Increase the structural resistance;
 - Increase the stiffness of the structure.

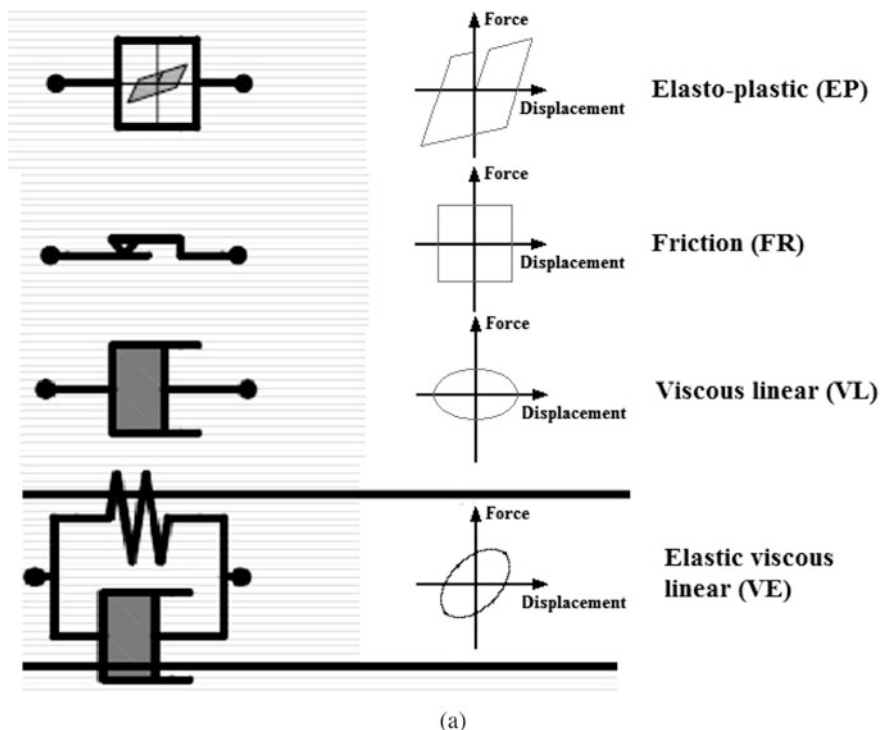


Fig. 17.34 Mechanical models of dampers

- Decouple the vertical and lateral resisting systems;
- The damping level is between 10% and 30% of the critical load.

Figure 17.35 shows the difference in the fundamental period between a structure equipped with a bracing system and another structure equipped with a damping system. The main advantage of dampers is that they increase the fundamental period of the structure significantly, and this causes the reduction of the corresponding ground acceleration. Therefore, the structure can then be designed for reduced forces.

17.6 Seismic Behavior of a Passive Brace

Figure 17.36 shows the difference in the behavior of elastic braces and dampers. Bracing systems increase the stiffness of the structure, which increases the strength to resist lateral forces. This is also accompanied by a reduction of the structure's fundamental period, which may cause the structure to be subjected to a higher ground acceleration. On the other hands, the damping systems increase the lateral

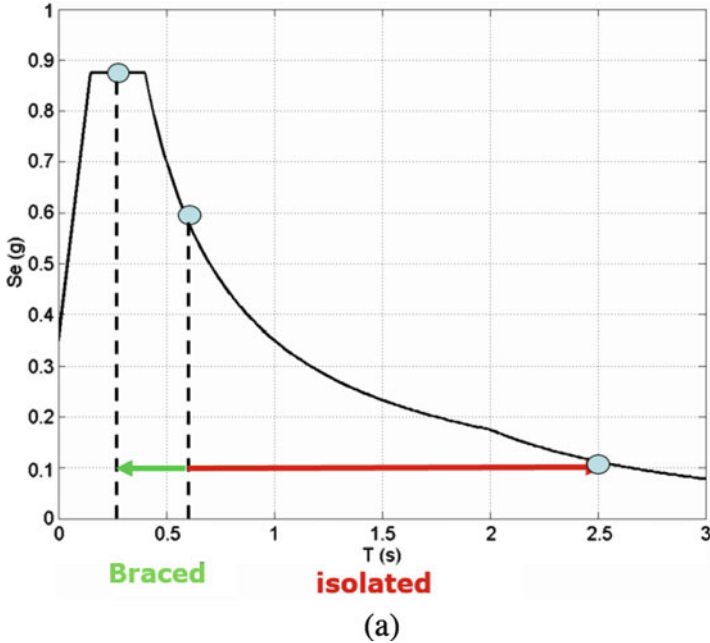


Fig. 17.35 Comparison between a rigid and a damped brace

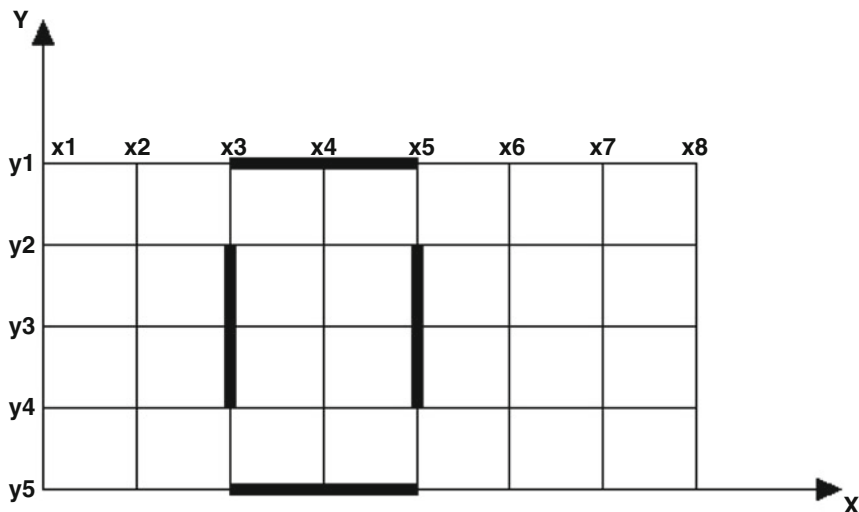
stiffness of the structure due to their initial elastic effect, they yield at low level of force, and therefore no additional stiffness is added to the structure stiffness. The global system then continues to have the initial stiffness of the structure until the yielding of the structural elements. The global system will be characterized by a higher lateral resistance.

17.7 Seismic Design of Damping Systems

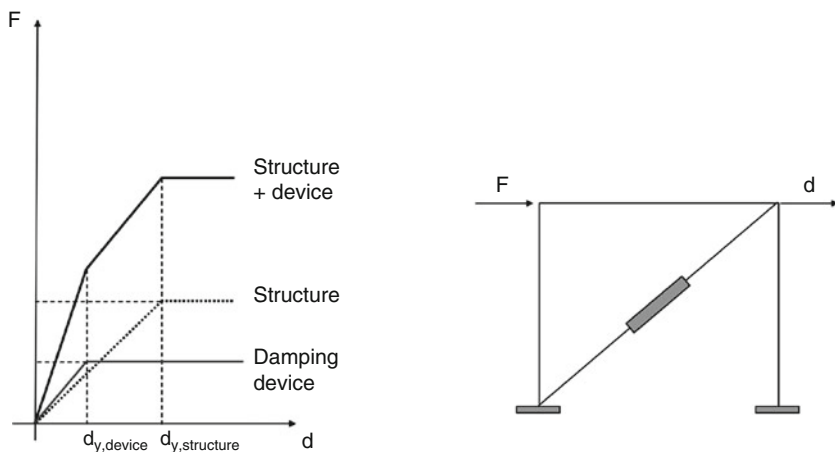
The design of damping systems is performed through an iterative method that is affected by many parameter, such as:

- The disposition of the device in plane and in elevation;
- The structural configuration of the device;
- The stiffness;
- The characteristics of the device.

The disposition of the device has to fit within the architectural constraints, but at the same time the devices must respect the geometric regularities and the torsional stiffness demand



a



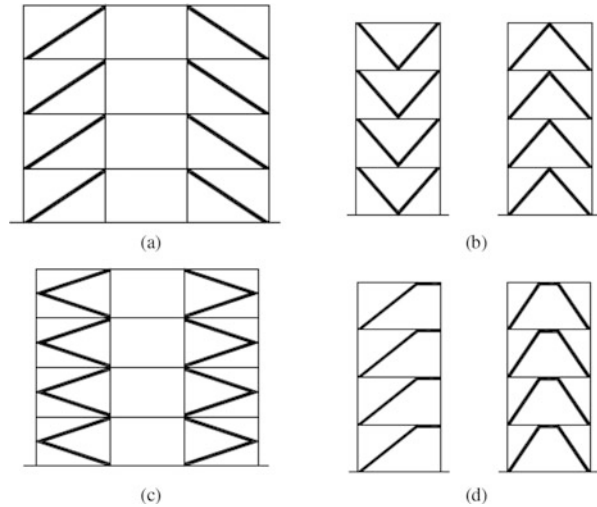
b

Fig. 17.36 Static behavior: (a) Elastic bracing device; (b) Damping device

In addition, the form of the device affects the global response. Regarding the geometric shape, two types of devices are identified:

1. Concentric devices;
2. Eccentric devices.

Fig. 17.37 Categories of damper devices: (a) Tension; (b) V form; (c) K form; (d) Structures with eccentric devices



The first type includes three configurations:

- Diagonal form, where the diagonals resist the horizontal forces and dissipate energy (Fig. 17.37a);
- V form, where both tension and compression elements resist the lateral forces (Fig. 17.37b).
- K form, which, although it is very similar to the V configuration, it is not considered as a damping system (Fig. 17.36c).

In the second case (eccentric devices), the horizontal forces are carried by the elements through their axial capacity. Due to the eccentricity, a part of the horizontal beam dissipates energy during the different seismic cycles (Fig. 17.37d).

An important rule for designing the passive dissipation system is that the structure is designed to resist 75% of lateral forces if the structure is regular, and 100% of the lateral forces in case of irregular structures.

The design of the global system (structure with dampers) is an iterative procedure with five ordered steps:

1. Defining the structural properties and analyzing the structure for vertical and seismic loads;
2. Choosing the desired dissipation level;
3. Choosing a structural configuration for the devices;
4. Choosing the mechanical properties of each device;
5. Verifying the behavior of the equipped structure.

Viscous dampers in particular are designed using the following procedure:

1. Defining the section;
2. Choosing a damping ratio, typically $\xi = 30\%$;
3. Calculating the period of the unequipped structure (without devices) T_u ;

4. Calculating the period of the equipped structure $T_f = \frac{T_u}{\sqrt{2\xi^2+1}}$;
5. Calculating the lateral stiffness at each story assuming a shear-type structure loaded by unitary forces.

17.8 Geometric Amplification of Dampers

Damper installed in-line with bracing element (diagonal) experiences a displacement between its two ends that is less than the inter-story drift. Damper installed horizontally at the chevron bracing system's top is subjected to a displacement between its two end points that is equal to the inter-story drift. The efficiency of the supplemental damping systems can be improved by providing a convenient geometrical configuration, which can amplify the damper displacement for the specified inter-story drift.

Figure 17.38 shows structural configurations for four different damping systems, including the two configurations mentioned in the previous paragraph (diagonal and chevron). Figure 17.39 shows real cases of the different configurations. The selection of the appropriate configuration depends on several factors, such as the architectural constraints and the energy dissipation demand. Therefore, there is no configuration that is characterized by a superior behavior.

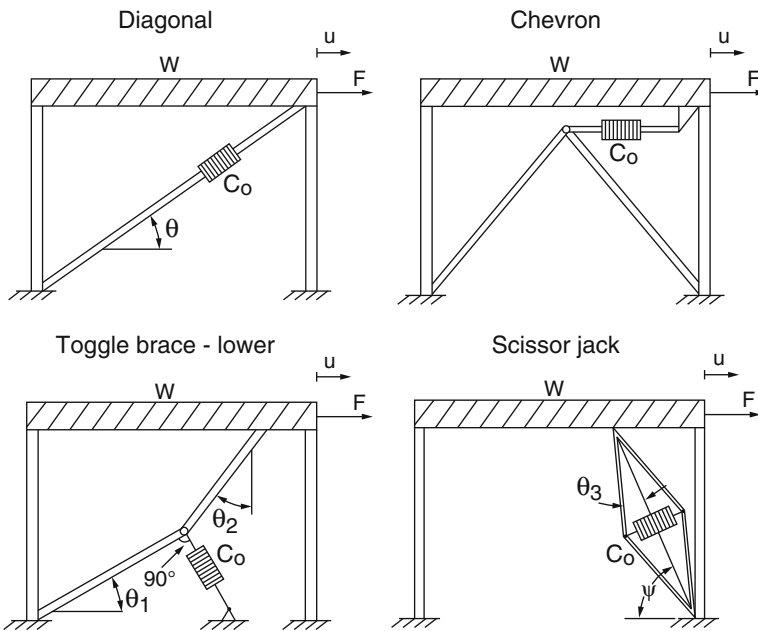


Fig. 17.38 Geometrical configurations of four damping systems

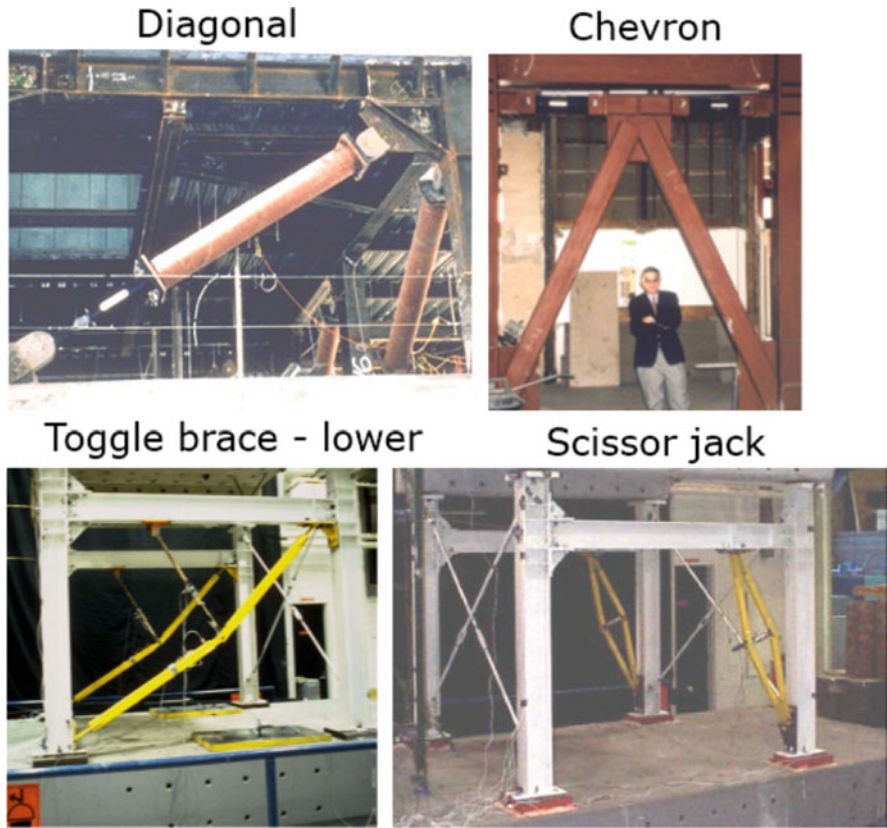


Fig. 17.39 Four types of dampers

The damping amplification provided by the Toggle-Brace (Constantinou et al. 2001) and the scissor jack systems can be established by re-writing the general forms of the equilibrium and compatibilities relationships.

References

- Aiken ID, Kelly JM (1990) Earthquake simulator testing and analytical studies of two energy-absorbing systems for multistory structures. Doctoral dissertation, University of California, Berkeley
- Chawla KK, Meyers M (1999) Mechanical behavior of materials. Prentice Hall, Upper Saddle River
- Christopoulos C, Filiatrault A (2003) Post-tensioned energy dissipating (PTED) steel frames for seismic regions
- Cimellaro GP, De Stefano A (2010) Correlation in spectral accelerations of European ground motion records. In: Proceedings of 9NCEE

- Cimellaro G, Soong T, Reinhorn AM (2009) Integrated design of controlled linear structural systems. *J Struct Eng ASCE* 135(7):853–862. [https://doi.org/10.1061/\(ASCE\)ST.1943-541X.0000032](https://doi.org/10.1061/(ASCE)ST.1943-541X.0000032)
- Constantinou MC, Symans M (1992) Experimental and analytical investigation of seismic response of structures with supplemental fluid viscous dampers. National Center for earthquake engineering research, Buffalo
- Constantinou MC, Tsopelas P, Hammel W, Sigaher AN (2001) Toggle-brace-damper seismic energy dissipation systems. *J Struct Eng* 127(2):105–112
- Filiatrault A, Restrepo J, Christopoulos C (2004) Development of self-centering earthquake resisting systems. In: 13th world conference on earthquake engineering, pp 1–6
- Fitzgerald T, Anagnos T, Goodson M, Zsutty T (1989) Slotted bolted connections in aseismic design for concentrically braced connections. *Earthq Spectra* 5(2):383–391
- Funakubo K, Sakamoto M (1987) Higher order contributions in finite temperature renormalization group. *Phys Lett B* 186(2):205–210
- Hoehler MS, Stanton JF (2006) Simple phenomenological model for reinforcing steel under arbitrary load. *J Struct Eng* 132(7):1061–1069
- Pall AS, Marsh C, Fazio P (1980) Friction joints for seismic control of large panel structures. *PCI J* 25(6):38–61
- Richter PJ, Nims DK, Kelly JM, Kallembach R (1990) The EDR-energy dissipating restraint. A new device for mitigation of seismic effects. In: Proceedings of the 1990 SEAOC convention, vol 1, pp 377–401
- Ricles JM, Sause R, Garlock MM, Zhao C (2001) Posttensioned seismic-resistant connections for steel frames. *J Struct Eng* 127(2):113–121
- Robinson W, Tucker A (1976) A lead-rubber shear damper. *Bull N Z Natl Soc Earthq Eng* 4:251–259
- Roh H, Cimellaro GP, Lopez-Garcia D (2011) Seismic response of adjacent steel structures connected by passive device. *Adv Struct Eng* 14(3):499–517. <https://doi.org/10.1260/1369-4332.14.3.499>
- Scholl RE (1990) Added damping and stiffness elements. US Patent 4,910,929
- Song G, Ma N, Li HN (2006) Applications of shape memory alloys in civil structures. *Eng struct* 28(9):1266–1274
- Soong T, Cimellaro G (2009) Future directions in structural control. *J Struct Control Health Monit* 16(1):7–16
- Tsai KC, Chih-Yu W (2013) Buckling restrained brace. US Patent 8,424,252
- Tsai KC, Chen HW, Hong CP, Su YF (1993) Design of steel triangular plate energy absorbers for seismic-resistant construction. *Earthq Spectra* 9(3):505–528
- Zhu S, Zhang Y (2007) Seismic behaviour of self-centring braced frame buildings with reusable hysteretic damping brace. *Earthq Eng Struct Dyn* 36(10):1329–1346

Chapter 18

Tuned-Mass Dampers



Abstract In this chapter Tuned-Mass-Dampers (TMDs) are explained. At the beginning the mechanical characteristics and their operation are discussed, and then the design criteria for these seismic isolation systems are defined. At the end of the chapter two practical examples of TMD and Active-Tuned-Mass-Dampers (ATMDs) are inserted.

18.1 Introduction

A tuned mass damper is a device mounted in structures to prevent discomfort, damage, or outright structural failure caused by vibration. They are used in high rise buildings to prevent failure of buildings during earthquakes (Filiatrault 1998). Usually these systems are collocated in the upper part of the buildings. In origin they were used to reduce the wind-induced vibrations in high rise structures and only recently they became a protection for seismic vibrations (Filiatrault and Christopoulos 2006). They are also known as active mass dampers (AMD), as they represent a protection for civil engineering structures. These systems have the capability to reduce the external dynamic disturbance. Typically they are composed by a mass, a damper and a spring, and they are located in strategic points of the structure. However the TMDs have their drawbacks: they need a large space for the installation, enough room to accommodate the large displacements that are due to the necessity of the system to be in resonance with the structure, and a smooth surface to reduce the friction and facilitate the movement (Carr 2005).

18.2 Undamped TMD Under Harmonic Loading

Figure 18.1 represents a primary structure with only a single degree of freedom, where m is a mass attached to the main mass M , and K is the elastic stiffness.

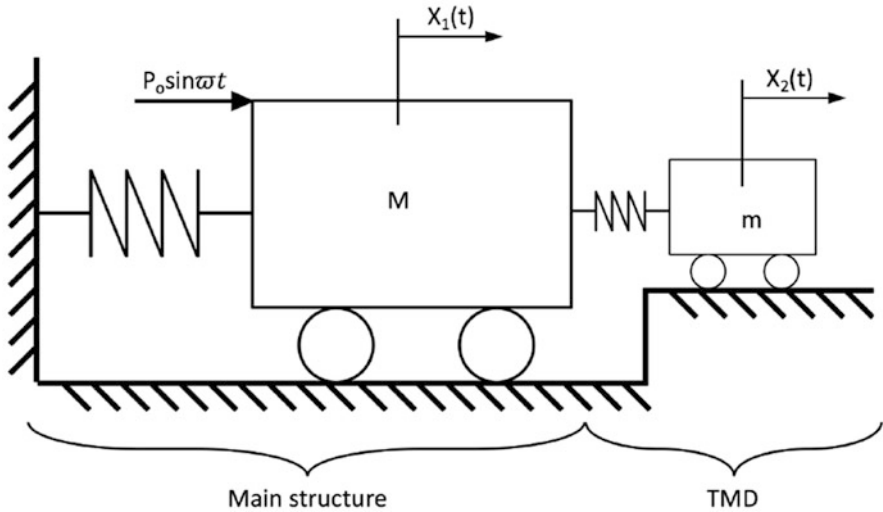


Fig. 18.1 Vibration Absorber (Adapted from Filiatrault and Christopoulos 2006)

These systems are subjected to the external sinusoidal dynamic force

$$P(t) = P_o \sin \omega t \quad (18.1)$$

By applying Newton's second law to the two masses, the following equations are obtained

$$\begin{aligned} M\ddot{x}_1 + (K + k)x_1 - kx_2 &= P_o \sin \omega t \\ m\ddot{x}_2 + k(x_2 - x_1) &= 0 \end{aligned} \quad (18.2)$$

The forced vibration has a simple response because the system is undamped

$$\begin{aligned} x_1(t) &= a_1 \sin \bar{\omega}t \\ x_2(t) &= a_2 \sin \bar{\omega}t \end{aligned} \quad (18.3)$$

In Eq. 18.3, a_1 and a_2 indicate the amplitude of the vibration of the primary and the secondary mass, respectively. Combining Eqs. 18.2 and 18.1

$$\begin{aligned} (-Ma_1\bar{\omega}^2 + (K + k)a_1 - ka_2) \sin \bar{\omega}t - ka_2 \sin \omega t &= P_o \sin \bar{\omega}t \\ (-ma_2\bar{\omega}^2 + k(a_2 - a_1)) \sin \bar{\omega}t &= 0 \end{aligned} \quad (18.4)$$

Equation 18.4 has to be satisfied at all times, so it is possible to rewrite it as

$$\begin{aligned} a_1(-M\bar{\omega}^2 + K + k) - ka_2 &= P_o \\ -ka_1 + a_2(-m\bar{\omega}^2 + k) &= 0 \end{aligned} \quad (18.5)$$

To simplify the equation and the next algebraic operation, it is possible to introduce the following variables:

$$\begin{aligned} x_{st} &= \frac{P_o}{K} : \text{static displacement of the primary structure} \\ \Omega_{st}^2 &= \frac{K}{M} : \text{natural frequency of the primary structure} \\ \omega_a^2 &= \frac{k}{m} : \text{natural frequency of the TMD} \end{aligned} \quad (18.6)$$

Normalizing Eq. 18.5 to the elastic stiffness K the following expression is obtained

$$\begin{aligned} a_1 \left(1 + \frac{k}{K} - \frac{\bar{\omega}^2}{\Omega_n^2} \right) - a_2 \frac{k}{K} &= x_{st} \\ a_1 &= a_2 \left(1 - \frac{\bar{\omega}^2}{\omega_a^2} \right) \end{aligned} \quad (18.7)$$

Solving the equation for the amplitudes a_1 and a_2

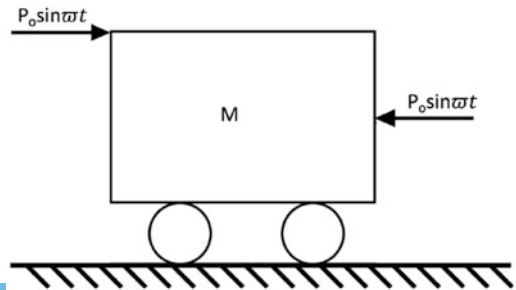
$$\begin{aligned} \frac{a_1}{x_{st}} &= \frac{\left(1 - \frac{\bar{\omega}^2}{\omega_a^2} \right)}{\left(1 - \frac{\bar{\omega}^2}{\omega_a^2} \right) \left(1 + \frac{k}{K} - \frac{\bar{\omega}^2}{\Omega_n^2} \right)} \\ \frac{a_2}{x_{st}} &= \frac{1}{\left(1 - \frac{\bar{\omega}^2}{\omega_a^2} \right) \left(1 + \frac{k}{K} - \frac{\bar{\omega}^2}{\Omega_n^2} \right)} \end{aligned} \quad (18.8)$$

Examining the first equation, it is clear that when the natural frequency $\omega_a = \sqrt{\frac{k}{m}}$ is selected so that it is equal to the frequency of the disturbing force $\bar{\omega}$, the main mass M does not vibrate. In the second equation, when $\omega_a = \bar{\omega}$ the expression becomes

$$a_2 = -\frac{K}{k} x_{st} = -\frac{P_o}{k} \quad (18.9)$$

Figure 18.2 shows the moment when the TMD has a motion $-\left(\frac{P_o}{k}\right) \sin \bar{\omega} t$ and the main mass stands still. In that case the external forces are opposite and equal. In the case where the vibration absorber is in resonance with the main system, the size of

Fig. 18.2 Diagram of free main mass for optimum tuning conditions (Adapted from Filiatrault and Christopoulos 2006)



the damper is determined by $\omega = \Omega_n$ or $\frac{k}{m} = \frac{K}{M}$ or $\frac{k}{K} = \frac{m}{M} = \mu$. Then, the Eq. 18.8 becomes

$$\begin{aligned} \frac{x_1(t)}{x_{st}} &= \frac{\left(1 - \frac{\bar{\omega}^2}{\omega_a^2}\right)}{\left(1 - \frac{\bar{\omega}^2}{\omega_a^2}\right)\left(1 + \mu - \frac{\bar{\omega}^2}{\omega_a^2}\right) - \mu} \sin \bar{\omega}t \\ \frac{x_2(t)}{x_{st}} &= \frac{1}{\left(1 - \frac{\bar{\omega}^2}{\omega_a^2}\right)\left(1 + \mu - \frac{\bar{\omega}^2}{\omega_a^2}\right) - \mu} \sin \bar{\omega}t \end{aligned} \quad (18.10)$$

The denominators of the two Eqs. 18.10 are quadratic functions and they have two roots $\frac{\omega^2}{\omega_a^2}$. Therefore, the two values of the external frequency ω and the denominators become zero, and x_1 and x_2 become infinitely large. These are the natural frequencies of the two-degrees-of-freedom system. By setting the denominator equal to zero the natural frequency is obtained

$$\left(\frac{\bar{\omega}}{\omega_a}\right)^4 - \left(\frac{\bar{\omega}}{\omega_a}\right)^2 (2 + \mu) + 1 = 0 \quad (18.11)$$

The solution is expressed below

$$\left(\frac{\bar{\omega}}{\omega_a}\right)^2 = \left(1 + \frac{\mu}{2}\right) \pm \sqrt{\mu + \frac{\mu^2}{4}} \quad (18.12)$$

Figure 18.3 represents an example of a combination of natural frequency for TMDs tuned to the main structure with $\omega_a = \Omega_n$ and $\mu = 0.2$. The natural frequencies are set at 1.25 and 0.8 of that of the primary structure (Den Hartog 1956). The spectral amplitudes of the two masses are shown in Fig. 18.4.

The left graphic shows how at the first resonance $\left(\frac{\bar{\omega}}{\omega_a} = \frac{\bar{\omega}}{\Omega_n} = 0, 8\right)$, the curve $\frac{x_1}{x_{st}}$ passes across zero from positive to negative infinite; when the excitation frequency is in resonance with the main structure and the TMD $(\bar{\omega} = \Omega_n = \omega_a)$, the curve passes across zero and, as the excitation increases, it becomes positive again. When there is the second resonance $\left(\frac{\bar{\omega}}{\omega_a} = \frac{\bar{\omega}}{\Omega_n} = 1, 25\right)$, the curve becomes negative. The right graphic shows the changes which occur at the resonant points; the phase between the TMD and the main mass motions are not relevant.

18.3 Undamped TMD Under Harmonic Base Motion

Figure 18.5 represents a two-degree-of-freedom system. The ground excitation is defined by

$$x_g(t) = x_o \sin \bar{\omega}t \quad (18.13)$$

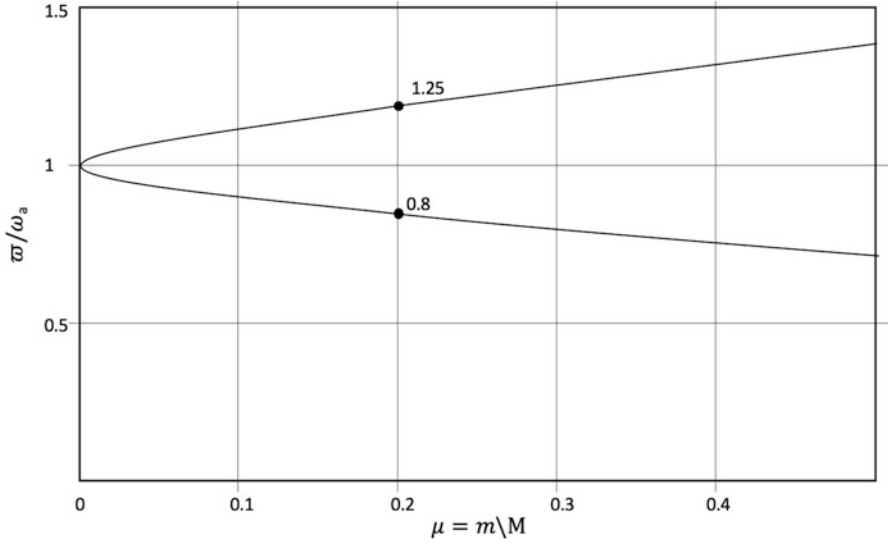


Fig. 18.3 Natural Frequencies combined with Vibration Absorbers Tuned to the main structure (Adapted from Den Hartog 1956)

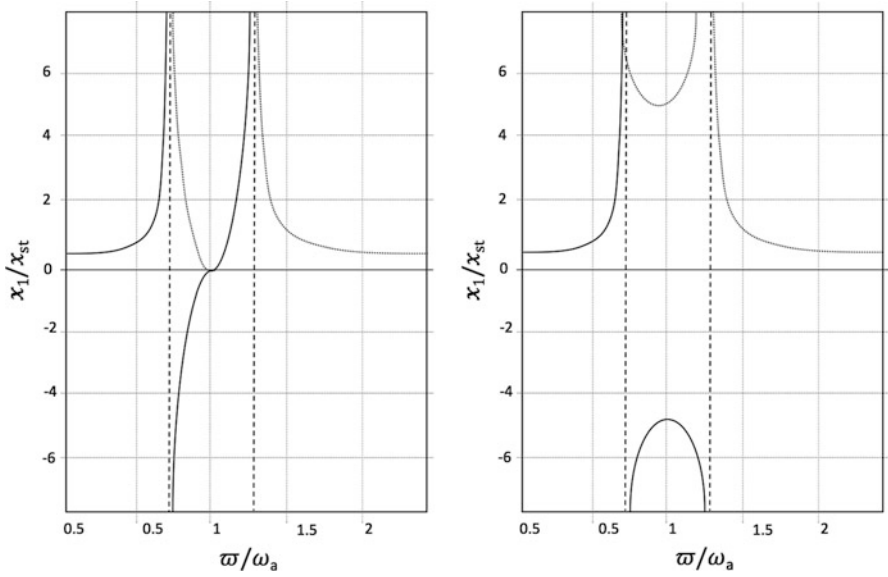


Fig. 18.4 Amplitude spectrum for Vibration Absorbers Tuned (Adapted from Den Hartog 1956)

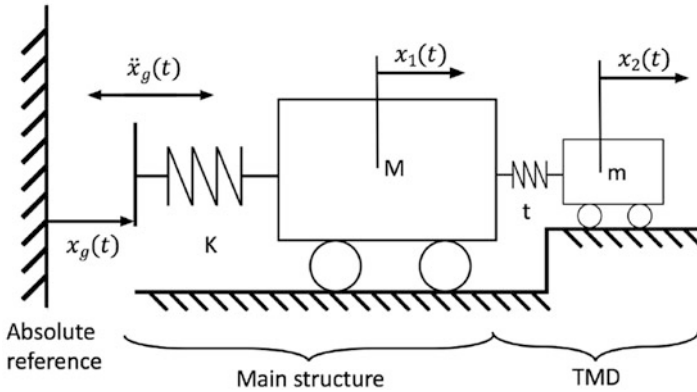


Fig. 18.5 Structure with TMD subject to a base excitation (Adapted from Filiatrault and Christopoulos 2006)

Applying Newton's second law for the two masses, the following equations of motion for a two-degree-of-freedom system are given

$$\begin{aligned} M\ddot{x}_1 + (K + k)x_1 - kx_2 &= M\bar{\omega}^2 x_o \sin \bar{\omega} t \\ m\ddot{x}_2 + k(x_2 + x_1) &= m\bar{\omega}^2 x_o \sin \bar{\omega} t \end{aligned} \quad (18.14)$$

Using Eq. 18.3, the solution of the single-degree-of-freedom system is obtained. Also in this case, the equation is satisfied at all times

$$\begin{aligned} a_1(-M\bar{\omega}^2 + K + k) - ka_2 &= M\bar{\omega}^2 x_o \\ -ka_1 + a_2(-m\bar{\omega}^2 + k) &= m\bar{\omega}^2 x_o \end{aligned} \quad (18.15)$$

Substituting the variables defined in Eq. 18.8, it is possible to solve the Eq. 18.15 for the amplitude a_1 and a_2

$$\begin{aligned} \frac{a_1}{x_o} &= \frac{\bar{\omega}^2 \left(\frac{1}{\Omega_n^2} \left(1 - \frac{\bar{\omega}^2}{\omega_a^2} \right) + \frac{1}{\omega_a^2} \left(\frac{k}{K} \right) \right)}{\left(1 - \frac{\bar{\omega}^2}{\omega_a^2} \right) \left(1 + \frac{k}{K} - \frac{\bar{\omega}^2}{\Omega_n^2} \right) - \frac{k}{K}} \\ \frac{a_2}{x_o} &= \frac{\frac{\bar{\omega}^2}{\Omega_n^2} + \frac{\bar{\omega}^2}{\omega_a^2} \left(1 + \frac{k}{K} - \frac{\bar{\omega}^2}{\Omega_n^2} \right)}{\left(1 - \frac{\bar{\omega}^2}{\omega_a^2} \right) \left(1 + \frac{k}{K} - \frac{\bar{\omega}^2}{\Omega_n^2} \right) - \frac{k}{K}} \end{aligned} \quad (18.16)$$

Two tuning conditions are obtained from Eq. 18.16. The first tuning condition exists when a_1 is equal to zero; the displacement of the main mass M is zero and it moves rigidly with the base. The absolute acceleration is equal to $x_g(t)$ and there is no force to induce the main spring K . This condition gives the equation

$$\frac{1}{\Omega_n^2} \left(1 - \frac{\bar{\omega}^2}{\omega_a^2} \right) + \frac{1}{\omega_a^2} \left(\frac{k}{K} \right) = 0 \quad (18.17)$$

Simplifying the previous equations this tuning condition on the natural frequency of the TMD can be obtained

$$\omega_a = \frac{\bar{\omega}}{\sqrt{1 + \mu}} \quad (18.18)$$

For a TMD with $\mu \approx 0$, the optimum tuning is obtained when the natural frequency of the TMD is equal to the frequency of the disturbing force. The second tuning condition is obtained when the main mass M is not moving and the absolute acceleration is zero during the movement of the base. In this case the force $-Kx_g(t)$ induces the main spring. This condition exists when a_1 is equal to x_o and gives

$$\frac{\bar{\omega}^2}{\Omega_n^2} \left(1 - \frac{\bar{\omega}^2}{\omega_a^2}\right) + \frac{\bar{\omega}^2}{\omega_a^2} \left(\frac{k}{K}\right) = - \left(\left(1 - \frac{\bar{\omega}^2}{\omega_a^2}\right) \left(1 + \frac{k}{K} - \frac{\bar{\omega}^2}{\Omega_n^2}\right) - \frac{k}{K} \right) \quad (18.19)$$

Simplifying the previous equations, this tuning condition on the natural frequency of the TMD can be obtained

$$\omega_a = \bar{\omega} \quad (18.20)$$

18.4 Damped TMD Under Harmonic Loading

Figure 18.6 shows a system where between the main mass M and the secondary mass m there is a dashpot c parallel to the damper k .

Also in this case, applying Newton's second law at the two masses the following equation is obtained

$$\begin{aligned} M\ddot{x}_1 + Kx_1 + k(x_1 - x_2) + c(\dot{x}_1 - \dot{x}_2) &= P - o \sin \bar{\omega}t \\ m\ddot{x}_2 + k(x_2 - x_1) + c(\dot{x}_2 - \dot{x}_1) &= 0 \end{aligned} \quad (18.21)$$

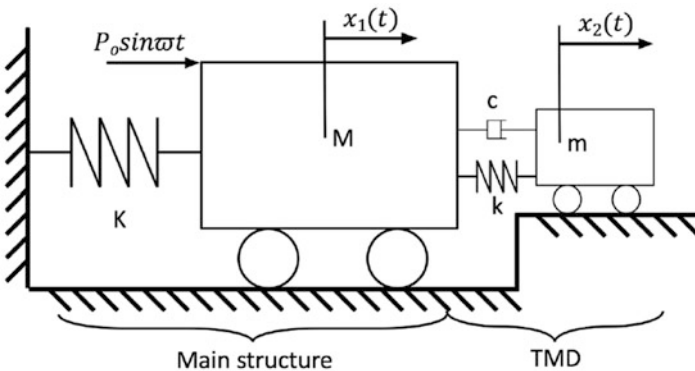


Fig. 18.6 Primary structure and damped TMD (Adapted from Filiatraut and Christopoulos 2006)

Transient free vibration is not considered, but only the forced vibration solution is investigated. At the frequency $\bar{\omega}$, the harmonic motion x_1 and x_2 can be considered as a complex number

$$\begin{aligned}x_1(t) &= C_1 e^{i\bar{\omega}t} \\x_2(t) &= C_2 e^{i\bar{\omega}t}\end{aligned}\quad (18.22)$$

C_1 and C_2 are unknown complex numbers with amplitude, phase and $i = \sqrt{-1}$. Substituting the Eq. 18.22 in the Eq. 18.21, the amplitude of the main mass a_1 is given.

$$\begin{aligned}-M\bar{\omega}^2 + KC_1 + k(C_1 - C_2) + i\bar{\omega}c(C_1 - C_2) &= P_o \\-m\bar{\omega}^2 C_2 + k(C_2 - C_1) + i\bar{\omega}c(C_2 - C_1) &= 0\end{aligned}\quad (18.23)$$

Equation 18.23 can be rewritten as

$$\begin{aligned}(-M\bar{\omega}^2 + K + k + i\bar{\omega}c)C_1 - (k + i\bar{\omega}c)C_2 &= P_o \\-(k + i\bar{\omega}c)C_1 + (-m\bar{\omega}^2 + k + i\bar{\omega}c)C_2 &= 0\end{aligned}\quad (18.24)$$

Then, it is possible to solve the equation for C_1

$$C_1 = P_o \frac{(k - m\bar{\omega}^2) + i\bar{\omega}c}{[(-M\bar{\omega}^2 + K)(-m\bar{\omega}^2 + k) - m\bar{\omega}^2 k] + i\bar{\omega}c[-M\bar{\omega}^2 + K - m\bar{\omega}^2]}\quad (18.25)$$

C_1 is a complex number and can be written as

$$C_1 = P_o (A_1 + iB_1)\quad (18.26)$$

A_1 and B_1 are real, the Eq. 18.26 can be rewritten as

$$C_1 = P_o \sqrt{A_1^2 + B_1^2}\quad (18.27)$$

To simplify the calculation, the following expression is introduced

$$\begin{aligned}A &= k - m\bar{\omega}^2 \\B &= \bar{\omega}c \\C &= (-M\bar{\omega}^2 + K)(-m\bar{\omega}^2 + k) - m\bar{\omega}^2 k \\D &= \bar{\omega}c(-M\bar{\omega}^2 + K - m\bar{\omega}^2)\end{aligned}\quad (18.28)$$

In this way, Eq. 18.25 can be written in the form

$$C_1 = P_o \frac{A + iB}{C + iD}\quad (18.29)$$

It is possible to write Eq. 18.29 as

$$C_1 = P_o \frac{(A + iB)(C - iD)}{(C + iD)(C + iD)} = P_o \frac{(AC + BD) + i(BC - AD)}{C^2 + D^2} \quad (18.30)$$

To find the amplitude a_1

$$\begin{aligned} \frac{a_1}{P_o} &= \sqrt{\left(\frac{(AC+BD)}{C^2+D^2}\right)^2 + \left(\frac{BC-AD}{C^2+D^2}\right)^2} \\ &= \sqrt{\frac{A^2C^2+B^2D^2+B^2C^2+A^2D^2}{(C^2+D^2)^2}} \\ &= \sqrt{\frac{(A^2+B^2)(C^2+D^2)}{(C^2+D^2)^2}} \\ &= \sqrt{\frac{(A^2+B^2)}{(C^2+D^2)}} \end{aligned} \quad (18.31)$$

The response's amplitude of the main mass M is obtained by replacing it with the terms of the Eq. 18.28

$$\frac{a_1}{P_o} = \sqrt{\frac{(k - m\bar{\omega}^2) + \bar{\omega}^2 c^2}{[(-M\bar{\omega}^2 + K)(-m\bar{\omega}^2 + k) - m\bar{\omega}^2 k]^2 + \bar{\omega}^2 c^2 (-M\bar{\omega}^2 + K - m\bar{\omega}^2)^2}} \quad (18.32)$$

The following variables are introduced

$$\begin{aligned} \mu &= \frac{m}{M} = \text{mass ratio} = \frac{TMD_{mass}}{main_{mass}} \\ \omega_a^2 &= \frac{k}{m} = \text{natural frequency of TMD} \\ \Omega_n^2 &= \frac{K}{M} = \text{natural frequency of main system} \\ f &= \frac{\omega_a}{\Omega_n} = \text{natural frequency ratio} \\ g &= \frac{\bar{\omega}}{\Omega_n} = \text{forced frequency ratio} \\ c_c &= 2\omega_a m = \text{critical viscous damping constant} \end{aligned} \quad (18.33)$$

Substituting these variables, the previous equation can be rewritten as below

$$\frac{a_1}{x_{st}} = \sqrt{\frac{\left(2\frac{c}{c_c}g\right)^2 + (g^2 - f^2)^2}{\left(2\frac{c}{c_c}g\right)^2 (g^2 - 1 + \mu g^2)^2 + [\mu f^2 g^2 - (g^2 - 1)(g^2 f^2)]^2}} \quad (18.34)$$

The amplitude of the vibration of the main mass depends on μ ; $\frac{c}{c_c}$; f and g .
The graphic represents the variation of the damping ratio of Lehr

$$\xi = \frac{c}{c_c} \quad (18.35)$$

When the value of ξ is equal to zero or to ∞ , the curve is infinite; between these two curves, there is the optimum value of c . Furthermore, the previous graphic shows

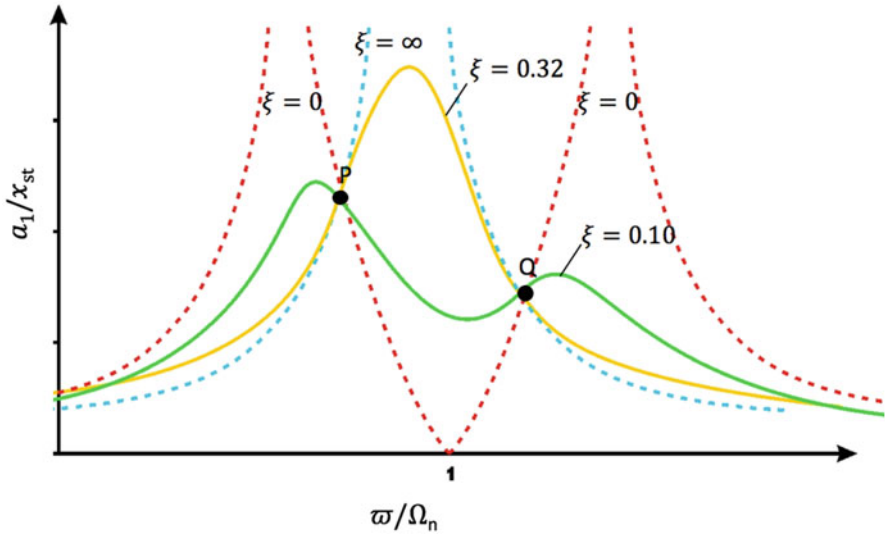


Fig. 18.7 Variation of the damping ratio of Lehr, $\mu = 0,25$ and $f = 0.8$ (Adapted from Den Hartog 1956)

that all the curves intersect in two points, P and Q (Fig. 18.7). Finding these two points, the curve which passes with an horizontal tangent through the higher point is the most favorable. These two points change their position as function of the natural frequency ratio, f . Selecting an appropriate value of f leads to find the points at an equal height and find the curve of ξ which passes with an horizontal tangent through one of the points. Using the values

$$\begin{aligned}
 A &= (2g)^2 \\
 B &= (g^2 - f^2)^2 \\
 C &= (2g^2)(g^2 - 1 + \mu g^2)^2 \\
 D &= (\mu f^2 g^2 - (g^2 - 1)(g^2 - f^2))^2
 \end{aligned}
 \tag{18.36}$$

Equation 18.34 can be rewritten as

$$\frac{a_1}{x_{st}} = \pm \sqrt{\frac{A\xi^2 + B}{C\xi^2 + D}}
 \tag{18.37}$$

By imposing the condition $\frac{A}{C} = \frac{B}{D}$, the Eq. 18.37 becomes independent of damping and gives

$$\left(\frac{1}{g^2 - 1 + \mu g^2} \right)^2 = \left(\frac{g^2 - f^2}{\mu f^2 g^2 - (g^2 - 1)(g^2 - f^2)} \right)^2
 \tag{18.38}$$

Considering the negative sign in Eq. 18.37, the solution is given by $g^2 = 0$, which means that the static response becomes independent of the damping. On the contrary, considering the positive sign, the solution is given by

$$g^4 - 2g^2 \frac{1+f^2 + \mu f^2}{2+\mu} + \frac{2f^2}{2+\mu} = 0 \quad (18.39)$$

The points P and Q are function of f and μ . To have an equal amplitude for the two points, the frequency has to be adjusted by using the two roots extracted from Eq. 18.38 and inserting them in Eq. 18.34. Thus, the relationship between the variable f and μ is obtained.

$$f = \frac{1}{1+\mu} \quad (18.40)$$

Substituting in Eq. 18.34 the values f that we obtain from Eq. 18.39, the optimum damping (ξ_{opt}) is evaluated. The solution gives two different results for the two points

$$\begin{aligned} \xi_{opt-P}^2 &= \frac{\mu \left(3 - \sqrt{\frac{\mu}{\mu+2}}\right)}{8(1+\mu)^3} \\ \xi_{opt-Q}^2 &= \frac{\mu \left(3 + \sqrt{\frac{\mu}{\mu+2}}\right)}{8(1+\mu)^3} \end{aligned} \quad (18.41)$$

Solving Eq. 18.40, the plot in Fig. 18.8 is obtained.

The two obtained curves are almost identical, then, the calculation used to find the optimum tuning with a single equation can be simplified as expressed below

$$\xi_{opt} = \sqrt{\frac{(3\mu)}{8(1+\mu)^3}} \quad (18.42)$$

18.5 Active TMD

The dimension of a TMD is characterized by a small mass ratio and a large structure; if the mass ratio is equal to 1%, the system becomes excessively large and heavy, and accommodating a massive TMD on the roof of high rise buildings could become a problem. The active tuned mass damper (ATMD) has the same structure of the TMD with the addition of an internal actuator that can be considered a force generator for frequencies (Chang and Yang 1995). These systems are based on a close-loop relying on sensors, actuators and control-power electronics. The mass of the ATMD does not depend on the mass of the structure and can be fixed on an existing device

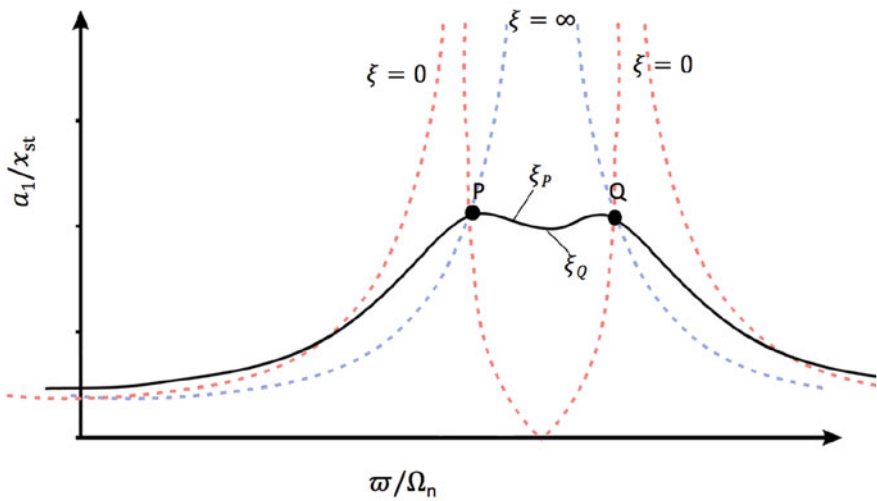


Fig. 18.8 Resonance curves, $\mu = 0.25$ and $f = 0.8$ (Adapted from Den Hartog 1956)

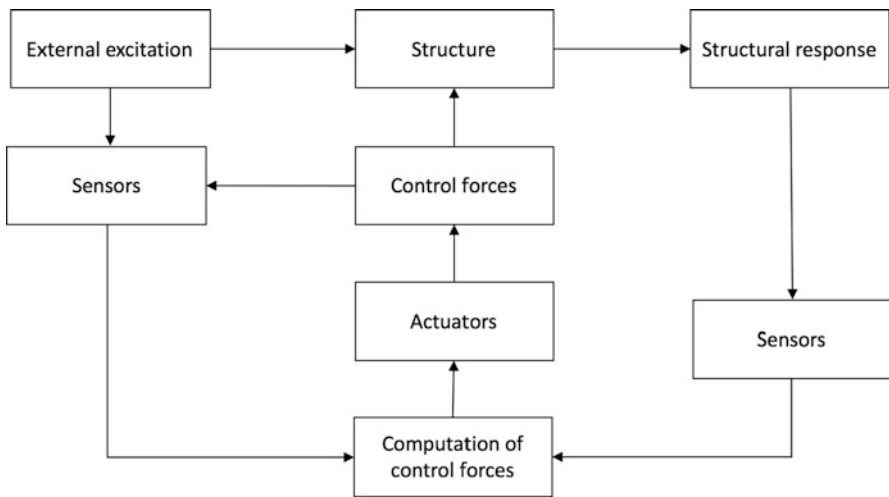


Fig. 18.9 Schematic diagram of an active control system (Adapted from Filiatrault and Christopoulos 2006)

with little design changes. The active force is introduced between the structure and the TMD as it increases their capacity (Li et al. 2003). However, since these systems add complexity to the structure of a TMD, they imply high maintenance costs.

As shown in Fig. 18.9, the systems are a combination of

- sensors to measure the response and the excitation

- actuator to drive the control force
- a computer to compute all the variables that the systems need, like the appropriate control force and the motion of the structure.

18.6 Analysis of a MDOF Structure Equipped with TMD

In reality, most buildings are multi-degree-of-freedom systems and the TMD can only be tuned to a single structural frequency. Thus the greatest efficacy of the TMD is obtained when the structure vibrates principally in a predominant mode (Fig. 18.10). For seismic applications, the TMDs are usually installed on the roof of the buildings to optimize the result.

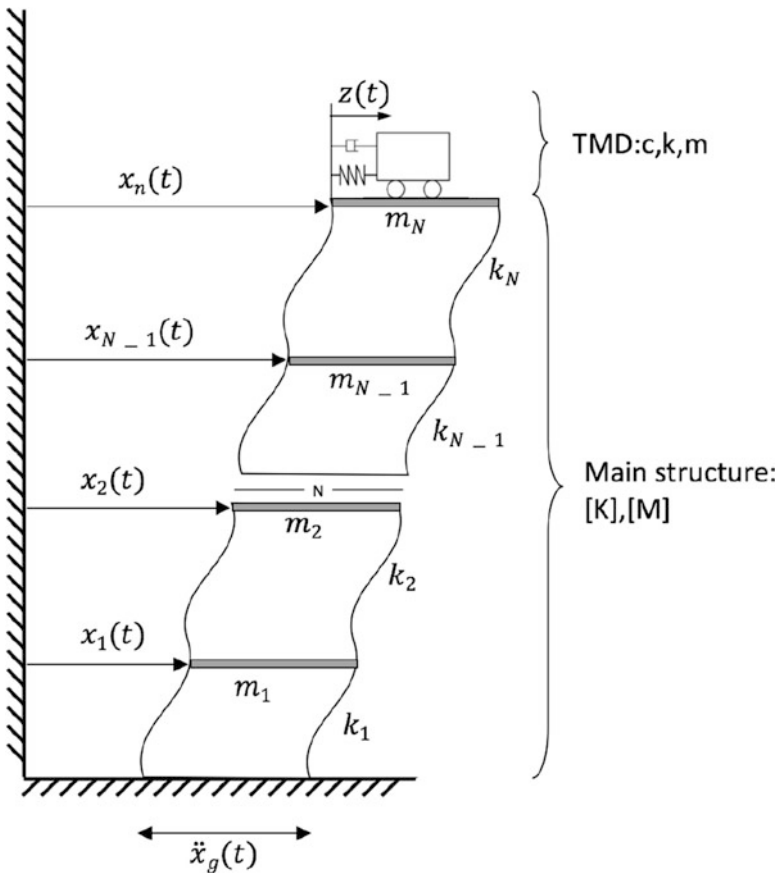


Fig. 18.10 First mode of a multi-storey building with installed TMD on the top

The coupled system for the case of undamped structure is described by the following equation

$$\begin{aligned} [M] \{\ddot{x}(t)\} + [K] \{x(t)\} &= -[M] \{r\} \ddot{x}_g(t) + \{P(t)\} \\ m\ddot{z} + c\dot{z} + kz &= -m\ddot{x}_N - m\ddot{x}_g \end{aligned} \quad (18.43)$$

The terms of Eq. 18.43 are below explained

- N = number of degree of freedom
- M = global mass
- K = stiffness matrices of the structure
- x = displacements
- \ddot{x} = acceleration of the structure relative to the ground
- r = dynamic coupling vector
- m = mass of the TMD
- c = damping constant of the TMD
- k = stiffness of TMD
- $z(t)$ = displacement of the TMD relative to the roof
- $P(t) = 0, 0, \dot{c}z + kz^T$

Equation 18.43 refers to a $N + 1$ dimensional space. If the main structure's response vector $x(t)$ is in the first mode of vibration, the following expression can be obtained

$$\{x(t)\} = \{A^{(1)}x_N(t)\} \quad (18.44)$$

where

- $A^{(1)}$ = first mode shape
- $X_N(t)$ = displacement, relative to the ground, of the roof

Using the orthogonality condition of the model's shape and substituting in Eqs. 18.43 and 18.45 simplified to $A^{(1)}$, the following expression is given

$$M_1\ddot{x}_N(t) + k_1x_N(t) = c\dot{z}(t) + kz(t) - \alpha_1M_1\ddot{x}_g \quad (18.45)$$

The terms of Eq. 18.45 are below expressed

$$\begin{aligned} M_1 &= \{A^{(1)}\}^T [m] \{A^{(1)}\} = \text{generalized mass} \\ K_1 &= \{A^{(1)}\}^T [k] \{A^{(1)}\} = \text{generalized stiffness coefficient} \\ \alpha_1 &= \frac{\{A^{(1)}\}^T [m] \{r\}}{M_1} = \text{modal participation factor} \end{aligned} \quad (18.46)$$

Comparing the second Eq. 18.43 with the first Eq. 18.21, and Eq. 18.45 with the first Eq. 18.21, they are practically identical. This consideration leads to notice that the single-degree-of-freedom system is the same as the multi-degree-of-freedom system except for the changing in the modal mass and the modal stiffness that are

employed. In a multi-degree-of-freedom, the tuning of a TMD can be performed with the Eqs. 18.40 and 18.42 with

$$\begin{aligned}\mu &= \frac{m}{M} = \text{mass ratio} \\ \Omega_N &= \omega_1 = \text{principal frequency of main structure}\end{aligned}\quad (18.47)$$

18.7 Design Considerations

For the design of a TMD for a building, it is possible to follow three steps

1. Evaluation of a mass ratio: this step provides the individuation of the equivalent viscous damping ratio of the structure. It is possible to use the procedure proposed by Luft (1979). This procedure starts to the individuation of the spectral acceleration, S_A , and the spectral displacement, S_D , and the equivalent viscous damping ratio ξ_{eq} that satisfies the following rules

$$\begin{aligned}\alpha_1 S_D(\omega_1, \xi_{eq}) &\leq x_{N(max)} \\ \alpha_1 S_A(\omega_1, \xi_{eq}) &\leq \ddot{x}_{N(max)}\end{aligned}\quad (18.48)$$

$x_{N(max)}$ and $\ddot{x}_{N(max)}$ are respectively the target maximum relative displacement and the maximum absolute acceleration at the roof of the building. The mass ratio is assessed through the equation proposed by Luft (1979)

$$\mu = 16(\xi_{eq} - 0.8\xi_1)^2 = \frac{m}{M_1}\quad (18.49)$$

ξ_1 is the first modal damping ratio of the main structure.

2. Tuning of TMD properties: using the optimum tuning conditions
3. Structural dynamic analysis check: control the selected TMD parameters result is in the range of the predominant response threshold.

18.8 Application of TMD

The optimization technique that is described in Eqs. 18.40 and 18.42 was performed to reduce a displacement in the structure such as a single-degree-of-freedom system that is subjected to sinusoidal force (Sadek et al. 1997). It is possible to implement this approach to seismic applications because many civil engineering structures can be considered as a single-degree-of-freedom system and if the structure is equipped with a TMD it has a nonlinear behavior. In Soong and Dargush (1997), there is a list of researches that considers the potential of the TMD in seismic applications. An example of this application is Taipei 101 in Taiwan (Fig. 18.11). This building

Fig. 18.11 Taipei 101

was designed to sustain the strong wind of typhoons and earthquakes that are typical of the Asian-Pacific area. In addition to the structural precautions, Taipei 101 has a spherical TMD of 800 tons between the 87th and 91st floors that were assembled in layers on site (Fig. 18.12). To dissipate the dynamic energy, 8 hydraulic pistons were installed.

18.9 Application of ATMD

Kyobashi Seiwa Building in Tokyo, Japan, is an 11 story building designed to resist at the earthquake motions and the wind incidents (Fig. 18.13). The ATMD system is collocate on the roof of the building but to detect the vibrations of the building, some accelerometers are located in the basement and at the 6th. The one in the roof are used to compute control force. The signals that are register by the sensors on the roof are transmitted to a control computer; the results of the analysis are sent to the hydraulic jacks that are located on the roof of the building. These jacks drive counter weights, thereby creating opposite forces that suppress the building's vibrations.



Fig. 18.12 TMD inside at Taipei 101

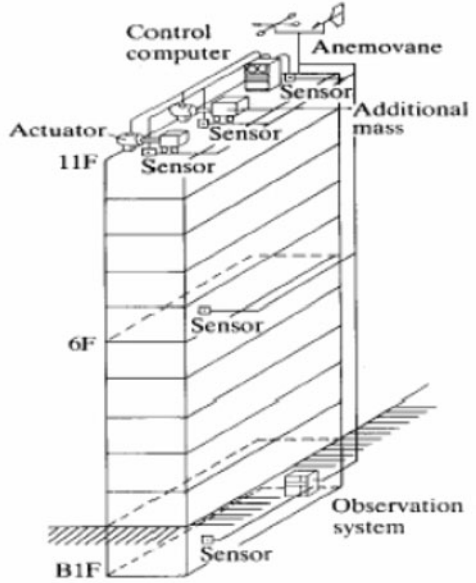


Fig. 18.13 Kyobashi Seiwa Building, Tokyo Japan (ATMD)

References

- Carr J (2005) Seismic response of buildings equipped with tuned-mass dampers. State University of New York, Buffalo
- Chang C, Yang HT (1995) Control of buildings using active tuned mass dampers. *J Eng Mech* 121(3):355–366
- Den Hartog JP (1956) Mechanical vibrations, 4th edn. McGraw-Hill, New York
- Filiatrault A (1998) Elements of earthquake engineering and structural dynamics. Polytechnic International Press, Montreal
- Filiatrault A, Christopoulos C (2006) Principles of passive supplemental damping and seismic isolation. IUSS Press, Pavia
- Li C, Liu Y, Wang Z (2003) Active multiple tuned mass dampers: a new control strategy. *J Struct Eng* 129(7):972–977
- Luft RW (1979) Optimal tuned mass dampers for buildings. *J Struct Div* 105(12):2766–2772
- Sadek F, Mohraz B, Taylor AW, Chung RM (1997) A method of estimating the parameters of tuned mass dampers for seismic applications. *Earthq Eng Struct Dyn* 26(6):617–636
- Soong T, Dargush G (1997) Passive energy dissipation systems in structural engineering. Wiley, New York

Chapter 19

Base Isolation



Abstract The chapter deals with the topic of base isolation system of structures. A description of the various systems that are used in structures is presented. In addition, different techniques for installing these systems in buildings are described and suggested.

19.1 Introduction

Base isolation is one of the most popular seismic protection system against earthquakes (Fig. 19.1). The basic idea of this system is to reduce the seismic forces acting on the structure instead of increasing its strength by decoupling the superstructure (upper part of the building) from its substructure resting on the shaking ground (Filiatrault and Christopoulos 2006).

The advantages of base isolation have been long recognized within the realms of mechanical engineering, in the use of spring mountings to reduce the transfer of accelerations from vibrating machinery into building floors. Later the benefits of this concept have been also realized throughout the civil engineering community as a means of seismic hazard mitigation. Base isolation systems, from an energy point of view, limit the seismic forces and protect the structure from the consequent vibrations (Den Hartog 1956). They also can be combined with energy dissipators (hybrid systems) to control the lateral displacements and obtain the desired performance.

The base isolation system is located below the structure and, since it has a lateral stiffness lower than the one of the fixed base structure, it shifts the natural period of the building from the main frequency energy content of the earthquake. Instead the energy dissipation system increases the damping to limit the forces that are transferred to the structure. Typically the range of spectral accelerations for elastic structures is between 0.1s and 1s with a maximum severity range between 0.2s and 0.6s. If the building has a natural period in that range, the probability to suffer damage during an earthquake is high (Kelly and Naeim 1999).

Figure 19.2 (upper left) illustrates the period shift, the most important characteristics of the seismic isolation system, while Fig. 19.2 (lower right) shows how

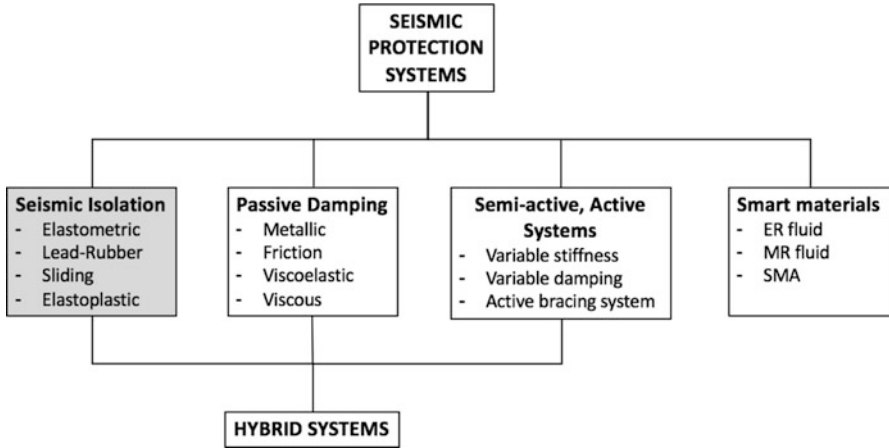


Fig. 19.1 Seismic protection system

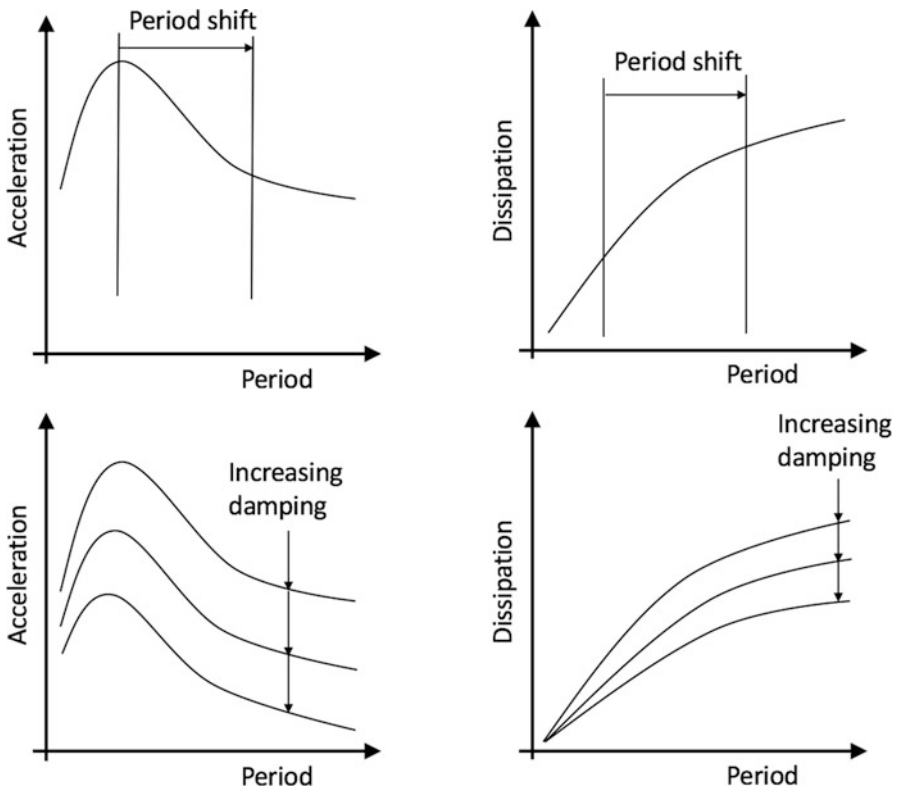


Fig. 19.2 Period shift and increase damping effect; (a) spectral accelerations, (b) spectral displacement (Adapted from Skinner et al. 1993)

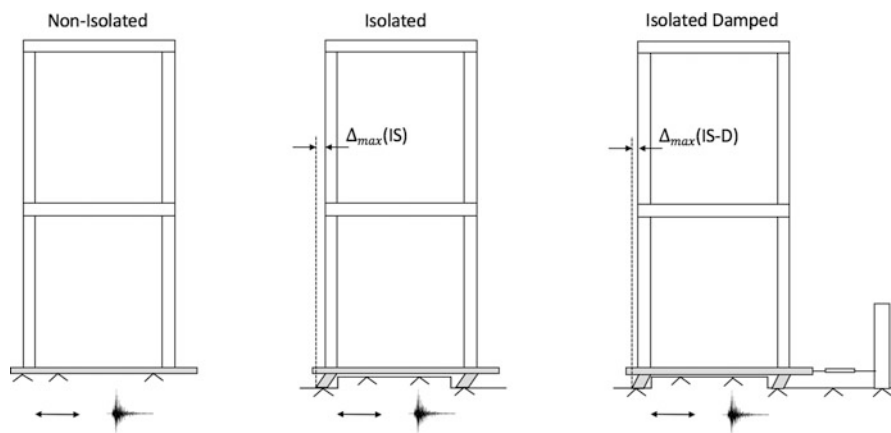


Fig. 19.3 Damped reinforced concrete frame (Adopted from Filiatrault and Christopoulos 2006)

the energy dissipation mechanism in the isolation system can control the excessive displacements by increasing damping.

Figure 19.3 shows three different cases of reinforced concrete frames:

- Non isolated (N-IS) with a natural period $T_1 = 0.55\text{s}$ and the viscous damping $\xi = 0.05$
- Isolated (IS) with a natural period $T_1 = 2.00\text{s}$ and the viscous damping $\xi = 0.05$ (Aiken 1997);
- Damping isolation system (IS-D) with a natural period $T_1 = 2.00\text{s}$ and the viscous damping $\xi = 0.20$.

19.2 History

Manufacturers have always been looking for appropriate systems to defend them against earthquakes. It seems that the Greeks in their ancient temples had already interposed, between the soil and the foundations, layers of material suitable to let the construction “slip” against the earth in the event of an earthquake (Fig. 19.4).

Therefore ancient buildings have survived several destructive earthquakes thanks to these rough seismic isolation systems. For example the misalignment of the blocks in the columns of the Temple of Ephesus (Fig. 19.5) is attributed to the effects on the earthquakes that occurred in the past.

The principles of seismic isolation have ancient origins. In fact the tomb of Cyrus the Great (Fig. 19.6) it is claimed to be the oldest base isolation building in the world.

However only in the 50 years with the diffusion of the computers it has been possible to analyze the performance of base isolation systems and start large mass

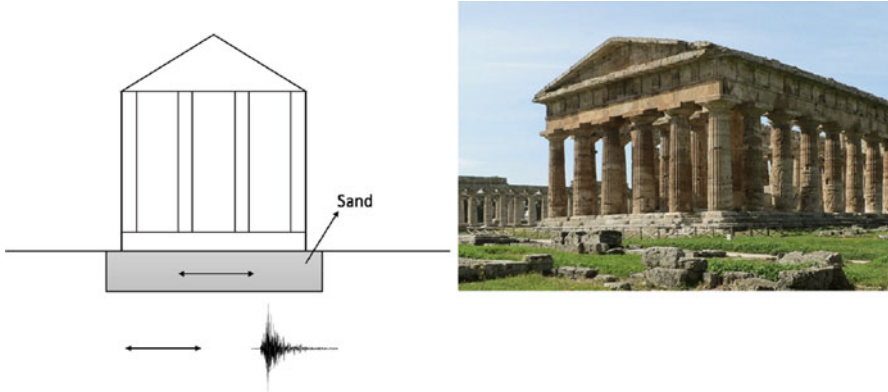


Fig. 19.4 Seismic protection systems in the ancient greek temples

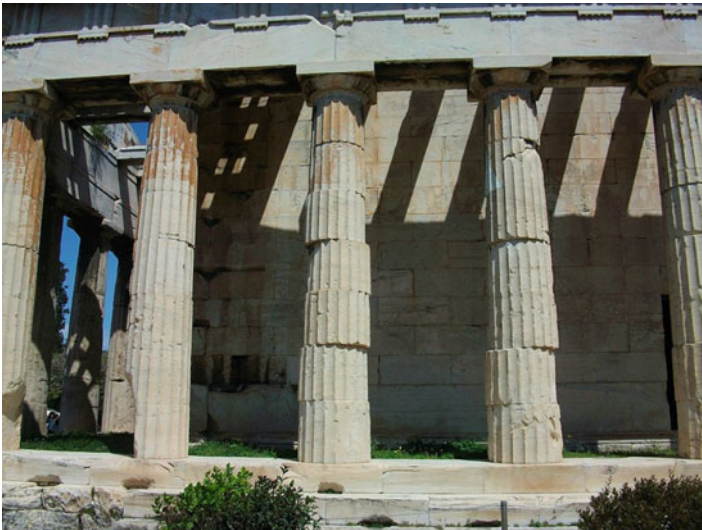


Fig. 19.5 Misalignment of the blocks in the columns of the Temple of Ephesus

applications in the civil engineering field. The first modern device to isolate the structure from the soil was used in bridge engineering: different standby devices in armored neoprene, steel-teflon and hydraulic devices were used in different countries to dissipate energy and absorb the forces caused by the traffic. 1995 Kobe earthquake in Japan gave a rapid impulse to the seismic engineering by pushing the application of the seismic isolation systems in buildings, because these devices were able to overcome the earthquake with almost no damage. However, the first idea of modern seismic isolator was developed in Italy almost 80 years before.



Fig. 19.6 Tomb of Cyrus the Great

19.2.1 First Base Isolation System

In 1909, after the Messina earthquake, the Commission for the reconstruction of the town of Messina in the South of Italy proposed two different solutions to isolate the buildings from the ground. The first one was to insert between the soil and the foundations a layers of sand, while the second one is to insert rollers between them. Eventually, both solutions were not approved. After few years, in 1911, the scientist Domenico Lodà invented the first seismic isolator in history (Fig. 19.7), which allowed to transfer the gravity loads of the buildings, but avoided the transmission of seismic waves.

19.3 Equation of Motion of a Base Isolated Building

In Fig. 19.8 is shown a single story building with mass m , stiffness k_s and viscous damping c_s (Kelly 1999). Under the structure there is a linear isolation system with a mass m_b , a linear spring k_b and a linear viscous dashpot c_b . This is an example of a two-degree-of-freedom system. u_g is the ground displacement and u_b and u_s are the lateral displacements at the level of the slab and the beam. To obtain the equation of motion, Newton's second law is applied

$$\begin{aligned} m\ddot{u}_s &= -c_s(\dot{u}_s - \dot{u}_b) - k_s(u_s - u_b) \\ m\ddot{u}_s + m_b\ddot{u}_b &= -c_b(\dot{u}_b - \dot{u}_g) - k_b(u_b - u_g) \end{aligned} \quad (19.1)$$

Fig. 19.7 Lodà's patent of the first base isolation system, Reggio Calabria, 1911

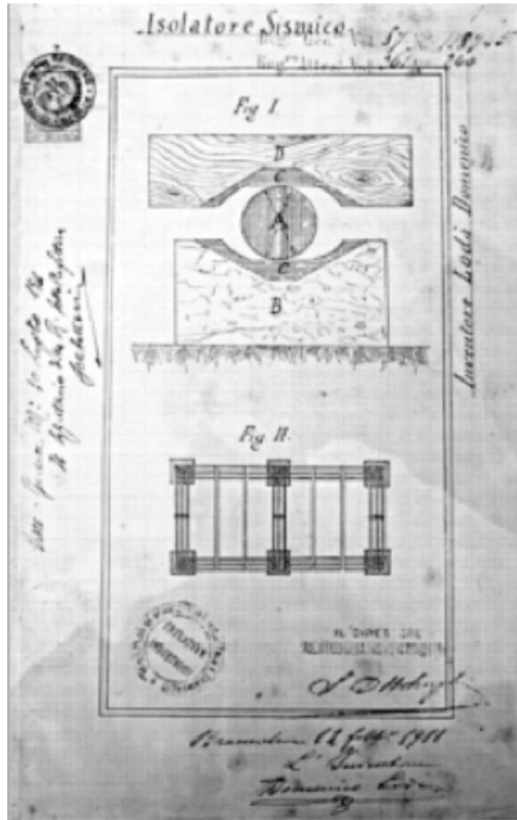
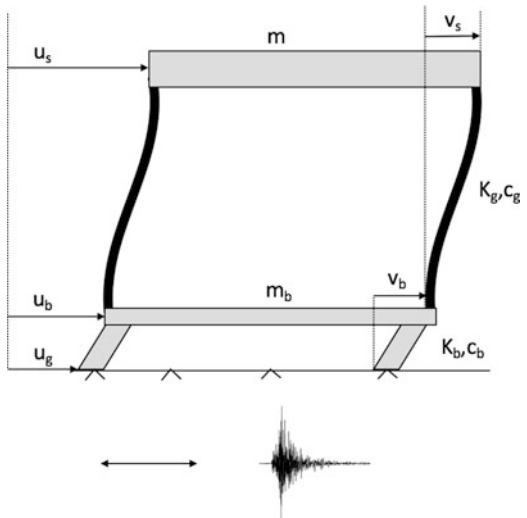


Fig. 19.8 Single-storey structure with linear isolation system (Adopted from Filiatrault and Christopoulos 2006)



where:

- \dot{u}_s is the absolute velocity at the top of the structure;
- \dot{u}_b is the absolute velocity at the base of the structure;
- \ddot{u}_s is the absolute accelerations at the top of the structure;
- \ddot{u}_b is the absolute accelerations at the base of the structure.

The relative displacements are

$$\begin{aligned} v_s &= u_s - u_b \\ v_b &= u_b - u_g \end{aligned} \quad (19.2)$$

Equation 19.1 can be rewritten in terms of relative displacements as follows

$$\begin{aligned} m\ddot{v}_b + m\ddot{v}_s + c_s\dot{v}_s + k_s v_s &= -m\ddot{u}_g \\ (m + m_b)\ddot{v}_b + m\ddot{v}_b + c_b\dot{v}_b + k_b v_b & \end{aligned} \quad (19.3)$$

If it assumed that the relative motion between the base and the upper structure is $v_s = 0$, Eq. 19.3 becomes the standard equation of a two-single-degree-of-freedom system

$$M\ddot{v}_b + c_b\dot{v}_b + k_b v_b = -M\ddot{u}_g \quad (19.4)$$

where $M = m + m_b$ is the total mass. If it is assumed that the relative motion between the foundation and the ground is $v_b = 0$, Eq. 19.3 becomes Eq. 19.5 that corresponds to the equation of a two-single-degree-of-freedom system with fixed-base

$$m\ddot{v}_s + c_s\dot{v}_s + k_s v_s = -m\ddot{u}_g \quad (19.5)$$

So the equation of motion of the two-degree-of-freedom system can be written in matrix form as follow

$$[M]\{\ddot{v}\} + [C]\{\dot{v}\} + [K]\{v\} = -[M]\{r\}\ddot{u}_g \quad (19.6)$$

where:

$$\begin{aligned} &= \begin{bmatrix} M & m \\ m & M \end{bmatrix} \\ [K] &= \begin{bmatrix} k_b & 0 \\ 0 & k_s \end{bmatrix} \\ [C] &= \begin{bmatrix} c_b & 0 \\ 0 & c_s \end{bmatrix} \\ \{v\} &= \begin{bmatrix} v_b \\ v_s \end{bmatrix} \\ \{r\} &= \begin{bmatrix} 1 \\ 0 \end{bmatrix} \end{aligned} \quad (19.7)$$

Some assumptions related to the proprieties of the base isolation system are given below:

- $m_b > m$ have the same order of magnitude;
- $\omega_s = \sqrt{\frac{k_s}{m}} \gg \omega_b = \sqrt{\frac{k_b}{M}}$ so it can be defined $\epsilon = \left(\frac{\omega_b}{\omega_s}\right)^2$ with an order of 10^{-2} of magnitude;
- the viscous damping ratio for the structure $\xi_s = \frac{c_s}{(2m\omega_s)}$ and for the isolation system $\xi_b = \frac{c_b}{(2M\omega_b)}$ have the same order of magnitude.

The following equation needs to be solved to find the natural frequencies of the system:

$$|[K] - \omega^2[M]| = 0 \quad (19.8)$$

that can be expressed explicitly as follow

$$\begin{vmatrix} k_b - \omega^2 M & -\omega^2 m \\ -\omega^2 m & k_s - \omega^2 m \end{vmatrix} = 0 \quad (19.9)$$

If the determinant of Eq. 19.9 is expanded, the following frequency equation is obtained:

$$(1 - \gamma)\omega^4 - (\omega_b^2 + \omega_s^2)\omega^2 + \omega_b^2\omega_s^2 = 0 \quad (19.10)$$

where $\gamma = \frac{m}{M}$. Solving Eq. 19.10 the following solutions are obtained:

$$\omega_1, \omega_2 = \frac{1}{2(1 - \gamma)} \left\{ (\omega_s^2 + \omega_b^2) \pm \sqrt{(\omega_s^2 + \omega_b^2)^2 - 4(1 - \gamma)(\omega_s^2\omega_b^2)} \right\} \quad (19.11)$$

Equation 19.11 can be written as

$$\sqrt{(\omega_s^2 + \omega_b^2)^2 - 4(1 - \gamma)(\omega_s^2\omega_b^2)} = (\omega_s^2 - \omega_b^2) \sqrt{1 + 4\gamma \frac{\omega_b^2\omega_s^2}{(\omega_s^2 - \omega_b^2)^2}} \quad (19.12)$$

Then the right-hand side of Eq. 19.12 can be converted in a binomial series, so:

$$\sqrt{(\omega_s^2 + \omega_b^2)^2 - 4(1 - \gamma)(\omega_s^2\omega_b^2)} \approx (\omega_s^2 - \omega_b^2)^2 \left(1 + \frac{2\gamma\omega_b^2\omega_s^2}{(\omega_s^2 - \omega_b^2)^2} \right) \quad (19.13)$$

Then the two natural frequencies of the system are obtained substituting Eq. 19.13 in Eq. 19.11:

$$\begin{aligned} \omega_1^2 &= \frac{\omega_b^2}{(1 - \gamma)} \left[1 - \frac{\gamma\omega_s^2}{(\omega_s^2 - \omega_b^2)} \right] \\ \omega_2^2 &= \frac{\omega_s^2}{(1 - \gamma)} \left[1 - \frac{\gamma\omega_b^2}{(\omega_s^2 - \omega_b^2)} \right] \end{aligned} \quad (19.14)$$

Considering that $\omega_s \gg \omega_b$ Eq. 19.14 becomes

$$\begin{aligned}\omega_1^2 &= \omega_b \sqrt{1 - \gamma \epsilon} \approx \omega_b \\ \omega_2^2 &= \frac{\omega_s}{\sqrt{1 - \gamma}} \sqrt{1 + \frac{\gamma \omega_b^2}{\omega_s^2}} \approx \frac{\omega_s}{\sqrt{1 - \gamma}}\end{aligned}\quad (19.15)$$

The first natural frequency, ω_1 , is not affected by the flexibility of the structure but by the frequency of the isolation system. The second natural frequency, ω_2 concerns the structural frequency and the mass at the base. It is possible to combine these two factors to enhance the separation of the frequency of the isolation and ed-base system. The first mode shape is $\{A^{(1)}\}$ and it is given by

$$\begin{bmatrix} k_b - \omega_b^2 M & (-\omega_b^2 m) \\ -\omega_b^2 m & k_s - \omega_b^2 m \end{bmatrix} \begin{Bmatrix} A_1^{(1)} \\ A_2^{(1)} \end{Bmatrix} = \begin{pmatrix} 0 \\ 0 \end{pmatrix}\quad (19.16)$$

Extrapolating the second equation from Eq. 19.16

$$(-\omega_b^2 m A_1^{(1)} + (k_s - \omega_b^2 m) A_2^{(1)}) = 0\quad (19.17)$$

and given $\{A_1^{(1)}\}$ the second mode shape can be determined.

$$A_2^{(1)} = \frac{\omega_b^2 m}{k_s - \omega_b^2 m} = \frac{\omega_b^2}{\omega_s^2 - \omega_b^2} = \frac{1}{(1 \setminus \epsilon) - 1} = \frac{\epsilon}{1 - \epsilon} \approx \epsilon\quad (19.18)$$

Consequently, ω_1 can be rewritten as

$$\{A^{(1)}\} = \begin{Bmatrix} 1 \\ \epsilon \end{Bmatrix}\quad (19.19)$$

Likewise, the second mode shape can be obtained $\{A^{(2)}\}$ as:

$$\begin{bmatrix} k_b - \frac{\omega_s^2}{1 - \gamma} M & -\frac{\omega_s^2}{1 - \gamma} m \\ -\frac{\omega_s^2}{1 - \gamma} m & k_s - \frac{\omega_s^2}{1 - \gamma} m \end{bmatrix} \begin{Bmatrix} A_1^{(2)} \\ A_2^{(2)} \end{Bmatrix} = \begin{pmatrix} 0 \\ 0 \end{pmatrix}\quad (19.20)$$

Extrapolating the first equation from Eq. 19.20

$$\left(k_b - \frac{\omega_s^2}{1 - \gamma} M\right) A_1^{(2)} - \frac{\omega_s^2}{1 - \gamma} m A_2^{(2)} = 0\quad (19.21)$$

and setting $\{A_1^{(2)}\}$ the following expression can be obtained:

$$A_2^{(2)} \frac{k_b - \frac{\omega_s^2}{1 - \gamma} M}{\frac{\omega_s^2}{1 - \gamma} m} = \frac{(1 - \gamma)\epsilon - 1}{\gamma}\quad (19.22)$$

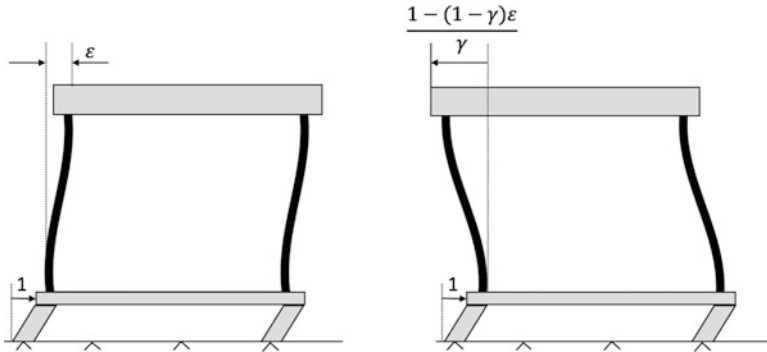


Fig. 19.9 Mode shape for a base isolated structure (Adopted from Filiatrault and Christopoulos 2006)

Consequently, ω_1 can be re-written as:

$$\{A^{(2)}\} = \left\{ \begin{array}{c} 1 \\ -\left(\frac{1-(1-\gamma)\epsilon}{\gamma}\right) \end{array} \right\} \quad (19.23)$$

Figure 19.9 shows two mode shapes. The first image represents the first mode shape and it can be assimilated to a rigid structure on a flexible base isolation system. The other image shows the second mode shape: the displacement at the top of the structure has the same order of magnitude as the isolation displacement, and they are both out of phase. This mode is similar to the free vibration of two masses with the combined system inside (at the center of the mass). It is possible to write the equation of the relative displacement $v_b(t)$ and $v_s(t)$ using the modal superposition method as

$$\begin{aligned} v_b(t) &= u_1(t)A_1^{(1)} + u_2(t)A_1(2) \\ v_s(t) &= u_1(t)A_2^{(1)} + u_2(t)A_2(2) \end{aligned} \quad (19.24)$$

$u_1(t)$ and $u_2(t)$ are modal response variables and if the damping is low enough to maintain the orthogonality of properties of the mode shape this can satisfy the modal equation of motion

$$\begin{aligned} M_1\ddot{u}_1 + C_1\dot{u}_1 + K_1u_1 &= P_1(t) \\ M_2\ddot{u}_2 + C_2\dot{u}_2 + K_2u_2 &= P_2(t) \end{aligned} \quad (19.25)$$

where

$$\begin{aligned} M_1 &= \{A^{(1)}\}^T [M] \{A^{(1)}\} & M_2 &= \{A^{(2)}\}^T [M] \{A^{(2)}\} \\ C_1 &= \{A^{(1)}\}^T [C] \{A^{(1)}\} & C_2 &= \{A^{(2)}\}^T [C] \{A^{(2)}\} \\ K_1 &= \{A^{(1)}\}^T [K] \{A^{(1)}\} & K_2 &= \{A^{(2)}\}^T [K] \{A^{(2)}\} \\ P_1 &= \{A^{(1)}\}^T [P] \{r\} \ddot{u}_g & P_2 &= \{A^{(2)}\}^T [P] \{r\} \ddot{u}_g \end{aligned} \quad (19.26)$$

It is possible to rewrite Eq. 19.25 as

$$\ddot{u}_1 + 2\xi_1\omega_1\dot{u}_1 + \omega_1^2u_1 = -\alpha_1\ddot{u}_g\ddot{u}_2 + 2\xi_2\omega_2\dot{u}_2 + \omega_2^2u_2 = -\alpha_2\ddot{u}_g \quad (19.27)$$

ξ_1 and ξ_2 are the modal damping ratios; α_1 and α_2 are the modal participation factors. These four factors are given by

$$\begin{aligned} \xi_1 &= \frac{C_1}{2\omega_1M_1} & \xi_2 &= \frac{C_2}{2\omega_2M_2} \\ \alpha_1 &= \frac{\{A^{(1)}\}^T[M]\{r\}}{M_1} & \alpha_2 &= \frac{\{A^{(2)}\}^T[M]\{r\}}{M_2} \end{aligned} \quad (19.28)$$

The equation of α_1 is composed of the following matrix operations

$$\alpha_1 = \frac{\begin{Bmatrix} 1 \\ \epsilon \end{Bmatrix}^T \begin{bmatrix} M & m \\ m & m \end{bmatrix} \begin{Bmatrix} 1 \\ 0 \end{Bmatrix}}{\begin{Bmatrix} 1 \\ \epsilon \end{Bmatrix}^T \begin{bmatrix} M & m \\ m & m \end{bmatrix} \begin{Bmatrix} 1 \\ \epsilon \end{Bmatrix}} = \frac{M + m\epsilon}{M + 2m\epsilon + m\epsilon^2} \quad (19.29)$$

If the term ϵ^2 is neglected the following equation is obtained

$$\alpha_1 = 1 - \frac{m\epsilon}{M + 2m\epsilon} = 1 - \frac{\epsilon}{(1 \setminus \gamma) + 2\epsilon} = 1 - \frac{\gamma\epsilon}{1 + 2\gamma\epsilon} \approx 1 - \gamma\epsilon \quad (19.30)$$

and it is possible to calculate the modal mass in the first mode as

$$M_1^* = \alpha_1^2 M_1 = (1 - \gamma\epsilon^2)(M + 2m\epsilon + m\epsilon^2) \approx M(1 - \gamma\epsilon^2(1 - 3\gamma)) \approx M \quad (19.31)$$

Using the same methodology for the second mode, the following equation is obtained

$$\alpha_2 = \gamma\epsilon \quad (19.32)$$

and

$$M_2^* = M \frac{(1 - \gamma)[1 - 2\epsilon(1 - \gamma)]}{\gamma} \quad (19.33)$$

From these calculations above it is possible to understand why this seismic isolation system performs well under earthquakes. α_2 is the modal participation factor of the second mode and it is involved in the structural deformation. This factor has the same order of amplitude of ϵ which has a small value if the original natural frequencies are separated.

It is possible that the natural frequency of the second mode moves to a higher value than the original fixed-base and, consequently, the isolated structure will be out of range if the earthquake motion is strong and has a large spectral acceleration.

Additionally, the second mode is orthogonal to the earthquake input because the modal participation factor α_2 is very small. Starting from Eq. 19.26, one can obtain the generalized load of the second mode as follows

$$P_2(t) = -\{A^{(2)}\}^T [m] \{r\} \ddot{u}_g(t) \quad (19.34)$$

where $\{r\}^T = \{10\}$. Observing Eq. 19.19 it is possible to see

$$\{r\} = \{A^{(1)}\} \quad (19.35)$$

and remembering the mass-orthogonality proprieties of model shape, it is obtained

$$\{A^{(2)}\}^T [M] \{A^{(1)}\} = 0 \approx \{A^{(2)}\}^T [M] \{r\} \quad (19.36)$$

Then it is correct to say:

$$P_2(t) \approx 0 \quad (19.37)$$

Equation 19.37 explains why when the ground motion contains energy at the second mode frequency, the energy is not transmitted to the structure. The seismic isolation system switches the seismic energy across these orthogonality proprieties and not only absorbs them. The energy dissipation, in the seismic isolation system can be described through linear viscosity damping. The modal damping ratios, ξ_1 and ξ_2 , can be determined by considering the base isolation system as independent from the structure.

For the natural rubber isolation system, the value of damping is usually between 10% and 20%. For conventional structures this value is about 5%. This means that when a conventional structure suffers a strong earthquake, some degree of structural and nonstructural damage will take place. With the use of a base isolated structure, there is a reduction of damage that the seismic force can cause on the structure. For this reason, it is correct to estimate a lower damping value for the structure. Starting from Eq. 19.28, the first modal damping ratio ξ_1 is given by

$$\xi_1 = \frac{\{A^{(1)}\}^T [c] \{A^{(1)}\}}{2\omega_1 M_1} = \frac{\begin{Bmatrix} 1 \\ \epsilon \end{Bmatrix} \begin{bmatrix} c_b & 0 \\ 0 & c_s \end{bmatrix} \begin{Bmatrix} 1 \\ \epsilon \end{Bmatrix}}{2\omega_1 (M + 2\omega\epsilon + m\epsilon^2)} = \frac{c_b + c_s\epsilon^2}{2\omega_b \sqrt{1 - \gamma\epsilon} (M + 2m\epsilon + m\epsilon^2)} \quad (19.38)$$

Neglecting ξ^2 from Eq. 19.38, the first modal damping ratio can be simplified as follow

$$\xi_1 \approx \frac{\xi_b(1 - 2\gamma\epsilon)}{\sqrt{1 - \gamma\epsilon}} \approx \epsilon_b \left(1 - \frac{2}{3}\gamma\epsilon\right) \quad (19.39)$$

Equation 19.39 shows that the deformation of the isolation system corresponds to the first modal damping ratio ξ_1 . Similarly the second modal damping ξ_2 can be determined from Eq. 19.28.

$$\xi_2 = \frac{\{A^{(2)}\}^T [c] \{A^{(2)}\}}{2\omega_2 M_2} = \frac{\left\{ \begin{array}{c} 1 \\ \frac{(1-\gamma)\epsilon-1}{\gamma} \end{array} \right\}^T \begin{bmatrix} c_b & 0 \\ 0 & c_s \end{bmatrix} \left\{ \begin{array}{c} 1 \\ \frac{(1-\gamma)\epsilon-1}{\gamma} \end{array} \right\}}{2\omega_s \frac{\sqrt{1+\gamma\epsilon}}{\sqrt{1-\gamma}} M \frac{(1-\gamma)[1-2\epsilon(1-\gamma)]}{\gamma}} \quad (19.40)$$

and by simplifying, it is possible to obtain

$$\xi_2 \approx \frac{\epsilon_s}{\sqrt{1-\gamma}} + \frac{\gamma \xi_b \sqrt{\epsilon}}{\sqrt{1-\gamma}} \quad (19.41)$$

The second modal damping ratio ξ_2 concerns the structure and the damping of the isolation system increases it.

If ξ_s is small, the relationship $\xi_b \sqrt{\epsilon}$ may mean that the structure has an increment of damping. The high damping in the isolated structure can contribute to the structural mode. Once the two modal damping ratios, ξ_1 and ξ_2 , and the two modal participation factors, α_1 and α_2 are determined, it is possible to determine the response of the base isolated system that is subjected to the ground acceleration time-history \ddot{u}_g . Duhamel integral can be used for this analysis

$$\begin{aligned} u_1(t) &= -\frac{\alpha_1}{\omega_1} \int_0^t \ddot{u}_g(t-\tau) e^{-\xi_1 \omega_1 \tau} \sin \omega_1(t-\tau) d\tau \\ u_2(t) &= -\frac{\alpha_2}{\omega_2} \int_0^t \ddot{u}_g(t-\tau) e^{-\xi_2 \omega_2 \tau} \sin \omega_2(t-\tau) d\tau \end{aligned} \quad (19.42)$$

The maximum values of the two responses are given by:

$$\begin{aligned} |u_1(t)|_{max} &= \alpha_1 S_D(\omega_1, \xi_1) \\ |u_2(t)|_{max} &= \alpha_2 S_D(\omega_2, \xi_2) \end{aligned} \quad (19.43)$$

where the term $S_D(\omega_i, \xi_i)$ is the relative displacement response spectrum for the ground motion \ddot{u}_g with a frequency ω_i and a damping ration ξ_i . It is possible to use the square root of the sum of the squares to estimate the maximum value of the relative displacement because the two natural frequencies are separated.

$$\begin{aligned} |v_s(t)|_{max} &= \sqrt{(A_2^{(1)} |u_1(t)|_{max})^2 + ((A_2^{(2)} |u_2(t)|_{max})^2} \\ |v_b(t)|_{max} &= \sqrt{(A_1^{(1)} |u_1(t)|_{max})^2 + ((A_1^{(2)} |u_2(t)|_{max})^2} \end{aligned} \quad (19.44)$$

Setting the following variables

$$\begin{aligned}
 A_1^{(1)} &= 1, A_2^{(1)} = \epsilon \\
 A_1^{(2)} &= 1, A_2^{(2)} = ((1 - \gamma)\epsilon - 1)/\gamma \\
 \alpha_1 &= 1 - \gamma\epsilon \\
 \alpha_2 &= \gamma\epsilon
 \end{aligned} \tag{19.45}$$

and substituting them in Eqs. 19.19, 19.23, 19.30, 19.32, and 19.43, the following expression is obtained

$$\begin{aligned}
 |v_b(t)|_{max} &= \sqrt{(1 - \gamma\epsilon)^2 [S_D(\omega_1, \xi_1)]^2 + \gamma^2 \epsilon^2 [S_D(\omega_2, \xi_2)]^2} \\
 |v_s(t)|_{max} &= \sqrt{\epsilon^2 (1 - \gamma\epsilon)^2 [S_D(\omega_1, \xi_1)]^2 + \gamma^2 \epsilon^2 \frac{1}{\gamma^2} [(1 - \gamma)\epsilon - 1]^2 [S_D(\omega_2, \xi_2)]^2} \\
 &= \epsilon \sqrt{(1 - \gamma\epsilon)^2 [S_D(\omega_1, \xi_1)]^2 + [(1 - \gamma)\epsilon - 1]^2 [S_D(\omega_2, \xi_2)]^2}
 \end{aligned} \tag{19.46}$$

Normally in the earthquake spectra, the displacement at high frequencies ω_2 is smaller than the displacement at lower frequencies ω_1 , so this term can be neglected and the two equations become

$$\begin{aligned}
 |v_b(t)|_{max} &\approx (1 - \gamma\epsilon) S_D(\omega_1, \xi_1) \\
 |v_s(t)|_{max} &\approx \epsilon \sqrt{[S_D(\omega_1, \xi_1)]^2 + [S_D(\omega_2, \xi_2)]^2}
 \end{aligned} \tag{19.47}$$

19.4 Characteristics of Base Isolation System

Base isolation systems are usually adopted in *critical facilities* such as hospitals, schools, police stations, bridges, etc (Moretti et al. 2014). In other words all the services that need to remain functional right after an earthquake to allow the emergency response operations. These systems can also be adopted in *plants with major-accident hazards* such as chemical and nuclear power plants for example where the safety requirements are quite high.

A base isolation system should be able to transfer the to the ground the vertical gravity loads of the building both in normal operating conditions and under seismic actions. The bearings are characterized by a low lateral stiffness to allow relative displacements between the upper and lower part of the building. However they still need an adequate lateral stiffness to withstand the horizontal forces of small entities such as wind, traffic and low intensity seismic actions. They should also have a certain dissipative and self-centering capacity.

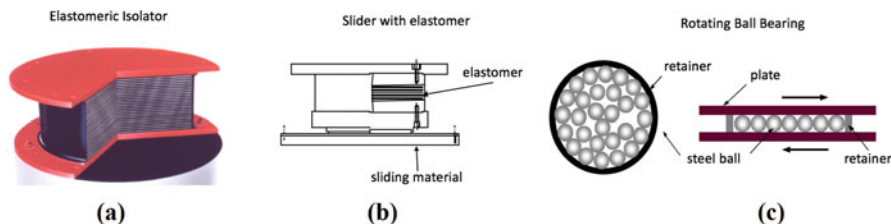


Fig. 19.10 Seismic isolation systems

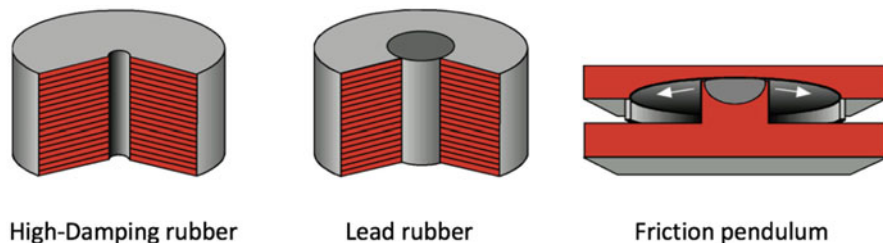


Fig. 19.11 Seismic isolation systems

19.5 Seismic Isolation Systems

Different types of isolators are developed for buildings, and it is possible to distinguish them in three categories:

1. *Elastomeric isolator* (Fig. 19.10a) (e.g. natural rubber bearing, lead plug rubber bearing or high damping rubber bearing) (Kelly 1997);
2. *Slider* (Fig. 19.10b);
3. *Rotating ball bearing* (Fig. 19.10c).

The main types of base isolation systems that are usually used in buildings are (Fig. 19.11):

1. *high-damping rubber bearings;*
2. *lead rubber bearings;*
3. *friction pendulum bearings.*

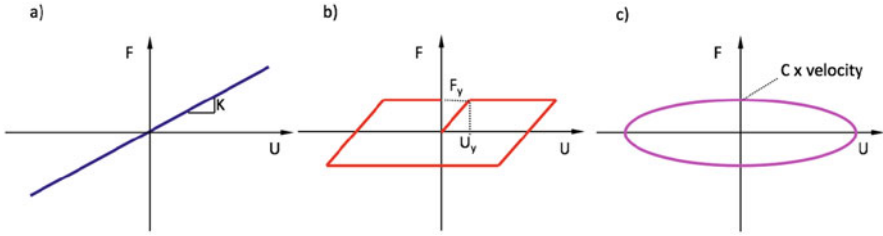


Fig. 19.12 Schematic representation of (a) linear spring, (b) EPP spring and (c) viscous dashpot

In the next sections is shown how each type of base isolation system can be modeled combining in parallel some basic *rheological* models or *mechanical* models (Fig. 19.12) that are:

1. *Linear spring*;
2. *EPP spring*;
3. *Viscous dashpot*.

19.5.1 Low-Damping Natural or Synthetic Rubber Bearings

Low Damping Rubber Bearings have a linear behavior in shear up to 100% shear strain, but they have a low damping ratio $\xi = 2 - 3\%$. The main advantages is that they are easy to manufacture and model and their response is not sensitive to the rate of loading, the history of loading, temperature and aging. However the main disadvantage is the relatively low damping provided by the rubber, but this problem can be partially solved with the use of high damping rubber and/or with the combination of supplemental damping systems. In fact in Japan they have been used with supplementary devices like dampers, steel bars, lead bars and so on. It is possible to design the bearing without damping and linear shear behavior, but it needs a viscous damping.

19.5.2 High-Damping Rubber Bearings (HDRBs)

The High-Damping Rubber Bearing (HDRB) (Fig. 19.13) is made of elastomeric rubber layers alternating with steel plates solidly joined together under high pressure and temperature, through the process of vulcanization. This stratigraphy allows to transmit the vertical loads due to permanent (gravity) and accidental effects. In fact the vertical capacity can be increased by reducing the thickness of the rubber layers, while the presence of the steel plates increases the vertical stiffness of the bearing. Moreover, the steel plates prevent the deformation of the rubber caused by the weight of the building. The damping in the rubber is increased by adding extra-fine

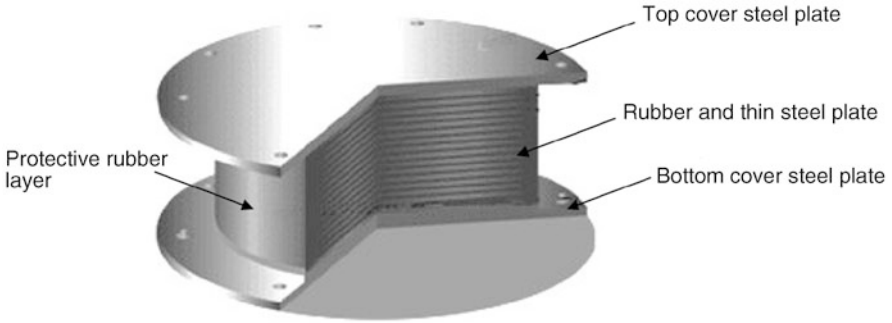


Fig. 19.13 Schematic of laminated rubber bearing

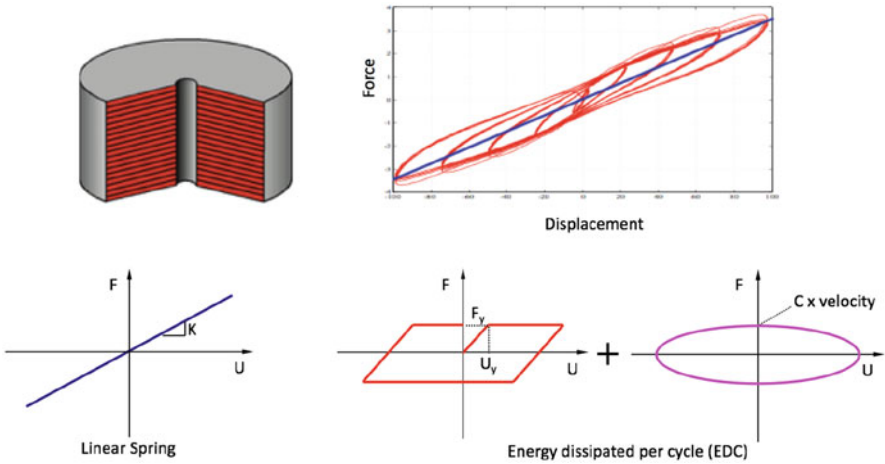


Fig. 19.14 Combination of linear spring, EPP spring and viscous dashpot in the HDRB

carbon black, oils or resins, and other proprietary fillers, so they can reach damping ratio $\xi = 10\text{--}20\%$ at shear strains of 100%. The effective stiffness and damping are not constant, but depend on:

1. *Elastomer and fillers;*
2. *Contact pressure;*
3. *Velocity of loading;*
4. *Load history (scragging);*
5. *Temperature;*

Figure 19.14 shows the combination of the basic elements to determine the behavior of the high-damping rubber bearings.

HDRB have been used in the construction of bridges, but in the last 20 years the use of this bearing has been extended also to the seismic isolation of buildings.



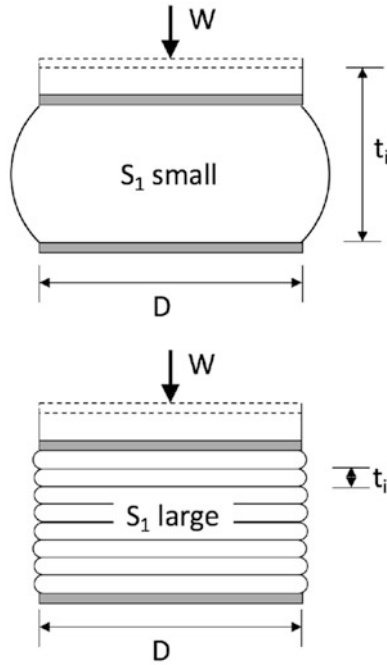


Fig. 19.15 Primary shape factor

19.5.2.1 Buckling in HDRB

It is important to avoid unstable behavior such as buckling in HDRBs. Two factors are used to define the shape of the rubber bearings, the *primary shape factor* S_1 and the *secondary shape factor* S_2 .

The *primary shape factor* S_1 is defined as follow

$$S_1 = A'/L \quad (19.48)$$

where A' is the area of the single steel plate and L is the load-free lateral area of the single layer of rubber. This parameter is connected to the vertical stiffness of the bearing (Fig. 19.15).

The *secondary shape factor* S_2 is defined as follow

$$S_2 = D/t_e \quad (19.49)$$

where D is the plan dimension of single steel plate and t_e is the total thickness of the layers of rubber. The parameter S_2 is related to the buckling of rubber bearings when the vertical load W is applied (Fig. 19.16). The buckling might occur with decreasing S_2 .

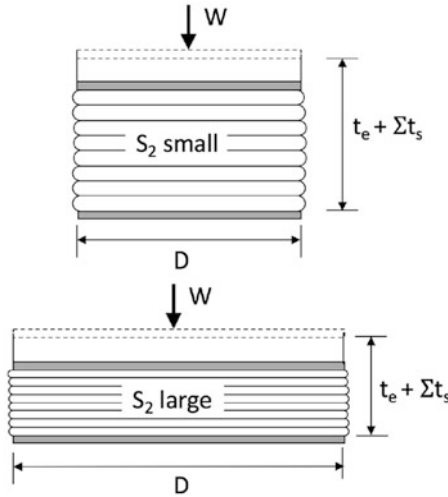


Fig. 19.16 Secondary shape factor

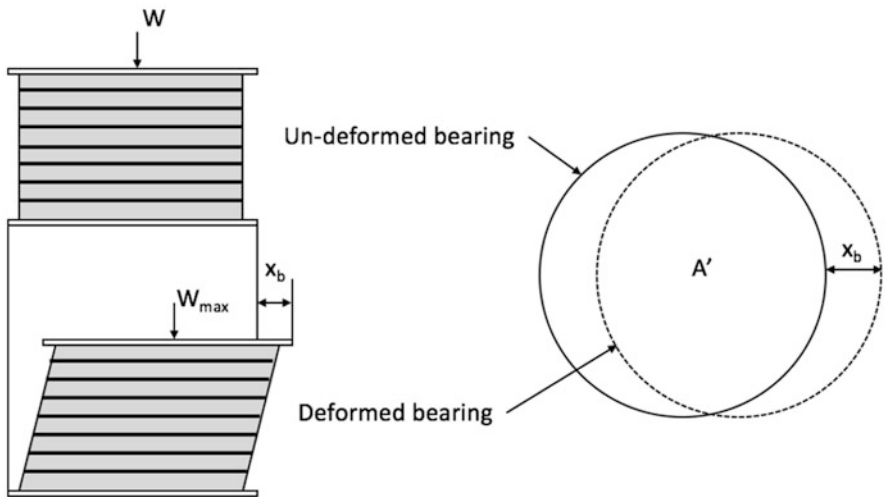


Fig. 19.17 Circular laminated rubber bearing under gravity and lateral loads (Adapted from Filiatrault and Christopoulos 2006)

19.5.2.2 Gravity Load Carrying Capacity of a HDRB

Figure 19.17 shows the effect of the gravity and the lateral loads on a circular laminated rubber bearing. The deformed shape of the device produces an overlap area A between the top and the bottom of the bearing.



The maximum allowed vertical load W_{max} is calculated with the following semi-empirical equation

$$W_{max} = A'G_rS\gamma_w \quad (19.50)$$

where G_r is the shear modulus of rubber (between 0.5 and 1 MPa), and γ_w is the allowable shear strain under gravity load which can be estimate as a function of the short-term failure strain of the rubber in pure tension ϵ_v as follows

$$\begin{aligned} \gamma_w &\approx 0.2\epsilon_v \\ \gamma_w &\approx 0.4\epsilon_v \text{ for design base earthquakes} \\ \gamma_w &\approx 0.7\epsilon_v \text{ for maximum credible earthquakes} \end{aligned} \quad (19.51)$$

where S is the shape factor of the rubber layers which coincides with the load area of a cylindrical bearing of diameter D divided by the load-free area of the rubber layers of thickness t_r .

$$S = \frac{\text{loaded area}}{\text{load free area}} = \frac{(\pi D^2)/4}{\pi D t_r} = \frac{D}{4t_r} \quad (19.52)$$

It is assumed that the rubber is fully constrained laterally and it interfaces with steel plates so the shear stress developed at the interface of the steel and the rubber τ_s is given by

$$\tau_s = \frac{W}{6A'S} \quad (19.53)$$

When the bearing has a *rectangular form* of sides $b \times d$ and is made of rubber layers of thickness t_r , the corresponding *shape factor* is given by

$$S = \frac{\text{loaded area}}{\text{load free area}} = \frac{bd}{2t_r(b+d)} \quad (19.54)$$

It is possible to assume that only the rubber layers suffer the pure shear deformation because the steel plates limit the flexural deformation. The lateral stiffness of the bearing, k_b , can be approximated as

$$k_b = \frac{G_r A_r}{h_r} \quad (19.55)$$

where A_r and h_r are the area and the total height of the rubber respectively and G_r is the shear modulus of the rubber. The natural period of vibration of a bearing that supports a portion of a rigid upper structure, W_b is given by

$$T_b = 2\pi \sqrt{\frac{W_b}{gk_b}} \quad (19.56)$$

Summing the entire weight of the building W_{Tot} and the total lateral stiffness k_{bTot} of the bearings that is obtained by summing the lateral stiffness of each bearing, the following period is obtained

$$T_b = 2\pi \sqrt{\frac{W_{Tot}}{gk_{bTot}}} \quad (19.57)$$

The vertical stiffness of a bearing is larger than its lateral stiffness so vertical deflections are usually neglectable however in some cases it might be important so it is necessary to know the associated vertical stiffness k_v that is given by

$$k_v = \frac{k_{vy}k_{vV}}{k_{vy} + k_{vV}} \quad (19.58)$$

where k_{vy} is the vertical stiffness due to rubber shear strains without volume change given by

$$k_{vy} = \frac{6G_r S^2 A_r}{h_r} \quad (19.59)$$

while k_{vV} is the vertical stiffness caused by the volume change of the rubber without shear given by

$$k_{vV} = \frac{\kappa_r A_r}{h_r} \quad (19.60)$$

κ_r is the compression modulus of the rubber that is typically $\kappa_r = 2000$ MPa.

The allowable lateral displacement $x_{b,all}$ is directly related to the allowable shear strain γ_s through the equation

$$x_{b,all} = h_r \gamma_s \quad (19.61)$$

and to the overlap factor AA_r . The relationship between AA_r and $x_{b,all}$ depends on the shear of the bearing. For example for a *cylindrical bearing* is given by

$$\frac{A_r}{A'} = 1 - \frac{2}{\pi} (\theta + \sin \theta \cos \theta) \quad (19.62)$$

where $\sin \theta = k_{b,all}/D$. For a *rectangular bearing* the equation is:

$$\frac{A_r}{A'} \approx 1 - \frac{x_{bb}}{b} - \frac{x_{bd}}{d} \quad (19.63)$$

where x_{bb} and x_{bd} are respectively the displacement parallel to each side of the dimension of the bearing.

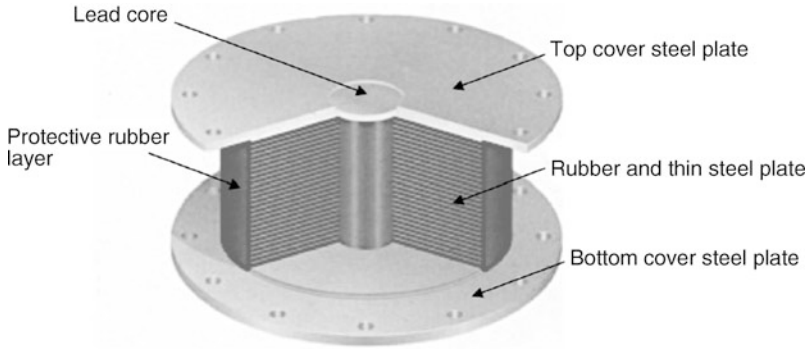


Fig. 19.18 Scheme of a lead rubber bearing

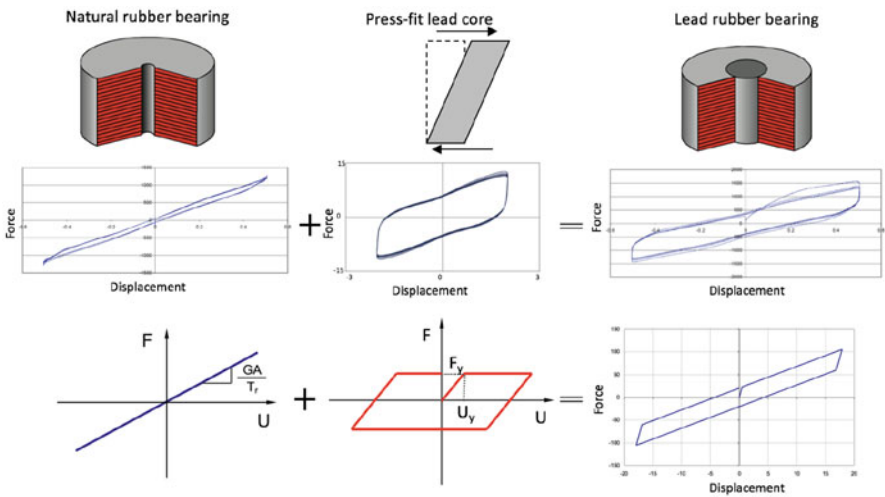


Fig. 19.19 Combination of linear spring and EPP spring in the HDRB

19.5.3 Lead Rubber Bearings

This device is made of a laminated-rubber bearing with a cylindrical lead plug in the center (Fig. 19.18) which serves to increase the damping by hysteretic shear deformation (Iwan 1965).

The material of this device, the lead, is chosen because its behavior is approximately elasto-plastic and the yield in shear is of about 10 MPa. Besides, this material is hot-worked at room temperature so its proprieties are continuously restored when cycled in the inelastic range.

Figure 19.19 shows how the lead rubber bearing works. The elastic stiffness k_1 is given by



$$k_1 \approx \frac{1}{h_r} (G_p A_p + G_r A_r) \quad (19.64)$$

where h_r is the total rubber height, A_p and A_r are the areas of the lead plug and the one of the rubber respectively, G_p and G_r are the shear modulus of lead (≈ 150 MPa at room temperature) and the one of the rubber (between 0.5 and 1 MPa). The post-yield stiffness k_2 is equal to the lateral shear stiffness of the rubber k_b

$$k_2 = k_b = \frac{G_r A_r}{h_r} \quad (19.65)$$

Using the shear force, it is possible to estimate the yield force F_y as

$$F_y = \tau_{py} A_p \left(1 + \frac{G_r A_r}{G_p A_p} \right) \quad (19.66)$$

where $\tau_{py} \approx 10$ MPa is the yield shear strength.

The presence of the lead core can improve the damping ratio reaching values $\xi = 15\text{--}35\%$ at shear strains of 100%.

19.5.4 Friction Pendulum System (FPS)

The Friction Pendulum Bearing (FPB) or Friction Pendulum System (FPS) is made of three main characteristics:

1. articulated friction slider;
2. spherical concave sliding surface;
3. enclosing cylinder for lateral displacement restraint.

Figure 19.20 shows the design of a FPS. There is a central spherical surface that is coated with a low-friction composite material. The articulated side is spherical and it is coated with stainless steel, while the other slide is a spherical cavity that is coated with a low-friction composite material.

Figure 19.21 shows how the basic elements are combined in the FPS.

Figure 19.22 shows the principle of operation of the device: W is the weight of the upper structure, δ is the amount of horizontal displacement; R is the radius of the

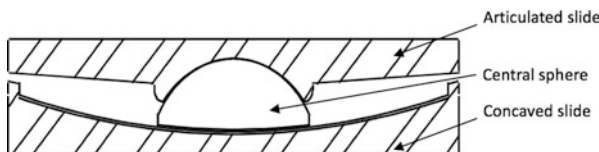


Fig. 19.20 Schematic representation of the FPS

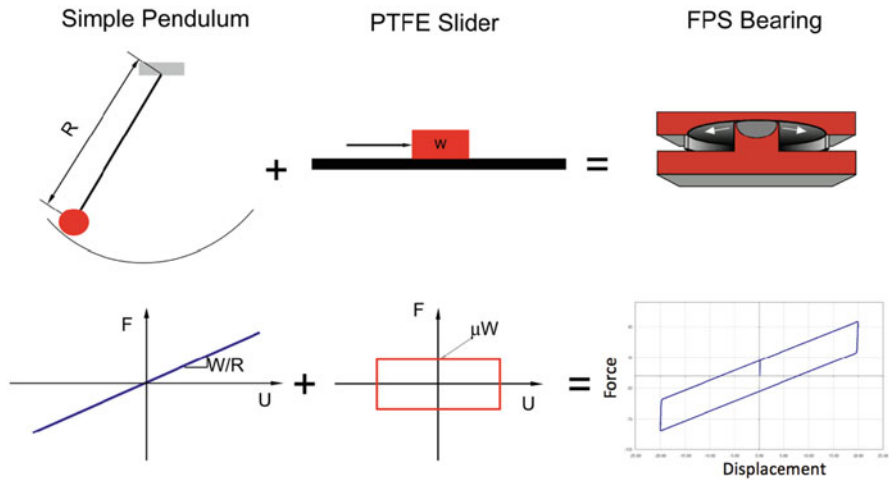


Fig. 19.21 Combination of simple pendulum and PTFE slider in the FPS bearing

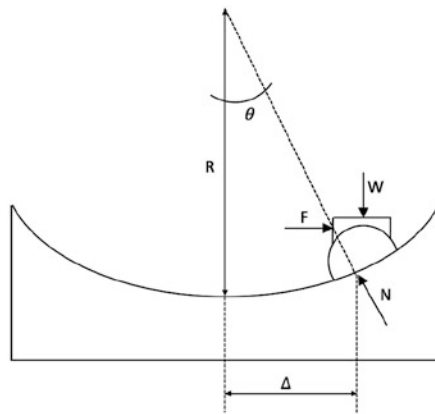


Fig. 19.22 Principle of operation of the FPS (Adopted from Filiatrault and Christopoulos 2006)

spherical concave surface; F is the horizontal force required for the displacement of the bearing and N is the normal force at the interface. The horizontal force that is required for the displacement is given by

$$F = N \sin \theta \tag{19.67}$$

and the equilibrium in the vertical direction is given by

$$W = N \cos \theta \tag{19.68}$$

Substituting Eq. 19.67 in Eq. 19.68, the following equation is obtained

$$F = W \tan \theta \quad (19.69)$$

From geometric considerations it is obtained that

$$\tan \theta = \frac{\delta}{R} \quad (19.70)$$

and substituting Eq. 19.70 in Eq. 19.69, the corresponding lateral force displacement is given by

$$F = \frac{W}{R} \delta \quad (19.71)$$

Instead the natural period of the FPS is given by

$$T = 2\pi \sqrt{\frac{W}{gk}} = 2\pi \sqrt{\frac{R}{g}} \quad (19.72)$$

So the period of the Friction Pendulum bearing is selected simply by choosing the radius of curvature of the concave surface. It is independent of the mass of the supported structure. The damping is selected by choosing the friction coefficient. Torsion motions of the structure are minimized because the center of stiffness of the bearings automatically coincides with the center of mass of the supported structure. Furthermore, the bearing's period, vertical load capacity, damping, displacement capacity, and tension capacity, can all be selected independently.

Variations of these devices have been proposed such as the *double concave friction pendulum* that is used to reduce the dimensions of standard bearings. In detail, this device is the union of two single friction pendulums where the two sides of the plates are made of spherical concave sliding interfaces and they are joined with an articulated double friction pendulum (Fig. 19.23). The double sliding contacts with upper/lower surfaces can provide the larger stroke for displacement with a compact footprint.

19.5.5 Spring-Type System

Spring-type systems are elastomeric bearing and they are used in case a full three-dimensional isolation is necessary. Originally GERB developed this system for the isolation of the power turbines. It is composed by a large helical steel spring that is flexible in the horizontal and vertical directions, while the vertical frequency is around 3–5 times the horizontal one. In all the three-dimensional systems, the center of gravity of the isolated structure is above the center of stiffness and this creates a strong link between horizontal and rocking motion; when the center of gravity and of stiffness are at the same level, this spring-type system becomes practical.

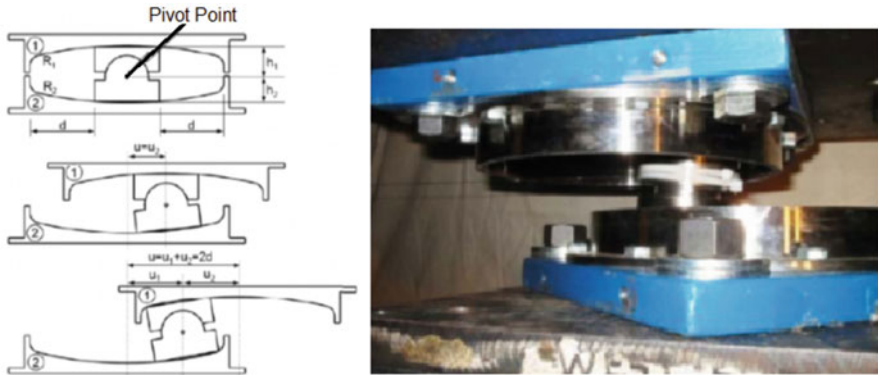


Fig. 19.23 Double concave friction pendulum

19.6 Limitations of a Base Isolation System

Although this retrofit is very effective, there are cases when it can not be applied. For example if:

1. *the structure is very flexible:* $T_{bf} \approx T_{IS}$. In this case the base isolation system allows to pass only the earthquake energy that corresponds to the frequency of the base isolated structure, therefore the seismic forces might be amplified;
2. *the structure is located on soft soil.* In this case the soil type amplifies the earthquake energy corresponding to the frequencies that are close to the period of the base isolated structure T_{IS} ;
3. *the seismic joints are not feasible.* In this case the lateral displacements of the base isolated structure are not allowed due to compatibility issues with the adjacent structures.

In all these case a valid alternative to base isolation system is the use of energy dissipation systems (Chap. 17).

19.7 Installation Methodology for New and Existing Buildings

19.7.1 Retrofit Construction Sequence for Existing Buildings

Six steps have been identified in the retrofit construction sequence.

1. *Basement excavation*
2. *Moat Excavation*
3. *Insertion of Rigid Layers and Jacking*

4. *Cutting of External Concrete/Masonry Walls*
5. *Placing of Isolators*
6. *Separation of building from Base*

19.7.1.1 Step 1: Basement Excavation

In *basement excavation* the logistics are the most complicated part in order to gain access to either the foundations of a structure, or remove a sufficient depth of soil to be able to install the isolators themselves. Problems such as site accessibility for excavation and removal equipment, entry into the basement itself and the co-ordination of various teams setting up around the area are probably the most usual kinds of trouble run into during the execution of this stage.

For many older buildings, the foundations simply consist of thick external walls extending down to bedrock. In this case, the basement must be excavated to a sufficient depth to allow the isolators to be installed, a new floor put in place and utilities to be connected. A typical depth to accommodate this scenario might be 6–7 ft.

19.7.1.2 Step 2: Moat Excavation

The *moat excavation* phase sees the initial shoring and temporary bracing of the exterior walls against the retaining walls put in place to ensure stability against relative building movements under construction loading. Once the retaining wall is in place, excavation can begin around the perimeter, while at the same time steel bracing is put place to prevent relative movement between any internal and external columns, while the soil around the footing is excavated to facilitate its enlargement. This is often necessary for it to be able to withstand the increased demand of seismic loading. Alternatively, for a smaller structure a mat slab might be poured to supply this resistance in addition to providing the necessary rigid layer below the level of isolation. A mat slab, in the event of an earthquake also has the advantage of having lower surface stress due to the movement of surrounding soil and will as a result settle less in the event of liquefaction.

19.7.1.3 Step 3: Insertion of Rigid Layers and Jacking

Two rigid layers must now be inserted into the building, one above and one below the intended soft isolation layer. There are several options below this level, the two most common being first a mat slab, and second reinforced cast-in-place concrete grade beams spanning the excavation. The problem with either solution is the connection detailing to both the internal columns and the external walls. A possible solution, for the exterior walls, is to core drill around the inner perimeter and grout in steel reinforcing bars, with a specified pull-out resistance. A set length of these

could remain exposed, with or without a bob, to provide sufficient anchorage to the slab. Although expensive, this is one of the more effective ways of providing for connection.

19.7.1.4 Step 4: Cutting of External Concrete/Masonry Walls

This step is only applicable to buildings with a continuous outer wall around the perimeter, and not one with external columns spanned by external cladding. The latter kind of structure facilitates the implementation of seismic isolation far better than the first. Once the jacks have been loaded and locked, the sections of concrete/masonry to be removed for isolator placement may be cut using either a circular, wire or plunge saw. The implement used is largely dependent upon the thickness of the walls.

19.7.1.5 Step 5: Placement of Isolators

Once again, the major problem here comes down to the accessibility of the basement to construction equipment. The manipulation and installation of large isolators is no easy task in confined conditions. In large scale retrofit projects the isolator is lowered by crane through the bubble in the moat onto the device cart used to remove the concrete cut outs, which is then towed to the desired location and the isolator positioned on the enlarged footing or foundation.

19.7.1.6 Step 6: Separation of Building from Base

Before separation, a new basement floor has to be installed and the utilities, electrical and mechanical need to be reconnected. Flexible connections are required for all of these. All the pipes that cross the joints of the isolated superstructure should remain functional during the displacement values corresponding to the Damage Limit State (SLD) (Figs. 19.24 and 19.25). Gas pipes and other service networks passing through the connection joints should be designed to allow the relative displacement of the isolated superstructure corresponding to the Ultimate Limit State (SLU) that is the same level of safety of the base isolated system.

Then the basement floor should rest upon the framework of steel I-Sections used to provide the rigid layer above the isolation. A hybrid construction is often used, both to prevent compression in the steel when subject to large seismic demand, and also for ease of construction. The final stage in the construction scheme is the disconnection of the building with its base. The remaining portions of concrete between the isolators are cut away with a wire saw, on a plane with the top and bottom of the isolation units respectively, in order to allow total freedom of movement under seismic loading. The tool used to cut the walls is again dependent upon their thickness, and the material.



Fig. 19.24 Flexible connection pipes for different types of infrastructures

19.7.2 Retrofit Construction Costs for New Buildings

The cost of a new base isolated building can vary according to its configuration, the material used, the intensity of the earthquake etc. As a general rule the inclusion of all aspects of seismic isolation in a new structure will add no more than 3% to total construction cost and considerably less when assessed against the benefits of isolation. An example is the Wellington Regional Hospital (Fig. 19.26), completed in December 2008. It is a seven storey building with a total floor area of 44,700 m² that has been retrofitted with 135 lead rubber bearings and 132 slider bearings. The hospital has been designed to withstand M7.8 on Wellington-Hutt fault and M8.3 on Wairarapa fault. The total construction cost \$165m, while the cost of seismic isolation bearings on their own was 1% of total construction cost. Instead

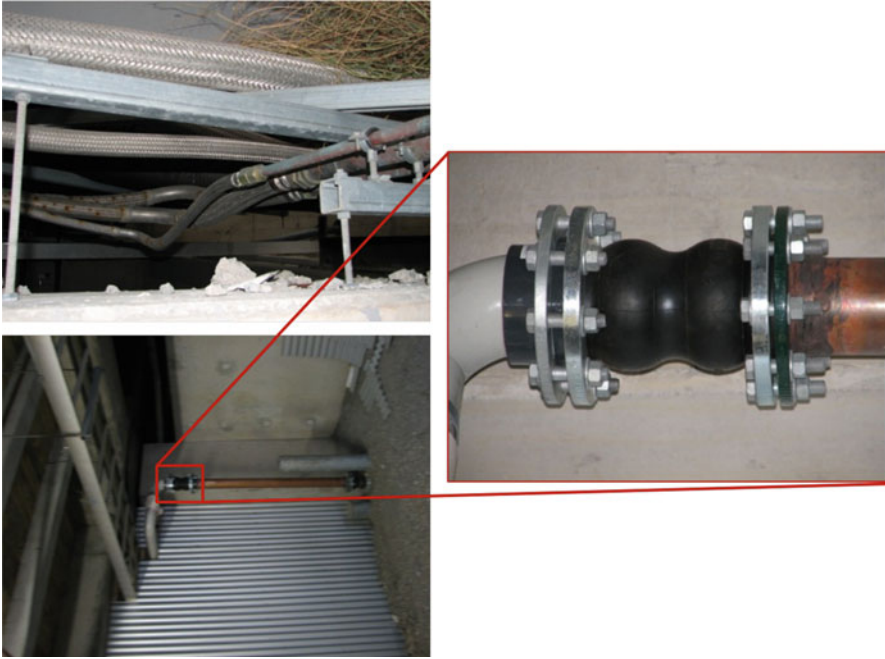


Fig. 19.25 Flexible connections in base isolated buildings (Wellington Hospital, New Zealand)

the cost of all components of the seismic isolation system (including installation, seismic gap and gaseant) was around 3% of total construction cost that translates to approximately \$110 m².

19.7.3 Mid-Story Base Isolation

Typically isolators are located at the bottom of the building in the basements, however also alternative locations are possible as shown in Fig. 19.27.

The main design concept is setting a layer of isolators at mid height to reduce the earthquake response of the upper structure. At the same time, the earthquake response of the whole structure is reduced because in the lower part the earthquake response is not increased as shown in Fig. 19.28.

Compared with a fixed-base structure, the first period of a mid-story base isolated building is longer and the damping ratio is higher; the modal participation factors are different according to the position of the layer of isolators. The deformation is concentrated at the isolation layer and the base shear is less than that one in the case of fixed-base structure.



Fig. 19.26 Installation of isolator in Wellington Hospital (new building), New Zealand

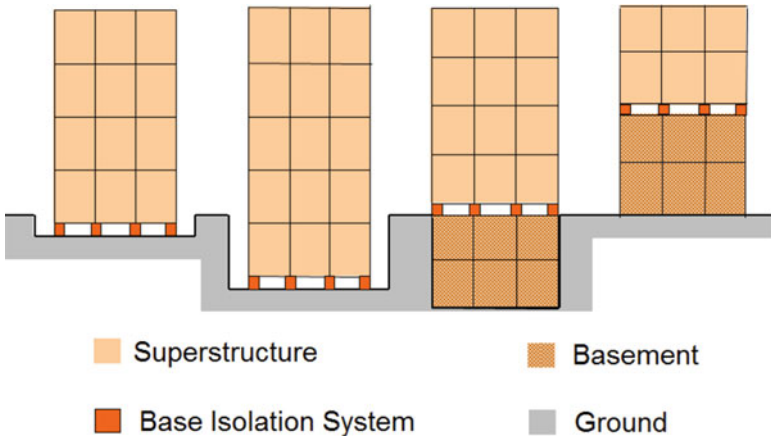


Fig. 19.27 Alternative locations of seismic isolators in tall buildings

Few example mid-story base isolation has been recently adopted both in US and Japan both in new buildings and for the rehabilitation of existing ones (e.g. control vibrations induced by subways (Fig. 19.29) or to increase the story high of existing buildings).

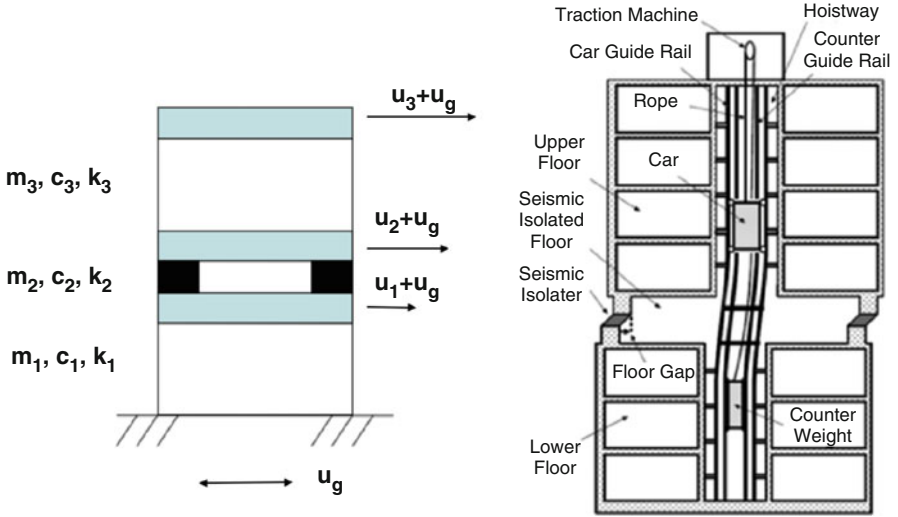


Fig. 19.28 Mid-story seismic isolated building



Fig. 19.29 Building located near Tokyo

The building shown in Fig. 19.29 is located near Tokyo and It was constructed in 1972 consisting of A & B blocks both of nine stories. Its 1st to 4th stories are of steel reinforced concrete (SRC) structure, and 5th to 9th stories of reinforced concrete (RC) structure. Structural analyses have shown that mid-story isolation could fully meet the seismic requirements and perform better than steel bracings.

After the analysis and the comparison, it was decided to install 24 laminated natural rubber bearings with diameters of 600 mm (Blakeley 1982). The isolators

were installed in all the columns of the 4th story: after one column was cut off at its mid-level, the rubber bearing was installed instantly between its two cuts, before another column was cut off. The dampers were installed in both longitudinal and transversal directions of the building.

19.8 Simplified Methodology to Design a Seismically Isolated Building with Rubber Bearings

Buildings with seismic isolation must meet the general safety requirements of seismic standards such as Eurocode 8 and NTC-08 (2008). In particular, the requirements regarding the stability (SLU), the damage limitations (SLD) and the ground foundations. The superstructure and the substructure must be substantially maintained in the elastic range. The base isolation system reduces the seismic forces acting on the superstructure, so the structure can be designed with lower forces corresponding to the low ductility (DC “B”) requirements.

Below are listed the steps necessary to design a base isolation system according to the Italian seismic standard NTC08:

First the *nominal life* of the structure V_N should be identified. V_N is defined as the period of time in which the structure, with ordinary maintenance, can be used for its purpose. Table 19.1 shows the three categories of nominal life.

Then the *Use Class* C_U which corresponds to the level of overcrowding of a structure in presence of seismic actions, with reference to the consequences of a lack of functionality. They correspond to the *Important Class* according to Eurocode 8. Table 19.2 shows the values of the *Use Class* C_U for four different categories.

Multiplying the *nominal life* V_N and the *Use Class* C_U the *reference period* V_R is obtained and the corresponding return period T_R (Sect. 12.5.1). Using this parameter it is possible to define the earthquake intensity used to design both the superstructure (Life Limit State SLV) and the isolators (Collapse Limit State – CLS).

Table 19.1 Nominal life

	Construction type	V_N (years)
1	Provisional structures	≤ 10
2	Ordinary structure	≥ 50
3	Great structure	≥ 100

Table 19.2 Use class

Usage classes	Description	C_u
I	Buildings of little importance	0.7
II	Buildings with normal crowds	1.0
III	Building whose use involves significant crowding	1.5
IV	Strategic construction	2

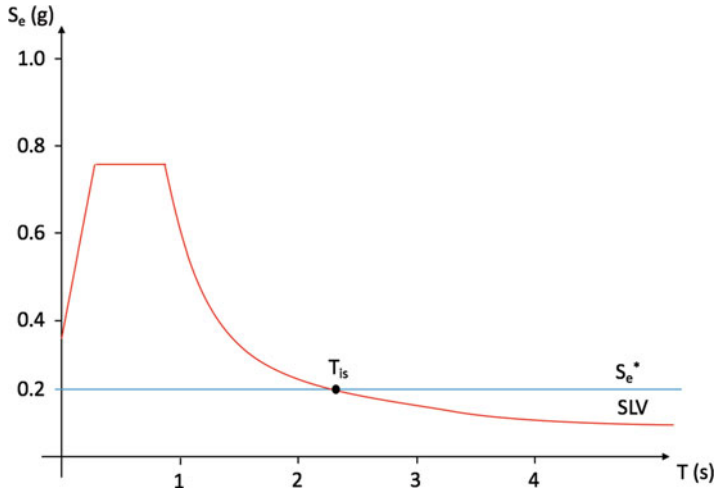


Fig. 19.30 Isolated period corresponding to the target spectral acceleration S_e

Third, the period T_{is} of the isolated building is chosen according to the following considerations:

- using the spectral acceleration S_e of the superstructure that is used as input in the response spectrum (Fig. 19.30) at the site to determine the target period of the isolated structure;
- the period of the isolated structure should be higher than the fixed-based period ($T_{is} \gg T_{bf}$), where T_{bf} is the period of the fixed base structure.
- the total displacements at the isolation level should be maintained within acceptable limits.

Regarding the first item the spectral acceleration S_e can be determined for *existing structures* from the vulnerability analysis corresponding to the Life Limit State (SLV) of the superstructure. Instead for new structures S_e^* is chosen according to architectural-functional and economic considerations. Then, the isolated period is:

$$T_{is} = 2\pi \sqrt{\frac{W}{k_{esi}}} \quad (19.73)$$

where k_{esi} is the global stiffness of the isolated system, and it is used to estimate the number of isolators using Eq. 19.74.

$$n = \frac{k_{esi}}{k_e} \quad (19.74)$$

where k_e is the stiffness of a single rubber bearing that can be selected from a catalog, using the stiffness k_e and the allowable displacements that should be

compatible with the spectral displacements corresponding to the target spectral accelerations and to the position of the rubber bearings. Multiple choices are possible, therefore the final design is selected by optimizing the dynamic behavior of the building and limiting the torsional effects of the superstructure that might cause excessive displacements on the bearings. The torsional effects can be minimized by reducing the distance between the projection of the center of mass of the building at the base isolation level and the center of stiffness of the bearings. The choice between the different technical options can be performed also on the basis of economic considerations. However at least eight rubber bearings are recommended and they should be located along the perimeter of the building. Finally in each bearing tension forces should be avoided or limited. The design vertical load V on each bearing during the seismic action should be always in compression or null. Furthermore it is also advisable to minimize the differences in behavior between bearings. For example the compression forces in normal operating conditions should be distributed uniformly among bearings.

References

- Aiken I (1997) Dampers for seismic protection: 1. Friction and viscous damper; 2. Viscoelastic and metallic dampers. In: Technical seminar on seismic isolation and energy dissipation technology, vol 11
- Blakeley R (1982) Code requirements for base isolated structures. In: Proceedings international conference on natural rubber for earthquake protection of buildings and vibration isolation
- Den Hartog JP (1956) Mechanical vibrations, 4th edn. McGraw-Hill Book Company, Inc., New York
- Filiatrault A, Christopoulos C (2006) Principles of passive supplemental damping and seismic isolation. IUSS press, Pavia
- Iwan WD (1965) The steady-state response of the double bilinear hysteretic model. ASME, New York
- Kelly J (1997) Earthquake-resistant design with rubber bearing. Springer, London
- Kelly JM (1999) The role of damping in seismic isolation. Earthq Eng Struct Dyn 28(1):3–20
- Kelly J, Naeim F (1999) Design of seismic isolated structures, from theory to practice. Wiley, New York
- Moretti S, Trozzo AC, Terzic V, Cimellaro GP, Mahin S (2014) Utilizing base-isolation systems to increase earthquake resiliency of hospitals and schools buildings. Proc Econ Finance 18(2014):969–976. [https://doi.org/10.1016/S2212-5671\(14\)01024-7](https://doi.org/10.1016/S2212-5671(14)01024-7)
- NTC-08 (2008) Nuove Norme Tecniche per le Costruzioni. Gazzetta Ufficiale della Repubblica Italiana
- Skinner RI, Robinson WH, McVerry GH (1993) An introduction to seismic isolation. Wiley, New York

Chapter 20

Masonry Structures



Abstract This chapter focuses on the seismic behaviour of masonry structures. A brief description of the types of masonry is provided. The collapse mechanisms related to masonry structures are discussed in details both for single-story and multi-story buildings.

20.1 Introduction

Masonry is a commonly used material for structural and non-structural components in buildings. Masonry structures provide more comfortable environment (e.g. reducing the amount of energy necessary for the internal air conditioning), give a nice appearance to buildings, and offer an excellent fire protection cover. Nevertheless, masonry structures are significantly vulnerable to the seismic excitation because they tend to be heavy (high vertical load in foundation). In addition, they are highly susceptible to extreme weather degradations (Paulay and Priestley 1992). Currently, approximately 10% of the new residential buildings in Italy are made using masonry as main structural element while a notable part of built environment in Europe (e.g. residential buildings, public offices, cathedrals, churches etc.) are made of masonry. Furthermore, the use of masonry as a construction material is growing in European and non-European Countries (Magenes 2006). The study of the seismic behaviour of masonry structures is fundamental to protect the cultural heritage (Arcidiacono et al. 2016) and to prevent severe damage on residential buildings. Recently NTC-08 (2008) and EN-1996 (2009) introduced new criteria for the safety and durability of masonry buildings.

20.2 Types of Masonry

Masonry is a construction material consisting of natural or artificial blocks and (not necessarily) a binder (Magenes et al. 2010). Figure 20.1 shows a dry masonry made of stone, while in Fig. 20.2 the units are artificial blocks (bricks) bounded together with mortar.

There are a number of bricks that can be used, but they can be divided in *solid bricks*, with a percentage of holes less than 15% of the brick volume, *hollow bricks*, with a percentage of holes between 15% and 45% of the brick volume, *perforated bricks*, in which holes are greater than 45% of the brick volume (Fig. 20.3).

Different thicknesses of the wall can be obtained using various types of bricks. For example, a layer of wall that is one unit thick is called “wythe”. In fact, walls with two wythes or core walls are common as well, especially in older buildings (Fig. 20.4). In addition, the wythe may consist of half brick or one brick.

Observing the various wall textures, different types of masonry can be identified. If different size units are used, the masonry is irregular (Fig. 20.5), whereas if stones are almost the same size and they are not modified, the result is a rough stone masonry where the units fit together like puzzle pieces (Fig. 20.6). Figure 20.7 shows a masonry consisting of cobblestones bounded with mortar. To improve the stability, one or two courses of bricks were alternated to cobblestones with a regular



Fig. 20.1 Dry masonry

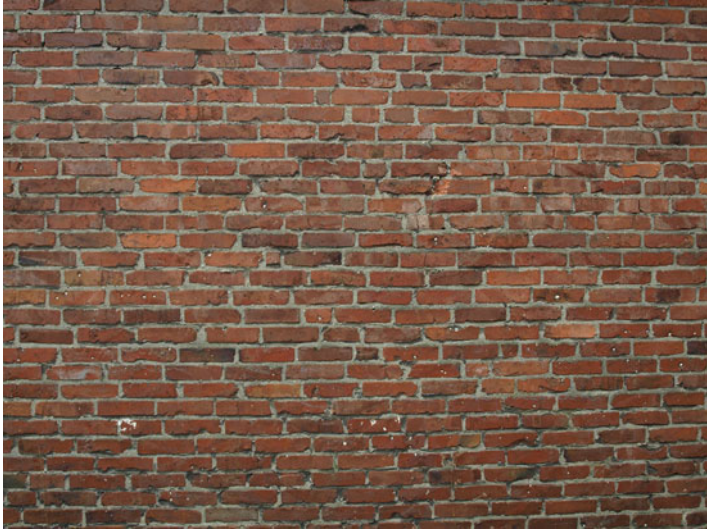


Fig. 20.2 Brick masonry

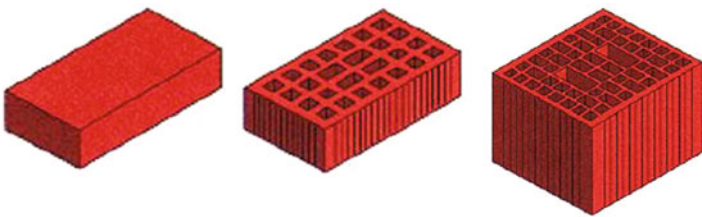


Fig. 20.3 Example of a solid, hollow, perforated brick

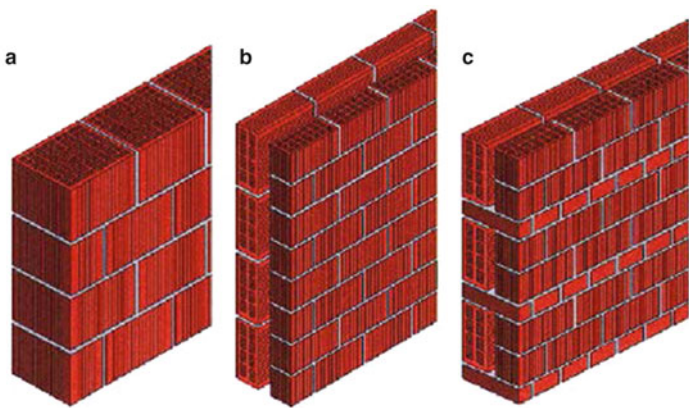


Fig. 20.4 (a) Single wythe wall; (b) two wythe wall; (c) core wall

Fig. 20.5 Irregular masonry

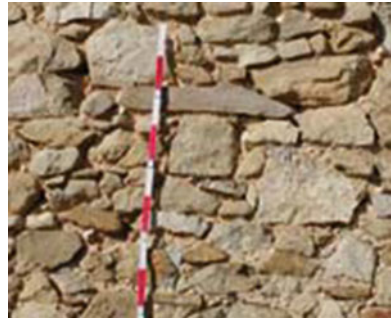
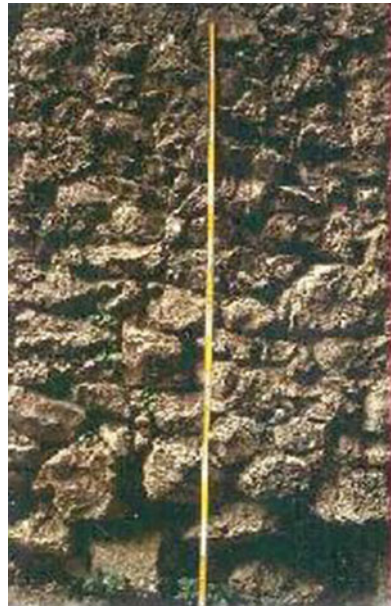


Fig. 20.6 Rough stone masonry



span: this is the so called *listatum masonry* (Fig. 20.8). Squared blocks of stone are instead used to obtain a better surface. In Fig. 20.9 there is an example of a wall consisting of an external wythe of squared stones and an internal wythe of cobbles bounded with mortar. Using squared and regular blocks leads to have horizontal courses, and consequently a better distribution of loads.

A classification of masonry has been done assigning a description and a code to each type of wall. Table 20.1 illustrates the classification of some walls made of artificial blocks, while Table 20.2 shows the ones made of natural blocks.

Fig. 20.7 Cobblestone masonry



Fig. 20.8 Listatum masonry



The mechanical behavior of a masonry wall depends on its construction quality. Figure 20.10 illustrates three kind of behavior grouped according to the construction quality. Good quality masonry has a monolithic behavior (a), while poor quality masonry (c) shows a chaotic disaggregation.

Fig. 20.9 Wall with two wythes: the external one is made of squared blocks, the internal one consists of cobblestones



The quality of masonry is strictly dependent on the construction empirical rules used to built it. The main principles to obtain a high quality masonry walls are resumed below

- presence of diatoms (or headers), bricks or units that are laid from side to side of the wall for a better tooting (Fig. 20.11) ;
- squared stones with proper dimensions;
- good properties of the mortar.
- staggered head joints, for a homogeneous distribution of load as shown in Fig. 20.12;

20.3 Collapse Mechanisms of Masonry Buildings

Collapse mechanisms can be divided in two categories that are summarized in Table 20.3: the first mechanism is due to out-of-plane forces and the second one is due to in plane actions (Milano et al. 2008; Giordano et al. 2002). Naturally, the wall's strength is dependent on the plane where the loads are applied. In-plane strength is higher than the out-of-plane strength. To give the appropriate resistance to the whole building, it is necessary that walls and floors are connected in an effective way to achieve the so called "box-like" behavior (Fig. 20.13).

Table 20.1 Types of masonry made of artificial blocks

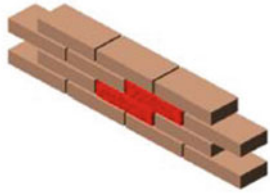
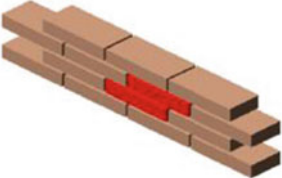
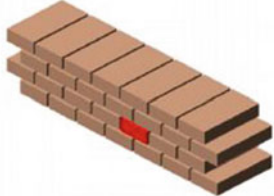
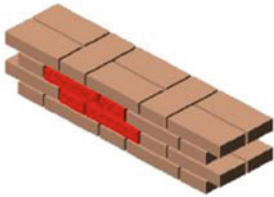
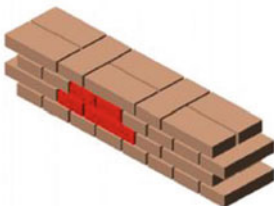








Type and texture pattern	Description	Code
	Half brick wall. Header joints staggered of 1/2 of the block length	A1a
	Half brick wall. Header joints staggered of 1/3 of the block length	A1b
	One brick wall only consisting of diatoms	A2a
	One brick wall. "Gothic" texture	A2b
	One brick wall. "Flemish" texture	A2c

Table 20.2 Types of masonry made of natural blocks

Type and texture pattern	Description	Code
	Stonework with worked and squared blocks	L1a
	Stonework with worked blocks	L1b
	Freestone wall with pseudo-rectangular units	P1a
	Freestone wall with pseudo-rectangular units laid in sub-horizontal courses	P1b

(continued)

Table 20.2 (continued)

Type and texture pattern	Description	Code
	Freestone wall with pseudo-rectangular units laid in a chaotic way	P1c
	Freestone wall with smoothed units	P1d
	Hewn stone wall with regular courses	S1a
	Hewn stone wall with courses of different height	S1b

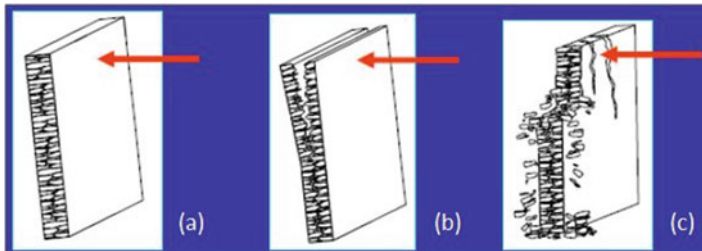


Fig. 20.10 (a) Good quality masonry; (b) medium quality masonry; (c) poor quality masonry (Giuffrè 1991)

Fig. 20.11 Diatoms and stretchers

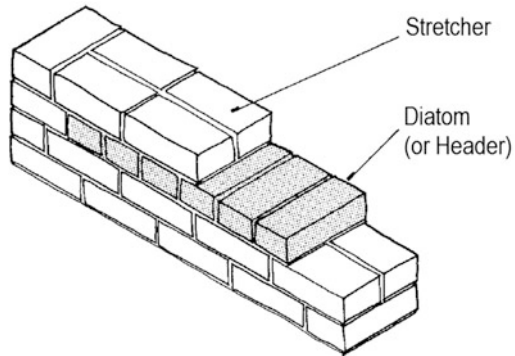
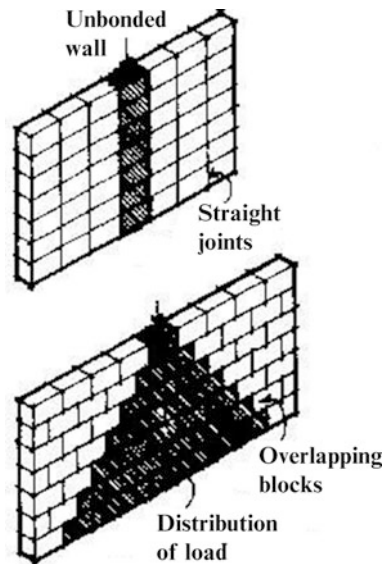


Fig. 20.12 Distribution of load in a straight joint wall and in a staggered joint wall



20.3.1 *In-Plane Failure Mechanisms of a Single-Story Masonry Building*

The failure mechanisms of a masonry wall will be analyzed in the following paragraph using a masonry wall subjected to compression and shear stress in the two upper and lower sections, as case study (Fig. 20.14, Tucker 2007).

The resulting stresses are contained in the middle plane of the wall. Considering a generic horizontal wall section, the value of the shear V , moment M , and axial actions N can be defined by imposing the translational (in vertical direction) and rotational equilibrium.

$$N_{inf} = N_{sup} + P \tag{20.1}$$

$$M = V \times H = N_{bot} \times e_{bot} + N_{top} \times e_{top} \tag{20.2}$$

Table 20.3 Types of collapse mechanisms (Touliatos 1996)

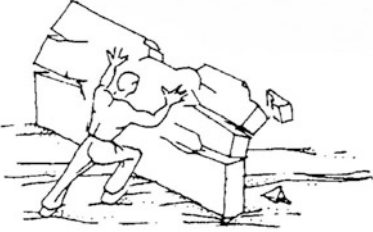
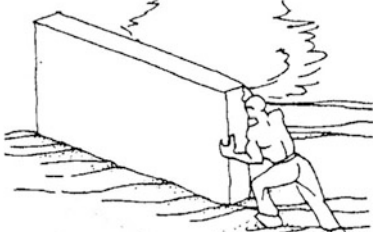
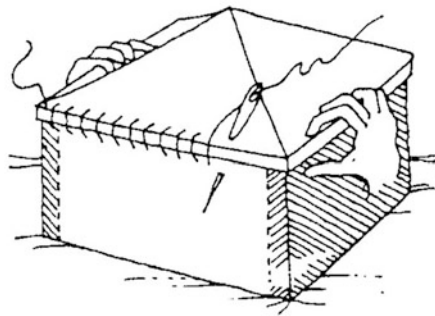
Collapse mechanisms	
Out-of-plane	In plane
	
<ul style="list-style-type: none"> • Simple overturning • Combined overturning • Vertical flexure • Horizontal flexure 	<ul style="list-style-type: none"> • Shear strain mechanisms • Settlement of the foundations

Fig. 20.13 The building like a box (Touliatos 1996)



where N_{bot} and N_{top} refers to the axial load acting on the top and bottom sections of the wall, respectively. The total weight of the masonry wall is identified by the term P , while H is the height of the wall and l its width. The compression load eccentricities are defined as e_{bot} and e_{top} , respectively on the bottom and on the top section of the wall. Three different failure modes are identified for the case study masonry wall (Fig. 20.15)

- failure of the wall caused by combined compressive and bending stress;
- failure of the wall caused by shear with diagonal cracking;
- failure of the wall caused by shear with sliding.

Fig. 20.14 Wall subjected to compression and shear

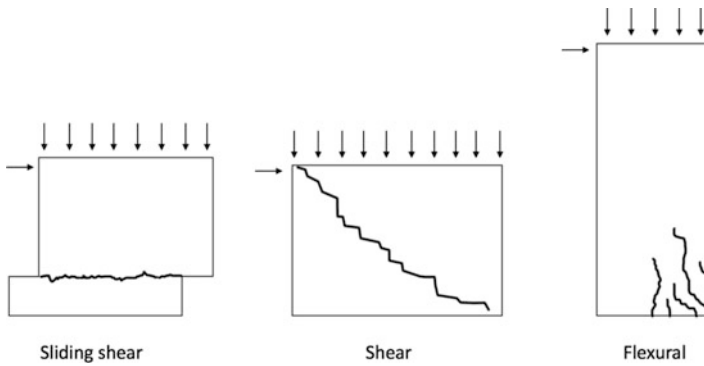
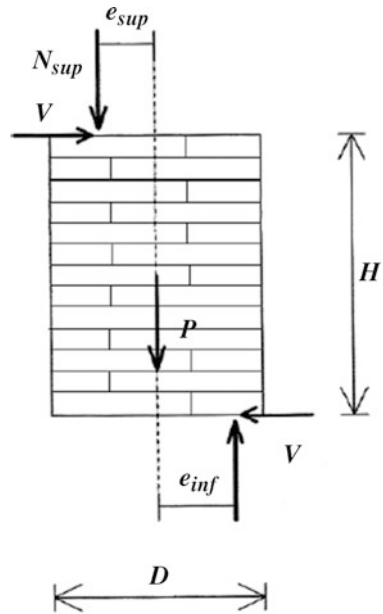


Fig. 20.15 Possible mechanisms of crisis for panels stressed in plane

20.3.1.1 Failure Caused by Combined Compressive and Bending Stress

This collapse mechanism occurs whenever low normal load values are applied on the panel. In fact, when the wall is subjected to a low axial stress, the compressed area is much smaller than the tensile area. This allows the formation of cracks in a wide part of the masonry panel. The analysis of break-through behavior for compression can be facilitated by using a suitable “stress-block” model of the compressed masonry (Fig. 20.16).



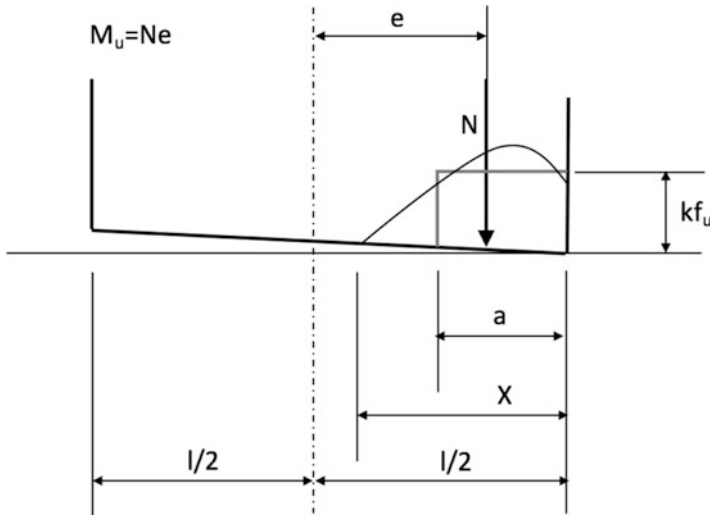


Fig. 20.16 Distribution of the tensions in the compressed strip

By imposing the equilibrium in the vertical direction, the equivalent compressed width a can be identified.

$$a = \frac{N}{k f_u t} \tag{20.3}$$

where k is a coefficient that takes into account the actual nonlinear distribution of the strain in the base section, and it can be assumed between 0.85 and 1.00. The compression strength of the wall is represented by f_u whereas the wall thickness is identified by t . Furthermore, the ultimate bending moment M_u is obtained through the rotational equilibrium equation.

$$M_u = N \left(\frac{l - a}{2} \right) = \frac{Nl}{2} \left(1 - \frac{N}{k f_u t} \right) \tag{20.4}$$

where l is the width of the masonry panel. Considering the mean values of compression acting on the top section (p), the ultimate shear V_u can be defined as below

$$V_u = \frac{p l^2 t}{2 H_0} \left(1 - \frac{p}{k f_u} \right) = \frac{p l t}{2 \alpha_v} \left(1 - \frac{p}{k f_u} \right) \tag{20.5}$$

where α_v represents the shear factor defined as below

$$\alpha_v = \frac{M}{V L} = \frac{H_0}{L} = \Psi' \frac{H}{D} \tag{20.6}$$

where H_0 is the distance from the base to the “null moment” section. The ratio $\frac{H}{D}$ represents the shape factor while Ψ' is a coefficient representing the restraint conditions of the wall. A value of 1.0 is assumed when the top section is free to

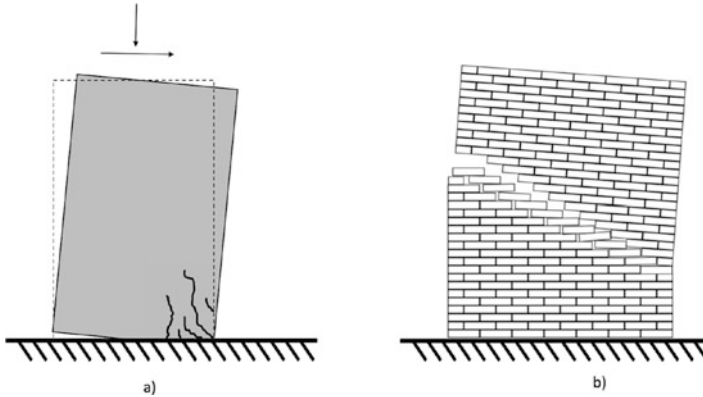


Fig. 20.17 Failure caused by combined compressive and bending stress

rotate and the bottom one is fully restrained (cantilever configuration), while it is equal to 0.5 if the top section can only translate without rotating (Fig. 20.17b).

20.3.1.2 Failure of the Wall Caused by Shear with Diagonal Cracks

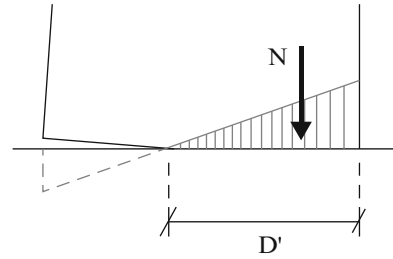
The failure mechanism caused by shear with diagonal cracking in simple masonry panels usually leads to the formation of one or more inclined cracks. These diagonal cracks are mainly propagated through the mortar joints or, in the case of high quality binders, through the bricks or the blocks. The diagonal cracks occurs when total shear values is close to the maximum shear resistance ($V_{crack} = (0.85 - 1.00)V_u$). The cracking will start at the center of the panel and then propagate towards the ends. The shear failure with diagonal cracking is considered as fragile mechanism. When the shear action is cyclic, it causes the formation of two systems of cross-diagonal cracks. Turnšek and Čačovič (1971) proposed a formulation to assess the resistance of walls subjected to diagonal cracks. The failure of the wall occurs when the main stress is equal to the tensile resistance f_{tu} . Assuming that the panel is sufficiently thin to be assimilated to a solid of De Saint Venant, the shear strength is given by the following equation

$$V_u = \frac{f_{tu}lt}{b} \sqrt{1 + \frac{N}{f_{tu}lt}} \quad (20.7)$$

where b is a coefficient dependent on the slenderness ratio H/B . This coefficient is equal to 1.5 when $H/D \geq 1.5$ and $b = 1.0$ when $H/D < 1.5$. The aforementioned mathematical formulation leads to accurate results when the rotation of the two extreme sections of the wall is limited. Alternatively, the conventional Mohr-Coulomb's approach can be used. In this case the shear strength of the masonry is expressed as below

$$\tau = c + \mu\sigma \quad (20.8)$$

Fig. 20.18 Normal stress on the base cross section of the panel subjected to bending moment and shear



where c and μ are the cohesion and the friction coefficient of the masonry. The tangential and normal stress are represented by τ and σ , respectively.

20.3.1.3 Failure of the Wall Caused by Shear with Sliding

Shear stress can also induce the formation of one or more sliding surfaces on the masonry wall due to the presence of cracks along the bed mortar. The crack propagation causes a rigid kinematic sliding between the two parts of the wall separated from the sliding surface. This mechanism occurs in masonry elements subjected to bending moment at the base which causes the partialization of the base cross section. According to the current technical standards, the shear strength of masonry element is expressed as shear masonry strength multiplied by the effective shear area, which can be identified as the compressed area of the considered cross section by neglecting the tensile resistance contribution (Fig. 20.18).

The shear strength is identified as expressed in the following equation.

$$V_u = f_{vk} t D' \quad (20.9)$$

where D' represents the length of the compressed base cross section, while f_{vk} is the considered shear strength which can be obtained as follow

$$f_{vk} = f_{vk0} + 0.4\sigma_d \quad (20.10)$$

where σ_d is the mean value of compression in the base cross section and f_{vk0} is the characteristic shear strength of the masonry.

20.3.2 In-Plane Failure Mechanisms of a Multi-story Masonry Building

This section summarizes the aforementioned mechanism of crisis in plane applied to a multi-story building.

- **Shear failure: discontinuity along the height** (Figs. 20.19 and 20.20)
- **Shear failure: shear strain** (Figs. 20.21 and 20.22)
- **Settlement of the foundations** (Figs. 20.23 and 20.24)

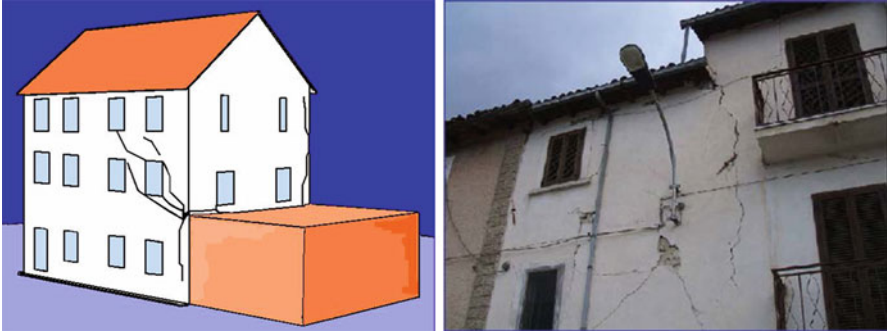


Fig. 20.19 Shear failure due to discontinuity along the height (Milano et al. 2008)



Fig. 20.20 Damages due to discontinuity along the height, Arquata 2016

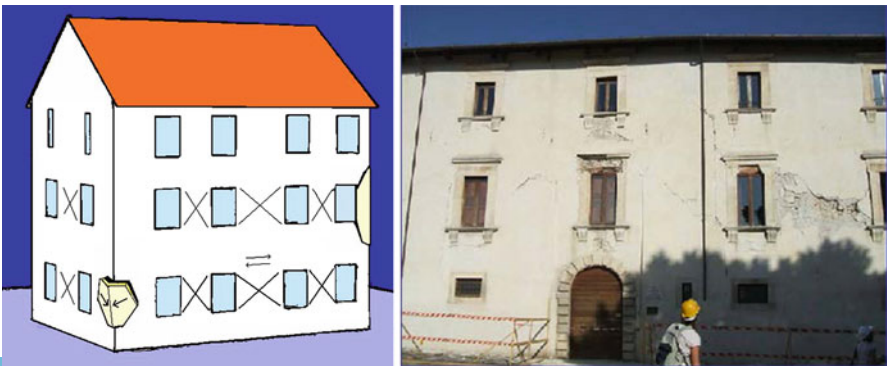


Fig. 20.21 Cracking due to shear strain (Milano et al. 2008)



Fig. 20.22 Diagonal cracks due to shear strain, Arquata 2016

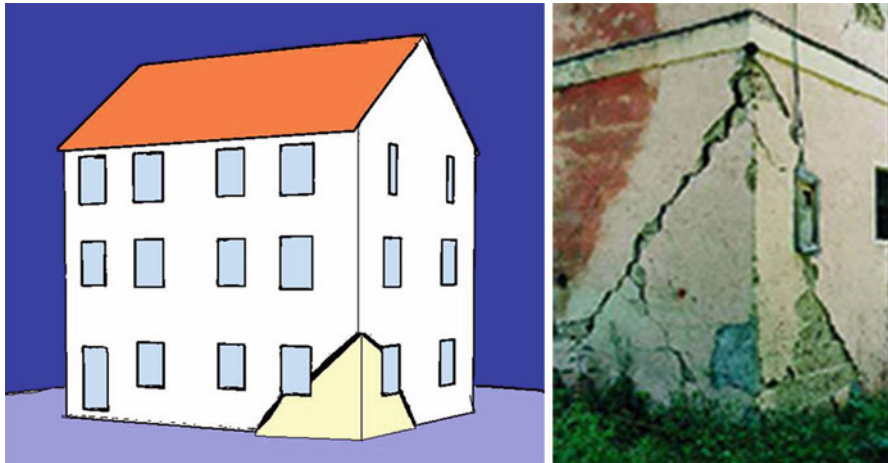


Fig. 20.23 Settlement of the foundations (Milano et al. 2008)

20.3.3 *Out-of-Plane Failure Mechanisms of a Single-Story Masonry Building*

The most frequent cases of out-of-plane collapse mechanism of ordinary single-story buildings are below listed and discussed in detail.



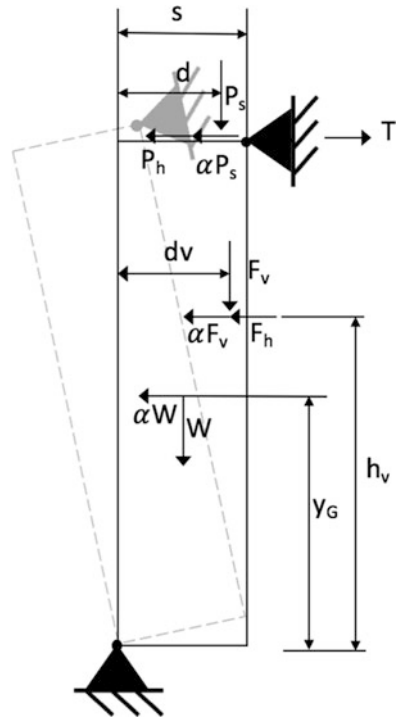
Fig. 20.24 Settlement of the foundations, Arquata 2016

- **Simple Overturning:** it can occur on buildings with monolithic and double curtain walls, and the overturning mechanism can involve one or multiple floors of the building in relation to the constraint conditions found at the various levels.
- **Composite Overturning:** it can occur on walls effectively connected to the orthogonal and free top walls, with different configurations of the detachment wedge and with the possibility that the tilting mechanism involves one or more floors of the building in relation to the constraint conditions observed at the various levels.
- **Vertical Flexure:** it is due to the effect of the orthogonal actions on the wall's plane, with the formation of a horizontal cylindrical hinge. The wall structure is divided into two rigid blocks rotating mutually around the hinge.
- **Horizontal Flexure:** it is due to the effect of the orthogonal actions on a wall's plane and is characterized by the formation of the detachment wedges consisting of macro-elements that rotate rigidly around cylindrical hinges located at their base.

20.3.3.1 Simple Overturning of a Single-Story Monolithic Wall

This is the case where the lack of connection at the top of the overturning wall concerns only the last floor of the building. The overturning of the entire wall or parts of it can be facilitated by a thrusting roof. The seismic action is represented by a horizontal force which is equal to the vertical loads multiplied by a coefficient α that is called collapse multiplier.

Fig. 20.25 Simple overturning mechanism



The collapse multiplier α_0 that determines the activation of the kinematic mechanism is evaluated imposing the rotational equilibrium in overturning conditions. In other words, the collapse multiplier can be obtained from the equilibrium equation between the overturning moment, given by the forces that determine the overturning, and the stabilizing moment, given by the forces that oppose to this rotation. Referring to Fig. 20.25 and considering the rotation around the hinge A, the following parameters are defined:

- W is the weight of the wall;
- F_V is the vertical component of the thrust of the arches;
- F_H is the horizontal component of the thrust of the arches;
- P_S is the weight of the floor calculated according to the influence area;
- P_H represents the static thrust of the roof;
- T represents the maximum value of the force exerted by the tie rod;
- s is the thickness of the wall;
- h is the height of the wall affected by the overturning with respect to the hinge A at the bottom;
- h_V is the distance between A and the point where the thrust of arches is applied;
- d is the horizontal distance between A and the point where the weight of the floor is applied;
- d_V is the horizontal distance of the force F_V from A;

- y_g is the height of the center of mass of the wall with respect to A ;
- α is the multiplier of loads.

Considering the rotation around point A , the stabilizing moment is given by

$$M_{S(A)} = W \frac{s}{2} + F_V d_V + P_S d + T h \quad (20.11)$$

while the overturning moment is given by

$$M_{R(A)} = \alpha [W y_G + F_V h_V + P_S h] + F_H h_V + P_H h \quad (20.12)$$

By equating the two terms, the collapse multiplier can be obtained

$$\alpha = \frac{W \frac{s}{2} + F_V d_V + P_S d + T h - F_H h_V - P_H h}{W y_G + F_V h_V + P_S h} \quad (20.13)$$

When calculating the forces' distances, it is important to consider the real geometry of the macro-elements. For instance, the presence of cracks in a wall generally modifies the position of its center of mass, resulting in a change of the value of the moment. In addition, the identification of different macro-elements with irregular geometry allows to consider a more realistic distribution of the horizontal loads applied to the structure.

Finally, removing the assumption of infinite strength of the masonry, it is possible to consider the position of the hinge within the thickness of the wall, corresponding to the position of the resultant compression force at the base. The simple overturning mechanism of a monolithic wall can involve many storeys when the floors are simply supported by the walls and there are no devices that can avoid the rotation at different levels. In this case, it should be considered the possibility that the wall, also subjected to the thrust exerted by the floors, undergoes overturning around different positions of the hinge. This means that the condition with the smaller collapse multiplier should be evaluated.

20.3.3.2 Simple Overturning on a Single-Story Two Wythe Wall

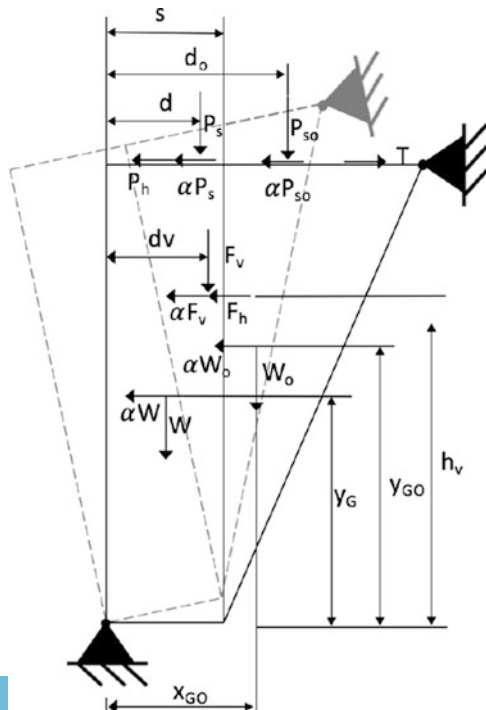
In historical buildings often there are masonry walls that do not guarantee monolithic behavior due to the lack of connecting diatoms between the wythes. In this case, the wythes have almost independent behavior, which makes difficult to define a reliable model. A simplified method could be to consider two separated walls with hinges at the base as constraints and a restraint distributed along the height. This restraint can be represented as a continuous distribution of mono-directional rollers which allows to transfer compression loads between the walls. During a seismic event, it is therefore possible that the inner wythe transfers part of its inertia to the external one. The resulting increased bending moment combined with a lower vertical force of compression, is the cause of collapse of the external wall. In this configuration, horizontal forces cannot be transferred from one wall to the other unless the rigid block assumption is removed.

20.3.3.3 Composite Overturning of a Diagonal Wedge

The overturning mechanism consists in the rigid rotation of the walls around horizontal cylindrical hinges and the dragging of masonry portions belonging to the counter walls. The activation of this type of mechanism requires a good connection between the corner walls involved and no effective connections at the top of the overturning macro-element, as in the case of simple overturning. The kinematic mechanism is also facilitated by pushing roofs and the poor quality of the spine walls. Also, the quality of the masonry of the facade determines the size of the detachment wedge and thus the value of the α coefficient, as α increases with the increase of the masonry portion involved in the overturning. Once the geometry of the macro-element and the boundary conditions are defined, all the variables of the model can be evaluated. Referring to Fig. 20.26, the following parameters are defined:

- W_0 is the dead weight of the detachment wedge (including any loads transferred by arches or vaults);
- P_{S0} is the weight of the floor supported by the wedge calculated according to the influence area;
- d_0 is the horizontal distance between the load P_{S0} and the point A;
- x_{G0} is the horizontal distance between the center of gravity and the point A;
- y_{G0} is the height of the center of gravity with respect to the hinge in A.

Fig. 20.26 Composite overturning mechanism



The *stabilizing moment* of the forces acting on the system is given by

$$M_{S(A)} = W\frac{s}{2} + F_V d_V + W_0 x_{G0} + P_S d + P_{S0} d_0 + Th \quad (20.14)$$

The *overturning moment* is

$$M_{R(A)} = \alpha [W y_G + W_0 y_{G0} + F_V h_V + P_S h + P_{S0} h] + F_H h_V + P_H h \quad (20.15)$$

By equating the two terms, the collapse multiplier is given by

$$\alpha = \frac{W\frac{s}{2} + F_V d_V + W_0 x_{G0} + P_S d + P_{S0} d_0 + Th + F_H h_V + P_H h}{W y_G + W_0 y_{G0} + F_V h_V + P_S h + P_{S0} h} \quad (20.16)$$

It should be noted that in the case of corner or isolated buildings the overturning can take place along both the longitudinal and transversal directions. This consideration can be neglected when the walls' lengths in the two main directions are not comparable. In this situation the building has a larger vulnerability to the overturning along the orthogonal direction of the larger facade. Also for this mechanism evaluating the position of the center of mass with respect to the cylindrical hinge is important and it allows to take into account irregular geometries of the macro-elements. Therefore, it is thus possible to define a more realistic distribution of the horizontal loads applied to the wall. Lastly, it is possible to consider a reduced strength of the masonry assuming the position of the cylindrical hinge within the wall thickness.

20.3.3.4 Composite Overturning Mechanism of the Angle

This mechanism involves the overturning of the upper part of the angle of the building. It consists in the rotation of a wedge delimited by cracks in the corner walls. The angle overturning mechanism is generally caused by the thrust of the roof, the lack of connection at the top of the orthogonal walls and the poor quality of the masonry. It is assumed that the overturning occurs around an axis passing through a point (hinge) and perpendicular to a plane containing the edge which forms a 45° angle with the walls. The 45° angle can be considered a good approximation of the thrust direction of a rafter in a hipped roof. The two schemes of Fig. 20.27 show a three-dimensional and in-plane view of the angle overturning mechanism. The following notations have been applied:

- W is the weight of detachment angle;
- P is the vertical load transferred by the rafter;
- P_H is the static thrust transferred by the rafter in the overturning direction;
- F_V is the vertical component of the thrust of the arches exerted on one of the two walls;
- P_H represents the projection of the horizontal component of the thrust of arches calculated as: $F'_H = (\frac{\sqrt{2}}{2})F_h$;
- P_{Vi} is the vertical load at the top of the i -th wall;

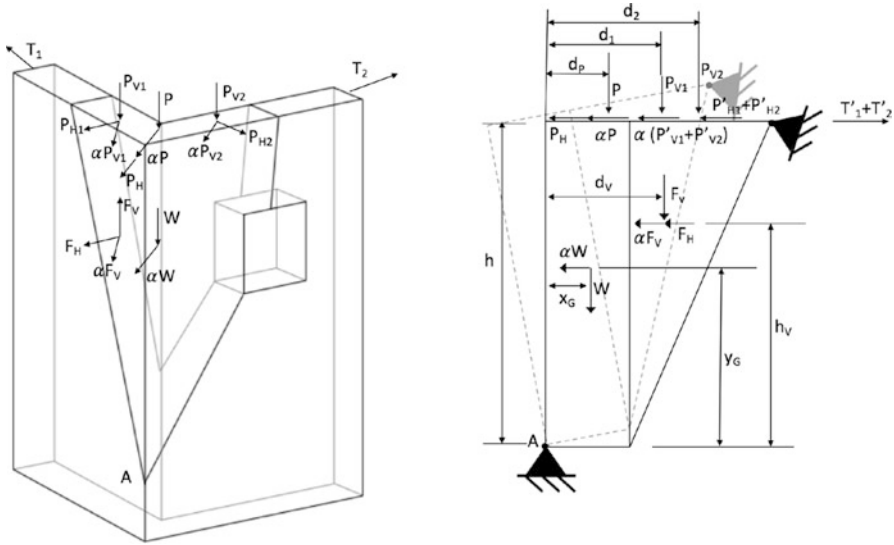


Fig. 20.27 Cantonal overturning mechanism and in-plane projection of the mechanism

- P'_{Hi} represents the projection in the overturning direction of the static thrust of the roof to the i -th wall, given by: $P'_{Hi} = (\frac{\sqrt{2}}{2})P_{hi}$;
- T'_i is the projection of the force exerted by the i -th tie rod, evaluated as: $T'_i = (\frac{\sqrt{2}}{2})T_i$;
- h is the height of the wedge with respect to the hinge in A ;
- h_v is the height of the point where the thrust of the arches with respect to the hinge A ;
- y_G is the position of the wedge's center of gravity with respect to the hinge in A ;
- d_p is the horizontal distance of the rafter's load with respect to A ;
- d_v represents the horizontal distance of the point where the load of the arches is applied with respect to the hinge in A ;
- d_i is the horizontal distance of the point where the vertical load at the top of the i -th wall is applied with respect to the hinge A ;
- x_G is the horizontal distance of the wedge's center of mass.

The stabilizing moment is given by

$$M_{S(A)} = Wx_g + F_v d_v + P d_p + P_{V1} d_1 + P_{V2} d_2 + (T'_1 + t'_2)h \tag{20.17}$$

The overturning moment is equal to

$$M_{R(A)} = \alpha[Wy_g + F_v h_v (P + P_{V1} + P_{V2})h] + F'_H h_v + (P_H + P'_{H1} + P'_{H2})h \tag{20.18}$$



- F_h is the horizontal component of the arch/vault's thrust on the wall;
- P_s is the effective weight of the floor acting on the wall;
- N is the weight of the wall;
- h_v is the vertical distance between the application point of the arch/vault's thrust and the point B shown in Fig. 20.28;
- d is the horizontal distance from the point B and the load N ;
- d_v is the horizontal displacement in the point where the hinge has formed;
- a is the horizontal distance between the point B and the load P_s ;
- h_1 is the height of body 1;
- h_2 is the height of body 2.

In order to describe the kinematic mechanism, the compatibility equations in terms of displacements have to be identified as $(\mu_{01}; v_{01}; \theta_{01}) = (\mu_A; v_A; \Psi) = (0; 0; 1)$ and $(\mu_{02}; v_{02}; \theta_{02}) = (\mu_B; v_B; \varphi) = (0; s; -\frac{h_1}{h_2})$

The geometric parameter h_2 can be expressed as ratio between the total height of the wall and a coefficient μ which assumes values greater than 1. Then, the virtual displacements due to the application of the considered load system are given below.

$$\begin{aligned} \delta_{1x} &= \frac{h}{2} \frac{\mu - 1}{\mu} & \delta_{1y} &= \frac{s}{2} \\ \delta_{2x} &= \frac{h}{2} \frac{\mu - 1}{\mu} & \delta_{2y} &= \frac{s}{2} (\mu + 1) \\ \delta_{Vx} &= h_v (\mu - 1) = -\delta_h & \delta_{Vy} &= s + d_v (\mu - 1) \\ \delta_{Px} &= s + a (\mu - 1) = -\delta_h & \delta_{Ny} &= s + d (\mu - 1) \end{aligned} \quad (20.20)$$

By applying the virtual work principle, Eq. 20.21 is obtained.

$$\alpha [W_1 \delta_{1x} + W_2 \delta_{2x} + F_V \delta_{Vx}] + F_H \delta_{Vx} - W_1 \delta_{1y} - W_2 \delta_{2y} - N \delta_{Ny} - P_s \delta_{Py} - F_V \delta_{Vy} = 0 \quad (20.21)$$

Then, the parameter α is identified.

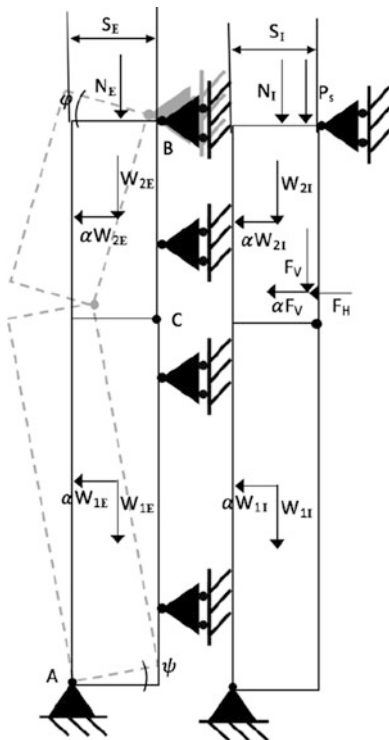
$$\alpha = 2 \frac{(\mu - 1)(Nd + P_s a + F_V d_v - F_H h_v) + s(W + N + P_s + F_V)}{(\mu - 1) \left(\frac{Wh}{\mu + 2F_V h_v} \right)} \quad (20.22)$$

Equation 20.22 shows that α depends on the parameter μ . The minimum value assumed by α is considered as representative of the collapse mechanism, and it is named as collapse multiplier. In order to evaluate the collapse multiplier, the first derivative of α with respect the coefficient μ has to be calculated and imposed equal to zero.

20.3.3.6 Vertical Flexure on a Single-Story Two-Wythes Wall

This case is similar to the previous one except for the number of wall's wythe. In this section the collapse mechanism of a two wythes wall is considered. The kinematic

Fig. 20.29 Vertical flexure on a single-story double curtain wall



mechanism is strictly dependent on the interaction between the two wythes. Usually the collapse mechanism can be described through the formation of an hinge in the external whyte, where the vertical loads are lower than the internal one. The scheme used to describe the kinematic mechanism is shown in Fig. 20.29.

The kinematic mechanism of the external whyte is substantially similar to that one analyzed in the previous section. The interaction between the two whytes is modeled through sliders. According to Fig. 20.29, the external whyte is divided in block 1 and 2, whereas the symbol *E* and *I* refers to the loads and displacements acting on the external and internal whyte, respectively. As explained in the previous section, the compatibility equations and the virtual displacements due to the application of the considered load system have to be identified. Then, the collapse multiplier is given by Eq. 20.23.

$$\alpha = \frac{(W_A s_A + N_A \frac{s_A}{2} (\mu + 1) - \rho F_H h_V (\mu - 1))}{\frac{h (\mu + 1)}{2 \mu} (W_A + \rho W_B) + \rho F_V h_V (\mu - 1)} \tag{20.23}$$

where ρ is the percentage of horizontal loads transmitted from the internal whyte to the external one. This coefficient depends on the characteristics of the internal whyte and on the level of connections between the two whytes. Also in this case, the first derivative of α with respect to the coefficient μ has to be calculated and fixed to zero.

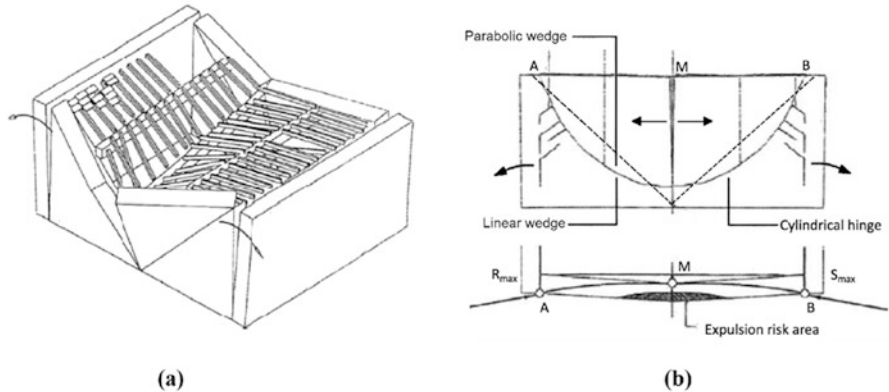


Fig. 20.30 Non-confined Horizontal flexure mechanism

20.3.3.7 Horizontal Flexure of a Non-confined Monolithic Wall

Figure 20.30 depicts the kinematic mechanism considered in the case of non-confined masonry wall.

The horizontal load acting on the wall causes the formation of inclined cylindrical hinges which identify unstable wedge macro-elements (detachment wedges). Furthermore, the side walls, which are not confined with the considered wall, rotates around their bases due to the arches/vaults’ thrust. The size and shape of the detachment wedges is affected by the presence of openings into the wall. In the case of wall without openings, the shape of the detachment wedge is parabolic, but usually, the wedge’s shape is simplified as triangular (Fig. 20.30b). The construction quality of the masonry wall influences the size of the detachment wedge. High quality masonry wall leads to a reduction of the height and maximum width of the wedge. The horizontal force also causes the formation of another additional vertical hinge. Then, the kinematic mechanism is described through the rotation of the wedge around the two inclined cylindrical hinges, and the two parts of wedge have a relative rotation around the vertical hinge. The aforementioned rotations around the hinges’ system cause three displacement components. The first component is parallel to the wall and it tends to separate the two wedge’s part, whereas the second component is vertical. Furthermore, a displacement orthogonal to the wall causes the out-of-plane overturning. Since the vertical displacement is smaller than the other two components, it is common to neglect it. This assumption leads to consider the collapse as a bi-dimensional kinematic model (Fig. 20.31).

In Fig. 20.31 H is the reaction of the arches/vaults’ thrust which is parallel to the wall, while P_{vi1} and P_{vi2} are the horizontal load components acting on the first and second wedges, respectively. As mentioned in the previous cases of out-of-plane mechanism, the collapse multiplier can be obtained through the virtual work principle in terms of displacements. The terms ψ refers to the virtual rotation of the first wedge, and it is assumed equal to 1. The compatibility equations and the virtual displacements due to the application of the considered load system are identified and the collapse multiplier is obtained (Eq. 20.24).

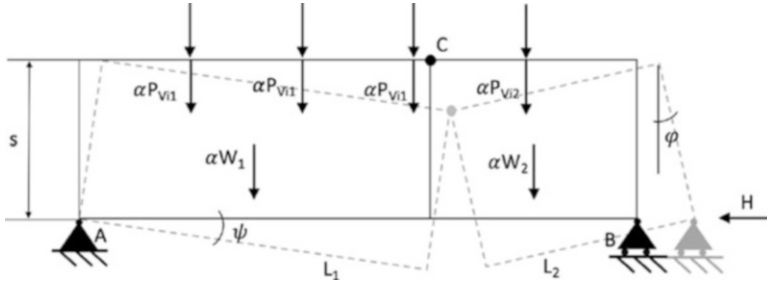


Fig. 20.31 Non-confined Horizontal flexure mechanism scheme

$$\alpha = \frac{Hs \left(1 + \frac{L_1}{L_2}\right) \frac{L_1}{L_2} d_{i2}}{W_1 x_{G1} + W_1 \frac{L_1}{L_2} x_{G2} + \sum_i P_{vi1} d_{i1} + \sum_i P_{vi2} \frac{L_1}{L_2} d_{i2}} \tag{20.24}$$

where d_{i1} and d_{i2} represents the distance between the loads applied on the wall and the associated rotation point (A and B for the first and second wedge, respectively).

20.3.3.8 Horizontal Flexure on a Confined Monolithic Wall

Masonry structures with tie bar system have a effective confinement into the wall plane. Nevertheless, the presence of arches/vaults generate an horizontal thrust on the masonry panel which can triggered a kinematic mechanism of horizontal flexure. This kinematic mechanism is similar to the previous one except for the additional restraint due to the orthogonal walls which are connected to the considered wall and/or to the tie bars system. Figure 20.32a depicts a top view of a masonry wall subjected to an uniformly distributed horizontal load due to the arches/vaults (p_H) and to αp which represents the monotonic horizontal load applied on the wall. F_H is the resultant of the horizontal loads system, while T and H represent the horizontal component of the arch/vault on the wall plan (R). L is the distance between the two orthogonal walls, f is the arch/vault's rise, and s is the thickness of the wall. The orthogonal walls and/or the tie bars system provide additional horizontal stiffness. Considering an effective confinement of the considered wall with the orthogonal ones, the horizontal thrust H is completely carried by the orthogonal walls. Thus, the overturning collapse mechanism is avoided.

The horizontal flexural mechanism is activated when the horizontal loads system leads to the formation of plastic hinges on the masonry wall. The horizontal flexure mechanism is studied by considering a portion of wall which have an height of b (Fig. 20.32c). Furthermore, the following assumptions are considered:

- Negligible tensile resistance of masonry;
- Formation of plastic hinges in the middle span and near the tie bars and or to the orthogonal walls;



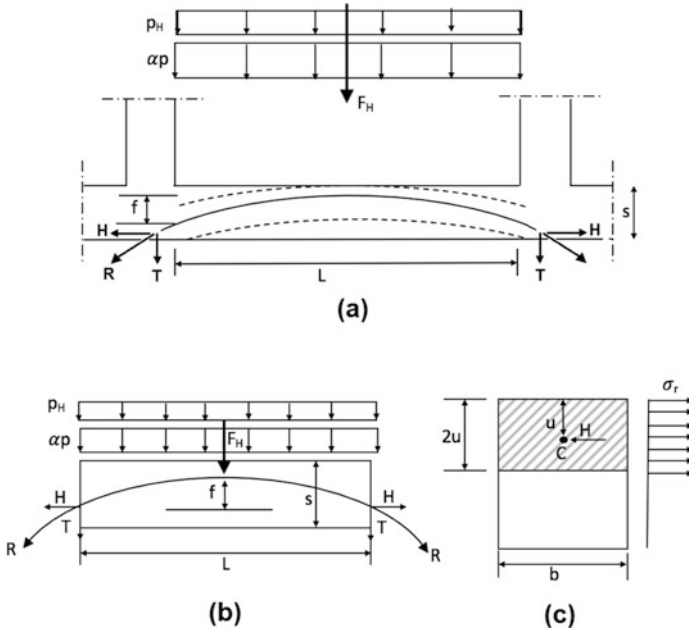


Fig. 20.32 Confined horizontal flexure mechanism scheme and section of the discharging arch in the masonry

- kinematic mechanism described through two rigid blocks with rotation point in the middle span;
- Parabolic shape of the thrust line with maximum rise in the middle span;
- Masonry compression strength equal to σ_r .

According to the hypotheses aforementioned, the value of the horizontal thrust H causing the collapse of the wall can be expressed as follow.

$$H = \frac{(\alpha p + p_H) + 2F_H L}{8f} \tag{20.25}$$

The maximum allowable normal load applied on the cross section is given by

$$H_u = 2\sigma_r u b \tag{20.26}$$

where u is a variable and it depends on the collapse multiplier α . Assuming a value of u equal to $(s-f)/2$, the collapse multiplier can be evaluated from Eqs. 20.25 and 20.26.

$$\alpha = \frac{16\sigma_r u b (s - 2u)}{pL^2} - \frac{p_H L + 2F_H}{pL} \tag{20.27}$$



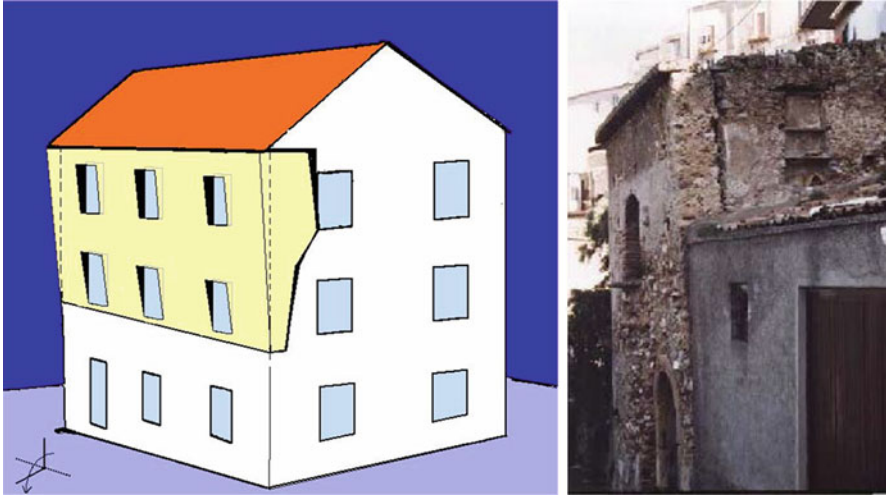


Fig. 20.33 Global overturning of a multi story wall (Milano et al. 2008)

20.3.4 *Out-of-Plane Failure Mechanisms of a Multi-story Masonry building*

This section summarizes the aforementioned mechanisms of crisis out-of-plane applied to a multi-story building and lists the possible *causes of collapse*.

- **Simple overturning: global overturning of a multi story wall (Figs. 20.33 and 20.34)**
 - high slenderness of the wall;
 - ineffective connection of horizontal structures;
 - lack of connection at the top;
 - lack of tothing with thorn walls.
- **Simple overturning: partial overturning of a multi story wall (Fig. 20.35) (Milano et al. 2008).**
 - high slenderness of the wall;
 - construction discontinuity;
 - effective connection of horizontal structures;
 - lack of connection at the top;
 - lack of tothing with thorn walls (Fig. 20.36).
- **Combined overturning (Fig. 20.37)**
 - high slenderness of the wall;
 - ineffective connection of horizontal structures;
 - lack of connection at the top;
 - effective tothing with thorn walls (Fig. 20.38).

Fig. 20.34 Global overturning of a multi story wall, Accumoli 2016

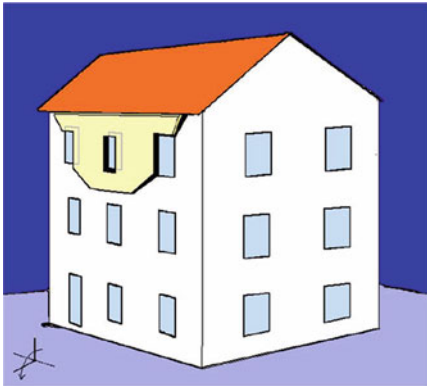


Fig. 20.35 Partial overturning of a multi story wall

• **Vertical flexure (Fig. 20.39)**

- effective connection at the top;
- lack of connection with the inter-story horizontal structures;
- constructive discontinuity.



Fig. 20.36 Partial overturning of a multi story wall, Accumoli 2016

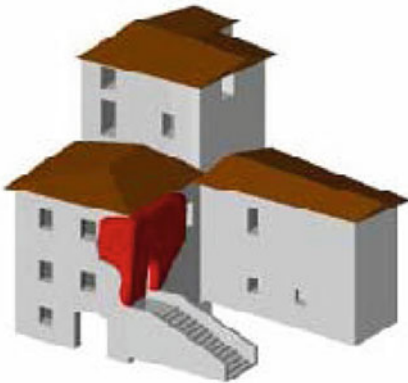


Fig. 20.37 Combined overturning of a multi story wall (Milano et al. 2008)

- **Horizontal flexure (Fig. 20.40)**

- ineffective connection at the top;
- effective tothing with thorn walls;
- high span between thorn walls.



Fig. 20.38 Combined overturning of a multi story wall, Pescara del Tronto 2016



Fig. 20.39 Vertical flexure of a multi story wall (Milano et al. 2008)



Fig. 20.40 Horizontal flexure (Milano et al. 2008)

20.4 Applications of Kinematic Equilibrium Method

20.4.1 Example 1: Simple Overturning

In existing masonry buildings there are often partial collapses after an earthquake, which are usually due to a loss of equilibrium of the masonry elements. The kinematic equilibrium method is based on the selection of a collapse mechanism and the evaluation of the horizontal force that activates the kinetic motion. The local collapse mechanisms that are significant for the building are determined by the examination of the seismic behaviour of similar buildings damaged by an earthquake, or identified through considerations about the cracking state. For each mechanism, the method considers the building or part of its as an unstable system (kinematic chain) which has to be congruent with the imposed constraints. Then, an increasing horizontal force is applied to the masses: $F = \alpha P$, where α is the *load multiplier* (NTC-08 2008). Thus the value of α_0 , which activates the mechanism, is the unknown variable of the problem. This is calculated through the principle of virtual works, by matching the total work of the external forces and the total work of the internal forces as shown in Eq. 20.28.

$$\alpha_0 \left(\sum_{i=1}^n P_i \delta_{x,i} + \sum_{j=n+1}^{n+m} P_j \delta_{x,j} \right) - \sum_{i=1}^n P_i \delta_{y,i} - \sum_{h=1}^o F_h \delta_h = L_i \quad (20.28)$$

Among all the possible kinematic mechanisms, the more probable one is the one associated with the lower load multiplier that corresponds also to the mechanisms which requires less energy. For example let's consider the case of *simple overturning*. This mechanism is initiated by the out-of-plane stresses and it causes a rigid rotation of entire building facades or portions of walls around an horizontal axis as shown in Fig. 20.41.

In this case the stabilizing moment M_S is given by

$$M_S = \sum_{i=1}^n W_i \cdot \frac{S_i}{2} + \sum_{i=1}^n F_{Vi} \cdot d_{Vi} + \sum_{i=1}^n P_{Si} \cdot d_i + \sum_{i=1}^n T_i \cdot h_i \quad (20.29)$$

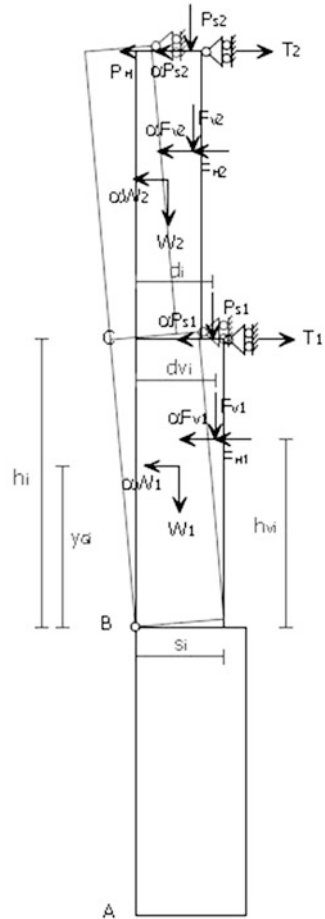
while the overturning moment M_R is

$$M_R = \alpha \cdot \left[\sum_{i=1}^n W_i \cdot y_{Gi} + \sum_{i=1}^n F_{Vi} \cdot h_{Vi} + \sum_{i=1}^n P_{Si} \cdot h_i \right] + \sum_{i=1}^n F_{Hi} \cdot h_{Vi} + P_H \cdot h_i \quad (20.30)$$

Then, by comparing the two moments it is possible to calculate the load multiplier that leads to collapse given in Eq. 20.31.

$$\alpha = \frac{\sum_{i=1}^n W_i \cdot \frac{S_i}{2} + \sum_{i=1}^n F_{Vi} \cdot d_{Vi} + \sum_{i=1}^n P_{Si} \cdot d_i + \sum_{i=1}^n T_i \cdot h_i - \sum_{i=1}^n F_{Hi} \cdot h_{Vi} - P_H \cdot h_i}{\sum_{i=1}^n W_i \cdot y_{Gi} + \sum_{i=1}^n F_{Vi} \cdot h_{Vi} + \sum_{i=1}^n P_{Si} \cdot h_i} \quad (20.31)$$

Fig. 20.41 Kinematic chain of simple overturning (Milano et al. 2008)



20.4.2 Example 2: Design of a Reinforcing Tie System

The kinematic mechanism shown in Example 1 (Sect. 20.4.1) can be avoided by using tie bars located at the floor levels (Fig. 20.42).

The tensile stresses on the tie bars can be calculated through the rotation equilibrium in hinges B (to determine T_2) and A (to determine T_1). For wall 2 the stabilizing moment M_S is given by

$$M_S = P_2 \left(\frac{b_2}{2} - t_2 \right) + N_2 (d_2 - t_2) + (T_2 - N_{2o}) \cdot h_2 \tag{20.32}$$

while the overturning moment M_R is given by

$$M_R = \alpha_0 \cdot \left(P_2 \cdot \frac{h_2}{2} + N_2 \cdot h_2 \right) \tag{20.33}$$



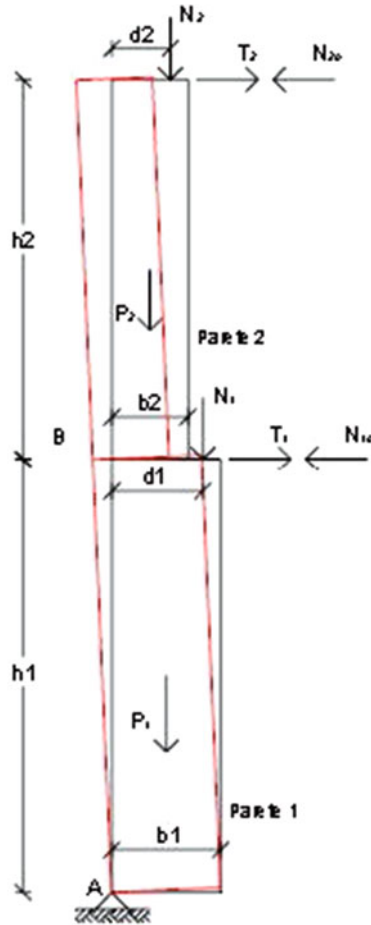


Fig. 20.42 Kinematic chain of simple overturning with tie bars (Milano et al. 2008)

Matching M_S to M_R the tensile stress T_2 is obtained. Similarly, T_1 is calculated by matching the stabilizing moment for wall 1 (Eq. 20.34) to the overturning moment (Eq. 20.35).

$$M_S = P_1 \left(\frac{b_1}{2} - t_1 \right) + P_2 \left(\frac{b_2}{2} - t_1 \right) + N_1 (d_1 - t_1) + N_2 (d_2 - t_1) + (T_1 - N_{1o}) \cdot h_1 + (T_2 - N_{2o}) \cdot h_{tot} \tag{20.34}$$

$$M_R = \alpha_0 \cdot \left(P_1 \cdot \frac{h_1}{2} + N_1 \cdot h_1 + P_2 \cdot \left(\frac{h_2}{2} + h_1 \right) + N_2 \cdot h_{tot} \right) \tag{20.35}$$

The design of a tie bar system is realized using the following four assumptions (Eqs. 20.36, 20.37, 20.38, and 20.39):

- Yielding of tie bars.

$$T_s = \pi \cdot \frac{\phi^2}{4} \cdot f_{yd} \quad (20.36)$$

- Punching of masonry in the anchor area.

$$T_m = 2s \cdot \sqrt{1 + \tan^2 \beta} \cdot (a + b + 2s \cdot \tan \beta) \cdot (\tau_0 + 0,4 \cdot \sigma_v) \quad (20.37)$$

- Contact pressure.

$$T_c = \sqrt{\frac{(a + 2s \cdot \tan \beta) \cdot (b + 2s \cdot \tan \alpha)}{a \cdot b}} \cdot \sigma_r \cdot a \cdot b \quad (20.38)$$

- Anchor plate strength.

$$T_r = \frac{f_{yd} \cdot t^2 \cdot a \cdot b}{3l^2} \quad (20.39)$$

where ϕ is the diameter of the tie bar, f_{yd} is the design strength, s is the thickness of the wall, β is the load distribution coefficient, a and b are the dimensions of the anchor plate, σ_r is the compressive strength of the masonry, t is the thickness of the anchor plate, l is a quarter of the diagonal of the anchor plate, σ_v is the vertical stress at the tie level, τ_0 is the shear strength of the masonry.

20.5 Retrofit Interventions

20.5.1 Traditional Retrofit Interventions

In the past the aim of the retrofit interventions was to maintain the stability of the building, preserving it from collapse (Doglioni 2000). However, damages were accepted in case of severe events. Frequent interventions were: metallic tie rods, hoops, flying buttresses, angled or clamped buttresses (Fig. 20.43).

20.5.2 Modern Retrofit Interventions

Modern interventions have established themselves since the beginning of the twentieth century, with the introduction of reinforced concrete technologies (Priestley and Seible 1995). Generally these interventions are inspired by the idea of reversibility, but sometimes their application to real cases has been incorrect (Cimellaro et al. 2011, 2012a,b). For instance, it happens that new technologies are used even if not

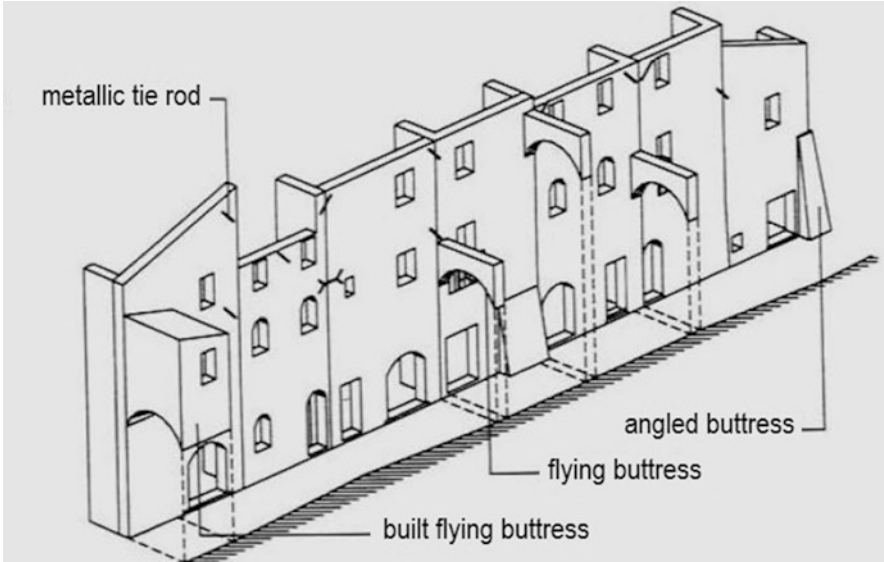


Fig. 20.43 Examples of traditional retrofit interventions

Fig. 20.44 Ineffective reinforced injections due to adhesion problems



tested enough or when they are not really necessary. It was the case of the first reinforced injections that resulted ineffective because of the lack of experimentation (Fig. 20.44). Similarly, in the recent past, hollow clay and concrete roofs and floors were highly recommended by the codes, but they turned out to be unsuccessful

Fig. 20.45 Masonry damages due to hollow clay and concrete floor or roof

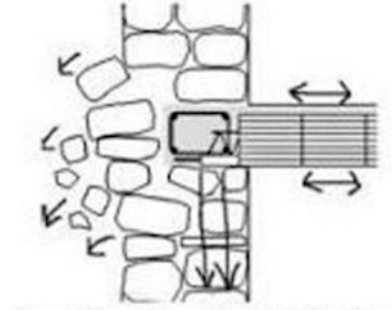
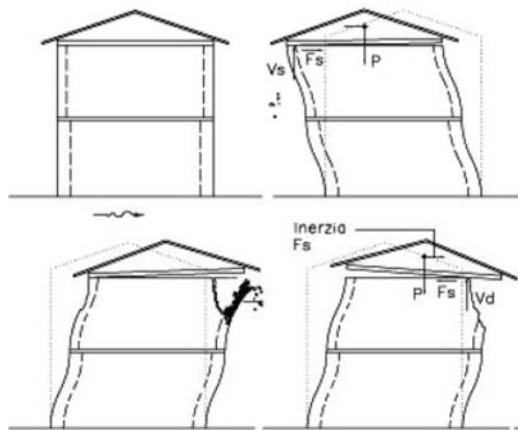


Fig. 20.46 Collapse mechanism due to a reinforced concrete roof



in most of the cases (Cimellaro and Marasco 2015). The bond beam at the perimeter indeed is much more stiff than the masonry, so the external walls are likely to collapse (Fig. 20.45). In addition, a dangerous modern intervention is the reconstruction of reinforced concrete roofs. The former one involves a significant increase of stiffness and a larger mass at the top of the building. Consequently, masonry, that is weaker than the roof, suffers damages under horizontal forces, and the roof can even overturn and crush the structure (Figs. 20.46 and 20.47).

20.5.3 Classification of Interventions

The most common retrofit interventions for masonry structures (G M 2012) are summarized and grouped below:

1. Retrofit interventions to reduce the lack of connections:

- Tie bars;
- Hoops;



Fig. 20.47 Overturning of the reinforced concrete roof. Pescara del Tronto, 2016



- Post tensioned ties;
- Top ring beams;
- Connection of floors to the walls.

2. Retrofit interventions to reduce the deformability of floors.

3. Retrofit interventions to increase the strength of the masonry piers (Tinè 1985):

- Replacing damaged units (patching);
- Face to face connectors;
- Injections;
- Reinforced injections;
- Stitching the angles;
- Repointing mortar joints;
- Repairing cracks;
- Reinforced plasters;
- Creating or replacing lintels;
- Inserting diatoms.

4. *Retrofit interventions on beams and columns:*

- Hoops;
- Tie bars;
- Distribution of the loads on other elements.

5. *Retrofit interventions on the foundations.*

Other possible Retrofit interventions are:

- *Retrofit interventions on arches and vaults.*
- *Retrofit interventions on the roof.*
- *Retrofit interventions to change the distribution of vertical structural elements.*
- *Retrofit interventions to reinforce walls around openings.*
- *Retrofit interventions on stairs.*
- *Retrofit interventions to ensure the connection of non-structural elements.*
- *Seismic joints.*

1. **Interventions to reduce the lack of connections.**

- **Tie bars.** These structural units are arranged in the two main directions of the building to guarantee a “box-like” behavior and to reduce the horizontal thrusts from other components of the structure. They have to be located at floor levels and connected to the bearing walls with anchors or anchor plates. If masonry is in poor condition, then a consolidation of the masonry is necessary in the anchor area because of the concentrated load (Figs. 20.48 and 20.49). To be effective, the anchor has to be placed correctly, as shown in Fig. 20.50. The advantages of this intervention are: significant increase of the structural performances of the building, small footprint, light system, long durability, reversibility. While the main disadvantage are the consolidation interventions on the masonry in the anchor areas.

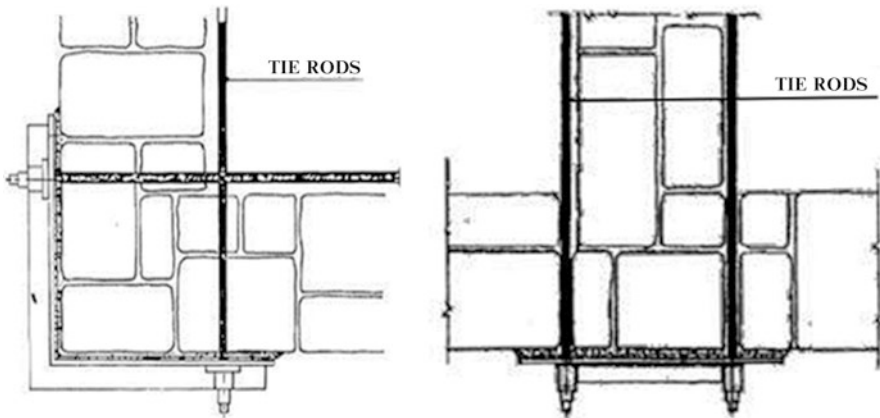


Fig. 20.48 Examples of configurations of tie bars

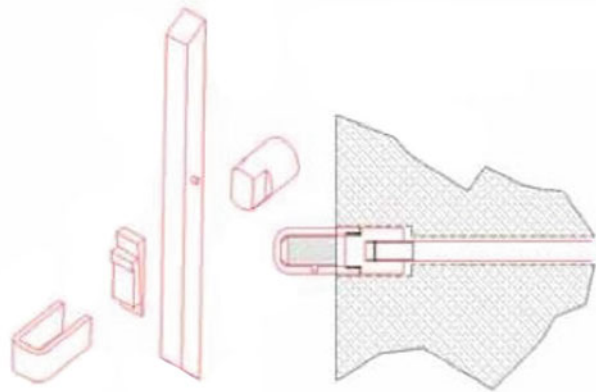
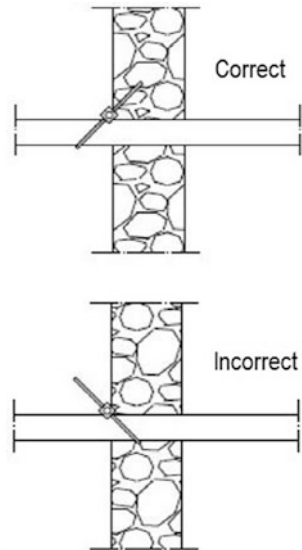


Fig. 20.49 Elements constituting a tie bar

Fig. 20.50 Correct and incorrect scheme to place the anchor



- **Hoops.** They are realized through metallic or composite stripes or strands placed along the perimeter of the building (Figs. 20.51, 20.52, and 20.53). It is necessary to avoid stress concentrations at the corners of the walls. The advantages are the small footprint and the lightness. The disadvantages are the sensitiveness to high temperatures and that a perfect adhesion to the substrate must be guaranteed.
- **Post tensioned ties** (Fig. 20.54).

Fig. 20.51 Example of metallic stripe hoops



Fig. 20.52 Example of FRP hoops

- **Top ring beams** Effective solution to connect walls each other, to the floors and to the roof. They can be made of reinforced masonry (Fig. 20.55), reinforced concrete (high weight and stiffness), steel (lighter and less intrusive, Fig. 20.56). To obtain a monolithic behavior the execution must be cured in detail.
- **Connection of floors to the walls.** Floors are anchored to the walls to avoid the slipping of the beams and to distribute horizontal forces to the vertical structures (Figs. 20.57 and 20.58).



Fig. 20.53 Example of steel strand hoops



Fig. 20.54 Horizontal post tensioned ties in a masonry building in Christchurch that withstood the 2011 earthquake

2. Interventions to reduce the deformability of floors.

Since floors distribute horizontal forces to the walls, it is necessary to improve their rigid behavior (Fig. 20.59). The stiffness increase can be positive or negative depending on the geometry of the building. The intervention can be done at the extrados with boards, metal or fiber reinforced strips (Fig. 20.60), or at the intrados with tie bars.

3. Interventions to increase the strength of the masonry piers.

- **Replacing damaged units (patching).** This intervention can be a solution for deep cracks. It consists in removing units nearby the crack, replacing them with new ones (Figs. 20.61 and 20.62). The materials used in the patching must be similar to the original ones and the mortar should have no shrinkage.



Fig. 20.55 Example of reinforced masonry top ring beam

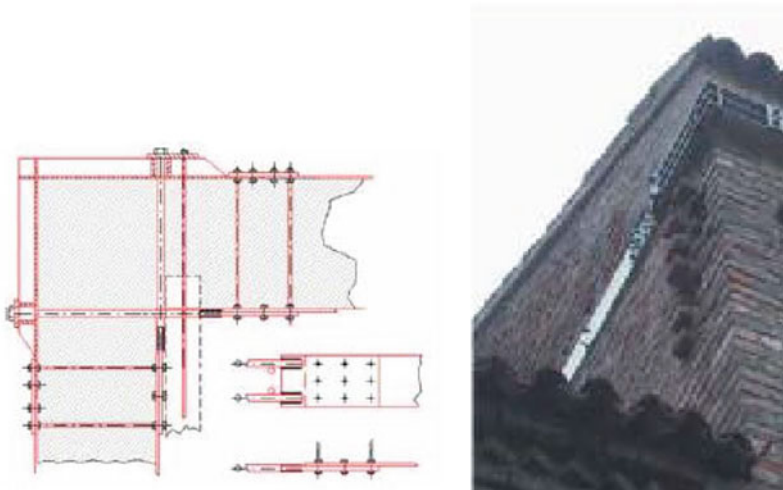
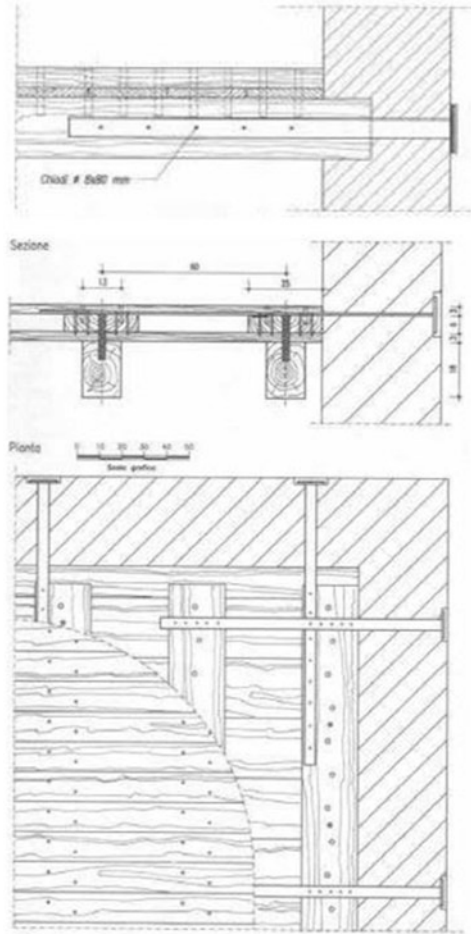


Fig. 20.56 Example of steel top ring beam

- **Face to face connectors.** These connectors avoid the disaggregation of the masonry keeping together the wythes, but they have low resistance to shear forces and the intervention is invasive (Figs. 20.63 and 20.64).
- **Injections.** Injections are used to fill internal voids, external cracks and to protect from the degradation, therefore they lead to a better compressive

Fig. 20.57 Example of steel connections between walls and a wooden floor



strength. The wall is perforated at the joints and a specifically designed mortar is injected through tubes (Figs. 20.65 and 20.66), without affecting the aesthetic aspect.

- **Reinforced injections.** In this case, reinforcement bars are placed into the holes and fixed with binder mixtures through injection. Generally they are used to improve the connection between perpendicular walls (Fig. 20.67), but, to be effective, masonry has to be of good quality. Bars are inclined in both vertical and horizontal directions, like Fig. 20.68 shows. With regard to the classic injections, an increase of ductility can be noticed.

Fig. 20.58 Example of connection of a wooden beam to the wall

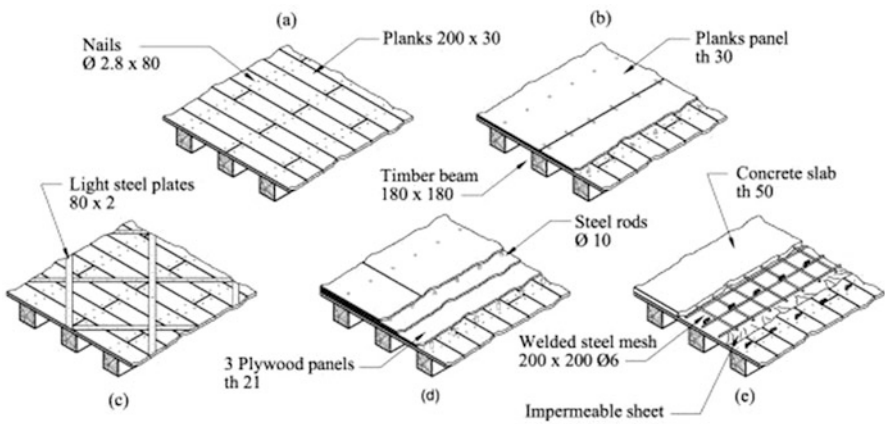
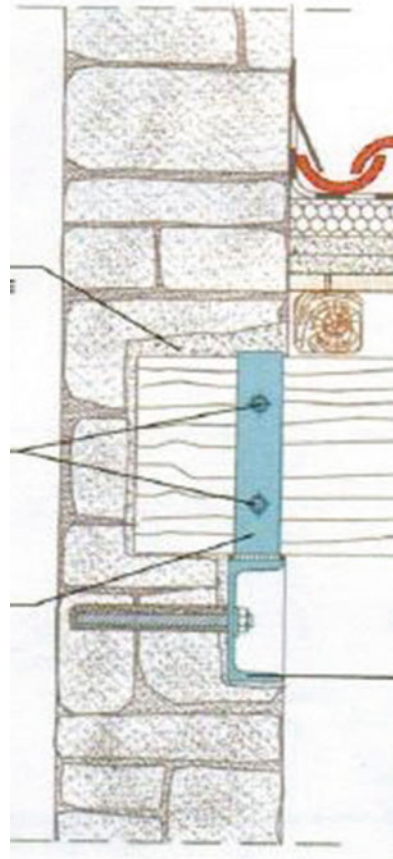


Fig. 20.59 Different ways to increase the stiffness of wooden floors



Fig. 20.60 Application of FRP stripes at the extrados

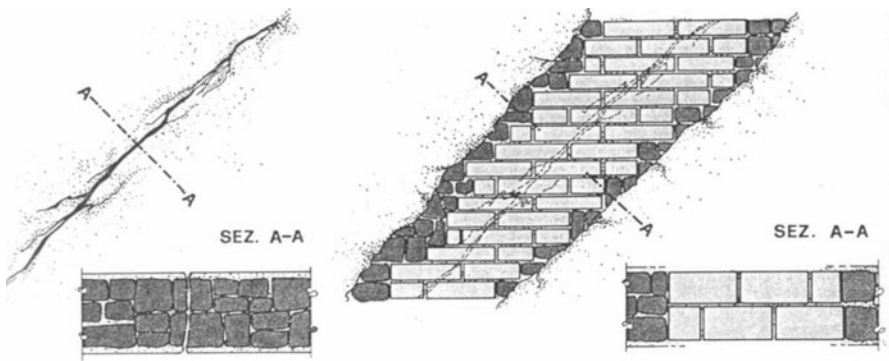


Fig. 20.61 Portion of the wall that should be repaired

- **Stitching the angles.** If the tothing of the angle is weak, the two perpendicular walls can separate. The intervention avoid this through reinforced injections in the two main directions of the walls (Fig. 20.69).
- **Repointing mortar joints.** The intervention is to remove the old mortar and then fill the joints with a better quality mortar. If the wall is not too thick and the intervention is applied on both sides, then grouting mortar joints can improve the mechanical properties of the wall. It is important to design an adequate kind of mortar. It is also possible to place FRP or steel bars in the joints before refilling them with mortar (Fig. 20.70).

Fig. 20.62 Example of patching



Fig. 20.63 Phases of laying the connectors

Fig. 20.64 Possible configurations of connectors

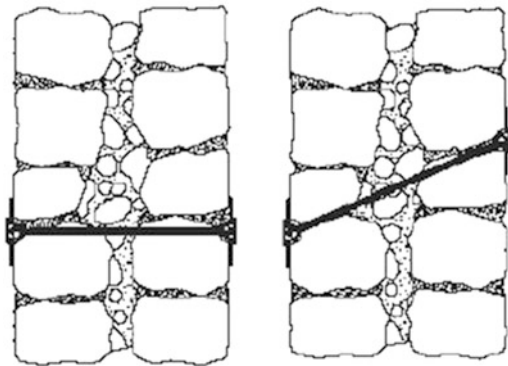


Fig. 20.65 Injection tubes

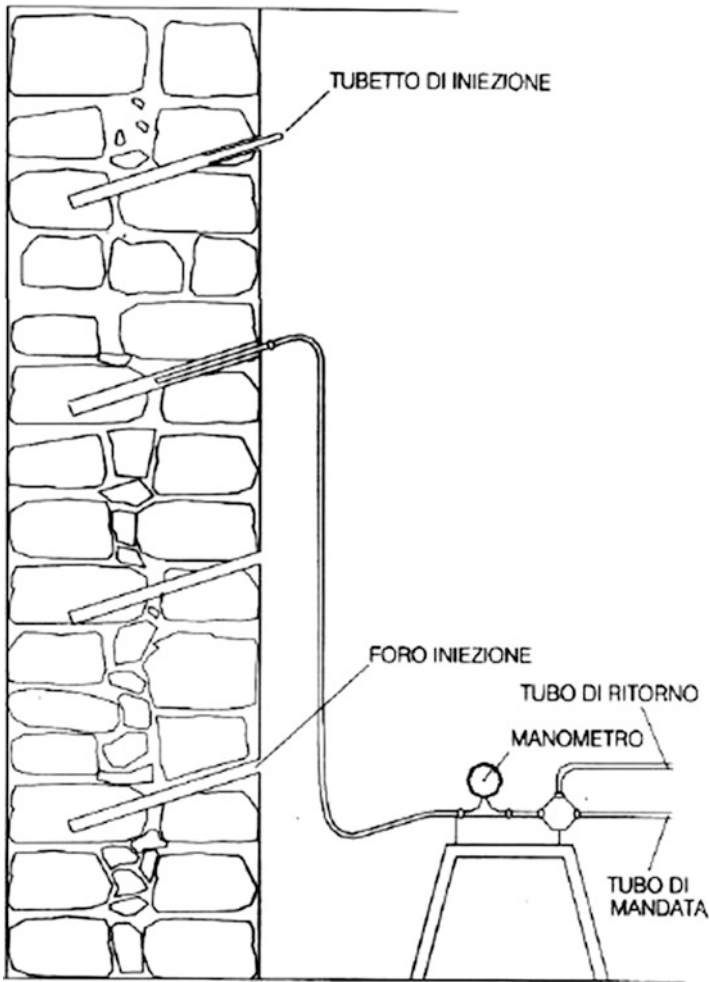


Fig. 20.66 Injection scheme

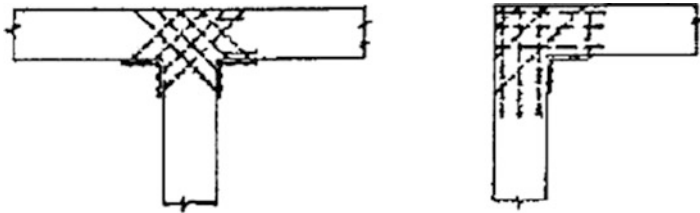


Fig. 20.67 Reinforced injections in perpendicular walls

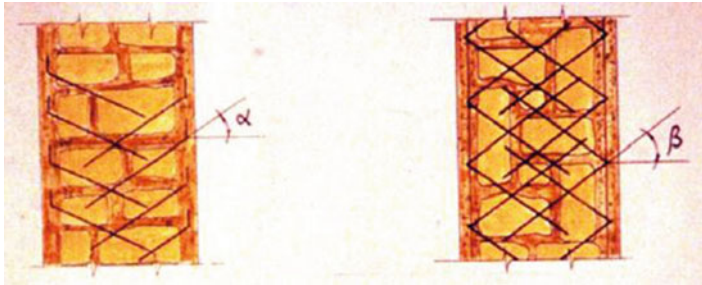


Fig. 20.68 Reinforced injections: α indicates the vertical inclination of the bars, β the horizontal one

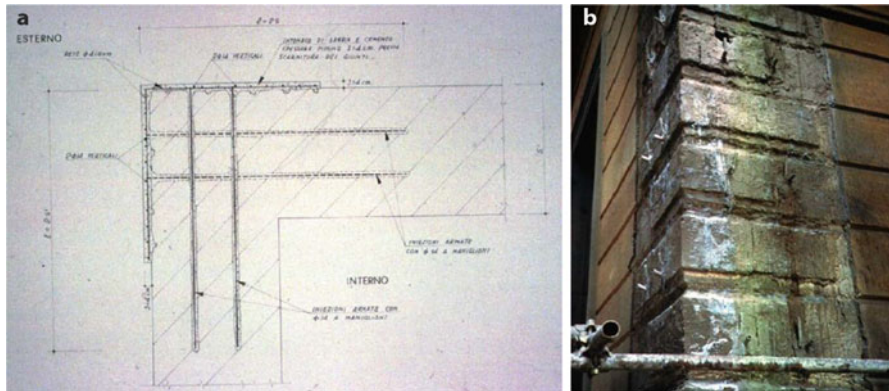


Fig. 20.69 Example of a stitched angle



Fig. 20.70 Execution phases of the repointing intervention

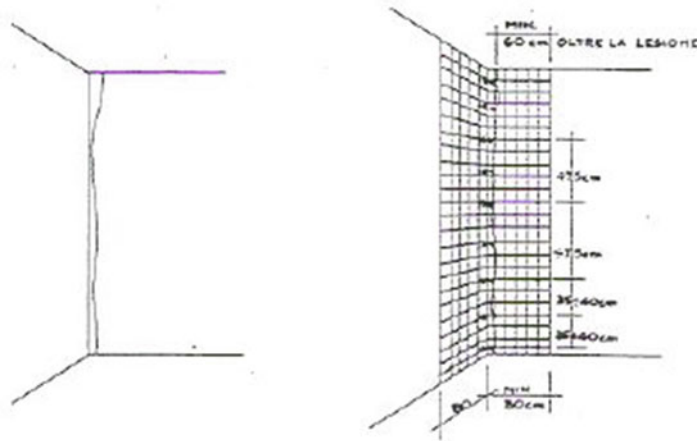


Fig. 20.71 Application of a grid at the corner



Fig. 20.72 Application of the welded grid from the inside

- **Repairing cracks.** If the crack is not too deep, it can be sealed and then filled with mortar. For deep cracks injections are necessary and then a reinforcement grid has to be applied along the crack over a layer of mortar (Fig. 20.71).
- **Reinforced plasters.** The plaster is reinforced with a welded grid fixed to the wall (Fig. 20.72). The purposes of this intervention are: confinement, increase



Fig. 20.73 Degradation of the reinforced plaster due to a lack of connection of the welded grid to the wall

of the section and of the stiffness. Its limits are: increased weight, degradation problems (Fig. 20.73), decrease of breath-ability, aesthetic alteration.

- **Creating or replacing lintels** (Fig. 20.74).

4. Interventions on beams and columns.

- **Hoops.** The purpose of this intervention is to confine the structural elements in order to increase their bearing capacity. The confinement can be obtained with metallic hoops, FRP stripes or thin concrete walls around the columns (Figs. 20.75 and 20.76).

5. Interventions on the foundations.

The most common interventions are the *enlargements of the base of foundations* and *micro piles*. In the first case, the base can be enlarged with concrete as depicted in Fig. 20.77 to have a better distribution of loads in the soil. Obviously the connection between foundation and concrete is extremely important and it is made through steel connectors. Micro piles instead consolidate the shallower layers of soil and also mobilize the deepest layers. The execution consists

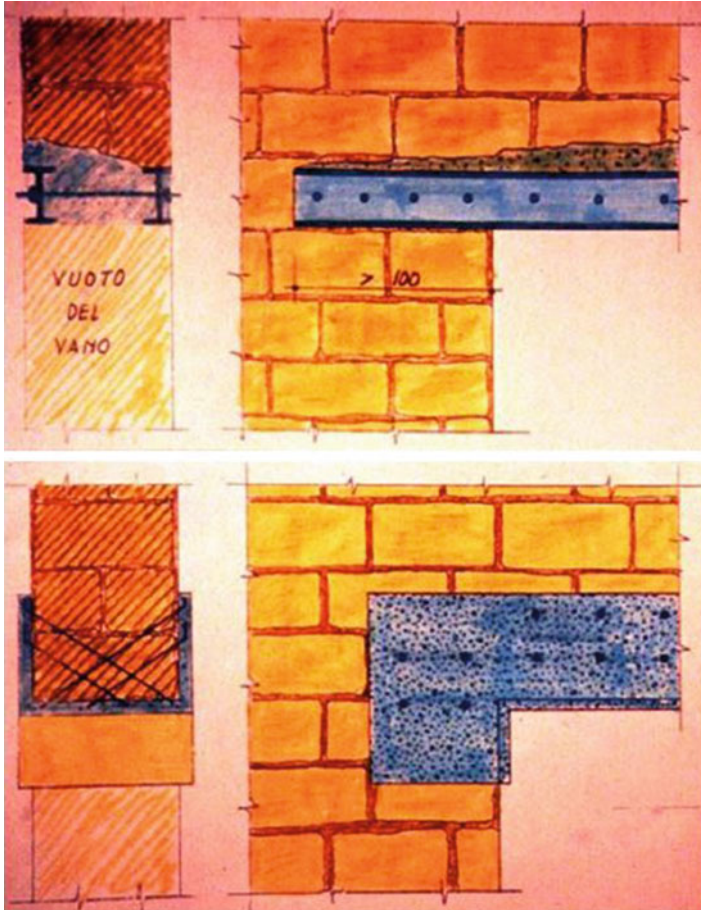


Fig. 20.74 Examples of configurations of steel lintels

of drilling inclined holes, placing steel casing and filling with cement grout (Fig. 20.78). Both solutions are effective in case of settlements or additional loads on the structure. Another possibility is to connect isolated foundations through a reinforced concrete raft foundation, like shown in Fig. 20.79.

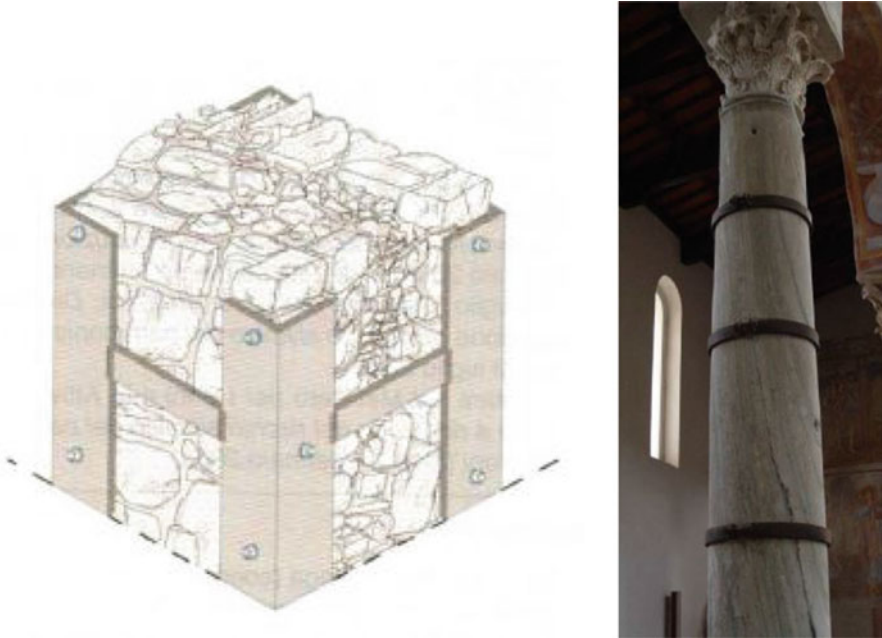


Fig. 20.75 Examples of metallic hoops for square and circular columns

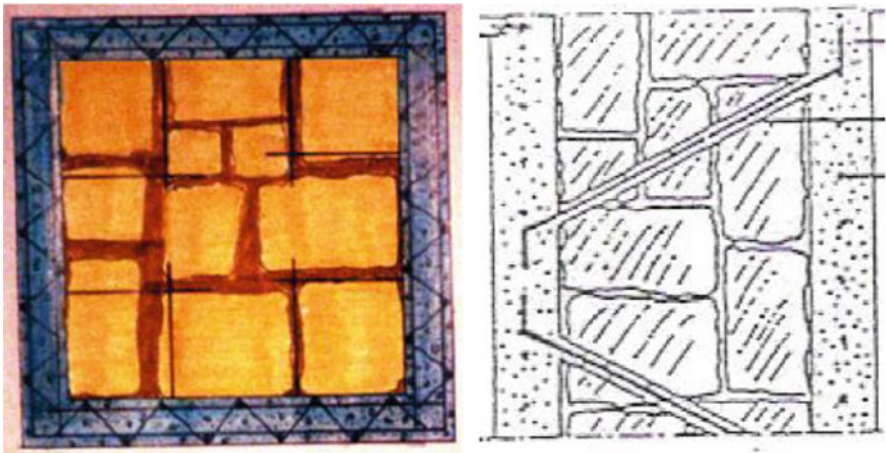


Fig. 20.76 Examples of confinement with concrete

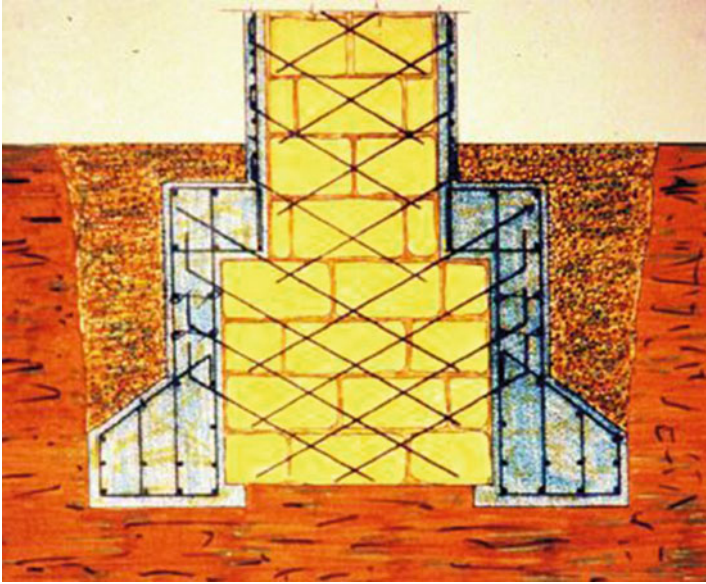
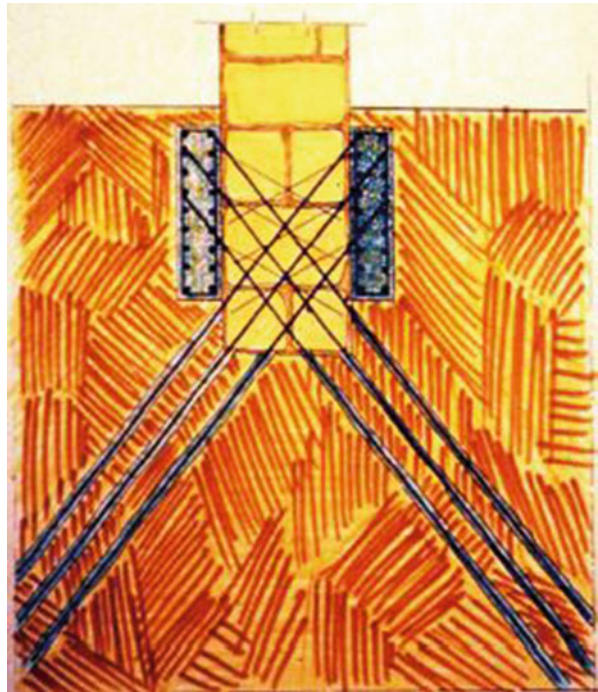


Fig. 20.77 Base enlargement of the foundation

Fig. 20.78 Positioning scheme of micro piles



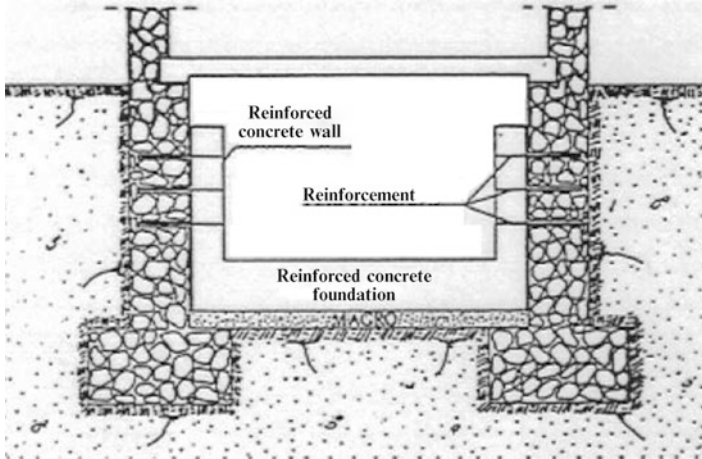


Fig. 20.79 Raft foundation connecting the existing foundations

References

- Arcidiacono V, Cimellaro GP, Piermarini E, Ochsendorf J (2016) The dynamic behavior of the basilica of San Francesco in assisi using simplified analytical models. *Int J Archit Herit* 10(7):938–953. <http://doi.org/10.1080/15583058.2016.1158333>, <Go to ISI>://WOS:000384652000008
- Cimellaro GP, Marasco S (2015) A computer-based environment for processing and selection of seismic ground motion records: Opensignal. *Front Built Environ* 1:17. <https://doi.org/10.3389/fbuil.2015.00017>
- Cimellaro G, Reinhorn AM, De Stefano A (2011) Introspection on improper seismic retrofit of basilica Santa Maria di Collemaggio after 2009 Italian earthquake. *Earthq Eng Eng Vib* 10(1):153–161
- Cimellaro GP, Reinhorn AM, De Stefano A (2012a) Reply to discussion 1 on introspection on improper seismic retrofit of basilica Santa Maria di Collemaggio after 2009 Italian earthquake by G.P. Cimellaro, A.M. Reinhorn and A. De Stefano by Vincenzo Ciampi. *Earthq Eng Eng Vib* 11(2):283–288. <http://doi.org/10.1007/s11803-012-0119-z>
- Cimellaro GP, Reinhorn AM, De Stefano A (2012b) Reply to discussion 2 on introspection on improper seismic retrofit of basilica Santa Maria di Collemaggio after 2009 Italian earthquake by G.P. Cimellaro, A.M. Reinhorn and A. De Stefano by Enzo Cartapati. *Earthq Eng Eng Vib* 11(2):291–292. <http://doi.org/10.1007/s11803-012-0121-5>
- Doglioni F (2000) Codice di pratica (linee guida) per la progettazione degli interventi di riparazione, miglioramento sismico e restauro dei beni architettonici danneggiati dal terremoto umbro marchigiano del 1997. *Bollettino Ufficiale Regione Marche* (15)
- EN-1996 (2009) General rules for reinforced and unreinforced masonry. European Committee for Standardization
- G M (2012) Edifici esistenti in muratura: analisi del comportamento sismico e interventi di rinforzo. In: *Atti del convegno: Pericolosità, recupero e prevenzione sismica alla luce del terremoto dell'Emilia Romagna*
- Giordano A, Mele E, De Luca A (2002) Modelling of historical masonry structures: comparison of different approaches through a case study. *Eng Struct* 24(8):1057–1069

- Giuffrè A (1991) Lectures on historical masonry mechanics (Lecture sulla Meccanica delle murature storiche). Edizioni Kappa, Rome, pp 69–85
- Magenes G (2006) Masonry building design in seismic areas: recent experiences and prospects from a European standpoint. In: First European conference on earthquake engineering and seismology
- Magenes G, Penna A, Galasco A, Rota M (2010) Experimental characterisation of stone masonry mechanical properties. In: Proceedings of the 8th international masonry conference, Dresden
- Milano L, Mannella A, Morisi C, Martinelli A (2008) Schede illustrative dei principali meccanismi di collasso locali negli edifici esistenti in muratura e dei relativi modelli cinematici di analisi. Allegato alle Linee Guida per la Riparazione e il Rafforzamento di elementi strutturali, Tamponature e Partizioni. Accessed 21 Feb 2012
- NTC-08 (2008) Nuove Norme Tecniche per le Costruzioni. Gazzetta Ufficiale della Repubblica Italiana
- Paulay T, Priestley MN (1992) Seismic design of reinforced concrete and masonry buildings. Wiley, New York
- Priestley M, Seible F (1995) Design of seismic retrofit measures for concrete and masonry structures. *Constr Build Mater* 9(6):365–377
- Tinè S (1985) La pratica del restauro. *Materiali-macchine-tecnologie*. Bema, 276 pp
- Touliatos PG (1996) Seismic behaviour of traditionally-built constructions. In: Protection of the architectural heritage against earthquakes. Springer, Vienna, pp 57–69
- Tucker C (2007) Predicting the in-plane capacity of masonry infilled frames: a dissertation presented to the Faculty of the Graduate School, Tennessee Technological University
- Turnšek V, Čačovič F (1971) Some experimental results on the strength of brick masonry walls. In: Proceedings of the 2nd international brick-masonry conference. British Ceramic Society, Stoke-on-Trent, pp 149–156

Chapter 21

Modeling of Structures in Seismic Zone



Abstract This chapters describes the general procedure used to model a 3D frame using SAP2000. A ten-storey reinforced concrete building is assumed as case study. Four types of methods of analysis are analyzed for the case study building.

21.1 Introduction

The response of a structural system to a seismic excitation generates a distribution of lateral forces on the building that depend on the ground motion intensity as well as on the its geometric and mechanical characteristics. In structural engineering a 3D multistory buildings is discretized as an assemblage of beam and column elements interconnected at nodal points where the DOFs are assumed located. The solution of dynamic problems requires the use of numerical methods. In the last decades, the availability, effectiveness, and utilization of computer technology has led to the application of the Finite Element Analysis (FEA) (Bathe and Wilson 1976) which are currently used extensively in academia and industry. The general concept of FEA is to approximate the response of a system (in terms of displacement, stress, etc.) at a discrete number of points. This approach leads to reduce the DOFs of the system and then the requested computational effort, by minimizing the deviation between the analytical and the real solution. Thus, the structural problems are currently solved through Finite Element software available in the market. SAP2000 is among the more largely diffused general-purpose software performing structural analysis (CSI 2010).

21.2 Structural Analysis

Assessment of building performance inherently entails significant uncertainty (FEMA 2012) associated with the model definition, material and geometry definition, and loads calculation. In order to reduce the inherent uncertainties, the

structural analysis requires a rigorous procedure. Generally, the structural analysis process involves in different ordered steps below resumed.

21.2.1 *Structural Idealization*

The results of structural analysis are highly affected on the idealization of the structure. Depending on how closely the model matches the real structure, the results provide accurate solution. The structural model is discretized into different members (beams, columns, walls, etc.). In the context of FEA, a large variety of elements are available. Conventionally, the structural elements are categorized into one-dimensional, two-dimensional, and three-dimensional members. In the first case, the members are significantly longer in one direction compared with the other two (beam, column, bar). The two-dimensional members are typically used to model elements having two dimensions greater than the third one (shell, plate), while for the three-dimensional elements all the dimensions are considered (solid). The structural model is realized by assembling the elements in the 2D or 3D system. Mostly, the model is extended in all three of the axis directions to better describe the real geometry of the structure. The selection of the appropriate model influences the final results in terms of stresses and displacements in the elements which compose the entire structural system.

21.2.2 *Materials*

The main properties of a structural system are the mass and stiffness which affect the static and dynamic response of the structure. The structural materials must be in compliance with specific harmonized rules which describe the process of identification, certification, and conformity of the material. UNI (2006) provides the standard procedure of specification, performance, production and conformity of concrete. The standardized characteristics of the steel for the reinforcement of concrete are contained in the EN (2005). The main parameters which characterize the structural elements are the strength and the elastic modulus. According to NTC-08 (2008) the *compressive strength of concrete is denoted by classes that are related to the characteristic (5%) cylinder strength f_{ck}* . According to the characteristic compressive strength, ten ordinary classes ($f_{ck} < 50$ MPa) and six classes for special concrete ($f_{ck} \geq 50$ MPa) (see 4.1.I NTC-08 2008) are provided. Concrete is used in a wide range of services and environmental conditions which can impact its service life. The recent design rules focus on protect the structure considering its intended use during the design working life. For this purpose, the exposure conditions (chemical and physical environmental conditions) must be considered in addition to the mechanical actions. According to UNI (2006), six *exposure classes* related to the environmental conditions are provided. The indicative compression

strength classes for the particular environmental exposure classes are suggested by Institution (2004). The behaviour of reinforcing steel is specified by the yield strength (f_{yk}), the tensile strength (f_t), the ductility parameters (ϵ_{uk} , and f_t/f_{yk}). NTC-08 (2008) provides the steel strength class B450A (low ductility) and B450C (high ductility), while their characteristics are given in Table 11.3.Ic and 11.3.Ib of the NTC-08 (2008), respectively. The materials strength classes must be selected according to the principle of durability and structural safety. A durable structure may meet the requirements of serviceability, strength and stability throughout its design working life, without significant loss of utility or excessive unforeseen maintenance (Narasimhan and Faber 2010). The design material strengths are assessed through the *partial safety coefficients method* which reduce the characteristic strength values that are affected by epistemic uncertainties.

21.2.3 Load Analysis

The loads applied on a structure are always affected on epistemic uncertainties. The common approach proposed to the national and international design standards is to provide different *design situations* in which the actions are defined according to their intensity through the time. The NTC-08 (2008) identifies the design situations as *permanent*, *variable*, *accidental*, and *seismic*. For the purpose of Limit State verification (global or local) the actions must be combined in different *load combinations* (see paragraph 2.5.3 of NTC-08 2008). Each load combination is given by superposition of the effects of the characteristics values of the action multiplied by the related *partial safety coefficients*. Furthermore, the variable loads are not considered applied on the structure with the maximum intensity. For this purpose, the design codes provide the *combination coefficients* which are intended to reduce the variable loads intensity (see Table 2.5.I of NTC-08 2008). The values of these coefficients are defined for three different categories which depend on the duration of the load application (*near-permanent*, *frequent*, *rare*).

21.2.4 Solution of the Problem Through a Given Method of Analysis

The solution of the structural problem is the core of the analyses and it represents the engineering approach used to solve the problem. The methods of analysis for multistory buildings are based on static or dynamic approaches depending on the characteristics of the action. If the load produces a stress which does not exceed the yield point of the elements (serviceability requirements), the linear method can be used. On the contrary, plastic dissipation on the structure occurs when the intensity of the action is increasing, then the nonlinear methods have to be

considered for assessing the stress and deformation level on the structural element (safety requirements). The methods of analysis for multistory buildings subjected to earthquake excitation have been explained in detail in Chap. 14.

21.2.5 Safety Assessment

The building design codes comply with the principles and requirements for the safety and serviceability of structures. Therefore, the verification procedures are based on the structural safety, serviceability and robustness under accidental loads during its design working life. Each verification procedure is applicable to a given performance level of the structures (identified through the Limit States (LS)). For each *design load combination* the structural systems have to be verified regarding to the structural safety (ULS) and serviceability (SLS). The design strength (R_d) must be greater or equal than the design action (E_d) considered for the local member or for the entire building.

21.3 Brief Introduction to SAP2000

SAP (Structural Analysis Program) is a general-purpose civil-engineering software for structural analysis and design. It was developed in the 1970s by a group of students directed by Professors Wilson and Bathe at the University of California, Berkeley. The software was initially developed for an educational purpose but it was then spread among engineering firms during the 1980s, just during the period in which the first personal computers appeared in the market. The first release of the program was known as SAP80, which has then evolved to SAP90, and then to the actual version SAP2000. The latest version of SAP2000 software offers a wide variety of features such as static and dynamic analysis, linear and nonlinear analysis, geometric nonlinearity, buckling analysis, etc. This section introduces the basic useful information to a beginner user who wants to perform seismic analysis of a multistory building.

21.3.1 Files Type

SAP2000 saves the structural model into .SDB, S2K or 2K file formats. The first one represents the main file project displayed in the SAP2000 environment, while the second file contains the ASCII version of the project. This last file can be used to modify the structure without using the graphical interface.

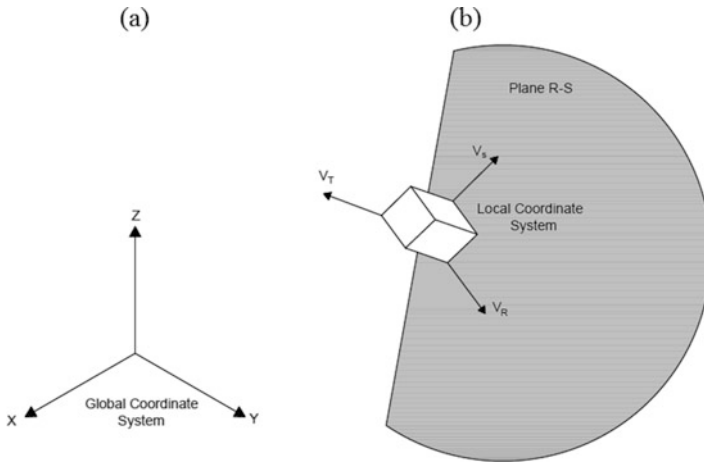


Fig. 21.1 Global and local coordinate systems

21.3.2 Coordinate System

All elements in a SAP2000 model are defined with respect to a single coordinate system, a three dimensional and right-handed Cartesian system. X and Y axes are the two horizontal axes defining the plane perpendicular to the gravity direction, and Z axis indicates the vertical direction. Other coordinate systems are defined by the user with respect to the global coordinate system (Fig. 21.1a), either directly or indirectly. In addition, each element is characterized by its own coordinate system, known as 'local coordinate system' (Fig. 21.1b), which is useful for extracting the stress information.

21.3.3 Elements

There are four main types of unit measures in SAP2000:

1. Force;
2. Length;
3. Temperature;
4. Time.

An important distinction is made by SAP2000 between the weight and the mass. The weight is a force that can be applied like any other force, while the mass is used only for calculating the dynamic inertial forces.

Four types of objects are found in SAP:

1. *POINT OBJECT*: there are two kinds of point objects, *Joint object*, which is automatically created at the edges of other objects, and *Grounded object*, which is used to create special supports, such as isolators, dampers, etc;
2. *FRAME OBJECT*: is an element used to model beams and columns;
3. *AREA OBJECT*: is used to model walls, floors and generally to model two-dimensional solid objects like shell;
4. *SOLID OBJECT*: is used to model three-dimensional solid objects.

The main element used to model the structural elements is the *frame object*. The frame element is modeled as a straight line connecting two points. It can support three different load types: (i) its own weight, (ii) the concentrated load, and (iii) the distributed load.

21.3.4 Materials and Sections

The material property may be defined as *isotropic*, *orthotropic*, or *anisotropic*. Choosing among them depends on the element type. Each material type can be used by more than one element. The materials are indirectly referenced through the section properties that are appropriate for that element type. For example, for concrete elements, it is necessary to define four parameters:

1. Weight per unit volume;
2. Modulus of elasticity;
3. Poisson's ratio;
4. Concrete compressive strength.

After the definition of the material parameters, it is necessary to define the section of all elements. In SAP2000, there is no limit of the number of sections. They are characterized by their name, dimension (depth and width) and material type.

21.3.5 Loads

The loads represent the actions applied to the structure and they can be of different types, such as pressure, force, support displacement, thermal effects, ground acceleration, etc.

21.3.5.1 Load Patterns

The term Load Pattern indicates a spatial distribution of load. In the creation of the model, it is possible to define any number of load cases. The different types of loads are:

- DEAD, SUPER-DEAD to define the permanent loads;
- LIVE, REDUCED LIVE to define the accidental loads;
- QUAKE to define the seismic loads;
- SNOW;
- WIND;

Different functions exist within SAP2000 to describe the variation of load in time. Those functions are used for dynamic analyses where the load changes with time. Some of these functions are:

- Response Spectrum Functions;
- Time-History;
- Steady-State Functions;
- Power-Spectral-Density Functions.

21.3.5.2 Load Cases

A “load case” defines how load patterns are applied:

- statically
- dynamically

how the structure responds:

- linearly
- nonlinearly

and how analyses are performed:

- static
- modal
- response spectrum
- time history
- power spectral density

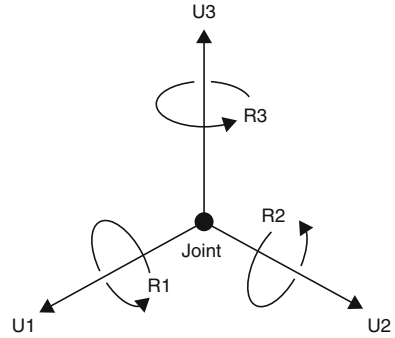
For each analysis to be performed, a load case is defined, and there is no limit for the number of load cases.

21.3.5.3 Load Combination

A “Load Combination” in SAP2000 is the combination of the results coming from different analysis cases. There are several types of combinations:

- Additive type: Results are added linearly;
- Absolute type: The absolute values of the results are added;
- SRSS type: Final result is the square root of the sum of the squares of the results;
- Envelope type: Results from analysis and combinations are enveloped to find the maximum and minimum values.

Fig. 21.2 Degrees of freedom



21.3.6 Restraints and Constraints

Every joint is characterized by a set of degrees of freedom, internal and external constraints, properties, and loads. To model the joints, the global coordinate system is used as local coordinate system. Six displacement components are associated with every joint of the model (Fig. 21.2).

- Three translations along local axes, U1, U2 and U3;
- Three rotations about local axes, R1, R2 and R3.

The external constraint 'Restraint' can be assigned to joints that need to be blocked from a specific movement. This gives the possibility of modeling different support types, such as roller, hinge, or fixed support. Internal Constraints are used to impose certain types of rigid body behavior, symmetry conditions, and to connect different parts together. Two types of constraints can be used to model a rigid-body behavior:

1. Rigid Body;
2. Rigid Diaphragm.

21.3.6.1 Rigid Body

Rigid body causes all of its constrained joints to move together as a three-dimensional rigid body. It can be used to model rigid connections, connect different parts of the structural model and to connect frame elements that are acting as eccentric stiffeners to shell elements.

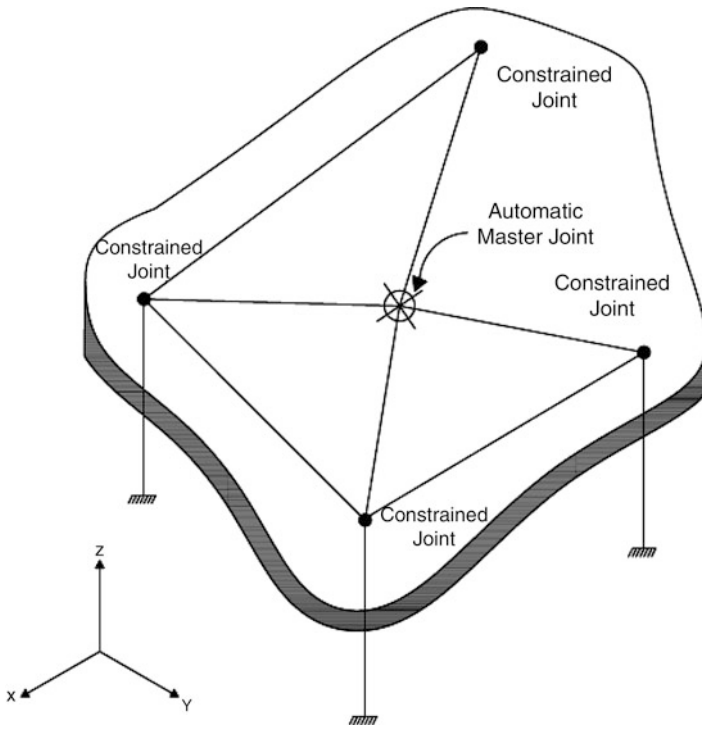


Fig. 21.3 Use of diaphragm constraint to model a rigid floor slab

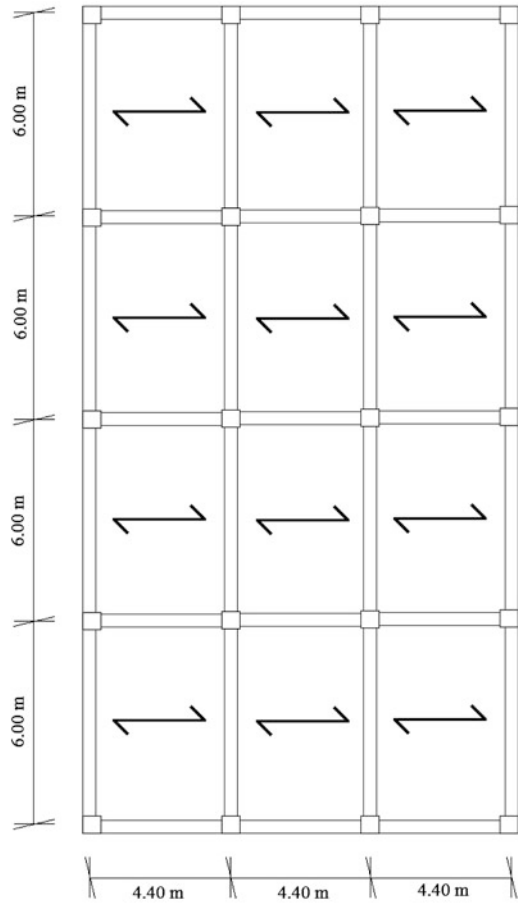
21.3.6.2 Rigid Diaphragm

Rigid diaphragm forces constrained joints to move together as a rigid planar diaphragm (Fig. 21.3). It prevents any membrane deformation, while it does not influence out-of-plane deformation. Diaphragm constraints can be used to model concrete floors in building structure with high in-plane stiffness and to model bridge superstructures.

21.4 SAP2000 Case Study

This section is intended to provide a general overview on the structural modeling and apply the methods of analysis for a multistory building. The design procedure is intentionally omitted because it is not relevant for achieving the main goal of the section. A five-story reinforced concrete building (residential occupancy) located in the town of L'Aquila in Italy (Lat. 42.3511, Long: -13.3980) is considered as case study and the entire structural analysis procedure in SAP2000 is discussed in detail. The lateral resisting system is a *moment resisting frame* having a footprint area of 316.80 m² (X direction: 13.20 m, Y direction: 24.00 m) and the story height of 3.00 m (Fig. 21.4).

Fig. 21.4 Plan layout of the building



The concrete strength class used is C30/37 with an elastic modulus equal to 33017 MPa (according to NTC-08 2008). The concrete weight per unit volume is assumed equal to 24,000 N/m³ while the Poisson coefficient is fixed to 0.2. Columns have a square sections of 0.45 × 0.45 m and the beams are designed as rectangular tick section with 0.3 × 0.5 m dimensions. The class B450C is used for the reinforcing steel bars with an elastic modulus equal to 200,000 MPa. A diameter of 20 mm is used for the steel bars ($\phi 20$). The reinforcement ratio in the columns is equal to 1.8% while the beams have a perfectly symmetric steel bars disposal arrangement. The arrangement of the steel bars in the cross section is reported in Fig. 21.5 both for beams (Fig. 21.5b) and columns sections (Fig. 21.5a).

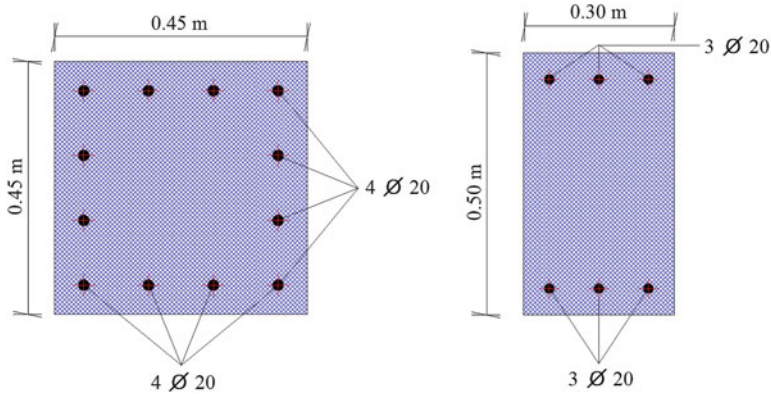


Fig. 21.5 Designed column (a) and beam (b) cross sections

21.4.1 Model Definition

It is common practice to start the model definition by setting the units measures used in the structural analysis. The units have to be specified in the drop-down list located in the bottom right corner of the interface. For the case study, N , m , $^{\circ}C$ are set for forces, distances, and thermal units, respectively. The idealization of the structural system is performed through the selection of the appropriate type of model. Figure 21.6 depicts the SAP2000 dialog box used to define a new structural model. In order to better describe the real geometry of the structure, a *3D Frame type* is selected for the case study building. SAP2000 allows also to identify the number of stories, number of bays (both in X and Y direction) and fixing the related dimensions of the objects in the global coordinate system. In addition, SAP2000 provides a *grid system* used to locate objects in the in the graphical user interface. Grids have no meaning in the analysis model and the related dialog box allows to fix the coordinates of the objects (a *X Grid Data*, a *Y Grid Data*, and a *Z Grid Data*).

Furthermore, the restraints have to be assigned to the frame model. After selecting the base joints, the restraints are assigned through the sequential commands: *Assign* \rightarrow *Joint* \rightarrow *Restraints*. A new dialog box appears and the six DOFs can be managed accordingly to the structural restraint characteristics. For the case study, all the DOFs are fixed in order to assume a fully restrained structure at the base. In the context of multistory building seismic analysis it is important to make some assumptions about the decks behavior. As explained in Chap. 4, the bending stiffness of the flooring system affects the rotational capacity of the beam-column connection. Moreover, the vertical elements can be assumed inextensible, because the axial stiffness is greater than the flexural one. This conditions should be considered in the analysis to reduce the problem complexity. For this purpose, the constraints are used to enforce certain types of rigid deck behaviors in which the constrained joints translate and rotate together as if connected by rigid links. The

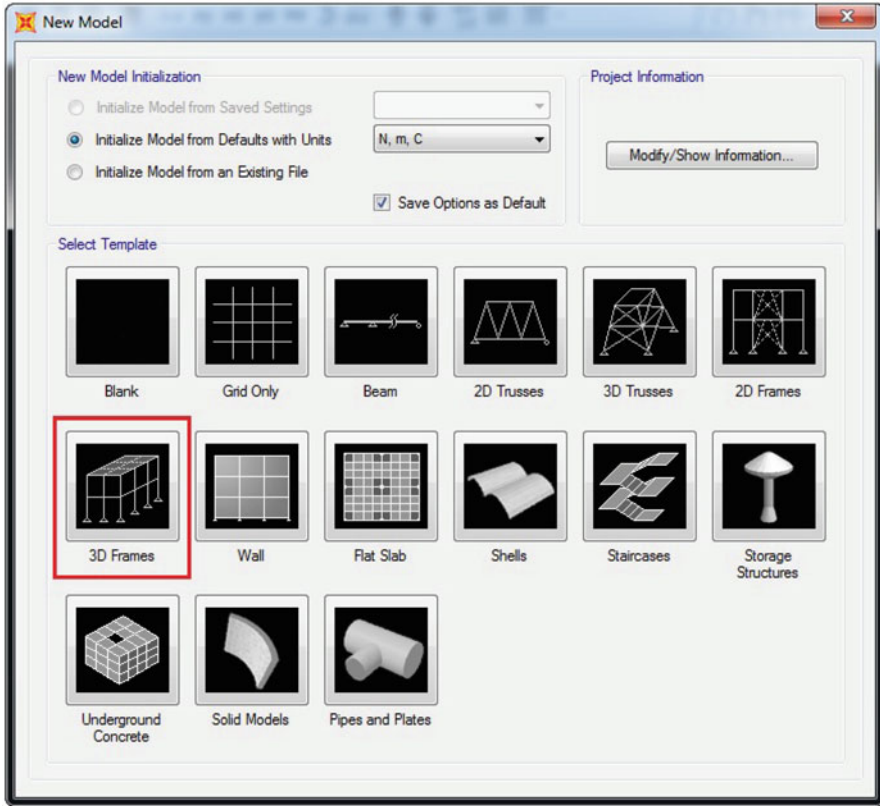


Fig. 21.6 New structural model SAP2000 dialog box

constraints are assigned to the selected joints through the sequential commands: *Assign* → *Joint* → *Constraints*. Shear type and bending type models can be used to simulate the seismic behaviour of multistory buildings.

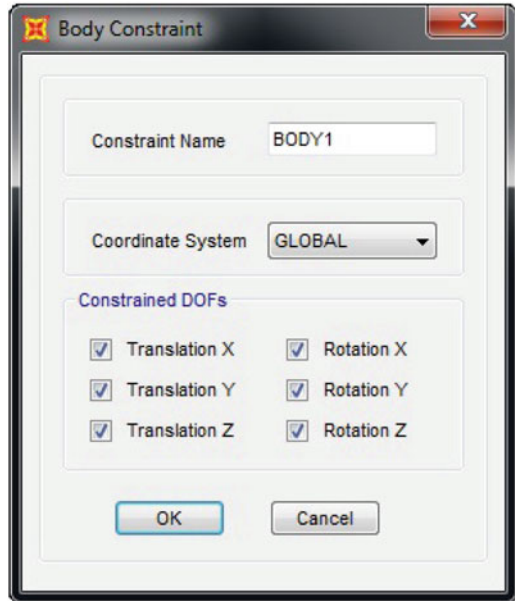
21.4.1.1 Shear Type Model

The large bending stiffness of the horizontal elements does not permit significant rotations in the beam-column connections. Therefore, the lateral strength can be described in terms of the translational displacements only. The shear type structures are governed by the following assumptions:

1. Columns and beams with infinite axial stiffness (inextensible elements);
2. Fully restrained beam-column joint (infinite joint rotational capacity);

The modeling of a shear type structure in SAP2000 is carried out by fixing the *Rigid Body* constraints for the joint located in the same horizontal plan (Fig. 21.7).

Fig. 21.7 Rigid body constraints



As depicted by Fig. 21.7, the Rigid Body constraint allows a fully rigid behaviour of the deck. This assumption leads to fix all the six relative displacements of the deck joints members to zero.

21.4.1.2 Bending Type Model

In the bending type systems the rotational DOFs are considered to evaluate the global stiffness contribution. The deck assumes a rigid membrane behaviour but the beam-column joints rotations are not neglected. A bending type building is modeled by using the *Rigid Diaphragm* constraints for the joint located in the same horizontal plan (Fig. 21.8).

These type of constraints ensures a rigid behavior in the horizontal plane allowing the rotations of the beam-column joints. Then, the translational relative displacements are fixed to zero, while the rotations in the global plane X-Z and Y-Z are allowed (rotations induced by the bending moment in the beams).

21.4.1.3 Beam-Column Joints Model

Structural modeling procedure has to be performed to accurately simulate the real behaviour of the structure. In a frame model, the analytical length of the element is considered as the distance between the two adjacent frame joints. This values does not correspond to the real deflection length of the element because the extreme zones of the elements constitutes the joints (Fig. 21.9).

Fig. 21.8 Rigid diaphragm constraints

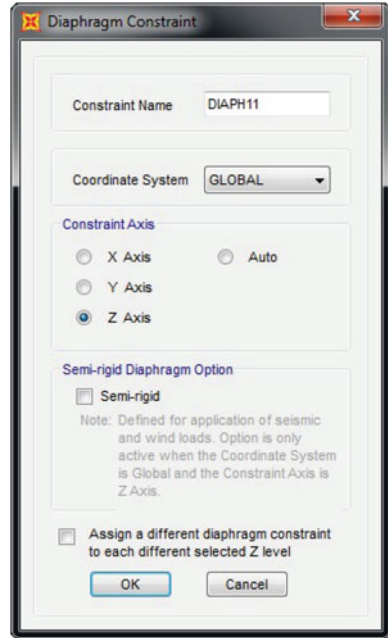
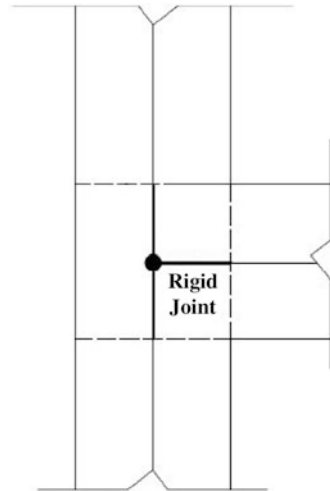


Fig. 21.9 Rigid zone in the beam/column joint



The part of the beams and columns that forms the joint has to be considered as a rigid zone in which the deflection of the beam and column is constrained. In order to take into account this physical aspect, the *Rigid Link* can be used to simulate the different rigidity of the nodes' zone. The assignment of this kind of constraints in SAP2000 is carried out by selecting all the frame's nodes and following this sequential command: *Assign* → *Frame* → *End (Length) Offsets*. The dialog box

requires the setting of the *Rigid Zone Factor* for the automatic detected connection zones (*Automatic from Connectivity*) or for the user specified length (*User Defined Length*). The rigid zone factor assumes values less than or equal to 1, where the unit value simulate the fully restrained conditions while 0 does not consider any rigid zone.

21.4.2 Materials Definition

The materials are used to define the mechanical, thermal, and density properties of the elements. As previously mentioned, this chapter is intended to provide the general information about structural performance analysis in SAP2000. The concrete properties are defined by clicking *Define* → *Materials*. A new dialog box appears and the materials properties can be customized through *Add New Material* button. SAP2000 provides new material definition accordingly to standard codes or user specifications. In the first case, the new material is defined by selecting *Region*, *Material type*, *Standard*, and *Grade*. In the case of user material definition, additional information have to be provided in the *Material Property Data* dialog box. For the case study, concrete and steel materials properties data are shown in Fig. 21.10.

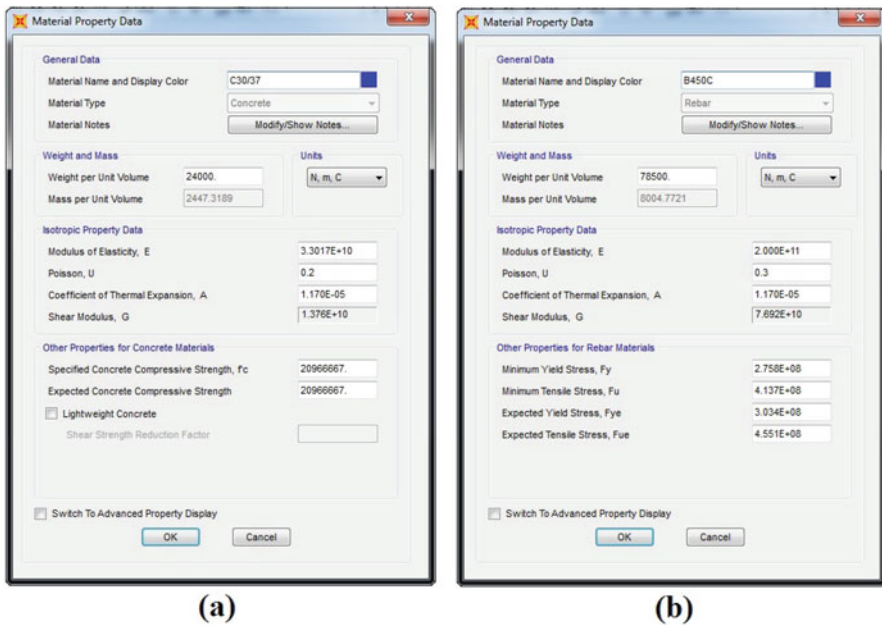


Fig. 21.10 Concrete (a) and steel reinforcing bars (b) material property data assignment



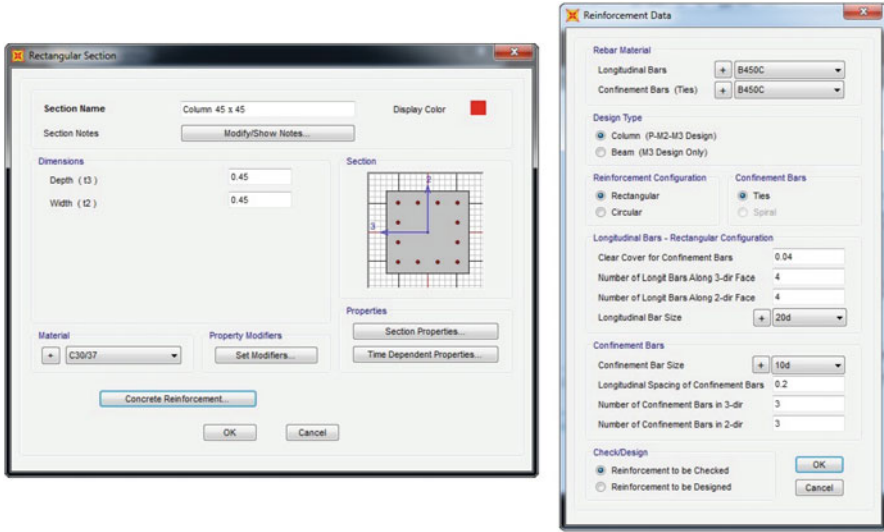


Fig. 21.11 Column section geometry definition (a) and associated steel reinforcing bars (b)

21.4.3 Sections Definition

The geometry of the frame elements (beams and columns) are assigned through the following sequential commands: *Define* → *Section Properties* → *Frame Sections*. In the new dialog box the section geometry is defined by clicking on *Add New Property* which will show the new dialog box *Add Frame Section Property*. SAP2000 provides some default frame section geometries associated with the *Frame Section Property type* which lists the type of materials used. Furthermore, the general section geometries (such as irregular shape section) are provided by selecting *Other* frame section property type. It is noteworthy to mention the *section designer* tool provided by SAP2000 for customizing the cross section geometry by using polygonal shapes. This tool is capable of modeling efficiently the section geometry of the frame element especially in those cases of reinforced concrete section with specific reinforcement distribution on the section. Given the simple geometry of the considered frame elements, the section definitions are performed by selecting *Concrete* → *Rectangular* in the *Add Frame Section Property* dialog box. Then, the *section name* is specified and the dimensions are set (*Depth* and *Width*). The *Material* associated with the element has to be fixed among the defined materials. Furthermore, the *Concrete Reinforcement* can be set by specifying the *Reinforcement Data* in the new dialog box. As an example, Figs. 21.11a and 21.5b illustrate the section definition for the column elements.

The defined frame elements have to be selected and then assigned by using the sequential commands *Assign* → *Frame* → *Frame Sections* and then choosing among the generated frame sections. Figure 21.12a displays the SAP2000 view of the frame section properties and Fig. 21.12b the 3D extruded view for the case study.

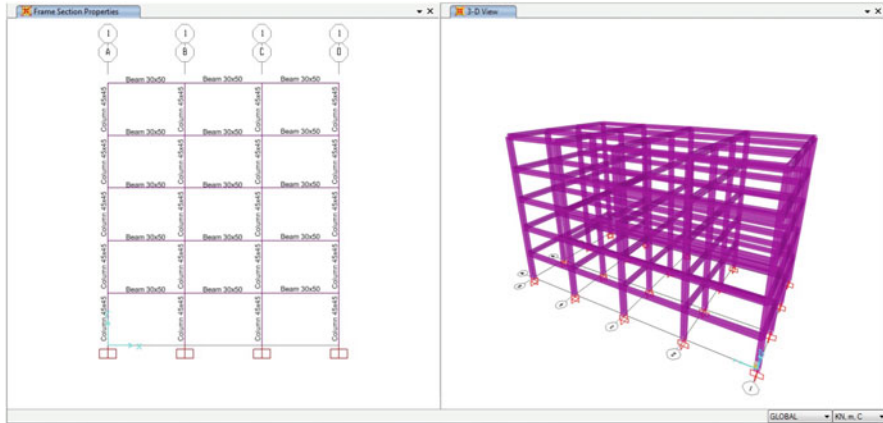


Fig. 21.12 Frame section properties (a) and 3D extruded view (b)

21.4.4 Vertical Load Definition

In SAP2000 the load definition has to be conducted through the definition of *Load Patterns*, *Load Cases*, and *Load Combinations*. A Load Pattern is a specified spatial distribution of forces, displacements, temperatures, and other effects that act upon the structure. A Load Pattern by itself does not cause any response of the structure, so it must be applied in *Load Cases* to produce results. The vertical loads are defined according to the *Seismic combination* as prescribed by the NTC-08 (2008). The permanent loads are always applied to the structures during its working period. For the case study, the weight of the deck (G) and of the external walls (W_{ext}) are defined as permanent loads. Furthermore, SAP2000 provides the permanent load, named *DEAD*, which defines the action due to the self-weight of the frame elements. The live loads (variable loads) are applied on the structure for a part of its working period. According to NTC-08 (2008) the variable load (Q) to be considered for a residential occupancy building is equal to 2000 and 500 N/m² for internal story and roof, respectively. Each Load Pattern has a design type (Dead, Live, Quake, etc.) which identifies the type of load applied. The definition of the *load pattern type* is required by the design algorithms to know how to treat the load when it is applied in a specific Load Case. Furthermore, the Load Pattern requires a self-weight multiplier which activates the self-weight of all elements in the model when it is set to unit values. Then the self-weight multiplier has to be set equal to 1 in the *DEAD* load pattern and 0 in the other cases. Figure 21.13 shows the Load Patterns dialog box with the set loads used in the case study.

A Load Case can apply a single Load Pattern or a combination of Load Patterns. Additionally, the results of the Load Cases can be combined after analysis by defining the Load Combinations. The definition of Load Cases and Load Combinations will be discussed in Sect. 21.4.5. Once the Load Patterns have been

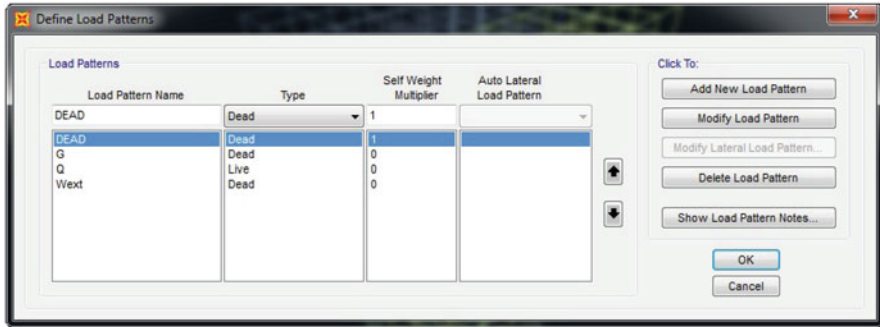


Fig. 21.13 Load pattern definition for the vertical loads

defined, the loads intensity have to be defined and assigned to the frame elements. In SAP2000 the loads can be applied on the frame as gravity, concentrated forces, distributed forces, temperatures, strains, deformations, etc. In SAP2000 the load intensity can be uniform or trapezoidal and the direction of loading may be specified in the global coordinate system or in the element local coordinate system. After selecting the frame elements, the assignment of the load is performed by the sequential commands *Assign* → *Frame Loads* → *Distributed*. The dialog box *Assign Frame Distributed Loads* requires general information (*Load Pattern Name*, *Coordinate System*, *Load Direction*, and *Load Type*). In the bottom part of the dialog box, the load values must be inserted by specifying the distance (relative or absolute). As example, Fig. 21.14 illustrates the Load Assignment used for the permanent load.

The same procedure has to be carried out for each Load Pattern.

21.4.5 Seismic Action

The seismic action on a structure is assessed through static and dynamic methods in the elastic field (linear methods) or considering also the plastic effects (nonlinear methods). In this section, four types of methods of seismic analysis are applied to the case study building in SAP2000.

21.4.5.1 Linear Static Analysis

The linear static analysis is performed by applying a distribution of equivalent static inertial forces in each center of mass at each story. The intensity of the equivalent forces are assumed proportional to the seismic weights at each story level. Due to the direction and center of the mass location (accidental eccentricity) unpredictability, the NTC-08 (2008) prescribes the use of different seismic load combinations to assess the response of the structure subjected to the earthquake excitation (see Table 14.2).

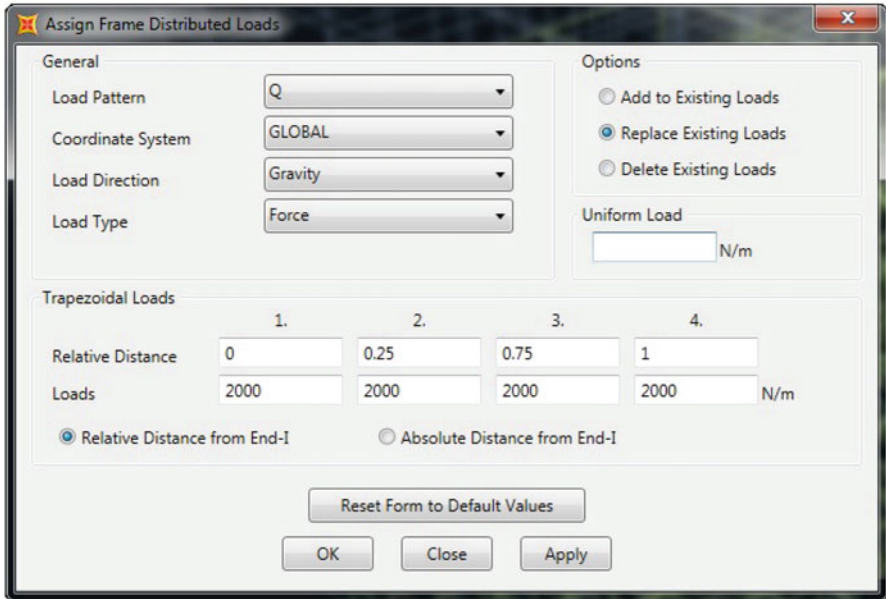


Fig. 21.14 Load frame assignment

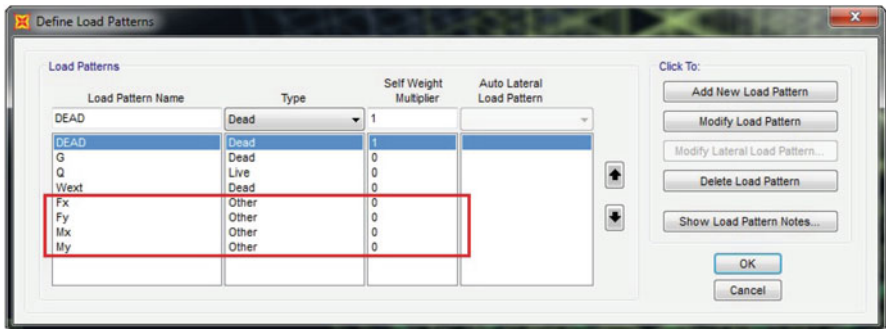


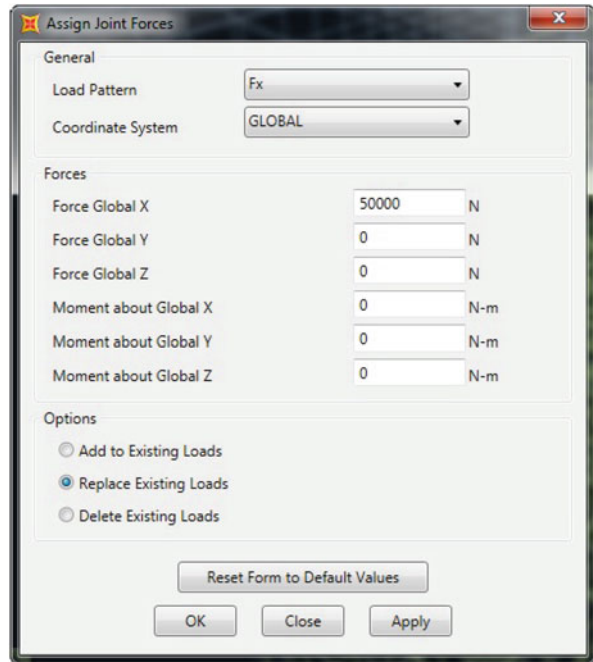
Fig. 21.15 Definition of the seismic load patterns

The definition of the seismic forces in SAP2000 can be carried out following different procedures. In this section, the definition of the seismic Load Pattern is performed through the use of two horizontal forces patterns (F_x and F_y), and the two generated torque moments (M_x and M_y) as *Other* Load Pattern Type (Fig. 21.15).

The assignment of the Load Pattern's values is carried out by selecting the center of the mass at the level of interest. The sequential commands *Assign* → *Joint Loads* → *Forces* are used. The *Load Pattern Name* and *Coordinate System* is fixed and then the values of the forces or moments are assigned (Fig. 21.16).



Fig. 21.16 Seismic actions assignment



When the center of the mass at a given level does not correspond to an existing node, it has to be defined (*Draw* → *Draw Special Joint*). Once the Load Pattern values are defined in both horizontal directions, the 32 Load Cases have to be defined accordingly to the Table 14.2 by setting *Static* as *Load Case Type* and inserting the previously defined Load Patterns. Figure 21.17 illustrates an example of Load Case definition.

Figure 21.17 depict the seismic combination considering the total positive contribution in X ($F_x \pm M_x$) direction and the 30% in Y direction ($F_y \pm M_y$).

The most critical response of the structure must be considered as result of the structural analysis. The NTC-08 (2008) prescribes to consider the envelope of the assumed seismic combinations as representative results. Thus, a Load Combination is defined in SAP2000 considering the 32 seismic combinations and the vertical load combinations and selecting the *Envelope* as *Load Combination Type* (Fig. 21.18).

As illustrative example, Fig. 21.19 shows the internal forces distribution, in a part of the frame, in terms of bending moment derived from the envelope of the 32 combinations.

21.4.5.2 Linear Dynamic Analysis

In this section the linear dynamic analysis (modal analysis) using response spectrum is illustrated. Modal analysis is used to determine the vibrational modes of a

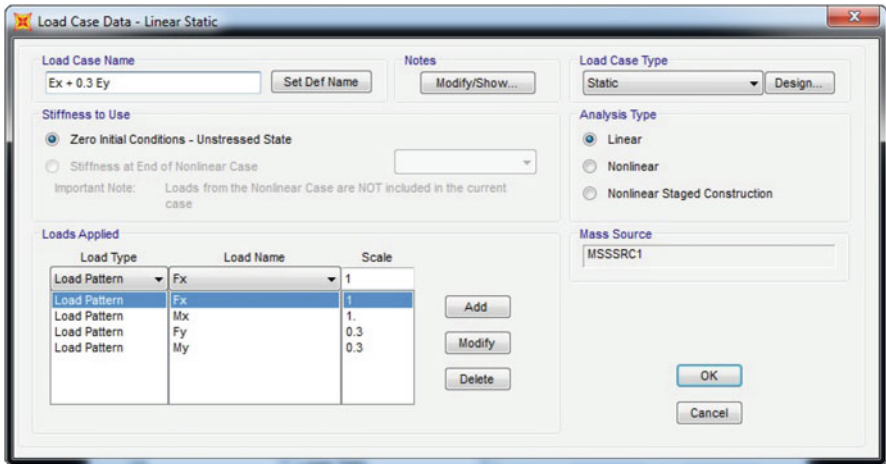


Fig. 21.17 Seismic load case definition

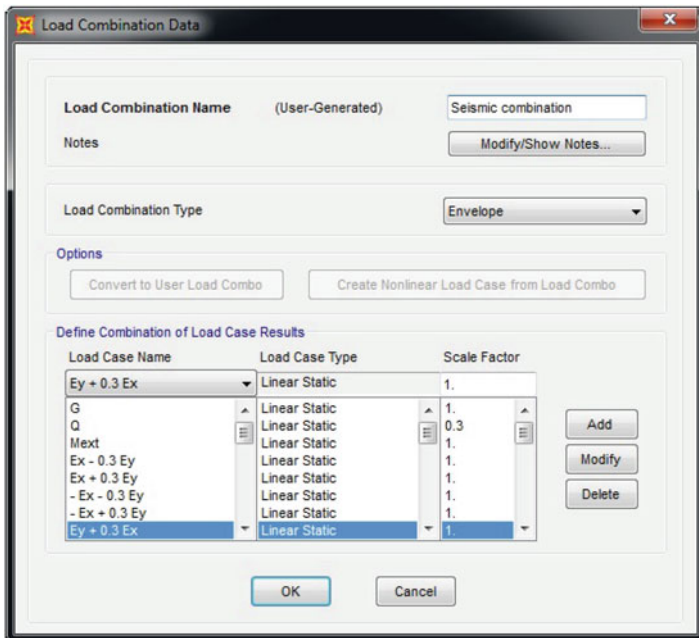


Fig. 21.18 Seismic envelope load combination definition

structure which are used to assess the structural response. They can also be used as the basis for modal superposition in the response spectrum analysis. The modal analysis is performed by defining of the Response Spectrum to be used in the analysis (*Define* → *Function* → *Response Spectrum*). SAP2000 is capable to

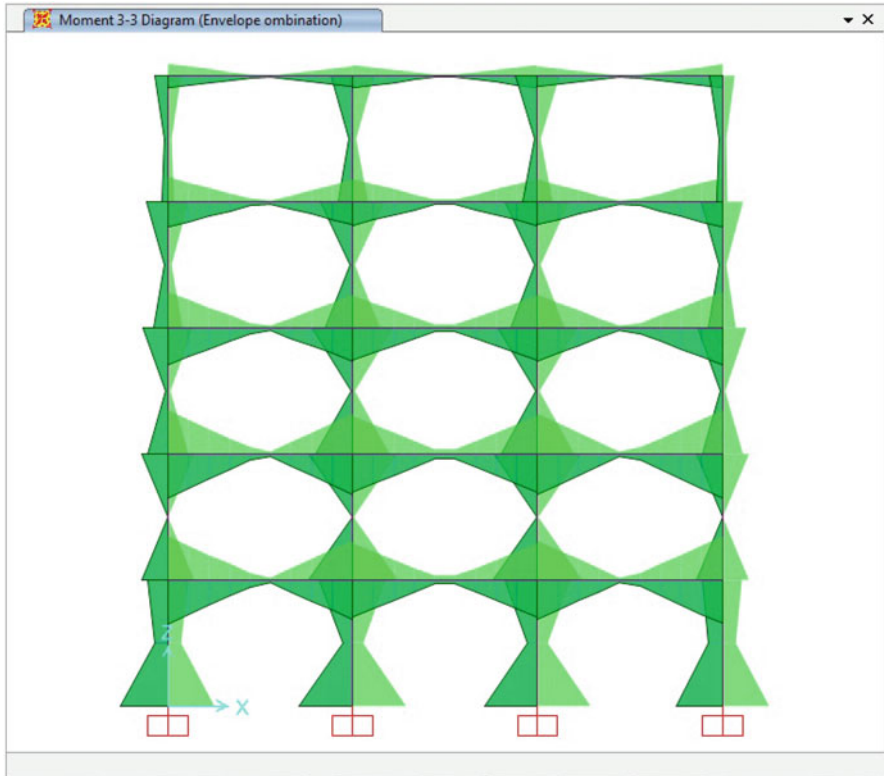


Fig. 21.19 Results in terms of bending moment (M3) for the envelope of the 32 combination

import a text file containing the periods and the associated spectral accelerations. In the case study the Response Spectrum RS_x and RS_y are defined in X and Y direction, respectively. According to NTC-08 (2008), the seismic excitation is obtained considering only the modes giving a total modal mass contributions of 85% and each mode having a modal mass contribution greater or equal than 5%. SAP2000 allows to both select the maximum number of modes to be considered in *Modal Load Case* (automatically generated), and the modal combination method. The directional effects on the structural response are assessed by SAP2000 through the *Directional Combination* (SRSS, CQC3, and Absolute combinations). For each response parameter, the modal combination produces a single, positive result for each direction of acceleration. These values for a given response quantity are combined to produce a single positive result. This allows to neglect the directional uncertainty of the seismic excitation. Anyway, due to the bi-directionality of the seismic excitation and the uncertainty in the center of the mass location 8 different Load Cases (Table 14.3) have to be defined by selecting *Response Spectrum* as *Load Case Type*. Then, the response spectrum function previously defined has to be inserted as *Accel Load Type*, U1-U2-R3 (translation in X – translation in Y

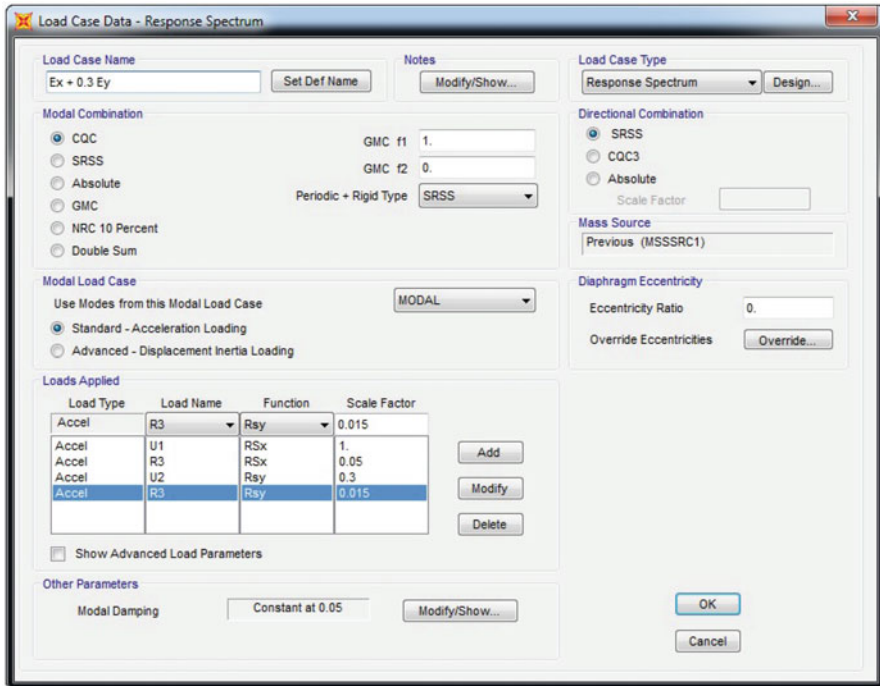


Fig. 21.20 Seismic load case definition

directions – rotation around Z axis, respectively) (Fig. 21.20). The torque moment caused by the eccentricity of the seismic excitation is obtained multiplying the response spectrum by the accidental eccentricity. In the same dialog box, the *Modal Combination* and *Directional Combination* can be selected.

The calculation of the built-in acceleration loads in the dynamic analysis requires the definition of the structural mass. SAP2000 calculates the mass for the model using the command *Define* → *Mass Source*. In the mass source data’s dialog box the load patterns which are converted in mass have to be specified (Vertical loads combination). The *DEAD* Load Pattern is considered by checking the *Element Self Mass and Additional Mass* while the other Load Patterns associated to the vertical actions have to be inserted after checking the *Specified Load Pattern* (Fig. 21.21).

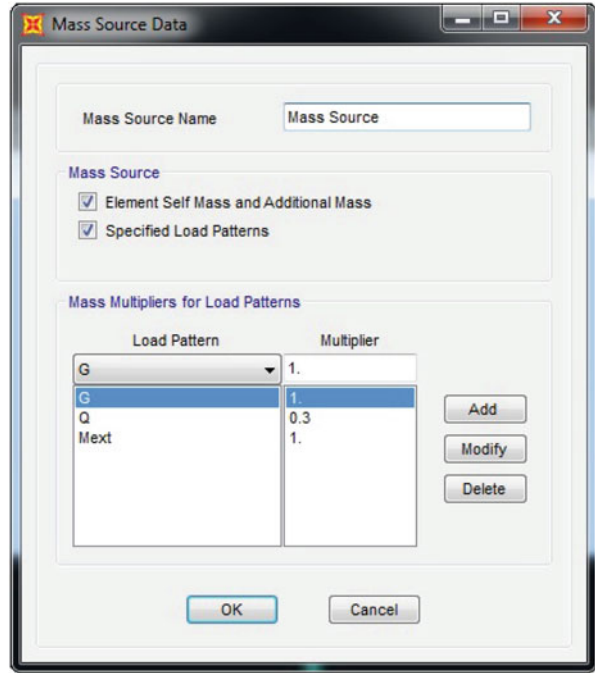
Similarly to the linear static analysis, a Load Combination is defined considering the 8 seismic combinations and the vertical load combinations (*Envelope as Load Combination Type*).

It is interesting to analyze the results coming from the Modal analysis to investigate the dynamic characteristics of the building. Figure 21.22 depicts the SAP2000 table containing the periods and the mass ratios of each mode.

Focusing the attention on the first three modes, the following information can be derived:



Fig. 21.21 Mass source definition



OutputCase	StepType	StepItem	Period	UX	UY	UZ	SumUX	SumUY	SumUZ	RX	RY	RZ	SumRX	SumRY	SumRZ
Modal	Mode	Unitless	Sec	Unitless	Unitless	Unitless	Unitless	Unitless	Unitless	Unitless	Unitless	Unitless	Unitless	Unitless	Unitless
1	MODAL	Mode	0.626126	0.00031	0.82741	0.362610	0.00031	0.82741	0.362610	0.04028	2.7476-05	0.00033	0.04028	2.7476-05	0.00033
2	MODAL	Mode	0.59847	0.78713	0.00046	2.544E-10	0.78714	0.82787	1.191E-09	2.513E-05	0.07279	0.00021	0.04032	0.07282	0.03054
3	MODAL	Mode	0.548022	0.03748	0.00019	1.090E-09	0.82489	0.82806	2.285E-09	1.523E-05	0.00432	0.794	0.04032	0.07714	0.03054
4	MODAL	Mode	0.379319	0.00531	4.396E-06	3.109E-11	0.8302	0.82806	2.318E-09	2.963E-06	0.00024	0.00117	0.04032	0.07739	0.03171
5	MODAL	Mode	0.301007	0.00173	7.528E-06	1.194E-12	0.83193	0.82807	2.318E-09	1.265E-06	0.00039	0.00117	0.04032	0.07778	0.03288
6	MODAL	Mode	0.242784	9.79E-06	2.658E-06	1.100E-10	0.83194	0.82807	2.428E-09	4.024E-05	1.100E-05	0.0003	0.04036	0.07778	0.03318
7	MODAL	Mode	0.198554	0.0445	0.04663	5.66E-09	0.87644	0.87475	8.66E-09	0.06298	0.12088	0.00411	0.10334	0.19865	0.03729
8	MODAL	Mode	0.187315	0.03641	0.05878	1.062E-09	0.91285	0.93352	9.15E-09	0.07939	0.08914	0.00335	0.18274	0.28779	0.04064
9	MODAL	Mode	0.179851	0.00287	6.839E-06	3.62E-09	0.91152	0.93352	1.277E-08	1.057E-05	0.00759	0.04174	0.18275	0.30038	0.08238
10	MODAL	Mode	0.175481	0.01049	7.918E-07	7.494E-09	0.92801	0.93352	2.628E-08	7.971E-07	0.0288	0.04317	0.18275	0.33386	0.02554
11	MODAL	Mode	0.154832	0.01122	8.889E-05	3.855E-12	0.93723	0.93361	2.627E-08	0.00013	0.03141	0.04407	0.18288	0.36039	0.02961
12	MODAL	Mode	0.150430	5.078E-05	0.00017	4.871E-10	0.93728	0.93378	2.674E-08	0.00025	0.00013	0.00774	0.18313	0.36852	0.03736

Fig. 21.22 Modal information

1. Mode 1: translational mode in Y direction ($T_1 = 0.626$ s and $m_{mod} = 82.74\%$);
2. Mode 2: translational mode in X direction ($T_2 = 0.598$ s and $m_{mod} = 78.71\%$);
3. Mode 3: rotational mode in Z direction ($T_3 = 0.548$ s and $m_{mod} = 79.40\%$);

This data confirm how almost all the participation mass (modal mass) is distributed in the first modes for regular buildings. The mode ratios of the higher modes assume low values (less than 0.5%), then they can be neglected in the modal analysis with response spectrum.



21.4.5.3 Nonlinear Static Analysis

Nonlinear static analysis (pushover analysis) is used to estimate the seismic vulnerability of a structural system. The structure is subjected to vertical loads and to a static inertial force distribution increasing in a quasi-static way that leads to a plastic hinge formation and also to a stress redistribution within the structural members. Pushover analysis is a method which permits the estimation of the *capacity* of a structure subjected to a given external lateral increasing load. The structural capacity is usually given by the base shear (V_b) versus the control node displacement (u_c). Differently to the linear analysis cases, the geometrical nonlinearity (second order effects) and material nonlinearity (concentrated or distributed nonlinearity models) have to be considered.

I. Material nonlinearity

The material nonlinearities are assumed in SAP2000 through the definition of the *Frame Hinge Properties* which represent the concentrated post-yield behavior in one or more DOFs. Hinges can be assigned to a frame element at its extreme points along the clear length of the element (length of plastic hinge).

SAP2000 provides different types plastic hinge according to the stress-state in the structural members. The following hinge types are among the most used plastic hinges for frame elements.

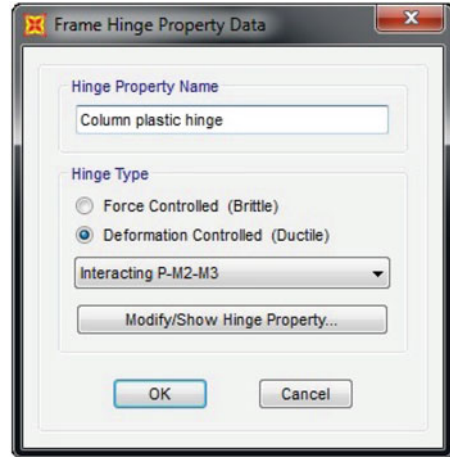
- (a) coupled P - $M2$ - $M3$ hinges which yield based on the interaction of axial force and bi-axial bending moments at the hinge location. This type of plastic hinge is feasible for 3D column members.
- (b) P - $M2$ and P - $M3$ hinges which yield based on the interaction of axial force and bending moment at the hinge location. This type of plastic hinge is feasible for 2D column members.
- (c) $M2$ - $M3$ hinges which yield based on the interaction of bi-axial bending moment at the hinge location. This type of plastic hinge is feasible for 3D beam members

The force-displacement behaviour is described by idealized hinge properties or by default hinge properties which are provided based on ASCE 41-13 (Deierlein et al. 2010).

For each force or moment degree of freedom, the force-displacement, moment-rotation or moment-curvature curves can be defined. These curves give the yield value and the plastic deformation following yield by means of five points:

- (a) A: origin of the curve;
- (b) B: yielding point;
- (c) C, D: characteristics plastic points useful to describe ultimate limit state;
- (d) E: ultimate point which corresponds to the maximum displacement capacity of the member.

Fig. 21.23 Frame hinge properties definition



Each plastic hinge is modeled as a discrete point in which all the plastic deformations occur within the point hinge. The plastic deformation is then integrated over a certain length (hinge length). Some guidelines suggest a formulation to assess the hinge length (e.g., ASCE 41-13).

The user-defined plastic hinge properties can be set through the sequential command: *Define* → *Section properties* → *Hinge Properties*. By clicking to *Add New Property* the type of plastic hinge can be fixed by selecting through *Steel*, *Concrete* or *User* type of hinge. A new dialog box will appear in which the *Hinge Property Name* and the *Hinge Type* can be selected. Figure 21.23 depicts an example of hinge type definition for column frame elements in the case study.

In the case study, the hinge types are defined as *Displacement Controlled* and *Interacting P-M2-M3* for the columns, and *Displacement Controlled – Interacting M2-M3* for the beams. The hinge type is defined according to the *Force Controlled* or *Displacement Controlled* curve, and based on the stress-state induced in the members. The scaled force-displacement curves are generated by default accordingly to ASCE 41-13. By selecting *Modify/Show Hinge Property*, the plastic characteristics can be modified through the new dialog box (Fig. 21.24).

This section is not intended to provide all the information about the definition of plastic hinges to be used in the analysis. For detailed information the SAP2000 user manual is suggested. In order to better clarify the characterization of the plastic capacity of a structural member, the moment-rotation curve is analyzed in this section. The five characteristic points of the moment-curvature curve can be modified or shown by clicking *Modify/Show Moment Rotation Curve Data*. The data are displayed in the new dialog box which shows the curve normalized with respect to the yield moment (Fig. 21.25).

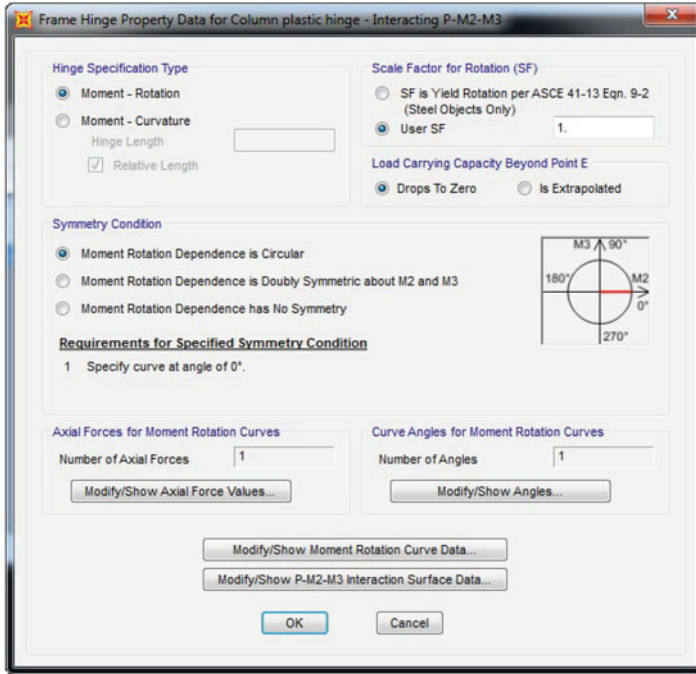


Fig. 21.24 Frame hinge property data

Automatic hinge properties can be also provided by SAP2000. They are based upon a simplified set of assumptions that may not be appropriate for all structures. The following types of automatic hinges are available in SAP2000 (according to FEMA 356 2000):

- (a) Concrete Beams in Flexure;
- (b) Concrete Columns in Flexure;
- (c) Steel Columns in Flexure;
- (d) Steel Braces in Tension/Compression.

Once the plastic hinges are defined, the assignment to each structural element is carried out by selecting the elements and following the sequential commands: *Assign* → *Frame* → *Hinges*. The hinge property name (*Auto* is given for the automatic hinge properties) and relative distance are required. This last parameter represents the relative distance between the extreme point of the element and the hinge location. For column and beam members it is suggested to use the relative distances of 0.05 and 0.95 which means to apply the plastic hinges at 5% and 95% far from the initial extreme point of the element. For the case study, the example of the columns plastic hinges assignment is illustrated in Fig. 21.26.

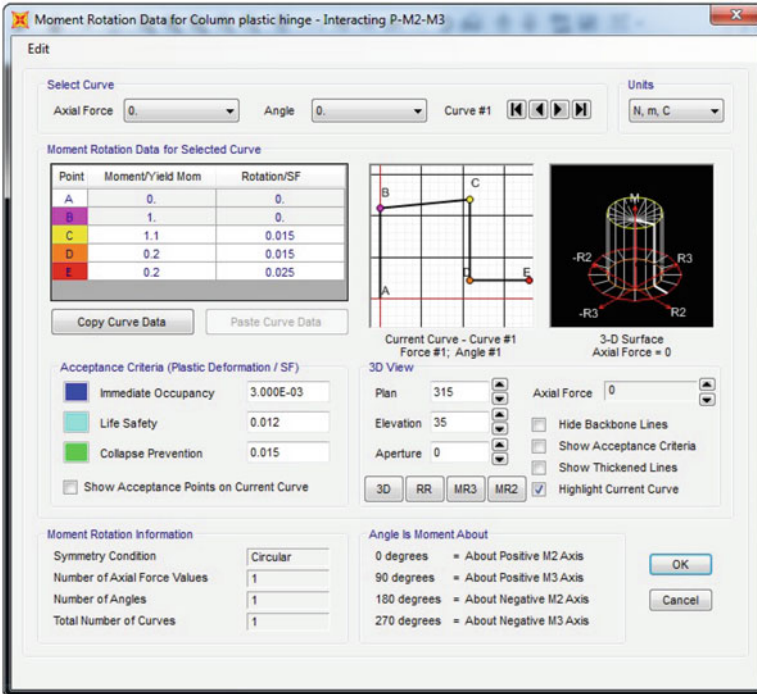


Fig. 21.25 Moment rotation data for column plastic hinge – interacting P-M2-M3

As illustrative example, the plastic hinge assignment for a part of the frame model used as case study is depicted in Fig. 21.27.

Due to the selection of the relative distance, the plastic hinge are displayed at a certain distance to the column and beam nodes. Furthermore, the name of the hinge properties are reported.

II. Load pattern shape

The capacity curve is strictly dependent on the force distribution along the building elevation. The Italian seismic standard (NTC-08 2008) prescribes the use of two different horizontal force distributions named principal distribution (Group 1) and secondary distribution (Group 2).

In Group 1 the distribution can be selected among one of the three below:

- distribution proportional to the forces obtained with the linear static procedure (Sect. 14.2);
- distribution corresponding to a distribution of accelerations proportional to the fundamental mode shape;
- distribution corresponding to a distribution of story shear derived through linear dynamic analysis (Sect. 14.3).

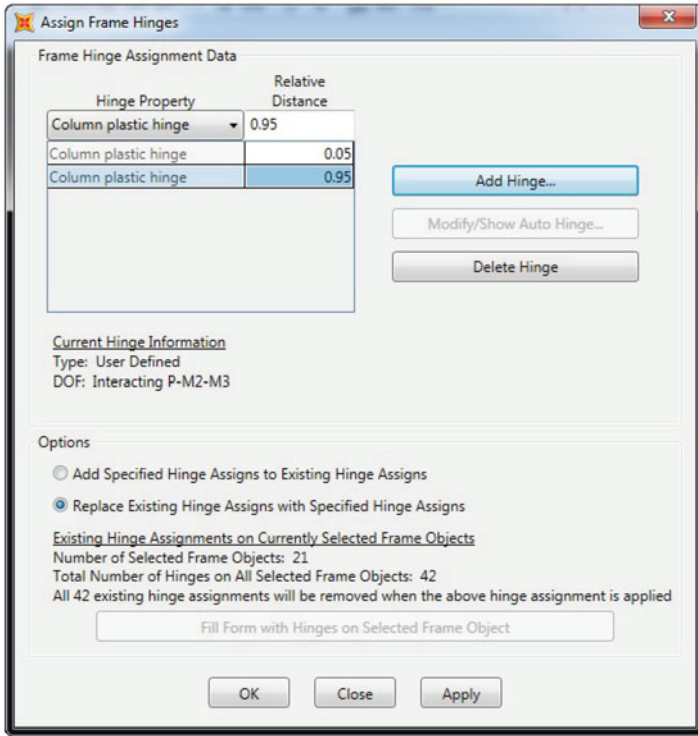


Fig. 21.26 Plastic hinge assignment

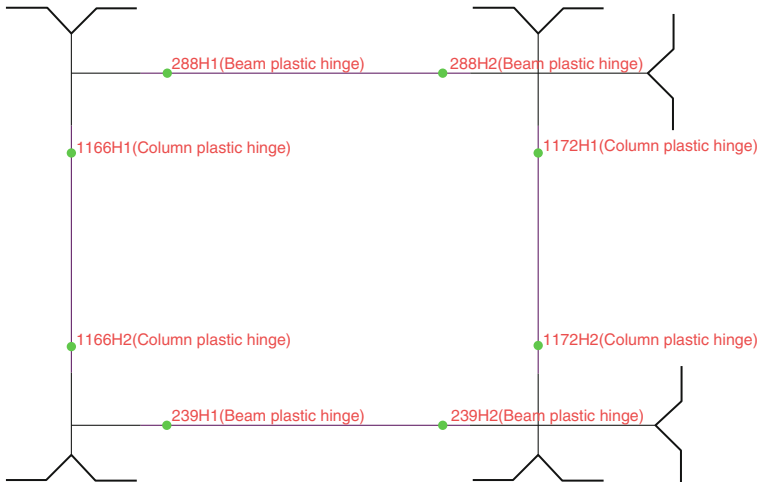


Fig. 21.27 Example of plastic hinge assignment in a part of the frame model

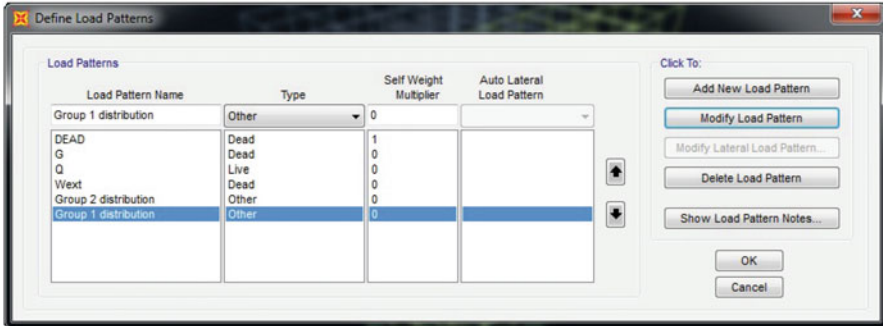


Fig. 21.28 Load pattern definition

In the first two cases the fundamental mode must have a modal participation factor greater than 75%.

Instead in Group 2 the distribution can be selected among one of the two below:

- uniform force distribution;
- adaptive force distribution which changes with the increment of the target displacement due to the formation of plastic hinges.

The horizontal forces distributions are applied consequently to the vertical load combination. In the case study building, two horizontal force distributions are used and the pushover analysis is performed in the X direction. The group 1 horizontal load pattern is selected as acceleration distribution proportional to the first mode in the X direction which have a modal participation factor of 78% (see Fig. 21.22). Additionally, a uniform distribution is considered as group 2 load horizontal pattern. Thus, the Load Pattern *Group 1 distribution* and *Group 2 distribution* are defined in SAP2000 as *Other* Load Pattern type. The vertical Load Pattern are defined as well (Fig. 21.28).

Similarly to the equivalent linear static forces, the defined seismic Load Patterns have to be assigned as Joint Forces in the center of mass at each story level. Since the pushover analysis is performed by increasing monotonically the horizontal force distribution, it is suggested to assign a proportional horizontal force having the unit value as top force. The definition of the Load Cases is then carried out for the two force distributions and for the vertical load combination. For the case study, the following Load Cases are defined as *Static* Load Case Type and *Nonlinear* Analysis type.

- Vertical where the dead load (*DEAD*), permanent load (*G*), external wall load (*Wext*), and live load (*Q*) with scale factor equal to 0.3 are considered.
- Pushover Group 1 where the *Group 1 distribution* Load Pattern is considered.
- Pushover Group 2 where the *Group 2 distribution* Load Pattern is considered.

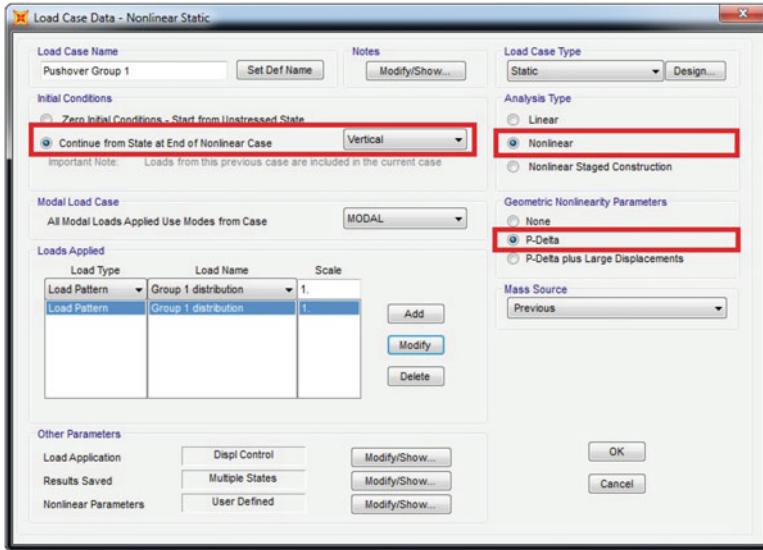


Fig. 21.29 Load case data definition

When the horizontal force pattern is proportional to a modal shape, SAP2000 allows to define the related Load Case by selecting *Mode* as Load Type and choose among the number of modes. For the *Pushover Group 1* and *Pushover Group 2* Load Cases the *Initial Conditions*, *Geometric Nonlinearity Parameters*, and *Other Parameters* have to be defined. The initial conditions specify the stress-state condition in the structure when the horizontal forces are applied. In the pushover analysis, the horizontal force distribution is applied after the application of the vertical loads. Thus, *Continue from State at End of Nonlinear Case* is checked and *Vertical Load Case* is selected as starting Nonlinear Case. The second order effects can be taken into account in the analysis by checking *P-Delta* as geometric Nonlinearity Parameters (Fig. 21.29).

The load application approach and the displacement control point can be selected by modifying the *Load Application* parameter. It is suggested to select *Displacement Control* as load Application control and considering the top center of the mass point as monitored joint in the direction of interest (Fig. 21.30).

The Joint number 120 is the joint corresponding to the center of the mass at the top of the building. Since the pushover analysis is performed in the X direction, the monitored displacement is *U1*. Furthermore, the *Results Saved* and *Nonlinear parameters* settings can be modified. For the case study building, a Group 1 force distribution proportional to the first mode in the X direction (mode 2, with modal participation factor equal to 78%) is considered. According to ASCE 41-13, the column and the beam plastic hinges are selected as Interacting P-M2-M3 and Interacting M2-M3, respectively. Figure 21.31 illustrates the



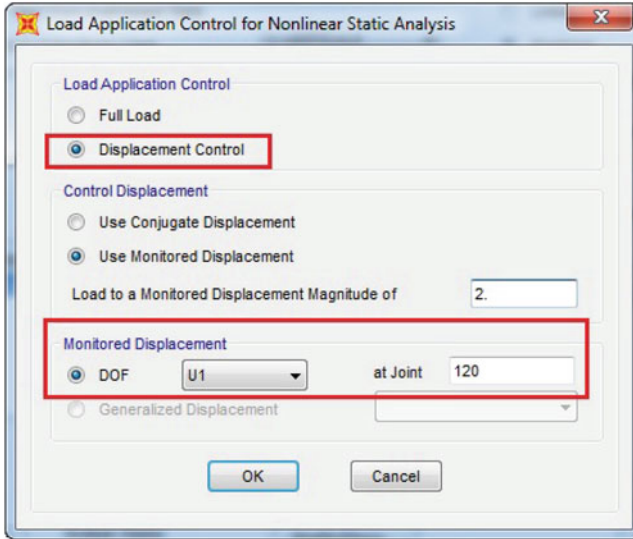


Fig. 21.30 Load application control data

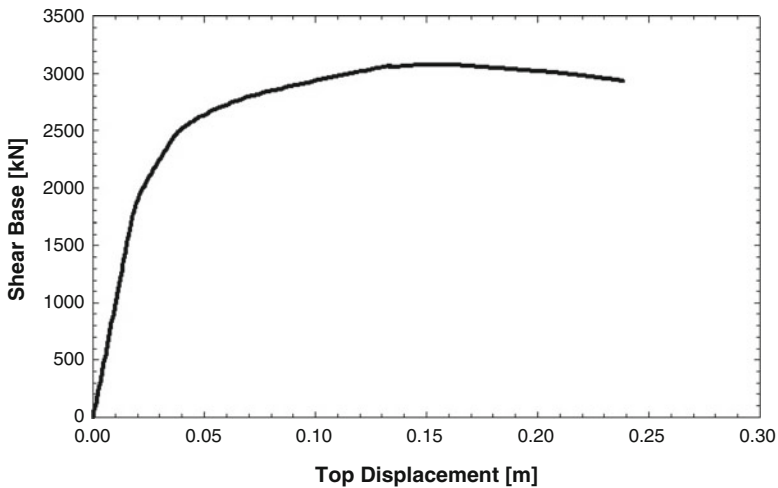


Fig. 21.31 Pushover curve in X direction

pushover curve in the X direction in which the building's top center of mass is the monitored joint. The P-Delta effects are also considered in the analysis.

SAP2000 provides also the deformed shape at each step of the pushover analysis and the plastic hinges formed in the structures are shown. Figure 21.32 depicts the last step of the pushover analysis for the case study building.

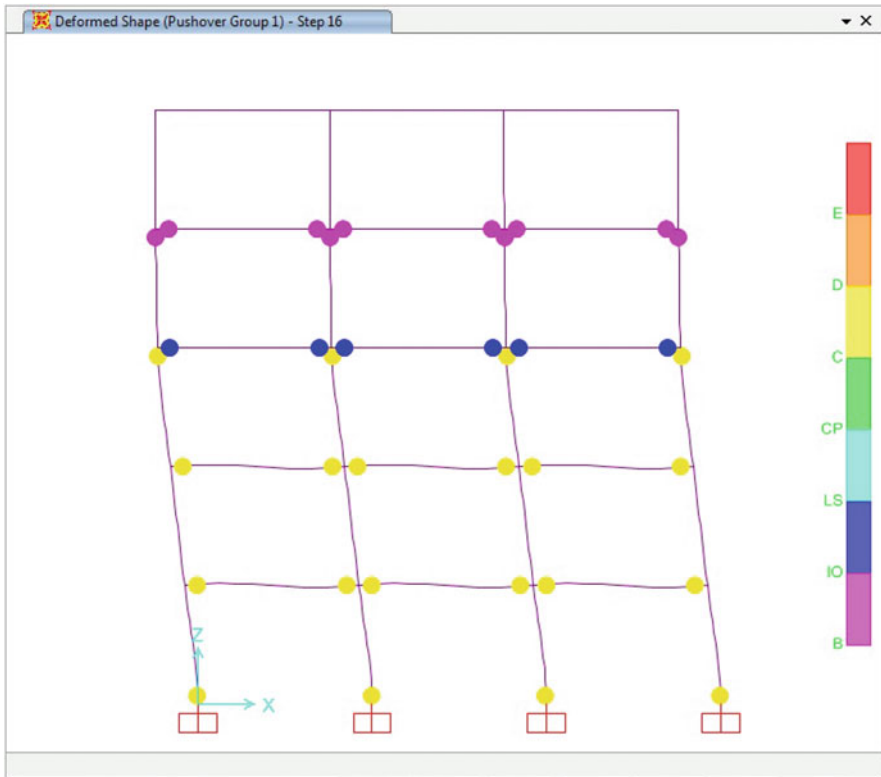


Fig. 21.32 Last step pushover deformed shape

The plastic hinge color’s legend is reported on the right in which each color corresponds to a given Limit State.

21.5 Seismic Retrofitting

The structural retrofit focuses on reducing the seismic risk for buildings by improving their dynamic response. The retrofitting methodologies are based on the modification of the structure to make it more resistant to the seismic action, and on the understanding of seismic demand (Moehle 2000). Thus, the goal of the modern retrofit techniques is to enhance the seismic performance of the structures through proper initial design or subsequent modifications. The seismic retrofit strategies are substantially different and they are classified in terms of basic approach used to achieve the structural performance enhancing (Reitherman 2012). Generally, the seismic retrofit strategies can be diversified as below:



1. *Global Strengthening* which increases the global capacity of the structural system (e.g., shear walls).
2. *Local Strengthening* which increases the local capacity of the structural system (e.g., strength beam-column joint connection)
3. *Passive Control* which reduces the seismic demand by means of proper devices (base isolation system, TMD and dampers)
4. *Selecting weakening* which consists in reducing the strength/stiffness of specific members within the structural system. This in turn results in a reduced demand on the structural members (Ireland et al. 2006; Viti et al. 2006).

In this section some of the common seismic retrofit techniques will be explained with practical examples of SAP2000 modeling.

21.5.1 Seismic Isolated Structures

Seismic isolation is a design strategy that has been used both for seismic rehabilitation of existing buildings and new buildings. In general, this system is feasible for strategic buildings whose stakeholder requires a larger seismic performance and can afford the costs associated with the technique. The idea of base isolation is to reduce the seismic demand by reducing the energy being transferred to the structure from the foundations. The superstructure in turn experiences low inter-story drifts which allow an elastic behaviour. Different base isolation design procedures have been proposed in the past. Generally, a complete design for base isolation should ensure that the isolators can support the maximum gravity service loads of the structure throughout its life, and the isolators can provide the dual function of period shift and energy dissipation to the isolated structure during earthquakes (Yang et al. 2003). In this section, a simplified design procedure for rubber bearing isolators is discussed below.

1. The period of the isolated structure T_{is} is selected to be higher than the non-isolated structure (fully restrained structure) (T_f). NTC-08 (2008) suggests to use a period of the isolated structure equal to three times the period of the fully restrained structure. A common procedure to fix the T_{is} is carried out by reducing the ground acceleration of 80% and evaluate the new period from the design spectrum at the corresponding site.
2. The equivalent stiffness of the isolation system (K_0) is assessed assuming an equivalent SDOF system in which the equivalent mass is given by the superstructure's mass (M) and the period is assumed equal to T_{is} . Thus, the equivalent stiffness of the isolated system is given by Eq. 21.1.

$$K_0 = M \cdot \left(\frac{2 \cdot \pi}{T_{is}} \right)^2 \quad (21.1)$$

- The number of isolators can be evaluated by selecting a commercial rubber bearing isolator having a certain lateral stiffness (K_{is}). Then, the number of devices (n_{is}) to be used is given by Eq. 21.2.

$$n_{is} = \frac{K_0}{K_{is}} \tag{21.2}$$

Different types of base isolators are available in the market. Each of them is classified according to the maximum displacement, capacity and stiffness/strength. The first parameters represents the maximum lateral absolute displacement that the isolators can reach. The stiffness/strength properties are expressed by the lateral stiffness (K_0) and the vertical stiffness (K_V). The principal strength parameters are represented by the maximum vertical axial force applicable on the isolators. These parameters must be in compliance with the maximum axial load acting on the base columns.

- The geometrical arrangement of the isolators must be carried out to reduce the torsional effects due to the offset between the center of mass at the base and the stiffness centroid of the isolation system. Furthermore, when the number of isolators is less than the number of base columns, additional sliding devices (sliders) must be located in the non-isolated columns.

The aforementioned concepts are applied to the case study structure. The calculation period of isolated structure is assessed in order to reduce the ground acceleration of 80%. NTC-08 (2008) prescribes the use of the Life Safety elastic response spectrum scaled with a reduction factor equal to 1.5. Figure 21.33 illustrates the Life Safety scaled elastic response spectrum for the considered site and the selected isolated structural period.

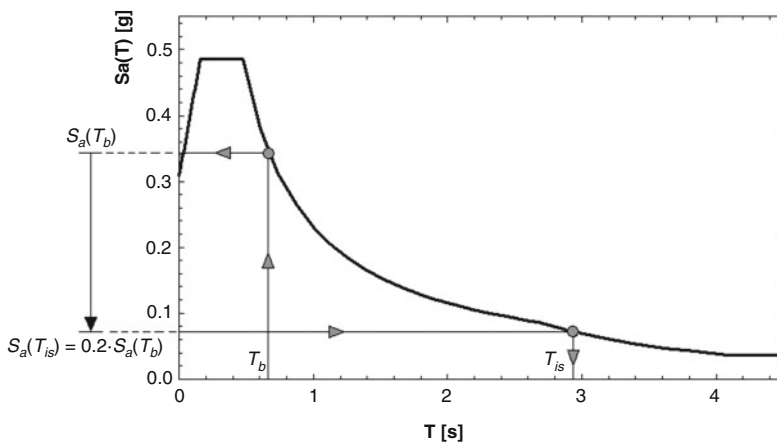
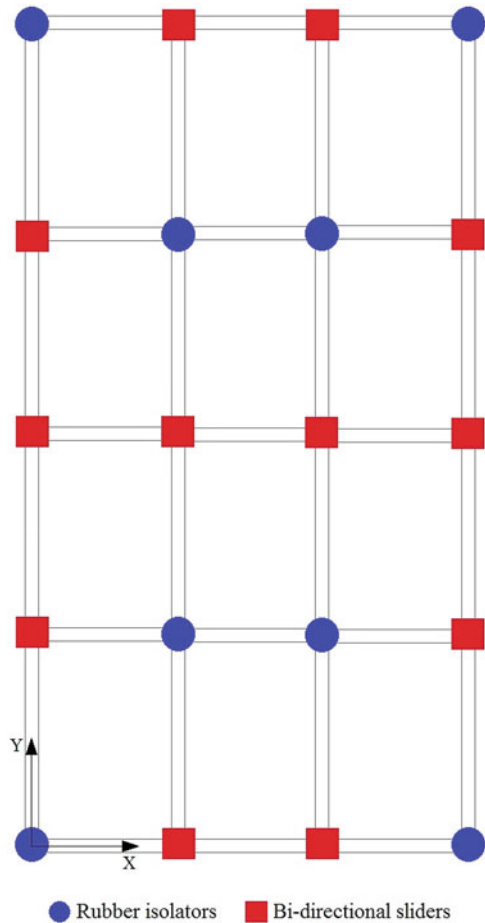


Fig. 21.33 Evaluation of the isolated structure period

Fig. 21.34 Geometrical arrangement of the base isolation system



The spectral acceleration at the period of the non-isolated structure is equal to 0.345 g. Reducing it of 80% the spectral acceleration of the isolated structure is equal to 0.069 g which corresponds to a period of 2.92 s. The total mass of the structure is equal to 691,278 kg which corresponds, through Eq. 21.1, an equivalent lateral stiffness of the base isolation system equal to 7.81 kN/mm. According to the plan of the building and its regularity, the isolators and sliders may be located as illustrated in Fig. 21.34.

This solution is suitable in terms of design and related costs. The lateral stiffness of each isolator is calculated accordingly to Eq. 21.2 and it is equal to 0.98 kN/mm. Furthermore, the maximum vertical load on the base column is equal to 1022 kN (derived by running the vertical combination on SAP2000). According to the two mentioned parameters and the maximum allowable base displacement, the type of isolators have to be selected among the available in the market. For this purpose, the catalog of *FIP industriale* is considered for the selection of the rubber isolators in the case study (Fig. 21.35).

Displacement 250 mm

SI-H	V kN	F _{zd} kN	K _o kN/mm	K _v kN/mm	D _g mm	t _o mm	h mm	H mm	Z mm	W kg
SI-H 300/128	65	1810	0.77	456	300	128	230	280	350	110
SI-H 350/125	350	2890	1.08	620	350	125	213	263	400	138
SI-H 400/125	1040	4680	1.41	911	400	125	213	263	450	179
SI-H 450/126	1880	6930	1.77	1111	450	126	226	276	500	239
SI-H 500/126	3520	9360	2.18	1489	500	126	226	276	550	294
SI-H 550/126	4220	9820	2.64	1753	550	126	217	267	600	338
SI-H 600/128	4910	10310	3.09	2006	600	128	213	263	650	389
SI-H 650/126	5580	10830	3.69	2344	650	126	205	255	700	440
SI-H 700/130	6250	11370	4.14	2590	700	130	216	276	750	575
SI-H 800/130	9080	14990	5.41	3752	800	130	216	276	850	747
SI-H 900/132	13790	21220	6.75	4514	900	132	222	282	950	963
SI-H 1000/140	15470	22590	7.85	5105	1000	140	236	316	1050	1402
SI-H 1100/140	19590	27460	9.50	6631	1100	140	236	316	1150	1691
SI-H 1200/144	22700	28700	11.00	7468	1200	144	236	316	1250	1979

Fig. 21.35 Selected rubber isolator (*FIP industriale*)

An hard series rubber isolator is selected, having a maximum allowable base displacement of 250 mm. Furthermore, the lateral stiffness is 1.08 kN/mm and the maximum vertical load at ultimate limit state is 2890 kN. Thus, this characteristics are in compliance with the design parameters previously calculated. The seismic isolation system is modeled in SAP2000 using *Link Elements* which describe the structural linear and nonlinear behaviour for each DOFs by specifying the force-deformation relationships. The mass, weight, and damping properties may also be specified. For the case study building, two link elements are defined to model the rubber isolators and the bi-directional sliders. The definition of the link elements is carried out through the following sequential commands: *Define* → *Section Properties* → *Link/Support Properties*. Several types of link elements are proposed in SAP2000, but for the case study considered the *Rubber Isolators* and *MultiLinear Elastic* elements are considered for modeling the rubber isolators and the bi-directional sliders, respectively. The *Directional Properties* can be set and the stiffness/strength and damping properties can be modified. The rubber isolators are defined by fixing the rotational DOFs, while the bi-directional sliders are defined by fixing the rotational DOFs and the vertical translations. In addition, the mass, the lateral stiffness, and the damping coefficients of the rubber isolators and the bi-directional sliders are set. An illustrative example of the link properties setting is shown in Fig. 21.36.

SAP2000 allows to add a link element between two joints. Then, the base plan of the building must be duplicated at a distance $\delta H = -h_{is}$, where h_{is} corresponds to the height of the rubber isolator. Therefore, the link elements can be modeled in the right location by means of the command *Draw* → *Draw 2 Joint Link*. Once all the link elements are modeled, the assignment of the previously defined properties is carried out through the sequential commands: *Assign* → *Link/Support* → *Link/Support Properties*.

The dynamic analysis is performed as explained in Sect. 21.4.5.2. SAP2000 requires to define 8 different Load Case as *Static Nonlinear*. The envelope of the 8 seismic combinations are considered as results of the structural analysis of the isolated structure. As illustrative example, the results of modal analysis is shown in Fig. 21.37.

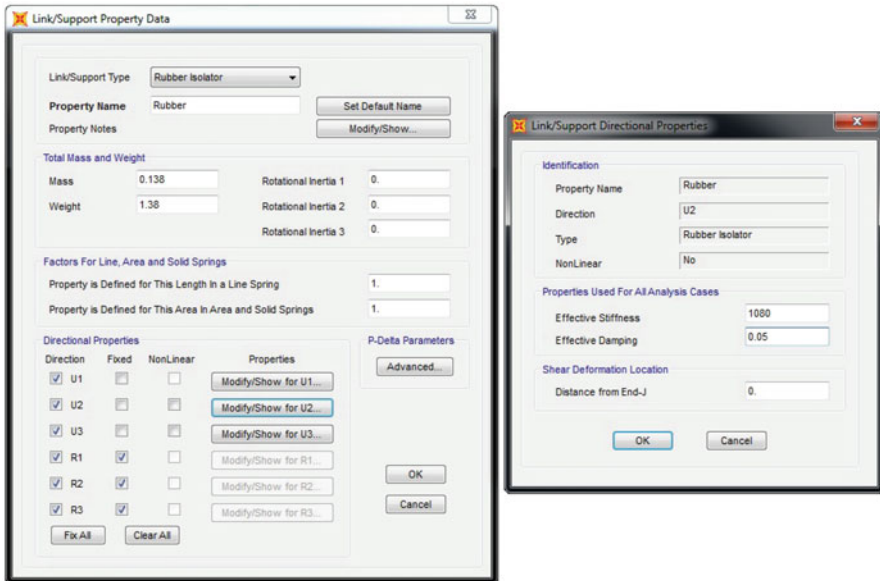


Fig. 21.36 Rubber isolator property definition

It is possible to notice that the first period is equal to 2.787 s which is close to the design period of the isolated structure ($T_{is} = 2.92$ s). The difference in the two periods values is due the use of a rubber isolator having a greater lateral stiffness than the design values K_0 . In addition, the efficiency of the base isolation is confirmed by the comparison between the base displacement and the displacements of the superstructure.

21.5.2 Shear Walls

A shear wall is a structural system composed of panels to counter the effects of lateral load acting on the building. Shear walls are considered as global strengthening retrofitting systems which reduce the lateral deformability with a consequent increment of internal stresses. A retrofitted system is then composed by the frame structure and the shear walls system which guarantee a coupled response to the lateral loads (dual system). In fact, the frame system has a flexural behaviour while the shear wall has a shear behaviour (Fig. 21.38).

Frame systems are usually characterized by large inter-stories drifts in the bottom part of the structure. On the contrary, in the shear wall the large displacement occurs at the top. According to the shear wall response to later loads, the following shear wall types can be identified:

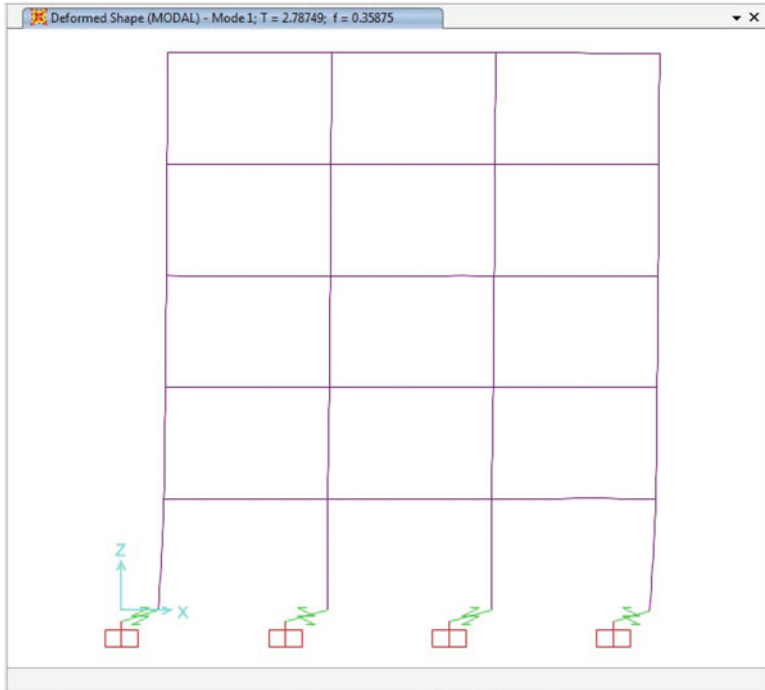


Fig. 21.37 First mode of the isolated structure

- *Ductile wall* : the relative rotation at the base is fixed then the energy is dissipated by a plastic joint at the base.
- *Weakly reinforced walls* : the length is 4 meters at least, or $2/3$ of wall height. This type of walls do not have plastic joints at the base due to the large dimensions.
- *Coupled wall*: a structural element that is made of at least two single walls connected by a ductile beam that reduces the total stress of almost 25%.

The failure mechanism of a shear wall can be summarized as: shear failure (Fig. 21.39a), bending failure (Fig. 21.39b), sliding (Fig. 21.39c), and overturning (Fig. 21.39d).

The design of shear walls system is substantially based on three main rules:

1. The walls must carry at least 50% of the total horizontal forces at each level.
2. The shear walls should be located to reduce the eccentricity between the center of mass and the stiffness centroid at each level.
3. The shear walls have to be mainly located along the building perimeter to increase the torsional inertia of the structure.

According to the last issue, Fig. 21.40 depicts some unstable and stable configurations.

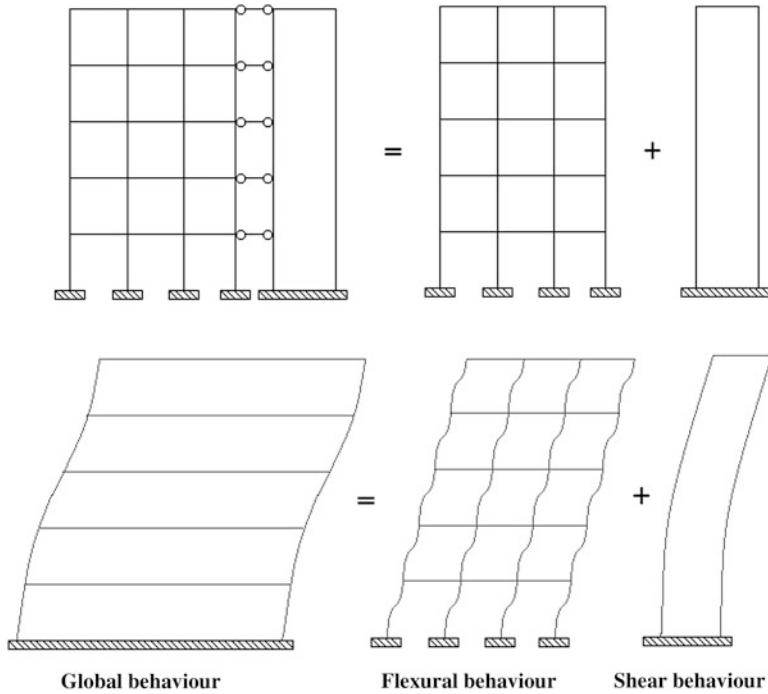


Fig. 21.38 Coupled behaviour of a frame system and shear wall

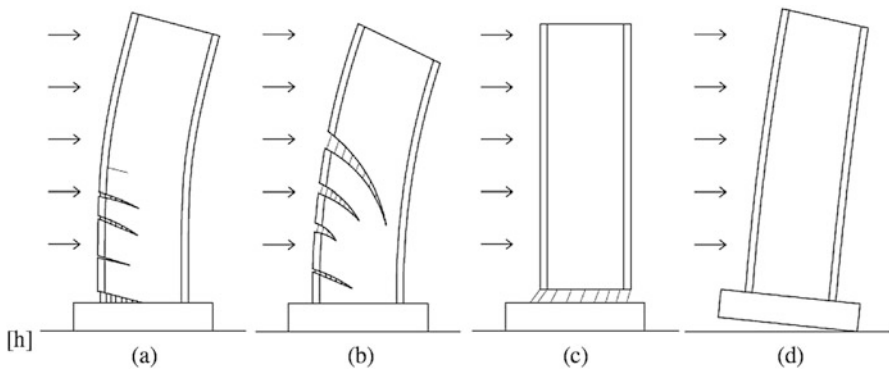


Fig. 21.39 Shear wall failure mechanisms. (a) Bending; (b) Shear; (c) Sliding; (d) Overturning

Shear walls can be integrated in the plan as elevator shafts or stair cases which can significantly increase the lateral stiffness in a multistory buildings. Figure 21.41a shows a configuration where the core is in the center of the plane. This configuration creates no torsional effect in the structure. Unlike in Fig. 21.41b, where the core lies on the perimeter. This can produce torsional effects once

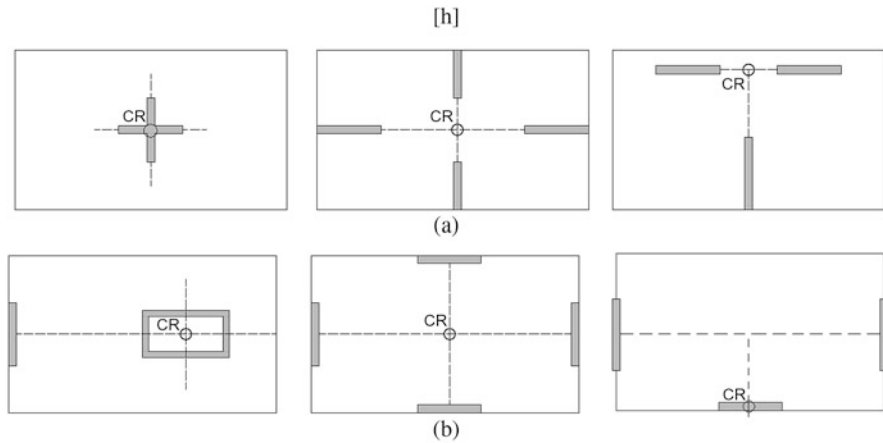


Fig. 21.40 Examples of torsional (a) unstable and (b) stable configurations

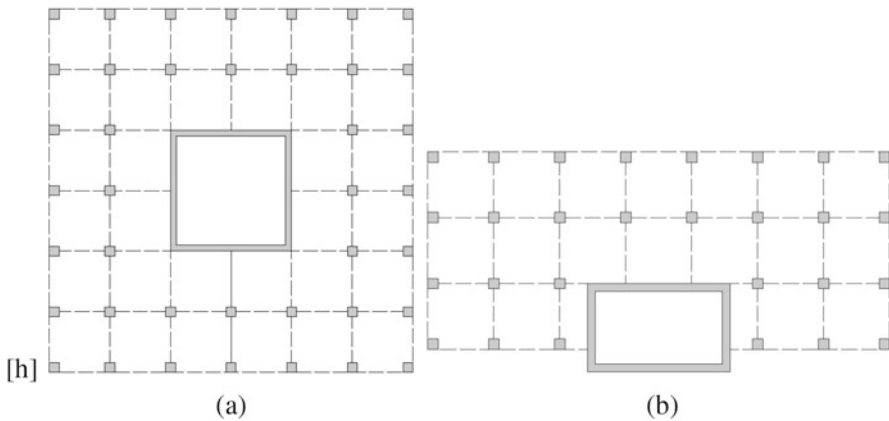


Fig. 21.41 Structural configurations of reinforced concrete core

subjected to lateral force. If the latter is considered, the structure should be balanced with additional walls along the other side to minimize the difference between the center of mass and the center of inertia.

The selection of an adequate shear wall cross section is crucial for the seismic behaviour of the building. Some sections like in Fig. 21.42b, d are optimum for peripheral walls because they provide stability against lateral buckling and improve the confinement of concrete in plastic hinge locations.

Normally, the section of the walls is constant in elevation for medium sized buildings, but for tall buildings the horizontal forces and strength demand decrease in the upper stories, so the section size can be reduced in elevation. Figure 21.43 shows some configurations.



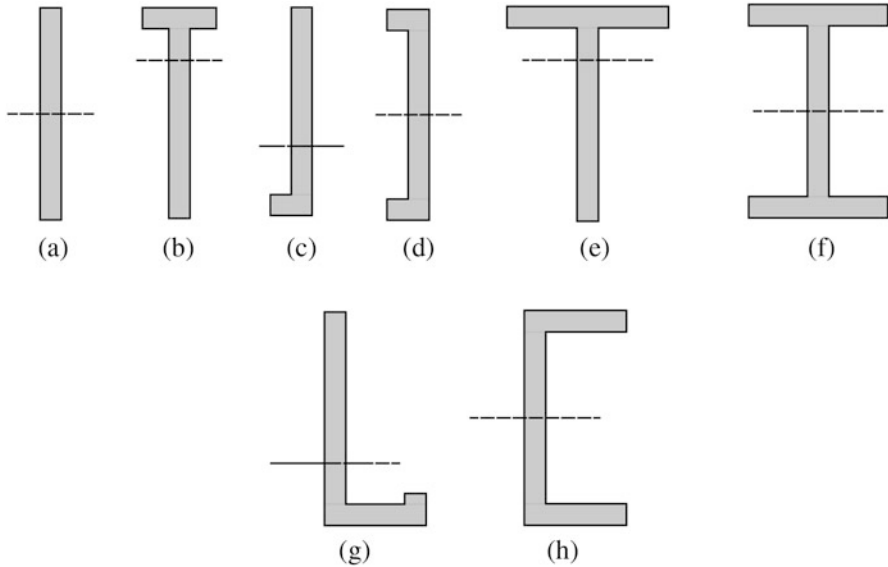


Fig. 21.42 Examples of wall sections



Fig. 21.43 Elevation configuration for shear walls

Another aspect related to the elevation is the presence of openings in the shear walls. In this case, it is crucial to ensure that the flexural strength of the walls meets the demand. Openings can be arranged with the inner edge along a line (Fig. 21.44a), however this configuration is not sufficiently ductile to avoid damage. Another possibility is to allow a diagonal space between the openings (Fig. 21.44b), but in this case a correlated compression and tension field creates diagonal cracks. A better solution is the *coupled wall system* (Figs. 21.44 and 21.45) where the two walls are connected by short and deep beams, which are weaker than the walls. Therefore, the walls behave as cantilevers without openings and beams dissipate energy over the entire height of the structure.

Fig. 21.44 Shear walls with opening

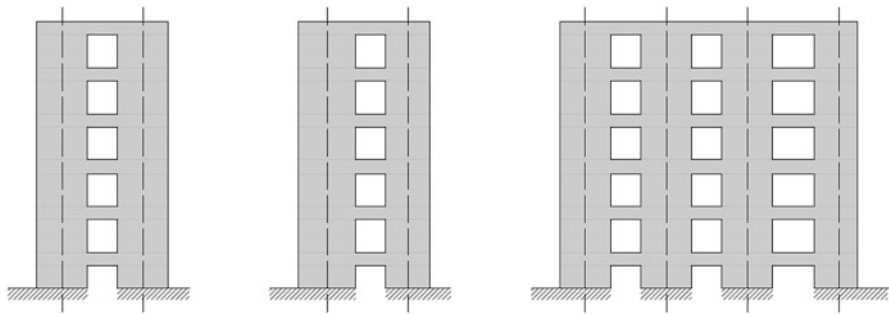
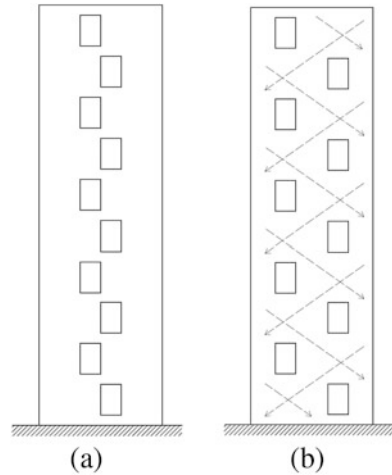


Fig. 21.45 Coupled walls

The definition of the cross section and the location of the shear walls system can be carried out using an iterative procedure. The shear walls dimensions can be preventively defined in order to carry at least 50% of the base shear calculated as expressed by Eq. 21.3.

$$V_b = M \cdot S_a(T_1) \quad (21.3)$$

where V is the base shear, M is the total mass and $S_a(T_1)$ is the spectral acceleration at the fundamental period. For the case study building, four perimeter shear walls are designed with the dimensions showed in Fig. 21.46.

The arrangement of the shear walls allows to have a center of mass coincident with the center of stiffness, neglecting the torsional effects. Furthermore, the calculated base shear is equal to 1567 kN and the associated shear load carried by the walls is almost equal to 70%. The shear walls are better modeled as bidimensional elements in SAP2000. Similarly to the frame element the following sequential

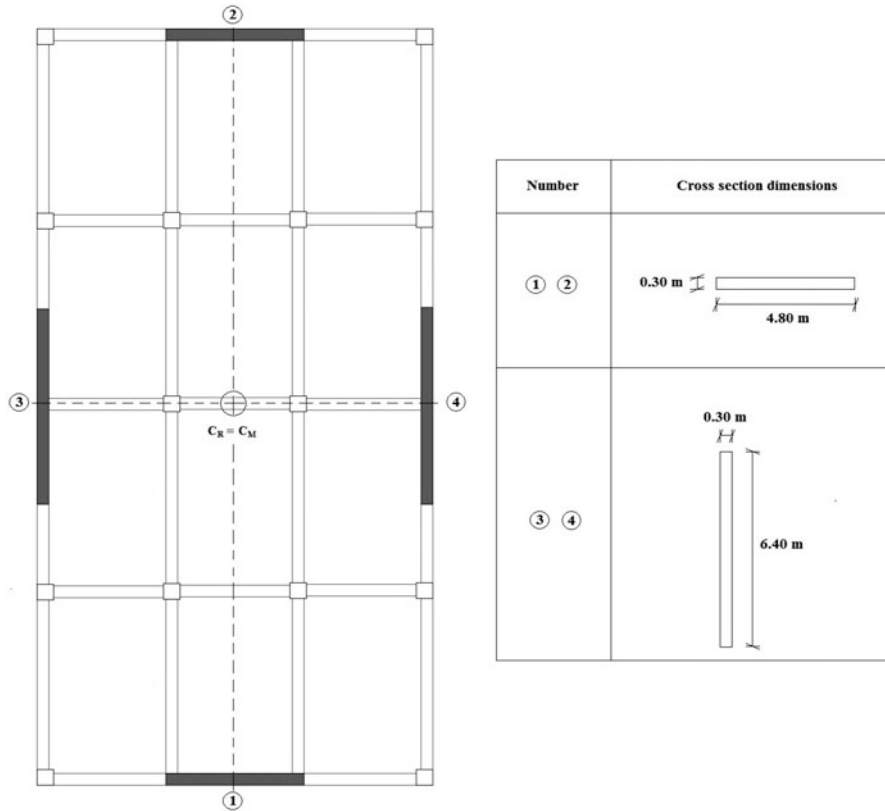


Fig. 21.46 Dimension and geometrical arrangement of the shear walls

commands are used to define the shell element: *Define* → *Section Properties* → *Area Sections* → *Shell*. In the new dialog box the geometrical characteristics can be assigned (Fig. 21.47).

It is also important to define new joints which are intended to model the connections between the shear walls (shell elements) and the frame system (frame elements). SAP2000 recommends that when the frame is in the 1–2 local plane of the shell, the frame has to be modeled such that it extends the length of the shell object and connects to the two shell joints. All forces but shear (axial, torsion, and moments) should be released at the far end of the frame object. Similarly, when the frame is normal to the 1–2 local plane of the shell, a small frame element has to be modeled within the plane of the shell, and release the moment at the far end of the frame object. Figure 21.48 illustrates an extrude view of the case study building retrofitted with shear walls and the results of the modal analysis.

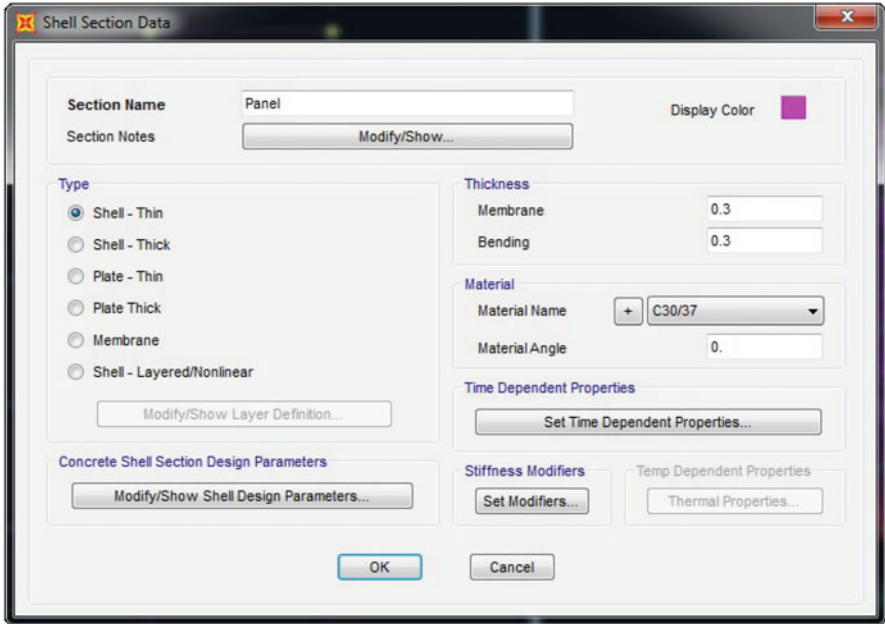


Fig. 21.47 Shear wall section geometry definition

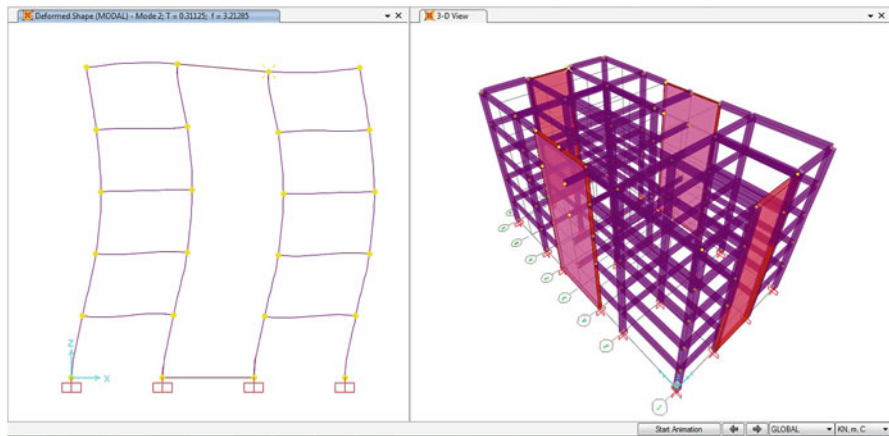


Fig. 21.48 Area section properties (a) and 3D extruded view (b)

21.5.3 Effects of the External Walls

The external walls located along the perimeter of the building have a lateral strengthening effects. Furthermore, the presence of the external walls increase the global dissipative capacity of the structure. The effects of the infill walls and the

Fig. 21.49 Compressed diagonal element model

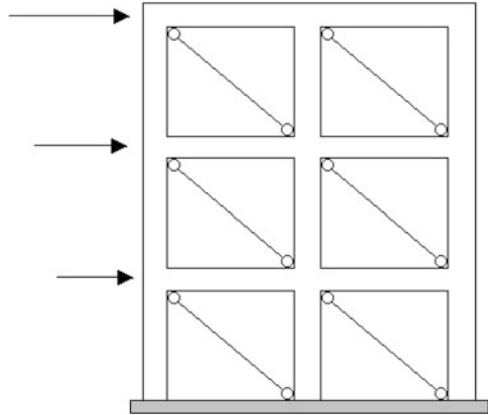
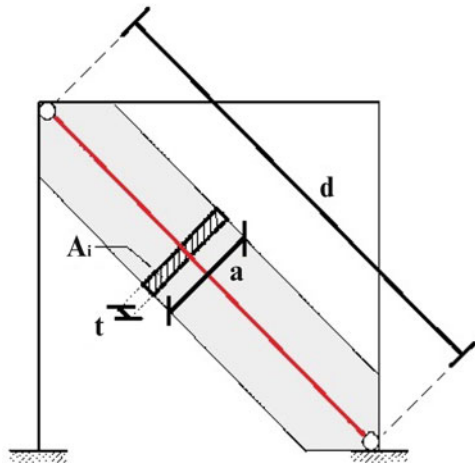


Fig. 21.50 Geometrical characterization of a diagonal element



analytical models which take into account the increase of lateral stiffness and strength have been explained in detail. In this section, the SAP2000 modeling of the external walls is explained. The equivalent compressed element model is among the most used simplified macro-models which simulate the behaviour of the external walls within a frame system. The response of the wall to lateral load is modeled through a diagonal compressed elements (Fig. 21.49).

The diagonal element is characterized by its length (d) and cross section ($A_i = ts$). Figure 21.50 illustrates the geometry of the diagonal element.

Different methods have been proposed for evaluating the equivalent stiffness and geometry of the diagonal element. In this section, the Al-Chaar et al. (2002) method is considered to assess the geometry, while the EN-1996 (2009) is assumed for evaluating the equivalent stiffness for each diagonal element for both horizontal directions. The diagonal element width is determined by evaluating the equivalent

Table 21.1 Geometrical and mechanical characteristics of the diagonal elements in X direction

$E_{m,eq}$ [MPa]	θ_2	λ_2	a_2 [m]	$a_{2,RED}$ [m]
1973	0.60	2.61	0.52	0.25

Table 21.2 Geometrical and mechanical characteristics of the diagonal elements in Y direction

$E_{m,eq}$ [MPa]	θ_1	λ_1	a_1 [m]	$a_{1,RED}$ [m]
1973	0.46	2.42	0.53	0.26

lateral rigidity (Smith and Carter 1969) and a distribution of opening equal to 20% is considered in the case study (Tables 21.1 and 21.2).

In SAP2000, the diagonal compressed elements are modeled through the *Gap Link* element which works in compression only (*Define* → *Section Properties* → *Link/Support Properties*). In order to take into account also the nonlinear behaviour of the wall, a *MultiLinear Plastic* element can be used. In this case, the force-displacement relationship can be set in SAP2000. For the case study, a gap element is assumed with the equivalent elastic modulus previously calculated. Figure 21.51 illustrates a 2D view of the SAP2000 model with the gap elements.

Due to the bidirectionality of the seismic excitation, the gap elements must be located in both diagonal directions of the walls.

21.6 Comparisons of the Structural Models

The efficiency of a seismic retrofit techniques can be compared in SAP2000 in terms of story displacements and modes. Thus, the following models listed below have been compared:

1. Regular structure;
2. Structure with base isolation system;
3. Structure with shear walls;
4. Regular structure considering the effects of the external walls.

For each model, the envelope of the 8 seismic combinations are considered and the results of the linear dynamic analysis (Fig. 21.52).

It is possible to observe how in the structure with base isolation system the story displacements assume low values, while the absolute displacement at the base is equal to 0.225 m. This leads to verify the selected isolators previously discussed which presented a maximum allowable displacement of 0.25 m. The ratio between the base and the top displacement is almost equal to 76%. This result remarks the efficiency of the base isolation system. The building retrofitted with shear walls presents the smallest story displacements. This result is in compliance with the concept of global strengthening system which characterizes the active seismic

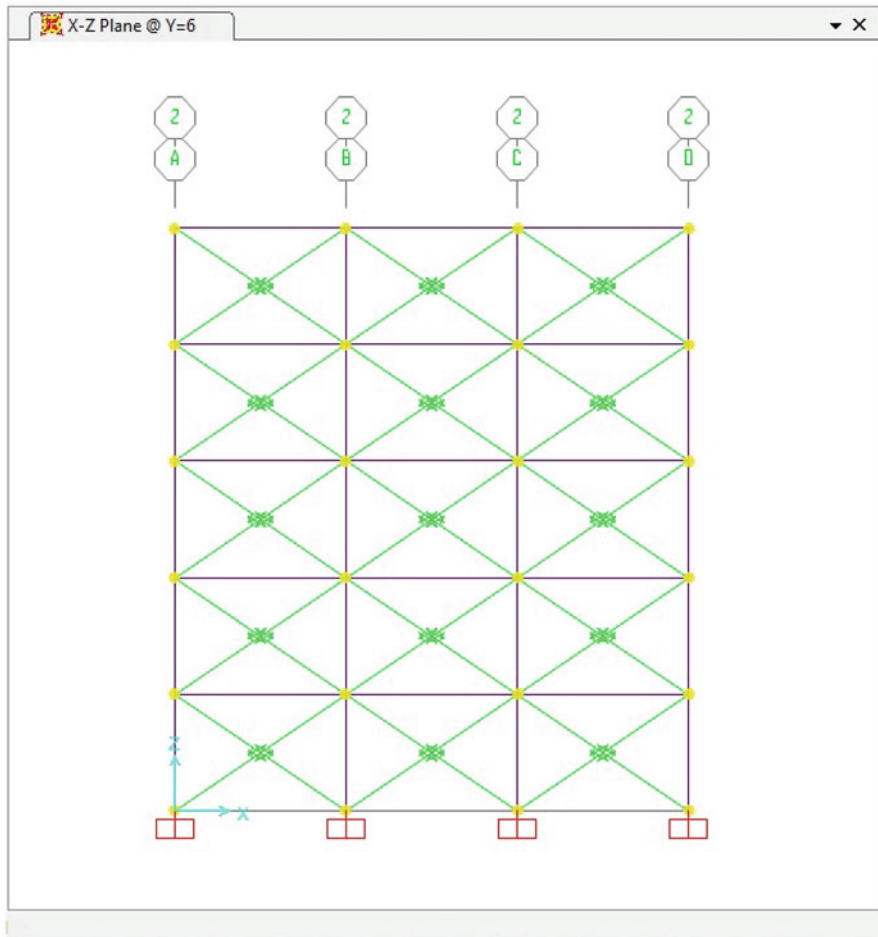


Fig. 21.51 2D view of SAP2000 model with gap elements

retrofitting methods. Furthermore, the presence of external walls provides a limited global strengthening of the building such that the inter-story drifts are less than the regular building ones. These differences in terms of displacements are more relevant in the upper stories. On the other hand, when the structure is flexible and the lateral displacements assume considerable values, the seismic action carried by the structures decreases. Figure 21.53 depicts a comparison in terms of base shear the four structural models considered.

It is possible to observe a substantial increment of stiffness and strength due to the presence of shear walls. On the contrary, the base shear of the isolated structure assumes lower values that ensures an elastic behaviour of the superstructure. In addition, the modal results are investigated for the first three modes in terms of periods and mass ratios (Table 21.3).

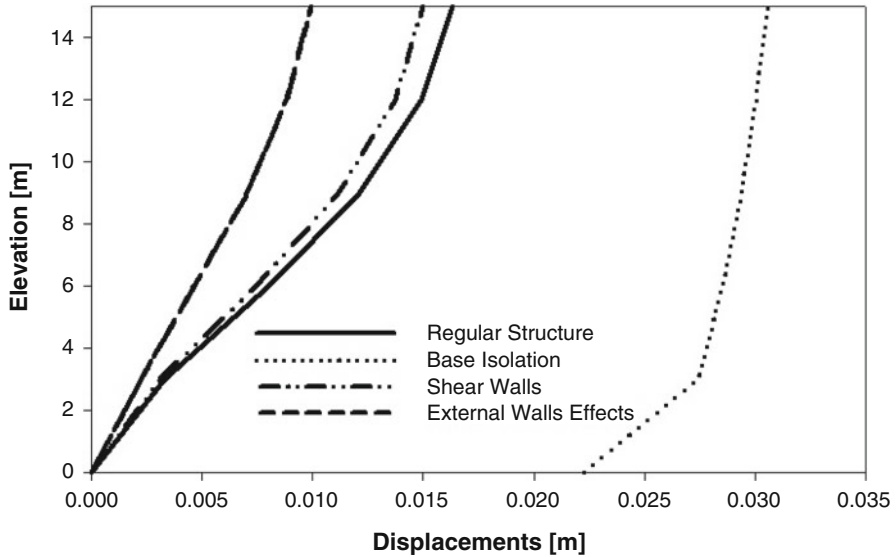
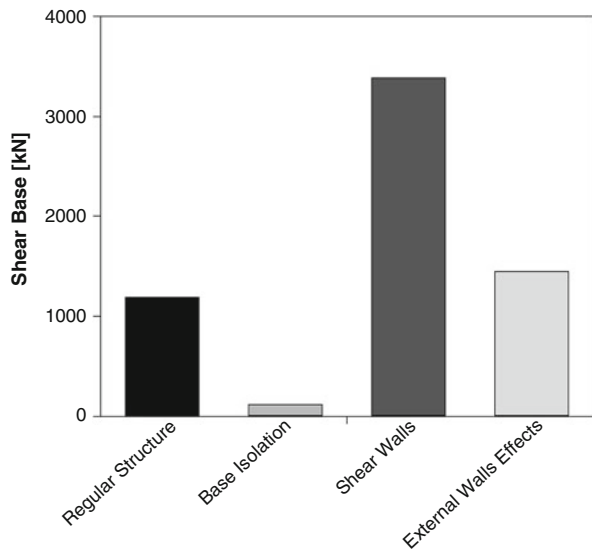


Fig. 21.52 Story displacements of the four analyzed structural models

Fig. 21.53 Base shear of the four analyzed structural models



Regarding the first modes, the most flexible system is the base isolated structure ($T = 2.78$ s) while in the other systems (e.g., shear walls and external walls models) the lateral stiffness and strength is larger and causes a reduction of the fundamental periods. The presence of the external walls in the model does not reduce the period significantly such as in the shear walls where the reduction of the period is of 62%. In all the cases the first two modes are mainly translational, while the third

Table 21.3 Modal information

Model	Mode	Period [s]	U_x	U_y	R_z
Regular structure	1	0.626	0.000	0.828	0.000
	2	0.592	0.807	0.000	0.026
	3	0.547	0.025	0.000	0.807
External walls effects	1	0.568	0.000	0.834	0.000
	2	0.559	0.828	0.000	0.007
	3	0.487	0.007	0.000	0.834
Base isolation	1	2.787	0.968	0.021	0.009
	2	2.777	0.021	0.978	0.000
	3	2.380	0.009	0.001	0.989
Shear walls	1	0.385	0.891	0.000	0.000
	2	0.226	0.000	0.686	0.001
	3	0.206	0.001	0.002	0.742

ones are torsional. When the first two modes of the shear walls model are mainly translational with considerable mass ratios, the location and the design of the shear walls is efficient and accurate. In the case study, the first two modes have a mass ratios of 89% and 69%, respectively.

References

- Al-Chaar G, Issa M, Sweeney S (2002) Behavior of masonry-infilled nonductile reinforced concrete frames. *J Struct Eng* 128(8):1055–1063
- Bathe KJ, Wilson EL (1976) Numerical methods in finite element analysis, vol 197. Prentice-Hall, Englewood Cliffs
- CSI SV (2010) Integrated finite element analysis and design of structures basic analysis reference manual. Computers and Structures Inc., Berkeley
- Deierlein GG, Reinhorn AM, Willford MR (2010) Nonlinear structural analysis for seismic design. NEHRP Seism Des Tech Brief 4:1–36
- EN B (2005) 10080–steel for the reinforcement of concrete–weldable reinforcing steel–general. Central Secretariat, Brussels
- EN-1996 (2009) General rules for reinforced and unreinforced masonry. European committee for standardization
- FEMA356 (2000) Prestandard commentary for the seismic rehabilitation of buildings. FEMA-356, Federal Emergency Management Agency, Washington, DC
- FEMA (2012) Fema p-58-1: seismic performance assessment of buildings. Volume 1–methodology
- Institution BS (2004) Eurocode 2: design of concrete structures: part 1–1: general rules and rules for buildings. British Standards Institution
- Ireland M, Pampanin S, Bull D (2006) Concept and implementation of a selective weakening approach for the seismic retrofit of RC buildings
- Moehle JP (2000) State of research on seismic retrofit of concrete building structures in the us. In: US-Japan symposium and workshop on seismic retrofit of concrete structures

- Narasimhan H, Faber MH (2010) Categorisation and assessment of robustness related provisions in European standards. In: Proceedings of the joint workshop of COST actions TU0601 and E, vol 55
- NTC-08 (2008) Nuove Norme Tecniche per le Costruzioni. Gazzetta Ufficiale della Repubblica Italiana
- Reitherman RK (2012) Earthquakes and engineers: an international history. American Society of Civil Engineers
- Smith BS, Carter C (1969) A method of analysis for infilled frames. Proc Inst Civ Eng 44(1):31–48
- UNI E (2006) 206-1:2006. Calcestruzzo-Specificazione, prestazione, produzione e conformità
- Viti S, Cimellaro G, Reinhorn AM (2006) Retrofit of a hospital through strength reduction and enhanced damping. Smart Struct Syst Int J 2(4):339–355
- Yang YB, Chang KC, Yau JD (2003) Base isolation. Earthquake engineering handbook. CRC Press LCC, Washington, DC

Appendix A

Fundamentals of Probability and Statistics

A.1 Important Definitions

In the terminology of set theory, the set of all possibilities in a probabilistic problem is collectively a sample space, and each of the individual possibilities is a sample point. An event is then defined as a subset of the sample space (Fig. A.1).

- *Impossible event*: denoted \emptyset , is the event with no sample point;
- *Certain event*: denoted S , is the event containing all the sample points in a sample space, it is the sample space itself;
- *Complementary event \bar{E}* : of an event E contains all the sample points in S that are not in E .

A.2 The Venn Diagram

A sample space and its subsets (or events) can be represented pictorially with a Venn diagram. In many practical problems, the event of interest may be a combination of several other events; there are only two ways that events may be combined: *the union* or *intersection* (Fig. A.2).

A.3 Mathematics of Probability

The theory of probability is based on certain fundamental assumptions, or axioms, that are not subject to proofs; these are as follows:

Fig. A.1 A Venn diagram of sample space S

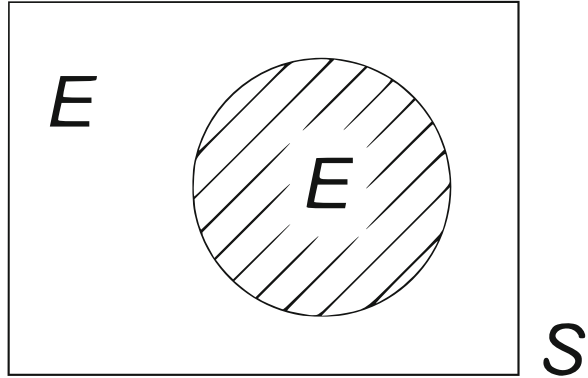
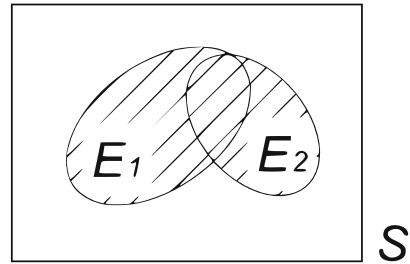


Fig. A.2 Venn diagram for $E_1 \cup E_2$



- **Axiom 1:** For every event E in a sample space S , there is a probability

$$P(E) \geq 0 \quad (\text{A.1})$$

- **Axiom 2:** The probability of the certain event S is

$$P(S) = 1.0 \quad (\text{A.2})$$

- **Axiom 3:** Finally, for two events E_1 and E_2 that are mutually exclusive (if the occurrence of one precludes the occurrence of the other event)

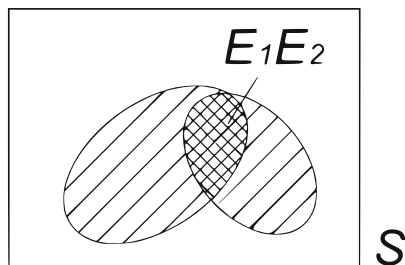
$$P(E_1 \cup E_2) = P(E_1) + P(E_2) \quad \text{Addition Rule} \quad (\text{A.3})$$

These equations constitute the basic axioms of probability theory, are essential assumptions and, therefore, cannot be violated (Fig. A.3).

A.4 Conditional Probability

There are occasions in which the probability of an event may depend on the occurrence (or nonoccurrence) of another event. If this dependence exists, the relevant probability is a *conditional probability*. For this purpose, we shall use the notation:

Fig. A.3 Venn diagram for $E_1 \cap E_2$



$P(E_1 | E_2)$ = the probability of E_1 assuming the occurrence of E_2 , or simply the probability of E_1 given E_2 .

The conditional probability $P(E_1 | E_2)$ may be interpreted as the likelihood of realizing a sample point of E_1 that is in E_2 ; hence the appropriate normalization, we obtain the conditional probability

$$P(E_1 | E_2) = \frac{P(E_1 \cap E_2)}{P(E_2)} \quad \text{Multiplication Rule} \quad (A.4)$$

A.5 The Theorem of Total Probability

On occasion, the probability of an event, say A , cannot be determined directly; its occurrence will depend on the occurrence or non occurrence of other events such as $E_i = 1, 2, \dots, n$ and the probability of A will depend on which of the E_i 's has occurred. On such an occasion, the probability of A would be composed of the conditional probabilities (conditioned on each of the E_i 's) and weighted by the respective probabilities of the E_i 's. Such problems require the theorem of total probability.

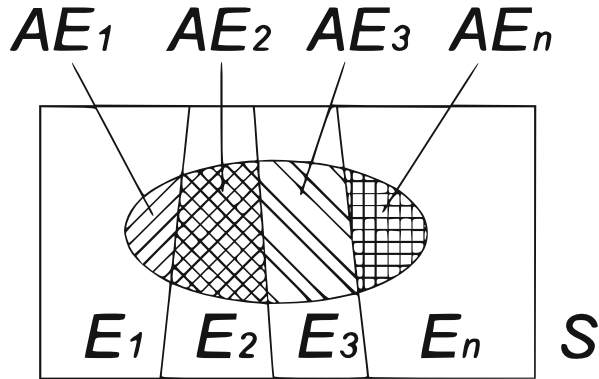
Formally, consider n events that are mutually exclusive and collectively exhaustive, namely E_1, E_2, \dots, E_n . That is, $E_1 \cup E_2 \cup \dots \cup E_n = S$. Then if A is an event in the same sample space S as shown in Fig. A.4, we derive the theorem of total probability as follows:

$$\begin{aligned} A &= AS \\ A &= A(E_1 \cup E_2 \cup \dots \cup E_n) \\ A &= AE_1 \cup AE_2 \cup \dots \cup AE_n \end{aligned} \quad (A.5)$$

Then

$$P(A) = P(AE_1) + P(AE_2) + \dots + P(AE_n)$$

Fig. A.4 Intersection of A and E_1, E_2, \dots, E_n in sample space S



And by virtue of the multiplication rule, we obtain the theorem of total probability as

$$P(A) = P(A | E_1)P(E_1) + P(A | E_2)P(E_2) + \dots + P(A | E_n)P(E_n) \tag{A.6}$$

A.6 Probability Distribution of a Random Variable

A random variable is a mathematical vehicle for representing an event in analytical form. In contrast to a deterministic variable that can assume a definite value, the value of a random variable may be defined within a range of possible values. If X is defined as a random variable, then $X = x$, or $X < x$, or $X > x$, represents an event, where $(a < x < b)$ is the range of possible values of X.

As the values of a random variable represent events, the numerical values of the random variable are associated with specific probability. These probability measures may be assigned according to prescribed a probability law that is called *probability distribution function* (PDF). If X is a random variable, its probability distribution can always be described by its *cumulative distribution function* (CDF) (Fig. A.5).

A random variable may be discrete, continuous or mixed. X is a discrete random variable if only discrete values of x have positive probabilities; X is a continuous random variable if probability measures are defined for all values of x; X is a mixed random variable if probability distribution is a combination of probabilities at discrete values of x as well as over a range of continuous values of x.

In the case of a continuous distribution, cumulative distribution function gives the area under the probability density function from minus infinity to x,

$$F(x) = P(X \leq x) = \int_{-\infty}^x f(t)dt \quad \text{Cumulative distribution function} \tag{A.7}$$



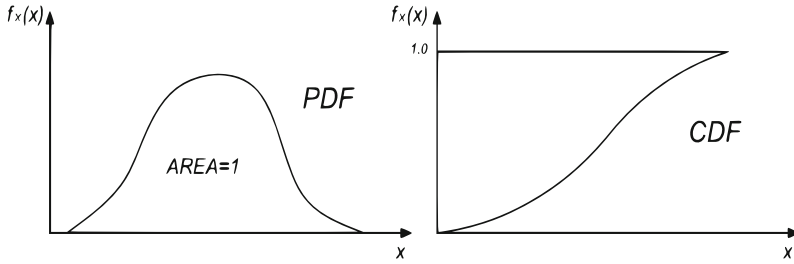


Fig. A.5 Probability distribution function and cumulative distribution function

A.7 Useful Probability Distributions

The best known and most used probability distribution is undoubtedly the Gaussian distribution also known as the normal distribution (Fig. A.6). Its PDF for a continuous random variable X, is given by

$$f_x(x) = \frac{1}{\sigma\sqrt{2\pi}} \exp\left[-\frac{1}{2}\left(\frac{x-\mu}{\sigma}\right)^2\right] \quad -\infty < x < +\infty \quad (\text{A.8})$$

where (in case of continuous random variable)

$$\mu = E(x) = \int_{-\infty}^{\infty} xf_x(x)dx \quad \text{Mean Value} \quad (\text{A.9})$$

$$\text{Var}(X) = \int_{-\infty}^{\infty} (x-\mu)^2 f_x(x)dx \quad \text{Variance of X} \quad (\text{A.10})$$

$$\sigma = \sqrt{\text{Var}(X)} \quad \text{Standard deviation} \quad (\text{A.11})$$

$$P(a < x \leq b) = \frac{1}{\sigma\sqrt{2\pi}} \int_b^a \exp\left[-\frac{1}{2}\left(\frac{x-\mu}{\sigma}\right)^2\right] dx \quad (\text{A.12})$$

The logarithmic normal or simply lognormal distribution is also a popular probability distribution (Fig. A.7). Its PDF is

$$f_x(x) = \frac{1}{\sqrt{2\pi}(\zeta x)} \exp\left[-\frac{1}{2}\left(\frac{\ln x - \lambda}{\zeta}\right)^2\right] \quad x \geq 0 \quad (\text{A.13})$$



Fig. A.6 The Gaussian distribution

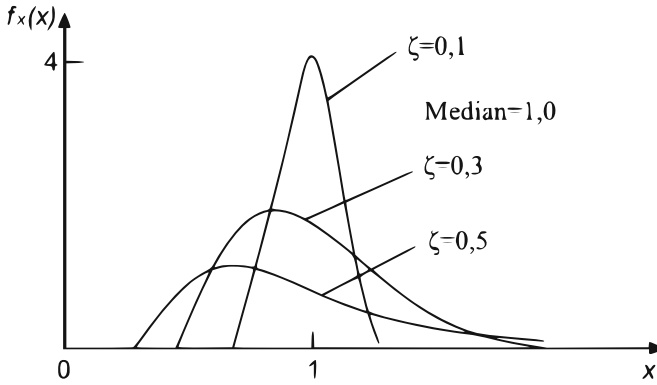
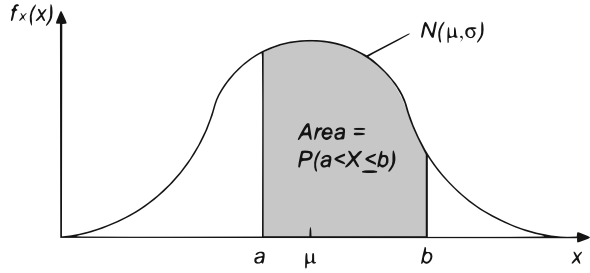


Fig. A.7 The lognormal PDFs for various values of ζ

where

$$\lambda = E(\ln X) \text{ Mean value} \tag{A.14}$$

$$\zeta = \sqrt{\text{Var}(\ln X)} \text{ Standard deviation} \tag{A.15}$$

$$P(a < X \leq b) = \frac{1}{\sqrt{2\pi}(\zeta x)} \int_b^a \exp \left[-\frac{1}{2} \left(\frac{\ln x - \lambda}{\zeta} \right)^2 \right] dx \tag{A.16}$$

A.8 Multiple Random Variables

The essential concepts of a random variable and its probability distribution can be extended to two or more random variables and their joint probability distribution. In order to identify events that are the results of two or more physical processes in numerical terms, the events in a sample space may be mapped into two (or more) dimensions of the real space; implicitly, we can recognize that this requires two or more random variables (Fig. A.8).

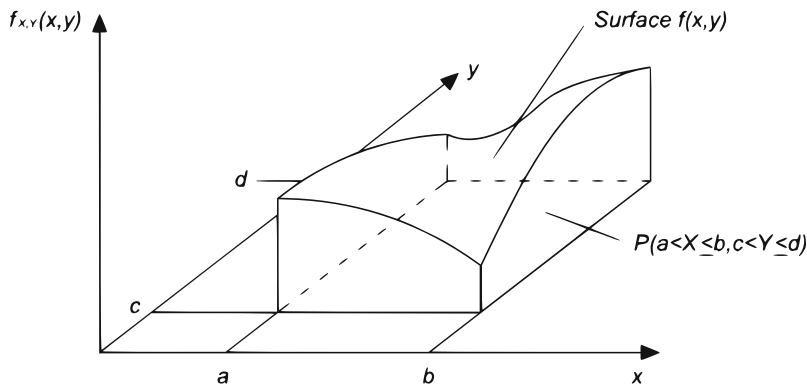


Fig. A.8 Volume under the PDF $f_{X,Y}(x,y)$

As any pair of values of the random variables X and Y represent events, there are probabilities associated with given values of x and y; if the random variables X and Y are continuous, the joint probability distribution may also be described with the joint PDF, $f_{X,Y}(x,y)$ that graphically is a surface

$$f_{X,Y}(x,y)dx dy = P(x < X \leq x + dx, y < Y \leq y + dy) \quad \text{Joint PDF} \quad (A.17)$$

Then

$$F_{X,Y}(x,y) = \int_{-\infty}^x \int_{-\infty}^y f_{X,Y}(u,v)dv du \quad \text{Joint CDF} \quad (A.18)$$

We observe the following probability

$$P(a < X \leq b, c < Y \leq d) = \int_a^b \int_c^d f_{X,Y}(u,v)dv du \quad (A.19)$$

Which is the volume under the PDF $f_{X,Y}(x,y)$

A.9 The Conditional and Marginal Distributions

For continuous X and Y, the conditional PDF of given Y is

$$f_{X|Y}(x|y) = \frac{f_{X,Y}(x,y)}{f_Y(y)} \quad (A.20)$$

From which we have

$$f_{X,Y}(x, y) = f_{X|Y}(x|y) f_Y(y) \text{ or } f_{X,Y}(x, y) = f_{Y|X}(x|y) f_X(y) \quad (\text{A.21})$$

Finally, through the theorem of total probability, we obtain the marginal PDFs

$$f_X(x) = \int_{-\infty}^{\infty} f_{X|Y}(x|y) f_Y(y) dy = \int_{-\infty}^{\infty} f_{X,Y}(x, y) dy \quad (\text{A.22})$$

This is called marginal density function and can be deduced from the probability density associated with, in a general case, the random variables X_1, \dots, X_n by integrating on all values of the $n - 1$ other variables.

In the probabilistic approach, it can be used to calculate the expected value of the resilience index considered a random variable dependent by other random variables.

Glossary

- ASD** Allowable-Stress Design method
- CM** center of mass
- CLS** Collapse Prevention Limit State
- CQC** complete quadratic combination
- DOF** degree of freedom
- DFT** discrete Fourier transform
- EC** Eurocode 8
- FFT** fast Fourier transform
- GMPE** ground motion prediction equation
- hazard** Conditions that increase the probability of loss
- HFM** Half-Power Method
- LSD** Limit State Design Method
- LDA** Logarithmic Decrement Analysis
- NDP** nonlinear dynamic procedures
- OLS** Operational Limit State
- resilience** is the ability [of a system] to cope with change
- RHA** response history analysis

RSA response spectrum analysis

SLS Serviceability Limit State

SDF single-degree-of-freedom

SRSS square root of the sum of the square

ULS Ultimate Limit State

Index

Symbol

3D MDOF system, 150

A

accuracy, 69

active TMD, 431

analytical methods, 57

Approximated solution, 181

Argand-Gauss plane, 24, 37

Arias Intensity, 225

artificial seismic records, 301

artificial time-history selection, 317

assembled system, 188

Attenuation Relationship, 214

Avezzano, Abruzzo, 232

B

band-eliminate filter, 222

band-pass filter, 222

Beam-column joint, 363

beam-column joints model, 545

beats phenomenon, 32

Belice, Sicily, 238

bending type, 99

bending type model, 545

body wave magnitude, 205

box-like behavior, 480

Butterworth filter, 223

C

Capacity Design, 355

Capacity Design of a multi-story building, 356

Central difference method, 82

Characteristics of base isolation system, 452

Classification of interventions, 513

classification of masonry, 478

comparison of the structural models, 579

condensation method, 107

Conditional mean spectrum, 296

constraint, 540

convection currents, 196

coupled wall, 571

CQC, 146

Crisafulli, 382

critical damping system, 24

D

damped systems, 20

damping, 10

damping energy, 161, 163

damping estimation, 164

damping matrix, 102, 106

degrees of freedom, 4

design approach by codes, 359

Design of beams, 360

Design of columns, 360

Design Response spectrum, 288

diatoms, 480

dip slip movement, 207

distributed mass, 173

double concave friction pendulum, 463

DSHA, 252

ductile wall, 571

ductility factor, 166

Duhamel's integral, 63
 duration, 226
 dynamic amplification function, 35, 43

E

earthquake genesis, 193
 earthquake response, 50
 EERA, 323
 elastic rebound theory, 199
 Elastic Response Spectra, 283
 Electromagnetic variations, 268
 energetic method, 316
 Energy balance equation, 161
 epicentral distance, 206
 equal acceleration criterion, 172
 equal displacement criterion, 171
 equal energy criterion, 171
 equations of motion, 13
 equivalent viscous damping, 12
 equivalent viscous damping ratio, 11
 ESMD, 323
 Example of a System with distributed mass and elasticity, 182
 example of kinematic equilibrium method, 508
 Explicit methods, 70
 external walls, 577

F

failure modes, 371
 Fast Fourier Transform (FFT), 218
 fault, 198
 fault-distance, 206
 Filter, 223
 Finite differences method, 70
 First Isolator, 443
 foundation, 515
 Fourier analysis, 216
 Fourier series, 65
 free vibrations, 15, 17, 118
 frequency ratio, 29
 friction pendulum system, 461

G

Garfagnana, Tuscany, 235
 gaussian distribution, 590
 generalized SDOF systems, 179
 GMPE, 214
 ground motion databases, 304
 Gutenberg-Richter law, 206

H

half-power method, 166
 Half-Power Method (HPM), 166
 harmonic excitation, 131
 harmonic excitations, 28
 HDRB, 454
 High-damping rubber bearing, 454
 Hokkaido, Japan, 249
 Hoops, 516, 527
 hypocentral distance, 207

I

Idealization of the structures, 3
 In-plane failure mechanisms of a multi-story masonry building, 489
 In-plane failure mechanisms of a single-story building, 484
 influence coefficient matrix, 143
 injections, 519
 input energy, 26
 introduction, 355
 Irpinia, Campania e Basilicata, 233
 isolated period, 472
 ITACA, 311, 323

K

kinetic energy, 161
 Kuril Islands, Russia, 247

L

Lâquila, Abruzzo, 239
 lagrangian approach, 179
 lead rubber bearing, 460
 Linear dynamic analysis, 336
 linear dynamic analysis, 552
 Linear static analysis, 334
 linear static analysis, 550
 load analysis, 535
 load cases, 539
 local magnitude, 203
 Logarithmic Decrement Analysis, 164
 Logarithmic Decrement Analysis (LDA), 164
 lognormal distribution, 589
 Love waves, 211
 lumped mass, 186

M

masonry, 476
 masonry collapse mechanisms, 480

mass, 9
 mass matrix, 103, 106
 materials, 534
 materials definition, 547
 mean value, 589
 mechanisms of failure, 371
 Mercalli-Cancani-Sieberg scale, 203
 Messina and Rreggio Calabria, 230
 modal analysis, 109
 modal coordinate, 116
 modal participation factor, 144
 Modern retrofit interventions, 511
 modes of vibration, 115
 modified Newton-Raphson method, 85
 moment magnitude, 203

N

natural frequencies, 114
 neo-deterministic seismic hazard analysis, 271
 Newmark Method, 83
 Newmark method, 75
 Newton Raphson Method, 85
 Nicastro, Calabria, 231
 nonlinear dynamic analysis, 350
 nonlinear static analysis, 557
 nonlinear system, 54
 normal fault, 207
 Northern Sumatra, Indonesia, 242, 244
 Nyquist frequency, 220

O

Offshore Maule, Chile, 243
 opensignal, 309
 Out-of-plane failure mechanisms of a multi-story masonry building, 504
 Out-of-plane failure mechanisms of a single-story masonry building, 491
 over strength factor, 167
 overdamped system, 25

P

P-waves, 210
 Partial overturning, 505
 Peak Ground Acceleration (PGA), 216
 Peak Ground Displacement (PGD), 216
 Peak Ground Velocity (PGV), 216
 PEER, 323
 periodic excitation, 49
 Peru, 248
 plastic energy, 162, 166
 plate tectonics, 193

Poisson process, 256
 Predicted Mean Spectrum, 326
 Prediction methods, 265
 Prince William Sound, Alaska, 241
 PSHA, 256
 pushover, 337, 557

R

radon emission, 267
 Rat Islands, Alaska, 245
 Rayleigh damping, 126
 Rayleigh waves, 211
 real time history selection, 315
 reduction of DOF, 107
 reinforced injections, 520
 reinforced plasters, 526
 relative stiffness, 370
 resonance, 30
 Restrains, 540
 return period, 255
 reverse fault, 208
 rigid body, 540
 rigid diaphragm, 541
 Runge-Kutta method, 71, 91

S

S-waves, 210
 Safety assessment, 536
 SAP2000, 536
 SDOF Systems, 17
 sections definition, 548
 seismic action, 550
 seismic isolated structures, 565, 566
 seismic isolation systems, 453
 seismic moment, 204
 Seismic Records Selection, 315
 seismograph, 201
 shear failure, 489
 shear type, 104
 shear type model, 544
 shear walls, 570
 signal processing, 312
 simple overturning, 504
 Single period matching, 321
 Site Response Analysis, 320
 Southern Sumatra, Indonesia, 246
 spreading ridges, 196
 SRSS, 145
 stability, 69
 Stafford Smith and Coull, 387
 Stafford-Smith and Carter, 378
 standard deviation, 589

stiffness, 7
 stiffness matrix, 99, 104
 stiffness methods, 377
 strength reduction factor, 167
 strike slip, 197
 Strong motion databases, 311
 structural analysis, 533
 structural idealization, 534
 subduction zone, 198
 surface wave magnitude, 205
 Synthetic seismic records, 303
 synthetic time-history selection, 317

T

Theorem of Total Probability, 587
 tie bars, 515
 time histories, 298
 time step, 69
 Tolmezzo, Friuli Venezia Giulia, 237
 Top ring beams, 517
 Traditional retrofit interventions, 511
 transfer function, 222
 Transmissibility function, 51
 transmissibility function, 53

trust fault, 208
 Tuned Mass Damper, 421
 type of masonry, 481

U

undamped systems, 18, 28
 Underdamped system, 22
 Uniform Hazard Spectrum, 285

V

Valdivia, Chile, 240
 variance, 589
 Venn diagram, 585
 vertical load, 549
 viscous, 407
 viscous wall, 411
 viscously damped systems, 32, 139

W

waveform and spectral matching, 315
 weakly reinforced wall, 571
 wythe, 476